

Table of Contents	Page
Foreword	iii
Abstract	v
Outputs of this work	vii
<i>List of Publications</i>	vii
<i>List of conference presentations</i>	viii
Table of Contents	ix
List of Figures	xiv
List of Tables	xx
List of Acronyms	xxii
Chapter 1. Introduction	1
The phenomenology of an atom in a molecule	1
On the nature of chemical bonding	3
Theoretical descriptions of atoms in molecules	4
Problem statement	6
Aims and general approach	9
Overview of this thesis	9
A note on the historical development of FALDI	13
References	14
Chapter 2. Theoretical Background and Developments.	17
<i>Theoretical Background</i>	
The electron density	18
The pair density and electron holes	19
The Quantum Theory of Atoms in Molecules	23
QTAIM atomic overlap matrices, localization and delocalization indices	26
Domain Averaged Fermi Holes	28
 <i>Novel Theoretical Developments</i>	
The FALDI density decomposition scheme	31
FALDI localized and delocalized natural density functions	34
FALDI exclusive localization and delocalization indices	36
Local bonding, nonbonding and antibonding classification scheme of	
FALDI components	42
FALDI decomposition of the gradient of the total ED	44
FALDI deformation densities	46
 <i>References</i>	51

Chapter 3. Exact and Exclusive Electron Localization Indices within QTAIM Atomic Basins	53
<i>Introduction</i>	54
<i>Theoretical Basis</i>	55
<i>Computational Details</i>	59
<i>Results and Discussion</i>	59
The H ₂ molecule	59
The N ₂ molecule	59
The ethene molecule	60
The ethylene molecule	62
Formamide	63
Benzene	64
<i>Conclusions</i>	66
<i>Acknowledgment</i>	66
<i>References</i>	66
Chapter 4. FALDI-based decomposition of an atomic interaction line leads to 3D representation of the multicenter nature of interactions	68
<i>Introduction</i>	69
<i>Computational Details</i>	70
<i>Theoretical Background and Development</i>	70
Domain averaged Fermi holes	70
The fragment, atom, localized, delocalized and interaction density decomposition	71
Partial second derivatives of <i>deloc</i> -ED distributions	72
<i>Results and Discussion</i>	72
Intramolecular H-bonding interaction in β -alanine	74
Multicenter bonding nature of boron-hydrogen interaction in diborane	75
Typical carbon-carbon covalent bonding interaction in “linear” <i>n</i> -butane	76
Comparison of two different M-C bonding interactions in carbene complexes	77
Comparative Analysis	78
<i>Conclusions</i>	79
<i>Acknowledgment</i>	80
<i>References</i>	80
Chapter 5. FALDI-Based Criterion for and the Origin of an Electron Density Bridge with an Associated (3,-1) Critical Point on Bader’s Molecular Graph	82
<i>Introduction</i>	85
<i>Theoretical Background</i>	89
The FALDI density decomposition scheme	93
Classification scheme for ED components	94
The decomposition of the gradient in bonding, nonbonding and antibonding terms.	95

Physical and chemical interpretations of FALDI components	98
<i>Computational Details</i>	100
<i>Results and Discussion</i>	100
H-bonding interaction in neutral and protonated ethylenediamine	100
Highly repulsive oxygen-oxygen interaction in similar organic molecules	105
Attractive chlorine-chlorine interaction in di- and hexa-chloroethane	109
H-H steric contact in cis-2-butene	112
<i>Conclusions</i>	114
<i>Acknowledgements</i>	115
<i>References</i>	116
Chapter 6. Toward deformation densities for intramolecular interactions without radical reference states using the fragment, atom, localized, delocalized, and interatomic (FALDI) charge density decomposition scheme	119
<i>Introduction</i>	120
<i>Theoretical Development</i>	122
Framework for conformational deformation densities	122
DAFH-based density decomposition	122
General properties of the DAFH	123
Introducing the FALDI density decomposition scheme	124
Decomposing atomic-ED distributions into localized, delocalized and interatomic contributions	124
Conformational deformation densities using the FALDI-DD decomposition	127
<i>Computational Details</i>	128
<i>Results and Discussion</i>	128
Total deformation density from orthodox $\Delta\rho(\mathbf{r})$ and FALDI $\Delta\rho_c(\mathbf{r})$	128
Atomic FALDI deformation densities	130
Fragment FALDI deformation densities	132
Diatomic and Intrafragment interactions from the FALDI perspective	133
<i>Conclusions</i>	134
<i>References</i>	136
Chapter 7. Exploring fundamental differences between red-and blue-shifted intramolecular hydrogen bonds using FAMSEC, FALDI, IQA and QTAIM	137
<i>Introduction</i>	138
<i>Theoretical Background</i>	140
<i>Computational Details</i>	141
<i>Results and Discussion</i>	141
Exploring the changes of the atomic electron population and bond charge polarization	142
FALDI-based atomic deformation densities of the W-X-H \cdots Y-Z fragment	144
FALDI-based interatomic delocalized deformation densities of the X-H \cdots Y fragment	145
1D FALDI cross-sections of X-H \cdots Y interactions	146

Validity of the AIL between atoms H and Y	148
FAMSEC-based interpretation of the W–X–H···Y–Z region	149
<i>Conclusions</i>	151
<i>References</i>	152
Chapter 8. Conclusions	154
<i>Summary</i>	154
<i>Implications</i>	157
<i>Future Work</i>	158
<i>References</i>	159
Appendix I. Evaluating common QTAIM and NCI interpretations of the electron density concentration through IQA interaction energies and 1D cross-sections of the electron and deformation density distributions	160
<i>Introduction</i>	161
<i>Methods and computational details</i>	162
<i>Results and discussion</i>	163
Water dimers	163
Energy profiles and molecular graphs	163
NCI analysis	163
IQA analysis	164
Density cross-sections and deformation density analysis	165
Bipyridine	166
NTPA	170
2,2,2-Tet	171
<i>Conclusions</i>	174
<i>Acknowledgments</i>	175
<i>References</i>	175
Appendix II. Synthesis, structure and DFT study of asymmetrical NHC complexes of cymantrene derivatives and their application in the dehydrogenative dimerization reaction of thiols	178
<i>Introduction</i>	179
<i>Experimental</i>	180
General	180
Synthesis of complexes 1-6	181
X-ray crystallography	181
Molecular Modelling	182
General procedure for the dimerization of thiols	182
<i>Results and discussion</i>	182
Synthesis and characterization	182
Spectroscopic characterization	182
Single crystal X-ray diffraction studies	183
Theoretical study	184

Table of Contents.

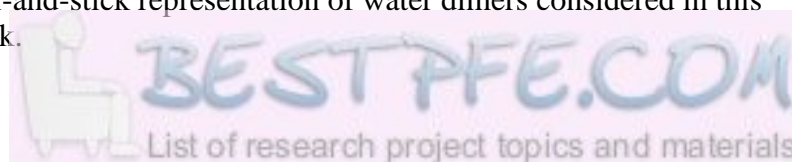
Ligand steric parameters	184
Wiberg bond indices and bond dissociation energies (BDEs)	185
Extended Transition State coupled with Natural Orbitals for Chemical Valence (ETS-NOCV)	185
Catalytic study	187
<i>Conclusion</i>	188
<i>Acknowledgements</i>	189
<i>References</i>	189
Appendix III. Gold (I) Hydrides as Proton Acceptors in Dihydrogen Bond Formation	191
<i>Introduction</i>	192
<i>Computational Details</i>	193
<i>Results and Discussion</i>	193
Adducts with Anionic and Neutral Gold Hydrides	193
The Role of Relativistic Effects	194
Energy Partitioning	194
The Role of Charge Transfer	194
Competing Reactions	195
1:2 and 3:1 Interactions of AuH ₂ ⁻ and Proton Donors	196
<i>Conclusions</i>	197
<i>Acknowledgements</i>	197
<i>References</i>	197

List of Figures	Page
 Chapter 3. Exact and exclusive electron localization indices with QTAIM atomic basins	
Figure 1. <i>Loc</i> -ED and <i>deloc</i> -ED distributions for H ₂ for orthodox QTAIM LIs and DIs and LO-free LIs and DIs.	59
Figure 2. Uncorrected <i>loc</i> -ED and <i>deloc</i> -ED distributions as well as selected uncorrected <i>loc</i> -NDFs and <i>deloc</i> -NDFs for N ₂ .	60
Figure 3. LO-free <i>loc</i> -ED and <i>deloc</i> -ED distributions as well as selected LO-free <i>loc</i> -NDFs and <i>deloc</i> -NDFs for N ₂ .	60
Figure 4. Uncorrected and LO-free <i>loc</i> -ED and <i>deloc</i> -ED distributions for ethene.	61
Figure 5. Selected LO-free <i>deloc</i> -NDFs for atom-pair C,C in ethene.	61
Figure 6. Uncorrected, LO-free and LDO-free LI and <i>loc</i> -ED distributions for the nitrogen atom in ethylamine.	62
Figure 7. LDO-free LI and <i>loc</i> -ED distributions for the nitrogen, carbon and oxygen atoms in formamide.	63
Figure 8. LDO-free <i>deloc</i> -NDF distributions and associated occupations for atom-pair C1,N4, atom-pair C1,O3 and atom-pair O4,N5 in formamide.	64
Figure 9. LDO-free <i>deloc</i> -NDF distributions and associated occupations for atom-pair C1,C2, atom-pair C1,C3 and atom-pair C1,C4 in benzene.	65
 Chapter 4. FALDI-based decomposition of an atomic interaction line leads to 3D representation of the multicenter nature of interactions	
Scheme 1. FALDI-based decomposition of the total static ED.	73
Scheme 2. Examples of cross-sections illustrating trends of bonding, nonbonding or antibonding ED distributions for a selected atom-pair as well their 2 nd partial derivatives.	73
Figure 1. Molecular graphs of β -alanine, diborane, "linear" <i>n</i> -butane, Schrock and Fischer carbene complexes, including vectors along which ED decomposition analyses are done.	74
Figure 2. FALDI-based decomposition of the <i>tot</i> -ED into <i>loc</i> - and <i>deloc</i> -ED in β -alanine. Subsequent FALDI-based decomposition of the <i>deloc</i> -ED into constructive (bonding nature), nonconstructive (nonbonding nature) and deconstructive (antibonding nature) electron correlation.	75
Figure 3. <i>Deloc</i> -ED 3D isosurfaces of the major constructive, bonding ED, nonconstructive and deconstructive electron correlation contributing factors in β -alanine.	75
Figure 4. FALDI-based decomposition of the constructive electron correlation with respect to BCP(H6,N11) in β -alanine, into the major contributing atom-pairs. Pie-chart summarizing percentage-wise the major contributing atom-pairs at the BCP(H6,N11).	76

Figure 5.	<i>Deloc</i> -ED 3D isosurfaces of the major constructive electron correlation contributing atom-pairs with respect to BCP(H6,N11) in β -alanine.	76
Figure 6.	FALDI-based decomposition of the constructive electron correlation (i.e., <i>deloc</i> -ED of a bonding nature) with respect to BCP(B1,H7) in diborane, into the major atom-pair contributions. Pie-chart summarizing percentage-wise the major contributing atom-pairs at the BCP(B1,H7).	77
Figure 7.	<i>deloc</i> -ED 3D-isosurfaces of the major constructive electron correlation contributing atom-pairs with respect to BCP(B1,H7) in diboran	77
Figure 8.	FALDI-based decomposition of the constructive electron correlation (i.e., <i>deloc</i> -ED of a bonding nature) in “linear” <i>n</i> -butane, into the major contributing atom-pairs. Pie-chart summarizing percentage-wise the major contributing factors at the BCP(C9,C12).	78
Figure 9.	<i>deloc</i> -ED 3D-isosurfaces of the major constructive electron correlation contributions with respect to BCP(C9,C12) in “linear” <i>n</i> -butane.	78
Figure 10.	Comparison of the FALDI-based decompositions of the constructive electron correlation (i.e., <i>deloc</i> -ED of a bonding nature) with respect to the M–C BCPs in the Schrock and Fischer carbene complexes, into the major contributions made by the indicated atom-pairs. Pie-charts summarizing percentage-wise the major contributions at the M–C BCPs in 4 and 5 .	79
Figure 11.	Comparison of the relative degree of multicenter bonding character of the five bonding interactions investigated in this study. Values of specific atom-pair <i>deloc</i> -ED contributions to the total bonding <i>deloc</i> -ED at a relevant BCP are expressed as percentages. Primary contributions indicate the <i>deloc</i> -ED associated with an indicated atom-pair that is connected by an AIL.	79
 Chapter 5. FALDI-Based Criterion for and the Origin of an Electron Density Bridge with an Associated (3,–1) Critical Point on Bader’s Molecular Graph		
Figure 1.	Molecular graph of energy optimised <i>cis</i> -2-butene, and associated cross-sections along various eigenvectors of the Hessian matrix	91
Figure 2.	Hypothetical ED distributions showing <i>bonding</i> - and <i>nonbonding</i> -ED distributions as well as their gradients.	97
Figure 3.	Equilibrium structures of a neutral (1) and a protonated (2) ethylenediamine also showing the λ_2 -eigenvectors.	100
Figure 4.	Comparison of the total <i>bonding</i> - and total <i>nonbonding</i> -ED along the λ_2 -eigenvector passing through the GCP(N7,H11) of neutral ethylenediamine (1) and the (3,–1) CP(N7,H11) of protonated ethylenediamine (2).	101
Figure 5.	Comparison of the 1st derivative curves of the total <i>bonding</i> - and total <i>nonbonding</i> -ED, as well as the <i>CP</i> (<i>r</i>) function, along the λ_2 -	102

	eigenvector passing through the GCP(N7,H11) in (1) and the (3,-1) CP(N7,H11) in (2) .	
Figure 6.	Molecular graphs of equilibrium structures (3) and (4) in the gas phase, including the λ_2 -eigenvectors.	105
Figure 7.	Comparison of the total <i>bonding</i> - and total <i>nonbonding</i> -ED along the λ_2 -eigenvector passing through the GCP(O6,O8) and (3,-1) CP(O6,O8) of the structures (3) and (4) .	106
Figure 8.	Comparison of the 1st derivative curves of the total <i>bonding</i> - and total <i>nonbonding</i> -ED along the λ_2 -eigenvector passing through the GCP(O6,O8) in (3) and the (3,-1) CP(O6,O8) in (4) .	106
Figure 9.	Molecular graphs of eclipsed conformations of C ₂ H ₄ Cl ₂ (5) and C ₂ Cl ₆ (6) structures in the gas phase, including the λ_2 -eigenvectors.	109
Figure 10.	Comparison of the total <i>bonding</i> - and total <i>nonbonding</i> -ED along the λ_2 -eigenvector passing through the GCP(Cl4,Cl6) in (5) and (3,-1) CP(Cl4,Cl6) in (6) .	110
Figure 11.	Comparison of the 1st derivative curves of the total <i>bonding</i> - and total <i>nonbonding</i> -ED along the λ_2 -eigenvector passing through the GCP(Cl4,Cl6) in (5) and the (3,-1) CP(Cl4,Cl6) in (6) .	111
Figure 12.	Comparison of the 1 st derivative curves of the total <i>bonding</i> - and total <i>nonbonding</i> -ED along the λ_2 -eigenvector passing through the (3,-1) CP(H1,H6) in <i>cis</i> -2-butene	113
Chapter 6.	Toward deformation densities for intramolecular interactions without radical reference states using the fragment, atom, localized, delocalized, and interatomic (FALDI) charge density decomposition scheme	
Figure 1.	Average electron density associated with a carbon atom in ethane. QTAIM-defined electron population, and DAFH-defined electron population.	123
Figure 2.	Interatomic-ED and delocalized-ED distributions for a C–C bond in ethane and an O···H interaction in a water dimer.	126
Scheme 1.	Proposed FALDI-DD decomposition of the deformation density.	128
Figure 3.	Molecular graphs of linear Hen ⁺ (<i>ref</i>) and equilibrium Hen ⁺ (<i>fin</i>) conformers for the calculation of conformational deformation densities using FALDI. The <i>ref</i> conformer is rotated around the N7,C1,C4,N8 dihedral angle.	128
Figure 4.	Total deformation densities: computed in ADF using indicated partitioning scheme and from FALDI, using the conformational approach.	129
Figure 5.	FALDI-on-promolecules generated Fragment-DD from the 2F ₁ and 3F partitioning schemes for –C ₄ H ₂ –C ₁ H ₂ – and combined terminal groups using orthodox promolecules as a reference state.	130
Figure 6.	ADD distributions and changes in QTAIM atomic net charges and atomic populations (both in <i>e</i>) obtained for indicated atoms on the <i>ref</i> → <i>fin</i> structural change.	131
Figure 7.	FDD distributions obtained for indicated fragments on the <i>ref</i> → <i>fin</i> structural change.	133

Figure 8.	IDD distributions obtained for the indicated diatomic and intrafragment interactions.	134
Chapter 7. Exploring fundamental differences between red- and blue-shifted intramolecular hydrogen bonds using FAMSEC, FALDI, IQA and QTAIM		
Figure 1.	Molecular graphs of <i>fin</i> structures of LEC and HEC showing the changes (at MP2) in atomic electron population, $\Delta N(A)$, on the <i>ref</i> (Lin) to <i>fin</i> structural change.	143
Figure 2.	Molecular graphs of <i>fin</i> structures of LEC and HEC showing the changes (at MP2) in charge polarisation between chemically bonded atoms, $\Delta Q(A) - Q(B) $, on the <i>ref</i> (Lin) to <i>fin</i> structural change.	143
Figure 3.	Relative to Lin , FALDI atomic deformation density isosurfaces for selected atoms in LEC and HEC and changes in atomic populations calculated at the B3LYP level.	144
Figure 4.	FALDI interatomic delocalized deformation density isosurfaces for selected interactions in LEC and HEC relative to Lin . Changes in delocalization indices as well as IQA interatomic exchange-correlation energies are shown; all calculated at the B3LYP level	145
Figure 5.	Cross-sections along the path defined by the λ_2 -eigenvector at the BCP of the X–H bond of LEC and HEC conformers, as shown by the blue line in the ball-and-stick representation at the top. The total deformation density as well as the change in selected FALDI atomic density, relative to Lin , is shown in the middle, and the change in selected FALDI interatomic delocalized densities is shown at the bottom; all calculated at the B3LYP level.	147
Figure 6.	Cross-sections along the path defined by the λ_2 -eigenvector at the BCP of the H \cdots Y interaction of LEC and HEC conformers. The total deformation density as well as the change in selected FALDI atomic density, relative to Lin , is shown at the top, and the change in selected FALDI interatomic delocalized densities is shown at the bottom. All calculated at the B3LYP level.	148
Figure 7.	FALDI-defined privilege of the H \cdots Y interaction, relative to local secondary interactions (X \cdots Y, X \cdots Z, W \cdots Y, H \cdots W and H \cdots Z) for LEC and HEC calculated at the B3LYP level.	149
Appendix I. Evaluating common QTAIM and NCI interpretations of the electron density concentration through IQA interaction energies and 1D cross-sections of the electron and deformation density distributions		
Figure 1.	Ball-and-stick representation of water dimers considered in this work.	163



List of Figures.

Figure 2.	Variation in E with interatomic distance for the indicated water dimers also showing representative molecular graphs.	164
Figure 3.	NCI isosurfaces (with RDG isovalue = 0.9 au) for water dimers: d1) $d(\text{O}---\text{H}) = 2.0 \text{ \AA}$; d2) $d(\text{O}---\text{O}) = 1.6 \text{ \AA}$; d3) $d(\text{O}---\text{O}) = 2.4 \text{ \AA}$; d4) $d(\text{H}---\text{H}) = 2.0 \text{ \AA}$.	164
Figure 4.	Cross section of the electron density and the deformation density along λ_2 eigenvector for d1 at $d(\text{O}---\text{H}) = 1.946 \text{ \AA}$ and d2 at $d(\text{O}---\text{O}) = 2.6 \text{ \AA}$.	166
Figure 5.	Cross-section of the electron density, its first and second order changes, along the λ_2 eigenvector for d4 for indicated distances of $d(\text{H}---\text{H})$.	167
Figure 6.	Cross-section of the deformation density along the λ_2 eigenvector for indicated distances of d4 .	167
Figure 7.	Molecular graphs of the <i>s-cis</i> and <i>s-trans</i> forms of bipyridine, L, HL and H2L.	168
Figure 8.	NCI isosurfaces of the <i>s-cis</i> forms of bpy (L) and HL.	168
Figure 9.	Cross-sections of the electron density along the λ_2 eigenvector for indicated interactions without a bond path, and with a bond path present, in indicated forms of bpy.	168
Figure 10.	Cross-sections of the deformation density along the λ_2 eigenvector for selected interactions without bond path in deprotonated bpy and with a bond path in indicated forms of bpy.	169
Figure 11.	Molecular graphs of the lowest and highest energy conformer of NTPA.	170
Figure 12.	NCI isosurfaces of the lowest and highest energy conformer of NTPA.	171
Figure 13.	Cross-sections of the electron density along the λ_2 eigenvector for indicated interactions in the lowest and highest energy conformers of NTPA.	171
Figure 14.	Cross-sections of the deformation density along the λ_2 eigenvector for the indicated interactions in the lowest and highest energy conformers of NTPA.	171
Figure 15.	Molecular graphs of the lower energy L1 and higher energy L2 conformer of 2,2,2-tet	172
Figure 16.	NCI isosurfaces of the lower L1 and higher energy L2 conformer of 2,2,2-tet.	172
Figure 17.	Cross-sections of the electron density along the λ_2 -eigenvector for indicated $\text{H}\cdots\text{N}$ interactions with an AIL, $\text{XH}\cdots\text{N}$ interactions without an AIL and $\text{CH}\cdots\text{HC}$ interactions in the lower energy conformer, LEC, of 2,2,2-tet.	172
Figure 18.	Cross-sections of the deformation density along the λ_2 -eigenvector for indicated $\text{XH}\cdots\text{N}$ with AIL present, $\text{XH}\cdots\text{N}$ without AIL present and $\text{CH}\cdots\text{HC}$ interactions in the lowest energy conformer of 2,2,2-tet.	173

Appendix II. Synthesis, structure and DFT study of asymmetrical NHC complexes of cymantrene derivatives and their application in the dehydrogenative dimerization reaction of thiols

List of Figures.

Figure 1.	Isomerisation of Ru-NHC complexes afforded through photochemical processes.	180
Figure 2.	NHC complexes of cymantrene and MMT and agostic interaction of the cymantrene NHC complex.	180
Figure 3.	Cymantrene derived NHC complexes of this study.	180
Figure 4.	NHC ligands used in this study.	181
Figure 5.	Perspective view of 3 with thermal ellipsoids drawn at the 50% probability level.	182
Figure 6.	Perspective view of 6 (molecule A) with thermal ellipsoids drawn at the 50% probability level.	183
Figure 7.	The angle between the Cp and carbene planes of 3 .	183
Figure 8.	Hydrogen interactions witnessed in 3 .	183
Figure 9.	Perspective view of C1 with thermal ellipsoids drawn at the 50% probability level.	183
Scheme 1.	Synthesis of group VII NHC complexes.	184
Figure 10.	NHC complexes 1-6 , A1 , A2 , phosphine complex B1 and acetonitrile complex C1 of the theoretical study.	184
Figure 11.	Graphical representation of the sphere defining the %V _{bur} of metal complexes 1-6 ; steric contour map of 3 and representation of the solid angle and GM of a complex.	185
Figure 12.	The G _M (Complex) of 1 , 3 , 5 and CpMn(CO) ₃ .	185
Figure 13.	Solid angle parameters of the MeCpMn(CO) ₃ , diethyl substituted NHC and complex 2 .	186
Figure 14.	Primary NOCV channels and associated orbital energy changes for 1 .	187
Figure 15.	Possible carbonyl substitution positions CO _a and CO _b available on 1-6 .	188
Figure 16.	Catalytic cycle associated with the dimerization of thiol substrates.	189
Appendix III. Gold (I) Hydrides as Proton Acceptors in Dihydrogen Bond Formation		
Figure 1.	Optimized structures, bond distances, angles and binding energies for HF adducts of gold hydrides (1)–(5).	193
Figure 2.	Selected distances and binding energies for indicated adducts.	194
Figure 3.	Correlations between: binding energy, quotient of the local electron potential and kinetic energy densities at the BCP of directly interacting atoms in the 1:1 adducts and the charge transfer (CT) from Au-containing complex to HF.	195
Figure 4.	Bond distances, angles and binding energy for products (6) and (7) where E_{bind} for, for example, (6) is $E(\mathbf{6}) - \{E(\text{AuH}) + E(\text{HF}) + E(\text{H}_2)\}$.	195
Figure 5.	Bond distances, angles and binding energies for the (1).(HF) ₂ and (1) ₃ .H ₃ O ⁺ complexes.	196
Figure 6.	Selected distances for the (1) ₂ .H ₂ O.(4)-H ₂ and (1) ₂ .H ₂ O.(4) structures. The binding energy for (1) ₂ .H ₂ O.(4) is also provided.	197

List of Tables	Page
Chapter 3. Exact and exclusive electron localization indices with QTAIM atomic basins	
Table 1. Interatomic LO-free DI contributions to atomic populations in ethene.	62
Table 2. Interatomic LO-free and LDO-free delocalized electron contributions to atomic populations in ethylamine.	63
Table 3. LDO-free DIs and <i>deloc</i> -NDF occupations for selected atom-pairs in formamide.	64
Table 4. LDO-free DIs and <i>deloc</i> -NDF occupations for all carbon-carbon interactions in benzene.	65
Chapter 5. FALDI-Based Criterion for and the Origin of an Electron Density Bridge with an Associated (3,-1) Critical Point on Bader's Molecular Graph	
Table 1. Selected contributions made to GCP(N7,H11) in ethylenediamine.	103
Table 2. Selected contributions made to (3,-1) CP(N7,H11) in protonated ethylenediamine.	103
Table 3. Selected contributions made to GCP(O6,O8) in (3).	108
Table 4. Selected contributions made to (3,-1) CP(O6,O8) in (4).	108
Table 5. Selected contributions made to GCP(Cl4,Cl6) in (5).	112
Table 6. Selected contributions made to (3,-1) CP(Cl4,Cl6) in structure (6).	112
Table 7. Selected contributions made to (3,-1) CP(H1,H6) in <i>cis</i> -2-butene.	114
Chapter 7. Exploring fundamental differences between red-and blue-shifted intramolecular hydrogen bonds using FAMSEC, FALDI, IQA and QTAIM	
Table 1. Molecular graphs and selected geometric features and properties of fin structures of β -alanine investigated in this work.	142
Table 2. Changes in QTAIM properties at the BCP of the X-H bond at B3LYP level.	146
Table 3. Energy components used for the interpretation of selected important molecular fragments in LEC and HEC .	150
Appendix I. Evaluating common QTAIM and NCI interpretations of the electron density concentration through IQA interaction energies and 1D cross-sections of the electron and deformation density distributions	
Table 1. Analysis of interactions in water dimers, d1-d4 , in terms of interaction energies and electron density in the interatomic bonding region.	165

Table 2.	Analysis of interactions in bpy and its protonated forms in terms of interaction energies and electron density in the interatomic region.	170
Table 3.	Analysis of interactions in the LEC and HEC of NTPA in terms of interaction energies and electron density in the interatomic region.	171
Table 4.	Analysis of interactions in the protonated lower (L1) and higher (L2) energy conformers of 2,2,2-tet and its protonated forms in terms of interaction energies and electron density in the interatomic region.	173
Table 5.	Comparative analysis of all interactions investigated in this work.	174
 Appendix II. Synthesis, structure and DFT study of asymmetrical NHC complexes of cymantrene derivatives and their application in the dehydrogenative dimerization reaction of thiols		
Table 1.	Selected bond lengths and angles.	182
Table 2.	Solid angle parameters for 1-6 .	185
Table 3.	Selected ETS-NOCV energy contributions.	187
Table 4.	Dimerization of ethylthiol by manganese(I) NHC complexes 1-6 .	188
 Appendix III. Gold (I) Hydrides as Proton Acceptors in Dihydrogen Bond Formation		
Table 1.	Analysis of QTAIM-defined net atomic charges and electron population in $[\text{AuH}_2]^-$, HF and (1).HF .	194
Table 2.	Competing reactions and associated reaction energies, ΔE_r .	196

List of Abbreviations

2,2,2-tet , <i>trien</i>	triethylenetetramine
AIL	atomic interaction line
AIM	atom in a molecule
AOM	atomic overlap matrix
<i>atom-DD</i> , ADD	atomic deformation density distribution
<i>atom-ED</i> , AED	atomic electron density distribution
BCP	bond critical point
bde	bond dissociation energy
bpy	bypridine
CCP	cage critical point
CP	critical point
DAFH	Domain Averaged Fermi Holes
DB	density bridge
DD	deformation density
<i>deloc-DD</i> , DDD	delocalized interatomic deformation density distribution
<i>deloc-ED</i> , DED	delocalized interatomic electron density distribution
<i>deloc-NDF</i>	delocalized interatomic natural density function
DFT	Density Functional Theory
DI	delocalization index
DI _{Excl}	exclusive delocalization index
DNO	domain natural orbitals
ED	electron density
EDA	Energy Decomposition Analysis
<i>en</i>	ethyldiamine
ETS	Extended Transition State
ETS-NOCV	The Extended Transition State coupled with Natural Orbitals for Chemical Valence
FALDI	Fragment, Atomic, Localized, Delocalized and Interatomic
FAMSEC	Fragment-attributed Molecular System Energy Change
<i>fin</i>	final
FMO	Frontier Molecular Orbital
<i>frag-DD</i> , FDD	fragment deformation density distribution
<i>frag-ED</i> , FED	fragment electron density distribution
GCP	geometric critical point
GIP	geometric interaction point
H-bond	hydrogen bond
HEC	highest energy conformer
HF	Hartree-Fock
HOMO	highest occupied molecular orbital
ICP	NCI-defined interaction critical point
IDD	interatomic deformation density
IQA	Interacting Quantum Atoms
λ_2 -eigenvector	eigenvector associated with the second eigenvalue of the Hessian matrix
LAP	linear aliphatic polaymine

List of Abbreviations.

LDM	localization-delocalization matrix
LDO	localized-delocalized overlap
LEC	lowest energy conformer
LI	localization index
LI _{Excl}	exclusive localization index
LO	localized overlap
<i>loc</i> -DD , LDD	localized atomic deformation density distribution
<i>loc</i> -ED , LED	localized atomic electron density distribution
<i>loc</i> -NDF	localized atomic natural density function
LUMO	lowest unoccupied molecular orbital
MMT	methylcyclopentadienyl manganese tricarbonyl
MO	molecular orbital
NBO	Natural Bonding Orbitals
NCI	Noncovalent Interactions
NDF	natural density function
NHC	N-heterocyclic carbene
NOCV	Natural Orbitals for Chemical Valence
NTA	nitrioloacetic acid
NTPA	nitriolo-3-propionic acid
PD	pair-density
QCT	Quantum Chemical Topology
QTAIM	The Quantum Theory of Atoms in Molecules
RCP	ring critical point
RDG	reduced density gradient
<i>ref</i>	reference
SAPT	Symmetry-Adapted Perturbation Theory
SD	single determinant
SDD	self deformation density
SEDI	shared electron delocalization index
SF	Source Function
SI	Supplementary Information
SPC	single point calculation
TJ	Tognetti and Joubert
TM	transition metal
<i>tot</i> -DD , TDD	total deformation density distribution
<i>tot</i> -ED , TED	total electron density distribution
VB	Valence Bond
vdW	Van der Waals
XC	exchange-correlation

Chapter 1: Introduction

1.1 The phenomenology of an atom in a molecule

The concept of an atom as a fundamental component of a molecule is a critically important cornerstone of conceptual and experimental chemistry. Most of modern conceptual chemistry, including (and especially) synthetic chemistry and separation sciences, relies on the properties of atoms as separate entities combined to form a molecule. In theoretical quantum chemistry, however, the concept of an atom is well-defined only on its own *in vacuo*, and the concept of an atom within a molecule does not form part of the axioms of molecular quantum mechanics. There is therefore quite a divide between theoreticians and experimentalists regarding their views on the most fundamental building blocks of matter.

The reason why the model of an atom in a molecule (AIM) is popular amongst general chemists but scorned by some of the theoretical community lies amongst the differences in philosophical paradigms which experimental and theoretical chemists typically ascribe to. Experimental and conceptual chemistry generally follow an *atomistic* philosophy^{1,2}: the reductive view that a molecule (an observable) is formed by the juxtaposition of two or more atoms (observable only when regarded separately). The atomistic view of chemistry provides three very useful properties which analytical research can exploit: (i) transferability – that information regarding the properties and functionalities of atoms and functional groups in one molecule can often be transferred to the same atoms or functional groups in a different molecule, (ii) additivity – that any observable molecular property is the sum of partial atomic properties, and (iii) identity – that an atom, and therefore its properties, is defined by the number of protons and neutrons in its nucleus, as well as the number and configuration of its electrons.^{1,2} These properties allow a large degree of generality and predictivity to empirical results, thereby accelerating the development of theorems describing chemical phenomena. It can be argued that the study of chemistry in the 18th, 19th and 20th centuries was made possible (despite of the immense physical and mathematical complexity of any chemical system) through the widespread adoption of the doctrine of atomism.

Molecular quantum chemistry, on the other hand, belongs inherently to a *holistic* philosophy^{3,4} in that a state function (the wavefunction) describes the structure and properties of a molecule, and that while similarities in the wavefunctions of two different molecules can be found, the wavefunction for each molecule is unique. Therefore, whereas general chemistry

sees the molecule as a collection of interacting atoms, quantum chemistry sees the molecule as a unique arrangement of only nuclei and electrons, interacting simultaneously. The holistic view of chemistry provides a much more precise approach to molecular phenomena, in that the properties of any molecule can be extracted using the same set of general physical laws. In a holistic approach to chemistry, no additional information regarding the arrangement and interactions of *atoms* is required – the laws governing the interactions and configuration of the molecules' particles are completely general and universal to all systems. On the other hand, the properties given by the atomistic view of chemistry is generally lacking in the holistic approach. As a result, it is considerably more difficult to reduce the inherent complexity of chemical science to manageable concepts in the holistic approach than the atomistic approach.

Molecular quantum chemistry is a relatively young sub-discipline of chemistry, yet has played a very large part in shaping of modern and post-modern chemical thinking. Early 20th century developments in quantum chemistry have led to many core chemical concepts – such as molecular orbitals, valency, covalency, resonance, electronegativity and aromaticity, to name but a small number. However, with the advent of high-throughput computing, molecular quantum chemistry has become an increasingly precise science, and the divide between holistic and atomist views of chemistry is growing more apparent in the 21st century. Such a divide translates into (i) a difficulty in reconciling computed, theoretical predictions and experimental results, and (ii) a difficulty in describing various important conceptual *noumena* (such as chemical bonding, partial charge or atomic valency) from a theoretical, computable and, most importantly, quantifiable point of view.

Of course, the holistic and atomistic approaches to chemistry are not entirely mutually exclusive. Many concepts in molecular quantum chemistry have been translated conceptually into an atomist's language, such as the description of transition metal bonding patterns through the use of ligand-field theory.⁵ Likewise, many computational chemists implicitly describe their results in terms of atoms, despite their results being intrinsically holistic, *e.g.* frontier molecular orbital theory as an indicator of reactivity.⁶ Unfortunately, most concepts from general chemistry is ill-defined in terms of quantum mechanics, with special mention of the concept of a chemical bond, and leads to a large degree of confusion amongst experimentalists and theoreticians alike.⁷ The lack of ease with regards to the flow of information between theoretical and experimental realms of chemical science strongly inhibits the development of chemical science, and it is therefore imperative to reconcile these two approaches as much as possible. It is therefore the phenomenology of an atom within a molecule – the manner through

which the atomic model is perceived – which has to be reconciled between general and quantum molecular chemistry.

1.2 On the nature of chemical bonding

If atoms and molecules form the building blocks of modern chemistry, then the chemical bond is its mortar, girders, windows, plumbing and *facade*. Chemical bond theory has been generally active throughout the 20th century, with a number of “*Nature of Chemical Bonding*” treatises published. From humble *hook-and-eye* models to sophisticated quantum mechanical treatments, the chemical bond remains one of the only fundamental questions which chemistry poses.⁸

The identity of chemical bonding, however, has been fractured between general chemists and theoreticians as much as the concept of an atom in a molecule. The phenomenology of chemical bonding also suffers from conflicting atomistic and holistic schools of thought. Prevalent models of chemical bonding – those built on the ideas of Lewis, Pauling, Hund and others – have their roots in quantum mechanics and are therefore holistic in origin, but have been forced into an atomistic viewpoint during their generalization and conceptualization. For instance, molecular orbital (MO) theory, as a method for approximating the electron structure of a molecule, describes the energy of electrons on a molecular system as a whole and, in principle, does not require any concept of an atom in order to be applied. MO *bonding* theory, however, describes the perturbations which *atomic* orbitals undergo upon formation of a molecule from a set of isolated atoms or molecular fragments. MO bond theory therefore operates in the holistic realm of molecular quantum mechanics but is interpreted from an atomistic school of thought. While such an approach yields clear results for systems where an AIM is conceptually fairly well defined, such as diatomic molecules, larger molecules become much more difficult to fully interpret from an MO point of view.

The often-stated fundamental property of a chemical bond is that the energy of a system is lower when a collection of atoms is *bonded* (*i.e.* close together) than when they are separated. This property necessitates chemical bonding as a function of relative states and introduces a severe conceptual problem of correlation: if a molecule is a collection of bound atoms, then a “bond” between atoms or fragments is only defined in relation to all other bonds within the system. As a result, any diatomic interaction or interactions between two fragments in a molecule cannot be tested whether it is a bond without breaking all other bonds in the process, hence rendering the concept of a molecule as a collection of bonds undefined. In order to

circumvent such a paradox, *aspects* of chemical bonding are usually investigated for diatomic or very small systems and then similar aspects are identified in polyatomic systems. Therefore, most concepts of chemical bonding are defined from an almost exclusively diatomic nature, and become very difficult to apply to the descriptions of intramolecular bonds, multicentre bonds, weak and dispersive interactions. That said, the progress of experimental chemistry shows that such a “definition” of a chemical bond is empirically viable; but it remains a mystery to theoreticians wishing to accurately define and quantify chemical bonds.

As for the perception of an AIM, trying to view holistic properties of molecules through strict atomistic lenses makes a general, precise and robust definition of chemical bonding in terms of molecular quantum mechanics impossible. It is the manner through which chemical bonding is perceived - by either general chemists, theoreticians or both - that needs to be reconciled before any precise “nature of the chemical bond” can be discovered. However, the benefits of the atomistic doctrine - transferability, additivity and identity - is critical to the utility of the chemical bond, and it is therefore perhaps beneficial to continue to investigate chemical bonding from the perspective of interacting atoms, rather than disregarding the concept of an AIM entirely from chemical bond theories. A robust understanding of an AIM would therefore be as important as understanding chemical bonding itself.

1.3 Theoretical descriptions of atoms in molecules

Many models of AIMs have been proposed after the rise of quantum mechanics. Early work by Moffitt⁹ regarding the theoretical treatment of hybridization of valence electrons included a soft definition of an AIM, as did Coulson’s long-standing treatise¹⁰ on valency in atoms. Mulliken was also an early pioneer in the development of AIM, and the still popular “Mulliken population analysis”¹¹⁻¹⁵ calculates the partial charge by considering elements of the density matrix of basis functions centred on a specific nucleus. Hirshfield’s, or ‘stockholder’ atoms¹⁶ represent a group of “fuzzy” AIMs– atomic basin definitions of atoms that contribute to all coordinates of molecular space with a given weight. Hirshfield’s approach calculates the contribution which each atom makes to any given coordinate based on the ratio between the promolecular atomic density and the total molecular density. As a result, the method is very dependent on the choice of reference density.¹⁷ Many iterations of Hirshfield’s atoms have since been developed,^{18,19} most of which introduce a manner of iteration and self-consistency during the calculation in order to reduce the dependency on reference density, yet still this dependency ultimately reduces the general nature of the theory. Arguably, the most popular

and developed AIM model is Richard Bader and co-workers' Quantum Theory of Atoms in Molecules (QTAIM).²⁰ As part of the discipline of Quantum Chemical Topology (QCT),²¹ despite historically preceding it, the QTAIM model of an atom is exact, robust and experimentally verifiable.^{17,22} It provides exact transferability and additivity;²³ however, the identities that QTAIM atoms are prescribed to do occasionally differ from classical expectations, and have often been critiqued.²⁴⁻²⁷ Regardless, QTAIM and QCT methods in general are a growing sub-discipline of theoretical and computational chemistry, and provide a very strong bridge between atomistic conceptual chemistry and holistic quantum mechanics. However, one aspect of QTAIM that has been critiqued quite often²⁸⁻³² is its description of the interactions between atoms. Specifically, *bond paths*, also called atomic interaction lines (AILs), line paths³³ or density bridges, are critical topological features of the molecular electron density distribution. Note that the term AIL or density bridge is preferred throughout this thesis, and will be consistently used. An AIL is a path in the gradient vector field originating from a nuclear critical point (a local maximum in the electron density, usually coinciding with the position of a nucleus) and terminating at a bond critical point (BCP) – a critical point often found between two nuclei. Along each coordinate of an AIL, including at the BCP, the electron density is a local maximum along two principle axes perpendicular to the internuclear vector. An AIL is therefore often seen as a 'bridge of density'³⁴ linking two nuclei. Interestingly, a very strong equivalence exists between the presence of an AIL and most atomic interactions generally recognized as chemical bonds, so much so that Bader originally interpreted an AIL as a chemical bond.^{35,36} Later, however, he revised³⁴ his statement and concluded that an AIL in an equilibrium structure represents a "bonding interaction". Since then, a number of examples of AILs found between interactions where a chemical bond is *not* expected have been reported,²⁸⁻³² as well as a few examples where a chemical bond is expected but no AIL is present.^{37,38} A very recent discussion by Shahbazian³⁹ highlights many of the misinterpretations commonly given to AILs, but does not further any support to the nature of an AIL itself.

An important feature of QTAIM is its analysis of atomic populations. Extended population analysis is a popular family of techniques in quantum chemistry where a specific field (such as the wavefunction, a set of molecular orbitals, or the electron density) is analysed in real-space with respect to a set of sub-spaces. In QTAIM, extended population analysis takes the form of the total atomic electron population (*i.e.* the number of electrons found, on average, within an atom) as well as the number of electrons *localized* to a domain and the number of electrons *delocalized* between 2 domains.^{40,41} Such measures of localized or delocalized electrons are QTAIM's counterpart to *core* and *valence* electron counts. Extended population analysis within

QTAIM therefore suffices to lend an identity to an atom, thereby describing its partial charge or oxidation state as well as the manner with which an atom interacts with its neighbours.

QTAIM powerfully addresses the distinct divide in the phenomenology of an atom in a molecule, and provides a very clear and precise common ground between experimental and theoretical results. However, it is not without fault, and the dichotomy of describing chemistry in atomistic terms using holistic methods plague QTAIM atoms, leading to imprecision and confusion. This thesis is focussed on extending the definition of QTAIM atoms and, in the process, provides additional tools to reconcile and extend conceptual and quantum mechanical descriptions of chemical bonding.

1.4. Problem statement

QTAIM provides a very precise and elegant definition of an atom in a molecule, and it recovers the principle utilities of an atomistic viewpoint – transferability and additivity – quite nicely. However, the identities which it confers to atoms are somewhat different than classically expected properties of atoms. Specifically, QTAIM-defined delocalization indices (DI)⁴⁰ are commonly associated with the bond order of an interaction.⁴²⁻⁴⁵ Classically, the formal bond order of a chemical bond provides the number of electron pairs which is shared or delocalized between two atoms. Therefore, for a carbon-carbon double bond (bond order = 2), the DI is usually around 2 as well. However, DI counts the number of electrons (not electron *pairs*), which suggests that only half of the expected number of electrons is delocalized across a double-bond. The QTAIM-defined localization index (LI), similarly, supposedly counts the number of electrons localized within an atom, and is generally much larger than classically expected core and non-bonded electron counts: in a sp^3 -hybridized nitrogen atom, which formally has 2 core and 2 non-bonded electrons (thus 4 localized electrons), the LI is usually around 5.5 electrons. The usefulness of the equivalence between the DI and bond order, however, has led to the scientific community mostly turning a blind eye toward these inconsistencies. Clearly, one or more of three hypotheses must be correct: (i) that our classical understanding of electron pair (de)localization across atoms and bonds is incorrect, even for well-understood systems, (ii) that QTAIM LIs and DIs are grossly misinterpreted, or (iii) that the concept of QTAIM's atom is still underdeveloped. While this inconsistency between classical and theoretical chemical thinking might seem moderately harmless, Bader and others has often argued⁴⁶⁻⁴⁸ that QTAIM's DIs provides a very strong link between classical molecular orbital theories of chemical bonding and QCT methods. In addition, DIs and LIs are being

incorporated in models of bonding and molecular structure more commonly – see for instance the work by Matta *et al*⁴⁹ or a recent discussion by a number of QCT frontrunners.⁵⁰ Therefore, it is of critical importance that DIs and LIs are clearly and explicitly defined and interpreted.

In this thesis, it is argued that the atomic identity of QTAIM atoms is incorrectly assigned, which leads to the above mentioned inconsistency, as well as a few other QTAIM-related problems (discussed later in this section). This problem is related to the inclusion of atomistic views in an otherwise inherently holistic discipline. Specifically, conceptual chemistry assigns a degree of electron ‘ownership’ to each atom, in that each atom consists of a nucleus and a number of core and non-bonded electrons, as well as a number of electrons shared with other atoms. In quantum chemistry, however, electrons are indistinguishable, and together with the holistic nature of the wavefunction, the concept of electron ‘ownership’ becomes irrelevant. Atomic electron populations within QTAIM atomic basins gives the average number of electrons which can be found in that basin, but cannot be interpreted as ‘belonging’ or ‘confined’ to a specific atom. Therefore, the interpretations of LIs and DIs are inexact through the indistinguishability of electrons – electrons which are counted by an LI can, in fact, be found in other basins, giving rise to the general undercounting of DIs and overcounting of LIs. This problem is discussed in detail in Chapter 3 of this thesis.

The deformation density is an extremely useful tool in both theoretical and experimental approaches. The deformation density calculates the change in charge density between a reference and a final state, thereby providing very valuable information with regards to chemical bonding, charge transfer and polarization. The deformation density is also often used in conjunction with the interaction or binding energy, and we show in Appendix F⁵¹ that the deformation density is a very good tool to measure the accumulation of density in an internuclear region for the fulfilment of Feynman’s theorem⁵² regarding the forces acting on nuclei. The deformation density, together with the binding energy, is the central approach of many energy decomposition analyses such as the Extended Transition State coupled with Natural Orbitals for Chemical Valence (ETS-NOCV).⁵³ However, a well-defined, chemically meaningful reference state is required for calculating a meaningful deformation density distribution, making this method only suitable for studying intermolecular interactions. Unchemical reference states, often containing radicals, are used for the study of the formation of intramolecular interactions regardless, but the lack of a suitable reference state places severe doubt on any such results. The nature of such deformation density experiments (*i.e.* severing parts of a molecule in order to study local chemical bonding) ties in with the general problem of defining chemical bonds as a property of diatomic interactions, as discussed earlier in this

chapter. However, the limitation of deformation densities (as well as binding energies) can be circumvented through a suitable AIM model which allows for the transferability of atoms between two states, thereby allowing the calculation of density changes as a result of conformational transformation. The immense utility of the deformation density makes a scheme for the calculation of conformational deformation densities very alluring, and allows for extension of the study of fundamental properties of chemical bonds to intramolecular interactions.

Unfortunately, none of the AIM theories mentioned in the previous section implicitly allows for the calculation of conformational deformation densities. Due to QTAIM's exhaustive decomposition of all molecular space into sub-domains, each coordinate \mathbf{r} is an element of only a single atomic domain. Again, while it provides the illusion of 'ownership' of each atom over a domain of molecular space, electron waves are distributed across the entire molecule and not localized to a single coordinate. As a result, calculating an atomic electron distribution in 3D space is meaningless. That means, however, that deformation density calculations as a result of conformational change is not possible using QTAIM-defined atoms. Therefore, QTAIM as an atoms-in-molecules theory cannot recover such a general chemical approach, and is therefore not a complete theoretical representation of a chemists' atom. In Chapter 6, we discuss the importance of the deformation density in analysing intramolecular chemical bonds – a quantity which is only sensible when calculated as a result of conformational change rather than fragmentation.

Finally, the interpretation of QTAIM's AILs has been a source of heated debate for many years,^{28-33,39} yet the remarkable equivalence^{20,36} between the presence of a bond path and *most* chemical bonds is a continued impetus for further study of this topological phenomenon. To date, the nature of an AIL and its relationship to chemical bonding (if any) is still mostly unknown. Since our general understanding of the nature of a chemical bond is philosophically irremovable from the concept of an atom, and since electron delocalization plays a critically important role in most bonding models, it is of paramount importance to fully understand the nature and distribution of (de)localized electrons within an atom in a molecule if we wish to fully elucidate the true meaning of an AIL, as well as chemical bonding from an atomistic, electron density perspective.

1.5. Aims and general approach

This thesis aims to (i) extend Bader's definition of an atom in a molecule, (ii) investigate the nature and characteristics of AILs, (iii) develop a scheme for calculating conformational deformation densities and (iv) to work towards a full rendering of general chemistry's atomistic philosophy into the universal, precise world of quantum mechanics. We introduce the Fragment, Atomic, Localized, Delocalized and Interatomic (FALDI) density decomposition scheme,⁵⁴⁻⁵⁷ which presents a holistic view of an atom in a molecule and recovers the notion of electron 'ownership' without distinguishing electrons. This goal was already achieved previously, in part, through Ponec and co-workers' Domain Averaged Fermi Hole (DAFH)⁵⁸⁻⁶⁰ approach, which calculates the real-space distribution of electrons found on average in a QTAIM atomic basin. FALDI extends the DAFH approach by also calculating the distribution of density fully localized to a single atomic basin and density delocalized across two or more basins.

Furthermore, this thesis then aims to use the FALDI decomposition to address some of the problems stated in the previous section. The nature of (de)localized electrons within QTAIM basins are investigated, and truly *exclusive* localization and delocalization indices are developed. A scheme for calculating deformation densities arising from conformational change will be presented, which to our knowledge, is the first of its kind. Finally, we will introduce a number of tools derived from FALDI components with which we will investigate the nature of AILs. Using these tools, we aim to show the relationship between QTAIM's atoms as extended with FALDI and classical molecular orbital bonding theories.

1.6. Overview of this thesis

This thesis is presented as a compilation of journal articles. Each results-containing chapter (Chapters 3 through 7, as well as Appendices I through III) has been published in international, peer-reviewed journals, with the exception of Chapter 5, which has been submitted at the time of writing. The manuscripts have been included in their published, peer-reviewed forms. For the interest of brevity, the supplementary information to each manuscript is not included, but a relevant link is given at the beginning of each chapter for finding its supplementary information online.

It should be noted that development of FALDI has occurred over a succession of publications, and many aspects of the approach were published separately. Therefore, the full derivation and implications of all features of FALDI are compiled in Chapter 2.

An additional three manuscripts are included as appendices. These manuscripts have also been published as part of the output of this work, but do not directly relate to FALDI. Rather, one of these publications describes a problem in QTAIM and other QCT techniques' interpretations, and led us to the development of the FALDI scheme. The other two appendices describe orthodox deformation densities involving fragmentation which we performed for applications in inorganic chemistry while we were still developing FALDI. This work will be revisited in the near future using the methods described in Chapter 2. A quick overview of each chapter is given below.

Chapter 2 provides the derivation of the full FALDI theory, as well as background information on existing theories and concepts upon which FALDI relies. Chapter 2 is divided into two sections. In the first section, the following topics are covered: (i) The electron density, (ii) the pair density and electron holes, (iii) The Quantum Theory of Atoms in Molecules, (iv) QTAIM localization and delocalization indices, and (v) Domain Averaged Fermi Holes. The second section covers the derivation and implementation of all aspects of the FALDI approach, in the following order: (i) The general FALDI density decomposition, (ii) Orthogonalization of FALDI matrices and FALDI natural density functions, (iii) Exclusive localization and delocalization indices, (iv) Classification of FALDI components as bonding, nonbonding and antibonding, (v) FALDI decomposition of the gradient of the total electron density, and (vi) Conformational deformation densities. This chapter also briefly comments on the computational implementation of FALDI.

Chapter 3, titled "Exact and Exclusive Localization Indices within QTAIM Atomic Basins", investigates the supposed exclusivity of QTAIM-defined LIs and DIs, and provides expressions for calculating truly exclusive measures of atomic electron (de)localization using FALDI. The concept of natural density functions (NDFs) is introduced, which provides a decomposition of FALDI's localized and delocalized electron density distributions into mostly orthogonal functions. Lack of exclusivity of orthodox QTAIM LIs and DIs is shown, together with the utility which the FALDI indices provide, on a number of small molecules.

Chapter 4, titled "FALDI-based Decomposition of an Atomic Interaction Line Leads to 3D Representation of the Multicenter Nature of Interactions", decomposes the electron density along a vector perpendicular to an internuclear vector into FALDI components. This paper introduces a classification of FALDI components, based on whether a specific component

concentrates, depletes or removes electron density in an internuclear region. We link the classification scheme to the formation of an AIL, and show that some components facilitate whereas other components hinder AIL formation. In this manner we show that many AILs should not be seen as a bicentric topological feature, but rather as an indication of a multi-centre interaction. We also link our classification scheme to the interference patterns of overlapping molecular orbitals, and therefore are able to classify each FALDI component as bonding, nonbonding or antibonding. We test a number of different atomic interactions, including an intramolecular H-bond, classical covalent bonds and organometallic carbene bonds.

Chapter 5, titled “FALDI-Based Criterion for and the Origin of an Electron Density Bridge with an Associated (3,-1) Critical Point on Bader’s Molecular Graph”, introduces an expression known as the $CP(\mathbf{r})$ function – a tool and methodology which can be used to investigate why AILs are present in some systems but absent in others. We build on the bonding, nonbonding and antibonding classification of FALDI components used in Chapter 4, and decompose the gradient of the electron density in a number of systems where changes in molecular composition leads to the appearance or disappearance of an AIL. Three types of intramolecular interactions are investigated – an attractive and classical H-bond, a repulsive O...O interaction and an attractive Cl...Cl interaction – and we show that the presence of an AIL for these interactions is a result of a larger rate of change of density of a bonding nature relative to density of a nonbonding or antibonding nature. We argue again that chemical interactions should always be considered on a multicentre basis, due to the holistic nature of the wavefunction. In addition, we relate the nature of FALDI’s bonding, nonbonding and antibonding distributions to both (i) physical forces acting on nuclei, and (ii) interference patterns of molecular orbitals overlapping simultaneously over multiple atomic basins.

Chapter 6, titled “Towards Deformation Densities for Intramolecular Interactions without Radical States using the Fragment, Atomic, Localized, Delocalized and Interatomic (FALDI) Charge Density Decomposition Scheme”, describes an approach for calculating the deformation density as a result of conformational change. This manuscript also introduced the FALDI decomposition scheme, designed originally for the application of conformational deformation densities. This work compares deformation densities for intramolecular interactions calculated in the orthodox manner, *i.e.* using radical states produced upon fragmenting a molecule, and the novel conformational deformation density approach. Using a number of small molecules with weak, intramolecular interactions, we show that the underlying

assumption of fragment-based deformation density schemes – that the presence of a radical in the reference state does not alter the deformation density significantly – is incorrect. We also show how the conformational deformation density, and its natural decomposition into FALDI components, can be a very useful tool for studying both inter- and intramolecular interactions.

Chapter 7, titled “Exploring Fundamental Differences between Red- and Blue-shifted Intramolecular Hydrogen Bonds using FAMSEC, FALDI, IQA and QTAIM”, uses the conformational deformation density developed in Chapter 6 to study the intramolecular H-bond which forms in some conformers of the amino acid β -alanine. We selected two conformers, where one conformer shows a distinct red-shifted H-bond and the other a distinct blue-shifted H-bond. We found, in contrast to the dominant trend in literature, that the nature of the H-bonds differs *fundamentally*, both locally and in terms of how the atoms involved in H-bonding interact with the remainder of the molecule. We also combine our FALDI density decomposition with other techniques, which are energy decompositions, in order to arrive at a very in-depth description of the H-bonds in β -alanine.

Chapter 8, Conclusions, conclude the major output of this work, and comment on the implications, and future work of the FALDI density decomposition scheme.

Appendix I, titled “Evaluating Common QTAIM and NCI Interpretations of the Electron Density Concentration through IQA Interaction Energies and 1D Cross-Sections of the Electron and Deformation Density Distributions.”, introduced a method for measuring the electron density along the vector associated with the λ_2 eigenvalue of the Hessian matrix. We used this approach to investigate how electron density is concentrated or depleted across an internuclear vector in a number of cases showing ‘controversial’ AILs. We concluded that AILs, as well as another QCT technique, the Non-Covalent Interactions (NCI) approach, should be interpreted with some care. We also suggested that the deformation density is a much more informative measure of an accumulation of density as an indication of bonding than the partial second derivative of the electron density.

Appendix II, titled “Synthesis, Structure and DFT Study of Asymmetrical NHC Complexes of Cymantrene Derivatives and their Application in the Dehydrogenative Dimerization Reaction of Thiols.”, is a joint synthetic and computational study on novel organometallic complexes. The part of this study which is significant to this thesis is a calculation and decomposition of the binding energies as well as deformation densities of a number of carbene complexes using the Extended Transition State coupled with Natural Orbitals for Chemical Valence (ETS-NOCV) energy and charge decomposition technique. ETS-NOCV is an

extremely useful analytical tool in computational chemistry, but uses orthodox fragments, often containing un-chemical reference states, in describing intramolecular bonds. In light of our conclusions in Chapters 6 and 7, this work is included in order to show what we wish to accomplish with FALDI conformational deformation densities as well as static density analysis, and we will revisit this work in the future.

Appendix III, titled “Gold (I) Hydrides as Proton Acceptors in Dihydrogen Bond Formation”, is a theoretical study of Au^I complexes with anionic dihydrides using QTAIM, FAMSEC and ETS-NOCV. Again, like Appendix II, this study was performed and published while we were developing FALDI, and we will return to this topic using the tools developed within this thesis.

1.7. A note on the historical development of FALDI

The development of the full set of FALDI tools occurred in a number of increments across multiple publications. The chapters in this thesis are grouped by theme, and not necessarily in the order in which they were published. As a result, some of the chapters reference work written in an earlier publication even though it is presented here in a later chapter. We therefore briefly discuss here the order in which the chapters were published in.

We originally showed a number of problems related to the interpretation of AILs using 1D cross-sections of the electron and deformation densities, published in 2015 and presented here in Appendix I. Stemming from this work, we set out to develop a methodology for calculating deformation densities resulting from conformational change in order to accurately study the formation of intramolecular interactions. We realized early on that a suitable density decomposition technique is a necessary requirement for calculating conformational deformation densities, and developed the FALDI density decomposition scheme. The first incarnation of the FALDI scheme was submitted in 2016, and published in early 2017, as part of our approach for calculating conformational deformation densities. This work is presented in Chapter 6. We note that this publication described additional FALDI components which we have not used again in subsequent publications. We followed on this work with an application of the FALDI conformational deformation densities on H-bond formation as a part of an invited article to a special edition of *Structural Chemistry*, and this work was published middle 2017 and is presented in Chapter 7.

During the development of FALDI we realized that while the scheme is a necessary component for the calculation of deformation densities, it could also be used to study and

decompose static electron density distributions. We then used the FALDI scheme to study the multi-centre natures of AILs and investigate the link between FALDI and molecular orbital bonding models, which resulted in a publication which was submitted in late 2017 and published early 2018. This work is presented in Chapter 4. We also noticed an alarming trend with regards to FALDI's localized density distributions – that these distributions also describe, to a certain degree, delocalized electrons. We realized that this non-exclusivity of FALDI distributions is related to the manner in which QTAIM LIs and DIs are calculated. We addressed this issue and developed truly exclusive FALDI distributions, as well as exclusive LIs and DIs. This work was published early in 2018, and is presented as the penultimate work of this thesis in Chapter 3. Finally, we revisited our research on the nature of AILs, but using the extended and exclusive FALDI distributions, and a manuscript describing an indicator of AILs has been submitted for publication and is presented in Chapter 5.

References

1. J. Schummer. *Endeavour* **2003**, 27, 37-41.
2. C. F. Matta. *Found Chem* **2013**, 15, 245-251.
3. H. Primas. In *Chemistry, quantum mechanics and reductionism: perspectives in theoretical chemistry*; Springer Science & Business Media, **2013**.
4. S. J. Weininger. *J. Chem. Educ.* **1984**, 61, 939.
5. B. N. Figgis. *Comprehensive Coordination Chemistry* **1987**, 1, 213-279.
6. K. Fukrd; T. Yomezawa; H. Skrlnga. *Chem. Phys* **1952**, 20, 722-725.
7. G. Frenking; A. Krapp. *J. Comput. Chem.* **2007**, 28, 15-24.
8. S. Shaik. *J. Comput. Chem.* **2007**, 28, 51-61.
9. W. Moffitt. *Proc. R. Soc. Lond. A* **1950**, 202, 534-547.
10. C. A. Coulson. In *Valence*; Clarendon Press, 1956.
11. R. Mulliken. *J. Chem. Phys.* **1955**, 23, 1841-1846.
12. R. Mulliken. *J. Chem. Phys.* **1955**, 23, 2338-2342.
13. R. Mulliken. *J. Chem. Phys.* **1955**, 23, 2343-2346.
14. R. Mulliken. *J. Chem. Phys.* **1955**, 23, 397-398.
15. R. S. Mulliken. *J. Chem. Phys.* **1955**, 23, 1833-1840.
16. F. L. Hirshfeld. *Theoretica chimica acta* **1977**, 44, 129-138.
17. R. F. Bader; C. F. Matta. *J. Phys. Chem. A* **2004**, 108, 8385-8394.
18. P. Bultinck; C. Van Alsenoy; P. W. Ayers; R. Carbó-Dorca. *J. Chem. Phys.* **2007**, 126, 144111.
19. T. C. Lillestolen; R. J. Wheatley. *Chem. Commun.* **2008**, 5909-5911.
20. R. F. Bader. In *Atoms in molecules*; Wiley Online Library, **1990**.

21. P. L. Popelier. In *The Chemical Bond II*; Springer, **2016**, p 71-117.
22. C. F. Matta; R. F. Bader. *J. Phys. Chem. A* **2006**, *110*, 6365-6371.
23. R. Bader. *Can. J. Chem.* **1986**, *64*, 1036-1045.
24. F. De Proft; C. Van Alsenoy; A. Peeters; W. Langenaeker; P. Geerlings. *J. Comput. Chem.* **2002**, *23*, 1198-1209.
25. C. Fonseca Guerra; J. W. Handgraaf; E. J. Baerends; F. M. Bickelhaupt. *J. Comput. Chem.* **2004**, *25*, 189-210.
26. A. Haaland; T. Helgaker; K. Ruud; D. Shorokhov. *J. Chem. Educ.* **2000**, *77*, 1076.
27. F. Jensen. In *Introduction to computational chemistry*; John Wiley & Sons, **2017**.
28. S. Grimme; C. Mück-Lichtenfeld; G. Erker; G. Kehr; H. Wang; H. Beckers; H. Willner. *Angew. Chem. Int. Ed.* **2009**, *48*, 2592-2595.
29. A. Krapp; G. Frenking. *Chem. Eur. J.* **2007**, *13*, 8256-8270.
30. J. Poater; M. Solà; F. M. Bickelhaupt. *Chem. Eur. J.* **2006**, *12*, 2889-2895.
31. J. Poater; M. Solà; F. M. Bickelhaupt. *Chem. Eur. J.* **2006**, *12*, 2902-2905.
32. J. Poater; R. Visser; M. Sola; F. M. Bickelhaupt. *J. Org. Chem.* **2007**, *72*, 1134-1142.
33. C. Foroutan-Nejad; S. Shahbazian; R. Marek. *Chem. Eur. J.* **2014**, *20*, 10140-10152.
34. R. F. Bader. *J. Phys. Chem. A* **2009**, *113*, 10391-10396.
35. R. F. Bader; T. H. Tang; Y. Tal; F. W. Biegler-Koenig. *J. Am. Chem. Soc.* **1982**, *104*, 946-952.
36. G. Runtz; R. Bader; R. Messer. *Can. J. Chem.* **1977**, *55*, 3040-3045.
37. L. J. Farrugia; C. Evans; M. Tegel. *J. Phys. Chem. A* **2006**, *110*, 7952-7961.
38. J. R. Lane; J. Contreras-García; J.-P. Piquemal; B. J. Miller; H. G. Kjaergaard. *J. Chem. Theory Comput.* **2013**, *9*, 3263-3266.
39. S. Shahbazian. *Chem. Eur. J.* **2018**, doi: 10.1002/chem.201705163.
40. R. F. Bader; M. E. Stephens. *J. Am. Chem. Soc.* **1975**, *97*, 7391-7399.
41. R. Daudel; R. Bader; M. Stephens; D. Borrett. *Can. J. Chem.* **1974**, *52*, 1310-1320.
42. C. F. Matta; R. J. Boyd. In *An introduction to the quantum theory of atoms in molecules*; Wiley Online Library, **2007**.
43. C. L. Firme; O. Antunes; P. M. Esteves. *Chem. Phys. Lett.* **2009**, *468*, 129-133.
44. C. F. Matta; J. Hernández-Trujillo. *J. Phys. Chem. A* **2005**, *109*, 10798-10798.
45. C. F. Matta; J. Hernández-Trujillo; T. H. Tang; R. F. Bader. *Chem. Eur. J.* **2003**, *9*, 1940-1951.
46. R. F. Bader. *Monatshefte für Chemie/Chemical Monthly* **2005**, *136*, 819-854.
47. F. Cortés-Guzmán; R. F. Bader. *Coord. Chem. Rev.* **2005**, *249*, 633-662.
48. X. Fradera; M. A. Austen; R. F. Bader. *J. Phys. Chem. A* **1999**, *103*, 304-314.
49. I. Sumar; R. Cook; P. W. Ayers; C. F. Matta. *Comput. Theor. Chem.* **2015**, *1070*, 55-67.
50. P. L. Ayers; R. J. Boyd; P. Bultinck; M. Caffarel; R. Carbó-Dorca; M. Causá; J. Cioslowski; J. Contreras-García; D. L. Cooper; P. Coppens. *Comput. Theor. Chem.* **2015**, *1053*, 2-16.

51. I. Cukrowski; J. H. de Lange; A. S. Adeyinka; P. Mangondo. *Comput. Theor. Chem.* **2015**, *1053*, 60-76.
52. R. P. Feynman. *Physical Review* **1939**, *56*, 340.
53. M. P. Mitoraj; A. Michalak; T. Ziegler. *J. Chem. Theory Comput.* **2009**, *5*, 962-975.
54. I. Cukrowski; D. M. van Niekerk; J. H. de Lange. *Struct. Chem.* **2017**, *28*, 1429-1444.
55. J. H. De Lange; I. Cukrowski. *J. Comput. Chem.* **2018**, doi: 10.1002/jcc.25223.
56. J. H. de Lange; D. M. van Niekerk; I. Cukrowski. *J. Comput. Chem.* **2018**, *39*, 973-985.
57. J. H. Lange; I. Cukrowski. *J. Comput. Chem.* **2017**, *38*, 981-997.
58. R. Ponec. *J. Math. Chem.* **1997**, *21*, 323-333.
59. R. Ponec. *J. Math. Chem.* **1998**, *23*, 85-103.
60. R. Ponec; D. L. Cooper. *J. Phys. Chem. A* **2007**, *111*, 11294-11301.

Chapter 2: Theoretical background and developments

Introduction

The primary novel development of this work is the derivation and implementation of the Fragment, Atomic, Localized, Delocalized and Interatomic (FALDI) density decomposition scheme.¹⁻⁴ The FALDI scheme, at its current development, has many different aspects related to calculation and decomposition of either deformation densities or static densities. Each of the aspects of FALDI and its applications are described separately, in publication form, in the various chapters of this thesis. This chapter serves as a consolidation of FALDI in its entirety. In addition, FALDI has gone through several developments as each aspect was published, with later developments also serving as an improvement of earlier aspects. This chapter will lay down a logical overview of FALDI in its current form, regardless of the historical timeline of its development.

The FALDI scheme is rooted in the first- and second-order density matrices, domain-averaged exchange-correlation electron holes, electron (de)localization, deformation densities and atoms-in-molecules atomic volumes. Section 2.1 of this chapter serves as a background to the reader, and will cover a brief background of the topics relevant to the discussion of FALDI. Specifically, the topics which will be covered in Section 2.1. are: (i) The electron density, (ii) The pair-density and electron holes, (iii) The Quantum Theory of Atoms in Molecules, (iv) Extended population analysis within QTAIM and (v) Domain Averaged Fermi Holes. Note that foundational quantum chemical theory, and specifically methods for approximating and calculating electronic structures will not be covered in this thesis. For interested readers we recommend Szabo and Ostlund⁵ as very good reference material.

Section 2.2 will cover the derivation, implementation and implications of FALDI itself. Specifically, the topics which will be covered in Section 2.2 are, in the discussed order: (i) the general FALDI decomposition, (ii) FALDI exclusive (de)localization indices and distributions, (iii) a classification scheme for identifying FALDI components as bonding, non-bonding and anti-bonding, (iv) the $CP(r)$ function, a tool for investigating the origins of atomic interaction lines, and (v) FALDI deformation densities.

2.1. Theoretical background

2.1.1. The electron density

The first-order electron density is a scalar distribution describing the probability of finding any of N electrons with arbitrary spin at a given coordinate in real-space, normalized to N . It arises from the probability interpretation of the square of the wavefunction, and the most general manner in which it can be calculated is by integrating the square of the wavefunction over all spin coordinates and all but one spatial coordinate and then normalizing to N :

$$\rho(\mathbf{r}) = N \int \Psi^*(\mathbf{x}_1, \mathbf{x}_2, \dots, \mathbf{x}_N) \Psi(\mathbf{x}_1, \mathbf{x}_2, \dots, \mathbf{x}_N) ds_1 dx_2 \dots dx_N \quad (1)$$

Eq. 1 is useful in general and illustrates the interpretation of the electron density (ED). In general though, the N -electron wavefunction is usually expressed in terms of a number (N) of 1-electron functions known as spin-orbitals (also called molecular orbitals, MO), which themselves are expressed as linear combinations of multiple basis functions. Spin-orbitals can take a variety of forms, from canonical MOs expressing the wavefunction as a single Slater determinant through Kohn-Sham orbitals used in Density Functional Theory (DFT), to MOs expressed as natural orbitals for wavefunctions containing multiple Slater determinants. Using the Müller approximation,⁶ the ED can be expressed in terms of weighted spin-orbitals:

$$\rho(\mathbf{r}) = \sum_i^{N_{MO}} v_i |\chi_i(\mathbf{r})|^2 \quad (2)$$

where $\chi_i(\mathbf{r})$ is the i th MO, v_i its occupation and N_{MO} the total number of occupied MOs. For restricted Hartree-Fock and DFT wavefunctions, v_i will be equal to two for all i and $N_{MO} = N/2$. For multi-determinant wavefunctions within the natural orbital expression, v_i is equal to the partial occupation of each spin-orbital.

The ED is an extremely critical element of quantum chemistry. It provides a spin-independent description of the average electron distribution in a molecule and can therefore be associated with a very large range of chemical phenomena. The ED is comparable to the wavefunction itself in that many physical properties of a specific state are inherently described by the ED alone. In addition, the ED is a quantum mechanical observable and can therefore be experimentally determined through, *e.g.* X-ray diffraction.

2.1.2. The pair density and electron holes

One of the biggest complexities in quantum chemistry is the particle-wave duality, as it requires that we have to treat all the particles in a chemical system (specifically electrons within the Born-Oppenheimer approximation) as both particles and waves. This requirement excludes the consideration of an independent particle model, which would've greatly simplified any chemical modelling, but rather necessitates explicit inclusion of correlation of electron positions and momenta. Inclusion of electron correlation in electron structure calculations is well-documented, and is the *raison d'être* for the Hartree-Fock (HF) approximation, DFT as well as post-SCF methods. Here, we are specifically interested in exploring how electron correlation affects the distribution of electrons throughout a chemical system.

The ED in Eqs. 1 and 2 is a first-order scalar field, which implicitly rather than explicitly depends on the correlated movement of electrons, *i.e.* if the wavefunction is correlated, the ED will represent the probability distribution as affected by averaged correlation effects. A correlated wavefunction (regardless of the degree of approximation) depends on all spatial and spin coordinates of all electrons simultaneously, and the position or momentum of a single electron will therefore simultaneously affect the distribution of all other electrons – an effect which is not immediately apparent in the ED.

A second order electron density is easily defined in the same fashion as Eq. 1:

$$\rho_2(\mathbf{x}_1, \mathbf{x}_2) = N(N - 1) \int \Psi^*(\mathbf{x}_1, \mathbf{x}_2, \dots, \mathbf{x}_N) \Psi(\mathbf{x}_1, \mathbf{x}_2, \dots, \mathbf{x}_N) d\mathbf{x}_3 \dots d\mathbf{x}_N \quad (3)$$

where the integration is over all but two spin-spatial coordinates. $\rho_2(\mathbf{x}_1, \mathbf{x}_2)$ is known as the pair-density (PD) and represents the probability of finding two electrons with spins σ_1 and σ_2 simultaneously at \mathbf{r}_1 and \mathbf{r}_2 . Note that we have used \mathbf{x}_1 and \mathbf{x}_2 instead of \mathbf{r} as the function's variables; where the ED in Eq.1 is a spin-independent quantity, the pair-density explicitly depends on the spins of both electrons. Finally, the $N(N - 1)$ normalization factor ensures that the PD is normalized to the correct number of electron pairs. For the remainder of this chapter, we will consider the PD without the effects of electron spin, unless explicitly stated, hence we will only consider the spinless PD obtained by integrating over the spin of two coordinates of Eq. 3, $\rho_2(\mathbf{r}_1, \mathbf{r}_2) = N(N - 1) \int \Psi^*(\mathbf{x}_1, \mathbf{x}_2, \dots, \mathbf{x}_N) \Psi(\mathbf{x}_1, \mathbf{x}_2, \dots, \mathbf{x}_N) d\omega_1 d\omega_2 d\mathbf{x}_3 \dots d\mathbf{x}_N$.

The PD allows us to investigate the effects of electron correlation directly. It can be calculated from the first order EDs and a correlation factor:

$$\rho_2(\mathbf{r}_1, \mathbf{r}_2) = \rho(\mathbf{r}_1)\rho(\mathbf{r}_2)[1 + f(\mathbf{r}_1; \mathbf{r}_2)] \quad (4)$$

If electrons were truly independent, *i.e.* marble-like point charges, then the PD would simply be equal to the product of two electrons at two spatial coordinates, independent of spin, *i.e.* $f(\mathbf{r}_1; \mathbf{r}_2) = 0$. The probability of finding two electrons simultaneously at \mathbf{r}_1 and \mathbf{r}_2 would be exactly the non-correlated product of finding each electron separately at the two coordinates, if electron movement was truly independent. In a correlated wavefunction, $f(\mathbf{r}_1; \mathbf{r}_2) \neq 0$ and the PD is either larger or smaller than the product of the first-order densities. Usually, electron correlation leads to a *reduction* of the PD, especially when \mathbf{r}_1 is close to \mathbf{r}_2 . It is prudent to define a conditional probability, *i.e.* the probability of finding an electron at \mathbf{r}_1 if an electron is already known to be at \mathbf{r}_2 :

$$\rho^{cond}(\mathbf{r}_1; \mathbf{r}_2) = \frac{\rho_2(\mathbf{r}_1, \mathbf{r}_2)}{\rho(\mathbf{r}_2)} \quad (5)$$

Again, if electrons were fully independent, then $\rho^{cond}(\mathbf{r}_1; \mathbf{r}_2) = \rho(\mathbf{r}_1)$; in other words, the ED at \mathbf{r}_1 would be unaffected regardless of the remaining electron positions. The difference between the uncorrelated and correlated $\rho^{cond}(\mathbf{r}_1; \mathbf{r}_2)$ for finding an electron at \mathbf{r}_1 describes how electron correlation changes the conditional probability:

$$\rho^{Hole}(\mathbf{r}_1; \mathbf{r}_2) = \rho(\mathbf{r}_1) - \frac{\rho_2(\mathbf{r}_1, \mathbf{r}_2)}{\rho(\mathbf{r}_2)} \quad (6)$$

This pseudo 2nd-order distribution is known as the *electron hole function*, or more commonly as the exchange-correlation (XC) hole. The XC-hole describes how the ED is diminished or increased at \mathbf{r}_1 due to the presence of a reference electron at \mathbf{r}_2 . Since electron correlation usually leads to decreased ED in the vicinity of the reference electron, the XC-hole commonly describes how an electron is *excluded* at \mathbf{r}_1 due to the reference electron. In addition, the XC-hole results in exactly -1 when integrated over all space – that is to say, if an electron is known to be at \mathbf{r}_2 , it cannot be found anywhere else and a single electron is entirely excluded from the remainder of the molecule.

Wavefunctions built from spin-orbitals generally need to account for two types of electron correlation. The first is *Fermi* or *exchange* electron correlation that is a spin-dependent property arising from the antisymmetry of a wavefunction. Specifically, and very importantly, Fermi correlation applies only to electrons of the same spin. Exchange electron correlation is a purely quantum mechanical term, and can best be understood by investigating the PD in a 2 electron, antisymmetric, single determinant wavefunction. We consider first the case of a single determinant (SD) wavefunction containing two electrons of opposite spin:

$$\Psi_{\text{SD}}^{\sigma_1 \neq \sigma_2} = \frac{1}{\sqrt{2}} [\phi_a(\mathbf{r}_1)\alpha(\omega_1)\phi_b(\mathbf{r}_2)\beta(\omega_2) - \phi_a(\mathbf{r}_2)\alpha(\omega_2)\phi_b(\mathbf{r}_1)\beta(\omega_1)] \quad (7)$$

where $\phi(\mathbf{r})$ are spatial orbitals, $\alpha(\omega)$ and $\beta(\omega)$ are spin functions and the determinant has been expanded. The PD – the probability of finding an electron with spin s_1 at \mathbf{r}_1 and an electron with spin s_2 at \mathbf{r}_2 – for $\Psi_{\text{SD}}^{\sigma_1 \neq \sigma_2}$ is equal to the square of the wavefunction:

$$\begin{aligned} \rho_2(\mathbf{x}_1, \mathbf{x}_2) &= \frac{1}{2} [|\phi_a(\mathbf{r}_1)|^2 |\alpha(\omega_1)|^2 |\phi_b(\mathbf{r}_2)|^2 |\beta(\omega_2)|^2 \\ &\quad + |\phi_a(\mathbf{r}_2)|^2 |\alpha(\omega_2)|^2 |\phi_b(\mathbf{r}_1)|^2 |\beta(\omega_1)|^2 \\ &\quad - 2\phi_a(\mathbf{r}_1)\alpha(\omega_1)\phi_b(\mathbf{r}_1)\beta(\omega_1)\phi_b(\mathbf{r}_2)\beta(\omega_2)\phi_a(\mathbf{r}_2)\alpha(\omega_2)] \end{aligned} \quad (8)$$

The spin-independent density can be obtained by integrating over the spins:

$$\begin{aligned} \int \rho_2(\mathbf{x}_1, \mathbf{x}_2) d\omega_1 d\omega_2 &= \frac{1}{2} [|\phi_a(\mathbf{r}_1)|^2 |\phi_b(\mathbf{r}_2)|^2 + |\phi_a(\mathbf{r}_2)|^2 |\phi_b(\mathbf{r}_1)|^2 + 0] \\ &= \rho(\mathbf{r}_1)\rho(\mathbf{r}_2) \end{aligned} \quad (9)$$

where we have used the orthonormality condition for integration of two spin functions, *i.e.* $\langle \alpha | \alpha \rangle = 1$, $\langle \beta | \beta \rangle = 1$ and $\langle \alpha | \beta \rangle = 0$. The PD for $\Psi_{\text{SD}}^{\sigma_1 \neq \sigma_2}$ therefore reduces to the totally uncorrelated product of the 1st-order EDs at \mathbf{r}_1 and \mathbf{r}_2 . Therefore, in a single-determinant wavefunction (such as for the HF approximation), electrons of opposite spin are entirely independent.

For a 2-electron wavefunction with electrons of parallel spin, $\Psi_{\text{SD}}^{\sigma_1 = \sigma_2}$, the PD is:

$$\begin{aligned} \rho_2(\mathbf{x}_1, \mathbf{x}_2) &= \frac{1}{2} [|\phi_a(\mathbf{r}_1)|^2 |\alpha(\omega_1)|^2 |\phi_b(\mathbf{r}_2)|^2 |\alpha(\omega_2)|^2 \\ &\quad + |\phi_a(\mathbf{r}_2)|^2 |\alpha(\omega_2)|^2 |\phi_b(\mathbf{r}_1)|^2 |\alpha(\omega_1)|^2 \\ &\quad - 2\phi_a(\mathbf{r}_1)\alpha(\omega_1)\phi_b(\mathbf{r}_1)\alpha(\omega_1)\phi_b(\mathbf{r}_2)\alpha(\omega_2)\phi_a(\mathbf{r}_2)\alpha(\omega_2)] \end{aligned} \quad (10)$$

and integrating the spins out,

$$\begin{aligned} \int \rho_2(\mathbf{x}_1, \mathbf{x}_2) d\omega_1 d\omega_2 &= \frac{1}{2} [|\phi_a(\mathbf{r}_1)|^2 |\phi_b(\mathbf{r}_2)|^2 + |\phi_a(\mathbf{r}_2)|^2 |\phi_b(\mathbf{r}_1)|^2 \\ &\quad - 2\phi_a(\mathbf{r}_1)\alpha(\omega_1)\phi_b(\mathbf{r}_1)\alpha(\omega_1)\phi_b(\mathbf{r}_2)\alpha(\omega_2)\phi_a(\mathbf{r}_2)\alpha(\omega_2)] \end{aligned} \quad (11)$$

is not equal to the product of 1st-order EDs at \mathbf{r}_1 and \mathbf{r}_2 . Therefore, in a single-determinant wavefunction, electrons of the same spin *are* correlated, and the conditional probability of finding an electron at \mathbf{r}_1 if an electron of the same spin is at \mathbf{r}_2 will be less than $\rho(\mathbf{r}_1)$.

Where Fermi correlation arises from the spins of electrons, *Coulomb* correlation arises from the instantaneous electrostatic repulsion between electrons. Spin-orbitals are inherently independent from each other, and as such, the electron-electron repulsion is calculated as an average between all spin-orbitals. However, in reality, electrons (regardless of spin) will experience both greater and weaker electron-electron repulsion than the average as they move around through space. Such instantaneous repulsions will change the PD – the probability of finding two electrons simultaneously at \mathbf{r}_1 and \mathbf{r}_2 will be much less than what the average would suggest if \mathbf{r}_1 and \mathbf{r}_2 were close together, independent of their spin. HF wavefunctions do not account for this effect at all, and only treat electron-electron repulsion in an averaged manner. The density distributions for HF wavefunctions are therefore entirely independent in terms of Coulomb correlation, whereas post-SCF corrections and multi-determinant wavefunctions account for Coulomb correlation in varying degrees.

The XC-hole describes the exclusion of an electron at \mathbf{r}_1 due to an electron at \mathbf{r}_2 resulting from both Fermi and Coulomb correlation. Hence, the XC-hole can be decomposed into a Fermi hole, $h_x(\mathbf{r}_1; \mathbf{r}_2)$ as well as a Coulomb hole, $h_c(\mathbf{r}_1; \mathbf{r}_2)$. The Fermi hole arises due to the antisymmetry of the wavefunction and can be directly related to the Pauli exclusion principle. The Fermi hole describes the exclusion of an electron of the same spin as the reference electron, and integrates to exactly -1 . In addition, the Fermi hole is always negative, and therefore always reduces the probability of finding another electron close to the reference electron. In this regard, the presence of the Fermi hole *reduces* the average electron-electron repulsion experienced by an electron in a spin-orbital. Such a reduction of the electron-electron repulsion is known as the *exchange* energy, and is an important component in covalent bonding.

On the other hand, the Coulomb hole arises from electrostatic correlation, and is typically much more difficult to calculate (as well as approximate) than the Fermi hole. The Coulomb hole integrates to exactly 0. In other words, if the Coulomb hole leads to a reduced probability of finding an electron at \mathbf{r}_1 relative to \mathbf{r}_2 , then an increased probability will be seen elsewhere in the molecule. Generally, the Coulomb hole also leads to reduced electron-electron repulsion, since regions where $h_c(\mathbf{r}_1; \mathbf{r}_2) < 0$ will be commonly seen when \mathbf{r}_1 and \mathbf{r}_2 are close together, whereas regions where $h_c(\mathbf{r}_1; \mathbf{r}_2) > 0$ generally occur when \mathbf{r}_1 and \mathbf{r}_2 are far apart and with a lesser influence on the electron-electron repulsion.

Both Fermi and Coulomb holes can have very complex and interesting distributions, and often can be unexpected and counter-intuitive. However, it is important to note that $h_x(\mathbf{r}_1; \mathbf{r}_2)$ and $h_c(\mathbf{r}_1; \mathbf{r}_2)$ can interact with each other, such that $h_c(\mathbf{r}_1; \mathbf{r}_2) > 0$ when the Fermi hole is

very large. Therefore, it is only the exchange-correlation hole, as well as the total exchange-correlation energy, which is sensible to analyse. In general however, the Fermi hole dominates the total XC-hole, and since the Fermi and Coulomb holes integrate to -1 and 0 , respectively, the total XC-hole also integrates to -1 . As a result, the total XC-hole always reduces the total electron-electron repulsion, and reduces the total molecular energy.

Finally, it is important to note that the XC-hole can be seen as a measure of electron delocalization. Since the XC-hole in Eq. 6 provides the origin of the excluded electron at \mathbf{r}_1 , *i.e.* $\rho(\mathbf{r}_1)$ is reduced by the probability of an electron in volume element $d\mathbf{r}_2$ being found at \mathbf{r}_1 . Therefore, by keeping \mathbf{r}_2 constant but varying \mathbf{r}_1 , the XC-hole can give a pseudo-dynamic distribution of the electron in $d\mathbf{r}_2$ throughout all molecular space. Charge-weighting the XC hole by $\rho(\mathbf{r}_2)$, $\rho(\mathbf{r}_2)\rho^{Hole}(\mathbf{r}_1; \mathbf{r}_2)$, then gives the molecular-wide distribution of *all* electrons in $d\mathbf{r}_2$.

2.1.3 The Quantum Theory of Atoms in Molecules

Richard Bader developed the Quantum Theory of Atoms in Molecules (QTAIM)⁷ together with various co-workers over the course of three decades. QTAIM is an example of a theory of an atom-in-a-molecule; while there have been many attempts towards defining atoms in molecules, QTAIM has been proven to be robust, powerful and general. Bader has shown⁷ that the atomic definition within QTAIM is a form of a generalized quantum mechanics of open systems, of which the molecule as a whole is a special case. While we will review a few critical concepts from QTAIM in this section, interested readers can further consult Bader's book⁷ or a work edited by Matta *et al.*⁸

QTAIM defines atoms within molecules through the topology of the ED, and QTAIM has opened up the field of Quantum Chemical Topology (QCT).⁹ While the topology of the ED has many subtleties and fine structure, we are principally concerned with critical points (local maxima or minima) within the ED distribution. A critical point (CP) in the electron density at a coordinate \mathbf{r}_c is a local maximum, minimum or a saddle point where the first derivative (and each of its three components) vanishes:

$$\nabla\rho(\mathbf{r}_c) = \mathbf{i}\frac{\partial\rho}{\partial x} + \mathbf{j}\frac{\partial\rho}{\partial y} + \mathbf{k}\frac{\partial\rho}{\partial z} = 0 \quad (12)$$

Each CP is a local maximum or minimum along each of the three principle axes corresponding to maximum curvature. The type of CP can be determined by evaluating components of the Hessian matrix, which describe the partial second derivatives of the ED at \mathbf{r}_c :

$$\mathbf{A}(\mathbf{r}_c) = \begin{pmatrix} \frac{\partial^2 \rho}{\partial x^2} & \frac{\partial^2 \rho}{\partial x \partial y} & \frac{\partial^2 \rho}{\partial x \partial z} \\ \frac{\partial^2 \rho}{\partial y \partial x} & \frac{\partial^2 \rho}{\partial y^2} & \frac{\partial^2 \rho}{\partial y \partial z} \\ \frac{\partial^2 \rho}{\partial z \partial x} & \frac{\partial^2 \rho}{\partial z \partial y} & \frac{\partial^2 \rho}{\partial z^2} \end{pmatrix} \quad (13)$$

The Hessian matrix can be diagonalized to give three curvatures along the principle axes at \mathbf{r}_c , yielding three eigenvalues, λ_1 , λ_2 and λ_3 , and associated eigenvectors. The sign of each eigenvalue reveals whether \mathbf{r}_c is a local minimum or maximum along the associated eigenvector, where positive and negative eigenvalues relate to local minima and maxima, respectively.

Each CP can be classified according to its partial first and second derivatives, and is given a rank, ω , and signature, σ . The rank determines the number of non-zero curvatures (eigenvalues of the Hessian matrix). In other words, a rank of (+3) indicates that a CP is a local maximum or minimum in all three principle axes. The signature is the algebraic sum of the signs of the eigenvalues, and a signature of (-1) indicates that \mathbf{r}_c is a local minimum in one axis but a local maximum in the remaining two axes (+1 -1 -1 = -1). While many CPs of rank 1 and 2 exist in any ED distribution, only a number of CPs of rank 3 will exist, subject to the Poincaré-Hopf relationship,⁷ and rank 3 CPs are therefore of particular use in QCT.

The topology of the ED is generally dominated by the electrostatic attractive force between nuclei and electrons, and as such, every nuclear coordinate is marked by a (+3,-3) CP – a local maximum in all three principle axes. (+3,-1) CPs are often found between pairs of nuclei and are known as bond critical points (BCPs). CPs found within a ring of nuclei are (+3,+1) CPs, known as ring critical points (RCPs), and a CP enclosed by a number of ring critical points is always a (+3,+3) CP, known as a cage critical point (CCP).

The presence of (+3,-3) CPs at nuclear positions and BCPs, RCPs and CCPs at various internuclear separations lead to a natural partitioning of space into subspaces, Ω , known as an atomic basin, with each basin Ω containing only a single nucleus. The surfaces separating atomic basins are uniquely defined by the gradient vector field of the ED:



$$\nabla\rho(\mathbf{r}) \cdot \mathbf{n}(\mathbf{r}) = 0 \quad (14)$$

where \mathbf{r} belongs to a surface $S(\Omega)$ beholden to the above condition, and $\mathbf{n}(\mathbf{r})$ is a unit vector normal to $S(\Omega)$. Eq. 14 describes a zero-flux surface, *i.e.* the gradient crossing $S(\Omega)$ at any coordinate will be equal to 0, and no gradient vector originating from any (+3,-3) critical point will cross $S(\Omega)$. Eq. 14 also holds for \mathbf{r} as it approaches infinity, and $S(\Omega)$ therefore stretches to infinity as well.

The atomic basins Ω provide an exhaustive partitioning of all molecular space. Bader has shown that the kinetic energy operator is not well-defined for any arbitrary subspace of a molecule, and that it is only well defined when operating on the entire molecular space *or* an atomic basin Ω . Among other proofs, including a derivation from Schwinger's principle of stationary action, QTAIM atomic basins therefore provide a fundamental, quantum mechanical description of an atom in a molecule. As a result, QTAIM atomic basins allow for the partitioning of any molecular property into atomic contributions:

$$\langle \hat{O} \rangle_{molecule} = \sum_i^{M_{Nuclei}} O(\Omega_i) \quad (15)$$

where $\langle \hat{O} \rangle_{molecule}$ is the expectation value of an operator \hat{O} acting on the molecular wavefunction. QTAIM atomic basins therefore provide an additive atomic count of any molecular property, including the total number of electrons, N , or the molecular charge, q . Eq. 15 is an extremely powerful tool and link between molecular quantum chemistry, the molecular structure hypothesis¹⁰ and conceptual chemistry.

QCT has revealed a peculiar property regarding the ED distribution between nuclei. A BCP is always observed at the interface between two zero-flux surfaces (Eq. 14) outside of the limit at infinity, *i.e.* interatomic zero-flux surfaces. Two gradient vectors originate at each of the enclosed nuclei and terminate at the BCP. The path defined by these two vectors is known as an *atomic interaction line* (AIL, also known as a *bond path* or a *line path*¹¹). The ED is at a local maximum perpendicular to the AIL at each and every coordinate of the AIL – an AIL is therefore a *bridge of density*¹² connecting two nuclei. As stated in Chapter 1, and stressed in the remaining chapters of this thesis, an AIL is a remarkable yet still misunderstood property of the ED. The collection of AILs gives rise to a *molecular graph*, which defines QTAIM-based atomic connectivity.

Two of the eigenvalues of the Hessian matrix (λ_1 and λ_2) will be negative at each and every coordinate of an AIL, indicating a negative partial second derivative along the principle vectors perpendicular to the AIL itself. A negative partial second derivative at \mathbf{r} , $\frac{\partial^2 \rho(\mathbf{r})}{\partial \mathbf{r}^2}$, can be seen as a measure of local *concentration* of the ED, in that the ED at \mathbf{r} is greater than the average of its neighbouring coordinates along a specific vector.⁷ Along the AIL, the third eigenvalue of the Hessian matrix (λ_3) will always be positive, indicating a local *depletion* of ED. Generally, at a given coordinate \mathbf{r} along an internuclear vector and as long the two nuclei are not part of a cage, $\lambda_1 < 0$ and $\lambda_3 > 0$. The sign of the remaining eigenvalue, λ_2 , then generally determines whether ED is concentrated at \mathbf{r} relative to its neighbouring environment, thereby forming an AIL if a CP is present, or whether the ED is depleted. Such concentrations and depletions have been used extensively by both QTAIM and other QCT techniques, such as the Noncovalent Interactions (NCI) technique,^{13,14} to indicate ‘*attractive*’ or ‘*repulsive*’ interactions. However, we showed¹⁵ in Appendix 1 that measures of ED concentration utilising λ_2 is only a relative to the local environment where it is measured. In Section 2.2.4, we will expand on the use of λ_2 as an absolute measure of ED concentration/depletion.

2.1.4. QTAIM atomic overlap matrices, localization and delocalization indices

Any exhaustive, real-space definition of an atom in a molecule, such as QTAIM’s topological definition through Eq. 5, provides a measure of the *atomic electron population* of an atom by integrating the ED over the atomic basin:

$$N(A) = \int_A \rho(\mathbf{r}) d\mathbf{r} \quad (16)$$

where the integration is applied over $\Omega(A)$. $N(A)$ therefore relates the average number of electrons which can be found in $\Omega(A)$, and, in accordance with Eq. 15, the sum of all atomic populations gives the total number of electrons in the molecule, N . The electron population of an atom is also related to the atomic charge, $q(A) = Z(A) - N(A)$, where $Z(A)$ is the nuclear charge.

Since $\rho(\mathbf{r})$ can be expressed in terms of MOs (Eq. 2), the atomic population for atom A can be written in terms of MOs integrated over $\Omega(A)$:

$$N(A) = \sum_i^{N_{MO}} \int_A v_i |\chi_i(\mathbf{r})|^2 d\mathbf{r} \quad (17)$$

The integration of the overlap between all MO pairs over $\Omega(A)$ can be written as a matrix associated with atom A, \mathbf{S}^A , and is known as an *atomic overlap matrix* (AOM). The elements of an N_{MO} by N_{MO} atomic overlap matrix,

$$S_{ij}^A = \sum_{ij} \int_A \chi_i^*(\mathbf{r}) \chi_j(\mathbf{r}) d\mathbf{r} \quad (18)$$

provide information on how each normalized MO (diagonal elements) or a MO-pair (off-diagonal elements) contribute to the ED distribution of atom A. The atomic population is therefore simply the sum of diagonal elements of the AOM weighted by the corresponding occupations:

$$N(A) = \sum_i^{N_{MO}} v_i S_{ii}^A \quad (19)$$

The off-diagonal elements of each AOM, however, provide valuable information regarding the 2nd-order density distribution across the atom, *i.e.* how MOs interfere (de)constructively within $\Omega(A)$.^{16,17} Such information can be used to indicate the degree of localization or delocalization of electrons within the atomic basin. Specifically, by integrating the pair density across two domains simultaneously, the total electron delocalization between electrons in each basin can be calculated:

$$\begin{aligned} \delta(A, B) &= 2 \sum_{ij} \int_A d\mathbf{r}_1 \int_B d\mathbf{r}_2 \sqrt{v_i v_j} \{ \chi_i^*(\mathbf{r}_1) \chi_j(\mathbf{r}_1) \chi_j^*(\mathbf{r}_2) \chi_i(\mathbf{r}_2) \} \\ &= 2 \sum_{ij} \sqrt{v_i v_j} S_{ij}^A S_{ji}^B \end{aligned} \quad (20)$$

where we have used the definition for the elements of the AOM from Eq. 18. $\delta(A, B)$ is known as the delocalization index (DI)^{18,19} for atom pair A, B. Note also that the integrations can be swapped ($d\mathbf{r}_1$ over $\Omega(B)$, $d\mathbf{r}_2$ over $\Omega(A)$) which will give the equivalent number of electrons, indicating that the number of electrons found on average in $\Omega(A)$ but delocalized into $\Omega(B)$ is the same as the number of electrons found on average in $\Omega(B)$ but delocalized into $\Omega(A)$; hence, the factor of 2 in Eq. 20.

Similarly, the number of electrons localized in one specific basin can be calculated as well:

$$\begin{aligned}
\lambda(A) &= \sum_{ij} \int_A d\mathbf{r}_1 \int_A d\mathbf{r}_2 \sqrt{v_i v_j} \{ \chi_i^*(\mathbf{r}_1) \chi_j(\mathbf{r}_1) \chi_j^*(\mathbf{r}_2) \chi_i(\mathbf{r}_2) \} \\
&= \sum_{ij} \sqrt{v_i v_j} S_{ij}^A S_{ji}^A
\end{aligned} \tag{21}$$

where $\lambda(A)$ is the localization index (LI) of atomic basin $\Omega(A)$.^{18,19} LIs and DIs therefore give an indication of the number of electrons either localized to a specific basin or delocalized between two atomic basins, and are decomposition products of the total atomic electron population:

$$N(A) = \lambda(A) + \sum_{B \neq A}^{M-1} \frac{1}{2} \delta(A, B) \tag{22}$$

where M is the number of atomic basins in the molecule. That is, the number of electrons which can be found on average in $\Omega(A)$ is equal to the number of electrons which, supposedly, can only be found in $\Omega(A)$ (localized) and the number of electrons which can be found in all other atomic basins as well (delocalized). Note that in Chapter 3 the exclusivity of QTAIM-defined LIs is extensively investigated and we have found that these LIs quite often describe electrons that are significantly *delocalized*.² Finally, the DI correlates well with the expected bond order of most covalent bonds, and is often used as such for interpretive purposes. However, this correlation is also strange,² as the DI describes the number of electrons shared between two basins, whereas the bond order describes the number of electron *pairs* shared between two atoms. These observations are also investigated in Chapter 3.

2.1.5. Domain averaged Fermi Holes

The Domain Averaged Fermi Hole (DAFH) approach by Ponec and co-workers^{20,21} is a highly visual, interpretive technique aimed originally at exploring the distribution of an electron-pair where one electron is described by the averaged distribution within a specific domain in real-space. It has evolved quite a lot since its original inception in 1997 and 1998,^{20,21} and in modern days represents a very powerful tool for analysing and visualizing electron (de)localization in various, physically correct and chemically sensible modes.

The concept of DAFH is simple. Starting from the definition of the spinless XC-hole, Eq. 6, one of the coordinates is averaged over a specific domain in real space. While the domain can be chosen arbitrarily, it has been shown that QTAIM-based atomic domains (given by the

condition in Eq. 14) give chemically meaningful results.²² For the remainder of this work, we will always refer to DAFH as defined in terms of QTAIM-based atomic domains. The central quantity in DAFH, the $g_A(\mathbf{r})$ function,

$$g_A(\mathbf{r}_1) = \int_A \rho(\mathbf{r}_2) \rho^{\text{Hole}}(\mathbf{r}_1; \mathbf{r}_2) d\mathbf{r}_2 \quad (23)$$

integrates (averages) one of the spatial coordinates of the electron hole over a chosen atomic basin. The electron hole is weighted by the charge density at the averaged coordinate ($\rho(\mathbf{r}_2)$) in order to evaluate the total charge at \mathbf{r}_2 rather than just a single electron.

$g_A(\mathbf{r})$ gives the number of electrons excluded at \mathbf{r} due to XC effects as a result of the electrons found on average in $\Omega(A)$. Since the domain-averaged XC-hole calculates the origin of the excluded electrons (*i.e.*, the electrons residing in $\Omega(A)$), $g_A(\mathbf{r})$ can also be interpreted as a pseudo-dynamic probability density of the electrons in $\Omega(A)$, and provides a normalized probability of finding any of the electrons found on average in $\Omega(A)$ at any given coordinate \mathbf{r} , even if $\mathbf{r} \notin \Omega(A)$. In other words, $g_A(\mathbf{r})$ gives the contribution at \mathbf{r} by atom A as a result of delocalized electron distributions, which automatically leads to a complete decomposition of the electron density at \mathbf{r} :

$$\rho(\mathbf{r}) = \sum_A^M g_A(\mathbf{r}) \quad (24)$$

A few interesting relationships can be drawn between DAFH's $g_A(\mathbf{r})$ and the QTAIM populations described in section 2.1.4:

- (i) Integration of $g_A(\mathbf{r})$ over *all* molecular space yields the atomic population, $N(A)$ (Eq. 16):

$$N(A) = \int_A \rho(\mathbf{r}) d\mathbf{r} = \int_{-\infty}^{\infty} g_A(\mathbf{r}) d\mathbf{r} \quad (25)$$

Interpreting Eq. 25 can, at first, seem strange, as it suggests that the same number of electrons which are found, on average, in $\Omega(A)$ can also be found throughout the molecule. Where $N(A)$ measures the static, first-order electron density and gives the average electrons found in $\Omega(A)$, $g_A(\mathbf{r})$ measures how these same electrons are delocalized throughout the molecule as a result of XC effects. $g_A(\mathbf{r})$ therefore represents a pseudo-2nd order, real-space distribution of the $N(A)$ electrons.

- (ii) Integration of $g_A(\mathbf{r})$ over only $\Omega(A)$ gives the QTAIM-defined localization index,

$$\lambda(A) = \int_A g_A(\mathbf{r}) d\mathbf{r} \quad (26)$$

which, supposedly, gives the number of electrons localized to $\Omega(A)$. If $N(A)$ electrons are fully localized to $\Omega(A)$, then $\lambda(A) = N(A)$, $g_A(\mathbf{r}) = \rho(\mathbf{r})$ for $\mathbf{r} \in \Omega(A)$ and $g_A(\mathbf{r}) = 0$ for $\mathbf{r} \notin \Omega(A)$.

- (iii) Integration of $g_A(\mathbf{r})$ over any other atomic basin gives half of the QTAIM-defined delocalization index, as well as integrating $g_B(\mathbf{r})$ over $\Omega(A)$:

$$\frac{1}{2} \delta(A, B) = \int_B g_A(\mathbf{r}) d\mathbf{r} = \int_A g_B(\mathbf{r}) d\mathbf{r} \quad (27)$$

Interpreting Eq. 27 is quite simple – since $g_A(\mathbf{r})$ gives the contribution of $\Omega(A)$'s electrons at \mathbf{r} , it therefore gives the contribution which those electrons make to other atomic basins' expected number of electrons – or, in other words, the electrons of $\Omega(A)$ which are sufficiently delocalized to be found *outside* of $\Omega(A)$.

- (iv) The atomic electron population, $N(A)$, can be decomposed in terms of DAFH functions:

$$\begin{aligned} N(A) &= \int_A g_A(\mathbf{r}) d\mathbf{r} + \sum_{B \neq A}^{M-1} \int_B g_A(\mathbf{r}) d\mathbf{r} \\ &= \int_A g_A(\mathbf{r}) d\mathbf{r} + \sum_{B \neq A}^{M-1} \int_A g_B(\mathbf{r}) d\mathbf{r} \end{aligned} \quad (28)$$

which is the corollary of Eq. 22. The average number of electrons in $\Omega(A)$, when taking XC-effects into account, is therefore equal to the contribution which atom A makes to $\Omega(A)$ itself (localized electrons, first term in Eq. 28) as well as the contribution which atom A makes to the remainder of the molecule (delocalized electrons, second term in Eq. 28). Alternatively, and equally true, is that the average number of electrons in $\Omega(A)$ is equal to the localized electrons and the number of electrons from all other atoms which are delocalized in $\Omega(A)$.

The above-mentioned properties of $g_A(\mathbf{r})$ show that it is the equivalent of atomic electron population, but taking into account the dynamic distribution of electrons due to XC-effects. As a result, DAFH is an extremely useful tool for understanding atomic populations, delocalization effects, conjugation and aromaticity, as well as general properties of chemical bonding. Since

$g_A(\mathbf{r})$ can be visualized as cross-sections, contour maps or isosurfaces, DAFH is also a very visual method and provides very useful pictures of atomic electron distributions.

To calculate the full $g_A(\mathbf{r})$, as defined by Eq. 23, can be quite time-consuming since the XC-hole incorporates the full second-order density matrix. A considerably quicker route can be followed using the AOM elements, as defined in Eq. 18:

$$g_A(\mathbf{r}) = \sum_{ij} \sqrt{v_i} \sqrt{v_j} \chi_i^*(\mathbf{r}) \chi_j(\mathbf{r}) S_{ji}^A \quad (29)$$

DAFH, in its current, modern form, is usually subjected to additional treatments. Firstly, $g_A(\mathbf{r})$ can be written in matrix-form and subsequently diagonalized, producing a set of 1-electron domain natural functions and occupations associated with each atomic basin. Secondly, Ponec, Cooper and Kohout introduced²³ Cioslowski's isopycnic transformations²⁴ during the calculation of $g_A(\mathbf{r})$; this produces a different set of 1-electron DAFH functions (the sum of which still gives the same $g_A(\mathbf{r})$) but which are differently localized, in chemically intuitive fashions. For the purposes of this work, only the general DAFH function, $g_A(\mathbf{r})$, is used and expanded upon.

Section 2.2. Novel theoretical developments

2.2.1. The FALDI density decomposition scheme

FALDI is derived from DAFH and uses QTAIM atomic basins, although any exhaustive decomposition of molecular space into spatial domains can be used. In its essence, FALDI decomposes the total electron density (ED) at any given coordinate into one or more FALDI, or FALDI-derived, components:

$$\rho(\mathbf{r}) = \sum_i \text{FALDI}(\mathbf{r}) \quad (30)$$

The FALDI components correspond to: (i) the density contribution of a chemical fragment, *frag*-ED, (ii) the density contribution of an atom, *atom*-ED, (iii) the density contribution of electrons localized to a specific atom, *loc*-ED, and (iv) the density contribution of electrons delocalized across a specific atom-pair, *deloc*-ED. A number of components derived from the above-mentioned FALDI fields will be discussed in the following sections.

The same elementary principle applies to all FALDI components, as it applies to the DAFH function $g_A(\mathbf{r})$ discussed above – each FALDI component is a distribution in real-space of a

corresponding QTAIM population or index. We will briefly discuss *atom*-ED and *frag*-ED distributions below, and then we will discuss the derivation of *loc*-ED and *deloc*-ED distributions.

Atom-ED distributions are identical to DAFH $g_A(\mathbf{r})$ functions, discussed above in Section 2.1.5, and therefore we use the same symbol.¹ Each *atom*-ED distribution gives the real-space distribution of the electrons contained, on average, in an atomic basin $\Omega(A)$ (as calculated by the atomic electron population, $N(A)$, Eq. 17). $g_A(\mathbf{r})$ is, in general, non-zero even *outside* of $\Omega(A)$ due to exchange-correlation effects, as discussed in Section 2.1.5. Therefore, the total ED at any \mathbf{r} can be expressed in terms of the contribution each atom, as a whole, makes through Eq. 30: $\rho(\mathbf{r}) = \sum_i^M g_i(\mathbf{r})$. *Frag*-ED distributions, $g^{\{F\}}(\mathbf{r})$, are then quite simply the sum of multiple *atom*-ED distributions, corresponding to selected chemical fragments, and a *frag*-ED distribution integrated over all space will give the sum of the fragment's electron populations, $N\{F\} = \sum N(A) = \int_{\infty} g^{\{F\}}(\mathbf{r})$.

While atom and fragment contributions can already provide useful insights into the total ED distribution of a molecule, we have found that it is quite often necessary to have a deeper degree of decomposition in order to understand certain phenomena. A natural decomposition of an atom's electron population is the number of electrons localized to the atom itself (a 1-body contribution) and the number of electrons delocalized among atom pairs (2-body contributions). QTAIM-defined Localization indices (LI), as discussed in Section 2.1.4, provides a count of the contributions which the atom's electrons make to its own basin. The LI can be calculated by integrating an *atom*-ED distribution, $g_A(\mathbf{r})$ over its own basin, $\Omega(A)$ (Eq. 26), which leads to the definition of an LI in terms of AOMs (Eq. 21). For single-determinant restricted wavefunctions, the LI can be written as the trace of the matrix product of the AOM with itself:

$$\lambda(A) = 2Tr(\mathbf{S}^A \mathbf{S}^A) \quad (31)$$

For multi-determinant wavefunctions, the LI can be approximated by the sum of the squares of all elements of the AOM. For the remainder of this chapter, we will focus on the equations dealing with single-determinant, restricted wavefunctions, and we will implement and test Eq. 31 for multi-determinant wavefunctions in the future.

¹ While it might seem unnecessary to assign a new name to an already existing function, we felt it was necessary for consistency in the context of the entire FALDI decomposition scheme, and especially in the deformation density calculations using FALDI fields.

In a similar fashion to the calculation of the DAFH function (Eq. 29), a distribution in 3D real space of an LI can be calculated:

$$\mathcal{L}_A(\mathbf{r}) = 2 \sum_{ij}^{N/2} \chi_i^*(\mathbf{r}) \chi_j(\mathbf{r}) (\mathbf{S}^A \mathbf{S}^A)_{ji} \quad (32)$$

$\mathcal{L}_A(\mathbf{r})$ is known within FALDI as a localized ED distribution for atom A (*loc*-ED), and describes the contribution to the total ED at \mathbf{r} resulting from the electrons which are localized to $\Omega(A)$. Integrating $\mathcal{L}_A(\mathbf{r})$ over all space gives the QTAIM-defined LI, and is therefore equivalent to integrating $g_A(\mathbf{r})$ over $\Omega(A)$. Correspondingly, QTAIM-defined DIs can also be calculated in terms of the matrix product of two AOMs:

$$\delta(A, B) = 2Tr(\mathbf{S}^A \mathbf{S}^B + \mathbf{S}^B \mathbf{S}^A) \quad (33)$$

and again, Eq. 33 holds for single-determinant wavefunctions but for multi-determinant wavefunctions the DI is equal to the sum of the scalar products of each corresponding element of the two AOMs. A 3D real space distribution of $\delta(A, B)$ can be calculated as:

$$\mathcal{D}_{A,B}(\mathbf{r}) = 2 \sum_{ij}^{N/2} \chi_i^*(\mathbf{r}) \chi_j(\mathbf{r}) (\mathbf{S}^A \mathbf{S}^B + \mathbf{S}^B \mathbf{S}^A)_{ji} \quad (34)$$

$\mathcal{D}(\mathbf{r})$ is known within FALDI as a delocalized ED distribution for atom-pair A,B (*deloc*-ED) and describes the contribution to the total ED at \mathbf{r} resulting from the electrons which are delocalized between $\Omega(A)$ and $\Omega(B)$. Integrating $\mathcal{D}(\mathbf{r})$ over all space gives the associated QTAIM-defined DI, and is therefore equivalent to integrating $g_A(\mathbf{r})$ over $\Omega(B)$ plus integrating $g_B(\mathbf{r})$ over $\Omega(A)$.

Each *atom*-ED is decomposed perfectly into 1- and 2-body contributions:

$$g_A(\mathbf{r}) = \mathcal{L}_A(\mathbf{r}) + \sum_{B \neq A}^{M-1} \frac{1}{2} \mathcal{D}_{A,B}(\mathbf{r}) \quad (35)$$

In other words, the contribution which each atom makes to the total ED at any given \mathbf{r} is a result of the electrons localized to $\Omega(A)$ and half the electrons delocalized between $\Omega(A)$ and the remainder of the molecule. The FALDI decomposition products therefore provide significant additional analysis tools to the DAFH function. In addition, the total ED at any given \mathbf{r} can be decomposed into only *loc*-ED and *deloc*-ED contributions, in order to gain insight on the overall localized and delocalized density distributions:

$$\rho(\mathbf{r}) = \sum_A^M \mathcal{L}_A(\mathbf{r}) + \sum_A^M \sum_{B \neq A}^{M-1} \frac{1}{2} \mathcal{D}_{A,B}(\mathbf{r}) \quad (36)$$

Note that Chapter 6, which historically first introduced the FALDI decomposition, described an additional method for calculating intra-atomic and interatomic density contributions. For the purposes of calculating and interpreting conformational deformation densities these distributions proved quite useful, but since then we have opted to focus on the definitions for *loc*-ED and *deloc*-ED distributions described above.

2.2.2. FALDI localized and delocalized natural density functions

Each of the matrix products $\mathbf{S}^A \mathbf{S}^A$ and $(\mathbf{S}^A \mathbf{S}^B + \mathbf{S}^B \mathbf{S}^A)$ can be diagonalized in order to produce a set of orthogonal localized and delocalized ED functions in conjunction with Eqs. 32 and 34. The diagonalization is done through a unitary transformation matrix of the associated matrix product, collectively referred to as $\mathbf{S}^A \mathbf{S}^X$:

$$\mathbf{S}^A \mathbf{S}^X \mathbf{U}^{AX} = n^{AX} \mathbf{U}^{AX} \quad (37)$$

where the columns of \mathbf{U}^{AX} are the eigenvectors associated with $\mathbf{S}^A \mathbf{S}^X$. The eigenvalues are calculated as:

$$n_i^{AX} = \sum_{jk}^{N_{MO}} U_{ji}^{AX} (\mathbf{S}^A \mathbf{S}^X)_{kj} U_{ki}^{AX} \quad (38)$$

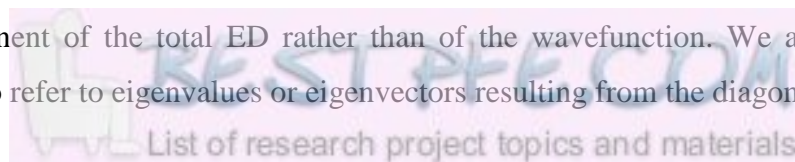
Each *loc*-ED and *deloc*-ED distribution can be expressed in terms of the eigenvectors and eigenvalues of Eq. 38. For the diagonalization of a *loc*-ED distribution:

$$\mathcal{L}_A(\mathbf{r}) = \sum_i^{N_{MO}} n_i^{AA} [\phi_i^{AA}(\mathbf{r})]^2 \quad (39)$$

where

$$\phi_i^{AA}(\mathbf{r}) = \sum_j^{N_{MO}} \chi_j(\mathbf{r}) U_{ji}^{AA} \quad (40)$$

The product of the eigenvalue and eigenvector in Eq. 39 is referred to as a generic natural density function (NDF) so as not to confuse with natural orbital approaches, since an NDF calculates a component of the total ED rather than of the wavefunction. We also use the superscripts 'AA' to refer to eigenvalues or eigenvectors resulting from the diagonalization of



the matrix product $\mathbf{S}^A \mathbf{S}^A$. Finally, the NDF described in Eq. 39 is a localized NDF (*loc*-NDF). The eigenvalues, n_i^{AA} , give the electron occupation of the NDF whereas the square of the eigenvector, $\phi_i^{AA}(\mathbf{r})$, describes the NDFs distribution through space. Note that the sum of the occupations gives the total LI, $\lambda(A) = \sum n_i^{AA}$, whereas the sum of *loc*-NDFs gives the associated *loc*-ED distribution (Eq. 39). Note also that for each *loc*-ED distribution N_{MO} (the number of canonical spin-orbitals in a single-determinant wavefunction) *loc*-NDFs will be produced. In addition, in restricted wavefunctions, the maximum occupation of any NDF will be 2 electrons, whereas in an unrestricted wavefunction it will be 1 electron. Finally, for single-determinant wavefunctions, *loc*-NDF occupations will always be nonnegative, and each *loc*-NDF itself will be positive throughout all space.

Similarly, NDFs for *deloc*-ED distributions can be calculated in the exact same fashion, but using the matrix product $\mathbf{S}^A \mathbf{S}^{X=}$ ($\mathbf{S}^A \mathbf{S}^{B+} + \mathbf{S}^B \mathbf{S}^A$) in Eq. 37 for calculating eigenvalues and eigenvectors:

$$\mathcal{D}_{A,B}(\mathbf{r}) = \sum_i^{N_{MO}} n_i^{AB} [\phi_i^{AB}(\mathbf{r})]^2 \quad (41)$$

where

$$\phi_i^{AB}(\mathbf{r}) = \sum_j^{N_{MO}} \chi_j(\mathbf{r}) U_{ji}^{AB} \quad (42)$$

and again, the sum of occupations gives the total DI for a specific atom-pair, $\delta(A, B) = \sum n_i^{AB}$. Unlike *loc*-NDFs, *deloc*-NDFs can be either positive or negative, depending on the sign of its occupation. The reason for this is that a MO pair simultaneously distributed across two atomic basins can lead to either constructive or deconstructive overlap, resulting in a positive or negative *deloc*-NDF occupation, respectively.

The introduction of NDFs extends the possibility of FALDI analysis quite extensively. Due to the nature of the eigenfunction equation in Eq. 37, the highest occupied *deloc*-NDFs will usually correlate with expected bonding modes (σ , π , etc.) whereas the highest occupied *loc*-NDFs will usually correlate with core-electron distributions of specific orbital symmetry (1s, 2s, 2p_x, etc.). While many localized natural orbital approaches provide similar distributions, they are usually holistic (molecular-wide) in nature and defined in Hilbert space. FALDI-defined NDFs, as well as 1-electron DAFH functions, give contributions to the density in real-space and are atom-centric. In addition, FALDI's separation of the total *atom*-ED into 1- and

2-body components provides a perfect analogy with atom- or atom-pair centred core, non-bonded and bonded electrons. Therefore, FALDI NDFs generate an extremely useful and direct link between conceptual chemistry, which is intrinsically atom-centric, and quantum theoretical chemistry.

2.2.3. FALDI exclusive localization and delocalization indices

QTAIM LIs, despite claims in the original derivations,^{18,19} are not *exclusive*, in that the electrons counted by orthodox LIs cannot be said to be restricted to a single atomic basin. In fact, as we show and extensively investigate in Chapter 3, QTAIM LIs describe the core electrons (electrons which are *exclusively* localized to a single atomic basin), plus the non-bonded electrons (electrons which are mostly localized to a single basin, such as lone-pairs) as well as a significant degree of delocalized electrons (electrons which can be found, often times in significant quantities, in two atomic basins). Therefore, orthodox LIs are very misleading and ambiguous in their descriptions. Similarly, QTAIM-defined DIs undercount the number of electrons delocalized amongst an atom-pair, since some of the delocalized electrons are already counted by QTAIM-defined LIs. This observation is the reason why orthodox DIs – a count of the number of *electrons* delocalized between two atomic basins – is often equal to the expected bond order – a count of the number of *electron-pairs* delocalized between two atomic basins. These interpretations are investigated and critiqued in Chapter 3, but the FALDI-based solution is given here as it is an additional set of tools in FALDI's arsenal.

Unfortunately, the *loc*-ED and *deloc*-ED distributions described by Eqs. 32 and 34 in the previous section are subject to the same lack of exclusivity as QTAIM-defined LIs and DIs. For this reason we will refer to *loc*-ED and *deloc*-ED distributions calculated in the manner described by Eqs. 32 and 34 as orthodox *loc*-ED and *deloc*-ED distributions. Our goal in this section is to define a truly exclusive *loc*-ED distribution, which, when integrated, gives an exclusive localization index (LI_{excl}). Generally undercounted *deloc*-ED distributions can then be suitably adjusted to give an integrated, exclusive delocalization index (DI_{excl}).

In order to arrive to a definition of LI_{excl} and DI_{excl} , we first note that orthodox *loc*-ED distributions generally overlap with each other, as well as with *deloc*-ED distributions. Such overlap is even more noticeable with *loc*-NDFs and *deloc*-NDFs, where two atoms will possess identical *loc*-NDFs and the associated atom-pair will possess a very similar *deloc*-NDF (all describing a specific channel of electron sharing between the two basins). Such overlap between *loc*-NDFs associated with different atomic basins can be accounted for.

Generally, the overlap between the i th NDF of a *loc*-ED distribution ($\mathcal{L}_A^i(\mathbf{r})$) with the j th NDF of any other *loc*-ED distribution ($\mathcal{L}_B^j(\mathbf{r})$) can be calculated as:

$$\mathbf{s}(\mathcal{L}_A^i; \mathcal{L}_B^j) = \sqrt{n_i^{AA} n_j^{BB}} [(\mathbf{U}^{AA})^\dagger \mathbf{U}^{BB}]_{ij} \quad (43)$$

where $n_i^{AA} n_j^{BB}$ is the product of the occupations of the associated *loc*-NDFs and \mathbf{U}^{XX} is the eigenvector of the associated AOM product (Eq. 37). The eigenvectors of a given AOM product are orthonormal, but the eigenvectors of different AOM products are not, with $0 \leq [(\mathbf{U}^{AA})^\dagger \mathbf{U}^{BB}]_{ij} \leq 1$. The overlap of eigenvectors is then normalized to the square-root of the product of the occupations, $\sqrt{n_i^{AA} n_j^{BB}}$, and the overlap of an NDF with itself is therefore $\mathbf{s}(\mathcal{L}_A^i; \mathcal{L}_B^j) = n_i^{AA} = \int_{\infty} n_i^{AA} [\phi_i^{AA}(\mathbf{r})]^2 d\mathbf{r}$. In addition, Eq. 43 describes a general equation for the overlap between any two NDFs; for instance, the overlap can be calculated between a *loc*-NDF and a *deloc*-NDF: $\mathbf{s}(\mathcal{L}_A^i; \mathcal{D}_{A,B}^j)$ using the eigenvalues and eigenvectors of $(\mathbf{S}^A \mathbf{S}^B + \mathbf{S}^B \mathbf{S}^A)$, n_j^{AB} and \mathbf{U}^{AB} .

Using Eq. 43, we can now calculate the total overlap between a specific *loc*-NDF, $\mathcal{L}_A^i(\mathbf{r})$, and other *loc*-NDFs associated with all other atomic basins:

$$\text{LO}(\mathcal{L}_A^i) = \sum_{X \neq A}^M \sum_j^{N_{\text{MO}}} \mathbf{s}(\mathcal{L}_A^i; \mathcal{L}_X^j) \quad (44)$$

where we have used Eq. 43 and $\text{LO}(\mathcal{L}_A^i)$ is the total localized overlap (LO). If the occupation of the i th NDF of basin A (n_i^{AA}) is larger than $\text{LO}(\mathcal{L}_A^i)$ then the occupation can be adjusted accordingly; otherwise, the NDF is completely overlapped by other *loc*-ED distributions with contributions to the same MOs, and the occupation can be set to zero. A new occupation for the i th NDF of basin A is then generated by this condition. The occupation is primed in order to indicate that it is free of any LO (LO-free):

$$n_i'^{AA} = \begin{cases} n_i^{AA} - \text{LO}(\mathcal{L}_A^i) & n_i^{AA} > \text{LO}(\mathcal{L}_A^i) \\ 0 & n_i^{AA} \leq \text{LO}(\mathcal{L}_A^i) \end{cases} \quad (45)$$

After adjusted occupations have been generated for every NDF of basin A, the adjusted occupations can be substituted into Eq. 39, using unadjusted eigenvectors, to produce a LO-free *loc*-ED distribution and LO-free *loc*-NDFs:

$$\mathcal{L}'_A(\mathbf{r}) = \sum_i^{N_{MO}} n'_i{}^{AA} [\phi_i^{AA}(\mathbf{r})]^2 \quad (46)$$

where, again, the *loc*-ED has been primed to indicate that it is LO-free. Finally, a LO-free localization index can be calculated by integrating the LO-free *loc*-ED over all space, or by summing the adjusted occupation values:

$$\begin{aligned} \lambda'(A) = \lambda_{LO-free}(A) &= \int_{-\infty}^{\infty} \mathcal{L}'_A(\mathbf{r}) d\mathbf{r} \\ &= \sum_i^{N_{MO}} n'_i{}^{AA} \end{aligned} \quad (47)$$

The process of generating LO-free *loc*-NDFs removes $n_i^{AA} - n'_i{}^{AA}$ electrons from the *i*th NDF, which is an indication of the component of orthodox LIs which is, in fact, delocalized across multiple basins. These electrons must then be added to specific *deloc*-NDFs. Specifically, the number of electrons which was removed from n_i^{AA} as a result of the overlap between the *loc*-ED distributions of basins A and B can therefore be added to the *deloc*-ED distribution of atom-pair A,B. The fraction of electrons which has to be added to the *j*th NDF of this *deloc*-ED distribution can be calculated as a weighted fraction of the total electrons removed from the *i*th NDF of the *loc*-ED distribution of basin A:

$$n'(\mathcal{L}_A^i \rightarrow \mathcal{D}_{A,B}^j) = w'(\mathcal{L}_A^i; \mathcal{D}_{A,B}^j) (n_i^{AA} - n'_i{}^{AA}) \quad (48)$$

where the weighting function, defined separately for each \mathcal{L}_A^i and $\mathcal{D}_{A,B}^j$ pair, is

$$w'(\mathcal{L}_A^i; \mathcal{D}_{A,B}^j) = \frac{\mathbf{s}(\mathcal{L}_A^i; \mathcal{D}_{A,B}^j)}{\sum_j \mathbf{s}(\mathcal{L}_A^i; \mathcal{D}_{A,B}^j)} \cdot \frac{\sum_k \mathbf{s}(\mathcal{L}_A^i; \mathcal{L}_B^k)}{LO(\mathcal{L}_A^i)} \quad (49)$$

$w'(\mathcal{L}_A^i; \mathcal{D}_{A,B}^j)$ is the overlap between \mathcal{L}_A^i and $\mathcal{D}_{A,B}^j$ (as defined by Eq. 43) as a fraction of the total overlap between \mathcal{L}_A^i and *all* NDFs of $\mathcal{D}_{A,B}$, as well as the overlap between \mathcal{L}_A^i and *all* NDFs of \mathcal{L}_B as a fraction of the total localized overlap of \mathcal{L}_A^i (as defined by Eq. 44). Eq. 49 ensures that the removed density from a single *loc*-NDF as a result of localized overlap is added as a fraction to each relevant *deloc*-NDF. $n'(\mathcal{L}_A^i \rightarrow \mathcal{D}_{A,B}^j)$ (Eq. 48) gives the adjusted, delocalized occupations which are transferred from \mathcal{L}_A^i to $\mathcal{D}_{A,B}^j$. A LO-free *deloc*-ED can be calculated, in terms of *deloc*-NDFs augmented by *loc*-NDFs with the adjusted occupations:

$$\begin{aligned}
 \mathcal{D}'_{A,B}(\mathbf{r}) &= \sum_j^{N_{\text{MO}}} n_j^{\text{AB}} [\phi_j^{\text{AB}}(\mathbf{r})]^2 \\
 &+ \sum_j^{N_{\text{MO}}} \sum_i^{N_{\text{MO}}} \left(n'(\mathcal{L}_A^i \rightarrow \mathcal{D}_{A,B}^j) [\phi_i^{\text{AA}}(\mathbf{r})]^2 + n'(\mathcal{L}_B^i \rightarrow \mathcal{D}_{A,B}^j) [\phi_i^{\text{BB}}(\mathbf{r})]^2 \right)
 \end{aligned} \tag{50}$$

The first term of Eq. 50 is the unadjusted *deloc*-NDFs, as calculated by Eq. 41. The second term consists of *loc*-NDFs (corresponding to basin A and basin B, respectively), adjusted by the weighted electron count (Eq. 48) which was removed from the respective *loc*-ED distributions due to LO. Finally, LO-free DIs can be calculated by integrating Eq. 50 over all space, or as the sum of all *deloc*-NDF occupations and adjusted *loc*-NDF occupations:

$$\begin{aligned}
 \delta'(A, B) &= \delta_{\text{LO-free}}(A, B) = \int_{-\infty}^{\infty} \mathcal{D}'_{A,B}(\mathbf{r}) d\mathbf{r} \\
 &= \sum_i^{N_{\text{MO}}} n_i^{\text{AB}} + \sum_j^{N_{\text{MO}}} \sum_i^{N_{\text{MO}}} \left(n'(\mathcal{L}_A^i \rightarrow \mathcal{D}_{A,B}^j) + n'(\mathcal{L}_B^i \rightarrow \mathcal{D}_{A,B}^j) \right)
 \end{aligned} \tag{51}$$

The procedure described above (the LO-procedure) fractionally removes any MO which contributes simultaneously to the LIs of two or more atomic basins. An MO which contributes only to a single atomic basin (*i.e.* a truly localized MO) will not be affected by the LO-procedure. For any other MO spanning multiple basins, a fraction is removed from the MO's contribution to the LIs of each basin and the same fraction is added to the corresponding atom-pair's DI. The result is LO-free LIs and DIs, expressed in terms of FALDI NDF occupations, and distributed in real-space through FALDI *loc*-ED and *deloc*-ED distributions and NDFs. Chapter 3 contains a number of examples detailing the difference between orthodox and LO-free LIs and DIs. We have also found that where orthodox LIs contain core, non-bonded (e.g. lone-pairs) and some of the delocalized electrons, LO-free LIs contain only core and non-bonded electrons. Orthodox DIs describe typically half of the number of electrons expected to be delocalized, hence matching the expected number of electron-pairs, whereas LO-free DIs typically correspond well with the expected number of electrons in bonded delocalized channels.

However, LO-free LIs and DIs still do not match the hypothetical LI_{excl} and DI_{excl} , as described earlier in this section. Specifically, while the LO-procedure removed overlap between *loc*-ED distributions of two atoms, it did not account for overlap between *loc*-ED and

deloc-ED distributions. For instance, it is entirely possible for electrons to be counted among only a single orthodox LI, but are still able to delocalize into other basins as a result of constructive or deconstructive overlap of *pairs* of MOs. We next present a second procedure which calculates the overlap of the *i*th NDF of a *loc*-ED distribution with *all* other electrons, *i.e.* the NDFs of all other *loc*-ED and *deloc*-ED distributions. The resulting LIs and *loc*-ED distributions are free of any localized and delocalized overlap (LDO). In principle, the LDO-procedure operates in exactly the same manner as the LO procedure, again by calculating the total localized and delocalized overlap associated with a single NDF of basin A ($\text{LDO}(\mathcal{L}_A^i)$):

$$\text{LDO}(\mathcal{L}_A^i) = \sum_{X \neq A}^M \sum_j^{N_{\text{MO}}} \mathbf{s}(\mathcal{L}_A^i; \mathcal{L}_X^j) + \sum_X^M \sum_{Y \neq A}^M \sum_j^{N_{\text{MO}}} \mathbf{s}(\mathcal{L}_A^i; \mathcal{D}_{X,Y}^j) \quad (52)$$

where we have used the definition for the general overlap between two NDFs (Eq. 43). The first term in Eq. 52 is identical to the calculation of LO (Eq. 44) and describes the overlap between \mathcal{L}_A^i and all other *loc*-NDFs. The second term describes the overlap between \mathcal{L}_A^i and all other *deloc*-NDFs. LDO-free occupations for *loc*-NDFs can be calculated, in analogy to Eq. 45:

$$n''_i^{\text{AA}} = \begin{cases} n_i^{\text{AA}} - \text{LDO}(\mathcal{L}_A^i) & n_i^{\text{AA}} > \text{LDO}(\mathcal{L}_A^i) \\ 0 & n_i^{\text{AA}} \leq \text{LDO}(\mathcal{L}_A^i) \end{cases} \quad (53)$$

where we have now used double primes to indicate LDO-free occupations, NDFs or FALDI components. Substituting n''_i^{AA} into Eq. 39 results in a LDO-free *loc*-ED distribution,

$$\mathcal{L}''_A(\mathbf{r}) = \sum_i^{N_{\text{MO}}} n''_i^{\text{AA}} [\phi_i^{\text{AA}}(\mathbf{r})]^2 \quad (54)$$

and integrating over all space *or* summing the occupations gives a LDO-free LI:

$$\begin{aligned} \lambda''(A) = \lambda_{\text{LDO-free}}(A) &= \int_{-\infty}^{\infty} \mathcal{L}''_A(\mathbf{r}) d\mathbf{r} \\ &= \sum_i^{N_{\text{MO}}} n''_i^{\text{AA}} \end{aligned} \quad (55)$$

Again, the fraction of electrons which were removed from each *loc*-NDF is added to an appropriate *deloc*-NDF using a fractional weighting function. The occupations detailing how many electrons are moved from the *i*th *loc*-NDF to the *j*th *deloc*-NDF is:

$$n''(\mathcal{L}_A^i \rightarrow \mathcal{D}_{A,B}^j) = w''(\mathcal{L}_A^i; \mathcal{D}_{A,B}^j)(n_i^{AA} - n''_i^{AA}) \quad (56)$$

where

$$w''(\mathcal{L}_A^i; \mathcal{D}_{A,B}^j) = \frac{\mathbf{s}(\mathcal{L}_A^i; \mathcal{D}_{A,B}^j)}{\sum_j \mathbf{s}(\mathcal{L}_A^i; \mathcal{D}_{A,B}^j)} \cdot \frac{\sum_k \mathbf{s}(\mathcal{L}_A^i; \mathcal{L}_B^k)}{\text{LDO}(\mathcal{L}_A^i)} \quad (57)$$

The LDO-free *deloc*-ED distribution can then be calculated as a sum of the unadjusted *deloc*-NDFs and adjusted *loc*-NDFs:

$$\begin{aligned} \mathcal{D}''_{A,B}(\mathbf{r}) &= \sum_j^{N_{\text{MO}}} n_j^{AB} [\phi_j^{AB}(\mathbf{r})]^2 \\ &+ \sum_j^{N_{\text{MO}}} \sum_i^{N_{\text{MO}}} \left(n''(\mathcal{L}_A^i \rightarrow \mathcal{D}_{A,B}^j) [\phi_i^{AA}(\mathbf{r})]^2 + n''(\mathcal{L}_B^i \rightarrow \mathcal{D}_{A,B}^j) [\phi_i^{BB}(\mathbf{r})]^2 \right) \end{aligned} \quad (58)$$

and LDO-free DIs can be calculated by integrating over all space, or summing all associated occupations:

$$\begin{aligned} \delta''(A, B) = \delta_{\text{LDO-free}}(A, B) &= \int_{-\infty}^{\infty} \mathcal{D}'_{A,B}(\mathbf{r}) d\mathbf{r} \\ &= \sum_i^{N_{\text{MO}}} n_i^{AB} + \sum_j^{N_{\text{MO}}} \sum_i^{N_{\text{MO}}} \left(n''(\mathcal{L}_A^i \rightarrow \mathcal{D}_{A,B}^j) + n''(\mathcal{L}_B^i \rightarrow \mathcal{D}_{A,B}^j) \right) \end{aligned} \quad (59)$$

$\lambda_{\text{LDO-free}}(A)$ and the associated *loc*-ED distribution, $\mathcal{L}''_A(\mathbf{r})$, represent electrons which can be found *only* and *exclusively* in $\Omega(A)$. $\lambda_{\text{LDO-free}}(A)$ therefore corresponds to the hypothetical LI_{excl} , and is a clear indicator of truly localized electrons. We show in Chapter 3 that $\lambda_{\text{LDO-free}}(A)$ describes only core electrons, and that it can be a very useful tool to investigate when supposed core-electrons are actually utilized and delocalized for bonding purposes. The associated $\delta_{\text{LDO-free}}(A, B)$ and $\mathcal{D}''_{A,B}(\mathbf{r})$ distribution describes the maximum electron distribution which can be delocalized across multiple atomic basins, even as a result of very weak interference patterns.

Orthodox, LO-free and LDO-free LIs, DIs, *loc*-EDs and *deloc*-EDs are interchangeable for the other FALDI analyses described in the following sections. Historically, the LO- and LDO-procedures were discovered quite late in FALDI's development, and as such, most of the

chapters in this thesis describe FALDI analyses on orthodox *loc*-ED and *deloc*-ED distributions. We are in the process of revisiting some of these applications in the future in order to test their utilities using significantly more (de)localized 1- and 2-body fields. Finally, note that the LO-free and LDO-free procedures have only been derived for single determinant wavefunctions. Deriving similar sets of equations for multi-determinant wavefunctions in a natural orbital basis is relatively simple; however, the computational load becomes far too demanding for our current implementation and we will revisit LO-free and LDO-free FALDI for multi-determinant wavefunctions after we have optimized our algorithms.

2.2.4. Local bonding, nonbonding and antibonding classification of FALDI components

The topology of the total ED, as discussed in Section 2.1.3, is quite rich in physically meaningful information. So too are the FALDI fields, and specifically *loc*-ED and *deloc*-ED distributions. However, finding patterns in the general topologies of FALDI fields can be quite a daunting task, considering that a large set of molecular-wide *loc*-ED and *deloc*-ED distributions is generated for any but the smallest systems. However, since FALDI is a complete decomposition of the total ED, many of the total ED's interesting topological features can be decomposed into FALDI contributions. Specifically, the concentration of ED in an internuclear region (as discussed thoroughly in Section 2.1.3) is of particular interest to us, as it is used in a number of QCT techniques, such as the Non-covalent Interactions approach (NCI),^{13,14,25} and the interpretation of an atomic interaction line (AIL).^{12,26} As mentioned earlier, each point of an AIL has the specific property that ED is concentrated perpendicular to the AIL (as measured by the second eigenvalue of the Hessian matrix, λ_2), a property which is often interpreted as an attractive component of chemical bonding with relation to the local virial theorem⁷ and Feynman's theorem.²⁷ However, the total ED is influenced simultaneously by all particles within the system and, as a result, λ_2 of the total ED gives the *net* concentration or depletion at a given point \mathbf{r} . As a consequence, λ_2 might change sign and with it the chemical interpretation, as a result of very small changes in the environment. In other words, the measure of concentration or depletion in a given region is extremely relative and locally dependent. If the second-derivative in an area of interest can be decomposed into chemically meaningful components, however, then the *net* concentration or depletion carries less importance than the *absolute* concentration or depletion of specific components. We have developed³ a scheme within FALDI using such a concept, described comprehensively in Chapter 4.

We start by considering the partial second derivatives of FALDI's decomposed ED distributions. We will consider FALDI distributions which are implied to be LDO-free (as discussed in Section 2.2.3), but note that the following investigations can be carried out on orthodox or LO-free distributions as well. First, we have to consider the sign of a specific FALDI component's contribution at a specific coordinate in space, \mathbf{r} . *Deloc*-ED distributions can be positive or negative, unlike *loc*-ED distributions. Regions where $\mathcal{D}_{A,B}(\mathbf{r}) > 0$ represent a constructive interference of one or more MOs simultaneously overlapping two atomic basins ($\Omega(A)$ and $\Omega(B)$) at \mathbf{r} , leading to an increase of the total ED. Regions where $\mathcal{D}_{A,B}(\mathbf{r}) < 0$, however, are due to deconstructive interference of one or more MOs simultaneously overlapping two atomic basins at \mathbf{r} , reducing the total ED.

Next, we can consider the sign of the partial second derivative of the specific FALDI component. As discussed in Section 2.1.3, the sign of the second derivative of the ED determines whether the ED is locally concentrated (*i.e.* the ED is greater at \mathbf{r} than at the average of its neighbouring points) or depleted (less than the average of its neighbouring points). Similarly, the sign of the partial second derivative of a FALDI component at \mathbf{r} determines whether that distribution is concentrated or depleted. Along the principle axis perpendicular to an internuclear vector (*i.e.* the eigenvector associated with λ_2), concentrated *deloc*- and *loc*-ED distributions will *facilitate* the formation of an AIL, whereas depleted *deloc*-ED distributions will *hinder* the formation of an AIL. Unlike the topology of the total ED, however, the sign of the partial second derivative for a single *deloc*-ED is not directly dependent on the local ED environment, and gives a description of the absolute concentration or depletion of that distribution.

In orthodox MO theory detailing chemical bonds, each spin-orbital can be classified in terms of bonding, nonbonding or antibonding with respect to a particular chemical interaction. Bonding orbitals are in-phase and their occupation results in an increase of ED in the internuclear region(s) and lowers the molecular energy as a result of constructive interference. Antibonding orbitals are out-of-phase and their occupation results in a decrease of ED in the internuclear region(s) and raises the molecular energy as a result of deconstructive interference. Occupation of nonbonding orbitals typically does not alter the ED distribution at the region of interest nor does it alter the molecular energy. Since the sign of $\mathcal{D}_{A,B}(\mathbf{r})$ is a result of MO interference across multiple atomic basins, each *loc*- and *deloc*-ED distribution can be labelled with respect to a specific interatomic region, in analogy to MO bond theory. FALDI distributions that concentrate ED in a specific region can be said to be *bonding*, distributions

that decrease ED can be said to be *antibonding* and distributions that deplete ED can be said to be *nonbonding*.

The overall classification scheme is discussed in detail (with examples) in Chapters 4 and 5, where we have used the scheme to show the multi-centre nature of various AIL or to investigate the existence of an AIL in the first place. Our classification scheme provides an answer to the locality dependency of most QCT approaches, provides support for the validity of Feynman's theorem with respect to chemical bonding in larger molecules (including the description of intramolecular bonds) and creates a very strong link between conceptual MO bond theory and real-space approaches.

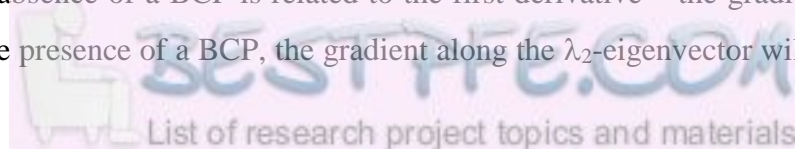
2.2.5. FALDI decomposition of the gradient of the total ED

The classification scheme of FALDI components at any given \mathbf{r} as *bonding*, *nonbonding* or *antibonding*, as discussed in the previous section, allows for a careful investigation of the formation of topological features in the total ED. Since the chemical significance of AILs is still being questioned and their interpretation is still a topic of investigation, we now present a FALDI-based tool with which AIL formation can be carefully investigated. Specifically, our tool allows researchers to investigate and understand why an AIL and BCP is present for a specific interaction in one molecule but absent in a different (even very similar) system. This tool is described in detail in Chapter 5.

We first define an exact coordinate to measure, \mathbf{r}^* . If a BCP is present between the nuclei of an interaction of interest, then $\mathbf{r}^* = \mathbf{r}_c$. If a BCP is not present, then we set \mathbf{r}^* to be the position of the geometric interaction point (GIP),¹⁵ which is defined as the coordinate on an internuclear vector where the ED is at a local minimum. The GIP is well-defined for any given atom-pair, and usually the GIP and BCP are close to each other, depending on how much an AIL is bent. Next, we measure the partial second derivative along the eigenvector associated with λ_2 (henceforth referred to as the λ_2 -eigenvector) and classify each *deloc*-ED and *loc*-ED distribution as bonding, nonbonding or antibonding, as discussed in the previous section. FALDI components of the same nature can be summed up to give total *bonding*, *nonbonding* and *antibonding* distributions and thus providing a total decomposition of the density at \mathbf{r}^* :

$$\rho(\mathbf{r}^*) = \rho_{\text{bonding}}(\mathbf{r}^*) + \rho_{\text{nonbonding}}(\mathbf{r}^*) + \rho_{\text{antibonding}}(\mathbf{r}^*) \quad (60)$$

The presence or absence of a BCP is related to the first derivative – the gradient – of the total ED at \mathbf{r}^* . In the presence of a BCP, the gradient along the λ_2 -eigenvector will be zero at



\mathbf{r}^* . We can therefore decompose the gradient of the total ED at \mathbf{r}^* into the same components as Eq. 60:

$$\partial\rho(\mathbf{r}^*) = \partial\rho_{\text{bonding}}(\mathbf{r}^*) + \partial\rho_{\text{nonbonding}}(\mathbf{r}^*) + \partial\rho_{\text{antibonding}}(\mathbf{r}^*) \quad (61)$$

For a BCP to be present, the sum of the terms in Eq. 61 should be equal to zero. Let us ignore the effects of antibonding contributions to the slope at \mathbf{r}^* for the moment, and assume that it is zero. That leaves the interplay between the rates of change of the bonding and nonbonding contributions which will determine whether a BCP is present or not. The two possibilities which will lead to the formation of a CP is if i) both the slopes of bonding and nonbonding contributions at \mathbf{r}^* are zero, or ii) the slopes of bonding and nonbonding contributions at \mathbf{r}^* are equal, but opposite in sign. We already know that the signs of the partial second derivatives along the λ_2 -eigenvector for the bonding and nonbonding contributions are negative and positive, respectively, and for a BCP to be present, the partial second derivative of the total ED is also negative ($\lambda_2 < 0$). Therefore, in the *vicinity* of a BCP, the absolute gradient of the bonding contribution will be greater than the absolute gradient of the nonbonding contributions, leading to the following conditions:

$$|\partial\rho_{\text{bonding}}(\mathbf{r}^*)| > |\partial\rho_{\text{nonbonding}}(\mathbf{r}^*)|, \text{ in the vicinity of a BCP}$$

$$|\partial\rho_{\text{bonding}}(\mathbf{r}^*)| < |\partial\rho_{\text{nonbonding}}(\mathbf{r}^*)|, \text{ outside the vicinity of a BCP, and}$$

$$|\partial\rho_{\text{bonding}}(\mathbf{r}^*)| - |\partial\rho_{\text{nonbonding}}(\mathbf{r}^*)| = 0, \text{ at the BCP}$$

The second condition will hold for most interactions of interest, regardless of whether a BCP is present or not. If a BCP is not present, then the first and third condition will not be met. If a RCP is present, then the first condition will not be met. In order to evaluate the interplay of these effects, we propose detecting AILs and CPs when measured along the λ_2 -eigenvector:

$$CP(\mathbf{r}) = -\text{sign}(\partial\rho_{\text{nonbonding}}(\mathbf{r})) \cdot [\partial\rho_{\text{bonding}}(\mathbf{r}) + \partial\rho_{\text{nonbonding}}(\mathbf{r}) + \partial\rho_{\text{antibonding}}(\mathbf{r})] \quad (62)$$

The $CP(\mathbf{r})$ function simply returns the slope of the total ED (Eq. 61), but modified by the sign of the net slope of the nonbonding contributions. The $CP(\mathbf{r})$ function will therefore also be equal to 0 at \mathbf{r}^* , if a BCP is present. However, in the *vicinity* of a BCP, a region along the λ_2 -eigenvector will always exist where $CP(\mathbf{r})$ is positive, in one or both directions, whereas $CP(\mathbf{r})$ will always be negative if a BCP is absent.

Ignoring antibonding contributions again for the moment, let us investigate the properties of the $CP(\mathbf{r})$ function in order to understand the chemical significance of a BCP. $CP(\mathbf{r})$ will

be positive if i) the total *bonding*-ED and total *nonbonding*-ED distributions have opposite slopes as well as ii) the slope of the total *bonding*-ED is greater in magnitude than the slope of the total *nonbonding*-ED. In other words, an AIL forms when the rate of change of the bonding contributions is greater than the rate of change of nonbonding contributions, in the absence of antibonding contributions. It is very important to note that it is not the *value* of the *bonding*-ED or *nonbonding*-ED contributions which determine AIL formation; it is possible that an AIL can be present even when the *nonbonding*-ED contributions are much greater in value than the *bonding*-ED contributions. However, for most accepted chemical bonds, both the slope and the value of the *bonding*-ED contributions are generally greater than the slope and the value of the *nonbonding*-ED contribution.

We note that antibonding contributions change the interpretation somewhat, but in general only for non-stable molecules or excited states. Generally, the antibonding contributions (and especially their slopes) are negligible for most interactions and AILs which we have investigated. If it is present, then antibonding contributions can either facilitate or hinder AIL formation, depending on whether it has the same slope as the bonding contribution or not.

The $CP(\mathbf{r})$ function is a tool which we hope to use to clearly investigate the nature of both accepted and controversial AILs. In conjunction with the full FALDI decomposition, the $CP(\mathbf{r})$ can be used to investigate *which* atoms or atom-pairs are primarily responsible for the formation or absence of an AIL. In addition, we discuss in Chapter 5 detailed physical and chemical interpretations of the *bonding*-, *nonbonding*- and *antibonding*-ED components and their slopes, thereby providing a set of general descriptive tools with which the nature of an AIL, as well as the ED distribution in general, can be understood.

2.2.6. FALDI deformation densities

The deformation density is a very useful and easily interpretable tool in a wide range of theoretical as well as experimental fields. It measures the change in density from an unbound state to a bound state:

$$\Delta\rho(\mathbf{r}) = \rho(\mathbf{r}) - \rho^0(\mathbf{r}) \quad (62)$$

where $\rho^0(\mathbf{r})$ is usually the sum of the densities of a number of non-interacting promolecules. Promolecules can be isolated atoms (such as is often used in conjunction with X-ray diffraction studies), isolated monomers or even isolated fragments (after breaking apart selected bonds in the final molecule). For the resulting $\Delta\rho(\mathbf{r})$ to be meaningful, it is necessary for the coordinate

system to be identical in the final (*fin*) state as well as promolecular or reference (*ref*) state. In other words, all nuclear coordinates in the *fin* state must be identical, or very easily transformed, as the corresponding nuclear coordinates in the *ref* state. If the *ref* state coordinates need to be transformed in order to match the *fin* state coordinates, then all atoms of the *ref* state must be transformed uniformly – such that the distance between each nuclear coordinate \mathbf{R}_i and every general coordinate of the molecule, \mathbf{r} , remain constant. If these conditions are met, then the different ED distributions in the *ref* and *fin* states are aligned so that the change between them is sensible. Chapter 6 discusses the deformation density, its uses and importance in detail.

The conditions mentioned above regarding the coordinate system of *fin* and *ref* states restricts the use of the deformation density to the study of intermolecular interactions (such as the intermolecular interaction formed by the dimerization of two monomers). For the study of intramolecular interactions, the molecule has to be fragmented into one or more unchemical states in order to calculate $\Delta\rho(\mathbf{r})$. These states often involve the inclusion of radical species, which muddles the chemical information which is extractable from $\Delta\rho(\mathbf{r})$.

In this section we will present a framework for calculating deformation densities using conformational change, rather than fully isolated promolecules. Two significant and necessary modifications must be made to the promolecular approach in order to calculate a *conformational* deformation density ($\Delta\rho_c(\mathbf{r})$): (i) the *ref* state will consist of interacting (as opposed to non-interacting) molecular fragments, and (ii) the change in nuclear coordinates from a *ref* conformer to a *fin* conformer must be accounted for, with respect to aligning ED distributions of each state. Both of these modifications can be accounted for by using a charge decomposition scheme which decomposes the total ED into molecular-wide components corresponding to a set of molecular fragments:

$$\rho(\mathbf{r}) = \sum_i^M \rho_i(\mathbf{r}) \quad (63)$$

where M is the number of fragments. Such decomposition allows a comparison of the density contribution which each fragment makes to \mathbf{r} in both *fin* and *ref* states, if \mathbf{r} can be suitably transformed from *ref* to *fin*:

$$\Delta_c\rho(\mathbf{r}) = \sum_i^M {}^{fin}\rho_i(\mathbf{r}) - \sum_i^M {}^{ref}\rho_i(\mathbf{A}_i\mathbf{r}) \quad (63)$$

where \mathbf{A}_i is a transformation matrix which transforms the i th fragment in the *ref* state to the associated coordinate system of the *fin* state. Each $^{fin}\rho_i(\mathbf{r})$ and $^{ref}\rho_i(\mathbf{A}_i\mathbf{r})$ pair is then compared separately and their contribution to the conformational deformation density is calculated.

We note that both DAFH and FALDI (Eqs. 24 and 30) adhere to the condition set in Eq. 63, as well as a number of other decomposition schemes, such as the Source Function.²⁸ FALDI, however, has the benefit of defining very clear 1- and 2-body contributions, which, as we shall see, is necessary for the calculation of $\Delta\rho_c(\mathbf{r})$. If we use DAFH functions, (FALDI's *atom*-ED distributions) in Eq. 63, and with suitable transformation matrices for each nucleus,

$$\Delta_c\rho(\mathbf{r}) = \sum_i^M {}^{fin}g_i(\mathbf{r}) - \sum_i^M {}^{ref}g_i(\mathbf{A}_i\mathbf{r}) \quad (64)$$

then we arrive to a surprisingly good first attempt at the conformational deformation density. However, as we have shown in Section 2.2.1, each *atom*-ED consists of electrons which are localized to the atom and electrons delocalized between the atom and all other atoms. *loc*-ED distributions, therefore, depend explicitly on the coordinates of only one nuclear centre, whereas *deloc*-ED distributions depend on the coordinates of two centres simultaneously. Therefore, a \mathbf{A}_i transformation matrix will be able to match the relative position and orientation of a *loc*-ED distribution from the *ref* state to the *fin* state, but it will not be able to do the same for a *deloc*-ED distribution. Accordingly, a first-order transformation matrix for an *atom*-ED distribution, as is used in Eq. 64, will only correctly align the localized components of $g_A(\mathbf{r})$, whereas the delocalized components will be unaligned. We have to consider the transformation and calculation of deformation density components separately for each FALDI component.

The change in *loc*-ED distributions from *ref* to *fin* is easy to calculate, and follows the same form as Eq. 64:

$$\Delta_c\mathcal{L}_A(\mathbf{r}) = {}^{fin}\mathcal{L}_A(\mathbf{r}) - {}^{ref}\mathcal{L}_A(\mathbf{A}_A\mathbf{r}) \quad (65)$$

where $\mathbf{A}_A\mathbf{r}$ relates the position and relative orientation of the *loc*-ED distribution in the *ref* state to the corresponding position and orientation of the *loc*-ED distribution in the *fin* state. \mathbf{A}_A transformation matrices are, at this stage, calculated by hand based on obvious conformational changes, but we are working towards automated procedures based on a number of different approaches. $\Delta_c\mathcal{L}_A(\mathbf{r})$ then gives the change in localized, 1-body electron contributions of basin A and is a *localized deformation density* distribution (*loc*-DD).

Transforming the *deloc*-ED distributions, however, is not as easy, since each $\mathcal{D}_{A,B}(\mathbf{r})$ depends on the positions and relative orientations of two nuclei and therefore needs to be transformed using two transformation matrices simultaneously (a second-order transformation). There are a number of different ways to approach such a problem, and it should be noted that the following approach is presented as a first and very approximate implementation at solving this non-trivial issue. Our approach uses a linear scaling scheme based on projections of the internuclear vector to generate a new set of coordinates which takes into account the linear transformations of both basins, as described below.

The linear transformation used to transform the *loc*-ED distributions (Eq. 65) can be used to generate new coordinates $\mathbf{r}_A^{\mathcal{R}}$ and $\mathbf{r}_B^{\mathcal{R}}$ for the *ref* state relative to the basins $\Omega(A)$ and $\Omega(B)$ in the *fin* state:

$$\begin{aligned}\mathbf{r}_A^{\mathcal{R}} &= \mathbf{A}_A \mathbf{r} \\ \mathbf{r}_B^{\mathcal{R}} &= \mathbf{A}_B \mathbf{r}\end{aligned}\tag{66}$$

Two parallel planes, perpendicular to the internuclear vector \mathbf{R}_{AB} , can be used to define which value of *deloc*-ED applies to the *ref* state. Any coordinate \mathbf{r} which is outside of the area enclosed by the two planes, *i.e.* any \mathbf{r} outside of the internuclear space, can use $\mathbf{r}_A^{\mathcal{R}}$ or $\mathbf{r}_B^{\mathcal{R}}$ as a *ref* coordinate. An altered value of the *deloc*-ED distribution for atom-pair A,B in the *ref* state, ${}^{ref}\mathcal{D}_{A,B}^{\mathcal{R}}(\mathbf{r})$, at any \mathbf{r} which lies *inside* the internuclear space, can be expressed as a weighted combination of $\mathcal{D}_{A,B}$ at $\mathbf{r}_A^{\mathcal{R}}$ and $\mathbf{r}_B^{\mathcal{R}}$, thereby using a portion of ${}^{ref}\mathcal{D}_{A,B}$ measured at two different positions:

$$\begin{aligned}{}^{ref}\mathcal{D}_{A,B}^{\mathcal{R}}(\mathbf{r}) &= w_A(\mathbf{r}) {}^{ref}\mathcal{D}_{A,B}(\mathbf{r}_A^{\mathcal{R}}) + w_B(\mathbf{r}) {}^{ref}\mathcal{D}_{A,B}(\mathbf{r}_B^{\mathcal{R}}) \\ &= w_{AB}(\mathbf{r}) {}^{ref}\mathcal{D}_{A,B}(\mathbf{r}_A^{\mathcal{R}}) + [1 - w_{AB}(\mathbf{r})] {}^{ref}\mathcal{D}_{A,B}(\mathbf{r}_B^{\mathcal{R}})\end{aligned}\tag{67}$$

for \mathbf{r} between \mathbf{R}_A and \mathbf{R}_B . The weight function,

$$w_{AB}(\mathbf{r}) = 1 - \frac{(\mathbf{r} - \mathbf{R}_A) \cdot \mathbf{R}_{AB}}{|\mathbf{R}_{AB}|^2}\tag{68}$$

is generated by projecting the vector from the nuclear coordinate of atom A to \mathbf{r} , $\mathbf{r} - \mathbf{R}_A$, onto the internuclear vector, \mathbf{R}_{AB} , and then taking the fraction along \mathbf{R}_{AB} where \mathbf{r} is projected. The altered ${}^{ref}\mathcal{D}_{A,B}^{\mathcal{R}}(\mathbf{r})$, for any \mathbf{r} is then:

$${}^{ref}\mathcal{D}_{A,B}^{\mathcal{R}}(\mathbf{r}) = \left\{ \begin{array}{l} w_{AB}(\mathbf{r}) {}^{ref}\mathcal{D}_{A,B}(\mathbf{r}_A^{\mathcal{R}}) + [1 - w_{AB}(\mathbf{r})] {}^{ref}\mathcal{D}_{A,B}(\mathbf{r}_B^{\mathcal{R}}) \\ {}^{ref}\mathcal{D}_{A,B}(\mathbf{r}_A^{\mathcal{R}}) \\ {}^{ref}\mathcal{D}_{A,B}(\mathbf{r}_B^{\mathcal{R}}) \end{array} \right\} \begin{array}{l} 0 < w_{AB}(\mathbf{r}) < 1 \\ w_{AB}(\mathbf{r}) \geq 1 \\ w_{AB}(\mathbf{r}) \leq 0 \end{array} \quad (70)$$

In other words, the transformed value of $\mathcal{D}_{A,B}$ depends on the relative position of \mathbf{r} in the *fin* molecule. If \mathbf{r} lies outside nuclei A and B, then we transform the *ref* coordinate relative to the nuclei to which \mathbf{r} is the closest. If \mathbf{r} lies inside the internuclear space defined by A and B, then we use a linear combination of both transformed coordinates based on how far \mathbf{r} lies relative to the internuclear vector. This approximation lets us calculate a value for the *deloc*-ED in the *ref* state, transformed to align approximately to the *fin* state. The change in *deloc*-ED is then:

$$\Delta_c \mathcal{D}_{A,B}(\mathbf{r}) = {}^{fin}\mathcal{D}_{A,B}(\mathbf{r}) - {}^{ref}\mathcal{D}_{A,B}^{\mathcal{R}}(\mathbf{r}) \quad (71)$$

giving a delocalized, 2-body deformation density, *deloc*-DD.

The total deformation density associated with a *conformational* change can be given by:

$$\Delta_c \rho(\mathbf{r}) = \sum_A^M \Delta_c \mathcal{L}_A(\mathbf{r}) + \sum_A^{M-1} \sum_{B=A+1}^M \Delta_c \mathcal{D}_{A,B}(\mathbf{r}) \quad (72)$$

or simply the sum of all *loc*-DD and all *deloc*-DD distributions. Similarly, an *atom*-DD as well as *frag*-DD distributions can be easily calculated, in line with the FALDI decomposition:

$$\Delta_c \mathbf{g}_A(\mathbf{r}) = \Delta_c \mathcal{L}_A(\mathbf{r}) + \sum_{B \neq A}^{M-1} \frac{1}{2} \Delta_c \mathcal{D}_{A,B}(\mathbf{r}) \quad (73)$$

$$\Delta_c \mathbf{g}^{\{F\}}(\mathbf{r}) = \sum_A^{M_{\{F\}}} \Delta_c \mathbf{g}_A(\mathbf{r}) \quad (74)$$

While the conformational deformation density itself, $\Delta_c \rho(\mathbf{r})$, is already quite useful, the decomposition (Eqs. 72 to 74) is both necessary for its calculation as well as useful for analysis. In Chapters 6 and 7 we show multiple applications^{1,4} of $\Delta_c \rho(\mathbf{r})$. In addition, Appendices 2 and 3 both use orthodox deformation densities^{29,30} – calculated using fragments, which we are busy revisiting using the FALDI-based conformational deformation density.

Finally, we note that orthodox, LO-free as well as LDO-free FALDI components can be used for the calculation of conformational deformation densities. Historically, $\Delta_c \rho(\mathbf{r})$ was calculated using orthodox FALDI components, as it was the application of calculating deformation densities related to conformational change which led us to develop the

decomposition scheme initially. We have since shown that orthodox *loc*-ED distributions describe a component of delocalized density as well, which, as mentioned earlier, is dependent on two components simultaneously and therefore not a true 1-body contribution. As a result, $\Delta_c\rho(\mathbf{r})$ calculated using orthodox FALDI fields can be somewhat full of artefacts, since the *loc*-ED distributions are scaled only using a single transformation matrix. LDO-free FALDI fields, and specifically the LDO-free *loc*-ED distributions produce extremely clean $\Delta_c\rho(\mathbf{r})$ distributions, and we will be exploring the applications of this method in the near future.

References

1. I. Cukrowski; D. M. van Niekerk; J. H. de Lange. *Struct. Chem.* **2017**, 28, 1429-1444.
2. J. H. De Lange; I. Cukrowski. *J. Comput. Chem.* **2018**, doi: 10.1002/jcc.25223.
3. J. H. de Lange; D. M. van Niekerk; I. Cukrowski. *J. Comput. Chem.* **2018**, 39, 973-985.
4. J. H. Lange; I. Cukrowski. *J. Comput. Chem.* **2017**, 38, 981-997.
5. A. Szabo; N. S. Ostlund. In *Modern quantum chemistry: introduction to advanced electronic structure theory*; Courier Corporation, **2012**.
6. A. Müller. *Phys. Lett. A* **1984**, 105, 446-452.
7. R. F. Bader. In *Atoms in molecules*; Wiley Online Library, **1990**.
8. C. F. Matta; R. J. Boyd. In *An introduction to the quantum theory of atoms in molecules*; Wiley Online Library, **2007**.
9. P. L. Popelier. In *The Chemical Bond II*; Springer, 2016, p 71-117.
10. R. F. Bader. *Chem. Rev.* **1991**, 91, 893-928.
11. S. Shahbazian. *Chem. Eur. J.* **2018**, doi: 10.1002/chem.201705163.
12. R. F. Bader. *J. Phys. Chem. A* **2009**, 113, 10391-10396.
13. J. Contreras-García; E. R. Johnson; S. Keinan; R. Chaudret; J.-P. Piquemal; D. N. Beratan; W. Yang. *J. Chem. Theory Comput.* **2011**, 7, 625-632.
14. A. Otero-de-la-Roza; E. R. Johnson; J. Contreras-García. *PCCP* **2012**, 14, 12165-12172.
15. I. Cukrowski; J. H. de Lange; A. S. Adeyinka; P. Mangondo. *Comput. Theor. Chem.* **2015**, 1053, 60-76.
16. R. F. Bader. *Monatshefte für Chemie/Chemical Monthly* **2005**, 136, 819-854.
17. F. Cortés-Guzmán; R. F. Bader. *Coord. Chem. Rev.* **2005**, 249, 633-662.
18. R. F. Bader; M. E. Stephens. *J. Am. Chem. Soc.* **1975**, 97, 7391-7399.
19. R. Daudel; R. Bader; M. Stephens; D. Borrett. *Can. J. Chem.* **1974**, 52, 1310-1320.
20. R. Ponec. *J. Math. Chem.* **1997**, 21, 323-333.
21. R. Ponec. *J. Math. Chem.* **1998**, 23, 85-103.
22. P. Bultinck; D. L. Cooper; R. Ponec. *J. Phys. Chem. A* **2010**, 114, 8754-8763.

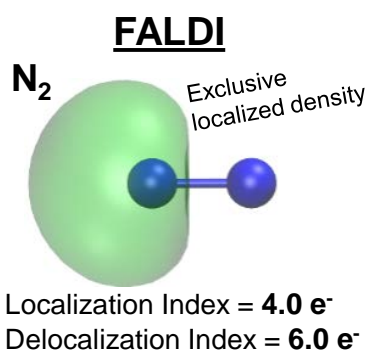
23. D. L. Cooper; R. Ponec; M. Kohout. *Mol. Phys.* **2015**, *113*, 1682-1689.
24. J. Cioslowski; S. T. Mixon. *J. Am. Chem. Soc.* **1991**, *113*, 4142-4145.
25. R. Chaudret; B. De Courcy; J. Contreras-Garcia; E. Gloaguen; A. Zehnacker-Rentien; M. Mons; J.-P. Piquemal. *PCCP* **2014**, *16*, 9876-9891.
26. R. F. Bader. *J. Phys. Chem. A* **1998**, *102*, 7314-7323.
27. R. P. Feynman. *Physical Review* **1939**, *56*, 340.
28. R. F. Bader; C. Gatti. *Chem. Phys. Lett.* **1998**, *287*, 233-238.
29. I. Cukrowski; J. H. de Lange; F. Groenewald; H. G. Raubenheimer. *ChemPhysChem* **2017**, doi: 10.1002/cphc.201700383.
30. R. Fraser; P. H. van Rooyen; J. de Lange; I. Cukrowski; M. Landman. *J. Organomet. Chem.* **2017**, *840*, 11-22.

Chapter 3. Exact and Exclusive Electron Localization

Indices within QTAIM Atomic Basins

Accepted for publication in:

Journal of Computational Chemistry, 2018, DOI: 10.1002/jcc.25223



A new method for calculating and visualizing electron (de)localization for atoms is presented. The resulting indices present exclusively (de)localized electrons and correspond to classically expected values for atoms involved with typical chemical bonds. We also show that traditional QTAIM-based (de)localization indices are non-exclusive and ambiguous in their physical meaning.

Exact and Exclusive Electron Localization Indices Within QTAIM Atomic Basins

Jurgens H. de Lange and Ignacy Cukrowski 

Novel measures of electron (de)localization within the Quantum Theory of Atoms in Molecules (QTAIM) atomic basins are presented which, unlike orthodox localization indices (LIs), are fully exclusive and can be easily visualized. This work shows that QTAIM-defined LIs describe a portion of interatomic delocalized electrons; hence, the chemical/physical interpretation of orthodox LIs is misleading. Using the recently introduced Fragment, Atomic, Localized, Delocalized, and Interatomic (FALDI) density decomposition technique we derive two novel sets of LIs and delocalization indices (DIs), by accounting for the overlap between localized and delocalized

density functions. The FALDI-based LIs and DIs perfectly recover chemically expected core and bonded electron count. Usefulness of new (de)localization indices and their 3D representations were demonstrated on a number of examples, including formamide and benzene. We therefore expect that the scheme reported in this work will provide a valuable stepping stone between classical conceptual chemistry and quantum chemical topology. © 2018 Wiley Periodicals, Inc.

DOI: 10.1002/jcc.25223

Introduction

The concept of localized and delocalized electrons within the atomistic ansatz is one of the most fundamental cornerstones of conceptual chemistry. It underlies a large number of chemical constructs such as valence and core electrons, covalency, aromaticity, lone-pairs, and bond orders. It is also a core concept in many conceptual interpretations of molecular structure, including Lewis structures, VSEPR theory, valence bond theory, molecular orbital theory, crystal-field theory, and general interpretations regarding trends in the periodic table. Computationally, however, atomic electron localization and delocalization still represents somewhat of a challenge, due in parts to both the ambiguity regarding the definition of an atom in a molecule and the necessity of including second-order density matrices in the description of electron (de)localization. Early work by Daudel et al.^[1] set the foundation for the study of *atomic* electron (de)localization by partitioning molecular space into well-defined spatial regions which maximizes the probability of finding a fully localized electron pair. Their work naturally led to the general field of extended population analysis—a set of approaches which investigate how the canonical or natural orbital distributions *or* first- and second-order density matrices are distributed across real-space domains. Since then, many different measures of localization and delocalization within atoms have been proposed, ranging from 1- to 2-center (de)localization indices^[2–5] to multi-center electron delocalization^[6–10] and aromaticity^[11–13] measures. More general (non-atomistic) measures of (de)localization are also commonly used in quantum chemical topology fields, such as the popular electron localization function.^[14] Arguably, one of the most popular measures are the localization and delocalization indices (LI and DI)^[2] of the Quantum Theory of Atoms in Molecules (QTAIM).^[15] DI, also sometimes referred to as the shared

electron delocalization index (SEDI),^[16] is a measure of the number of electrons shared between two topologically defined atomic basins, whereas LI is a measure of the number of electrons localized to a specific atomic basin.

DI and LI, since their introduction in 1975,^[2] are popular measures of electron (de)localization, and their widespread usage has been steadily growing. A quick Google Scholar search reveals ~19,400 hits involving terms “Delocalization Index QTAIM,” and Scopus analytics reveal that the latter term within only the Title, Abstracts and Keywords of listed documents have grown exponentially from a single hit in 1978 to an average of 28 hits per year in the last 3 years. These publications are also not restricted to computational and theoretical chemistry and include many biochemical, medicinal, and pharmacological applications. Richard Bader’s book, “Atoms in Molecules,”^[15] have garnered 16,145 citations since published in 1990, and Bader and Stephens’ original publication introducing DIs and LIs have generated 548 citations. Recently, Matta and coworkers have also incorporated LIs and DIs within their conceptual chemical graph theory as comprehensive Localization–Delocalization Matrices.^[17] It is clear that DI and LI within QTAIM is a very significant and robust measure of the fundamental concept of electron (de)localization in chemistry and related fields.

The interpretation of LIs and DIs is, however, somewhat strange in relation to classical chemical thinking. The DI is commonly seen as a measure of the bond order between two atoms, and many correlations between DI and bond order

J. H. de Lange, I. Cukrowski

Department of Chemistry, Faculty of Natural and Agricultural Sciences, University of Pretoria, Lynnwood Road, Hatfield, Pretoria 0002, South Africa
E-mail: jurgens.delange@up.ac.za; E-mail: ignacy.cukrowski@up.ac.za

Contract grant sponsor: The National Research Foundation of South Africa; Contract grant number: 105855

© 2018 Wiley Periodicals, Inc.

have been reported.^[18–20] Such a correlation is remarkable but highlights one of the inherent misunderstandings about DI: while the DI measures the number of *electrons* delocalized within two atomic basins, it is only correlated with the number of *electron pairs* (bond order). For instance, in ethane, the DI between the two carbon atoms will be ~ 1.0 , indicating that 1 electron is fully shared between the two atoms, whereas the bond order suggests that 1 electron pair, i.e. 2 electrons are fully shared between the two atoms. Similarly, the LI measures the number of electrons “*exclusively*”^[21,22] localized to a single atomic basin, but this number does not correlate with any conceptual measure of core and non-bonding (such as a lone-pair) electrons. As an example, consider the H₂ molecule. The LI of each H atom is 0.5 e[−] (depending on the level of theory used), which, according to the definition of LI, indicates that 0.5 electrons on each H atom *cannot* be found on the other atom. The DI between the two H atoms is usually 1.0 e[−], indicating that one electron is fully shared between both atoms. In contrast, an investigation of the electronic structure would reveal that both electrons are fully delocalized across the entire molecule, and no electrons are localized to either atomic basin, in line with classical chemical thinking and in direct contrast with the quantity given by the LI. Note that the QTAIM interpretation of H₂ is discussed and critiqued in detail later in this work.

The fact that the DI correlates almost perfectly with the expected bond order for bonded atoms has, in our opinion, lead to an ambiguity with regards to the interpretations of both DIs and LIs. In this work, we will highlight the very statistical nature of DIs and LIs by considering the 3D real-space distribution of (de)localized electrons using the Fragment, Atom, Localized, Delocalized, and Interaction (FALDI) density decomposition technique.^[23,24] We also introduce two new sets of localization and delocalization indices calculated through FALDI which measures and corrects for the overlap between localized electron density distributions. Our novel indices represent (de)localization measures which fully recover traditional interpretations of electronic structures within QTAIM atomic basins, but are not pigeonholed into a classical paradigm. We present our results for orthodox and our novel LIs and DIs, as well as associated FALDI distributions, on H₂, N₂, ethene, ethylamine, formamide, and benzene. All of our results, as well as the Theoretical Basis, are discussed in terms of single-determinant, spin-restricted wavefunctions for simplicity.

Theoretical Basis

The number of electrons which can be found, on average, in the QTAIM-defined atomic basin of atom A (Ω_A) can be calculated by integrating the molecular electron density (ED) distribution over the relevant atomic domain (Ω_A):^[14]

$$N(A) = \int_A \rho(\mathbf{r}) d\mathbf{r} \quad (1)$$

where $N(A)$ is known as the atomic population. $N(A)$ can also be directly expressed in terms of the various canonical

molecular orbitals (MOs, spin-orbitals) of an electronic structure calculation:

$$N(A) = \text{tr}(\mathbf{S}^A) \quad (2)$$

where \mathbf{S}^A is known as the atomic overlap matrix (AOM) of basin Ω_A and its elements are given as the overlap between all MO pairs over the atomic domain:

$$S_{ij}^A = \sum_{ij} \int_A \chi_i^*(\mathbf{r}) \chi_j(\mathbf{r}) d\mathbf{r} \quad (3)$$

The atomic population for any given atom is therefore simply the sum of the expectation values of each MO integrated over the atomic domain. However, most MOs are delocalized across multiple atomic domains and therefore a portion of the electrons given by $N(A)$ can be found elsewhere as well.

The Domain Averaged Fermi Hole (DAFH)^[25,26] approach presents an alternative for calculating $N(A)$ and highlights the localized and delocalized nature of the electrons found within Ω_A . The exchange–correlation (XC) electron hole gives the ED which is excluded at \mathbf{r}_1 as a result of a reference electron at \mathbf{r}_2 :

$$\rho^{\text{Hole}}(\mathbf{r}_1; \mathbf{r}_2) = \frac{2\rho_2(\mathbf{r}_1, \mathbf{r}_2)}{\rho(\mathbf{r}_2)} - \rho(\mathbf{r}_1) \quad (4)$$

where $\rho_2(\mathbf{r}_1, \mathbf{r}_2)$ is the electron pair density. $\rho^{\text{Hole}}(\mathbf{r}_1; \mathbf{r}_2)$ is an excellent measure of XC effects at \mathbf{r}_1 as a result of an electron at \mathbf{r}_2 . Since $\rho^{\text{Hole}}(\mathbf{r}_1; \mathbf{r}_2)$ gives the *origin* of the XC effects, it can be used as a pseudo 2nd-order probability distribution of an electron at \mathbf{r}_2 , i.e. the delocalization of an electron at \mathbf{r}_2 as measured at \mathbf{r}_1 .^[20] In DAFH, the reference electron of the charge-weighted XC electron hole is averaged over an atomic domain to calculate how the electrons in Ω_A are distributed throughout the entire molecule:

$$g_A(\mathbf{r}_1) = - \int_A \rho(\mathbf{r}_2) \rho^{\text{Hole}}(\mathbf{r}_1; \mathbf{r}_2) d\mathbf{r}_2 \quad (5)$$

$g_A(\mathbf{r})$ is the central quantity in DAFH analysis and gives the contribution of atom A to the ED at any coordinate throughout the molecule (both inside and outside Ω_A), and the total molecular ED at \mathbf{r} is the sum of all atoms' contributions, $\rho(\mathbf{r}) = \sum g_A(\mathbf{r})$. Integrating $g_A(\mathbf{r})$ over all molecular space therefore recovers the atomic population from eq. (1):

$$N(A) = \int_{-\infty}^{\infty} g_A(\mathbf{r}) d\mathbf{r} \quad (6)$$

Since $g_A(\mathbf{r})$ is generally non-zero outside of Ω_A , eqs. (1) and (6) neatly illustrate that the average electrons in Ω_A ($N(A)$) can be found outside of Ω_A as well. In other words, $N(A)$ contains electrons which are localized to Ω_A as well as electrons which are delocalized (as a result of XC effects) throughout the molecule. Specifically, the number of electrons localized to Ω_A can be calculated by integrating $g_A(\mathbf{r})$ over only Ω_A :

$$\lambda_{\text{QTAIM}}(A) = \int_A g_A(\mathbf{r}) d\mathbf{r} \quad (7)$$

$\lambda_{\text{QTAIM}}(A)$ is known as the localization index (LI) of atom A in QTAIM, and gives the number of electrons which can be found “exclusively” in Ω_A .^[2,22] Similarly, the number of electrons delocalized between two atoms A and B can be calculated by integrating $g_A(\mathbf{r})$ over Ω_B and $g_B(\mathbf{r})$ over Ω_A :

$$\delta_{\text{QTAIM}}(A, B) = \int_B g_A(\mathbf{r}) d\mathbf{r} + \int_A g_B(\mathbf{r}) d\mathbf{r} \quad (8)$$

$\delta_{\text{QTAIM}}(A, B)$ is known as the delocalization index (DI) between atoms A and B in QTAIM, and gives the number of electrons delocalized (shared) within Ω_A and Ω_B .^[2] Note that the two terms on the right-hand side of eq. (8) are equal, i.e. the number of electrons of atom A which can be found in Ω_B is equal to the number of electrons of atom B which can be found in Ω_A . $N(A)$ can therefore be written as the sum of localized and delocalized electrons:

$$N(A) = \lambda_{\text{QTAIM}}(A) + \sum_{X \neq A} \frac{1}{2} \delta_{\text{QTAIM}}(A, X) \quad (9)$$

LIs and DIs provide an interesting picture regarding the atomic populations of a molecule, especially when expressed in terms of $g_A(\mathbf{r})$. Since $g_A(\mathbf{r})$ gives the contribution of the average number of electrons in A to the total ED at any coordinate in space, all contributions to coordinates *within* Ω_A are considered localized and all contributions to coordinates *outside* Ω_A are considered delocalized. $N(A)$ is therefore intrinsically a pseudo 2nd-order quantity which is revealed by its decomposition into $\lambda_{\text{QTAIM}}(A)$ and $\delta_{\text{QTAIM}}(A, X)$. The same argument can be made, however, for $\lambda_{\text{QTAIM}}(A)$ as well: just as the ED in Ω_A can be found simultaneously in other basins, the localized ED in Ω_A can also be found in other basins, i.e. $\lambda_{\text{QTAIM}}(A)$ describes electrons which are only “exclusive” on average. To investigate such an apparent lack of true exclusivity in LIs, we first discuss our FALDI density decomposition.

FALDI, similarly to the manner in which DAFH provides real-space distributions of atomic populations, provides real-space distributions of (de)localization indices.^[23,24] A short description of the FALDI equations follows. Within FALDI, $g_A(\mathbf{r})$ is known as an atomic ED distribution (*atom-ED*). In both FALDI and DAFH schemes, $g_A(\mathbf{r})$ is usually calculated using an AOM in terms of overlap of all MOs at \mathbf{r} :

$$g_A(\mathbf{r}) = \sum_{ij} \chi_i^*(\mathbf{r}) \chi_j(\mathbf{r}) S_{ji}^A \quad (10)$$

where \mathbf{S}^A is the AOM describing Ω_A [eq. (3)]. Note that eq. (10) is specific for single-determinant wavefunctions. While it can be easily adjusted for multi-determinant wavefunctions using natural orbital expansions (as has been done before^[16,22,27,28]), the same cannot be said for the equations which follow. We will restrict the remainder of this paper to derivations specific to single-determinant wavefunctions, as it provides a much simpler understanding of the various components involved, and we will derive and investigate suitable general expressions for multi-determinant wavefunctions in the future.

FALDI further defines localization and delocalization ED distributions (*loc-ED* and *deloc-ED*) in a similar fashion:

$$\mathcal{L}_A(\mathbf{r}) = \sum_{ij} \chi_i^*(\mathbf{r}) \chi_j(\mathbf{r}) (\mathbf{S}^A \mathbf{S}^A)_{ji} \quad (11)$$

$$\mathcal{D}_{A,B}(\mathbf{r}) = \sum_{ij} \chi_i^*(\mathbf{r}) \chi_j(\mathbf{r}) (\mathbf{S}^A \mathbf{S}^B)_{ji} \quad (12)$$

where $\mathbf{S}^A \mathbf{S}^A$ is the matrix product of \mathbf{S}^A with itself and $\mathbf{S}^A \mathbf{S}^B$ is the sum of matrix products $\mathbf{S}^A \mathbf{S}^B + \mathbf{S}^B \mathbf{S}^A$. Note that integrating the *loc-ED* distribution for atom A ($\mathcal{L}_A(\mathbf{r})$) over all molecular space recovers the total, QTAIM-defined LI, in complete analogy to eq. (6):

$$\int_{-\infty}^{\infty} \mathcal{L}_A(\mathbf{r}) d\mathbf{r} = \text{tr}(\mathbf{S}^A \mathbf{S}^A) = \lambda_{\text{QTAIM}}(A) \quad (13)$$

and the same for the QTAIM-defined DI and the *deloc-ED* distribution between atoms A and B, $\int_{-\infty}^{\infty} \mathcal{D}_{A,B}(\mathbf{r}) d\mathbf{r} = \text{tr}(\mathbf{S}^A \mathbf{S}^B) = \delta_{\text{QTAIM}}(A, B)$. Therefore, the FALDI fields represent real-space distributions of orthodox LI and DIs, so that *loc-ED* and *deloc-ED* distributions form a complete decomposition of each $g_A(\mathbf{r})$ as well as the total ED:

$$g_A(\mathbf{r}) = \mathcal{L}_A(\mathbf{r}) + \sum_{B \neq A} \frac{1}{2} \mathcal{D}_{A,B}(\mathbf{r}) \quad (14)$$

$$\rho(\mathbf{r}) = \sum_A g_A(\mathbf{r}) = \sum_A \mathcal{L}_A(\mathbf{r}) + \sum_{AB} \mathcal{D}_{A,B}(\mathbf{r}) \quad (15)$$

$\mathcal{L}_A(\mathbf{r})$, like $g_A(\mathbf{r})$, is non-zero outside of Ω_A , which shows that the localized electrons as measured by LIs within QTAIM can only be seen as “exclusively localized” within purely statistical interpretations. In the Results section, we will illustrate that the exclusivity, as indicated by orthodox LIs varies wildly and carries little chemical information.

The general procedure to calculate either DAFH’s $g_A(\mathbf{r})$ distributions or FALDI’s *loc-ED* distributions can be applied sequentially to AOMs to generate successively more localized distributions, i.e. $[\lambda_{\text{QTAIM}}(A)]^{(n)} = [\mathbf{S}^A]^{(n)}$. If the procedure is followed *ad infinitum* then no electrons will be found to be localized, and all electrons of an atom will be seen as delocalized. Such a result is chemically meaningless. However, orthodox LI and associated *loc-ED* distributions, which partly describe delocalized electrons in addition to localized electrons, are difficult to interpret. Therefore, our aim of this work is to arrive at a measure of exclusive electron localization within QTAIM atomic basins, i.e., an exclusive LI and *loc-ED* distribution (LI_{excl} and $\text{loc-ED}_{\text{excl}}$) that describe electrons which can only be found within a single atomic basin. Such an exclusive localization measure can be derived by considering the overlap of *loc-ED* distributions with other FALDI fields in 3D space. Specifically, any MO which (i) contributes to the LI of a specific atom and (ii) spans over multiple atomic basins needs to be accounted for when calculating LI_{excl} . To do so, we first express FALDI fields in a basis of MOs as natural functions, as discussed below.

Equation (10) is usually diagonalized in the DAFH procedure, to produce (i) a set of domain natural orbitals (DNOs), $\phi_i^A(\mathbf{r})$ of

the eigenvectors of \mathbf{S}^A in an MO basis and (ii) corresponding occupations, $n_i^{A, [15]}$

$$g_A(\mathbf{r}) = \sum_i^{N_{MO}} n_i^A [\phi_i^A(\mathbf{r})]^2 \quad (16)$$

where N_{MO} is the number of MOs and the sum of the occupations recovers the electron population, $\sum_i^{N_{MO}} n_i^A = N(A)$. The FALDI fields, *loc*-ED and *deloc*-ED distributions, can also be diagonalized to produce sets of orthogonal functions. This is accomplished by diagonalizing the matrices $\mathbf{S}^A \mathbf{S}^A$ and $\mathbf{S}^A \mathbf{S}^B$ (collectively referred to as $\mathbf{S}^A \mathbf{S}^X$), as introduced in eqs. (11) and (12), through a unitary transformation matrix:

$$\mathbf{S}^A \mathbf{S}^X \mathbf{U}^{AX} = n^{AX} \mathbf{U}^{AX} \quad (17)$$

where the columns of \mathbf{U}^{AX} are the eigenvectors associated with $\mathbf{S}^A \mathbf{S}^X$. The eigenvalues (occupations) can then be calculated as:

$$n_i^{AX} = \sum_{jk}^{N_{MO}} U_{ji}^{AX} (\mathbf{S}^A \mathbf{S}^X)_{kj} U_{ki}^{AX} \quad (18)$$

Each *loc*-ED and *deloc*-ED distribution can be expressed in terms of the eigenvectors ((de)localized DNOs) and eigenfunctions of eq. (17). For the diagonalization of a *loc*-ED distribution:

$$\mathcal{L}_A(\mathbf{r}) = \sum_i^{N_{MO}} n_i^{AA} [\phi_i^{AA}(\mathbf{r})]^2 \quad (19)$$

where

$$\phi_i^{AA}(\mathbf{r}) = \sum_j^{N_{MO}} \chi_j(\mathbf{r}) U_{ji}^{AA} \quad (20)$$

We refer to $n_i^{AA} [\phi_i^{AA}(\mathbf{r})]^2$ as a generic natural density function (NDF), to differentiate from natural orbital approaches. The sum of occupations gives the total LI, $\lambda_{QTAIM}(A) = \sum n_i^{AA}$. Similarly, NDFs for *deloc*-ED distributions can be calculated by $\mathcal{D}_{A,B}(\mathbf{r}) = \sum n_i^{AB} [\phi_i^{AB}(\mathbf{r})]^2$ with $\delta_{QTAIM}(A, B) = \sum n_i^{AB}$. Note that NDF occupations will always be positive for *loc*-ED distributions, but can be either positive or negative for *deloc*-ED distributions. Various examples of NDFs and their occupations are given throughout the Results section. We note that NDFs will produce similar results to the DAFH functions subjected to Cioslowski's isopycnic transformations^[29,30] in some molecules while very different results in others. However, we also note that our approach provides direct transferability to the total LI and DI values with straightforward interpretations.

Using the NDFs defined in eqs. (17–20), we can now calculate the overlap of *loc*-ED distributions with other FALDI fields. Generally, the overlap between the *i*th NDF of a *loc*-ED distribution ($\mathcal{L}_A^i(\mathbf{r})$) with the *j*th NDF of any other *loc*-ED ($\mathcal{L}_B^j(\mathbf{r})$) distribution, in an MO basis, can be calculated as:

$$\mathbf{s}(\mathcal{L}_A^i; \mathcal{L}_B^j) = \sqrt{n_i^{AA} n_j^{BB}} \left[(\mathbf{U}^{AA})^\dagger \mathbf{U}^{BB} \right]_{ij} \quad (21)$$

Note that the overlap is normalized to the square root of the occupations of the NDFs. Therefore, the overlap of $\mathcal{L}_A^i(\mathbf{r})$ with itself will be equal to its occupation, n_i^{AA} . The overlap between $\mathcal{L}_A^i(\mathbf{r})$ and an NDF of a *deloc*-ED distribution ($\mathcal{D}_{A,B}^j(\mathbf{r})$), $\mathbf{s}(\mathcal{L}_A^i; \mathcal{D}_{A,B}^j)$, can be calculated in exactly the same manner, using the eigenvalues and eigenvectors of $\mathbf{S}^A \mathbf{S}^B$: n_j^{AB} and \mathbf{U}^{AB} .

The first step which we take toward LI_{excl} is to calculate the overlap between all *loc*-ED distributions. Using eq. (21), the total localized overlap (LO) of the *i*th NDF of $\mathcal{L}_A(\mathbf{r})$ with all other NDFs of all other *loc*-EDs can be calculated:

$$\text{LO}(\mathcal{L}_A^i) = \sum_{X \neq A}^{M_{\text{Atoms}}} \sum_j^{N_{MO}} \mathbf{s}(\mathcal{L}_A^i; \mathcal{L}_X^j) \quad (22)$$

If the occupation of the NDF (n_i^{AA}) is larger than $\text{LO}(\mathcal{L}_A^i)$ then the occupation can be adjusted accordingly; otherwise, the NDF is completely overlapped by other *loc*-ED distributions with contributions to the same MOs, and the occupation can be set to zero:

$$n_i'^{AA} = \begin{cases} n_i^{AA} - \text{LO}(\mathcal{L}_A^i) & , n_i^{AA} > \text{LO}(\mathcal{L}_A^i) \\ 0 & , n_i^{AA} \leq \text{LO}(\mathcal{L}_A^i) \end{cases} \quad (23)$$

where the occupation of the *i*th NDF is primed to indicate that it is LO-free. The adjusted occupations ($n_i'^{AA}$) can be substituted into eq. (19) to produce a LO-free *loc*-ED distribution,

$$\mathcal{L}'_A(\mathbf{r}) = \sum_i^{N_{MO}} n_i'^{AA} [\phi_i^{AA}(\mathbf{r})]^2 \quad (24)$$

and integrated over all space [eq. (13)] to produce a LO-free LI:

$$\lambda_{\text{LO-free}}(A) = \int_{-\infty}^{\infty} \mathcal{L}'_A(\mathbf{r}) d\mathbf{r} \quad (25)$$

where we have used the subscript "LO-free" to distinguish from orthodox LIs ($\lambda_{QTAIM}(A)$).

The occupation of a specific *loc*-ED's NDF which is removed through eq. (23) is $n_i^{AA} - n_i'^{AA}$, and is an indication of delocalized density included in an orthodox LI as a result of averaging. The overlap between the *loc*-ED distributions of atoms A and B can therefore be added to the *deloc*-ED distribution of atom-pair A and B as a fraction of the total removed density:

$$n'(\mathcal{L}_A^i \rightarrow \mathcal{D}_{A,B}^j) = w'(\mathcal{L}_A^i; \mathcal{D}_{A,B}^j) (n_i^{AA} - n_i'^{AA}) \quad (26)$$

where

$$w'(\mathcal{L}_A^i; \mathcal{D}_{A,B}^j) = \frac{\mathbf{s}(\mathcal{L}_A^i; \mathcal{D}_{A,B}^j)}{\sum_j \mathbf{s}(\mathcal{L}_A^i; \mathcal{D}_{A,B}^j)} \cdot \frac{\sum_k \mathbf{s}(\mathcal{L}_A^i; \mathcal{L}_B^k)}{\text{LO}(\mathcal{L}_A^i)} \quad (27)$$

is the overlap between $\mathcal{L}_A^i(\mathbf{r})$ and $\mathcal{D}_{A,B}^j(\mathbf{r})$ as a fraction of the total overlap between $\mathcal{L}_A^i(\mathbf{r})$ and all NDFs of $\mathcal{D}_{A,B}^j(\mathbf{r})$, as well as the overlap between $\mathcal{L}_A^i(\mathbf{r})$ and $\mathcal{L}_B^j(\mathbf{r})$ as a fraction of the total overlap between $\mathcal{L}_A^i(\mathbf{r})$ and all other *loc*-ED distributions [eq.

(22)]. The weighting function in eq. (27) ensures that the fraction of the removed density, $n_i^{AA} - n_i'^{AA}$, is added to a suitable NDF of the relevant *deloc*-ED distribution. The LO-free *deloc*-ED distribution, in terms of NDFs, then becomes:

$$\mathcal{D}'_{A,B}(\mathbf{r}) = \sum_j^{N_{MO}} n_j^{AB} [\phi_j^{AB}(\mathbf{r})]^2 + \sum_j^{N_{MO}} \sum_i^{N_{MO}} (n'(\mathcal{L}_A^i \rightarrow \mathcal{D}_{A,B}^j) [\phi_i^{AA}(\mathbf{r})]^2 + n'(\mathcal{L}_B^i \rightarrow \mathcal{D}_{A,B}^j) [\phi_i^{BB}(\mathbf{r})]^2) \quad (28)$$

where we have used the adjusted occupations from eq. (26). The first term of eq. (28) are NDFs related to the matrix $\mathbf{S}^A \mathbf{S}^B$ and the second term contains the contributions which was removed from *loc*-ED distributions due to LO-overlap. Finally, LO-free DIs can be calculated by integrating eq. (28) over all space:

$$\delta_{LO\text{-free}}(A, B) = \int_{-\infty}^{\infty} \mathcal{D}'_{A,B}(\mathbf{r}) d\mathbf{r} \quad (29)$$

After the procedure described above, the fraction of any MO which contributes simultaneously to the LIs of two or more atoms will be removed from the LIs and added to the associated DI. The result is LO-free LIs and DIs. The primed occupation ($n_i'^{AA}$) is the LO-free occupation and can be used during the calculation of a NDF to produce a LO-free NDF, and their sum gives the LO-free *loc*-ED distribution. Finally, the density which was removed from the *loc*-ED NDFs, as given by $n'(\mathcal{L}_A^i \rightarrow \mathcal{D}_{A,B}^j)$, eq. (26), is added to the *j*th NDF of the associated *deloc*-ED distribution to ensure that the total ED remains the same after calculating the LO. In summary, accounting for LO results in a set of *loc*-ED distributions (and LIs) which effectively describes the core and non-bonded electrons of an atom, i.e. the electrons which are localized only to a single atom and cannot be found in the *loc*-ED distributions of other atoms.

The LO-free LI and *loc*-ED distributions are still not exclusively localized, however. We next present a second set of equations which calculates the overlap of the *i*th NDF of a *loc*-ED distribution with *all* other electrons, i.e. the NDFs of all other *loc*-ED and *deloc*-ED distributions. The resulting LIs and *loc*-ED distributions are free of any localized and delocalized overlap (LDO). The same procedure for calculating LO-free indices is followed, except the overlap is calculated between both localized and delocalized NDFs. Therefore, the total LO of eq. (22) changes to include overlap with the delocalized density of the molecule:

$$LDO(\mathcal{L}_A^i) = \sum_{X \neq A}^{M_{Atoms}} \sum_j^{N_{MO}} \mathbf{s}(\mathcal{L}_A^i; \mathcal{L}_X^j) + \sum_X^{M_{Atoms}} \sum_{Y \neq A}^{M_{Atoms}} \sum_j^{N_{MO}} \mathbf{s}(\mathcal{L}_A^i; \mathcal{D}_{X,Y}^j) \quad (30)$$

All other equations remain, in principle, the same, and produce new occupations for NDFs of *loc*-ED distributions, $n_i''^{AA}$, given by:

$$n_i''^{AA} = \begin{cases} n_i^{AA} - LDO(\mathcal{L}_A^i) & , n_i^{AA} > LDO(\mathcal{L}_A^i) \\ 0 & , n_i^{AA} \leq LDO(\mathcal{L}_A^i) \end{cases} \quad (31)$$

Note that we have used double primes to indicate the occupations of NDFs for LDO-free FALDI fields. Substituting $n_i''^{AA}$ into eq. (19) gives a LDO-free *loc*-ED distribution,

$$\mathcal{L}''_A(\mathbf{r}) = \sum_i^{N_{MO}} n_i''^{AA} [\phi_i^{AA}(\mathbf{r})]^2 \quad (32)$$

and integrating over all space gives a LDO-free LI:

$$\lambda_{LDO\text{-free}}(A) = \int_{-\infty}^{\infty} \mathcal{L}''_A(\mathbf{r}) d\mathbf{r} \quad (33)$$

Again, the fraction of electrons which was removed from each NDF [eq. (31)] for each LDO-free *loc*-ED distribution is added to the appropriate NDF of a *deloc*-ED distribution using a fractional weighting function:

$$n''(\mathcal{L}_A^i \rightarrow \mathcal{D}_{A,B}^j) = w''(\mathcal{L}_A^i; \mathcal{D}_{A,B}^j) (n_i^{AA} - n_i''^{AA}) \quad (34)$$

where

$$w''(\mathcal{L}_A^i; \mathcal{D}_{A,B}^j) = \frac{\mathbf{s}(\mathcal{L}_A^i; \mathcal{D}_{A,B}^j)}{\sum_j \mathbf{s}(\mathcal{L}_A^i; \mathcal{D}_{A,B}^j)} \cdot \frac{\sum_k \mathbf{s}(\mathcal{L}_A^i; \mathcal{L}_B^k)}{LDO(\mathcal{L}_A^i)} \quad (35)$$

The LDO-free *deloc*-ED distribution is then given by:

$$\mathcal{D}''_{A,B}(\mathbf{r}) = \sum_j^{N_{MO}} n_j^{AB} [\phi_j^{AB}(\mathbf{r})]^2 + \sum_j^{N_{MO}} \sum_i^{N_{MO}} (n''(\mathcal{L}_A^i \rightarrow \mathcal{D}_{A,B}^j) [\phi_i^{AA}(\mathbf{r})]^2 + n''(\mathcal{L}_B^i \rightarrow \mathcal{D}_{A,B}^j) [\phi_i^{BB}(\mathbf{r})]^2) \quad (36)$$

and LDO-free DIs can be calculated by integrating over all space:

$$\delta_{LDO\text{-free}}(A, B) = \int_{-\infty}^{\infty} \mathcal{D}''_{A,B}(\mathbf{r}) d\mathbf{r} \quad (37)$$

$\lambda_{LDO\text{-free}}(A)$ [eq. (33)] as well as the associated *loc*-ED distribution [$\mathcal{L}''_A(\mathbf{r})$, eq. (32)] represent electrons which can be found exclusively in only a single atomic basin, and therefore corresponds to the hypothetical LI_{excl} and $loc\text{-ED}_{\text{excl}}$ distributions mentioned earlier. $\delta_{LDO\text{-free}}(A, B)$ [eq. (37)] as well as the associated *deloc*-ED distribution [$\mathcal{D}''_{A,B}(\mathbf{r})$, eq. (36)] therefore describes electrons which are delocalized (in any way) between atomic basins.

In conclusion, $\lambda_{LDO\text{-free}}(A)$ is a localized electron count of electrons which are exclusive to a single atomic basin and it describes what chemists would typically call core electrons. $\lambda_{LO\text{-free}}(A)$ is a localized electrons count of electrons which are not necessarily exclusively localized to an atom as a whole, but it accounts for electrons which cannot be found in the localized distributions of other atoms. Generally, $\lambda_{LO\text{-free}}(A)$ describes core as well as non-bonded electrons, such as lone-pairs. In contrast, $\lambda_{QTAIM}(A)$ is a statistically localized electron count of electrons which are not exclusively found in a single atomic basin and can be found in the localized electron

counts of other atoms as well; $\lambda_{\text{QTAIM}}(A)$ contains core and non-bonded electrons as well as a significant portion of delocalized electrons. Note that the LO-free delocalized electrons associated with a single atom correspond to the typical number of valence electrons chemists assign to simple organic molecules, which is why the LO procedure is included within this work in conjunction with the LDO procedure.

For simplicity, the following conventions in nomenclature will be used: (i) $\lambda_{\text{QTAIM}}(A)$, $\lambda_{\text{LO-free}}(A)$, and $\lambda_{\text{LDO-free}}(A)$ refer to the uncorrected (orthodox), LO-free and LDO-free LIs, respectively, of atom A, (ii) $\delta_{\text{QTAIM}}(A, B)$, $\delta_{\text{LO-free}}(A, B)$, and $\delta_{\text{LDO-free}}(A, B)$ refer to the uncorrected, LO-free and LDO-free DIs, respectively, of atom-pair A,B, and (iii) superscripted LIs or DIs refer to the occupation of a specific NDF associated with that LI or DI, e.g. $\lambda_{\text{QTAIM}}^2(A)$ refers to the occupation of the 2nd NDF of the uncorrected *loc*-ED distribution for atom A, and $\delta_{\text{LDO-free}}^4(A, B)$ refers to the occupation of the 4th NDF of the LDO-free *deloc*-ED distribution for atom-pair A,B.

Computational Details

Optimizations of all structures were performed using restricted Hartree–Fock with a 6-311++G(d,p) basis set in Gaussian 09, rev. D.^[31] Cartesian coordinates of optimized ethene and ethylamine are shown in Tables S1 and S2 in the Supplementary Information. Atomic populations, as well as AOMs, were computed using AIMAll v. 17.01.25.^[32] All FALDI-based calculations, as well as orthodox LIs and DIs, were calculated with our in-house code. Isosurfaces of FALDI fields were visualized using VMD.^[33]

Results and Discussion

The H₂ molecule

The H₂ molecule, using a restricted Hartree–Fock (HF) wavefunction, has 1 molecular orbital (MO) fully delocalized across both atomic basins. Each atomic basin therefore consists of 50% of the total molecular space, and the average number of electrons in each atomic basin is one ($N(\text{H}) = 1.0 e^-$). In orthodox QTAIM population analysis, $\lambda_{\text{QTAIM}}(\text{H})$ is 0.5 and $\delta_{\text{QTAIM}}(\text{H}, \text{H})$ is 1.0, leading to the interpretation that, on average, 0.5 electrons will be found “exclusively” in each atomic basin and 1 electron will be fully delocalized across both basins. However, since only one MO is occupied, both electrons have equal probability to be found in both basins. It is therefore expected from the electronic structure that no electrons are localized in H₂, and that both electrons are fully shared across the molecule. The orthodox QTAIM LIs and DIs therefore only make sense from a purely 1st-order, statistical point of view. FALDI allows visualization of the localized and delocalized electrons, as shown in Figure 1a. The *loc*-ED distribution for a single H atomic basin, which gives the probability of finding an electron localized to the specified basin reveals that, in fact, this supposedly “exclusively localized” electron ($\lambda_{\text{QTAIM}}(\text{H1}) = 0.5 e^-$) is fully delocalized across both basins.

$\lambda_{\text{LO-free}}(A)$ and its associated *loc*-ED distribution, calculated as discussed in the Theoretical Basis, gives the core and non-

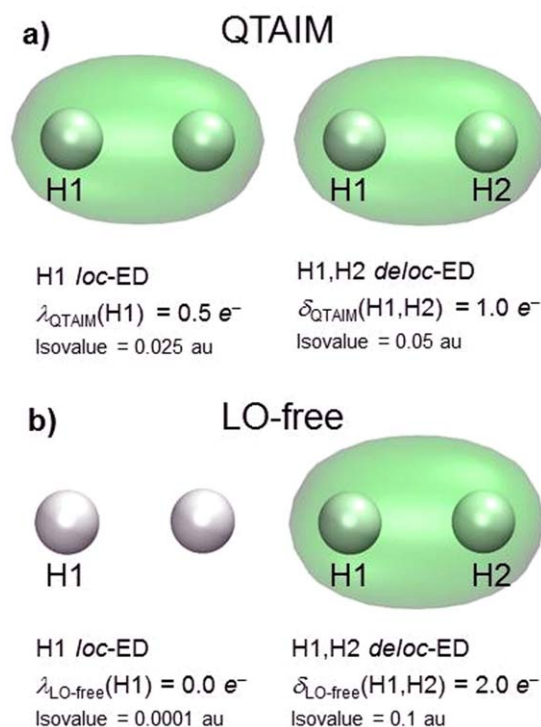


Figure 1. *Loc*-ED and *deloc*-ED distributions for H₂ for a) orthodox QTAIM LIs and DIs and b) LO-free LIs and DIs. [Color figure can be viewed at wileyonlinelibrary.com]

bonded electrons of an atom. In the case of an H-atom in H₂ there are no non-bonded electrons; hence, $\lambda_{\text{LO-free}}(\text{H})$ is 0.0 and the associated *loc*-ED is zero throughout the molecule (as shown in Fig. 1b). However, $\delta_{\text{LO-free}}(\text{H}, \text{H})$ is exactly 2.0 and the associated *deloc*-ED distribution is equal to the total ED distribution, coinciding with the electronic structure of the molecule, i.e. a single electron pair fully delocalized across both atoms.

The N₂ molecule

Figure 2a shows the uncorrected *loc*-ED distribution associated with a single N atom basin and *deloc*-ED distribution associated with the N,N atom-pair in N₂. As found for a single H atom in H₂, the localized electrons of N (with $\lambda_{\text{QTAIM}}(\text{N}) = 5.48 e^-$) are not exclusively localized at all. However, unlike H₂, the *loc*-ED distribution of a single N atom is much larger within the atomic basin whereas $\delta_{\text{QTAIM}}(\text{N}, \text{N}) = 3.04 e^-$ is much smaller than any of the LIs. The orthodox LI therefore describes the core electrons, non-bonded electrons (lone-pairs) as well as a portion of the delocalized electrons. Each LI and DI, as well as *loc*-ED and *deloc*-ED distributions, can be decomposed into natural density functions (NDFs) and associated populations, as discussed in the Theoretical Basis. The two highest occupied *loc*-NDFs for a single N atom with populations of 2.0 and 1.98 e⁻ (Fig. 2b) contribute ~4 electrons to $\lambda_{\text{QTAIM}}(\text{N})$. These distributions resemble the 1s orbital density and lone-pair density of the nitrogen, respectively, and both are clearly localized to the atomic basin. However, the remaining *loc*-NDFs, with a population of 0.5 e⁻ each, are fully

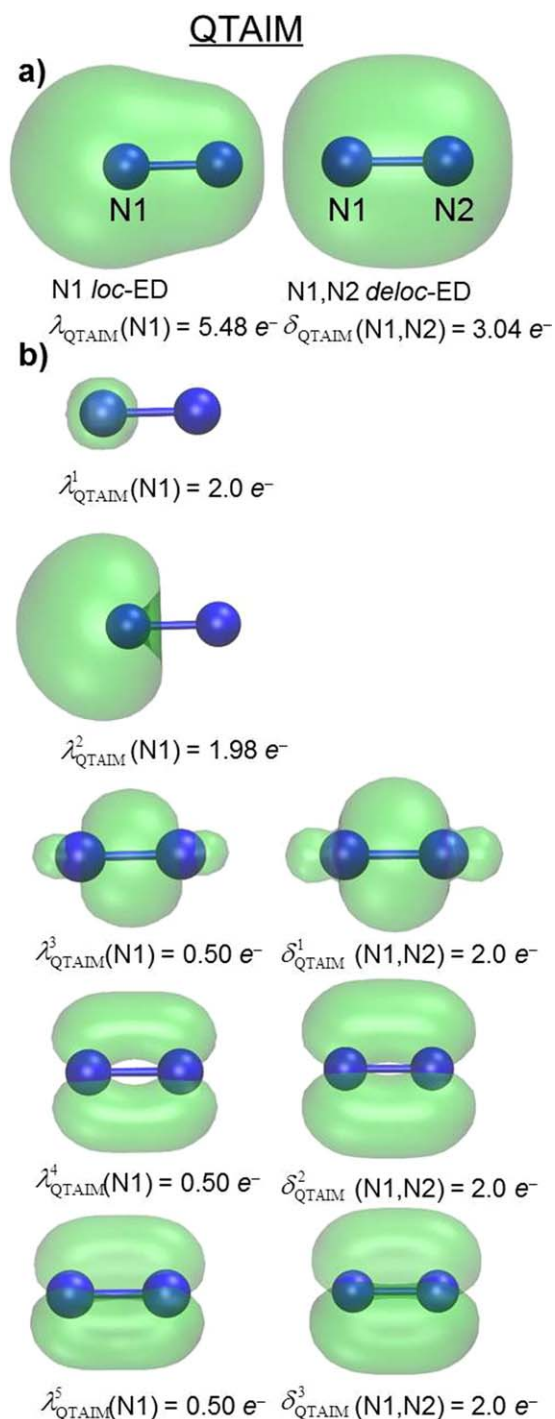


Figure 2. Uncorrected *loc*-ED and *deloc*-ED distributions a), as well as selected uncorrected *loc*-NDFs and *deloc*-NDFs b) for N₂. Orthodox LIs, DIs as well as NDF occupations are shown. All isovalues are at 0.01 a.u. [Color figure can be viewed at wileyonlinelibrary.com]

delocalized across both basins and resemble σ and π orbital densities. In fact, these NDFs are smaller, but otherwise identical, versions of the *deloc*-NDFs (with a population of 1.0 e⁻ each). Again, the interpretation given by orthodox QTAIM populations is somewhat difficult to comprehend: while 5.48 electrons are statistically *localized* to an atomic basin, 1.5 of these electrons can clearly be found on the other atomic basin.

Figure 3a shows the LO-free *loc*-ED distribution associated with a single N atom basin and *deloc*-ED distribution associated with the N,N atom-pair for N₂. Note that $\lambda_{\text{LO-free}}(\text{N})$ is 3.97 e⁻, matching the number of core and non-bonded electrons from the electronic structure, whereas $\delta_{\text{LO-free}}(\text{N,N})$ is 6.06 e⁻, corresponding to three electron pairs forming the triple bond of N₂. The LO-free *loc*-ED and *deloc*-ED distributions therefore correspond to exclusively localized and delocalized electrons, respectively. LO-free *loc*-NDFs and *deloc*-NDFs are shown in Figure 3b. It is clearly seen that (i) only two *loc*-NDFs are occupied that correspond to the 1s orbital density and the nitrogen-atom lone-pair and (ii) three occupied *deloc*-NDF (each containing 2 electrons) correspond to three bonding orbital densities in N₂.

The ethene molecule

Ethene is included as an example of a polyatomic molecule, with orthodox QTAIM atomic populations calculated as

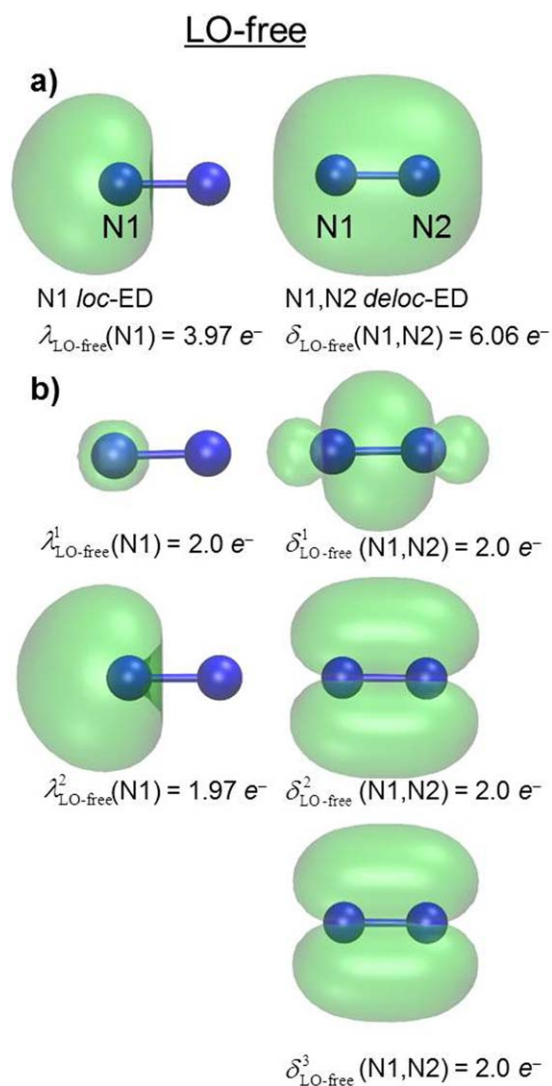


Figure 3. LO-free *loc*-ED and *deloc*-ED distributions a), as well as selected LO-free *loc*-NDFs and *deloc*-NDFs b), for N₂. LO-free LIs, DIs as well as NDF occupations are shown. All isovalues are at 0.01 a.u. [Color figure can be viewed at wileyonlinelibrary.com]

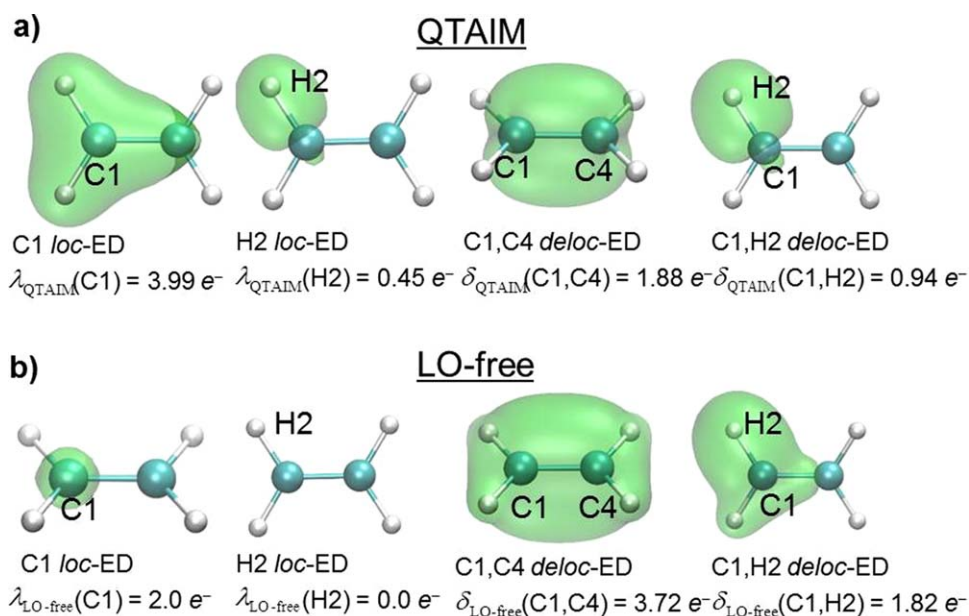


Figure 4. a) Uncorrected and b) LO-free *loc*-ED and *deloc*-ED distributions for ethene. Orthodox as well as LO-free LIs and DIs are shown. All isovalues are at 0.01 a.u. [Color figure can be viewed at wileyonlinelibrary.com]

$N(\text{C}) = 5.98 e^-$ and $N(\text{H}) = 1.01 e^-$. All atomic populations, as well as uncorrected and LO-free LI and DI values are shown in Tables S3 and S4 in the Supporting Information. $\lambda_{\text{QTAIM}}(\text{C})$ is equal to $3.99 e^-$, and the *loc*-ED distribution of a C atom (shown in Fig. 4a) clearly illustrates how the orthodox localized electrons of C can be found elsewhere in the molecule. Specifically, a carbon atom's *loc*-ED distribution completely overlaps its neighboring H atomic basins, and partially overlaps the other C atomic basin. $\lambda_{\text{LO-free}}(\text{C})$, however, is equal to exactly $2.0 e^-$ and its associated *loc*-ED distribution (shown in Fig. 4b) resembles the exclusively localized carbon 1s electrons. Similarly, the localized electrons of one of the H atoms ($\lambda_{\text{QTAIM}}(\text{H}) = 0.45 e^-$) extends into one of the C atomic basins, but $\lambda_{\text{LO-free}}(\text{H})$ becomes zero, i.e., no electrons are exclusively localized in any of the H atomic basins. Finally, the DI as well as *deloc*-ED distributions for the C,C and a C,H atom-pairs are shown in Figure 4a. The orthodox $\delta_{\text{QTAIM}}(\text{C,C})$ is equal to $1.88 e^-$, indicative of a bond order of two, and $\delta_{\text{QTAIM}}(\text{C,H}) = 0.94 e^-$. $\delta_{\text{LO-free}}(\text{C,C})$, however, is equal to $3.72 e^-$ —corresponding to slightly less than 2 electron pairs shared between the carbon atoms, and $\delta_{\text{LO-free}}(\text{C,H})$ is $1.82 e^-$. The fact that $\delta_{\text{LO-free}}(\text{C,C})$ and $\delta_{\text{LO-free}}(\text{C,H})$ is slightly smaller than what is formally expected is understandable, because each atom shares electrons with *all* other atoms. Accordingly, the portion of $N(\text{C})$ which is delocalized into other atomic basins is, after accounting for LO, equal to $4.02 e^-$, which is the number of formal valence electrons of a sp^3 hybridized C atom. Our LO-free FALDI indices therefore can recover the classically expected valence state of an atom, a quantity which is not obtainable from orthodox QTAIM analyses.

Selected LO-free *deloc*-NDFs, as well as their occupations, are shown in Figure 5; additional NDFs associated with *loc*-ED and *deloc*-ED of ethene are shown in Figures S1 and S2 in the Supporting Information. The results are generally as expected:

$1.87 e^-$ and $1.64 e^-$ are shared between C atoms in σ - and π -bonding fashions, respectively. The least occupied *deloc*-NDFs are also shown in Figure 5. The eigenvalues associated with these functions are negative, and the presence of these functions *reduces* the total ED. FALDI therefore recovers *deloc*-ED of an “antibonding” nature, even though the virtual orbitals are not included during calculations of atomic overlap matrices. The “antibonding” *deloc*-NDFs shown in Figure 5 resemble the LUMO and LUMO + 1 orbital densities of ethene, and result from destructive interference of MOs overlapping both atomic basins.

Accounting for LO introduces an interesting effect regarding the DIs. In orthodox QTAIM populations, the total $\delta_{\text{QTAIM}}(\text{A,B})$

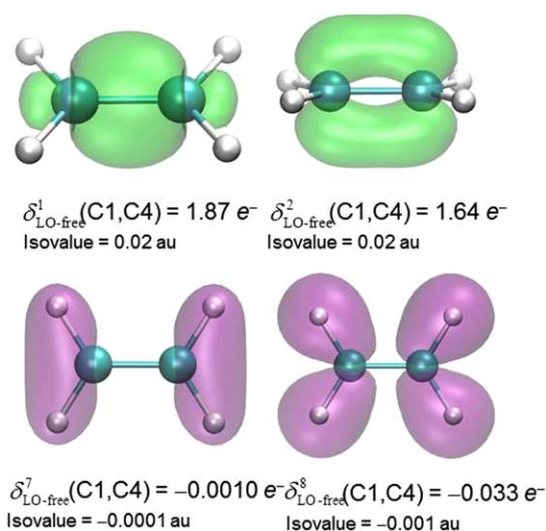


Figure 5. Selected LO-free *deloc*-NDFs, for atom-pair C,C in ethene. NDF occupations are shown. [Color figure can be viewed at wileyonlinelibrary.com]

Table 1. Interatomic LO-free DI contributions to atomic populations in ethane.

Atom A	Atom B			
	C1	H2	C4	H5
C1	–	0.97	1.86	0.09
H2	0.85	–	0.07	0.03
C4	1.86	0.09	–	0.97
H5	0.07	0.03	0.85	–

for any given atom-pair A,B is equally shared between both atoms; that is, $\delta_{\text{QTAIM}}(A,B) = 1/2\delta_{\text{QTAIM}}(A,B) + 1/2\delta_{\text{QTAIM}}(B,A)$. In LO-free DIs, however, the electrons are unequally shared between two atomic basins.

Table 1 shows how electrons are shared between selected atoms of ethane. For instance, $\delta_{\text{LO-free}}(\text{C1},\text{H2})$ is $1.92 e^-$. Of these electrons, $0.85 e^-$ is found on H2 and $0.97 e^-$ is found on C1. It is therefore expected that the electrons shared between C1 and H2 will be found $\sim 50.5\%$ of the time on C1 and 49.5% on H2.

The ethylamine molecule

LO-free LIs, Dis, and FALDI fields for H_2 , N_2 , and ethene have produced results in line with typical interpretations of electronic structures. Ethylamine is included in this study to investigate the (de)localization of the lone-pair electrons on the nitrogen atom. The uncorrected, as well as LO-free LIs and associated *loc*-ED distributions for the N atom are shown in Figures 6a and 6b, respectively (selected NDFs are shown in Figure S3 in the Supporting Information). The computed (i) $\lambda_{\text{QTAIM}}(\text{N}) = 6.71 e^-$ indicates core and non-bonded electrons as well as a portion of the delocalized electrons whereas (ii)

$\lambda_{\text{LO-free}}(\text{N}) = 3.80 e^-$ reflects only the core and lone-pair electrons present on N (all orthodox, LO-free and LDO-free indices are shown in Tables S5 and S6 in the Supporting Information). The uncorrected *loc*-ED distribution of N shows that the “localized” electrons are indeed somewhat delocalized, and a significant portion of these electrons can be found on the neighboring carbon as well as hydrogen atoms of the NH_2 group. However, even after accounting for LO, the localized electrons can still be found on hydrogen atoms as well as elsewhere in the molecule. The LO procedure accounts for electrons of a specific uncorrected *loc*-ED distribution which can be found in other *loc*-ED distributions. These electrons generally form the bulk of the diagonal elements of atomic overlap matrices. However, if significant electrons are localized or delocalized as a result of overlap of off-diagonal elements, the LO procedure will not account for these electrons. This is the case of the *loc*-ED distribution of N in ethylamine.

An additional step has been applied, the LDO-procedure, taking into account the overlap of a specific *loc*-ED with all other electron distributions in the molecule; i.e. other *loc*-ED distributions as well as all *deloc*-ED distribution of the molecule. The computed $\lambda_{\text{LDO-free}}(\text{N})$ of $1.99 e^-$ reflects the core $1s$ orbital density, as shown in Figure 6c. The LDO-free *loc*-ED distribution, from which even weakly delocalized effects have been excluded, can be interpreted as the electrons which cannot be found anywhere else in the molecule, and therefore gives a complete, exclusively localized electron count.

An additional step has been applied, the LDO-procedure, taking into account the overlap of a specific *loc*-ED with all other electron distributions in the molecule; i.e. other *loc*-ED distributions as well as all *deloc*-ED distribution of the molecule. The computed $\lambda_{\text{LDO-free}}(\text{N})$ of $1.99 e^-$ reflects the core $1s$ orbital density, as shown in Figure 6c. The LDO-free *loc*-ED distribution, from which even weakly delocalized effects have been excluded, can be interpreted as the electrons which cannot be found anywhere else in the molecule, and therefore gives a complete, exclusively localized electron count.

The difference between the LO- and LDO-free *loc*-ED distribution of N (Figs. 6b and 6c) reveals that the lone-pair density is not *exclusively* localized to the N atom, but can be found in other atomic basins as a result of overlap of off-diagonal terms of the AOMs. This finding is quite interesting with regards to our understanding of lone-pairs within atoms in molecules. While the lone-pair is predominantly localized to the N atom in ethylamine (as evidenced by the LO-free *loc*-ED distribution), the lone-pair density is “constructed” from different sets of mutually overlapping molecular orbitals across multiple atoms. As a result, the lone-pair density is not as strongly localized as say the $1s$ density of N. This point can be further explained by examining LO- and LDO-free DIs shown in Table 2 where $\delta_{\text{LO-free}}(\text{N8},\text{H9})$ for the N atom and one of its neighboring hydrogens, H9, is $1.77 e^-$. These electrons are delocalized in such a manner so that 1.18 and $0.59 e^-$ is found in N8's and H9's atomic basins, respectively. Looking at $\delta_{\text{LDO-free}}(\text{N8},\text{H9})$, it shows that a total of $2.07 e^-$ is shared between N8 and H9, with 1.50 and $0.57 e^-$ found in N8's and H9's atomic basins, respectively. The ~ 0.3 additional electrons in $\delta_{\text{LDO-free}}(\text{N8},\text{H9})$

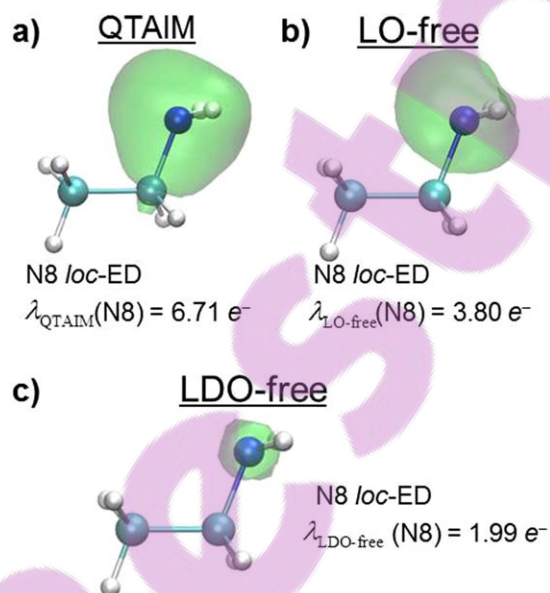


Figure 6. a) Uncorrected, b) LO-free and c) LDO-free LI and *loc*-ED distributions for the nitrogen atom in ethylamine. Orthodox, LO-free and LDO-free LIs are shown. All isosurfaces are at 0.01 a.u. [Color figure can be viewed at wileyonlinelibrary.com]

Table 2. Interatomic LO-free (part a) and LDO-free (part b) delocalized electron contributions to atomic populations in ethylamine.

Part a) LO-free DI					Part b) LDO-free DI				
Atom B					Atom B				
Atom A	C1	C5	N8	H9	Atom A	C1	C5	N8	H9
C1		0.98	0.12	0.02	C1		0.89	0.15	0.03
C5	0.92		0.70	0.02	C5	0.84		0.71	0.04
N8	0.20	1.33		1.18	N8	0.44	1.50		1.50
H9	0.01	0.02	0.59		H9	0.01	0.02	0.57	

as opposed to $\delta_{\text{LO-free}}(\text{N8}, \text{H9})$ therefore only contribute to the average atomic population of N8, despite the fact that these electrons can be found in H9 as well. The results in Table 2 (as well as the full table of all interatomic delocalized electron populations, Tables S6 and S7 in the Supporting Information) show a general trend of increased interatomic delocalized electrons for LDO-free DIs, but only increasing in N8's atomic basin.

Based on the findings in Figure 6 and Table 2, the "localized" lone-pair ED on N8 is a result of molecular-wide XC effects that leads to constructive interference *exclusively* in the N8 atomic basin. This observation explains why the LO-procedure does not account for the possibility of finding the lone-pair electrons in other basins, whereas the LDO-procedure accounts for the delocalized nature of the lone-pair electrons. Such an interpretation of a lone-pair is quite strange, but we hope that it should help to describe the peculiar properties and reactivity of lone-pairs, such as lone-pairs acting as good H-bond acceptors, Lewis bases and the so-called "lone-pair effect."

Formamide

All the above examples are well-understood chemical systems that were calculated at HF level to demonstrate that FALDI can recover classically expected atomic core, non-bonding and bonding populations. Formamide, calculated at RB3LYP/6-311++g(d,p) level, is included as an example of a highly conjugated system.

The carbon, nitrogen, and oxygen atoms have total atomic populations of 4.56, 8.13, and 9.13 electrons, respectively, indicating that the carbon atom is highly cationic whereas the nitrogen and oxygen atoms are highly anionic. LDO-free *loc*-ED distributions, as well as LDO-free LIs, for each heavy atom in formamide is shown in Figure 7. The *loc*-ED distributions for the nitrogen and carbon atoms match the typical 1s orbital density. Interestingly, the number of localized electrons in C1 is slightly less than 2 electrons ($\lambda_{\text{LDO-free}}(\text{C1}) = 1.82$), indicating that it is energetically favorable to delocalize some of the core 1s electrons in C1 and utilize these electrons for interatomic bonding. The number of core electrons in N4, however, is close to the expected value of 2 electrons ($\lambda_{\text{LDO-free}}(\text{N4}) = 1.98$), and the lone-pair on N4 is therefore highly delocalized. Oxygen, however, contains 3.42 exclusively localized electrons, and NDFs reveal that these electrons correspond to the 1s orbital density ($\lambda_{\text{LDO-free}}^1(\text{O3}) = 1.99$) and a partially occupied 2s

orbital ($\lambda_{\text{LDO-free}}^2(\text{O3}) = 1.44$), indicating that only a small fraction of the electrons forming the expected two lone-pairs are, indeed, exclusively localized.

Of considerable more interest is the distribution of density channels through which electrons are delocalized between atoms. Figure 8 shows the first three occupied LDO-free *deloc*-NDFs, as well as the sum of all remaining *deloc*-NDFs, for the electrons delocalized between heavy atoms, and Table 3 reports the total LDO-free DI as well as NDF occupations. In all three atom-pairs shown in Figure 8, three distinct modes of delocalization are always seen: typical σ - and π -bonding orbital densities, as well as a second π -bonding orbital density within the plane of the molecule. C1 and N4 shares a total of 2.86 electrons, indicating a partial double bond, which is predominantly of σ character (50.5%), but with significant π_1 and π_2 character as well (35.8% and 11.7%, respectively). Atom-pair C1,O3, however, present almost full double bond character (sharing a total of 3.70 electrons), of very nearly equal contributions of σ and π_1 bonding modes (36.4% and 35.1%, respectively) and significant π_2 contribution as well (23.4%). Finally, the long-range delocalization between atoms O3 and N4 delocalize 2.07 electrons, indicating that these supposedly non-bonded atoms share slightly more than a full electron pair. The highest occupied *deloc*-NDF for this atom-pair is of π -character (47.2% of the total LDO-free DI), but most surprising is a very significant, long-range σ -delocalization (34.7%). The antibonding contributions, shown as part of the remaining *deloc*-NDFs in Figure 8, is quite interesting as well: atom-pair C1,N4 has antibonding contributions on O3, atom-pair C1,O3 has antibonding contributions on N4, and atom-pair O3,N4 displays antibonding contributions in a π fashion between C1 and N4.

The LDO-free FALDI investigation of formamide challenges the classical conceptual model of formamide somewhat. Classically, C1 and N4 is singly bonded, C1 and O3 is doubly bonded and it is expected that a degree of delocalization exists between

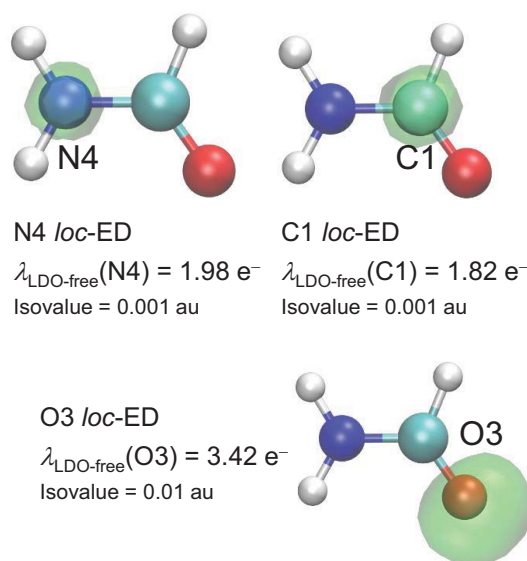


Figure 7. LDO-free LI and *loc*-ED distributions for the nitrogen, carbon and oxygen atoms in formamide. [Color figure can be viewed at wileyonlinelibrary.com]

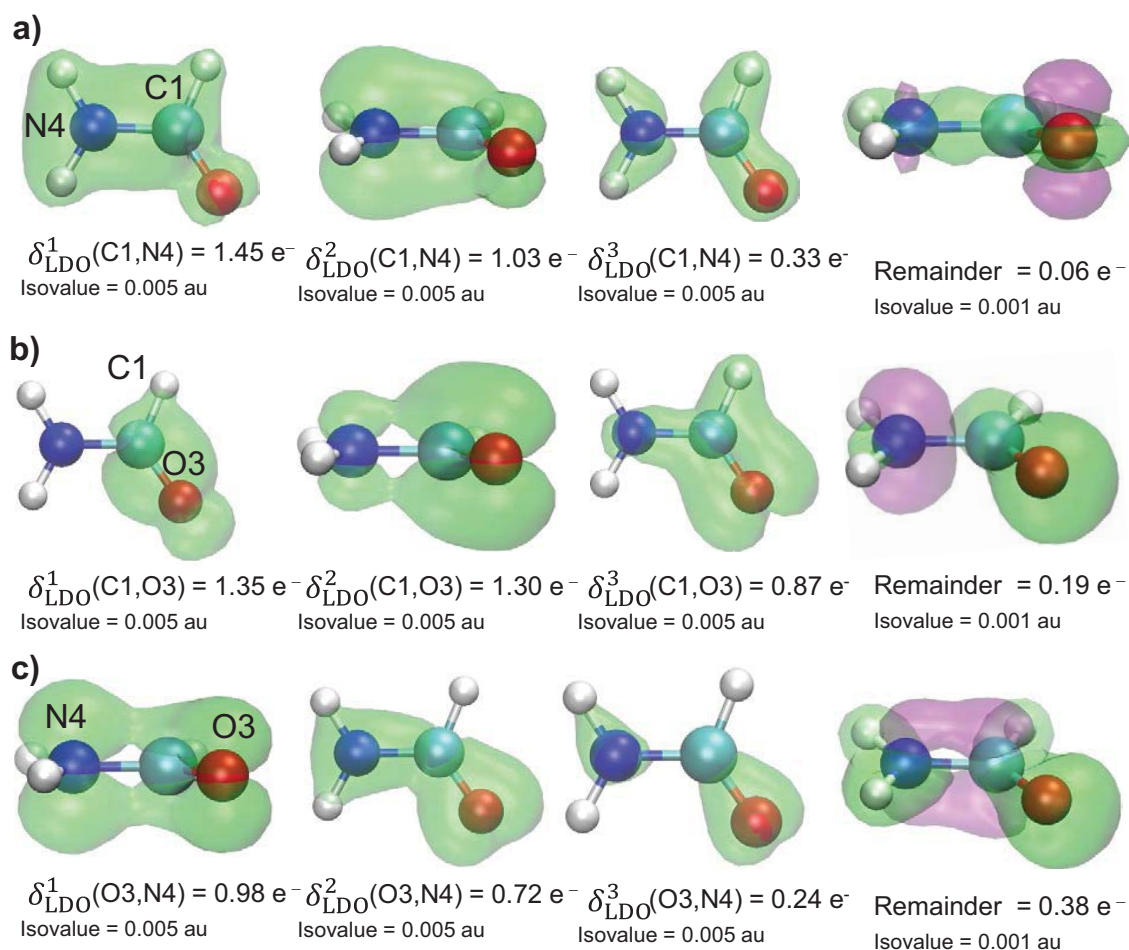


Figure 8. LDO-free *deloc*-NDF distributions and associated occupations for a) atom-pair C1,N4, b) atom-pair C1,O3 and c) atom-pair O3,N4 in formamide. [Color figure can be viewed at wileyonlinelibrary.com]

O3 and N4. However, the fact that O3 and N4 shares a *full* electron pair, and shares these electrons in a conjugated σ as well as π fashion, is reminiscent of the classical definition of covalency. Interestingly, this pair of electrons is shared through a 3D space occupied by the backbone of the molecule (via C-atom) rather than directly between O3 and N4, increasing the total density between both atom-pairs C1,N4 and C1,O3. This observation highlights the multi-center nature of even seemingly simple bonds (as we have observed before^[34]) and also challenges the habit of chemists of assigning mutually exclusive diatomic bond-orders. In addition, C1 and N4 shares a non-negligible number of electrons in a π -bond, clearly indicating a partial double-bond. Finally, the delocalization of electrons in a σ -fashion across all three atoms reveals the possibly larger role of σ -conjugation in highly delocalized systems.

Atom-pair	δ_{LDO}	δ_{LDO}^1	δ_{LDO}^2	δ_{LDO}^3	$\% \delta_{\text{LDO}}^\sigma$	$\% \delta_{\text{LDO}}^{\pi_1}$	$\% \delta_{\text{LDO}}^{\pi_2}$	% Remaining
C1,N4	2.86	1.45	1.03	0.33	50.5	35.8	11.7	2.0
C1,O3	3.70	1.35	1.30	0.87	36.4	35.1	23.4	5.0
O3,N4	2.07	0.98	0.72	0.24	34.7	47.2	11.5	6.7

Benzene

As a final example, we investigate benzene—a benchmark molecule for measuring electron delocalization—using RB3LYP and LDO-free FALDI components. We are specifically interested in the delocalization between carbon atoms, and we define short-range delocalization between neighboring carbon atoms and long-range delocalization between non-neighboring carbon atoms. Selected LDO-free *deloc*-NDF distributions are shown for each unique carbon–carbon interaction in Figure 9.

For each atom-pair (with the second atom corresponding to the ortho, meta and para carbons), three dominant modes of electron delocalization are again observed: channels associated with σ -, π_1 -, and π_2 -bonding orbital densities. The neighboring atom-pair, C1,C2, delocalizes 2.31 electrons in total, to give the expected partial double bond character. 1.41 electrons (61.2% of the total LDO-free DI) are delocalized in a σ fashion, 0.70 electrons (30.2%) in a primary π fashion due to the overlap of $2p_y$ orbitals and 0.23 electrons (9.9%) in a secondary, in-plane π fashion, due to the overlap of $2p_x$ orbitals. Note that the π_2 electrons are shared in a manner similar to the σ electrons, in the sense that the topologies at the bond critical point are qualitatively the same. Finally, the remaining electrons show a small σ contribution between the atom-pair but antibonding

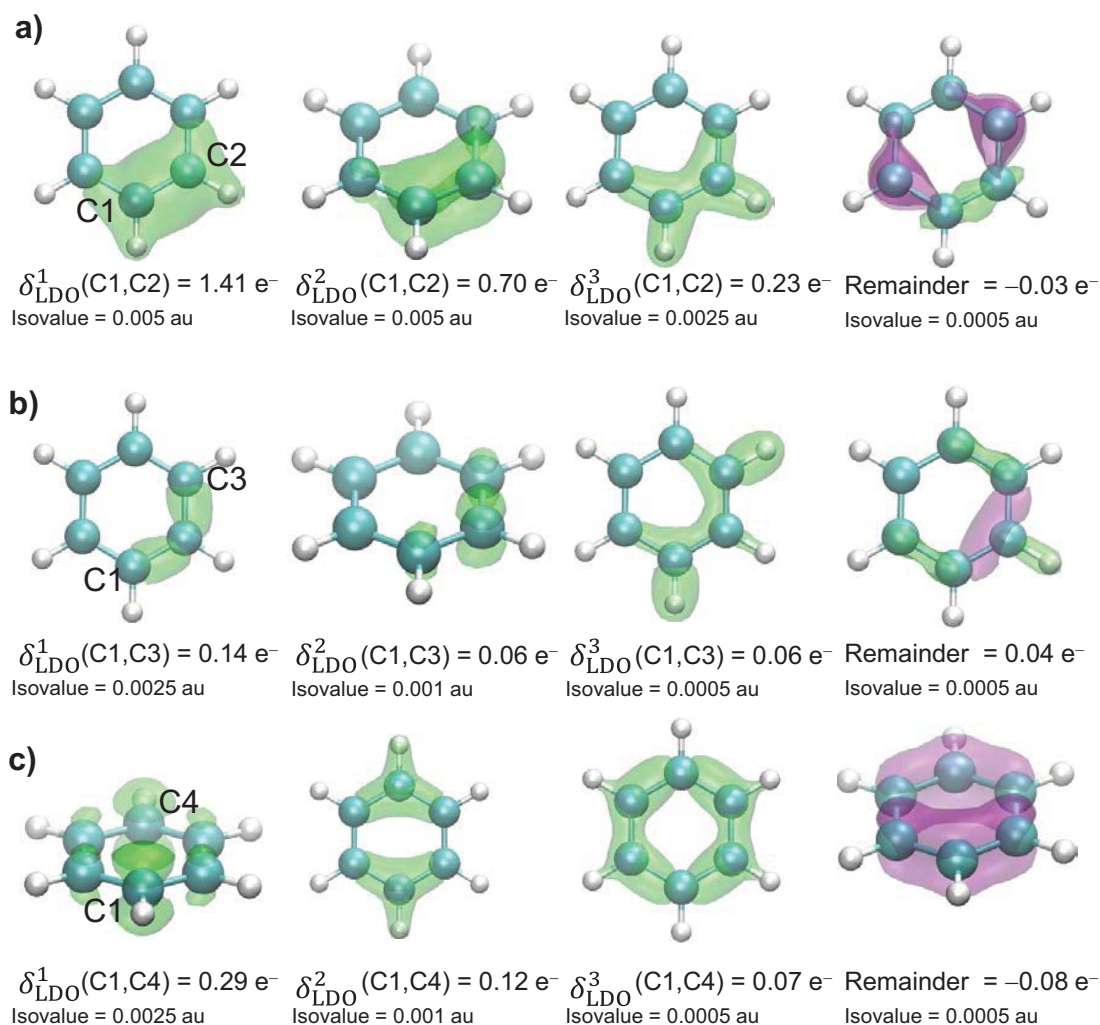


Figure 9. LDO-free *deloc*-NDF distributions and associated occupations for a) atom-pair C1,C2, b) atom-pair C1,C3 and c) atom-pair C1,C4 in benzene.

density distributions on the neighboring atoms (C3 and C6) lower the total LDO-free DI by -0.03 electrons.

The long-range delocalization patterns, between atom-pairs C1,C3 and C1,C4, show the same delocalization channels but at different occupations. The total LDO-free DI for atom-pair C1,C3 is 0.30 electrons, consisting of 48.3% σ , 20.8% π_1 , and 18.5% π_2 , whereas the LDO-free DI for atom-pair C1,C4 is 0.40 electrons, consisting of 16.9% σ , 73.6% π_1 , and 30.5% π_2 . Therefore, as expected, more electrons are delocalized between C1 and the *para* carbon atom, and mostly through π delocalization assisted by conjugation through the remaining carbon atoms.

Classically, aromaticity in benzene is usually ascribed to electron delocalization along $2p$ orbitals, forming a π -ring above the plane of the molecule. LDO-free FALDI allows for an in-depth investigation, from an atomic point of view, to the classical assertion. Table 4 shows the distribution of short- and long-range delocalized electrons in terms of their various delocalized channels; corresponding isosurfaces are shown in Figure S4 in the Supporting Information. In total, 16.84 electrons are delocalized between carbon atoms, of which 13.85 electrons are delocalized between short-range carbon-carbon

contacts (i.e., neighboring atoms) and 2.99 electrons are delocalized between long-range carbon-carbon contacts. For short-range contacts, 8.48 electrons (61.24%) are delocalized in a σ fashion, 4.18 (30.15%) in a π_1 fashion and 1.37 (12.29%) in a π_2 fashion. These numbers reflect the expected C-C bond in benzene—a primarily σ -bond with partial π -character. The electrons delocalized between long-range contacts (and the electrons responsible for the long-range conjugation properties of benzene) display 1.07 electrons in σ channels (35.69%), 1.26 electrons in π_1 channels (42.00%) and 0.70 electrons in π_2 channels (23.33%).

Classically, it would've been expected that long-range delocalization occurs predominantly in an above-the-plane π -ring. However, the long-range σ -delocalization is quite significant,

Table 4. LDO-free DIs and *deloc*-NDF occupations for all carbon-carbon interactions in benzene.

	$\delta_{\text{LDO}}^{\text{Total}}$	$\delta_{\text{LDO}}^{\sigma}$	$\delta_{\text{LDO}}^{\pi_1}$	$\delta_{\text{LDO}}^{\pi_2}$	Remaining
Short-range	13.85	8.48	4.18	1.37	-0.18
Long-range	2.99	1.07	1.26	0.70	-0.03
Total	16.84	9.55	5.43	2.07	-0.21

and in addition, the π_2 electrons are delocalized in-plane and in a very similar fashion as the σ electrons. Therefore, in terms of long-range electron delocalization, σ -modes (circular, in-plane conjugation) plays a larger role than out-of-plane π delocalization. This observation is in line with a number of other studies^[35–37] focusing on σ -delocalization, but, to our knowledge, it has not been shown from a topological or atoms-in-molecules approach before.

Conclusions

QTAIM-defined LIs and DIs, while quite popular, are somewhat ambiguous in their description of localized and delocalized electrons within atoms in a molecule. While the DI physically describes the electrons delocalized across basins, its correlation with bond order (i.e., electron pairs) has led to the term losing some physical meaning. We have shown in this work, by employing FALDI-defined *loc*-ED distributions in 3D real-space, that LIs do not describe electrons which are “exclusively” localized to an atom as each LI incorporates core electrons, non-bonded electrons (such as lone-pairs) as well as bonded (delocalized) electrons.

We have introduced two novel approaches for calculating LIs and DIs (as well as associated FALDI fields) that account for the Localized Overlap (LO) and Localized-Delocalized Overlap (LDO) densities. The LO procedure was designed for electrons which are simultaneously described by two or more LIs. By accounting for LO, the resultant (i) LO-free LIs are chemically meaningful electron localization indices which count the core and non-bonded electrons but do not contain any of the bonded electrons and (ii) the LO-free DIs correlate with the expected number of shared electrons rather than the number of electron-pairs.

Interestingly, LO-free *loc*-ED distributions are not necessarily exclusive to atomic basins, and we have shown that the lone-pair electrons of an N atom in ethylamine are not fully localized to its atomic basin. Rather, the lone-pair is formed from multiple overlapping MOs across several basins, and is therefore somewhat delocalized. The LDO-procedure produces localized electron distributions and counts (LDO-free LIs) which contain only core electrons that are truly exclusive to a single basin. Considering LDO-free DIs, they might be somewhat larger than what is typically expected as they also illustrate the delocalized nature of non-bonded electrons, such as lone-pairs. We note that, barring errors introduced during atomic basin integrations as well as basis set superposition errors, LDO-free LIs are examples of fully exclusive localization indices within QTAIM atomic basins.

We have also introduced natural density functions for FALDI fields. Natural orbital methods, such as NBO and NOCV, have seen widespread usage due to the simplification these methods provide to otherwise complex MO descriptions. FALDI NDFs provide atom-centric density distributions which fully recover conceptual orbital expectation densities, such as π -bonds and 1s electrons, even in larger systems. We expect that the LO- and LDO-free NDFs should provide a useful

interpretive tool in computational studies using electron density or topological approaches.

Formamide and benzene were included as examples of systems with a high degree of conjugation and electron delocalization. LDO-free NDFs and their associated occupations proved to be a useful tool to quantify and visualize both long-range and short-range electron delocalization in various different (e.g., σ , π) modes of bonding. Our approach revealed strong σ - and π -delocalization between N and O atoms in formamide, surmounting to more than a full electron-pair being shared despite the atoms not being adjacent to each other. In addition, previous notions^[35–37] about the role of σ -delocalization in benzene were recovered in an easy to understand, visual manner.

Finally, all the results as well as the theoretical developments were carried out at a restricted single determinant level. The LO- and LDO-procedures presented herein can, however, be modified for multi determinant wavefunctions using the Müller approximation^[38] or a similar approach as described by Cooper and Ponec,^[39] and we will test such applications in the near future.

Acknowledgment


We wish to thank Dr. David Cooper for insightful comments during the development of this work.

Conflict of Interest

There are no conflicts of interest to declare.

Keywords: QTAIM · localized density · delocalized density · FALDI

How to cite this article: J. H. de Lange, I. Cukrowski. *J. Comput. Chem.* **2018**, DOI: 10.1002/jcc.25223

 Additional Supporting Information may be found in the online version of this article.

- [1] R. Daudel, R. F. W. Bader, M. E. Stephens, D. S. Borrett, *Can. J. Chem.* **1974**, *52*, 1310.
- [2] R. F. W. Bader, M. E. Stephens, *J. Am. Chem. Soc.* **1975**, *97*, 7391.
- [3] I. Mayer, *Chem. Phys. Lett.* **1983**, *97*, 270.
- [4] A. Michalak, R. L. DeKock, T. Ziegler, *J. Phys. Chem. A* **2008**, *112*, 7256.
- [5] E. D. Glendenning, F. Weinhold, *J. Comput. Chem.* **1998**, *19*, 610.
- [6] P. Bultinck, R. Ponec, S. Van Damme, *J. Phys. Org. Chem.* **2005**, *18*, 706.
- [7] R. Ponec, I. Mayer, *J. Phys. Chem. A* **1997**, *101*, 1738.
- [8] R. Ponec, G. Yuzhakov, D. L. Cooper, *Theor. Chim. Acta* **2004**, *5*, 419.
- [9] P. Bultinck, M. Rafat, R. Ponec, B. Van Gheluwe, R. Carbó-Dorca, P. Popelier, *J. Phys. Chem. A* **2006**, *110*, 7642.
- [10] M. Giambiagi, M. S. de Giambiagi, K. Mundim, *Struct. Chem.* **1990**, *1*, 423.
- [11] C. W. Bird, *Tetrahedron* **1985**, *41*, 1409.
- [12] E. Matito, M. Duran, M. Solá, *J. Chem. Phys.* **2005**, *112*, 014109.
- [13] Z. Chen, C. S. Wannere, C. Corminboeuf, R. Puchta, P. vR. Schleyer, *Chem. Rev.* **2005**, *105*, 3842.
- [14] A. Savin, R. Nesper, S. Wengert, T. F. Fässler, *Angew. Chem. Int. Ed.* **1997**, *36*, 1808.
- [15] R. F. W. Bader, In *Atoms in Molecules: A Quantum Theory*; Oxford University Press: Oxford, **1990**.

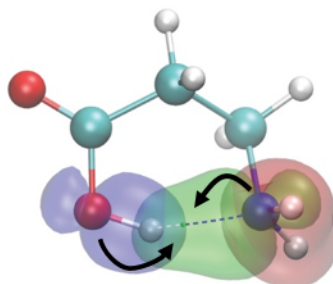
- [16] R. Ponec, D. L. Cooper, *Faraday Discuss.* **2007**, *135*, 31.
- [17] I. Sumar, R. Cook, P. W. Ayers, C. F. Matta, *Comput. Theor. Chem.* **2015**, *1070*, 55.
- [18] C. F. Matta, J. Hernández-Trujillo, T.-H. Tang, R. F. W. Bader, *Chem. Eur. J.* **2003**, *9*, 1940.
- [19] C. F. Matta, J. Hernández-Trujillo, *J. Phys. Chem. A* **2005**, *109*, 10798.
- [20] C. L. Firme, O. A. C. Antunes, P. M. Esteves, *Chem. Phys. Lett.* **2009**, *468*, 129.
- [21] C. F. Matta, R. J. Boyd, In *The Quantum Theory of Atoms in Molecules: From Solid State to DNA and Drug Design*; C. F. Matta, R. J. Boyd, Eds.; Wiley-VCH: Weinheim, **2007**; Chapter 1, pp. 1–34.
- [22] E. Francisco, A. M. Pendás, A. Costales, *Phys. Chem. Chem. Phys.* **2014**, *16*, 4586.
- [23] J. H. de Lange, I. Cukrowski, *J. Comput. Chem.* **2017**, *38*, 981.
- [24] I. Cukrowski, D. M. E. van Niekerk, J. H. de Lange, *Struct. Chem.* **2017**, *28*, 1429.
- [25] R. Ponec, *J. Math. Chem.* **1997**, *21*, 323.
- [26] R. Ponec, *J. Math. Chem.* **1998**, *23*, 85.
- [27] R. Ponec, D. L. Cooper, *J. Phys. Chem. A* **2007**, *111*, 11294.
- [28] P. Bultinck, D. L. Cooper, R. Ponec, *J. Phys. Chem. A* **2010**, *114*, 8754.
- [29] J. Cioslowski, *Int. J. Quant. Chem.* **1990**, *38*, 015.
- [30] D. L. Cooper, R. Ponec, M. Kohout, *Mol. Phys.* **2015**, *113*, 1682.
- [31] M. J. Frisch, G. W. Trucks, H. B. Schlegel, G. E. Scuseria, M. A. Robb, J. R. Cheeseman, G. Scalmani, V. Barone, B. Mennucci, G. A. Petersson, H. Nakatsuji, M. Caricato, X. Li, H. P. Hratchian, A. F. Izmaylov, J. Bloino, G. Zheng, J. L. Sonnenberg, M. Hada, M. Ehara, K. Toyota, R. Fukuda, J. Hasegawa, M. Ishida, T. Nakajima, Y. Honda, O. Kitao, H. Nakai, T. Vreven, J. A., Jr. Montgomery, J. E. Peralta, F. Ogliaro, M. Bearpark, J. J. Heyd, E. Brothers, K. N. Kudin, V. N. Staroverov, R. Kobayashi, J. Normand, K. Raghavachari, A. Rendell, J. C. Burant, S. S. Iyengar, J. Tomasi, M. Cossi, N. Rega, J. M. Millam, M. Klene, J. E. Knox, J. B. Cross, V. Bakken, C. Adamo, J. Jaramillo, R. Gomperts, R. E. Stratmann, O. Yazyev, A. J. Austin, R. Cammi, C. Pomelli, J. W. Ochterski, R. L. Martin, K. Morokuma, V. G. Zakrzewski, G. A. Voth, P. Salvador, J. J. Dannenberg, S. Dapprich, A. D. Daniels, Ö. Farkas, J. B. Foresman, J. V. Ortiz, J. Cioslowski, D. J. Fox, *Gaussian 09, Revision D.01*; Gaussian, Inc.: Wallingford, CT, **2009**.
- [32] T. A. Keith, AIMAll (Version 17.01.25); TK Gristmill Software: Overland Park KS, USA, **2017**. Available at: aim.tkgristmill.com.
- [33] W. Humphrey, A. Dalke, K. J. Schulten, *Mol. Graph.* **1996**, *14*, 33.
- [34] J. H. de Lange, D. M. E. van Niekerk, I. Cukrowski, *J. Comput. Chem.* **2018**, doi:10.1002/jcc.25175.
- [35] I. Fernandez, G. Frenking, *Faraday Discuss.* **2007**, *135*, 403.
- [36] S. Shaik, A. Shurki, D. Danovich, P. C. Hiberty, *Chem. Rev.* **2001**, *101*, 1501.
- [37] S. C. A. H. Pierrefixe, F. M. Bickelhaupt, *Chem. Eur. J.* **2007**, *13*, 6321.
- [38] A. M. K. Müller, *Phys. Lett. A* **1984**, *105*, 446.
- [39] D. L. Cooper, R. Ponec, *Phys. Chem. Chem. Phys.* **2008**, *10*, 1319.

Received: 16 January 2018
Revised: 12 March 2018
Accepted: 18 March 2018
Published online on 00 Month 2018

Chapter 4. FALDI-Based Decomposition of an Atomic Interaction Line Leads to 3D Representation of the Multicenter Nature of Interactions

Published in:

Journal of Computational Chemistry, 2018, 39, 973–985



Atom-pairs' bonding contributions to a multicentre AIL in 3D space

3D decomposition of an atomic interaction line (AIL) into contributions made by multiple atom-pairs to the total delocalized electron density at a BCP reveals the holistic nature of Bader's bond path linking only two atoms. A novel method, applied on five classical bonding interactions, reveals main atom-pairs' bonding, nonbonding or antibonding contributions to and various degrees of multicenter character of these interactions.

FALDI-Based Decomposition of an Atomic Interaction Line Leads to 3D Representation of the Multicenter Nature of Interactions

Jurgens H. de Lange, Daniel M. E. van Niekerk, and Ignacy Cukrowski 

Atomic interaction lines (AILs) and the QTAIM's molecular graphs provide a predominantly two-center viewpoint of interatomic interactions. While such a bicentric interpretation is sufficient for most covalent bonds, it fails to adequately describe both formal multicenter bonds as well as many non-covalent interactions with some multicenter character. We present an extension to our Fragment, Atomic, Localized, Delocalized and Interatomic (FALDI) electron density (ED) decomposition scheme, with which we can measure how any atom-pair's delocalized density concentrates, depletes or reduces the electron density in the vicinity of a bond critical point. We apply our method on five classical bonds/interactions, ranging from formal either two- or three-center bonds, a non-covalent

interaction (an intramolecular hydrogen bond) to organometallic bonds with partial multicenter character. By use of 3D representation of specific atom-pairs contributions to the delocalized density we (i) fully recover previous notion of multicenter bonding in diborane and predominant bicentric character of a single covalent C—C bond, (ii) reveal a multicenter character of an intramolecular H-bond and (iii) illustrate, relative to a Schrock carbene, a larger degree of multicenter M—C interaction in a Fischer carbene (due to a presence of a heteroatom), whilst revealing the holistic nature of AILs from multicenter ED decomposition. © 2018 Wiley Periodicals, Inc.

DOI: 10.1002/jcc.25175

Introduction

The concept of multicenter bonding has been known to chemists for almost 75 years, yet most physical properties of a bond (such as bond lengths, dissociation and interaction energies or even degrees of atomic orbital overlap) are reported and interpreted in terms of a two-center interaction. Multicenter bonding is “paradoxically counter intuitive in chemistry” because of chemists’ lingering tradition of representing a bond as a line, to paraphrase Silvi.^[1] Despite such conceptual difficulties, a large number of interactions have been formally classified (by a multitude of methods) as multicenter bonds. For instance, the remarkable differences observed between the structures of B₂H₆ and C₂H₆ led to the discovery of a large number of diborane structures with multicenter bonds.^[2–6] Moreover, multiple ligands which can bridge metal–metal bonds—such as chlorine atoms or carbonyl ligands—have been discovered and are well-known examples of formal M...X...M multicenter bonds.^[7–11] Relatively recently, unusually long, multicenter bonds between dimers of tetracyanoethylene have attracted a large amount of interest,^[12–14] as well as 4-center-2-electron bonding.^[15] Even metallic bonding, consisting of a “sea of delocalized electrons,” has been classified as multicenter bonding.^[16]

A great number of two-center bonds with known partial multicenter character exist, however, which are often overlooked. Hydrogen bonding is generally accepted to be an interaction caused by the combined effect of at least three atoms: an H-bond donor atom (X), a hydrogen atom (H) and an H-bond acceptor atom (Y). IUPAC suggests that the backbone atom bonded to Y, known as atom Z, could also be

included in the definition in specific cases,^[17,18] and we recently provided evidence^[19] of the considerable role that the atom bonded to X (atom W) plays in the formation of an intramolecular H-bond in β -alanine. Clearly, an H-bond involves contributions from more than only atoms H and Y as a conceptual line drawn between only these two atoms suggests. The nature and strength of many reported non-covalent interactions are greatly affected by their local environment and neighboring atoms,^[20] potentially an indication of some degree of multicenter character (including an agostic bond in a ruthenium complex, which has been formally characterized as a multicenter bond^[11]). Aromatic bonds in electron delocalized molecular systems are examples of partially multicenter bonding, as are any interactions involving an entire π -ring consisting of overlapping p -orbitals. Finally, the important influence of heteroatoms on organometallic C=M carbene bonds^[21] is a clear indication of multicenter character on what is normally interpreted as a diatomic “double” bond. For instance, the presence of a heteroatom in Fischer carbene complexes typically enhances π -backbonding from the metal atom, as well as σ -donation from the ligand in comparison to most Schrock carbenes.

The Quantum Theory of Atoms in Molecules (QTAIM)^[22] is a widely used tool in multiple applications of computational

J. H. de Lange, D. M. E. van Niekerk, I. Cukrowski
Department of Chemistry, Faculty of Natural and Agricultural Sciences,
University of Pretoria, Lynnwood Road, Hatfield, Pretoria 0002, South Africa
E-mail: ignacy.cukrowski@up.ac.za

Contract grant sponsor: National Research Foundation of South Africa;
Contract grant number: 105855

© 2018 Wiley Periodicals, Inc.

chemistry. QTAIM's molecular graphs present a topologically condensed view of the electron density (ED) as a series of critical points, where nuclear critical points (+3, -3) can be connected to bond critical points, BCPs (+3, -1) by atomic interaction lines (AILs, also known as bond paths). The discovery that AILs are found concomitant with every *generally accepted* chemical bond is a remarkable achievement of modern chemistry, despite the somewhat controversial occurrences of AILs being found where no chemical bond is expected.^[23–26] However, the connectivity provided by a molecular graph is strictly a two-center viewpoint. An AIL is present between atoms H and Y in a typical H-bond, for instance, lending a two-center impression of the bond rather than the multicenter interpretation as suggested by IUPAC. In electron delocalized systems, such as benzene, a two-center interpretation becomes problematic and raises the question: to what extent does an AIL between two neighboring carbon atoms in benzene represent a diatomic bonding interaction and/or the degree of aromatic delocalization of electrons from other atomic centers?

The extent to which a chemical interaction is multicenter seems to be a surprisingly difficult question to answer. Silvi suggested a density-based approach using the Electron Localization Function which is able to differentiate multicenter bonding (such as in B₂H₆) from two-center bonding (such as in C₂H₆).^[1] Silvi's approach, however, produces very strict categorization (i.e., an interaction is strictly either two- or three-center) and does not provide any insight regarding partial multicenter character (such as in the aforementioned carbon-carbon interaction in benzene). Ponec et al.^[9,27–29] have studied multicenter bonding within the QTAIM framework extensively, particularly with the use of the Domain Averaged Fermi Holes (DAFH) analysis as well as approaches based on the so-called generalized population analysis. In the latter approach the authors presented indices for electrons shared simultaneously in three or more atomic basins, which is very useful for formal three-center bonds but can be difficult to interpret with respect to partial multicenter bonding resulting from multiple contributions across a molecule. The source function^[30] has also been used to investigate the multicenter nature of various interactions at BCPs using QTAIM atomic basins.^[31,32]

The DAFH approach presents a very generalized and powerful tool for investigating the delocalization over all molecular space of the electrons found within an atomic basin. Making use of some DAFH concepts, we recently developed a theoretical framework which, among other uses, can provide a real-space distribution of electrons delocalized between two atomic basins.^[33] In this work, we will introduce an extension of the Fragment, Atomic, Localized, Delocalized and Interatomic (FALDI) electron density decomposition scheme with which we can identify and quantify atom-pairs contributing significantly toward the formation of an AIL. This work does not aim to present another multicenter bond index. Rather, our approach allows for the investigation of the holistic, multicenter nature of the AIL itself by decomposing the total ED into contributions made by multiple atom-pairs. Finally, we note that our approach is fully applicable to any point **r** in

molecular space; hence, it is also applicable to interacting regions where AILs are absent, as identified by the Non-Covalent Interaction (NCI) technique.^[34]

Computational Details

All structures were optimized in Gaussian 09, Rev. D.,^[35] using B3LYP with Grimme's D3 empirical dispersion^[36] and the 6-311++G(d,p) basis set, in the gas phase. Coordinates of all optimized structures are given in PART 1 of the Supporting Information. QTAIM molecular graphs, as well as atomic overlap matrices, were calculated using AIMAll version 16.10.31.^[37] FALDI data were calculated using in-house software, and FALDI isosurfaces were visualized using VMD.^[38] We note that preliminary testing using multi-determinant wavefunctions within the Müller approximation^[39] give the same qualitative results. A 1-electron implementation of FALDI for correlated wavefunctions should also be possible by following an approach reported by Cooper and Ponec.^[40] QTAIM and FALDI analyses of the two carbene complexes were done for structures in the singlet spin state only; the Fischer carbene complex is only stable in the singlet spin state while the Schrock carbene complex is approximately 10 kcal mol⁻¹ less stable in the triplet spin state. Finally, our FALDI software is currently limited to smaller, Gaussian basis sets due to memory constraints. We intend to optimize it in the future to handle larger basis sets, e.g., as suggested by Bühl and Kabrede,^[41] to more accurately describe the transition metals, such as those used in this study.

Theoretical Background and Development

The recently introduced FALDI density decomposition scheme^[33] provides an exhaustive decomposition of the ED at any coordinate **r** in real-space into contributions from all of *M* domains. These domains are usually chosen to be atomic basins as defined by QTAIM,^[42] yielding atomic contributions to the ED throughout an entire molecular system. While our previous work using FALDI^[33] focused primarily on calculating and decomposing conformational deformation EDs, we focus here on the decomposition of the static ED, i.e. the ED distribution of a single molecular state, regardless whether being at equilibrium or not.

Domain averaged Fermi holes

FALDI decomposes the total ED (*tot*-ED) at any point **r** into contributions from all atoms (domains),

$$\rho(\mathbf{r}) = \sum_i^M g_i(\mathbf{r}) \quad (1)$$

where $g_i(\mathbf{r})$ is the atomic ED (*atom*-ED) distribution associated with the *i*th atomic basin. Calculation of $g_i(\mathbf{r})$ was originally developed by Ponec and is a central concept from DAFH analysis.^[43–46] $g_i(\mathbf{r})$ is defined by averaging the reference electron of the charge-weighted exchange–correlation (XC) electron hole over an atomic basin (Ω_i):

$$g_i(\mathbf{r}_1) = - \int_j \rho^{\text{Hole}}(\mathbf{r}_1; \mathbf{r}_2) \rho(\mathbf{r}_2) d\mathbf{r}_2 \quad (2)$$

where $\rho^{\text{Hole}}(\mathbf{r}_1; \mathbf{r}_2) = \rho(\mathbf{r}_1) - \rho^{\text{cond}}(\mathbf{r}_1; \mathbf{r}_2)$ gives the reduced probability of ED at \mathbf{r}_1 as a result of an electron at \mathbf{r}_2 , and $\rho^{\text{cond}}(\mathbf{r}_1; \mathbf{r}_2) = 2\rho_2(\mathbf{r}_1, \mathbf{r}_2)/\rho(\mathbf{r}_2)$ gives the conditional probability of finding an electron at \mathbf{r}_1 given an electron at \mathbf{r}_2 . The XC hole provides the *origin* of the excluded electron at \mathbf{r}_1 , and therefore can be used as a pseudo-dynamic distribution of an electron within volume element $d\mathbf{r}_2$. Charge-weighting the XC hole by $\rho(\mathbf{r}_2)$ [as in eq. (2)] then gives the molecular-wide distribution of *all* electrons found on average in $d\mathbf{r}_2$.

An *atom*-ED distribution provides the distribution throughout all molecular space of the electrons that are found, on average, within a particular atomic basin. Integrating $g_i(\mathbf{r})$ over all molecular space yields the QTAIM-defined atomic population, $N(\Omega_i)$, and is equivalent to $N(\Omega_i)$ obtained by integrating the *tot*-ED over an atomic basin, Ω_i . The *atom*-ED distributions and the QTAIM atomic basins therefore describe the same electrons, but where QTAIM produces non-overlapping, 1st-order atomic domains, *atom*-ED distributions produce fuzzy, pseudo-2nd-order fields due to the inclusion of XC effects. To avoid the expensive integration of the pair density over multiple atomic basins, $g_i(\mathbf{r})$ is usually calculated through elements of atomic overlap matrices (AOM):

$$g_i(\mathbf{r}_1) = 2 \sum_{\lambda\sigma} \chi_\lambda(\mathbf{r}_1) \chi_\sigma(\mathbf{r}_1) S_{\sigma\lambda}^i \quad (3)$$

where

$$S_{\sigma\lambda}^i = \langle \chi_\sigma | \chi_\lambda \rangle_i = \int_j \chi_\sigma(\mathbf{r}_1) \chi_\lambda(\mathbf{r}_1) d\mathbf{r}_1 \quad (4)$$

$S_{\sigma\lambda}^i$ is an element of the AOM associated with a specific domain Ω_i , and $\chi(\mathbf{r})$ are natural molecular orbitals (which reduce to canonical molecular orbitals in single-determinant wavefunctions).

The procedure of a full DAFH analysis includes the diagonalization and subsequent isopycnic transformation of the AOMs to produce domain-localized natural orbitals associated with each DAFH function.^[45] However, our approach uses a different decomposition of each DAFH function, related to QTAIM atomic populations, as discussed next.

The fragment, atom, localized, delocalized and interaction density decomposition

FALDI decomposes each *atom*-ED into two components, i.e. the density that is localized to a specific atomic basin (*loc*-ED, $\mathcal{L}_i(\mathbf{r})$) and the density that is delocalized by two atomic basins (*deloc*-ED, $\mathcal{D}_{ij}(\mathbf{r})$), as shown in eq. (5):

$$g_i(\mathbf{r}) = \mathcal{L}_i(\mathbf{r}) + \sum_{j \neq i} \frac{1}{2} \mathcal{D}_{ij}(\mathbf{r}) \quad (5)$$

FALDI-generated *loc*-ED distributions and atom-pair *deloc*-ED distributions are real-space, i.e. 3D distributions of the QTAIM-

defined electron localization index (LI, $\lambda(\Omega_i)$) and electron delocalization index (DI, $\delta(\Omega_i, \Omega_j)$), respectively. *loc*-ED and *deloc*-ED distributions are calculated similarly to *atom*-ED distributions:

$$\mathcal{L}_i(\mathbf{r}) = 2 \sum_{\lambda\sigma} \chi_\lambda(\mathbf{r}) \chi_\sigma(\mathbf{r}) (\mathbf{S}^i \mathbf{S}^i)_{\sigma\lambda} \quad (6)$$

$$\mathcal{D}_{ij}(\mathbf{r}) = 2 \sum_{\lambda\sigma} \chi_\lambda(\mathbf{r}) \chi_\sigma(\mathbf{r}) (\mathbf{S}^i \mathbf{S}^j)_{\sigma\lambda} \quad (7)$$

where $(\mathbf{S}^i \mathbf{S}^i)_{\sigma\lambda}$ and $(\mathbf{S}^i \mathbf{S}^j)_{\sigma\lambda}$ are elements of the matrix products of the AOMs associated with domain Ω_i with itself and domain Ω_i with Ω_j , respectively. Note that $\text{LI}(\Omega_i) = \text{tr}(\mathbf{S}^i \mathbf{S}^i)$, and $0.5\text{DI}(\Omega_i, \Omega_j) = \text{tr}(\mathbf{S}^i \mathbf{S}^j)$. Integration of a *loc*-ED or *deloc*-ED distribution over all space gives the corresponding QTAIM-defined LI or DI term, respectively. Historically, the $\text{LI}(\Omega_i)$ and $\text{DI}(\Omega_{ij})$ terms have been interpreted as the number of electrons that are *localized* to the *i*th basin and the number of electrons that are *delocalized* between the *i*th and *j*th basins, respectively.^[47–49] This interpretation implies that $\text{LI}(\Omega_i)$ is a measure of the number of electrons found *exclusively* in Ω_i . However, due to averaging involved during the calculation of LI by QTAIM, such an interpretation is not correct, which we will elaborate on thoroughly in near future. Due to this general interpretation with regards to LI, which we do not agree with, we focus here on exploring multicenter character of AILs from only the *deloc*-ED distributions.

Deloc-ED distributions ($\mathcal{D}_{ij}(\mathbf{r})$) can be interpreted as the probability of finding an electron at any coordinate \mathbf{r} which is simultaneously correlated with two different atomic basins. 3D isosurfaces of $\mathcal{D}_{ij}(\mathbf{r})$ that are calculated from FALDI analyses therefore illustrate the molecular-wide distribution of electrons which can statistically be found in both the *i*th and *j*th atomic basins. These *deloc*-ED distributions are directly related to the magnitude of the interatomic XC energy, with increasing interatomic delocalization resulting in more stabilizing XC effects. DIs and *deloc*-ED distributions can be used as a measure of the covalency of an interaction, and DI is often used as an indication of the bond order between two atoms connected by an AIL.^[47–49] DI is usually calculated by considering the mutual overlap of MOs across two atomic basins, and is therefore a very good link between MO-theory and Quantum Chemical Topology (QCT).^[49] The full sets of LIs and DIs in a molecule have been combined as localization–delocalization matrices (LDMs) by Matta and coworkers^[50] This approach has been used to understand the complex network of localized and delocalized contributions to atomic populations.^[51,52] While an LDM provides a very valuable condensed overview of ED localization and delocalization at an atomic level, it does not provide valuable chemical information inherent in the real-space distributions of correlated ED. To our knowledge, FALDI is the first technique able to calculate the distribution of DI in real-space and we utilize this feature in this study to show that the *manner* in which electrons are delocalized is equally as important, and more informative than just the *amount* of delocalized electrons.

There is, however, a fundamental difference between the DI term and *deloc*-ED distribution. DI is always an integrated, positive value. However, *deloc*-ED distributions can be either a positive or negative values at a specific point \mathbf{r} . Regions where $\mathcal{D}_{ij}(\mathbf{r}) > 0$ represent a constructive interference of MOs simultaneously overlapping with two atomic basins Ω_i and Ω_j at \mathbf{r} , indicate regions in 3D space where electrons are positively correlated between both basins. Such a constructive overlap results in an increase in the *tot*-ED. Regions where $\mathcal{D}_{ij}(\mathbf{r}) < 0$, however, are due to deconstructive interference at \mathbf{r} of MOs overlapping with two atomic basins, indicate the regions in space where electrons are negatively correlated between the basins, thereby reducing the *tot*-ED.

Partial second derivatives of *deloc*-ED distributions

Our FALDI decomposition produces a large set of *deloc*-ED distributions. Each *deloc*-ED is a component of the *tot*-ED (hence, a contribution made by a specific atom-pair). However, only some components of the *tot*-ED will contribute to the formation of an AIL. This brings us to the primary objective of this work: isolating the components of the *tot*-ED that contribute to the formation of a specific AIL, as well as quantifying and visualizing their contributions. Each point of an AIL has the specific property that ED is concentrated perpendicular to the AIL (as measured by the second eigenvalue of the Hessian matrix, λ_2). Therefore, the second derivative (and more specifically, λ_2) of any *deloc*-ED distribution can be determined at any given point \mathbf{r} . In doing so, one can precisely determine whether a particular contribution made by a specific atom-pair is concentrating (negative partial 2nd derivative) or depleting (positive partial 2nd derivative) the *tot*-ED. *Deloc*-ED distributions that are concentrating the *tot*-ED therefore facilitate the formation of an AIL, whereas *deloc*-ED distributions that are depleting the *tot*-ED hinder the formation of an AIL. One must also realize that a specific component of *deloc*-ED, e.g. $\mathcal{D}_{ij}(\mathbf{r})$, might be concentrating in the interatomic region of Ω_i and Ω_j but depleting in another, e.g. in the interatomic region of Ω_i and Ω_k . The FALDI-based decomposition of the total density distribution of a molecular state implemented in this work is shown in Scheme 1.

In the orthodox MO theory, each orbital can be classified in terms of a bonding, nonbonding or antibonding contribution with respect to a particular chemical interaction; the effects of (de)constructive interference on both the binding energies and electron density concentration have been well documented and can be found in any textbook on electronic structure. Similarly, the sign of the partial second derivative of a *deloc*-ED distribution is a result of constructive or deconstructive interference of MOs overlapping simultaneously across two atomic basins. Therefore, in analogy to MO bonding theory, we label each atom-pair's *deloc*-ED distribution accordingly, i.e. an atom-pair contribution to the total *deloc*-ED as *bonding*, *nonbonding* or *antibonding* based on whether it concentrates (*bonding*), depletes (*nonbonding*) or reduces (*antibonding*) ED in a specific region of space, as illustrated in Scheme 2.

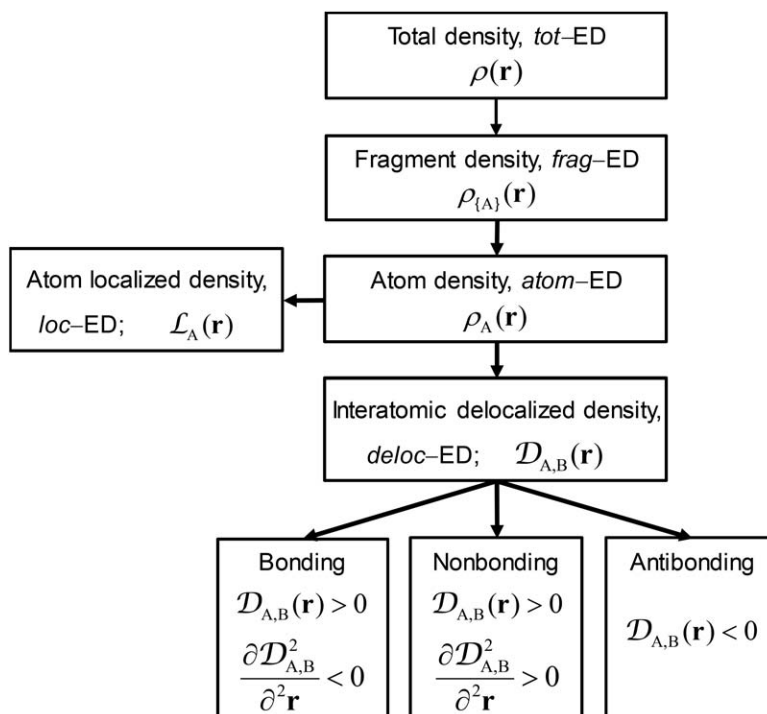
The above classification of each *deloc*-ED contribution to the *tot*-ED allows for the identification of atom-pairs and quantification of their contributions in the formation of a particular AIL (bonding *deloc*-ED), as well as of the atom-pairs that hinder formation of the AIL (nonbonding and antibonding contributions to the total *deloc*-ED). The presence of multiple contributions toward bond formation also allows us to extend the connectivity allowed by an AIL to more than just two atoms, a conceptual development which can have wide-ranging implications. Specifically, in our approach each AIL can be interpreted as the net effect of a number of bonding and competing (non- and antibonding) contributions. Hence, the presence of an AIL must imply that bonding *deloc*-ED distributions dominate.

We note that Gatti and Baders' source function (SF)^[30] also provides a full decomposition of $\rho(\mathbf{r})$ at any given \mathbf{r} into contributions from all atomic basins, thereby satisfying eq. (1). The SF has been used to interpret various chemical phenomena,^[31,32] including multicenter contributions at bond-critical points,^[31] from a QTAIM-based perspective in real-space. The second derivatives of the various atomic SFs in a molecule can therefore be calculated and classified according to how each atom facilitates or hinders the formation of an AIL that, in some respect, is similar to the approach discussed above. The SF, which is a Green's function based on the Laplacian of the total ED, has the advantage that it is quite quick to calculate, also from experimental densities. One must stress, however, that in terms of atom-pair contributions and explicit exchange–correlation effects it provides less information than the FALDI approach. Clearly, it would be of great interest and importance to explore advantages (limitations) of to both, SF- and FALDI-based, approaches and we plan to embark on such studies in near future.

Results and Discussion

We aim to determine the multicenter nature of the AILs in five "classical" bonding interactions from a delocalized ED perspective. Moreover, we hope to provide convincing evidence that (i) observed BCPs from *tot*-ED topological analyses, as obtained from QTAIM, should not be simply viewed or interpreted as an indication of a favorable bonding interaction between two atoms alone and (ii) the emergence of a BCP, and therefore the nature of an interaction (between the atoms linked by the associated AIL) depends on contributing (bonding) *deloc*-ED coming from other/distant atoms in a molecular system.

The first structure that we selected to investigate is the lowest energy conformer of β -alanine (**1** in Fig. 1) as it presents a very good example of a multicenter, intramolecular bonding interaction. QTAIM calculations of **1** show that an AIL is present between hydrogen atom H6 (H) and nitrogen atom N11 (Y) and thus BCP(H6,N11). This molecular graph alone does not provide any information regarding the multicenter bonding nature of this interaction. Moreover, it does not provide evidence to suggest how other atoms, such as O5 (X), C8 (Z) or C1 (W), influence (i.e., by either facilitating or hindering) the emergence of AIL(H6,N11). To compare with **1**, we decided to investigate the interactions of two systems that, relative to each other, should display quite opposing degrees of

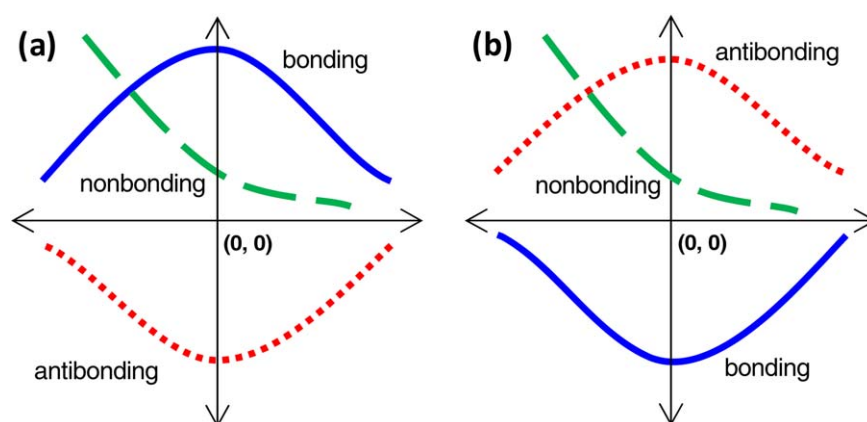


Scheme 1. FALDI-based decomposition of the total static ED (i.e., the ED distribution of a single molecular state) implemented in this work.

multicenter bonding nature. The interaction between a boron (B1) and hydrogen (H7) atom in diborane, **2** in Figure 1, is well-known as consisting of a large degree of multicenter character.^[2–6] However, the interaction between carbon atoms C9 and C12 in *n*-butane, **3** in Figure 1, which is representative of a classic single covalent C–C bond, provides an example of a bicentric interaction. We therefore expect that our ED decomposition scheme should be able to clearly distinguish between the multicenter natures of these two interactions, as well as agree qualitatively with that reported in the literature.

Lastly, we decided to compare the nature of two different metal–carbon (M–C) carbene bonding interactions, i.e. one of a typical Schrock carbene complex, $[(\text{Cp})_2\text{Ti}=\text{CH}_2]$, and one of a typical Fischer carbene complex, $[(\text{CO})_5\text{Cr}=\text{C}(\text{OCH}_3)\text{CH}_3]$. The

molecular graphs of the two complexes are shown in Figure 1 (**4** and **5**, respectively). In the case of **5**, oxygen atom O13 is expected to yield an additional degree of *deloc*-ED of a bonding nature to the carbene bond, since such heteroatoms are known to facilitate π -backbonding.^[21] As a consequence, this M–C carbene bonding interaction is expected to have more multicenter bonding character as compared to its counterpart in **4** (no heteroatom), even though the magnitude of the *tot*-ED at BCP(Cr1,C12) in **5** ($\rho = 0.09973$ a.u.) is considerably less than at BCP(Ti1,C22) in **4** ($\rho = 0.13851$ a.u.). In the following sections, we discuss results obtained from the ED decomposition along the indicated vectors whereas quantitative analyses (decomposition of either total or delocalized EDs) are reported at BCPs, as indicated in Figure 1.



Scheme 2. a) Examples of the cross-sections illustrating trends of bonding, nonbonding or antibonding ED distributions (computed for a selected atom-pair) as well as b) their 2nd partial derivatives. [Color figure can be viewed at wileyonlinelibrary.com]

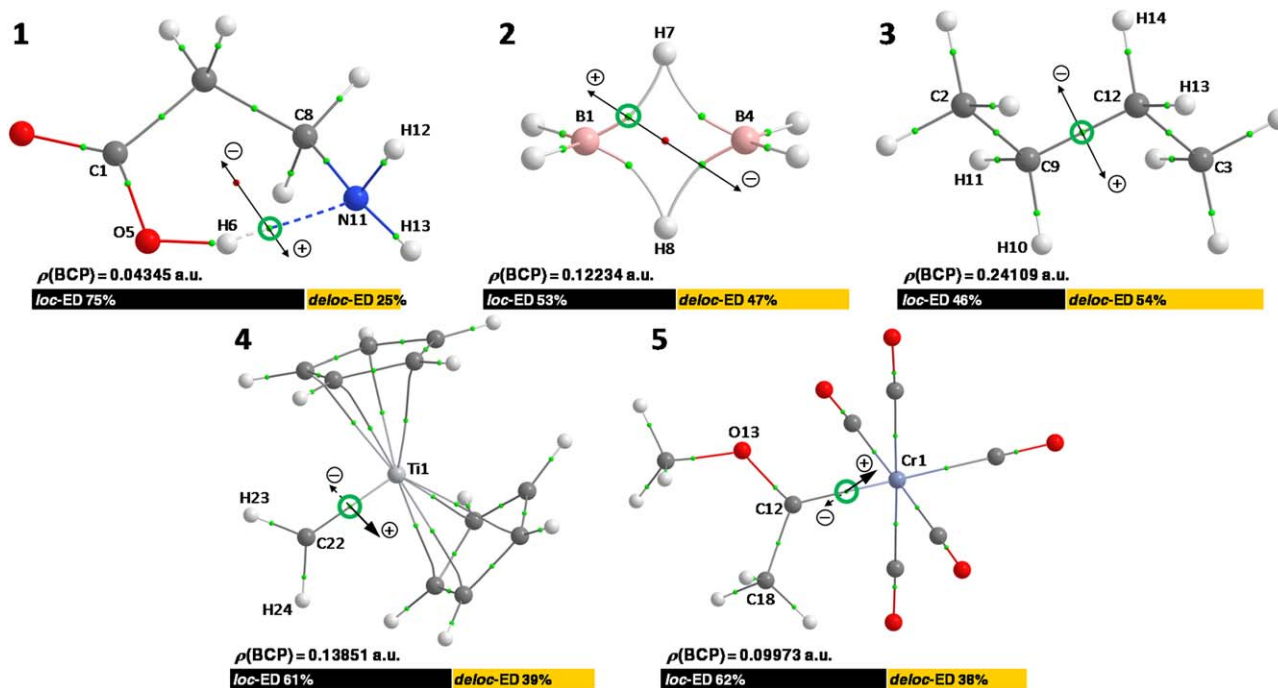


Figure 1. Molecular graphs of β -alanine (1), diborane (2), "linear" *n*-butane (3), Schrock, $[(\text{Cp})_2\text{Ti}=\text{CH}_2]$ (4) and Fischer, $[(\text{CO})_5\text{Cr}=\text{C}(\text{OCH}_3)\text{CH}_3]$ (5) carbene complexes, including the vectors along which ED decomposition analyses are done. Encircled (green) are the BCPs at which the multicenter bonding nature of an interaction is explored. *tot*-ED (ρ) and percentage of *loc*-ED and *deloc*-ED at these BCPs is given directly below the relevant molecular graphs. All (+3,+1) and (+3,+3) critical points in 4 have been omitted for clarity. [Color figure can be viewed at wileyonlinelibrary.com]

Intramolecular H-bonding interaction in β -alanine

Figure 2a shows the FALDI-based decomposition of the *tot*-ED (silver) into ED contributions that are localized (black) and delocalized (gold). We note that both trends have a local maximum in the vicinity of BCP(H6,N11) and a local minimum close to the RCP (small red sphere, 1 in Fig. 1). The decomposition of the total *deloc*-ED, Figure 2b, yields the sum totals of all contributions that are of a *bonding* (blue line), *nonbonding* (green line) and *antibonding* (red line) nature with respect to BCP(H6,N11).

Figure 2b clearly illustrates that the total *deloc*-ED (0.01102 a.u.) consists of a significant quantity of ED of a bonding nature (0.01107 a.u.) and it is the only one, among the three types of contributions that directly contributes toward the emergence of BCP(H6,N11). Nonbonding and antibonding *deloc*-ED components are approximately equal in magnitude but of a different sign, at 0.00104 and -0.00109 a.u., respectively.

Atom-pair O5,N11, i.e. atoms X and Y, is mainly responsible for the overall deconstructive electron correlation at BCP(H6,N11). It accounts for -0.00079 a.u. (72%) of the total antibonding *deloc*-ED, where it is also a local minimum along the analysed vector. Of all five the structures studied in this work, β -alanine is the only one to show a significant quantity of *deloc*-ED of an antibonding nature at BCP of interest (see PART 2 of the Supporting Information for *deloc*-ED decomposition graphs pertaining to the other four structures).

Figure 3 illustrates the 3D-isosurfaces of the major (either summed or individual) contributions to the total *deloc*-ED that are of a bonding, nonbonding or antibonding nature with respect to BCP(H6,N11). These three real-space ED distributions clearly illustrate how a particular atom-pair in the molecule (i)

concentrates, Figure 3a, (ii) depletes, Figure 3b (but concentrates ED elsewhere in the molecule) or (iii) specifically reduces, Figure 3c, ED in the vicinity of BCP(H6,N11).

Figure 3a reveals how the atom-pairs' contributions collectively form a channel of constructive electron correlation between the nuclei involved in the intramolecular interaction, thereby naturally facilitating the emergence of BCP(H6,N11). *deloc*-ED of a nonbonding or antibonding nature in this interatomic region, Figures 3b and 3c, respectively, both naturally hinder the emergence of this BCP and can therefore be classified as "competing secondary interactions" according to the nomenclature of Tognetti and coworkers^[53,54] Of the atom-pairs that deplete *deloc*-ED in the vicinity of BCP(H6,N11), Figure 3b, C1,O5 and C8,N11 are the largest in magnitude; their constructive electron correlation is mainly distributed all along their own covalent bonds, i.e. C1—O5 and C8—N11, respectively.

Since our study focuses on the multicenter nature of a particular AIL, we further decompose the total *deloc*-ED of a bonding nature (blue line in Fig. 2b). In doing so, we identify and quantify the major contributing atom-pairs that concentrate ED at BCP(H6,N11).

From Figure 4a we note that atom-pair H6,N11 (atoms H and Y), i.e. the two atoms linked by the AIL (which we will henceforth refer to as the primary interaction), does *not* make the largest contribution to the *deloc*-ED of a bonding nature.*

*In a simulated aqueous phase (using implicit solvent model PCM) the intramolecular H-bonding distance (H6...N11) is much shorter and the largest contribution to the *deloc*-ED of a bonding nature is from the atom-pair corresponding to the primary interaction, i.e. H6,N11. The same phenomena has been observed using the SF.^[32]

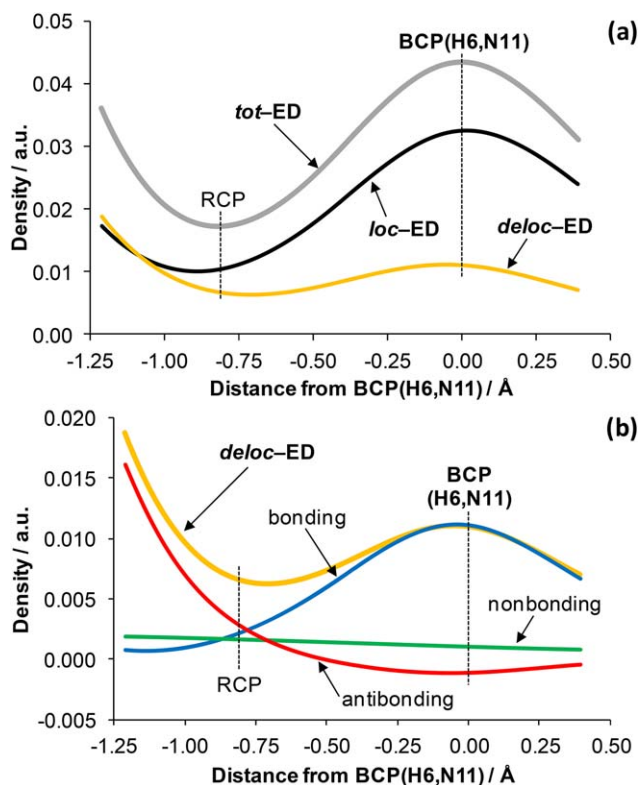


Figure 2. a) FALDI-based decomposition of the *tot*-ED (silver) into *loc*- (black) and *deloc*-ED (gold) in β -alanine along the vector indicated in Figure 1. b) Subsequent FALDI-based decomposition of the *deloc*-ED into constructive (blue, bonding nature), nonconstructive (green, nonbonding nature) and deconstructive (red, antibonding nature) electron correlation with respect to the BCP(H6,N11). [Color figure can be viewed at wileyonlinelibrary.com]

Only one-third (see the pie chart in Fig. 4b) of the total constructive *deloc*-ED at BCP(H6,N11) is made by the primary interaction. From the FALDI-based decomposition data, the major contribution to the *deloc*-ED of a bonding nature is in fact from atom-pair O5,H6 (atoms X and H), which accounts for 41% of the total. The third largest contribution comes from N11,H12 and N11,H13 atom-pairs. Each one contributes $\sim 7\%$ to the total and thus a collective sum of 14% is yielded by the N11–{H12,H13} “group.” All other atom-pairs made rather small contributions—we therefore summed their individual values together to get the “Remaining bonding” percentage, which is 13% of the total, Figure 4b. The FALDI-based decomposition of the *deloc*-ED at BCP(H6,N11) has revealed quantitatively (percentage-wise) the multicenter bonding nature of the intramolecular H-bonding interaction in β -alanine. Furthermore, we note that atom-pair combinations involving the three atoms O5 (X), H6 (H) and N11 (Y) account for the vast majority of *deloc*-ED of a bonding nature. This is an important result, not only in terms of quantifying the multicenter character (in this context, we can now approximate this interaction as three-center), but also in that the result is in full agreement with IUPAC’s basic recommendation^[17,18] of depicting an H-bond to comprise a series of at least three chemically bonded atoms, namely atoms X—H...Y.

Figure 5 shows the 3D-isosurfaces of the three major bonding contributions (see pie chart in Fig. 4b) to the total *deloc*-ED; it is clear that all of them concentrate ED in the vicinity of

BCP(H6,N11). The primary interaction, Figure 5b, forms a very clear channel of constructive electron correlation all along AIL(H6,N11). This particular isosurface may be related to the so-called “privileged exchange-channel” as per thinking by Pendás et al.^[55] However, the maximum value for this atom-pair does not occur at the same coordinate as the BCP along the analysed vector, Figure 4a, indicating that the overall or resultant “privileged exchange-channel” (i.e., the AIL) is the sum of all constructive electron correlation contributions and hence does not coincide with a simple two-atom interpretation of a BCP. Counter intuitively, the electrons shared by O5 and H6 (Fig. 5a), as well as the electrons shared by N11 and its bonded hydrogens (Fig. 5c), extend into the H6,N11 interatomic region along the AIL. These three FALDI-based isosurfaces, when considered individually and then as a collective group (as shown in Fig. 3a), provide a qualitative understanding of the multicenter nature of the AIL between atoms H6 and N11 in β -alanine.

Multicenter bonding nature of a boron–hydrogen interaction in diborane

Figures 6a and 6b show results obtained for the constructive *deloc*-ED distributions in diborane with respect to BCP(B1,H7). Additional FALDI decompositions are included in PART 2 of the Supporting Information. The largest contribution to the bonding *deloc*-ED comes from the atom-pair linked by the AIL, B1 and H7 (the primary interaction), and accounts for one-third (33%) of the total. Interestingly, the ED that is delocalized between the *other* boron atom with the same hydrogen, i.e. atom-pair B4,H7, contributes approximately the same amount (31%) of bonding *deloc*-ED. These two B,H atom-pairs therefore contribute almost equally to BCP(B1,H7) and (due to

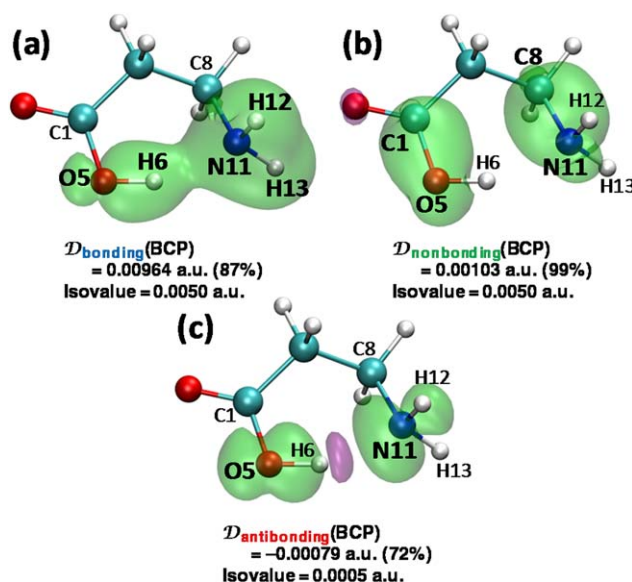


Figure 3. *Deloc*-ED 3D-isosurfaces of the major constructive, a) 87% of bonding ED, comprising (O5,H6) + (H6,N11) + (N11–{H12,H13}), nonconstructive, b) 99% of nonbonding ED, comprising (C1,O5) + (C8,N11) and deconstructive, c) 72% of antibonding ED, comprising (O5,N11) electron correlation contributing factors with respect to BCP(H6,N11) in β -alanine. Color coding: green = positive, purple = negative. [Color figure can be viewed at wileyonlinelibrary.com]

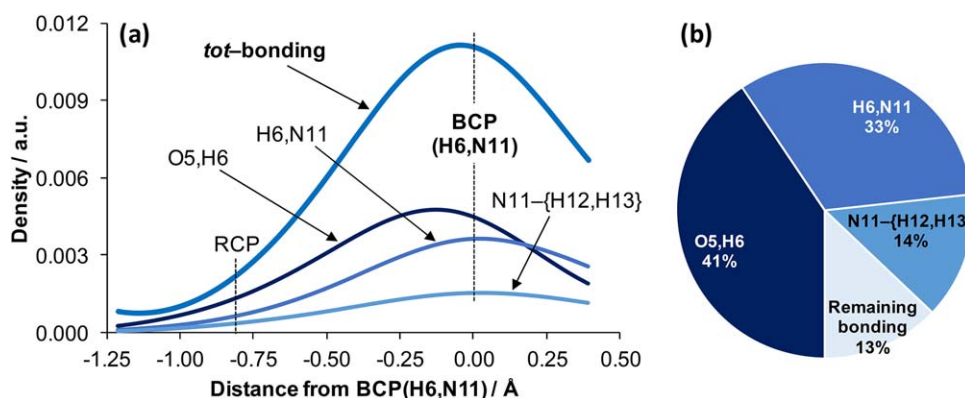


Figure 4. a) FALDI-based decomposition, along the indicated vector for **1** in Figure 1, of the constructive electron correlation (blue line in Figure 2b, bonding nature) with respect to the BCP(H6,N11) in β -alanine, into the major contributing atom-pairs. b) Pie-chart summarizing percentage-wise the major contributing atom-pairs at the BCP(H6,N11). [Color figure can be viewed at wileyonlinelibrary.com]

symmetry) BCP(B4,H7). Not only is this result an indication of a 3-center B—H—B interaction but it is also to a large extent consistent with the picture of $3c2e$ bonding.^[6] The third and fourth largest contributions are from atom-pairs that are not directly linked to each other with an AIL, namely H7,H8 (9%) and B1,B4 (6%). These two atom-pairs, together with the remainder of the constructive *deloc*-ED, collectively account for $\sim 36\%$ of the total amount at BCP(B1,H7). This is quite a substantial figure, indicating that the B1—H7 bonding interaction displays considerably more multicenter character than what is suggested by the rather oversimplified $3c2e$ model. This finding supports earlier results by Ponec and Uhlík^[56] who suggested that delocalized 3-center interactions require significant (non-vanishing) 2-center delocalization between all atom-pairs involved. Due to the symmetry (D_{2h}) of this diborane structure, the same observations apply to the remaining three B—H interactions involving H7 and H8.

Figure 7 illustrates the 3D-isosurfaces computed for four atom-pairs that made major contributions of bonding nature to the total *deloc*-ED at BCP(B1,H7). The *deloc*-ED distributions for atom-pairs B1,H7 and B4,H7 are remarkably similar, Figures 7a and 7b. Both distributions extend fully in-between the atomic basins of B1, H7 and B4, clearly indicating the tricentric manner in which electrons are shared across these centers. Note that Ponec and coworkers^[27–29] have previously shown (within the framework of DAFH) that a boron atom's ED distribution takes place across the B...H...B region. However, FALDI clearly shows the three-center nature of *each* B—H delocalized channel.

The ED that is delocalized between atom-pair H7,H8 occurs largely through the associated B,H BCPs (explaining why this atom-pair contributes to *deloc*-ED concentration at all four BCPs related to B1, B4, H7 and H8), as well as through a direct channel between their own nuclei, Figure 7c. Finally, the manner in which electrons are shared between atoms B1 and B4 occurs primarily through the channel between atoms H7 and H8, Figure 7d. This is quite an unexpected finding, revealing that boron atoms share ED “through bond” (i.e., by means of or *via* the two bridging hydrogen atoms) rather than “through space” (i.e., in a direct manner). Interestingly, based on IQA-defined interatomic exchange–correlation energies ($V_{XC}^{A,B}$), Pendás and coworkers^[57]

have previously shown that an AIL between atoms H7 and H8 is more likely to form than between atoms B1 and B4, but less likely than the existing AIL-linked H-atoms. Their results can easily be rationalized with the isosurfaces in Figures 7c and 7d; they show that the manner through which electrons are delocalized contributes cooperatively to the H-atoms linked by an AIL as well as the AIL-free interaction between H7 and H8.

All the above analyses demonstrate that atom-pairs which made major contributions at BCP(B1,H7) delocalize a substantial quantity of their ED in regions other than directly between each other, highlighting the large multicenter character of most AILs in diborane.

Typical carbon–carbon covalent bonding interaction in “linear” *n*-butane

Figures 8a and 8b show the FALDI-based decomposition of the constructive electron correlation in “linear” *n*-butane (with

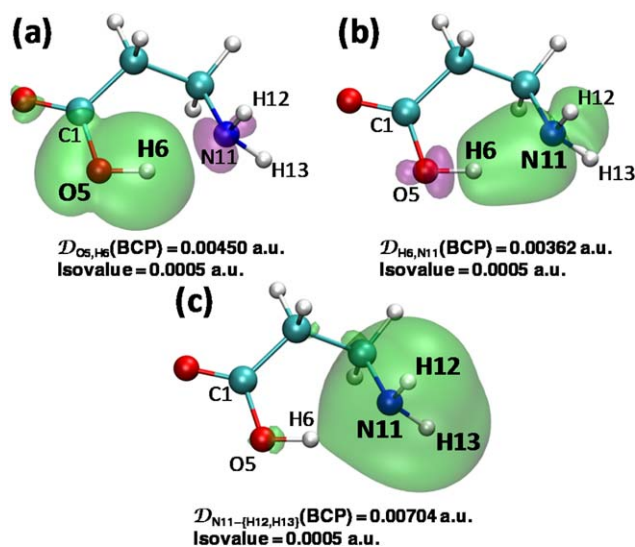


Figure 5. *Deloc*-ED 3D-isosurfaces of the major constructive electron correlation contributing atom-pairs with respect to the BCP(H6,N11) in β -alanine: a) $D_{O5,H6}$ (41%), b) $D_{H6,N11}$ (33%) and c) $D_{N11-\{H12,H13\}}$ (14%). Color coding: green = positive, purple = negative. [Color figure can be viewed at wileyonlinelibrary.com]

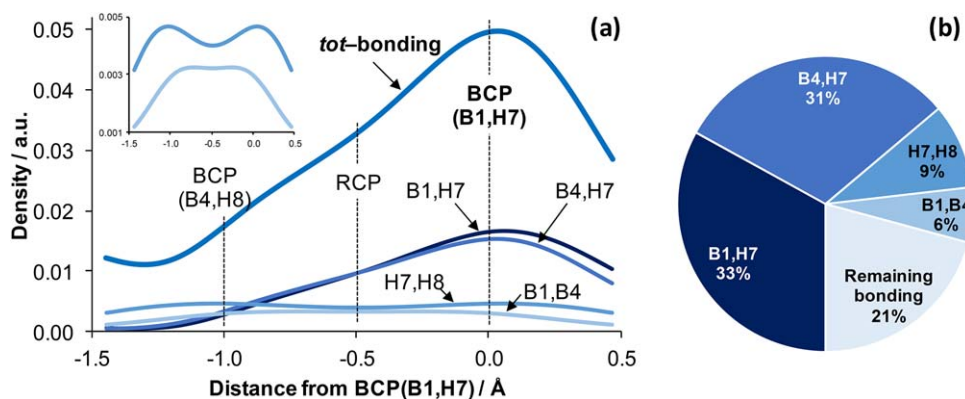


Figure 6. a) FALDI-based decomposition of the constructive electron correlation (i.e., *deloc*-ED of a bonding nature) with respect to BCP(B1,H7) in diborane, along the indicated vector for **2** in Figure 1, into the major atom-pair contributions. Inset: magnified trends for atom-pairs H7,H8 and B1,B4. b) Pie-chart summarizing percentage-wise the major contributing atom-pairs at the BCP(B1,H7). [Color figure can be viewed at wileyonlinelibrary.com]

respect to BCP(C9,C12)). Additional FALDI decompositions are included in PART 2 of the Supplementary Information. Unsurprisingly, atom-pair C9,C12 contributes by far the greatest amount of *deloc*-ED of a bonding nature, accounting for 84% of the total. This result is in agreement with the general interpretation of a covalent “single” bond as being a two-center interaction. A 3D-isosurface of atom-pair C9,C12 *deloc*-ED distribution is shown in Figure 9a; it reveals a clear XC-channel generally confined within the C9,C12 interatomic region. The C9,C12 *deloc*-ED distribution is therefore qualitatively very different from that of the atom-pair B1,H7 in diborane (Fig. 7a). Interestingly, our FALDI analyses reveal that this carbon–carbon interaction is not entirely bicentric. Note that 16% of the total *deloc*-ED resulting from constructive electron correlation at BCP(C9,C12) is due to other (secondary) atom-pairs. These secondary contributions come mostly from (i) the sum of four equivalent “carbon atom–hydrogen atom” atom-pairs, abbreviated as C–H (i.e., C9–{H13,H14} plus C12–{H10,H11}), accounting for 7% and (ii) the four “carbon atom–carbon atom” atom-pairs (i.e., C2–{C9,C12} plus C3–{C12,C9}) accounting for 6% of the total. 3D-isosurfaces of these contributions, Figures 9b and 9c, reveal how atom-pairs of these “distant” interactions also concentrate ED along ALL(C9,C12). In this context, the C9–C12 covalently bonded interaction, as measured at its associated BCP, can only be approximated as two-center.

Comparison of two different M–C bonding interactions in carbene complexes

The differences between M–C bonding interactions in Schrock, Fischer and several other types of carbene complexes have been a constant focal point of inorganic chemistry research for a number of decades.^[21] It is generally accepted that heteroatoms bonded directly to the carbene carbon atom in Fischer carbene complexes (such as an oxygen, **5** in Fig. 1) enhance π -backbonding from the metal atom, as well as σ -donation from the ligand. From a QTAIM, i.e. *tot*-ED topology perspective, however, the M–C bonds of the Schrock and Fischer carbene complexes appear to be almost identical, as both consist of (i) an AIL connecting the metal and carbon

atoms, (ii) a positive Laplacian value at BCP, (iii) a $|V|/G$ ratio larger than one and (iv) a DI in the range of $1.0 < DI(M,C) < 1.5$ (shown in PART 3 of the Supplementary Information). It was then of interest and importance to find out whether the approach presented in this work can quantify the degree and point correctly at the reason for the difference of multicenter bonding characters of the two M–C AILs in the Schrock and Fischer (**4** and **5**, respectively, in Fig. 1) carbene complexes.

Figures 10a and 10c show the FALDI-based decomposition of concentrated *deloc*-ED in **4** and **5** with respect to the

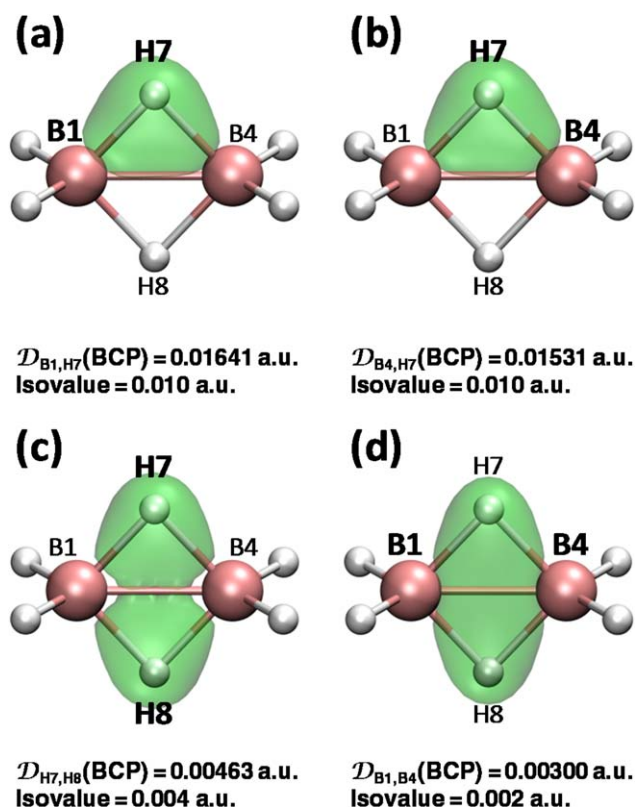


Figure 7. *deloc*-ED 3D-isosurfaces of the major constructive electron correlation contributing atom-pairs with respect to BCP(B1,H7): a) $D_{B1,H7}$ (33%), b) $D_{B4,H7}$ (31%), c) $D_{H7,H8}$ (9%) and d) $D_{B1,B4}$ (6%). [Color figure can be viewed at wileyonlinelibrary.com]

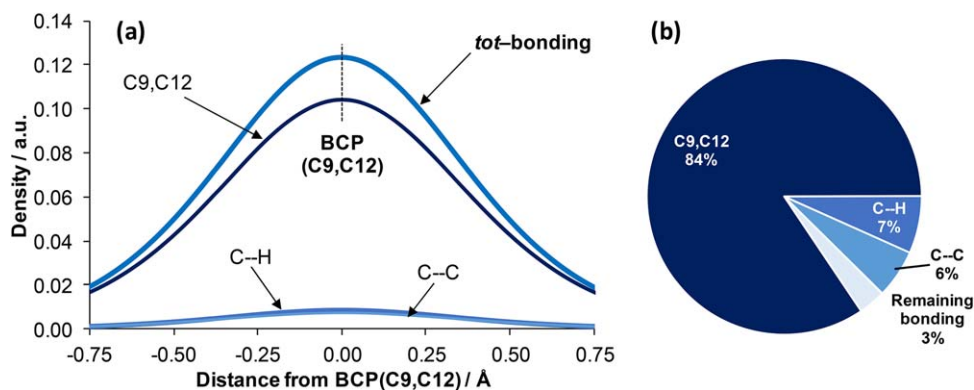


Figure 8. a) FALDI-based decomposition of the constructive electron correlation (i.e., *deloc*-ED of a bonding nature) along the indicated vector for **3** in Figure 1, in "linear" *n*-butane, into the major contributing atom-pairs. b) Pie-chart summarizing percentage-wise the major contributing factors at the BCP(C9,C12). [Color figure can be viewed at wileyonlinelibrary.com]

relevant M–C BCPs. Additional FALDI decompositions are included in PART 2 of the Supporting Information. Figures 10a and 10c show that the general shapes of the trends pertaining to structures **4** and **5** are similar as they only differ in relative magnitude. The primary M–C interaction in **4** accounts for comparatively more (80%) of the total *deloc*-ED of a bonding nature as compared to that in **5** (63%).

Clearly, the AIL linking the M and carbene C atoms in the Schrock complex is considerably more bicentric than in the Fischer complex. Importantly, the heteroatom O13 is indeed mainly responsible for the comparatively larger degree of multicenter bonding character in **5** (Fig. 10b), in accord with common knowledge. Two atom-pairs containing atom O13, that with the carbene carbon atom ($\rho_{\text{BCP}} = 0.00309$ a.u.) and with the carbene metal atom ($\rho_{\text{BCP}} = 0.00096$ a.u.) account for a significant 12% of the total constructive electron correlation at BCP(Cr1,C12). In comparison, atom-pair combinations of the *non*-heteroatoms H23 or H24 (equivalent due to symmetry of the molecular structure) in **4**, with the carbene carbon atom ($\rho = 0.00200$ a.u.) and with the carbene metal atom ($\rho = 0.00134$ a.u.) account for a much smaller 7% of the total *deloc*-ED of a bonding nature at BCP(Ti1,C22).

3D-isosurfaces of the major contributions to the *deloc*-ED of a bonding nature in both carbenes are comparable, showing similar features as found in the *n*-butane; they are included in PART 4 of the Supporting Information together with short discussion.

Comparative analysis

A comparison of the relative contributions made to the total *deloc*-ED of a bonding nature by the primary, largest secondary and sum of remaining interactions at BCPs associated with the five investigated bonding interactions is shown in Figure 11. The most striking observation one can make is the fact that "pure" (i.e., 100%) bi-center interactions might not exist at all, except in an isolated diatomic molecules; note a significant (16%) contribution made by atom-pairs other than the C9–C12 interaction (a classical single covalent bond) in *n*-butane.

The second surprising observation is the comparable degree of multicenter character discovered for the well-known case of diborane (as discussed in detail for atom-pair B1,H7) and classical intramolecular H-bonding interaction in β -alanine. In both cases, the primary interactions (atom-pairs H6,H11 and B1,H7 in β -alanine and diborane, respectively) account for just 33% of the total *deloc*-ED of bonding nature. It is important to stress that in the gas phase the largest secondary interaction (the atom pair O5,H6, or the X–H bond) contributed more (41%) to the concentrated *deloc*-ED at BCP(H6,N11) in β -alanine than the primary interaction (Fig. 4). However, the reverse trend holds in the aqueous phase. Considering diborane's most significant secondary contribution to the bonding *deloc*-ED at BCP(B1,H7), it amounts to 31%, which is nearly the same as found for the primary interaction. This nicely exemplifies the predominant tricentric character of a B,H AIL.

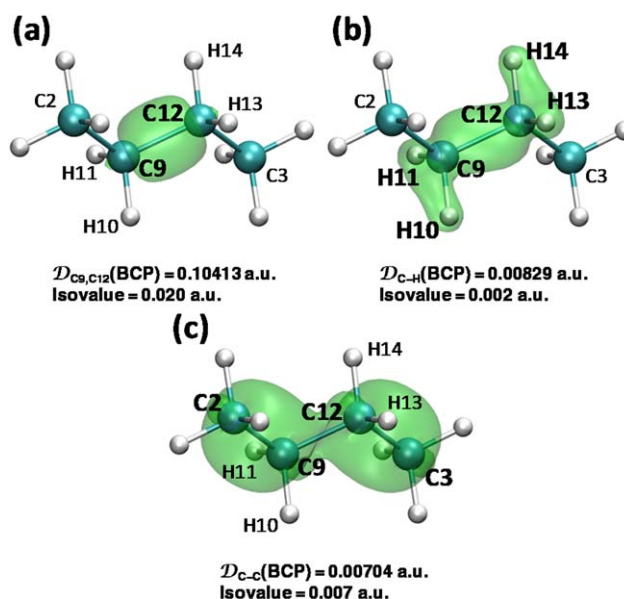


Figure 9. *deloc*-ED 3D-isosurfaces of the major constructive electron correlation contributions with respect to BCP(C9,C12) in "linear" *n*-butane: a) $D_{\text{C9,C12}}$ (84%), b) $D_{\text{C-H}}$ (7%) and c) $D_{\text{C-C}}$ (6%). [Color figure can be viewed at wileyonlinelibrary.com]

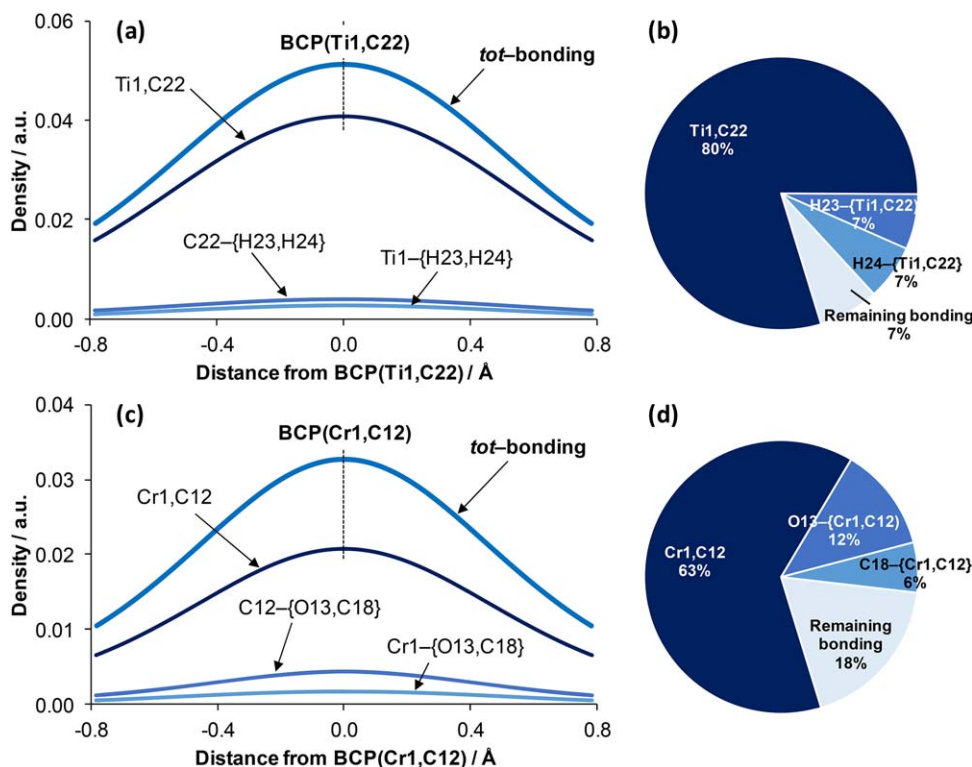


Figure 10. a) Comparison of the FALDI-based decompositions of the constructive electron correlation (i.e., *deloc*-ED of a bonding nature) with respect to the M—C BCPs in the Schrock and Fischer carbene complexes, into the major contributions made by the indicated atom-pairs. b) Pie-charts summarizing percentage-wise the major contributions at the M—C BCPs in **4** and **5**. [Color figure can be viewed at wileyonlinelibrary.com]

Finally, relative to the Schrock carbene, a larger degree of multicenter character of the M—C bonding interaction was fully confirmed in the Fischer carbene (atom-pair Cr1,C12). Possibly surprisingly, we have discovered that the degree of bicenter M—C bonding interaction in the Schrock carbene is comparable to that found for the classical single covalent bond in *n*-butane; we found that the primary interactions, Ti1,C22 and C9,C12, contributed 80% and 84%, respectively, to the total concentrated *deloc*-ED at the respective BCPs.

All these results show how the presence of an AIL, connecting only two nuclei, can be misleading in multi-atomic molecules. In fact, our results reveal that AILs are surprisingly

holistic in nature, despite their simple connectivity within a molecular graph. Figure 11 clearly illustrates that there are many atom-pairs that contribute significantly to the total *deloc*-ED in a constructive (concentrating) manner, hence facilitating the emergence of the AIL. This clearly demonstrates that care should be taken whenever an AIL is used to indicate and interpret the interaction between just two atoms. This comment applies, of course, to any method based on ED concentration, including NCI.

Conclusions

The concept of two-center interatomic interactions is, for the most part, a chemist's simplification within a molecular collection of nuclei and electrons interacting holistically and simultaneously. The AIL, which is also a physical observable, is usually interpreted as the result of a two-center interaction and is commonly followed by an analysis of topological properties at a specific BCP to describe a di-atomic interaction. While many multicenter indices have been reported in the literature, which can recover the multicenter nature of interatomic interactions, none of these indices address the real-space AIL itself.

Our FALDI density decomposition scheme, which measures the ED contributions of atoms and atom-pairs throughout all molecular space, provides the tools that are necessary to understand AILs on a holistic level. We have extended FALDI in this work by decomposing one of the fundamental ED properties of interatomic interactions—the concentration, depletion or reduction of ED—into contributions from all atomic pairs

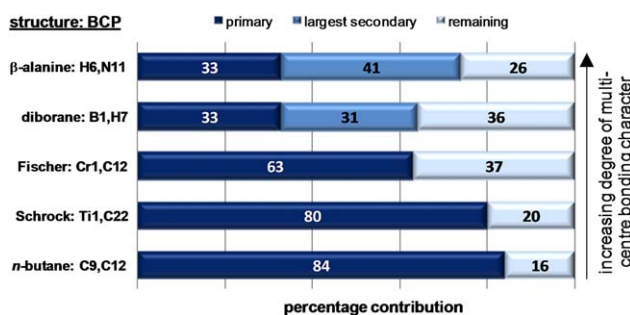


Figure 11. Comparison of the relative degree of multicenter bonding character of the five bonding interactions investigated in this study. Values of specific atom-pair *deloc*-ED contributions to the total bonding *deloc*-ED at a relevant BCP are expressed as percentages. Primary contributions indicate the *deloc*-ED associated with an indicated atom-pair that is connected by an AIL. [Color figure can be viewed at wileyonlinelibrary.com]

within the molecule. Such an approach allows a quantification and visualization of how the atoms of a primary interaction (atoms linked by an AIL) contribute to ED relative to all other atom-pairs, thereby arriving at a multicenter interpretation of an AIL. We have investigated five simple interactions linked by an AIL, ranging from formal two-center to formal three-center as well as interactions with partial multicenter character. Our results are fully consistent with general interpretations of multicenter bonding, despite focusing on the multicenter character of the AIL as measured in the vicinity of a BCP. We also note that our approach is not limited to atoms linked by an AIL, and can be used in conjunction with other QCT techniques, such as NCI.

AILs have previously been interpreted as “privileged exchange channels” by Pendás et al.^[55] This interpretation has been tested by Tognetti and Joubert^[53,54] by comparing the QTAIM-defined DI or the IQA-defined interatomic XC energy of the primary interaction (linked by an AIL) with the largest competing secondary interaction. While they could show that the primary interaction is indeed privileged (i.e., larger DI or XC energy than competing interactions) for strong interactions, they identified a number of cases where their approach did not give consistent results. We have shown that, unlike the total integrated DI (as defined in QTAIM), real-space distributions of FALDI-defined *deloc*-ED can be negative in certain regions of space. The sign of *deloc*-ED at any given coordinate, as well as the sign of its partial second derivative, is a result of constructive, nonconstructive or deconstructive simultaneous overlap of MOs across two atomic basins. Some of these atom-pairs’ delocalized ED concentrates ED in the same interatomic region, thereby facilitating the formation of an AIL, whereas some atom-pairs’ delocalized ED depletes or reduces ED, thereby hindering and competing against the formation of an AIL. This observation led to our labels of *bonding*, *nonbonding* or *antibonding* of any specific atom-pair’s *deloc*-ED in a given region of space in analogy to MO bonding theory. Therefore, any AIL, hence also a “privileged exchange channel,” is not simply a bridge of ED linking two atoms but rather the result of *multiple* bonding contributions that compensate over the competing nonbonding and antibonding contributions. This can be seen as a new interpretation of a “privileged exchange channel” that does not impose largest contribution to be made by the atom-pair linked by an AIL. As a matter of fact, the intramolecular H-bonding in β -alanine fully supports this, as the primary interaction (linked by an AIL) contributed significantly less when compared with a secondary one. Furthermore, because our approach also has the capability for the visualization and quantification of “privileged exchange channels” (e.g., Fig. 9) we noted, by inspecting *deloc*-ED isosurfaces, that most of the secondary bonding contributions investigated in this work occur *through* the primary interaction, i.e. along the AIL, as opposed to forming direct channels through space.

Cortés-Guzmán and Bader have previously stated^[49] that QTAIM and MO theories are fully consistent, with the primary link between the two being the DI. We note, however, that only through the visualization in real-space of FALDI’s *deloc*-ED

distributions can the information inherent in MO theory be fully expanded within the realms of QTAIM. For instance, DIs alone do not recover the manner in which atom-pair O5,H6 concentrates *deloc*-ED at BCP(H5,N11) in β -alanine, nor the manner in which electrons shared between atoms B1 and H7 in diborane are delocalized almost equally across the entire B...H...B region. In addition, DI values are always positive whereas, as shown in Figure 3c, due to deconstructive electron correlation, the electrons shared between two atoms can *reduce* the *tot*-ED, leading to a different energetic consequence for an interaction. Importantly, the decomposition of the total *deloc*-ED in the vicinity of a BCP in terms of bonding, nonbonding and antibonding is consistent with both Bader’s as well as MO theories.

The ability for chemists to understand and quantify the holistic nature of AILs should help alleviate conceptual challenges within QCT, especially for controversial AILs, since the properties of the ED at a BCP are commonly used in the classification and evaluation of interatomic interactions. Our assertion that the *manner* in which electrons are delocalized between atoms (*deloc*-ED distributions) is as important as the total *amount* of delocalized electrons (DI), should also aid the distillation of the wealth of information within MOs and the wavefunction into an atom-centric, density-based view of chemical bonding.

Conflict of Interest


There are no conflicts of interest to declare.

Acknowledgment

The authors gratefully acknowledge the Centre for High Performance Computing (CHPC), South Africa, for providing computational resources to this research project.

Keywords: atomic interaction line · electron density decomposition · FALDI · multicenter interaction · computational chemistry

How to cite this article: J. H. de Lange, D. M. E. van Niekerk, I. Cukrowski. *J. Comput. Chem.* **2018**, *39*, 973–985. DOI: 10.1002/jcc.25175

 Additional Supporting Information may be found in the online version of this article.

- [1] B. Silvi, *J. Mol. Struct.* **2002**, *614*, 3.
- [2] W. C. Price, *J. Chem. Phys.* **1947**, *15*, 614.
- [3] J. S. Kasper, C. M. Lucht, D. Harker, *Acta Cryst.* **1950**, *3*, 436.
- [4] K. Hedberg, M. E. Jones, V. Shomaker, *J. Am. Chem. Soc.* **1951**, *73*, 3538.
- [5] C. E. Nordman, W. N. Lipscomb, *J. Chem. Phys.* **1953**, *21*, 1856.
- [6] L. Lavine, W. N. Lipscomb, *J. Chem. Phys.* **1954**, *22*, 614.
- [7] M. Elian, R. Hoffman, *Inorg. Chem.* **1975**, *14*, 1058.
- [8] R. H. Summerville, R. Hoffman, *J. Am. Chem. Soc.* **1979**, *101*, 3821.
- [9] R. Ponec, G. Lendvay, J. Chaves, *J. Comput. Chem.* **2008**, *29*, 1387.
- [10] N. M. Kostic, R. F. Fenske, *Inorg. Chem.* **1983**, *22*, 666.
- [11] R. Bau, R. G. Teller, S. W. Kirtley, T. F. Koetzle, *Acc. Chem. Res.* **1979**, *12*, 176.

- [12] F. Mota, J. S. Miller, J. J. Novoa, *J. Am. Chem. Soc.* **2009**, *131*, 7699.
- [13] I. Garcia-Yoldi, J. S. Miller, J. J. Novoa, *J. Phys. Chem. A* **2009**, *113*, 7124.
- [14] W. Wang, Y. Kan, L. Wang, S. Sun, Y. Qiu, *J. Phys. Chem. C* **2014**, *118*, 28746.
- [15] J. S. Miller, J. J. Novoa, *Acc. Chem. Res.* **2007**, *40*, 189.
- [16] B. Silvi, C. Gatti, *J. Phys. Chem. A* **2000**, *104*, 947.
- [17] E. Arunan, G. R. Desiraju, R. A. Klein, J. Sadlej, S. Scheiner, I. Alkorta, D. C. Clary, R. H. Crabtree, J. J. Dannenberg, P. Hobza, H. G. Kjaergaard, A. C. Legon, B. Mennucci, D. J. Nesbitt, *Pure Appl. Chem.* **2011**, *83*, 1619.
- [18] E. Arunan, G. R. Desiraju, R. A. Klein, J. Sadlej, S. Scheiner, I. Alkorta, D. C. Clary, R. H. Crabtree, J. J. Dannenberg, P. Hobza, H. G. Kjaergaard, A. C. Legon, B. Mennucci, D. J. Nesbitt, *Pure Appl. Chem.* **2011**, *83*, 1637.
- [19] I. Cukrowski, D. M. E. van Niekerk, J. H. de Lange, *Struct. Chem.* **2017**, *5*, 1429.
- [20] I. Cukrowski, J. H. de Lange, A. S. Adeyinka, P. Mangondo, *Comput. Theor. Chem.* **2015**, *1053*, 60.
- [21] D. Bourissou, O. Guerret, F. P. Gabbaï, G. Bertrand, *Chem. Rev.* **2000**, *100*, 39.
- [22] R. F. W. Bader, *Atoms in Molecules: A Quantum Theory*; Oxford University Press, Oxford, **1990**.
- [23] P. Dem'yanov, P. Polestshuk, *Chem. Eur. J.* **2012**, *18*, 4982.
- [24] M. Mandado, A. M. Graña, R. A. Mosquera, *Phys. Chem. Chem. Phys.* **2004**, *6*, 4391.
- [25] L. J. Farrugia, H. M. Senn, *J. Phys. Chem. A* **2011**, *116*, 738.
- [26] C. F. Matta, J. Hernández-Trujillo, T. H. Tang, R. F. W. Bader, *Chem. Eur. J.* **2003**, *9*, 1940.
- [27] P. Bultinck, M. Rafat, R. Ponec, B. Van Gheluwe, R. Carbo-Dorca, P. Popelier, *J. Phys. Chem. A* **2006**, *110*, 7642.
- [28] R. Ponec, I. Mayer, *J. Phys. Chem. A* **1997**, *101*, 1738.
- [29] R. Ponec, G. Yuzhakov, D. L. Cooper, *Theor. Chim. Acta* **2004**, *5*, 419.
- [30] R. F. W. Bader, C. Gatti, *Chem. Phys. Lett.* **1998**, *287*, 233.
- [31] C. Gatti, F. Cargnoni, L. Bertini, *J. Comput. Chem.* **2003**, *24*, 422.
- [32] E. Monza, C. Gatti, L. L. Presti, E. Ortoleva, *J. Phys. Chem. A* **2011**, *115*, 12864.
- [33] J. H. de Lange, I. Cukrowski, *J. Comput. Chem.* **2017**, *38*, 981.
- [34] E. R. Johnson, S. Keinan, P. Mori-Sanchez, J. Contreras-Garcia, A. J. Cohen, W. Yang, *J. Am. Chem. Soc.* **2010**, *132*, 6498.
- [35] M. J. Frisch, G. W. Trucks, H. B. Schlegel, G. E. Scuseria, M. A. Robb, J. R. Cheeseman, G. Scalmani, V. Barone, B. Mennucci, G. A. Petersson, H. Nakatsuji, M. Caricato, X. Li, H. P. Hratchian, A. F. Izmaylov, J. Bloino, G. Zheng, J. L. Sonnenberg, M. Hada, M. Ehara, K. Toyota, R. Fukuda, J. Hasegawa, M. Ishida, T. Nakajima, Y. Honda, O. Kitao, H. Nakai, T. Vreven, J. A. Jr. Montgomery, J. E. Peralta, F. Ogliaro, M. Bearpark, J. J. Heyd, E. Brothers, K. N. Kudin, V. N. Staroverov, R. Kobayashi, J. Normand, K. Raghavachari, A. Rendell, J. C. Burant, S. S. Iyengar, J. Tomasi, M. Cossi, N. Rega, J. M. Millam, M. Klene, J. E. Knox, J. B. Cross, V. Bakken, C. Adamo, J. Jaramillo, R. Gomperts, R. E. Stratmann, O. Yazyev, A. J. Austin, R. Cammi, C. Pomelli, J. W. Ochterski, R. L. Martin, K. Morokuma, V. G. Zakrzewski, G. A. Voth, P. Salvador, J. J. Dannenberg, S. Dapprich, A. D. Daniels, Ö. Farkas, J. B. Foresman, J. V. Ortiz, J. Cioslowski, D. J. Fox, *Gaussian 09, Revision D.01*; Gaussian, Inc.: Wallingford, CT, **2009**.
- [36] S. Grimme, *Wiley Interdiscip. Rev. Comput. Mol. Sci.* **2011**, *1*, 211.
- [37] T. A. Keith, AIMAll (Version 16.10.31); TK Gristmill Software: Overland Park KS, USA, **2016**. Available at: aim.tkgristmill.com.
- [38] W. Humphrey, A. Dalke, K. Schulten, *J. Mol. Graph.* **1996**, *14*, 33.
- [39] A. M. K. Müller, *Phys. Lett. A* **1984**, *105*, 446.
- [40] D. L. Cooper, R. Ponec, *Phys. Chem. Chem. Phys.* **2008**, *10*, 1319.
- [41] M. Bühl, H. Kabrede, *J. Chem. Theory Comput.* **2006**, *2*, 1282.
- [42] P. Bultinck, D. L. Cooper, R. Ponec, *J. Phys. Chem. A* **2010**, *114*, 8754.
- [43] R. Ponec, *J. Math. Chem.* **1997**, *12*, 323.
- [44] R. Ponec, *J. Math. Chem.* **1998**, *23*, 85.
- [45] R. Ponec, D. L. Cooper, *Faraday Discuss.* **2007**, *135*, 31.
- [46] E. Francisco, A. M. Pendás, A. Costales, *Phys. Chem. Chem. Phys.* **2014**, *16*, 4586.
- [47] R. F. W. Bader, M. E. Stephens, *J. Am. Chem. Soc.* **1975**, *97*, 7391.
- [48] X. Fradera, M. A. Austen, R. F. W. Bader, *J. Phys. Chem. A* **1999**, *103*, 304.
- [49] F. Cortés-Guzmán, R. F. W. Bader, *Coord. Chem. Rev.* **2005**, *249*, 633.
- [50] I. Sumar, R. Cook, P. W. Ayers, C. F. Matta, *Comput. Theor. Chem.* **2015**, *1070*, 55.
- [51] I. Sumar, R. Cook, P. W. Ayers, C. F. Matta, *Phys. Scr.* **2016**, *91*, 013001.
- [52] M. J. Timm, C. F. Matta, L. Massa, L. Huang, *J. Phys. Chem. A* **2014**, *118*, 11304.
- [53] V. Tognetti, L. Joubert, *J. Chem. Phys.* **2013**, *138*, 024102.
- [54] O. A. Syzgantseva, V. Tognetti, L. Joubert, *J. Phys. Chem. A* **2013**, *117*, 8969.
- [55] A. M. Pendás, E. Francisco, M. A. Blanco, C. Gatti, *Chem. Eur. J.* **2007**, *13*, 9362.
- [56] R. Ponec, F. Uhlík, *J. Mol. Struct. (Theochem)* **1997**, *391*, 159.
- [57] M. García-Revilla, E. Francisco, P. L. A. Popelier, A. M. Pendás, *Chem. Phys. Chem.* **2013**, *14*, 1211.

Received: 2 November 2017

Revised: 7 December 2017

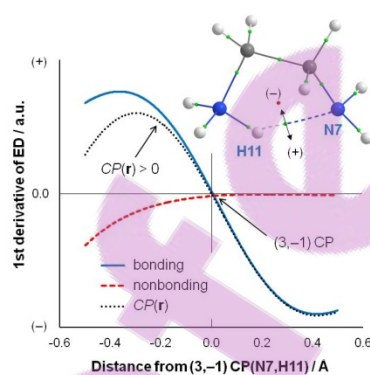
Accepted: 14 January 2018

Published online on 5 February 2018

Chapter 5. FALDI-Based Criterion for and the Origin of an Electron Density Bridge with an Associated (3,-1) Critical Point on Bader's Molecular Graph

Accepted by:

Journal of Computational Chemistry, 2018, June. DOI: 10.1002/jcc.25548



A novel quantum chemical function is introduced which can be used to study and understand the presence or absence of a density bridge in an internuclear region. The $CP(r)$ function uses the gradients of bonding, nonbonding and antibonding density contributions from the FALDI density decomposition scheme in order to assess the origin and nature of density bridges for inter- and intramolecular interactions in equilibrium and non-equilibrium structures.

FALDI-Based Criterion for and the Origin of an Electron Density Bridge with an Associated (3,-1) Critical Point on Bader's Molecular Graph

*Jurgens H. de Lange, Daniël M.E. van Niekerk, Ignacy Cukrowski**

Correspondence to: Ignacy Cukrowski (E-mail: ignacy.cukrowski@up.ac.za)

Department of Chemistry, Faculty of Natural and Agricultural Sciences, University of Pretoria, Lynnwood Road, Hatfield, Pretoria 0002, South Africa

KEYWORDS:

Atomic Interaction Line, Bond path, FALDI, Chemical bond, Intramolecular interaction

Abstract

The total electron density (ED) along the λ_2 -eigenvector is decomposed into contributions which either *facilitate* or *hinder* the presence of an electron density bridge (DB, often called an atomic interaction line or a bond path). Our FALDI-based approach explains a DB presence as a result of a dominating rate of change of facilitating factors relative to the rate of change of hindering factors; a novel and universal criterion for a DB presence is thus proposed. Importantly, facilitating factors show, in absolute terms, a concentration of ED in the internuclear region as commonly observed for most chemical bonds, whereas hindering factors show a depletion of ED in the internuclear region. We test our approach on four intramolecular interactions, namely (i) an attractive classical H-bond, (ii) a repulsive O...O interaction, (iii) an attractive Cl...Cl interaction and (iv) an attractive C–H...H–C interaction. (Dis)appearance of a DB is (i) shown to be due to a ‘small’ change in molecular environment and (ii) quali- and quantitatively linked with specific atoms and atom-pairs. The protocol described is equally applicable (a) to any internuclear region, (b) regardless of what kind of interaction (attractive/repulsive) atoms are involved in, (c) at any level of theory used to compute the molecular structure and corresponding wavefunction, and (d) equilibrium or non-equilibrium structures. Finally, we argue for a paradigm shift in the description of chemical interactions, from the ED perspective, in favour of a multicenter rather than diatomic approach in interpreting ED distributions in internuclear regions.

Introduction

From a general chemist's perspective, conceptual understanding of a chemical bond is an amalgamation of various chemical bond theories, empirical observations and intuition. Existing chemical bond theories are, for the most part, deductive inferences on calculations and experiments performed on very small and simple systems. Even modern developments in the field will almost always develop from a bottom-up approach, and our conceptual understanding of a chemical bond is therefore always much clearer for di- or few-atomic molecules. As it stands, there is no general and universal theory of a chemical bond and terms such as 'chemical bonding' rather than 'a chemical bond' dominate titles of chapters in two dedicated books^{1,2} published recently.

Unfortunately, complexity in chemical systems scales exponentially with an increasing number of atoms and bonds, and so does the difficulty of interpreting chemical bond models. For instance, both molecular orbital (MO) and valence bond (VB) theories are simple to understand and interpret for diatomic molecules, but their interpretation becomes increasingly convoluted as the number of MOs or allowable states increase. The same problem applies to many modern theoretical and computational approaches, such as calculations of bond dissociation energy and deformation densities. One of the biggest hurdles facing chemical bond theory is that the current paradigm places immense focus on bonds as a diatomic property of a molecule, whereas the wavefunction and changes within the wavefunction occur on a molecular-wide, hence a polyatomic scale. The irreducible cornerstone of a bond – that a chemical bond requires energy to break – is usually exemplified through measurements of energy differences between an interacting and non-interacting states. Such experiments study the *process* assumed to be a single diatomic, intra- or intermolecular, bond formation and do not consider the intrinsic property of a molecule as a collection of atoms interacting simultaneously with each other. The usage and interpretation of binding energies particularly fails in the case of the interpretation of intramolecular interactions, as it always involves more than just two atoms and requires breaking multiple bonds.

Quantum Chemical Topology (QCT)³ encompasses a range of approaches which, in principle, do not suffer from the above-mentioned complexity scaling. The most prominent QCT method is Bader's Quantum Theory of Atoms in Molecules (QTAIM).⁴ QTAIM's molecular graphs – a series of electron density bridges (DBs, but also commonly called atomic interaction lines, line paths^{5,6} or bond paths⁷) – are equally applicable to simple, small, large, hence complex molecules. Historically, the interpretation of a DB was associated, by

induction, with a chemical bond: remarkably, a DB is observed wherever chemists can *unanimously* agree that a chemical bond should exist. Since the first observations of the equivalence between a DB and a chemical bond,^{7,8} many questions regarding the validity and universality of a DB as an indicator of a chemical bond lead to a fierce scientific discourse,^{5,6,9-15} which will be discussed shortly. However, the large degree of correspondence between the presence of a DB and the general chemist's chemical bond is the impetus for continued research into the nature and interpretation of a DB. A range of properties of a DB, and specifically topological and energetic properties at the (3,-1) critical point (CP, commonly known as a bond critical point) associated with a DB, have been linked to and successfully applied in describing chemical phenomena, *e.g.*, bond strengths,^{16,17} open- and closed-shell natures of interactions,¹⁷ bond orders, degrees of π -bonding,¹⁸ and many more.

The critique that cautions the over-interpretation of DBs, critique that has been growing steadily over the last two decades, focuses on the two cases which places doubt on the universality of the interpretation of a DB as a bond path: (i) cases where a DB is observed but no chemical bond is expected,⁹⁻¹³ and (ii) cases where a chemical bond is expected but no DB is observed.^{19,20} The most prominent example of the former situation is of DBs which exist between H-atoms in a wide range of molecules and lead to a long series of debates regarding the chemical nature of CH \cdots HC interactions.^{11-13,15,21,22} The existence of a DB in these and other non-conventional types of interactions, many of which can be attractive or repulsive in nature, have placed considerable doubt on the conceptual homeomorphism between QTAIM molecular graphs and the lines which chemists draw to indicate bonds. For the inverse case – where a chemical bond is expected but no DB is observed – researchers have found evidence from other descriptors, such as the Non-covalent Interactions (NCI) technique,^{23,24} the source-function and delocalization indices that indicate the presence of some form of chemical interaction but it is not supported by a (3,-1) CP on a DB.^{19,20} These examples further illustrate that the relationship between various theoretical approaches and the topology of the electron density (ED) is not fully understood yet. In addition, the presence or absence of DBs is often seemingly inexplicable, which adds to the ambiguity regarding the interpretation of a DB. For instance, we have previously shown¹⁴ that the presence of a DB is strongly subjected to effects of the local environment, proving that the *nature* of an interaction might remain the same regardless of the presence or absence of a DB.

The interpretation of a DB has evolved somewhat over time as well. Originally, Bader had all but suggested that a DB and a chemical bond are synonymous.^{7,8,25} Later on, he stressed

that DBs are not chemical bonds, but rather represent ‘bonding interactions’^{15,16} – a mechanism of the molecular ED distribution that serves to lower the molecular energy. Pendás *et al.* presented an alternative interpretation by postulating that a DB represents a ‘privileged exchange channel’.²⁶ Their concept of a DB was further explored by Tognetti and Joubert^{27,28} (TJ). TJ studied a number of intramolecular interactions where a DB was present in some but not other molecules, and investigated whether the presence of a DB could be linked with ‘privileged exchange’. Their approach involved calculating the IQA-defined²⁹ interatomic exchange correlation (XC) energies, $V_{XC}^{X,Y}$, of the interaction between two atoms of interest (the ‘primary interaction’) as well as neighbouring ‘secondary interactions’. They found that if the ratio, $\beta = V_{XC}^{primary} / V_{XC}^{secondary} > 1.59$ (where secondary refers to a pair of atoms for which the $V_{XC}^{X,Y}$ term is largest among all secondary interactions) then a DB was always present whereas for $\beta < 1.35$ no DB was observed. β -ratios between 1.35 and 1.59 were found to be ambiguous – DBs might or might not be present in this range. TJ interpreted the presence of a DB as (i) evidence of privilege in support of Pendás *et al.*’s ideas²⁶ and (ii) the primary interaction being successful in *competing against* various exchange channels of the secondary interactions. Unfortunately, the ambiguity inherent in their β -ratios suggests that either (i) not all DBs represent ‘privileged exchange channels’, (ii) the exclusive use of the integrated $V_{XC}^{X,Y}$ for just a diatomic interaction is not ideal for measuring privilege, or (iii) possibly, the concept of ‘privileged exchange channels’ in predicting the presence/absence of a DB is incorrect.

All previous interpretations of a DB step into the same ‘trap’ as for the interpretation of chemical bonds – that the interaction between atoms in a molecule can be reduced to bicentric nature (*i.e.* line structures) that is subconsciously re-enforced by DBs linking two (and only two) nuclei at a time. However, the ED (as well as critical points in the ED) is a field influenced by *all particles* of a molecule, and therefore the notion that a DB is a diatomic property is false. In fact, we have previously shown³⁰ that the ED at a (3,-1) CP is a result of contributions from delocalized electrons arising from multiple atoms, thereby concluding that a DB is inherently multicenter in nature even in the case of a classical covalent bond. A similar problem facing existing interpretations of a DB is the use of the second eigenvalue of the Hessian matrix as a measure of electron concentration for the fulfilment of Feynman’s theorem³¹ (the basis for Bader’s interpretation^{15,16} as well as the interpretation of other methods such as NCI^{23,24}). This approach is flawed,¹⁴ as it only

measures the *local*, relative electron concentration rather than the absolute, and resultantly shows a large dependence on the local environment. Our own Fragment, Atom, Localized, Delocalized and Interatomic (FALDI) density decomposition scheme^{30,32-34} provides absolute measures of electron concentration for 1- and 2-centre ED distributions. Hence, FALDI provides a much more trustworthy measure³⁰ with regards to a concentration (and its origin) of ED within an internuclear region.

This work presents a new theoretical methodology that provides meaningful explanation of the presence (or absence) of a DB. Although our approach appears as simple in its final implementation, it required a paradigm shift in searching for the origin and meaning of a DB. Our approach comes from a realization that the nature of a DB is inherently not chemical, only its interpretation. Hence, the main focus should be on the ED itself and the elementary conditions required for the presence of a DB, rather than a direct link to chemical concepts such as atoms and linking the bonds. We propose here a set of topological criteria; with the gradient of the ED (along the eigenvector associated with the λ_2 eigenvalue of the Hessian matrix) determining *if* a critical point is present and the second derivative of the ED determining *which* type of critical point is present. To link the mathematics of DB presence with chemical meaning, we decompose the gradient of the ED (which in itself is difficult to interpret from a chemist's point of view) into components with clear chemical and physical interpretations. In principle, this approach can be taken with a large number of established ED decompositions. However, we have chosen our recently developed FALDI density decomposition scheme,^{30,32-34} as FALDI is (i) inherently linked to QTAIM atomic basins and populations, and (ii) FALDI can provide visualisation and quantify electron exchange-correlation channels in real 3D space.

Our primary aim in this work is to derive and introduce the tools necessary to detect and explain the presence or absence of a DB. We will refrain from providing in depth and universal interpretations of a DB in terms of chemical bonding. This is because a sound interpretation of a DB should be extremely robust, general, predictive and physically and chemically meaningful – an endeavour which is not taken lightly. Rather, we will provide a general criterion for the presence of a DB in terms of the gradients of our FALDI decomposition components, culminating in an approach that we hope ourselves or others can use to understand the difficult relationship between the ED distribution and chemical bonding. We present our approach with four case studies focusing on intramolecular interactions, as possibly they represent the most difficult case for chemists to interpret.

However, our approach is of general nature; it applies equally to inter- and intramolecular, weak and strong interactions. In three of the case studies, two similar molecules are investigated, and in each system a non-local perturbation results in the appearance of a DB linking atoms involved in an interaction of interest. Our case studies include an attractive intramolecular H-bond, a repulsive O...O interaction, an attractive Cl...Cl interaction and lastly, an attractive CH...HC interaction.

Theoretical Background

A critical point (CP) in the ED at a coordinate \mathbf{r}_c is a local maximum, minimum or a saddle point where the first derivative, and each of its three components, vanish:⁴

$$\nabla\rho(\mathbf{r}_c) = \mathbf{i} \frac{\partial\rho}{\partial x} + \mathbf{j} \frac{\partial\rho}{\partial y} + \mathbf{k} \frac{\partial\rho}{\partial z} = 0 \quad (1)$$

The unit vectors in Eq. 1 are the principle axes at \mathbf{r}_c , and are determined by the eigenvectors of the matrix of partial second derivatives (the Hessian matrix) of the ED at \mathbf{r}_c . The type of CP can be determined by evaluating the eigenvalues (λ_1 , λ_2 and λ_3) of the Hessian matrix. A CP found wherever a DB is present is a local minimum along one of the axes and local maxima along the other two axes, labeled as (+3,-1), where the *rank* (+3) denotes the number of non-zero eigenvalues at \mathbf{r}_c and the *signature* (-1) is the algebraic sum of the signs of the eigenvalues. A (+3,-1) CP has historically been called a number of names, from Bader's original bond critical point⁴ to more recent line or edge critical point^{5,6}. In this work, we will only refer to this CP as (3,-1) CP in order to reduce as much secondary and implied meanings as possible. For the case of a (3,-1) CP, λ_1 and λ_2 are negative (local maxima) whereas λ_3 is positive (local minimum) and, by convention, $\lambda_1 \leq \lambda_2 \leq \lambda_3$. A CP close to a nucleus is a (+3,-3) CP (a local maximum along all three axes) where all eigenvalues are negative. Therefore, in an interatomic region between two nuclei, λ_3 will always be positive, corresponding to a region of local minimum ED along the internuclear vector. Furthermore, unless the two nuclei are part of a cage, λ_1 will always be negative, corresponding to a local maximum along one of the axes perpendicular to the internuclear vector. The sign of the remaining eigenvalue, λ_2 , corresponding to the other perpendicular axis, determines whether the CP is of (3,-1) ($\lambda_2 < 0$, a local maximum) or a (3,+1) ($\lambda_2 > 0$, a local minimum), also called a ring critical point. The sign of λ_2 therefore contains very valuable information regarding the nature of the CP at \mathbf{r}_c . In addition, the second derivative of the ED is a measure of density concentration ($\nabla^2\rho(\mathbf{r}) < 0$) or depletion ($\nabla^2\rho(\mathbf{r}) > 0$). At any coordinate of a DB the ED is

therefore depleted along the internuclear vector ($\lambda_3 > 0$) but concentrated along all perpendicular vectors ($\lambda_1 < 0$, $\lambda_2 < 0$). It is for this reason that a DB is often called a ‘bridge of density’.¹⁵

A DB will always exist if an associated (3,-1) CP is present, and therefore it is enough to investigate when such a CP may (or may not) be present. Since the presence of a CP depends on the gradient of the ED rather than the ED itself or components of its second derivative, it is important to understand the directional first derivatives of the ED along principle axes in an internuclear region in both the presence and absence of a (3,-1) CP. Note that all derivatives – including components of the Hessian matrix as well as its eigenvalues and eigenvectors – can be calculated at any coordinate \mathbf{r} regardless of whether a critical point is present at \mathbf{r} or not. A local minimum in the ED along the internuclear vector is always present between two (3,-3) CPs of atomic basins that share an interatomic surface, hence the directional derivative of the ED along the internuclear vector will always vanish at some coordinate regardless of the presence or absence of a (3,-1) CP. Generally, the principle axis along which this derivative vanishes is the direction of the eigenvector associated with λ_3 . We label such a local minimum on the internuclear vector as a *geometric minimum density point* (MDP, previously also called a geometric interaction point¹⁴). The internuclear vector, an MDP and the direction of the 3rd eigenvector of the Hessian matrix at the MDP is shown, as an illustrative example, for the internuclear region between two H-atoms in close contact (*i.e.* H1 and H6) in *cis*-2-butene in Figure 1(a). Figure 1(b) shows the ED along the internuclear vector, clearly illustrating the local minimum in the ED and demonstrates how an MDP can easily be found. The perpendicular principle axes at the MDP correspond to the directions of the eigenvectors associated with λ_1 and λ_2 . As mentioned above, λ_1 is usually negative unless the internuclear region is part of a cage, and in most cases, the directional derivative along the direction of the eigenvector associated with λ_1 will vanish or be close to vanishing at the MDP, as shown in Figure 1(c). That leaves the directional derivative along the direction of the 2nd eigenvector of the Hessian matrix as the deciding factor for the presence or absence of most (3,-1) CPs. If this derivative vanishes, then the slope of the ED will be zero and a (3,-1) CP will be present. If this derivative does not vanish, then a (3,-1) CP will be absent regardless of the fact that the ED at the MDP is a local maximum and minimum along the directions of the 1st and 3rd eigenvectors of the Hessian matrix, respectively. Hence, in order to understand when a DB may be present between two atoms that share an interatomic surface, the component of the slope of the ED along the principle

axis λ_2 in the interatomic region should be investigated. Note that the position of the MDP and a (3,-1) CP, if present, does not always coincide, leading to bent DBs, but the deviation between MDP and (3,-1) CP always occurs on the direction of the 2nd eigenvector of the Hessian matrix, as measured at the MDP. The example showed in Figure 1(a) displays a (3,-1) CP quite far removed from the MDP between H-nuclei, but Figure 1(d) clearly illustrates a local maximum in the ED at the (3,-1) CP and vanishing directional derivative along the direction of the 2nd eigenvector of the Hessian matrix.

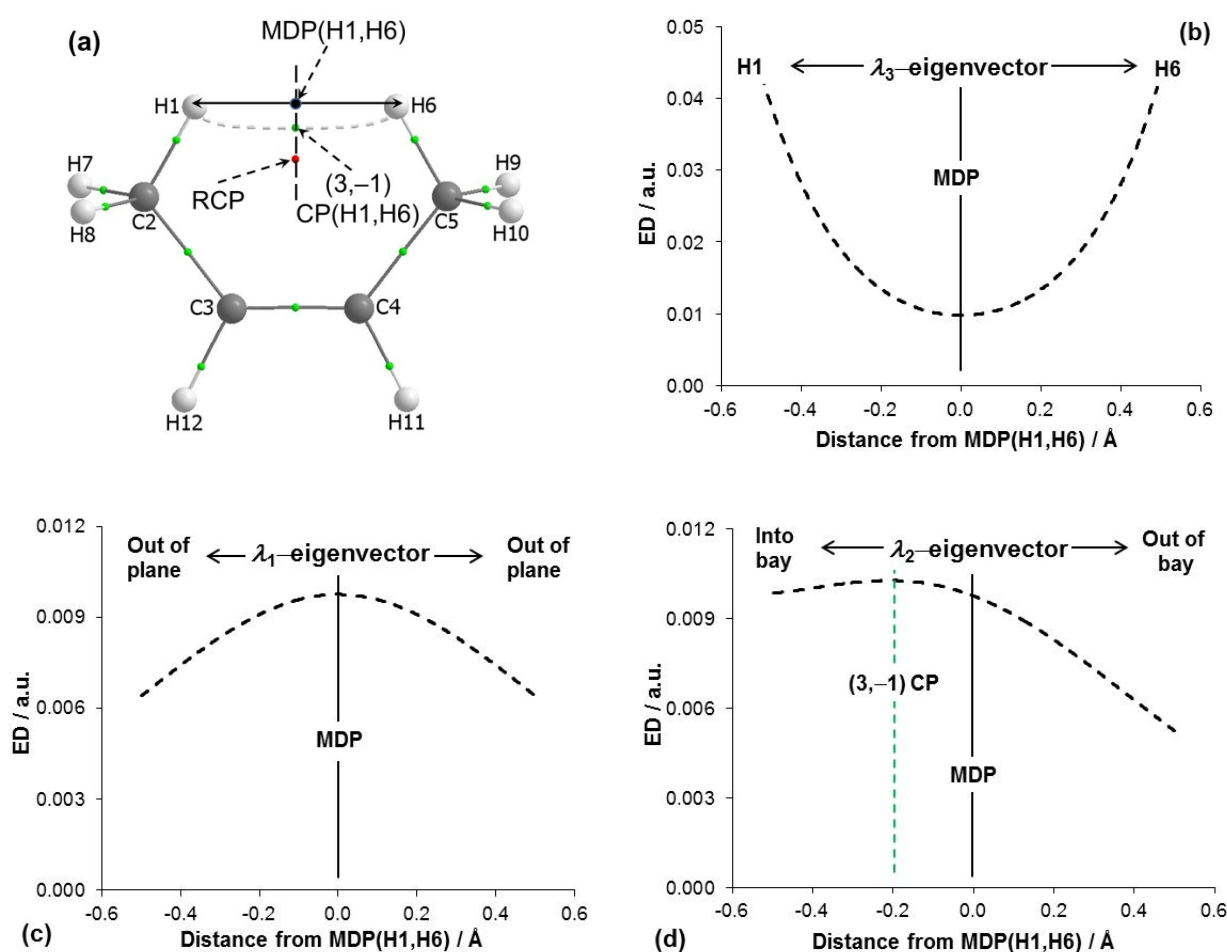


Figure 1. Part (a) - a molecular graph of energy optimised *cis*-2-butene showing a (3,-1) CP as a small green sphere on a density bridge between H1 and H6 atoms, RCP = (3,+1) CP as a small red sphere, and a minimum density point (MDP) on line geometrically linking 3D-coordinates of H1 and H6 nuclei. Part (b) - the total ED computed along the line geometrically linking 3D-coordinates of H1 and H6 nuclei with the MDP located at the minimum. Part (c) - variation in the total ED along the λ_1 -eigenvector. Part (d) - change in the total ED along the λ_2 -eigenvector also showing locations of the (3,-1) CP (at the maximum of ED) and MDP.

In a diatomic molecule, the slope of the ED along the eigenvector associated with λ_2 (henceforth referred to as the λ_2 -eigenvector) will always vanish at some \mathbf{r} on the

internuclear vector, hence a DB and (3,-1) CP will always be present. However, in the presence of other (3,-1) CPs (in any polyatomic molecule), the slope of the ED along the λ_2 -eigenvector is not guaranteed to vanish, and thus a (3,-1) CP will not be present between every nuclear pair. The presence of such CPs in polyatomic molecules depends on the environment. Typically, a strong interaction (such as a covalent bond) contains highly concentrated ED perpendicular to the internuclear vector, and a (3,-1) CP exists despite the presence of factors that hinder its presence. On the other hand, weak interactions (such as an intramolecular H-bond) have significantly less concentrated ED perpendicular to the internuclear vector, and a (3,-1) CP will only appear if the environment is favorable (*i.e.* in the absence of dominating factors which topologically hinder the presence of a (3,-1) CP). Regrettably, the precise chemical conditions required to foretell the presence of a (3,-1) CP (particularly for weak interactions) are not yet known exactly, despite previous attempts,^{27,28} and therefore the chemical significance of a DB is difficult to determine.

The slope of the ED along the λ_2 -eigenvector is an exact predictor for the existence of a (3,-1) CP and is easy to measure in most systems. In order to determine when a (3,-1) CP may form from a chemical point of view, however, one must understand first the physical factors which lead to a given ED distribution. To achieve that, the ED must be decomposed along the λ_2 -eigenvector into chemically and physically meaningful components in order to understand the ED distribution on a fundamental level. Specifically, provided that the contribution made to the total ED (*tot-ED*) by a primary interaction as well as by all other ones can be quantified, then it should be possible to determine whether a (3,-1) CP will exist in a given environment based on criteria other than the topology of the *tot-ED*. Subsequently, the components giving rise to a (3,-1) CP could then be scrutinized analytically in order to understand why the CP exists. Finally, if and only when the components themselves carry chemical significance, such information could be useful in determining the chemical conditions necessary for the existence of a (3,-1) CP and, therefore, a presence of a DB could be meaningfully interpreted in terms of chemical bonding.

We present in this work a scheme that determines components of the molecular system *tot-ED* that either facilitate or hinder the presence of a (3,-1) CP in the interatomic region of an interaction of interest. We also measure the exact contribution made by each component to arrive at a criterion which explains the presence or absence of a (3,-1) CP. We first describe a suitable *tot-ED* decomposition technique, followed by a classification scheme which

determines whether a decomposition component facilitates or hinders the presence of a DB, and finally we introduce an index to condense the information.

The FALDI density decomposition scheme

We recently introduced the Fragment, Atomic, Localized, Delocalized and Interatomic (FALDI) ED decomposition scheme.^{30,32,34} FALDI uses concepts from the Domain Averaged Fermi Hole (DAFH)^{35,36} approach in order to calculate pseudo-2nd order contributions arising from electrons within QTAIM-defined atomic basins. FALDI decomposes the *tot*-ED at any coordinate \mathbf{r} into 1- and 2-centre contributions:

$$\rho(\mathbf{r}) = \sum_A^M \mathcal{L}_A(\mathbf{r}) + \sum_A^{M-1} \sum_{B=A+1}^M \mathcal{D}_{A,B}(\mathbf{r}) \quad (2)$$

where M is the number of QTAIM-defined atomic basins. $\mathcal{L}_A(\mathbf{r})$ is known as a 1-centre localized ED (*loc*-ED) distribution, and describes the ED that is localized *exclusively* within an atomic basin Ω_A , as shown in Eq. 3,

$$\mathcal{L}_A(\mathbf{r}) = \sum_i^N n_i^{\prime\prime AA} [\phi_i^{AA}(\mathbf{r})]^2 \quad (3)$$

where N is the number of MOs, $\phi_i^{AA}(\mathbf{r})$ is a natural density function (NDF) obtained by diagonalizing the product of the atomic overlap matrices, $\mathbf{S}^A \mathbf{S}^A$. $n_i^{\prime\prime AA}$ is the occupation of the associated NDF that is double-primed to indicate that it is free of any localized-delocalized overlap, as previously described.³⁴ $\mathcal{D}_{A,B}(\mathbf{r})$ is known as a 2-centre delocalized ED (*deloc*-ED) distribution, and describes the ED that is delocalized between the atomic basins Ω_A and Ω_B :

$$\mathcal{D}_{A,B}(\mathbf{r}) = \sum_j^N n_j^{\prime\prime AB} [\phi_j^{AB}(\mathbf{r})]^2 + \sum_j^N \sum_i^N \left\{ n^{\prime\prime}(\mathcal{L}_A^i \rightarrow \mathcal{D}_{A,B}^j) [\phi_i^{AA}(\mathbf{r})]^2 + n^{\prime\prime}(\mathcal{L}_B^i \rightarrow \mathcal{D}_{A,B}^j) [\phi_i^{BB}(\mathbf{r})]^2 \right\} \quad (4)$$

where $\phi_j^{AB}(\mathbf{r})$ is an NDF obtained by diagonalizing the product of atomic overlap matrices, $\mathbf{S}^A \mathbf{S}^B$, and $\mathcal{D}_{A,B}(\mathbf{r})$ is corrected in the second term of Eq. 4 by any overlap that it has with NDFs of associated *loc*-ED (Eq. 3). Specifically, the degree of overlap which the i th NDF of a *loc*-ED distribution (\mathcal{L}_A^i) has with the j th NDF of a *deloc*-ED distribution ($\mathcal{D}_{A,B}^j$) is calculated by the function $n^{\prime\prime}(\mathcal{L}_A^i \rightarrow \mathcal{D}_{A,B}^j)$, which relates the relative overlap between \mathcal{L}_A^i

and $\mathcal{D}_{A,B}^j$ to the total overlap of \mathcal{L}_A^i with the remainder of the molecule's NDFs, as detailed in our previous work.³⁴

From the particular ED decomposition expressed by Eq. 2 it follows that the *loc*-ED distributions describe the core (not shared) electrons of each atomic basin while the *deloc*-ED distributions then describe the electrons shared between two atoms (corresponding to valence electrons of the two atomic basins). Integrating *loc*-ED and *deloc*-ED distributions over all molecular space yields the associated exclusive localization and delocalization indices (LI_{excl} and DI_{excl}); these distributions are similar to orthodox QTAIM (de)localization indices but intentionally designed to be free of any mutual overlap between *loc*-ED and *deloc*-ED distributions. To this effect, *e.g.*, in ethane (i) the *loc*-ED for each carbon atom describes the core 1s ED; it yields exactly 2 electrons when integrated over entire molecular space, and (2) the *deloc*-ED for the two carbon atoms describes the σ -bond ED shared between them (yielding exactly 2 electrons when integrated over molecular space).

We have previously used FALDI *loc*-ED and *deloc*-ED distributions for calculating deformation densities,^{32,33} multicenter interactions³⁰ as well as re-evaluating QTAIM-based localization and delocalization indices.³⁴ Eq. 2 therefore provides a complete decomposition, at any coordinate, of the 1-centre contributions from each atom as well as the 2-centre contributions from each atom-pair.

Classification scheme for ED components

We previously described a classification scheme for each *deloc*-ED contribution relative to \mathbf{r} .³⁰ We have expanded the scheme for the purposes of this study as it was necessary to also account for *loc*-ED contributions.

Firstly, let us define a specific coordinate of interest, \mathbf{r}^* : (i) if a (3,-1) CP is present with associated a DB linking the nuclei of the interaction under investigation, then $\mathbf{r}^* = \mathbf{r}_c$, and (ii) when a (3,-1) CP, hence also a DB, are absent, then we set \mathbf{r}^* to be the position of the MDP. The MDP is used as it is at specific coordinates that are well-defined for any atom-pair sharing an interatomic surface, regardless of the presence or absence of a (3,-1) CP. We would also like to make it clear and stress that these two points, MDP and (3,-1) CP, belong to distinctively different paths: (i) MDP is located at a density minimum along a geometric straight (hence shortest) line linking two nuclei and (ii) (3,-1) CP is located on a real and physical DB (experimental observable) that links two nuclei. It is for this reason why we also would rather not use the term 'line critical point' to describe (3,-1) CPs, as it intuitively

indicates the MDP rather than the CP. We also recommend to exclusively use the MDP at \mathbf{r}^* in experiments where the geometry is continuously perturbed in order to avoid discontinuities when a (3,-1) CP (dis)appears.

Each FALDI component (any particular *loc*-ED or *deloc*-ED distribution) can then be classified at \mathbf{r}^* according to its sign as well as the sign of its partial second derivative along the λ_2 -eigenvector. Specifically, if a FALDI component concentrates ED along the λ_2 -eigenvector in the vicinity of \mathbf{r}^* (implying negative partial second derivative), it facilitates the presence of a (3,-1) CP and can be said to be of a *bonding nature* (*bonding*-ED). On the other hand, if a FALDI component depletes ED along the λ_2 -eigenvector in the vicinity of \mathbf{r}^* (positive partial second derivative applies), it hinders the presence of a (3,-1) CP and can be said to be of a *nonbonding nature* (*nonbonding*-ED). Note that the sign of the component itself is positive, regardless of a bonding or nonbonding nature. It is important to note, however, that FALDI components can also be negative due to deconstructive interference of molecular orbitals. Accordingly, these components are labeled as *antibonding* regardless of the sign of the partial second derivative (*antibonding*-ED). Antibonding components can either facilitate or hinder the presence of a (3,-1) CP (in terms of topology), but regardless, these distributions decrease the amount of ED in the region of interest.

From the above it follows that each FALDI component can be classified as bonding, nonbonding or antibonding at any coordinate \mathbf{r} . Therefore, a FALDI component can be bonding in one region (such as the *deloc*-ED of two covalently bonded carbon atoms within their internuclear space) but nonbonding in another (such as in the internuclear space of a different nearby interaction, or a pair of atoms). For the purpose of the present work, we classify each FALDI component in terms of their topologies relative to \mathbf{r}^* , *i.e.*, at the (3,-1) CP or MDP of interest. Hence, the decomposition of the *tot*-ED (Eq. 2) at a (3,-1) CP or MDP can therefore be rewritten as:

$$\rho(\mathbf{r}^*) = \rho_{\text{bonding}}(\mathbf{r}^*) + \rho_{\text{nonbonding}}(\mathbf{r}^*) + \rho_{\text{antibonding}}(\mathbf{r}^*) \quad (5)$$

The decomposition of the gradient in bonding, nonbonding and antibonding terms

While the above classification pertains to the sign of the second derivative of a FALDI component at \mathbf{r}^* , it is obvious that the presence or absence of a (3,-1) CP is solely related to the gradient of the *tot*-ED at the vicinity of \mathbf{r}^* . As mentioned above, the gradient of the *tot*-ED along the λ_2 -eigenvector vanishes at \mathbf{r}^* when a (3,-1) CP is present. To achieve our goal

and understand the chemical (physical) conditions necessary for the existence of a (3,-1) CP, one must re-write the gradient (Eq. 1) in terms of the bonding, nonbonding and antibonding classification discussed in details above (Eq. 5):

$$\partial\rho(\mathbf{r}^*) = \partial\rho_{\text{bonding}}(\mathbf{r}^*) + \partial\rho_{\text{nonbonding}}(\mathbf{r}^*) + \partial\rho_{\text{antibonding}}(\mathbf{r}^*) \quad (6)$$

Although it is obvious, we want to make it absolutely clear that for a (3,-1) CP to be present, the sum of the terms in Eq. 6 must be zero.

From our experience it follows that antibonding distributions and their slopes at a MDP or (3,-1) CP are generally very small; hence, we will ignore the effects of their contributions for the moment. Eq. 4 then reduces to the sum of the rates of changes in just the *bonding*- and *nonbonding*-EDs along the λ_2 -eigenvector. In such a case, for a (3,-1) CP to be present, these two terms must be equal but have opposite sign at \mathbf{r}^* to meet the $\partial\rho(\mathbf{r}^*) = 0$ requirement. However, the partial second derivatives of the *bonding*- and *nonbonding*-EDs are always negative and positive, respectively. Therefore, due to the partial second derivative of the *tot*-ED being negative ($\lambda_2 < 0$) the following must hold: (i), the absolute slope of the sum (total) of all *bonding*-ED contributions must be greater than the absolute slope of the sum (total) of *nonbonding*-ED contributions in the vicinity of a (3,-1) CP ($|\partial\rho_{\text{bonding}}| > |\partial\rho_{\text{nonbonding}}|$) and (ii) exactly at the (3,-1) CP, $|\partial\rho_{\text{bonding}}| - |\partial\rho_{\text{nonbonding}}| = 0$. As such, a complex interplay takes place between the two components in the inward and outward directions making an interpretation a bit awkward. To ease and aid the interpretation of *bonding*-ED and *nonbonding*-ED we propose the following $CP(\mathbf{r})$ function for detecting DBs when measured along the λ_2 -eigenvector:

$$CP(\mathbf{r}) = -\text{sign}(\partial\rho_{\text{nonbonding}}(\mathbf{r})) \left[\partial\rho_{\text{bonding}}(\mathbf{r}) + \partial\rho_{\text{nonbonding}}(\mathbf{r}) + \partial\rho_{\text{antibonding}}(\mathbf{r}) \right] \quad (7)$$

The $CP(\mathbf{r})$ function returns the slope of the *tot*-ED, but with an adjusted sign depending on the sign of the slope of the *nonbonding*-ED contribution. Since the sign of the directional derivative in one dimension depends on the direction in which it is measured, the $-\text{sign}(\partial\rho_{\text{nonbonding}}(\mathbf{r}))$ factor is used in order to enforce the $CP(\mathbf{r})$ function to be negative throughout *except* for regions where the sum of the gradients $\partial\rho_{\text{bonding}}(\mathbf{r})$ and $\partial\rho_{\text{antibonding}}(\mathbf{r})$ is (i) greater, in absolute value, than $\partial\rho_{\text{nonbonding}}(\mathbf{r})$ and (ii) has an opposite sign than $\partial\rho_{\text{nonbonding}}(\mathbf{r})$. Furthermore, like the slope of the *tot*-ED, the $CP(\mathbf{r}^*)$ function is equal to zero at a (3,-1) CP. However, there will always be a region along the λ_2 -eigenvector close to a

(3,-1) CP where $CP(\mathbf{r})$ is positive, in one or both directions. By contrast, in the absence of a (3,-1) CP, $CP(\mathbf{r})$ will be negative throughout.

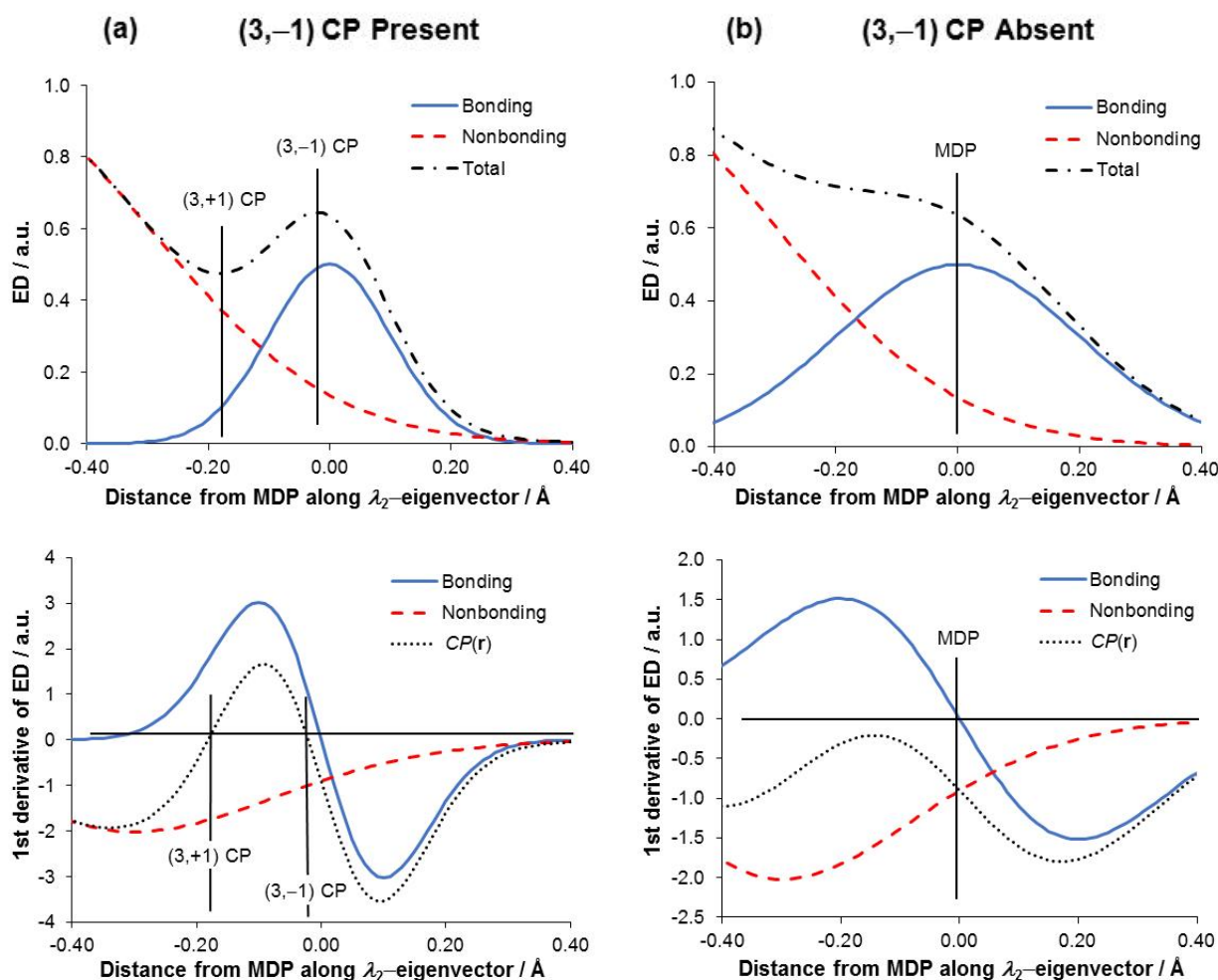


Figure 2. Hypothetical ED distributions showing *bonding*- and *nonbonding*-ED distributions as well as their gradients resulting in the presence (part a) or absence (part b) of the (3,-1) CP.

As an example, consider two hypothetical distributions in Figure 2, displaying *bonding*- and *nonbonding*-ED distributions in a system with a (3,-1) CP either present (part a) or absent (part b). In both Figures 2(a) and 2(b) a region exists where the gradient of *bonding*-ED is opposite in sign than the gradient of *nonbonding*-ED. Figure 1(a) illustrates a region where the $CP(\mathbf{r})$ function is positive, however, due to a larger magnitude of *bonding*-ED than *nonbonding*-ED gradient. When a (3,-1) CP is absent (Figure 2(b)), the $CP(\mathbf{r})$ function is negative throughout because the *bonding*-ED gradient is smaller in magnitude than the *nonbonding*-ED gradient.

Note that in this hypothetical example, the total gradient (not shown in Fig.1) and the $CP(\mathbf{r})$ function (dotted line in Figure 1) are identical; however, more complex systems can be

found where this is not the case. In addition, the $CP(\mathbf{r})$ function remains the same regardless of the direction in which the gradient is measured. The $CP(\mathbf{r})$ function therefore provides an additional criterion for the existence of a DB: if $CP(\mathbf{r})$ is positive anywhere on the λ_2 -eigenvector for a given internuclear region, then a (3,-1) CP as well as a DB will be present. Note that in the case of an intramolecular interaction, the presence of (3,-1) CP must be accompanied by a (3,+1) CP (commonly called a ring CP) and this is shown in Figure 1(a). Furthermore, the $CP(\mathbf{r})$ function is only well-defined in a region along the λ_2 -eigenvector where the directional first derivative of the total *nonbonding*-ED does not change sign, which would indicate a different nature of some of the components of the *nonbonding*-ED distribution relative to an internuclear region other than the region of interest.

Clearly, the presence of a DB, and the associated (3,-1) CP, is an interplay between facilitating and hindering factors; to gain an insight on the origin of these factors, each term in Eq. 7 can be decomposed into individual FALDI components, such as the valence ED delocalized across two atomic basins or the core ED localized to a particular atomic basin. Doing so reveals exactly which atoms or atom-pair interactions are important towards the presence of a DB, or which atoms and interactions hinder the presence of a DB. To this end the often-times strange presence of a DB can be investigated at a fundamental level, and the physical and chemical significance of a DB can be studied much more efficiently than in the past.

Physical and chemical interpretations of FALDI components

While the $CP(\mathbf{r})$ function (as well as further decomposition) can be used to understand the interplay of various 1- and 2-centre contributions towards the presence of a DB, it gains significantly more value if the various decomposition terms can be interpreted in a meaningful manner. The decomposition of ED at any coordinate \mathbf{r} into *bonding*-, *nonbonding*- and *antibonding*-ED contributions (Eq. 5) can be interpreted from both physical and chemical points of view. Below, we present interpretations that can be inferred from the mathematical derivation of FALDI; however, like all interpretations of mathematical formulae, these can (and should be) thoroughly tested, refined and generalized before they can be accepted as universal interpretations of FALDI fields. We nevertheless present these interpretations as suggestions towards a better understanding of ED distributions pertaining to chemical interactions.

Physically, each term of Eq. 5 represents a measure of the absolute concentration, depletion or reduction of various FALDI components (1- and 2-centre) along the λ_2 -eigenvector. *Bonding*-ED distributions contain all the FALDI components that (i) increase the *tot*-ED and (ii) *concentrate* the *tot*-ED at \mathbf{r} . Concentration of ED can be viewed in terms of Feynman's theorem,³¹ as explored by Bader:^{15,16} a concentration of ED can maximize the attractive forces acting on a nuclei, thereby facilitating a "bonding interaction". The use of the FALDI decomposition removes the dependency of the second partial derivative of the Hessian matrix on its local environment – each FALDI component is measured absolutely relative only to itself. In contrast, *nonbonding*-ED distributions contain all the FALDI components that (i) increase the *tot*-ED, but (ii) *deplete* the *tot*-ED at \mathbf{r} , thereby hindering the attractive forces acting on nuclei. Finally, *antibonding*-ED distributions always reduce the *tot*-ED at \mathbf{r} .

Chemically, each term of Eq. 5 can be interpreted in terms of MO overlap. The FALDI components are derived from the overlap of all MOs and MO pairs simultaneously across atomic basins and at any coordinate \mathbf{r} . *Bonding*-ED distributions arise from MOs or MO pairs overlapping a single basin (in the case of *loc*-ED distributions) or simultaneously overlapping two basins (in the case of *deloc*-ED distributions) in a constructive fashion, thereby increasing and concentrating ED at \mathbf{r} . In orthodox MO bond theory, such phenomena can be linked with chemical bonding in model systems. *Nonbonding*-ED distributions, on the other hand, describe MOs or MO-pairs overlapping in a non-constructive fashion, thereby reducing the concentration of ED at \mathbf{r} . Finally, *antibonding*-ED distributions describe MOs or MO-pairs that interfere destructively at \mathbf{r} , thereby reducing the *tot*-ED.

Clearly, each FALDI component can therefore be interpreted from both physical and chemical points of view. From a physical point of view, a DB can be linked to a larger rate of change of 1- and 2-centre components that concentrate ED (and therefore maximize the forces acting on nuclei) in the internuclear region. From a chemical point of view, a DB can be linked to a larger rate of change of MOs that simultaneously overlap one and two atomic basins in a constructive fashion. While these interpretations are only aspects of chemical bonding, they can be used to investigate the properties of ED distributions in multicenter chemical interactions in a descriptive manner. We will explore the utility of these interpretations for the four case studies throughout the results section.

Computational Details

All structures were optimized in Gaussian 09, Rev. D.,³⁷ using B3LYP with Grimme's D3 empirical dispersion³⁸ with 6-311++G(d,p) in the gas phase. QTAIM molecular graphs, as well as atomic overlap matrices, were calculated using AIMAll v. 16.10.31.³⁹ FALDI data was calculated using in-house software, and FALDI isosurfaces were visualized using VMD.⁴⁰ Tables of cartesian coordinates for all optimized structures are given in Section 1 of the supplementary information (SI).

Results and discussion

To link our study with work by TJ,^{27,28} we will use their term of '*primary interaction*' that refers to an interaction of an atom-pair of interest. TJ defines a '*secondary interaction*' as a neighbouring interaction between one of the atoms involved in the primary interaction and an atom that is linked by a DB to the second atom involved in the primary interaction. Secondary interactions in TJ's approach are seen as '*competing*' against the presence of a DB between the nuclei of the primary interaction. The secondary interaction with the largest absolute interatomic XC energy is then used for calculating TJ's β -ratio. Due to the holistic nature of our approach, we consider *all* interactions in our analysis, including the primary, secondary and all other atom-pairs. In addition, unlike TJ, we consider the possibility that any of the primary, secondary and other interactions can facilitate or hinder the presence of a DB. Furthermore, all molecular structures are presented as molecular graphs to illustrate the presence or absence of a DB between atoms of the primary interaction.

H-bonding interaction in neutral and protonated ethylenediamine

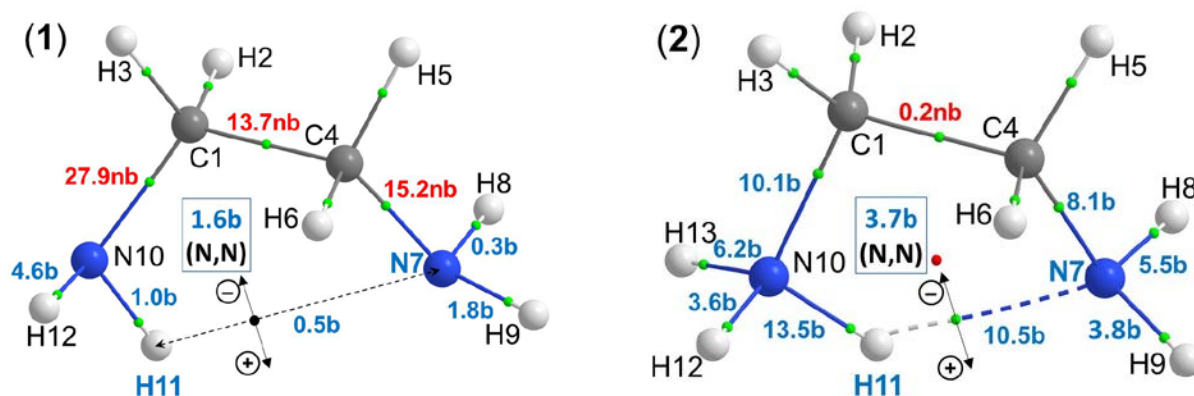


Figure 2. Molecular graphs of equilibrium structures of a neutral (1) and a protonated (2) ethylenediamine also showing the directions of λ_2 -eigenvectors crossing either the minimum density point (black small sphere in (1)) or (3,-1) CP on density bridge (green small sphere in (2)). Percentage-slope contributions made by atom-pairs that facilitate and hinder the presence of a DB(N7,H11) are shown as of bonding (b) and non-bonding (nb) nature, respectively.

Figure 3 shows that a DB between atoms N7 and H11 (primary interaction investigated) is present only in the protonated ethylenediamine (**2**) even though $d(\text{N7,H11}) < \{\text{sum of van der Waals (vdW) radii, N} = 1.55 \text{ \AA}, \text{H} = 1.20 \text{ \AA}\}^{41}$ in both equilibrium structures with $d(\text{N7,H11}) = 2.5893$ and 1.9912 \AA in structure (**1**) and (**2**), respectively.

From the IQA perspective, there is no qualitative difference in the nature of the primary interaction in both structures; atoms H11 and N7 are involved in highly attractive interactions ($E_{\text{int}}^{\text{N7,H11}} = -46.6$ and -104.3 kcal/mol in (**1**) and (**2**), respectively) that are predominantly of an ionic nature.

The computed TJ's β -ratios,^{27,28} $V_{\text{XC}}^{\text{N7,H11}}/V_{\text{XC}}^{\text{N7,N10}}$ of $(-3.16)/(-3.62) = 0.87$ for (**1**) and $(-16.7)/(-9.1) = 1.84$ for (**2**), not only predict the absence of a DB in (**1**) correctly, but also are within the respective ranges, namely: no DB for $\beta < 1.35$ and DB present for $\beta > 1.59$. The FALDI-based decomposition of the *tot*-ED along the λ_2 -eigenvectors passing through the MDP(N7,H11) in (**1**) and (3,-1) CP(N7,H11) in (**2**) (Figure 2) yields the distributions of total *bonding*- and *nonbonding*-EDs shown in Figure 3. We note that (i) qualitatively trends are similar in both structures and, focusing on values at MDP(N7,H11) in (**1**) and (3,-1) CP(N7,H11) in (**2**), (ii) the amount of *tot*-ED, *bonding*-ED as well as the ratio of *bonding*-ED/*nonbonding*-ED are always larger in (**2**) where a DB(N7,H11) is observed.

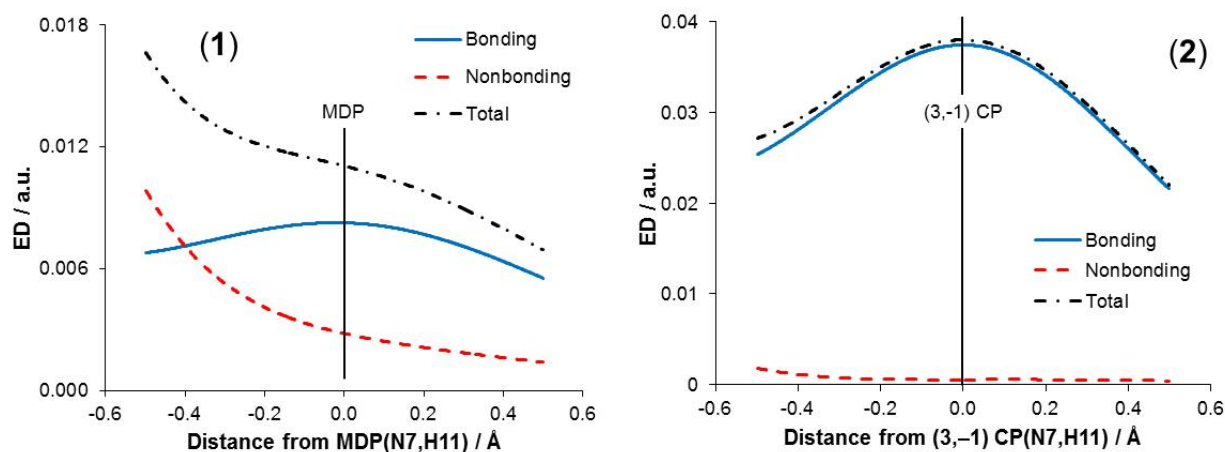


Figure 4. Comparison of the total *bonding*- and total *nonbonding*-ED along the λ_2 -eigenvector passing through the MDP(N7,H11) of neutral ethylenediamine (**1**) and the (3,-1) CP(N7,H11) of protonated ethylenediamine (**2**).

It is quite clear from the shapes of the *tot*-ED distributions in Figure 4 that a (3,-1) CP (and therefore a DB) is present in (**2**) but absent in (**1**), providing a good opportunity to explore the use of our $CP(\mathbf{r})$ function. We note again that there are no *antibonding*-ED

contributions present anywhere on the λ_2 -eigenvectors of **(1)** and **(2)**, as for all structures studied in this work.

It is immediately seen in Figure 5 that the $CP(\mathbf{r})$ function (dotted line) is negative in the entire region in **(1)** whereas it is positive in the inward region and zero at \mathbf{r}^* – the position of the (3,-1) CP(N7,H11) where the change in *bonding*- and *nonbonding*-ED is opposite but equal in value. As a matter of fact, the curves in Figure 5 serve as a nice and convenient pictorial representation of our $CP(\mathbf{r})$ function computed along relevant λ_2 -eigenvectors. Just as an example, see how slope of *bonding*-ED dominates that of *nonbonding*-ED in **(2)**, thereby meeting the criteria for the (3,-1) CP(N7,H11) and explaining the presence of the DB(N7,H11) in the protonated form of ethylenediamine. The trend observed in **(1)** are exactly opposite, hence no DB is present.

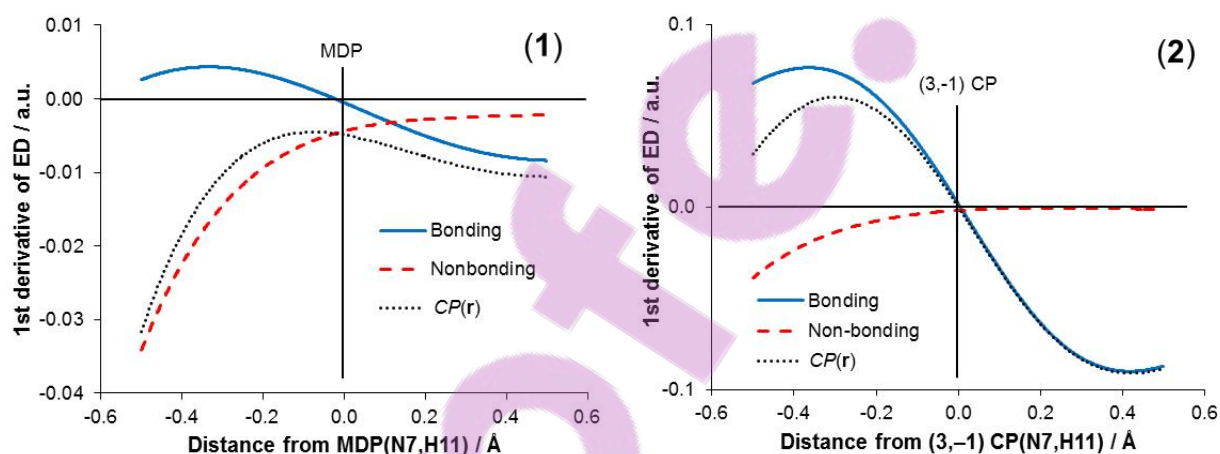


Figure 5. Comparison of the 1st derivative curves of the total *bonding*- and total *nonbonding*-ED, as well as the $CP(\mathbf{r})$ function, along the λ_2 -eigenvector passing through the MDP(N7,H11) in **(1)** and the (3,-1) CP(N7,H11) in **(2)**.

Atom-pairs that made most significant contributions towards *tot*-ED at \mathbf{r}^* are included in Tables 1 and 2; a full set of data is included in Tables S7 and S8 in the SI. There are several important observations we would like to make:

(1) The atom-pair N7,H11 (H-bond acceptor and H-atom) involved in the primary interaction has not made the largest contribution to the ED at \mathbf{r}^* in both structures, **(1)** and **(2)**, just 4.8 and 14.1% of the *tot*-ED, respectively. This is not entirely surprising, as we have noted similar observation in another case of a classical intramolecular H-bond.²⁷

(2) The N10,H11 (H-bond donor and H-atom) atom-pair is the largest contributor to the *tot*-ED at \mathbf{r}^* in both structures, namely 20.7% and 16.5% in **(1)** and **(2)**, respectively.

Table 1. Selected contributions made to MDP(N7,H11) in ethylenediamine. Percentages refer to contributions towards the *tot*-ED and its slope.

Component	$\rho_{\text{bonding}}(\mathbf{r}^*)$	$\partial\rho_{\text{bonding}}(\mathbf{r}^*)$	$\rho_{\text{nonbonding}}(\mathbf{r}^*)$	$\partial\rho_{\text{nonbonding}}(\mathbf{r}^*)$
N10,H11	0.00229 (20.7%)	0.00006 (1.0%)	-	-
N7,H9	0.00081 (7.3%)	0.00011 (1.8%)	-	-
N7,H8	0.00060 (5.5%)	0.00002 (0.3%)	-	-
N10,H12	0.00054 (4.9%)	-0.00027 (4.6%)	-	-
N7,H11	0.00053 (4.8%)	0.00003 (0.5%)	-	-
N7,N10	0.00030 (2.7%)	-0.00010 (1.6%)	-	-
C4,N7	-	-	0.00097 (8.8%)	-0.00090 (15.2%)
C1,N10	-	-	0.00079 (7.1%)	-0.00165 (27.9%)
C1,C4	-	-	0.00021 (1.9%)	-0.00081 (13.7%)
Total	0.00826	-0.00042	0.00278	-0.00444

Table 2. Selected contributions made to (3,-1) CP(N7,H11) in protonated ethylenediamine. Percentages refer to contributions towards the *tot*-ED and its slope.

Component	$\rho_{\text{bonding}}(\mathbf{r}^*)$	$\partial\rho_{\text{bonding}}(\mathbf{r}^*)$	$\rho_{\text{nonbonding}}(\mathbf{r}^*)$	$\partial\rho_{\text{nonbonding}}(\mathbf{r}^*)$
N10,H11	0.00628 (16.5%)	-0.00156 (13.5%)	-	-
N7,H11	0.00537 (14.1%)	0.00122 (10.5%)	-	-
N7,N10	0.00135 (3.6%)	0.00043 (3.7%)	-	-
N10,H13	0.00096 (2.5%)	-0.00072 (6.2%)	-	-
N10,H12	0.00085 (2.2%)	-0.00042 (3.6%)	-	-
N7,H9	0.00257 (6.8%)	0.00044 (3.8%)	-	-
N7,H8	0.00243 (6.4%)	0.00064 (5.5%)	-	-
C4,N7	0.00316 (8.3%)	-0.00093 (8.1%)	-	-
C1,N10	0.00115 (3.0%)	-0.00117 (10.1%)	-	-
C1,C4	-	-	0.00041 (1.1%)	-0.00003 (0.2%)
Total	0.03743	0.00063	0.00056	0.00006

(3) The functional groups that essentially serve as a proton donor, N10H₂ in **(1)** and N10H₃⁺ in **(2)**, contributed most to the *tot*-ED in a bonding fashion, 25.6 and 21.2%, respectively.

(4) The N7H₂ functional groups that essentially serve as a proton acceptor in **(1)** and **(2)**, made second largest *bonding*-ED contributions to the *tot*-ED, 12.8 and 9.4%, respectively.

(5) The nature of the contribution made by atom-pairs C1,N10 and C4,N7 changed from the largest *nonbonding*-ED component in **(1)** to a *bonding*-ED component in **(2)**.

(6) In both structures, the strongest ‘*competing*’ secondary interaction involving N7,N10 atom-pair has made constructive, hence a *bonding*-ED contribution of 2.7 and 3.6% in **(1)** and **(2)**, respectively, to the *tot*-ED.

(7) There are numerous secondary interactions that contributed in a constructive manner to the *tot*-ED at r^* , *i.e.*, MDP(N7,H11) in (1) and (3,-1) CP(N7,H11) in (2); hence, they must not be seen as competing interactions.

The FALDI-based investigation reveals that a DB is a holistic, multicenter phenomenon³⁰ that, in the case of structures (1) and (2), involves the entire skeleton and both terminal functional groups (nearly entire molecules) in contributing to the ED in the internuclear region of the primary interaction. Furthermore, upon protonating (1), multiple atom-pairs either concentrated ED in a much stronger fashion, or concentrated ED in (2) even though they were depleting ED in the neutral structure. In this regard, the intramolecular interactions in (1) and (2) differ qualitatively: (i) physically, in that we expect stronger attractive forces to act on the N7, N10 and H11 nuclei due to increased ED concentration from multiple sources, and (ii) chemically, in that we expect greater constructive interference in the N7, N10 and H11 internuclear regions due to simultaneous MO overlap over a number of atomic basins. The MO overlap pattern is significantly different in (1) and (2) as well.

The added advantage of FALDI is in that makes it possible to extract separate contributions to the slope of the total *bonding*- and *nonbonding*-EDs in any structure. Analysis of data in Tables 1 and 2 reveals some surprising observations:

(a) There is no direct correlation between the ED contributed by an atom-pair to the primary interaction and this contribution's slope at r^* ; this observation equally applies to *bonding*- and *nonbonding*-ED contributions. Just as an example: (i) the largest *bonding*-ED contribution in (1) was made by N10,H11 (20.7% of the *tot*-ED), but this ED did not vary significantly in the proximity of MDP resulting in just 1% of the total slope at the MDP(N7,H11); (ii) the largest *nonbonding*-ED contribution in (1) was made by C4,N7 but its slope at MDP(N7,H11) of 15.2% was largely 'outperformed' by the second largest *nonbonding*-ED contribution (C1,N10) that contributed 27.9 % to the slope of the total *nonbonding*-ED at MDP(N7,H11).

(b) The change (or slope) of *bonding*-ED contributions made by primary interactions in both structures at r^* is not the most significant in terms of their contribution to the final slopes of the *tot*-ED. Hence, the primary interactions have no control over the presence/absence of a (3,-1) CP or DB in these two molecules.

(c) Finally, we note that the most significant in value secondary interaction between N7 and N10, constructively contributed to the internuclear region of the primary interaction in

both structures, by adding ED and increasing the slope of *bonding*-ED. Clearly, this is not a competing interaction and this finding is in direct contrast to TJ's interpretation.^{27,28}

Highly repulsive oxygen-oxygen interaction in similar organic molecules

The molecular graphs of two structurally similar organic structures, (3) and (4), are shown in Figure 5. The atom neighbouring C1 is different in these two equilibrium structures: element 2 in (3) is a F-atom and in (4), a H-atom. Atoms O6 and O8 of primary interaction (vdW radius of O = 1.52 Å) are not linked with a DB in (3), ($d(\text{O6},\text{O8}) = 2.8892 \text{ \AA}$), but a DB is present in (4) ($d(\text{O6},\text{O8}) = 2.8838 \text{ \AA}$).

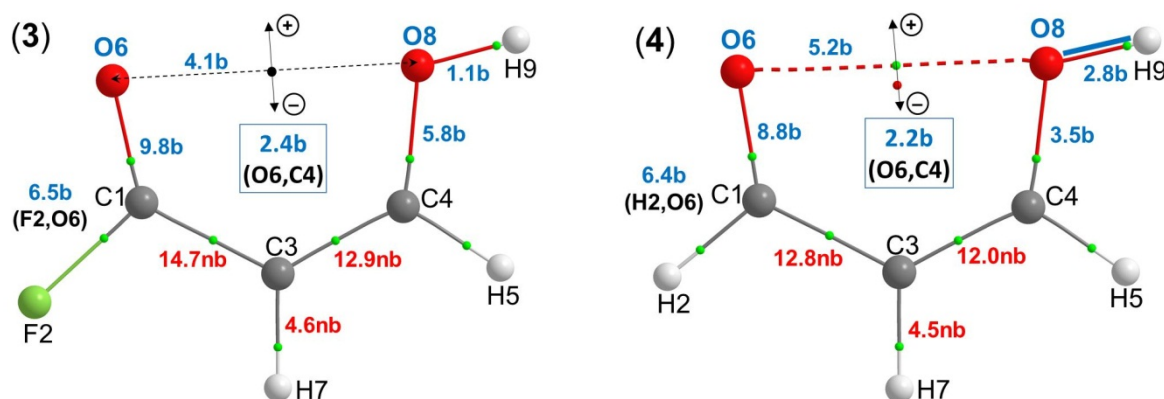


Figure 6. Molecular graphs of equilibrium structures (3) and (4) in the gas phase, including the λ_2 -eigenvectors. Blue and red colourings indicate selected individual atom-pairs that facilitate and hinder, respectively, the presence of DB(O6,O8) as well as their percentage-slope contributions.

There is no qualitative difference in the nature of the primary interaction from the IQA perspective as atoms O6 and O8 are involved in a highly repulsive and comparable in value interactions with $E_{\text{int}}^{\text{O6},\text{O8}}$ in (3) and (4) of +125.8 and +120.4 kcal mol⁻¹, respectively. The computed TJ's β -ratios,^{27,28} $V_{\text{XC}}^{\text{O6},\text{O8}}/V_{\text{XC}}^{\text{O6},\text{C4}}$ of $(-5.56)/(-3.42) = 1.63$ for (3) and $(-6.07)/(-4.29) = 1.41$ for (4), yield very inconclusive results:

(a) Structure (3) has a β -ratio in the specified range in which a *primary* (3,-1) CP is predicted to be due to $\beta > 1.59$, but no DB is present.

(b) The trend of the β -ratio criterion does not hold for these molecules as the comparatively smaller β -ratio in structure (4) does yield a DB.

This implies that either the DB(O6,O8) in (4) is of a different nature (*i.e.* not a “privileged exchange channel”) or that the β -ratio does not represent an accurate criterion for the presence of a DB.

Figures 7(a) and 7(b) show the values and trends (along the λ_2 -eigenvectors) computed for structures (3) and (4), respectively, shown in Figure 6. The respective *bonding*- and *nonbonding*-ED trends of the two structures are nearly identical, suggesting that the nature of the multicenter O6...O8 interaction in the two structures are highly comparable from an ED perspective.

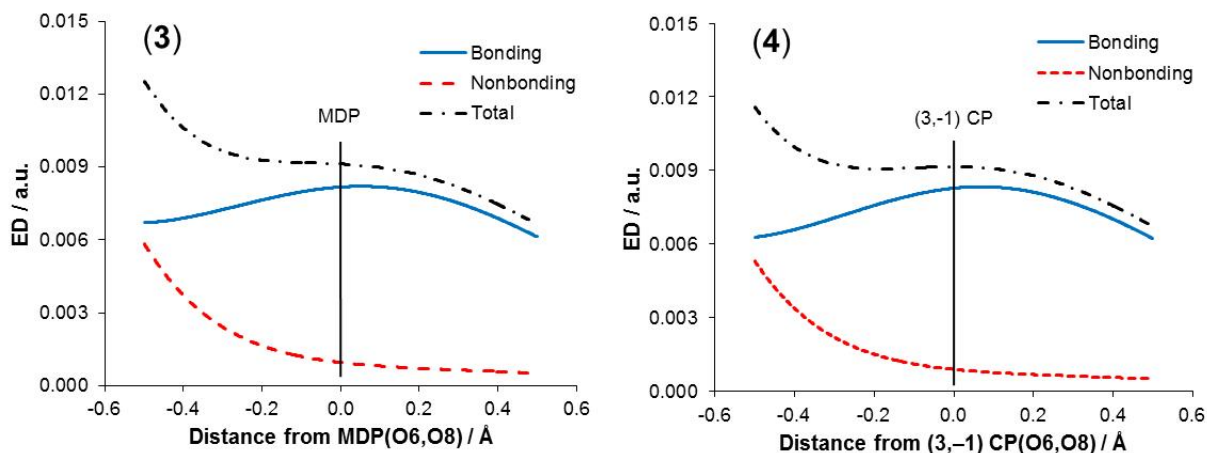


Figure 7. Comparison of the total *bonding*- and total *nonbonding*-ED along the λ_2 -eigenvector passing through the MDP(O6,O8) and (3,-1) CP(O6,O8) of the structures (3) and (4).

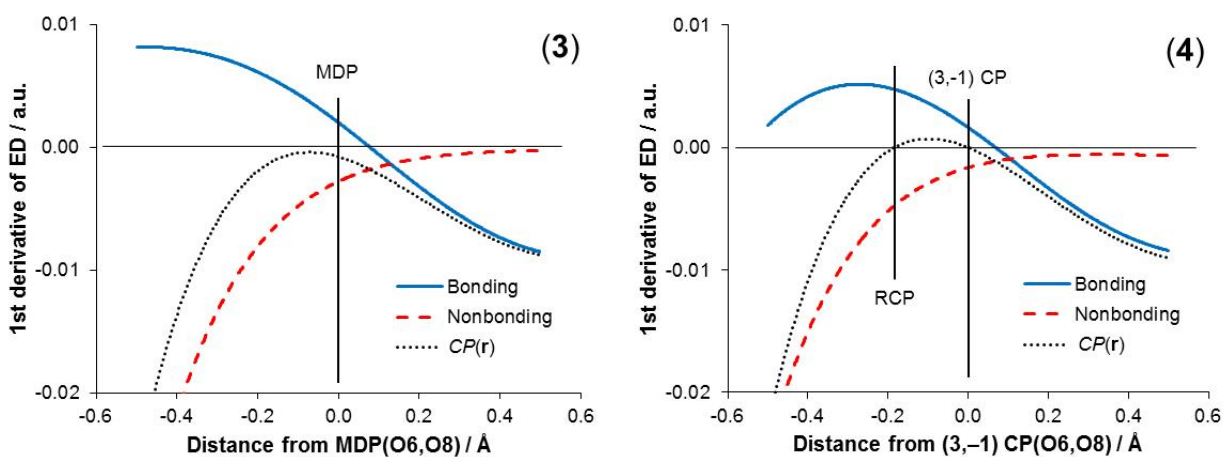


Figure 8. Comparison of the 1st derivative curves of the total *bonding*- and total *nonbonding*-ED along the λ_2 -eigenvector passing through the MDP(O6,O8) in (3) and the (3,-1) CP(O6,O8) in (4).

Figures 8(a) and 8(b) depict the gradients of the total *bonding*- and total *nonbonding*-ED values along the λ_2 -eigenvectors in (3) and (4), respectively, as well as the $CP(\mathbf{r})$ functions computed for both structures. $CP(\mathbf{r})$ exhibits an almost identical shape for both structures, but is positive in a small region only in (4), where the slope of the *bonding*-ED is greater in

magnitude than the slope of the *nonbonding*-ED. The rate of change of the *nonbonding*-ED is slightly smaller in magnitude in (4) than in (3), whereas the rate of change of *bonding*-ED is almost identical in both structures. However, this small difference results in a positive $CP(\mathbf{r})$ in (4) and, hence, the presence of a DB.

We have also tested the $CP(\mathbf{r})$ function's reliability at larger basis sets (aug-cc-pvqz), as shown in Section 3 of the SI. It is important to note that a DB between O atoms is absent in both (3) and (4) at this basis set and, correspondingly, our $CP(\mathbf{r})$ function is negative throughout in both structures. This nicely illustrates sensitivity of the $CP(\mathbf{r})$ function that was able to explain the presence/absence of a DB regardless of extremely small variations in topological differences generated by basis sets used in the calculations.

Tables 3 and 4 show selected contributions in (3) and (4), respectively, to the *tot*-ED and its gradient at the MDP(O6,O8) and (3,-1) CP(O6,O8); a full set of data is included in Tables S9 and S10 in the SI. The most pertinent results from this comparison are:

(1) The ED delocalized between the atoms of the primary interaction (O6...O8, a repulsive, closed-shell interaction) is predominantly of a bonding nature in *both* (3) and (4), regardless of the presence or absence of a DB.

(2) Interestingly, there is no specific atom or atom-pair which is decisively responsible for the presence of a DB in (4) or absence of one in (3).

(3) Components that facilitate the presence of a DB between O6 and O8 are generally from the neighbouring atoms, whereas the carbon backbone generally hinders DB presence.

(4) The atom-pair O6,O8 involved in the primary interaction has not made the largest contribution to the ED at \mathbf{r}^* in *both* (3) and (4), just 7.1 and 7.7% of the *tot*-ED, respectively.

(5) Interactions that might be interpreted as '*competing*' (such as C4...O6) in fact facilitate the presence of a DB between O6 and O8.

(6) The C1,O6 atom-pair is the largest contributor to the *tot*-ED at \mathbf{r}^* in both structures, namely 15.2 and 13.4% in (3) and (4), respectively.

(7) The factors that hinder or facilitate the presence of a DB(O6,O8) in (4) are the same as in (3).

(8) Numerous small differences in the magnitudes of the various factors' contributions are such that the slope of the *nonbonding*-ED in (3) is slightly greater than in (4), and as a result, a DB doesn't appear in (3).

Table 3. Selected contributions made to MDP(O6,O8) in (3). Percentages refer to contributions towards the *tot*-ED and its slope.

Component	$\rho_{\text{bonding}}(\mathbf{r}^*)$	$\partial\rho_{\text{bonding}}(\mathbf{r}^*)$	$\rho_{\text{nonbonding}}(\mathbf{r}^*)$	$\partial\rho_{\text{nonbonding}}(\mathbf{r}^*)$
C1,O6	0.00138 (15.2%)	-0.00048 (9.8%)	-	-
O6,O8	0.00065 (7.1%)	0.00020 (4.1%)	-	-
C4,O6	0.00024 (2.7%)	0.00012 (2.4%)	-	-
O6 loc	0.00021 (2.3%)	0.00046 (9.4%)	-	-
C1,C3	-	-	0.00023 (2.5%)	-0.00072 (14.7%)
C3,C4	-	-	0.00022 (2.4%)	-0.00064 (12.9%)
Total	0.00818	0.00114	0.00094	-0.00189

Table 4. Selected contributions made to (3,-1) CP(O6,O8) in (4). Percentages refer to contributions towards the *tot*-ED and its slope.

Component	$\rho_{\text{bonding}}(\mathbf{r}^*)$	$\partial\rho_{\text{bonding}}(\mathbf{r}^*)$	$\rho_{\text{nonbonding}}(\mathbf{r}^*)$	$\partial\rho_{\text{nonbonding}}(\mathbf{r}^*)$
C1,O6	0.00123 (13.4%)	-0.00041 (8.8%)	-	-
O6,O8	0.00071 (7.7%)	0.00024 (5.2%)	-	-
C4,O6	0.00027 (3.0%)	0.00010 (2.2%)	-	-
O6 loc	0.00021 (2.3%)	0.00039 (8.5%)	-	-
C1,C3	-	-	0.00022 (2.4%)	-0.00060 (12.8%)
C3,C4	-	-	0.00022 (2.4%)	-0.00056 (12.0%)
Total	0.00828	0.00173	0.00087	-0.00168

The above analyses of *bonding*- and *nonbonding*-ED distributions (Figure 6) and their slopes (Figure 7) as well as the IQA-defined interaction energies show that the physical nature of the two multicentre O6...O8 interactions is fundamentally the same. However, the *bonding*-ED contribution at the (3,-1) CP(O6,O8) in (4) is slightly larger than at MDP(O6,O8) in (3) (0.00071 and 0.00065 a.u., respectively) as well as its rate of change along the λ_2 -eigenvector. Therefore, we expect that the attractive forces acting on the nuclei to be greater in (4) than in (3) – a statement corroborated by a slightly less repulsive IQA interaction energy, by 5.4 kcal·mol⁻¹ in (4). From a chemical point of view, we expect increased constructive interference from MO overlap across both O6 and O8 atomic basins – again, corroborated by slightly greater $V_{\text{XC}}^{\text{O6,O8}}$ term of the interaction energy, by 0.5 kcal·mol⁻¹ in (4). Furthermore and importantly, our analysis shows that the ED in the internuclear region is of multicenter nature; hence, all contributions need to be taken into account in order to fully understand this interaction in both molecules. This is possibly why TJ’s β -ratio fails to correctly predict the DB(O6,O8) in (4).

In summary and to conclude, the total *bonding*-ED (as well as its rate of change) increases from (3) to (4), whilst the total *nonbonding*-ED (as well as its rate of change) decreases in magnitude from (3) to (4). Therefore, it seems likely that the multicenter intramolecular O6...O8 interaction is slightly less repulsive in (4) than in (3) (from both physical and

chemical points of view), due to manner in which ED is distributed. The consequence of these changes is the presence of a DB in (4). However, the changes between (3) and (4) are extremely small, and this case study clearly demonstrates that a DB can appear due to almost insignificant changes that have no bearing on the overall interpretation of an interaction on a fundamental level.

Attractive chlorine-chlorine interaction in di- and hexa-chloroethane

The third case study involves the comparison of a Cl...Cl interaction in eclipsed conformations (non-equilibrium structures) of chlorine-substituted ethane. The molecular graphs of di- and hexachloroethane ($C_2H_4Cl_2$ (5) and C_2Cl_6 (6)) in Figure 8 show that a DB is present between each pair of eclipsed chlorine atoms only in (6). The interaction between Cl4 and Cl6 atoms in both structures is characterised by rather small in value, repulsive in nature classical term that is compensated over by the $V_{XC}^{Cl_4,Cl_6}$ term. As a result, these atoms are involved in an overall attractive interactions, with $E_{int}^{Cl_4,Cl_6} = -5.29 \text{ kcal mol}^{-1}$ ($V_{XC}^{Cl_4,Cl_6} = -9.87 \text{ kcal mol}^{-1}$) in (5) and $E_{int}^{Cl_4,Cl_6} = -12.34 \text{ kcal mol}^{-1}$ ($V_{XC}^{Cl_4,Cl_6} = -13.70 \text{ kcal mol}^{-1}$) in (6) even though one can see them as being involved in a steric clash as $d(Cl_4,Cl_6) = 3.2142$ and 3.0196 \AA , respectively, in (5) and (6) (vdW radius of Cl = 1.75 \AA).

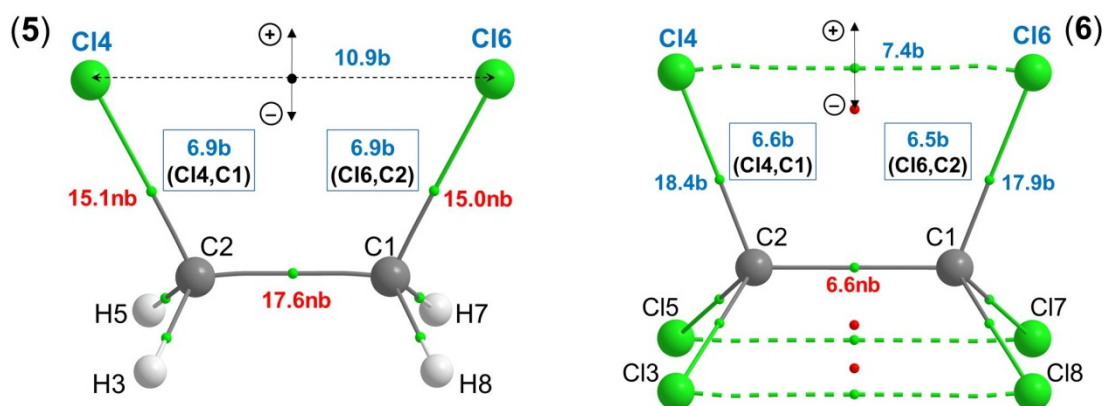


Figure 9. Molecular graphs of eclipsed conformations of $C_2H_4Cl_2$ (5) and C_2Cl_6 (6) structures in the gas phase, including the λ_2 -eigenvectors. Blue and red colourings indicate selected individual atom-pairs that facilitate and hinder, respectively, the presence of DB(Cl4,Cl6) as well as their percentage-slope contributions.

The computed TJ's β -ratios,^{27,28} $V_{XC}^{Cl_4,Cl_6} / V_{XC}^{Cl_4,C1}$ of $(-9.87)/(-5.06) = 1.95$ for (5) and $(-13.70)/(-4.79) = 2.86$ for (6), are both larger than the specified upper limit value of 1.59; hence the β -ratio incorrectly predicts a DB linking Cl4 with Cl6 in both structures. Furthermore, $V_{XC}^{Cl_4,Cl_6}$ in (5) is almost twice as large as that of the largest secondary

interaction, and therefore this interaction is considered privileged in such a context, yet no DB is present. This must raise some questions regarding the arbitrariness of TJ's interpretation of Pendás *et al.*'s concept of privileged exchange channels.²⁶

Figures 10(a) and 10(b) show the FALDI-based ED decomposition of the total *bonding*- and *nonbonding*-ED along the λ_2 -eigenvectors indicated in Figure 9. In this case study we see some very large differences in the ED distributions. While the *tot*-ED distributions in the vicinity of the MDP(CI4,CI6) in (5) and (3,-1) CP(CI4,CI6) in (6) are comparable in magnitude, the ratio of *bonding*- to *nonbonding*-ED in (6) is much larger. Furthermore, we note in (5) that *nonbonding*-ED dominates the negative range of the eigenvector (a direction 'towards' the carbon backbone) whereas in (6) it makes rather small (nearly negligible) contribution throughout entire region.

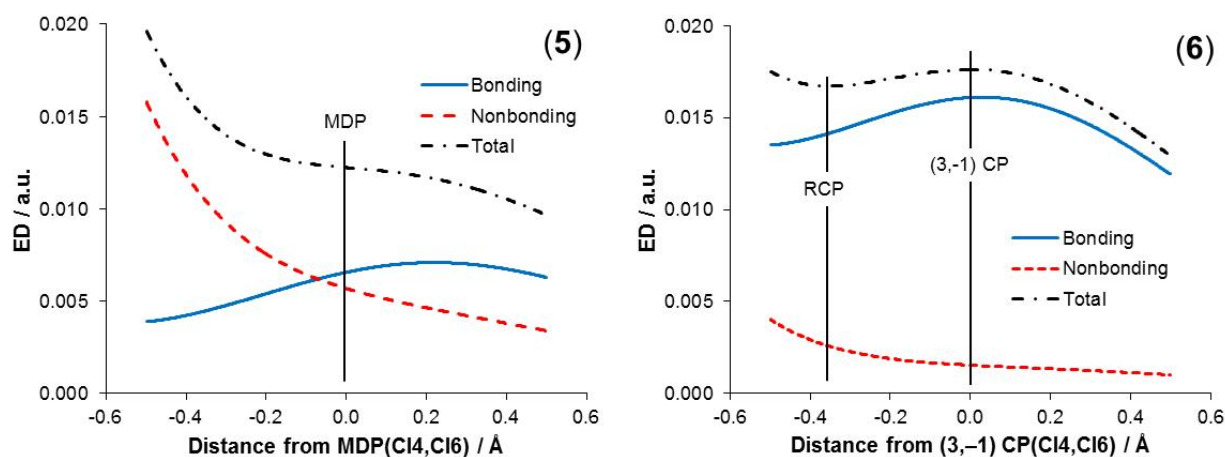


Figure 10. Comparison of the total *bonding*- and total *nonbonding*-ED along the λ_2 -eigenvector passing through the MDP(CI4,CI6) in (5) and (3,-1) CP(CI4,CI6) in (6).

Slopes of the total *bonding*- and total *nonbonding*-ED distributions, as well as the $CP(\mathbf{r})$ function, with respect to the λ_2 -eigenvector, are plotted in Figures 10(a) and (b). The criterion and mechanism leading to a DB existence using the $CP(\mathbf{r})$ function once again holds, in that $CP(\mathbf{r})$ is always negative between CI4 and CI6 atoms in (5) but displays a positive region in (6). This provides an evidence that the $CP(\mathbf{r})$ function is equally applicable and successful in its predictive ability for either equilibrium or non-equilibrium structures.

The substitution of H-atoms in (5) for Cl atoms in (6) has a very significant influence on the *bonding*- and *nonbonding*-ED distributions, as well as their slopes, between Cl-atoms.

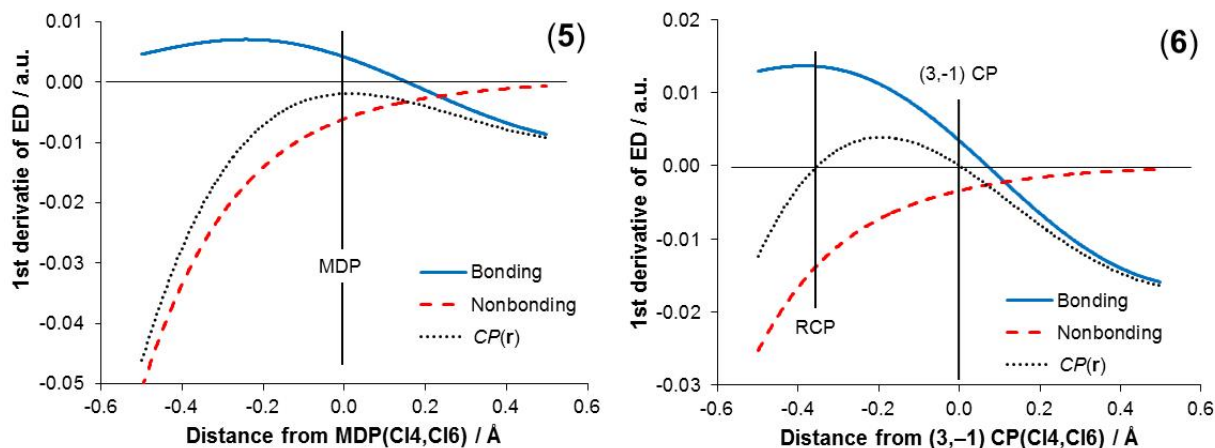


Figure 11. Comparison of the 1st derivative curves of the total *bonding*- and total *nonbonding*-ED along the λ_2 -eigenvector passing through the MDP(CI4,CI6) in (5) and the (3,-1) CP(CI4,CI6) in (6).

The largest contributions to are shown in Tables 5 and 6; a full set of data is included in Tables S11 and S12 in the SI. There are several important observations we would like to make:

(1) In contrast to previous molecules, the atom-pair CI4,CI6 involved in the primary interaction made the largest contribution to the ED at \mathbf{r}^* in both structures (5) and (6), 14.9 and 12.3% of the *tot*-ED, respectively.

(2) Atom-pairs C1,C2 and C2,CI4 hinder DB(CI4,CI6) presence in (5) (on average by ~16% of the total slope, nonbonding) but C2,CI4 facilitates DB(CI4,CI6) presence in (6) (~18% of total slope, bonding) whereas C1,C2 atom-pair's *nonbonding*-ED contribution decreased by about 50%.

(3) Long-range Cl...Cl interactions present in (6), such as from atom-pair CI3,CI4, facilitate the presence of DBs between eclipsed Cl-atoms. Each of the long-range Cl...Cl interactions contributes ~3.7% to the total slope at the (3,-1) CPs in a bonding fashion; in total, they contribute ~24% to the total slope and ~35% to the *tot*-ED at, *e.g.* the (3,-1) CP(CI4,CI6).

(4) The ED delocalized amongst various Cl atom-pairs (both eclipsed and non-eclipsed) is therefore distributed in a manner that *concentrates* ED between *all* eclipsed Cl...Cl contacts, as a result of molecular-wide MOs that show constructive interference between neighbouring Cl atoms.

Table 5. Selected contributions made to MDP(Cl4,Cl6) in (5). Percentages refer to contributions towards the *tot*-ED and its slope.

Component	$\rho_{\text{bonding}}(\mathbf{r}^*)$	$\partial\rho_{\text{bonding}}(\mathbf{r}^*)$	$\rho_{\text{nonbonding}}(\mathbf{r}^*)$	$\partial\rho_{\text{nonbonding}}(\mathbf{r}^*)$
Cl4,Cl6	0.00182 (14.9%)	0.00122 (10.9%)	-	-
C1,C14	0.00085 (6.9%)	0.00078 (6.9%)	-	-
C2,C14	-	-	0.00176 (14.4%)	-0.00169 (15.1%)
C1,C2	-	-	0.00053 (4.3%)	-0.00197 (17.6%)
Total	0.00658	0.00465	0.00563	-0.00653

Table 6. Selected contributions made to (3,-1) CP(Cl4,Cl6) in structure (6). Percentages refer to contributions towards the *tot*-ED and its slope.

Component	$\rho_{\text{bonding}}(\mathbf{r}^*)$	$\partial\rho_{\text{bonding}}(\mathbf{r}^*)$	$\rho_{\text{nonbonding}}(\mathbf{r}^*)$	$\partial\rho_{\text{nonbonding}}(\mathbf{r}^*)$
Cl4,Cl6	0.00218 (12.3%)	0.00066 (7.4%)	-	-
C1,C14	0.00095 (5.4%)	0.00058 (6.6%)	-	-
C2,C14	0.00193 (10.9%)	-0.00163 (18.4%)	-	-
Cl3,Cl4	0.000991 (5.6%)	0.000328 (3.7%)	-	-
C1,C2	-	-	0.00041 (2.3%)	-0.00058 (6.6%)
Total	0.01611	0.00153	0.00129	-0.00115

Clearly, from the MOs perspective, interactions between eclipsed Cl-atoms in (5) and (6) might be seen as distinctively different even though, from the IQA perspective, they are nearly identical. It is therefore not the Cl...Cl interaction itself which is different between the two structures, but rather a remarkably different environment in (6) which leads to a predominantly multicenter interaction involving considerable *bonding*-ED contributions. These additional *bonding*-ED contributions in (6) result in a relative increase in the slope of the factors that concentrate ED in the Cl4,Cl6 internuclear region, and as a result, a DB(Cl4,Cl6) is observed.

H--H steric contact in *cis*-2-butene

Finally, as requested by one of the reviewers, analysis of the H--H steric contact, with $d(\text{H1},\text{H6}) = 2.1150 \text{ \AA} < \text{sum of vdW radii}$, was performed using exactly the same approach as discussed for the remaining molecular systems – the molecular graph and λ_2 -eigenvector is shown in Figure 1a. Importantly, from NBO-based analysis it was recently concluded⁴² the H...H interaction in the *cis* isomer of 2-butene is repulsive and responsible for this conformer higher energy relative to the *trans*-conformer. Looking at trends shown in Figure 12, however, it is

apparent that the presence of a DB and the associated (3,-1) CP(H1,H6) is the result of the same fundamental process that lead to DBs in molecules discussed above:

- a) The total ED peaks at the (3,-1) CP is dominated by bonding contributions (part a).
- b) The $CP(\mathbf{r})$ function is positive in the region between RCP and (3,-1) CP(H1,H6) (part b) and this is a result of the larger slope computed for the *bonding*-ED relative to *nonbonding*-ED – Table 7.

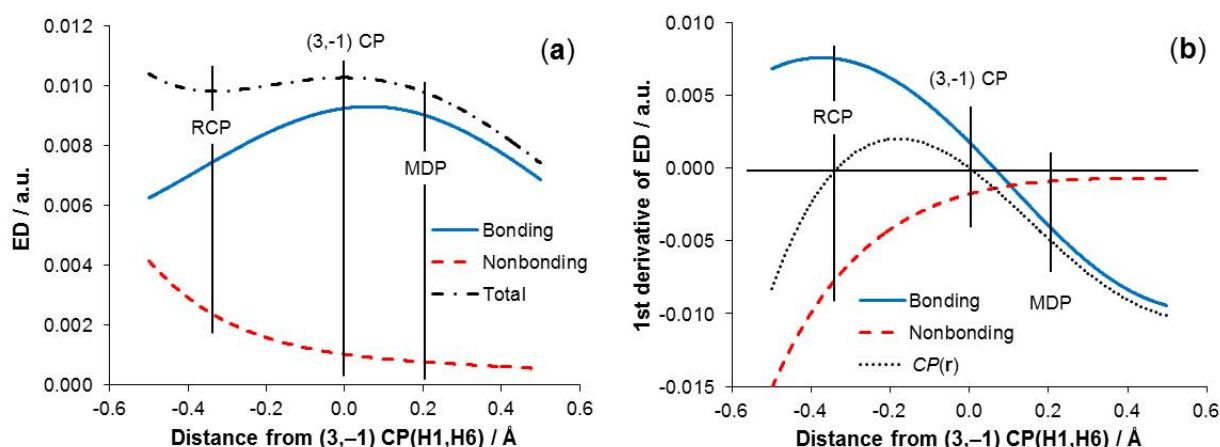


Figure 12. Comparison of the 1st derivative curves of the total *bonding*- and total *nonbonding*-ED along the λ_2 -eigenvector passing through the the (3,-1) CP(H1,H6) in *cis*-2-butene.

Data in Table 7 provides further and important insight when atom-pairs' main contributions are considered:

- 1) The largest contributions of a bonding nature came from C2,H1 (C5,H6) atom pairs (0.00268 a.u. each and when combined constitutes 52.2 % of the *tot*-ED) that is an order of magnitude larger when compared with contribution (also of *bonding* nature) made by the H1,H6 atom-pair. This (i) correlates perfectly well with these two fragments' stabilizing contributions made to the molecular energy of *cis*-2-butene when the *trans*- to *cis*-conformer structural change took place⁴³ and (ii) strongly suggests that a for-atom notation, CH••HC, for this kind of interaction is most representative.

- 2) Major contributions of nonbonding nature came from atom-pairs of the molecular backbone, among them the middle C3,C4 atom pair that became somewhat strained when in *cis*-conformer.⁴³

Table 7. Selected contributions made to (3,-1) CP(H1,H6) in *cis*-2-butene. Percentages refer to contributions towards the *tot*-ED and its slope.

Component	$\rho_{\text{bonding}}(\mathbf{r}^*)$	$\partial\rho_{\text{bonding}}(\mathbf{r}^*)$	$\rho_{\text{nonbonding}}(\mathbf{r}^*)$	$\partial\rho_{\text{nonbonding}}(\mathbf{r}^*)$
C2,H1	0.00268 (26.1%)	0.00066 (16.3%)	-	-
C5,H6	0.00268 (26.1%)	0.00066 (16.3%)		
H1,H6	0.00030 (2.9%)	0.00007 (1.7%)		
C2,H7	0.00031 (3.1%)	-0.00004 (0.9%)	-	-
C2,C3	-	-	0.00032 (3.1%)	-0.00061 (14.9%)
C4,C5	-	-	0.00032 (3.1%)	-0.00061 (14.9%)
C3,C4	-	-	0.00010 (1.0%)	-0.00029 (7.1%)
C3,H12	-	-	0.00003 (0.3%)	-0.00007 (1.8%)
Total	0.00925	0.00178	0.00103	-0.00178

Conclusions

A set of analytical quantum chemical tools were developed in order to study and understand the presence or absence of a DB linking two atoms on a molecular graph. Applicability and usefulness of the tools was successfully tested on four very different case studies involving intramolecular interactions: (1) a classical H-bond, (2) a highly repulsive O...O interaction, (3) an attractive Cl...Cl interaction and (4) an attractive CH...HC interaction. The first three case studies involved two similar molecules showing either an absence or presence of a DB.

We have consistently shown that the presence or absence of a DB cannot be solely linked to the β -ratio of IQA-defined $V_{\text{XC}}^{\text{X,Y}}$ terms of the interaction of interest (the so-called ‘*primary interaction*’) and the $V_{\text{XC}}^{\text{X,Y}}$ terms of ‘*competing*’ neighbouring interactions (‘*secondary interactions*’). Rather, we showed that all of the DBs studied in this work displayed very large degrees of multicenter character, illustrating that a simple bicentric approach for introducing a criterion for the presence of a DB represents a grossly misleading picture of the topology of the ED. In fact, in all four systems studied in this work, the atom-pair of the interactions that display a DB only contributed a relatively small fraction of the *tot*-ED as well as its slope at the (3,-1) CP. While Pendás *et al*’s concept of DBs as “privileged exchange channels”²⁶ might still hold, it must be redefined within a framework of multiple exchange channels resulting in a single density bridge.

Using the FALDI ED decomposition scheme, we have shown that for a specific internuclear region, multiple atoms and atom-pairs can either facilitate or hinder the presence of a DB due to the manner in which (de)localized ED is distributed across the molecule. We

have labelled each component as bonding, nonbonding or antibonding, related to each components' partial second derivative along the λ_2 -eigenvector. In all of our model systems we noticed multiple, unexpected bonding or nonbonding contributions to an internuclear region of interest; for instance, multiple Cl,Cl atom-pairs *facilitate* the presence of DBs between eclipsed Cl,Cl contacts in hexachloroethane (**6**), a factor which is missing in dichloroethane (**5**). Ultimately, we showed that the relative slopes (rates of change) of *bonding*-, *nonbonding*- and *antibonding*-ED determines the presence of a DB, and in the absence of *antibonding*-ED, a DB will always exist if the slope of the *bonding*-ED is greater in magnitude than the slope of the *nonbonding*-ED in a given internuclear region. Since each FALDI component can be interpreted from a physical (*i.e.* in terms of the forces acting on nuclei) and chemical (*i.e.* in terms of interference patterns of MOs overlapping multiple atoms) points of view, we present a criterion that provides a very useful and descriptive language for interpreting QTAIM's molecular graphs.

Analysis of the ED distributions of our model systems revealed that many contributions of a bonding nature are present regardless of whether a primary interaction is (i) linked by a DB (ii) repulsive or attractive, and/or (iii) considered as chemically bonded. As such, we cannot suggest using the presence of a DB as a condition for any chemical phenomena. That said, the presence of a DB proves that some ED contributions in an internuclear region are of a bonding nature; hence any (multicenter) interaction with a DB present displays a degree of bonding character, thereby strengthening or weakening attractive or repulsive interatomic forces, respectively.

Our observations point towards a necessary paradigm shift in the relationship between ED distributions in internuclear regions and chemical bonding, especially for the description of intramolecular interactions. While we hope, as many chemical theoreticians do, for the discovery of a universal, general theory of the chemical bond, we suggest that, perhaps, it is necessary to fully understand the inherently multicenter characteristics of bonding, nonbonding and antibonding in terms of ED distributions first, regardless of whether a chemical interaction can ultimately be considered as bonded or not.

Acknowledgements

This work is based on the research supported in part by the National Research Foundation of South Africa (Grant Number 105855). The authors gratefully acknowledge the Centre for

High Performance Computing (CHPC), South Africa, for providing computational resources to this research project.

The authors declare no conflict of interest.

References

1. The Chemical Bond: Chemical Bonding Across the Periodic Table; G. Frenking, S. Shaik, Eds.; Wiley-VCH: Weinheim, **2014**.
2. The chemical bond: fundamental aspects of chemical bonding; The Chemical Bond: Chemical Bonding Across the Periodic Table; G. Frenking, S. Shaik, Eds.; Wiley-VCH: Weinheim, **2014**.
3. P. L. Popelier, In The Chemical Bond II; D. Mingos, Ed.; Springer:Cham, **2016**; Vol. 170, p 71-117.
4. R. F. W. Bader, In Atoms in molecules: A Quantum Theory; Oxford University Press: Oxford, **1990**.
5. C. Foroutan-Nejad, S. Shahbazian, R. Marek, *Chem. Eur. J.* **2014**, *20*, 10140–10152.
6. S. Shahbazian, *Chem. Eur. J.* **2018**, *24*, 5401–5405.
7. G. Runtz, R. F. W. Bader, R. Messer, *Can. J. Chem.* **1977**, *55*, 3040–3045.
8. R. F. W. Bader, T. H. Tang, Y. Tal, F. W. Biegler-Koenig, *J. Am. Chem. Soc.* **1982**, *104*, 946–952.
9. S. Grimme, C. Mück-Lichtenfeld, G. Erker, G. Kehr, H. Wang, H. Beckers, H. Willner, *Angew. Chem. Int. Ed* **2009**, *48*, 2592–2595.
10. A. Krapp, G. Frenking, *Chem. Eur. J.* **2007**, *13*, 8256–8270.
11. J. Poater, M. Solà, F. M. Bickelhaupt, *Chem. Eur. J.* **2006**, *12*, 2889–2895.
12. J. Poater, M. Solà, F. M. Bickelhaupt, *Chem. Eur. J.* **2006**, *12*, 2902–2905.
13. J. Poater, R. Visser, M. Solà, F. M. Bickelhaupt, *J. Org. Chem.* **2007**, *72*, 1134–1142.
14. I. Cukrowski, J. H. de Lange, A. S. Adeyinka, P. Mangondo, *Comput. Theor. Chem.* **2015**, *1053*, 60–76.
15. R. F. W. Bader, *J. Phys. Chem. A* **2009**, *113*, 10391–10396.
16. R. F. W. Bader, *J. Phys. Chem. A* **1998**, *102*, 7314–7323.
17. D. Cremer, E. Kraka, *Croat. Chem. Acta* **1985**, *57*, 1259–1281.
18. R. F. W. Bader, T. Slee, D. Cremer, E. Kraka, *J. Am. Chem. Soc.* **1983**, *105*, 5061–5068.
19. L. J. Farrugia, C. Evans, M. Tegel, *J. Phys. Chem. A* **2006**, *110*, 7952–7961.

20. J. R. Lane, J. Contreras-García, J.-P. Piquemal, B. J. Miller, H. G. Kjaergaard, *J. Chem. Theory Comput.* **2013**, *9*, 3263–3266.
21. C. F. Matta, J. Hernández-Trujillo, T. H. Tang, R. F. W. Bader, *Chem. Eur. J.* **2003**, *9*, 1940–1951.
22. R. F. W. Bader, *Chem. Eur. J.* **2006**, *12*, 2896–2901.
23. J. Contreras-García, E. R. Johnson, S. Keinan, R. Chaudret, J.-P. Piquemal, D. N. Beratan, W. Yang, *J. Chem. Theory Comput.* **2011**, *7*, 625–632.
24. A. Otero-de-la-Roza, E. R. Johnson, J. Contreras-García, *Phys. Chem. Chem. Phys.* **2012**, *14*, 12165–12172.
25. R. F. W. Bader, *Can. J. Chem.* **1986**, *64*, 1036–1045.
26. A. M. Pendás, E. Francisco, M. A. Blanco, C. Gatti, *Chem. Eur. J.* **2007**, *13*, 9362–9371.
27. O. A. Syzgantseva, V. Tognetti, L. Joubert, *J. Phys. Chem. A* **2013**, *117*, 8969–8980.
28. V. Tognetti, L. Joubert, *J. Chem. Phys.* **2013**, *138*, 024102–024111.
29. M. Blanco, A. M. Pendás, E. Francisco, *J. Chem. Theory Comput.* **2005**, *1*, 1096–1109.
30. J. H. de Lange, D. M. van Niekerk, I. Cukrowski, *J. Comp. Chem* **2018**, *39*, 973–985.
31. R. P. Feynman, *Phys. Rev.* **1939**, *56*, 340–343.
32. J. H. Lange, I. Cukrowski, *J. Comp. Chem.* **2017**, *38*, 981–997.
33. I. Cukrowski, D. M. van Niekerk, J. H. de Lange, *Struct. Chem.* **2017**, *28*, 1429–1444.
34. J. H. de Lange, I. Cukrowski, *J. Comp. Chem.* **2018**, DOI: 10.1002/jcc.25223.
35. R. Ponec, *J. Math. Chem.* **1997**, *21*, 323–333.
36. R. Ponec, *J. Math. Chem.* **1998**, *23*, 85–103.
37. M. Frisch, G. Trucks, H. Schlegel, G. Scuseria, M. Robb, J. Cheeseman, G. Scalmani, V. Barone, B. Mennucci, G. Petersson, H. Nakatsuji, X. Li, M. Caricato, A. Marenich, J. Bloino, B. Janesko, R. Gomperts, B. Mennucci, H. Hratchian, J. Ortiz, A. Izmaylov, J. Sonnenberg, D. Williams-Young, F. Ding, F. Lipparini, F. Egidi, J. Goings, B. Peng, A. Petrone, T. Henderson, D. Ranasinghe, V. Zakrzewski, J. Gao, N. Rega, G. Zheng, W. Liang, M. Hada, M. Ehara, K. Toyota, R. Fukuda, J. Hasegawa, M. Ishida, T. Nakajima, Y. Honda, O. Kitao, H. Nakai, T. Vreven, K. Throssell, J. J. Montgomery, J. Peralta, F. Ogliaro, M. Bearpark, J. Heyd, E. Brothers, K. Kudin, V. Staroverov, T. Keith, R. Kobayashi, J. Normand, K. Raghavachari, A. Rendell, J. Burant, S. Iyengar, J. Tomasi, M. Cossi, J. Millam, M. Klene, C. Adamo, R. Cammi, J. Ochterski, R. Martin, K. Morokuma, O. Farkas, J. Foresman, D. Fox, Gaussian, Inc., Wallingford CT, **2009**.
38. S. Grimme, *Wiley Interdiscip. Rev. Comput. Mol. Sci.* **2011**, *1*, 211–228.

39. T. Keith, TK Gristmill Software (aim.tkgristmill.com): Overland Parks KS, USA, **2016**.
40. W. Humphrey, A. Dalke, K. Schulten, *J. Mol Graph.* **1996**, *14*, 33–38.
41. A. Bondi, *J. Phys. Chem.* **1964**, *68*, 441–451.
42. F. Weinhold, P. R. Schleyer, W. C. McKee, *J. Comp. Chem.* **2014**, *35*, 1499–1508.
43. I. Cukrowski, F. Sagan, M. P. Mitoraj, *J. Comp. Chem.* **2016**, *37*, 2783–2798.

Chapter 6. Toward deformation densities for intramolecular interactions without radical reference states using the fragment, atom, localized, delocalized, and interatomic (FALDI) charge density decomposition scheme

Published in:

Journal of Computational Chemistry, 2017, 38, 981–997.



A novel methodology for calculating deformation densities for intramolecular interactions without the need for radical fragments is presented. A density decomposition scheme is introduced (FALDI) which is used to calculate and transform the density contributions of atoms, fragments and interatomic interactions of a molecule undergoing structural or conformational change. The FALDI scheme also provides visualization of atomic and interatomic density in real-space, and is a useful analysis tool applicable on static electron densities, conformational and fragment-based deformation densities.

Electronic supplementary information available at:

<https://onlinelibrary.wiley.com/doi/full/10.1002/jcc.24772>

Toward Deformation Densities for Intramolecular Interactions without Radical Reference States Using the Fragment, Atom, Localized, Delocalized, and Interatomic (FALDI) Charge Density Decomposition Scheme

Jurgens Hendrik de Lange and Ignacy Cukrowski *

A novel approach for calculating deformation densities is presented, which enables to calculate the deformation density resulting from a change between two chemical states, typically conformers, without the need for radical fragments. The Fragment, Atom, Localized, Delocalized, and Interatomic (FALDI) charge density decomposition scheme is introduced, which is applicable to static electron densities (FALDI-ED), conformational deformation densities (FALDI-DD) as well as orthodox fragment-based deformation densities. The formation of an intramolecular NH...N interaction in protonated ethylene diamine is used as a

case study where the FALDI-based conformational deformation densities (with atomic or fragment resolution) are compared with an orthodox EDA-based approach. Atomic and fragment deformation densities revealed in real-space details that (i) pointed at the origin of density changes associated with the intramolecular H-bond formation and (ii) fully support the IUPAC H-bond representation. The FALDI scheme is equally applicable to intra- and intermolecular interactions. © 2017 Wiley Periodicals, Inc.

DOI: 10.1002/jcc.24772

Introduction

Recent years have seen a large resurgence in research investigating the chemical nature of many weak intermolecular and intramolecular interactions. Some of these interactions have been known to chemists for decades, but new theoretical evidence suggests that their chemical nature and properties might not be as clear as classical chemistry thought. Examples include the classically repulsive homopolar hydrogen–hydrogen contacts,^[1–5] dihydrogen interactions,^[6–8] and the large number of different hydrogen bonds.^[9–13] Conversely, investigations into the nature of known interactions have also led to the discovery of new interactions which might be of interest to chemists, such as halogen bonding,^[14–16] anion–anion interactions,^[17] and chalcogen bonds.^[18] While many debates related to weak interactions are ongoing in the theoretical community (e.g., the debates regarding the nature of hydrogen–hydrogen contacts^[19–27]), research into these areas of interest have revealed how underdeveloped our theoretical understanding of all chemical bonds still is. Specifically, despite many excellent treatises on the physical events on bond formation,^[28] there is still a scientific need to shed more light on the nature of many intramolecular interactions commonly found in experimental conditions, and how a network of intramolecular interactions contributes to the chemical properties and reactivity of a molecular system. To this end, many tools, techniques, and methodologies have been developed over the last few decades which are able to probe specific aspects of intramolecular interactions. Many of these can be classified as decomposition and transformation of (i) the molecular energy, including FAMSEC,^[29] EDA,^[30] ETS,^[31] IQA,^[32] and SAPT,^[33] or (ii) the molecular charge density distribution, including

QTAIM,^[34] FMO,^[35] NBO,^[36] NCI,^[37] and NOCV.^[38] Some of these methods have been combined, such as ETS–NOCV,^[39] to give a holistic viewpoint toward the energy and electron density phenomena regarding intermolecular and intramolecular interactions. While many of these techniques provide clear insights with regards to intermolecular bonding, discussions involving intramolecular interactions are generally much more muddled. Hence, obtaining a better understanding of intramolecular bonding is a very desirable goal, due to the extreme prevalence of intramolecular interactions in many physical sciences.

Bader's quantum theory of atoms in molecules^[34] (QTAIM) and his concept of a bond path (BP) or atomic interaction line (AIL) have experienced significant success. This is because a relatively inexpensive calculation is required to identify and classify intermolecular and intramolecular interactions. Many of his claims regarding the chemical significance of BPs have been questioned,^[25–27] leading to unorthodox interpretations of an AIL,^[22] improvements of QTAIM's charge decomposition scheme, including the noncovalent interaction^[37] (NCI) approach as well as a proposal to change the Bader's nomenclature from a bond path to a line path.^[40] The interpretation of both QTAIM's AILs and NCI's 'attractive regions of density concentration', as well as the interpretation of most charge

J. H. de Lange, I. Cukrowski

Department of Chemistry, Faculty of Natural and Agricultural Sciences,
University of Pretoria, Lynnwood Road, Hatfield, Pretoria 0002, South Africa
E-mail: ignacy.cukrowski@up.ac.za

Contract grant sponsor: National Research Foundation of South Africa;
Contract grant number: 87777; Contract grant sponsor: University of
Pretoria

© 2017 Wiley Periodicals, Inc.

decomposition analyses, is inherent in one of Feynman's theorems,^[41] that the most attractive forces on atoms are observed when an influx of charge is seen in the interatomic region. It is generally accepted that an accumulation of electron density within the interatomic region of two or more atoms is indicative of an interaction with a predominantly bonding character. However, it was shown that accumulation of density with an accompanying AIL is also observed when atoms are involved in a repulsive interaction even when a molecular system is at a true equilibrium state.^[27] Moreover, the manner in which an accumulation of electron density is measured differs significantly between different methods, leading to inconsistent interpretations and conclusions. For instance, we have previously shown that the measure of charge concentration (whether it be AILs or regions of concentration as used by QTAIM and NCI, respectively) cannot be used to consistently differentiate between IQA-defined attractive and repulsive intermolecular interactions in water dimers^[42] or intramolecular interactions in metal complexes.^[43]

The question then arises as to which specific measure of charge concentration gives the correct description of the nature of an interaction. To this end, the simplest and clearest measure of an accumulation or depletion of electron density is the deformation density, also known as the difference density, $\Delta\rho(\mathbf{r})$. It is defined at any given co-ordinate \mathbf{r} [eq. (1)] as the change in electron density in real space between the final (*fin*) and initial (or reference, *ref*) state,

$$\Delta\rho(\mathbf{r}) = \rho(\mathbf{r}) - \rho^0(\mathbf{r}) \quad (1)$$

where

$$\rho^0(\mathbf{r}) = \sum_i^{M_0} \rho_i^0(\mathbf{r}) \quad (2)$$

describes the contribution at \mathbf{r} to the *fin* state of density coming from an i number of noninteracting promolecules M_0 . In such an approach, for the resulting $\Delta\rho(\mathbf{r})$ to be meaningful, it is necessary for the co-ordinate system to be identical in the *fin* as well as *ref* state of a molecular system. In other words, all nuclear positions in the *fin* system must be the same as in promolecular state, with the only difference that each promolecule contains a subset of the total number of nuclei. The result is such that the distance between each nuclear co-ordinate \mathbf{R}_i and each co-ordinate \mathbf{r} , $d_{\mathbf{R}_i, \mathbf{r}}$ remains constant, but different electron distributions in the different states lead to the change in density between promolecules and a *final* molecule, $\Delta\rho(\mathbf{r})$.

The deformation density is an extremely valuable and easily interpretable tool. Not only does $\Delta\rho(\mathbf{r})$ give the change (accumulation or depletion) of density within the bonding region of an interaction (in a manner directly in line with Feynman's theorem), but also the change in density outside of the bonding region, revealing the various polarizations and charge transfers resulting from the formation of an interaction. Moreover, $\Delta\rho(\mathbf{r})$ is often used in conjunction with the so-called interaction energy (or bond formation energy, defined as the energy

difference between promolecular and molecular states). This is the central approach of many EDA schemes, such as the extend transition state coupled with natural orbitals for chemical valence (ETS-NOCV) approach,^[39] because visualizing and investigating electron density changes is a powerful tool in explaining bond formation energies.

Using $\Delta\rho(\mathbf{r})$ works well when intermolecular interactions are investigated because each separate molecule of a molecular system constitutes a well-defined and chemically viable reference state. Unfortunately, molecular reference states are usually not available in the case of intramolecular interactions and it is necessary to fragment the molecule into one or more unchemical states (usually radicals). Even though such radical states are physically and mathematically well-defined, extracting specific chemical information for intramolecular interactions can be troublesome. For instance, on reconstructing a molecule, formation of a covalent bond must unavoidably distort a picture related to the formation of a much weaker intramolecular bond/interaction. In addition, the presence of a radical in the reference state will affect the charge distribution on all atoms, which can lead to a distorted interpretation regarding formation of an intramolecular bond. Finally, it is extremely difficult to extract information regarding the density changes on atoms *not* involved in the formation of an intramolecular bond (such as a carbon backbone) using orthodox $\Delta\rho(\mathbf{r})$ calculations. This is because the density changes related to the formation of new covalent bonds tends to mask any other, causal changes. Nonetheless, due to the extreme usefulness of $\Delta\rho(\mathbf{r})$, ETS-NOCV and other theories based on $\Delta\rho(\mathbf{r})$ have been used to study intramolecular interactions and, with careful attention to the choice of reference state and final interpretation, have yielded some interesting results.^[44,45] The use of unchemical reference states, however, has also been the cause for a few strong and critical arguments.^[46] Since the use of *any* reference state carries a degree of ambiguity, whether the reference is chemically viable or not, it is obvious that any approach which can utilize nonradical reference states will be a welcome complement to the orthodox $\Delta\rho(\mathbf{r})$ studies involving intramolecular interactions.

This article is primarily focused on providing an alternative methodology which can utilize nonradical reference states. To this effect, a novel approach is presented to approximate the deformation density resulting from a structural change of a molecule involving physically and chemically sound states, typically conformers. We use a few concepts originating from the domain averaged Fermi hole (DAFH)^[47,48] method to decompose the electron density into fragment, atomic, localized, delocalized, and Intra- as well as interatomic contributions, hence arriving at the fragment, atom, localized, delocalized, and interatomic (FALDI) charge density decomposition scheme. These decomposition products are computed for each conformer. When individual changes are summed up, a FALDI-deformation density (DD) distribution in real space for a relevant *ref* \rightarrow *fin* structural change is obtained. Moreover, all components of the FALDI-DD distribution can be examined individually to gain an additional insight and aid interpretation of more complex systems. Applicability and usefulness of the

FALDI-DD approach is demonstrated using two conformers of protonated ethylenediamine (Hen^+). The linear, higher energy conformer is used as a *ref* state. The formation of an intramolecular H-bond in spontaneously formed *fin* state of Hen^+ is investigated by different modes of FALDI. Results obtained are compared with an orthodox $\Delta\rho(\mathbf{r})$ approach involving a number of partitioning schemes of the *fin* state of Hen^+ . We conclude this work by pointing at possible applications of the FALDI charge decomposition scheme as well as future extension(s) toward more accurate description of conformational deformation density distributions in real chemical systems.

Theoretical Development

Framework for conformational deformation densities

For the deformation density resulting from a *conformational* change of a molecule (*reference* to *final* state, *ref* \rightarrow *fin*) to be calculated in real space, two significant and necessary modifications must be made to the basic approach described by eq. (1): (i) molecular fragments in the *ref* state must be interacting to eliminate partitioning of a molecule to radical state fragments and (ii) the change in the co-ordinate system, caused by variation in nuclear distances and relative orientations on the *ref* \rightarrow *fin* structural change, must be accounted for. These modifications can both be addressed using a suitable charge partitioning scheme in computing the density distributions of both *ref* and *fin* states into smaller components. Next, each component should be separately transformed to allow for a change in the co-ordinate system, while still be interacting in both *ref* and *fin*.

Many different density partitioning schemes satisfy a general expression

$$\rho(\mathbf{r}) = \sum_i^M \rho_i(\mathbf{r}) \quad (3)$$

where the molecular density is recovered by summing up contributions made by M fragments or atoms. For instance, exhaustive and nonoverlapping schemes, such as the partitioning of the molecular density into atomic basins Ω_i separated by zero-flux surfaces (as used in QTAIM^[34]), can be used to decompose the density completely in a set of M domains, Ω_i , eq. (4):

$$\rho_i(\mathbf{r}) = \begin{cases} \rho(\mathbf{r}) & \mathbf{r} \in \Omega_i \\ 0 & \mathbf{r} \notin \Omega_i \end{cases} \quad (4)$$

It is important to note, however, that the shape and volume of each domain Ω_i changes from the *ref* to *fin* state. This results in regions of space for which the *change* in density cannot be uniquely attributed to a specific fragment, rendering a nonoverlapping scheme, such as QTAIM, unsuitable for conformational deformation density calculations. From this follows that the desired density decomposition scheme in eq. (3) needs to be based on molecular-wide distributions for each $\rho_i(\mathbf{r})$ and with $\rho_i(\mathbf{r}) \neq 0$ for all \mathbf{r} . In other words, whereas QTAIM partitions the molecular electron density into exclusive

and rigid domains, with the electron density associated with an atom or fragment given as an average count of all the electrons found from the nucleus up to the domain surface, we need a scheme which rather gives the electron density associated with an atom as a *distribution* across the entire space. We have found that the DAFH analysis, first developed by Ponec,^[47,48] provides a density decomposition satisfying this requirement.

DAFH-based density decomposition

DAFH analysis evolved around the concept of the exchange-correlation electron hole, which arises from the correlated movements of electrons

$$C(\mathbf{r}_1, \mathbf{r}_2) = 2\rho_2(\mathbf{r}_1, \mathbf{r}_2) - \rho(\mathbf{r}_1)\rho(\mathbf{r}_2) \quad (5)$$

where $C(\mathbf{r}_1, \mathbf{r}_2)$ is the correlation function,^[49] which relates the degree to which the pair density deviates from the completely uncorrelated product of first-order densities. The exchange-correlation electron hole function, located at \mathbf{r}_2 and evaluated at \mathbf{r}_1 is expressed in eq. (6)

$$\rho^{\text{Hole}}(\mathbf{r}_1; \mathbf{r}_2) = \rho(\mathbf{r}_1) - \rho^{\text{cond}}(\mathbf{r}_1; \mathbf{r}_2) \quad (6)$$

where

$$\rho^{\text{cond}}(\mathbf{r}_1; \mathbf{r}_2) = \frac{\rho_2(\mathbf{r}_1, \mathbf{r}_2)}{\rho(\mathbf{r}_2)} \quad (7)$$

is the conditional probability of finding an electron at \mathbf{r}_1 if an electron is already present at \mathbf{r}_2 . The electron hole function [eq. (6)] always integrates over the molecular system to -1 and is used to measure the degree to which the electron density is reduced (or rather excluded) at \mathbf{r}_1 due to correlated movement with an electron at \mathbf{r}_2 . By substituting eqs. (6) and (7) into eq. (5) one obtains

$$C(\mathbf{r}_1, \mathbf{r}_2) = \rho_2(\mathbf{r}_1, \mathbf{r}_2) - \rho^{\text{Hole}}(\mathbf{r}_1; \mathbf{r}_2)\rho(\mathbf{r}_2) \quad (8)$$

giving the correlation function in terms of the electron hole weighted with the charge density at \mathbf{r}_2 . Since the hole calculates the origin (\mathbf{r}_2) of the excluded electron (at \mathbf{r}_1), plotting eq. (8) by varying \mathbf{r}_1 but keeping \mathbf{r}_2 constant is effectively plotting the pseudo-dynamic probability density distribution of a single electron at \mathbf{r}_2 .^[50]

If we vary \mathbf{r}_1 over all space, it then gives the total, molecular-wide density distribution of the electrons which can be found in a volume element $d\mathbf{r}_2$. Finally, \mathbf{r}_2 can be averaged across a domain Ω_i (through integrating the correlation function through $d\mathbf{r}_2$ over a domain Ω_i) to reduce the second-order electron hole and correlation functions to pseudo-second order distributions,

$$g_i(\mathbf{r}_1) = - \int_{\Omega_i} C(\mathbf{r}_1, \mathbf{r}_2) d\mathbf{r}_2 \quad (9)$$

which gives the DAFH quantity, $g_i(\mathbf{r})$ associated with domain Ω_i . In principle, therefore, in the same way that the correlation

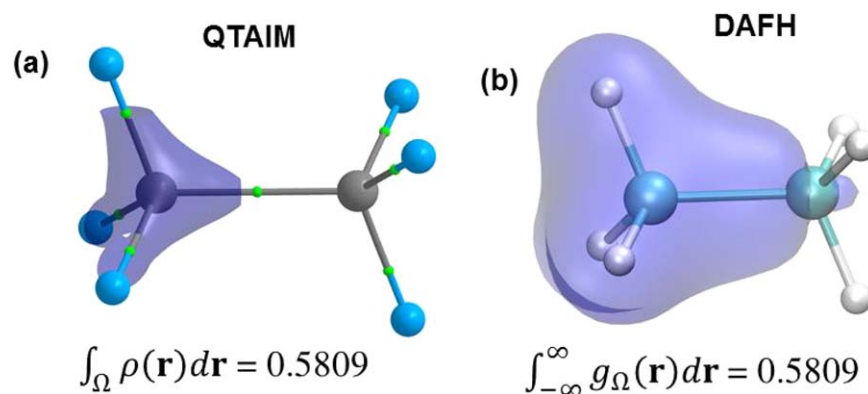


Figure 1. Average electron density associated with a carbon atom in ethane. a) QTAIM-defined electron population, and b) DAFH-defined electron population. [Color figure can be viewed at wileyonlinelibrary.com]

function [eq. (8)], when plotted as a function of varying \mathbf{r}_1 gives a probability distribution of an electron currently in $d\mathbf{r}_2$ (due to exchange-correlation effects), so does $g_i(\mathbf{r})$, when plotted as a function of varying \mathbf{r} , by giving a probability distribution of the electrons found on average in Ω_i across entire space. The $g_i(\mathbf{r})$ quantity, therefore, is of critical importance in this work, as it gives us the contribution made to any coordinate \mathbf{r} by electrons found on average in a domain, or, alternatively, the portion of the electron density at any coordinate \mathbf{r} associated with a specific domain Ω_i . This concept is shown visually in Figure 1. Figure 1a shows the QTAIM-defined electron population for a carbon atom in ethane, represented as an isosurface, and completely contained within the atomic domain defined by a set of zero-flux surfaces.

On average, 0.5809 electrons are found within the carbon atomic basin, which is calculated by integrating the electron density over only the basin. It is important to note that the isosurface shown in Figure 1a contains the electrons localized to C1's atomic basin as well as electrons delocalized to C1's basin from other basins. Correspondingly, the DAFH electron population (shown in Fig. 1b) is identical to the QTAIM-defined population, but it is calculated by integrating $g_i(\mathbf{r})$ over the entire molecule and shows how the 0.5809 electrons are delocalized throughout the molecule. In other words, Figure 1b displays the probability distribution of finding an electron anywhere in the molecule which can also be found, on average, in C1's atomic basin.

It is obvious that selection of the domains Ω_i is, in principle, an arbitrary choice. We have decided to use QTAIM atomic basins for the reasons stated by Bultinck et al.,^[51] however, we will investigate different specifications of atoms in molecules in future studies. We also use the absolute values of $g_i(\mathbf{r})$, for practical reasons when dealing with the deformation density. In addition, we restrict ourselves to spin-independent functions, although it is not difficult to define spin-dependent variants of eq. (9).^[50] Finally, to avoid the expensive integration of the correlation function over irregular QTAIM basins, we calculate $g_i(\mathbf{r})$ through comparison of the elements of various atomic overlap matrices (AOM)

$$g_i(\mathbf{r}_1) = - \sum_{\lambda\sigma}^N \phi_\lambda(\mathbf{r}_1) \phi_\sigma(\mathbf{r}_1) S_{\sigma\lambda}^\Omega \quad (10)$$

where

$$S_{\sigma\lambda}^\Omega = \langle \phi_\sigma | \phi_\lambda \rangle_\Omega = \int_{\Omega} \phi_\sigma(\mathbf{r}_1) \phi_\lambda(\mathbf{r}_1) d\mathbf{r}_1 \quad (11)$$

and $S_{\sigma\lambda}^\Omega$ stands for elements of the AOM associated with a specific domain Ω_i . In single determinant wavefunctions, using the elements of all AOM's related to each domain, $g_i(\mathbf{r})$ is calculated exactly and corresponds to the actual correlation function. However, for more correlated wavefunctions, this does not hold true anymore and it is either necessary to calculate and integrate the exact correlation function in eq. (5) or approach Coulomb correlation in an approximate manner. We have opted for the latter option through the use of the Müller approximation by linearly expanding the first-order density matrix with partial occupation numbers.^[52] However, we note that multiple methods have been suggested for more accurate and efficient treating of Coulomb correlation in DAFH analyses, and it is something we will incorporate in our own scheme in the future.

In traditional DAFH analyses, $g_i(\mathbf{r})$ is expressed as a matrix equation that is diagonalized to decompose $g_i(\mathbf{r})$ into N one-electron functions. Such an approach is counter-productive when the conformational deformation density is concerned, as the relative order of the one-electron DAFH functions might change within a matrix when the *ref* \rightarrow *fin* structural change takes place, creating additional difficulties. Furthermore, in this work we are more interested in the concept of $g_i(\mathbf{r})$, which we take from DAFH, rather than the full natural orbital approach.

General properties of the DAFH

It is important to point at a number of properties of $g_i(\mathbf{r})$ that are relevant to constructing conformational deformation density distributions:

1. $g_i(\mathbf{r})$ is a complete decomposition of the molecular electron density, at any point \mathbf{r} , into contributions from all M domains, as shown in eq. (12),

$$\rho(\mathbf{r}) = \sum_i^M g_i(\mathbf{r}). \quad (12)$$

Therefore, $g_i(\mathbf{r})$ satisfies eq. (3), but is not limited by the restriction in eq. (4); hence, it is well-suited for studying the change of density associated with a specific domain.

2. Integration of $g_i(\mathbf{r})$ over the entire molecular space yields the associated average density within a specific domain Ω_i :

$$N(\Omega_i) = \int_{\Omega_i} \rho(\mathbf{r}) d\mathbf{r} = \int_{-\infty}^{\infty} g_i(\mathbf{r}) d\mathbf{r} \quad (13)$$

where $N(\Omega_i)$ is the QTAIM-defined electron population of the domain. Integrating the electron density over the volume of Ω_i , or integrating $g_i(\mathbf{r})$ over the entire molecular system gives the same result. In this regard, the change in the atomic electron population from a *ref* to a *fin* conformer, $\Delta N(\Omega_i)$, is recovered whether $\rho(\mathbf{r})$ or $g_i(\mathbf{r})$ is used. Importantly, however, using $g_i(\mathbf{r})$ to calculate deformation density does not depend on changing domain shapes and volumes.

3. Integration of $g_i(\mathbf{r})$ over only a single domain Ω_i leads to the often used localization index, (LI), eq. (14)

$$\lambda(\Omega_i) = \int_{\Omega_i} g_i(\mathbf{r}) d\mathbf{r} \quad (14)$$

giving the number of electrons localized to a single atomic basin, whereas integration over any other domain Ω_j leads to the halved delocalization index (DI), eq. (15),

$$\delta(\Omega_i, \Omega_j) = \int_{\Omega_j} g_i(\mathbf{r}_1) d\mathbf{r}_1 + \int_{\Omega_i} g_j(\mathbf{r}_2) d\mathbf{r}_2 = 2 \int_{\Omega_j} g_i(\mathbf{r}_1) d\mathbf{r}_1 \quad (15)$$

giving the number of electrons delocalized between two atomic basins. The LI and DI are related to the electron population of domain Ω_i through

$$N(\Omega_i) = \lambda(\Omega_i) + \sum_{X \neq i}^M \frac{1}{2} \delta(\Omega_i, \Omega_X). \quad (16)$$

Note that the contribution which $g_i(\mathbf{r})$ makes at \mathbf{r} (regardless if it is toward the localized or delocalized density of Ω_i) depends only on whether $\mathbf{r} \in \Omega_i$. Hence, eq. (16) can be rewritten in terms of $g_i(\mathbf{r})$ as:

$$N(\Omega_i) = \int_{\Omega_i} g_i(\mathbf{r}) d\mathbf{r} + \int_{\Omega_j} g_i(\mathbf{r}) d\mathbf{r} \quad (17)$$

4. The distribution of $g_i(\mathbf{r})$ can be interpreted as the probability of finding any one of $N(\Omega_i)$ electrons (contained on average in Ω_i), at any \mathbf{r} . Also, $g_i(\mathbf{r})$ can be visualized as the distribution of the electrons of Ω_i over the molecular system through electron delocalization (exchange-correlation) effects. If $g_i(\mathbf{r}) = 0$, then none of the electrons in Ω_i can be found at \mathbf{r} and if all $\mathbf{r} \notin \Omega_i$, then the electrons of Ω_i are fully localized and $\rho(\mathbf{r}) = g_i(\mathbf{r})$ for $\mathbf{r} \in \Omega_i$.

Introducing the FALDI density decomposition scheme

The properties of $g_i(\mathbf{r})$ make it ideal for the calculation of conformational deformation densities. This is because density at

any co-ordinate \mathbf{r} in a final molecular state can be decomposed into atomic contributions and compared to relevant $g_i(\mathbf{r})$ at transformed $\mathbf{r}' = \mathbf{A}_i \mathbf{r}$ in a reference state,

$$\Delta_c \rho(\mathbf{r}) = {}^{fin} \rho(\mathbf{r}) - {}^{ref} \rho(\mathbf{A}_i \mathbf{r}) = \sum_i^M {}^{fin} g_i(\mathbf{r}) - \sum_i^M {}^{ref} g_i(\mathbf{A}_i \mathbf{r}) \quad (18)$$

where we have introduced $\Delta_c \rho(\mathbf{r})$ to signify the conformational deformation density, M is the total number of atoms and \mathbf{A}_i is the relevant transformation matrix relating the translation and rotation of the i th atom's co-ordinates in the *fin* state to the *ref* state. The difference between each ${}^{fin} g_i(\mathbf{r})$ and ${}^{ref} g_i(\mathbf{A}_i \mathbf{r})$ pair results in the deformation density associated with a specific atom (or domain) Ω_i , and hence we introduce here the first two terms in our FALDI decomposition scheme, an atomic electron density (atomic-ED, AED) distribution, defined as the static $g_i(\mathbf{r})$ for the i th atom in a conformer, and when used in the deformation density context, an atomic deformation density (atomic-DD, ADD) distribution, defined for the i th atom as ${}^{fin} g_i(\mathbf{r}) - {}^{ref} g_i(\mathbf{A}_i \mathbf{r})$ from two states.

The sum of various atomic-ED and atomic-DD distributions gives rise to the next two terms in our FALDI decomposition scheme, a fragment electron density (fragment-ED, FED) distribution, defined as the sum of $g_i(\mathbf{r})$ for any number of atoms forming a molecular fragment, and a fragment deformation density (fragment-DD, FDD) distribution, defined as the sum of $\{ {}^{fin} g_i(\mathbf{r}) - {}^{ref} g_i(\mathbf{A}_i \mathbf{r}) \}$ changes resulting from two states. The sum of FDD distributions computed for all fragments a molecule is made of (or the sum of all atomic-DD distributions) gives the total (molecular) deformation density (total-DD, TDD) distribution $\Delta_c \rho(\mathbf{r})$ defined in eq. (18). We want to stress again that atomic- and fragment-DD distributions require a separate transformation matrix ($\mathbf{A}_i \mathbf{r}$) for each atomic basin Ω_i as this is critical for the calculation of $\Delta_c \rho(\mathbf{r})$. Finally, they are very useful separate analysis tools in exploring the origin of the total change in density between two states at either atomic or fragment level.

Decomposing atomic-ED distributions into localized, delocalized, and interatomic contributions

The conformational deformation density calculated by eq. (18) can be difficult to interpret for certain systems and molecular transformations. The reason for this is the manner through which density shared between two atomic basins is transformed from the *ref* to the *fin* conformer: density delocalized between two atomic basins (Ω_i and Ω_j) with different transformation matrices (\mathbf{A}_i and \mathbf{A}_j) should be uniquely and separately transformed to take into account its dependence on two transformation matrices, as opposed to density localized to one atom (which only depends on \mathbf{A}_i). As it stands though, $\Delta_c \rho(\mathbf{r})$ calculated through eq. (18) presents the interatomic delocalized density simultaneously as half transformed via the transformation matrix of one atom (\mathbf{A}_i) and half through the transformation matrix of the other atom (\mathbf{A}_j). As an example of this problem, consider a system with two atoms, A and B , where A is transformed from *ref* to *fin* via \mathbf{A}_A and B remains untransformed ($\mathbf{A}_B = \mathbf{1}$). The density localized only to the basin

of A in *ref* is correctly transformed through \mathbf{A}_A and compared with the density localized to the basin of A in *fin*. However, half of the density delocalized between A and B in *ref* is transformed relative to A through \mathbf{A}_A and compared to the interatomic delocalized density in *fin*, resulting in an apparent density change as if B was also transformed through \mathbf{A}_A . Correspondingly, half of the density delocalized between A and B in *ref* remains untransformed, and results in an apparent density change as if A remained untransformed. When another atom C is transformed in the same manner as A (with $\mathbf{A}_A = \mathbf{A}_C$, if A and C are parts of the same fragment) then the density shared by A and C is correctly transformed from *ref* to *fin*, but not so the density shared between C and B . This problem of density delocalized across atoms with different transformation matrices appears as apparent artefacts on the total-DD distribution, and although $\Delta_c\rho(\mathbf{r})$ can still be interpreted correctly with some care, it becomes very difficult with anything but the simplest molecules. Note that the apparent artefacts in $\Delta_c\rho(\mathbf{r})$ are self-eliminating in that $\Delta_c\rho(\mathbf{r})$ integrated over all space is 0 because regions where the delocalized density apparently increases due to the problem described above is cancelled out by regions where the delocalized density apparently decreases.

We present next an approximation to the way in which $\Delta_c\rho(\mathbf{r})$ is calculated, which greatly aids the interpretation of $\Delta_c\rho(\mathbf{r})$ while keeping $\Delta_c\rho(\mathbf{r})$ integrated over all space to 0. Since it is only the density *shared* between atomic basins which is affected by incorrect transformation, we first develop expressions for two additional decompositions of the static density into (i) atomically localized and interatomically delocalized contributions, and (ii) intra-atomic (self) and interatomic contributions. These expressions form the final terms of our FALDI density decomposition and they will be discussed below. We then develop a method to approximate a process of transforming delocalized density distributions from *ref* to *fin* through multiple transformation matrices.

We start with expressions for localized and delocalized distributions in real-space in atomic resolution. The number of electrons delocalized across two basins, known as the delocalization index in QTAIM, can be calculated in terms of atomic overlap matrices as

$$\delta(\Omega_i, \Omega_j) = \delta_{ij} = 2 \left| - \sum_{\lambda\sigma}^N S_{\lambda\sigma}^{\Omega_i} S_{\sigma\lambda}^{\Omega_j} \right| \quad (19)$$

giving the overlap of the elements of each AOM for domains Ω_i and Ω_j . Alternatively, the delocalization index can be calculated as the trace of the product of each domains' AOM:

$$\delta_{ij} = 2\text{tr}(\mathbf{S}^{ij}) \quad (20)$$

where

$$\mathbf{S}^{ij} = S^{\Omega_i} S^{\Omega_j} \quad (21)$$

The real-space distribution of the electrons at \mathbf{r} shared between basins Ω_i and Ω_j can be calculated similarly to the calculation of $g_i(\mathbf{r})$ in eq. (10):

$$\delta_{ij}(\mathbf{r}) = -2 \sum_{\lambda\sigma}^N \phi_{\lambda}(\mathbf{r}) \phi_{\sigma}(\mathbf{r}) S_{\sigma\lambda}^{ij} \quad (22)$$

using the product of the atomic overlap matrices as defined in eq. (21). The distribution of the absolute value of $\delta_{ij}(\mathbf{r})$ gives the real-space distribution of electrons shared between the i th and j th basins, and is known within the FALDI decomposition as delocalized electron density (delocalized-ED, DED) distributions. Integrating $\delta_{ij}(\mathbf{r})$ over entire space gives the total delocalization index defined in eqs. (19) and (20):

$$\delta_{ij}(\mathbf{r}) = \int_{-\infty}^{\infty} \delta_{ij}(\mathbf{r}) d\mathbf{r} \quad (23)$$

The electrons localized on average to an atomic basin, known as the localization index in QTAIM terminology, can be calculated in a similar fashion to eqs. (19) and (20):

$$\lambda(\Omega_i) = \lambda_i = \left| - \sum_{\lambda\sigma}^N S_{\lambda\sigma}^{\Omega_i} S_{\sigma\lambda}^{\Omega_i} \right| = \text{tr}(\mathbf{S}^{ii}) \quad (24)$$

Then, similarly to eq. (22), the real space distribution of electrons localized to the i th basin at \mathbf{r} can be calculated as

$$\lambda_i(\mathbf{r}) = - \sum_{\lambda\sigma}^N \phi_{\lambda}(\mathbf{r}) \phi_{\sigma}(\mathbf{r}) S_{\sigma\lambda}^{ii} \quad (25)$$

and $\lambda_i(\mathbf{r})$ is known in the FALDI decomposition as localized electron density (localized-ED, LED) distributions, and, similarly to eq. (23), integrates to the exact localization index:

$$\lambda_i = \int_{-\infty}^{\infty} \lambda_i(\mathbf{r}) d\mathbf{r} \quad (26)$$

Each atomic $g_i(\mathbf{r})$ can therefore be decomposed into a respective localized-ED distribution and the sum of all delocalized-ED distributions involving the i th basin:

$$g_i(\mathbf{r}) = \lambda_i(\mathbf{r}) + \sum_{X \neq i}^M \frac{1}{2} \delta_{i,X}(\mathbf{r}) \quad (27)$$

Finally, the total electron density at \mathbf{r} can be fully decomposed into atom-localized and interatomically delocalized contributions, as

$$\rho(\mathbf{r}) = \sum_i^M \lambda_i(\mathbf{r}) + \sum_i^{M-1} \sum_{j=i+1}^M \delta_{ij}(\mathbf{r}) \quad (28)$$

The above approach is an exact and elegant decomposition of the electron density into 1- and 2-center contributions and relates well to often-used QTAIM parameters. However, an alternative decomposition of the total as well as atomic electron densities in terms of the direct overlap between atomic distributions can also be introduced as

$$\rho(\mathbf{r}) = \sum_i^M g_i(\mathbf{r})g_i(\mathbf{r})\rho^{-1}(\mathbf{r}) + 2 \sum_i^{M-1} \sum_{j=i+1}^M g_i(\mathbf{r})g_j(\mathbf{r})\rho^{-1}(\mathbf{r}) \quad (29)$$

and, accordingly, the $g_i(\mathbf{r})$ distribution of each atom can be decomposed by

$$g_i(\mathbf{r}) = g_i(\mathbf{r})g_i(\mathbf{r})\rho^{-1}(\mathbf{r}) + \sum_{j \neq i}^M g_i(\mathbf{r})g_j(\mathbf{r})\rho^{-1}(\mathbf{r}) = \gamma_i(\mathbf{r}) + \sum_{j \neq i}^M \kappa_{ij}(\mathbf{r}) \quad (30)$$

This decomposition calculates the fraction of the electron density which any atom contributes at \mathbf{r} ($g_i(\mathbf{r})/\rho(\mathbf{r})$), weighted with either the same atom's contribution [as in the first term in eq. (30)] or another atom's contribution [the second term in eq. (30)]. The result is a full decomposition of the electron density [eq. (29)] or the atomic density contribution [eq. (30)] at a specific co-ordinate \mathbf{r} in terms of intra- ($g_i(\mathbf{r})g_i(\mathbf{r})\rho^{-1}(\mathbf{r})$) and interatomic ($\sum_{j \neq i}^M g_i(\mathbf{r})g_j(\mathbf{r})\rho^{-1}(\mathbf{r})$) density. These two terms, $\gamma_i(\mathbf{r})$ and $\kappa_{ij}(\mathbf{r})$ in eq. (30), are known in our FALDI decomposition scheme as self and Interatomic Electron Density (self-ED or SED, and interatomic-ED, IED) distributions, respectively.

Both decompositions (either through localized and delocalized density or through self and interatomic density) sum up to the same atomic or total electron density. In addition, both decompositions, when used to calculate the conformational deformation density, give the same $\Delta_c \rho(\mathbf{r})$ distribution. However, the interpretation of the individual terms is different as it depends on the kind of decomposition used. Whereas $\lambda_i(\mathbf{r})$ and $\delta_{i,j}(\mathbf{r})$ (localized and delocalized density) distributions give the real-space representations of the analogous QTAIM localization and delocalization indices, $\kappa_{ij}(\mathbf{r})$ (interatomic density distribution) gives the *contribution* which each diatomic interaction makes to the density, in terms of mutual atomic overlap and irrespective of their delocalization patterns. $\gamma_i(\mathbf{r})$ (intra-atomic or self-density) distributions are then the remaining, non-overlap density of each atom. We have found that interatomic-ED and self-ED distributions reveal very distinct features of atomic interactions, especially in noncovalent interactions and interactions involving more than two atoms, such as H-bonds. Examples of delocalized and interatomic density distributions are given for a covalent C—C bond in ethane as well as for a van der Waals (vdW) interaction between O...H in a water dimer in Figure 2. Note that for both interactions, interatomic- and delocalized-ED distributions present very unique topologies, clearly illustrating the difference in delocalization patterns (delocalized-ED) and interaction contributions (interatomic-ED). We will be employing primarily localized- and delocalized-ED distributions in the remainder of this work, but note that the alternative decomposition in terms of self- and interatomic-ED distributions can be used in the exact same fashion for the calculation of identical conformational deformation densities; both approaches carry a unique and useful interpretation.

Having introduced a suitable decomposition of the atomic $g_i(\mathbf{r})$ distributions in 1- and 2-center contributions, we will

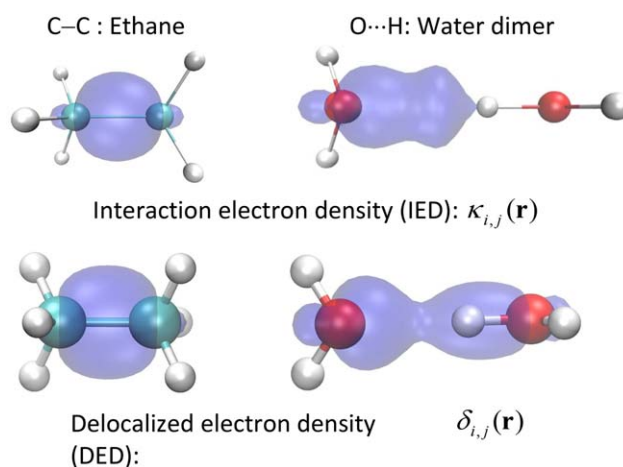


Figure 2. Interatomic-ED and delocalized-ED distributions for a C—C bond in ethane, isovalue = 0.01 au, and an O...H interaction in a water dimer, isovalue = 0.001 au. [Color figure can be viewed at wileyonlinelibrary.com]

now discuss how the decomposition terms can be used to calculate conformational deformation densities. The change in the localized density distribution, $\lambda_i(\mathbf{r})$, for two different states, $\Delta \lambda_i(\mathbf{r}) = \lambda_i^{\text{fin}}(\mathbf{r}) - \lambda_i^{\text{ref}}(\mathbf{r})$, gives the deformation of the density localized to an atom, which we call a localized deformation density (localized-DD, LDD) distribution.

As mentioned at the beginning of this section, the localized density of an atom (a LED distribution) in the *ref* state is easily transformed via $\mathbf{A}_i \mathbf{r}$ and compared to the *fin* state to generate a localized-DD distribution. Conversely, interatomic delocalized density (a DED distribution) needs to be transformed using two transformation matrices simultaneously to calculate delocalized deformation density (delocalized-DD, DDD) distributions. While there are a number of different ways to approach this problem of asymmetrical 2-center transformation, we have opted to use (as a very first and approximate solution) a scaling scheme based on projections of the internuclear vector to generate \mathbf{r}' from the transformed co-ordinates of domains Ω_i and Ω_j , \mathbf{r}'_i and \mathbf{r}'_j . The derivation of this approach is discussed below.

Given the transformations for \mathbf{r} to the relevant \mathbf{r}'_i and \mathbf{r}'_j of two atomic basins Ω_i and Ω_j ,

$$\begin{aligned} \mathbf{r}'_i &= \mathbf{A}_i \mathbf{r} \\ \mathbf{r}'_j &= \mathbf{A}_j \mathbf{r} \end{aligned} \quad (31)$$

we can calculate the value of $\delta_{i,j}(\mathbf{r})$ in the *ref* state at \mathbf{r} as a weighted combination of $\delta_{i,j}$ at \mathbf{r}'_i and \mathbf{r}'_j , as shown in eq. (32),

$$\begin{aligned} \delta_{i,j}^{\text{ref}}(\mathbf{r}) &= w_i(\mathbf{r}) \delta_{i,j}^{\text{ref}}(\mathbf{r}'_i) + w_j(\mathbf{r}) \delta_{i,j}^{\text{ref}}(\mathbf{r}'_j) = w_{ij}(\mathbf{r}) \delta_{i,j}^{\text{ref}}(\mathbf{r}'_i) \\ &+ [1 - w_{ij}(\mathbf{r})] \delta_{i,j}^{\text{ref}}(\mathbf{r}'_j) \end{aligned} \quad (32)$$

The weighting factors w_{ij} can be generated, eq. (33), by projecting the vector from the nuclear co-ordinate of the *i*th atom \mathbf{R}_i to \mathbf{r} , $\mathbf{r} - \mathbf{R}_i$, onto the internuclear vector, \mathbf{R}_{ij} , and calculating the fraction along \mathbf{R}_{ij} where \mathbf{r} is projected,

$$w_{ij}(\mathbf{r}) = 1 - \frac{(\mathbf{r} - \mathbf{R}_i) \cdot \mathbf{R}_{ij}}{|\mathbf{R}_{ij}|^2} \quad (33)$$

For co-ordinates \mathbf{r} between \mathbf{R}_i and \mathbf{R}_j , ${}^{ref}\delta'_{ij}(\mathbf{r})$ can be calculated as a weighted combination of ${}^{ref}\delta_{ij}(\mathbf{r})$ in terms of \mathbf{r}'_i and \mathbf{r}'_j , whereas outside of \mathbf{R}_i and \mathbf{R}_j , ${}^{ref}\delta'_{ij}(\mathbf{r})$ depends only on \mathbf{r}'_i or \mathbf{r}'_j :

$${}^{ref}\delta'_{ij}(\mathbf{r}) = \begin{cases} w_{ij}(\mathbf{r}){}^{ref}\delta_{ij}(\mathbf{r}'_i) + [1 - w_{ij}(\mathbf{r})]{}^{ref}\delta_{ij}(\mathbf{r}'_j) & 0 < w_{ij}(\mathbf{r}) < 1 \\ {}^{ref}\delta_{ij}(\mathbf{r}'_i) & w_{ij}(\mathbf{r}) \geq 1 \\ {}^{ref}\delta_{ij}(\mathbf{r}'_j) & w_{ij}(\mathbf{r}) \leq 0 \end{cases} \quad (34)$$

This approximation lets us calculate ${}^{ref}\delta'_{ij}(\mathbf{r})$ at \mathbf{r} , (where the prime indicates the use of the approximation) and compare directly to ${}^{fin}\delta_{ij}(\mathbf{r})$, which gives the change in interatomic or interfragment density contributions resulting from two states. This protocol generates approximated transformed delocalized-DD distributions for all interactions. We wish to emphasize that the above linear scaling approach is fairly arbitrary, and is only a first approximation to solving the asymmetrical diatomic transformation problem. However, this approach serves to illustrate how the FALDI decomposition can be used to calculate deformation densities, and we fully expect to improve on this approach in the future. In the following final section, we will put all of the FALDI terms together to form expressions for calculating conformational deformation densities.

Conformational deformation densities using the FALDI-DD decomposition

The total conformational deformation density, using the approximation for ${}^{ref}\delta'_{ij}(\mathbf{r})$, is then

$$\Delta_c \rho(\mathbf{r}) = \Delta_c \lambda(\mathbf{r}) + \Delta_c \delta(\mathbf{r}) \quad (35)$$

where

$$\Delta_c \lambda(\mathbf{r}) = \sum_i^M \left[{}^{fin}\lambda_i(\mathbf{r}) - {}^{ref}\lambda_i(\mathbf{A}_i; \mathbf{r}) \right] \quad (36)$$

gives the total localized density change for each atomic basin Ω_i (a LDD distribution), and

$$\Delta_c \delta(\mathbf{r}) = 2 \sum_i^{M-1} \sum_{j=i+1}^M \left[{}^{fin}\delta_{ij}(\mathbf{r}) - {}^{ref}\delta'_{ij}(\mathbf{r}) \right] \quad (37)$$

gives the total delocalized density change for each unique atomic pair Ω_i and Ω_j (a DDD distribution). Note that the sum of all DDD distributions associated with atom Ω_i gives the complete delocalized density distribution of atom Ω_i

$$\Delta_c \delta_{i,X}(\mathbf{r}) = \sum_{j \neq i}^M \Delta_c \delta_{ij}(\mathbf{r}) \quad (38)$$

and the sum of the atomic delocalized- and localized-DD distributions of atom Ω_i gives the atomic-DD distribution

$$\Delta_c g_i(\mathbf{r}) = \Delta_c \lambda_i(\mathbf{r}) + \Delta_c \delta_{i,X}(\mathbf{r}). \quad (39)$$

The sum of all atomic-DD distributions for atoms within a fragment $\{F\}$ gives the fragment-DD distribution

$$\Delta_c g^{\{F\}}(\mathbf{r}) = \sum_i^{M_{\{F\}}} \Delta_c g_i(\mathbf{r}). \quad (40)$$

where $M_{\{F\}}$ is the total number of fragments.

Each FDD distribution can also be decomposed into the density localized to a fragment, as well as the density delocalized between different fragments

$$\Delta_c g^{\{F\}}(\mathbf{r}) = \Delta_c \lambda^{\{F\}}(\mathbf{r}) + \Delta_c \delta^{\{F\}}(\mathbf{r}) \quad (41)$$

where

$$\Delta_c \lambda^{\{F\}}(\mathbf{r}) = \sum_i^{M_{\{F\}}} \Delta_c \lambda_i(\mathbf{r}) + 2 \sum_i^{M_{\{F\}}-1} \sum_{j=i+1}^{M_{\{F\}}} \Delta_c \delta_{ij}(\mathbf{r}) \quad (42)$$

and

$$\Delta_c \delta^{\{F\}}(\mathbf{r}) = \sum_i^{M_{\{F\}}} \sum_k^M \Delta_c \delta_{i,k}(\mathbf{r}) \quad (43)$$

where $k \notin \{F\}$.

Finally, the sum of all M FDD distributions gives again the conformational deformation density, as defined in eq. (35)

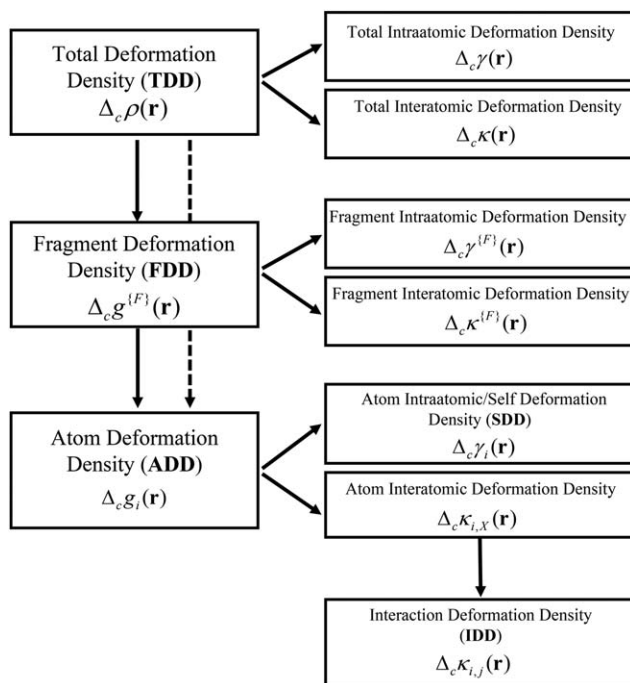
$$\Delta_c \rho(\mathbf{r}) = \sum_i^{\{M\}} \Delta_c g^{\{i\}}(\mathbf{r}) \quad (44)$$

where $\{M\}$ is the total number of fragments.

Note that, as mentioned earlier, the total deformation density calculation can be performed with the alternative decomposition involving the intra-atomic (self) and interatomic density distributions instead of localized and delocalized distributions. Both approaches lead to the same total deformation density but reveal different information regarding the contributions made by atomic interactions.

Scheme 1 shows the full decomposition scheme, and Scheme S1 in the Supporting Information shows the alternative decomposition in terms of self- and interatomic-DD. With regards to our proposed nomenclature, we will use (1) FALDI-ED, where ED can stand for either fragment, atomic, localized, delocalized, intra (self) or interatomic electron density (FED, AED, LED, DED, SED, or IED, respectively) to describe the FALDI decomposition when it is applied to the static electron density distribution of a single molecule, and (2) FALDI-DD, where DD can stand for either FDD, ADD, LDD, DDD, SDD, and IDD to describe the FALDI decomposition when it is applied to the change in density arising from a conformational change.

Lastly, we wish to note that the same decomposition is applicable to an orthodox fragmentation of the molecular system that involves promolecular deformation densities by setting ${}^{ref}\delta_{ij}(\mathbf{r}) = 0$, $\Delta_c \delta_{ij}(\mathbf{r}) = {}^{fin}\delta_{ij}(\mathbf{r})$ and $\mathbf{A}_i = \mathbf{1}$ for all i . The



Scheme 1. Proposed FALDI-DD decomposition of the deformation density.

FALDI-DD scheme can therefore be used to interpret and analyse orthodox deformation densities, as well as compare various FALDI-DD terms of both orthodox and conformational deformation densities. Hence, our decomposition scheme can be used in conjunction with the very useful natural orbital expansion of the various components of $\Delta\rho(\mathbf{r})$ (as is implemented in ETS-NOCV), to provide additional insight to the changes occurring during bond formation.

Computational Details

All systems were optimized in Gaussian 09, rev.D,^[53] using RB3LYP-D3/6-311++G(d,p) in gas-phase. AIMAll version 16.05.18^[54] was used to calculate atomic overlap matrices for all systems, using suitable wavefunction files generated by Gaussian and at the same level of theory and basis set. Atomic

overlap matrices were used to perform the FALDI decomposition and conformational deformation densities using in-house software. All FALDI isosurfaces were visualized using VMD.^[55] Orthodox deformation density calculations were performed and visualized with ADF 2014,^[56] using RB3LYP-D3/ATZP; however, similar calculations were also performed in Gaussian and visualized with VMD for comparison. Gaussian co-ordinates for all optimized molecules as well as promolecules are included in Section S1 of the Supporting Information.

Results and Discussion

Our focus is on gaining an insight on the density changes associated with the formation of an intramolecular interaction from the FALDI perspective and, as a case study, we will analyse a classical intramolecular H-bond in the lowest energy conformer of protonated ethylenediamine (Hen^+) used here as a *fin* state of Hen^+ . The $\text{N8-H11}\cdots\text{N7}$ bond (Fig. 3), with $d(\text{N7},\text{H11}) = 2.110 \text{ \AA}$, is formed spontaneously and, relative to a linear conformer, used here as a *ref* state, the molecular energy decreases, for example, by $-4.1 \text{ kcal}\cdot\text{mol}^{-1}$ at the MP2/6-311++G(d,p) in aqueous solution. In sections that follow we will perform a brief comparative analysis between an orthodox approach, using various fragmentation schemes, and the FALDI method reported in this work. Furthermore, we will demonstrate some unique features of FALDI by exploring deformation densities resulting from a *ref* \rightarrow *fin* structural change with a main focus on the $\text{H}_2\text{N8-H11}\cdots\text{N7H}_2\text{-C1}$ region.

Total deformation density from orthodox $\Delta\rho(r)$ and FALDI $\Delta\rho_c(r)$

An orthodox decomposition approach requires partitioning of a molecule to promolecules (or fragments). Four partitioning schemes were tested here where (i) Hen^+ was cut in the middle, which resulted in two, $-\text{CH}_2\text{NH}_2$ and $-\text{CH}_2\text{NH}_3^+$ fragments ($2F_1$ scheme), (ii) NH_2 group was cut off, hence $-\text{NH}_2$ and $-\text{CH}_2\text{CH}_2\text{NH}_3^+$ fragments were formed ($2F_2$ scheme), (iii) NH_3^+ group was cut off resulting in two, $-\text{NH}_3^+$ and $-\text{CH}_2\text{CH}_2\text{NH}_2$ fragments ($2F_3$ scheme), and (iv) both terminal groups were

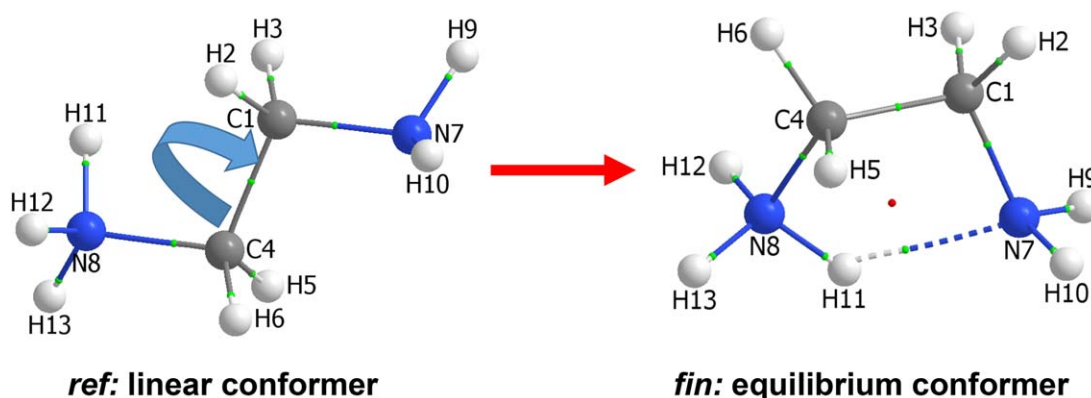


Figure 3. Molecular graphs of linear Hen^+ (*ref*) and equilibrium Hen^+ (*fin*) conformers for the calculation of conformational deformation densities using FALDI. The *ref* conformer is rotated around the $\text{N7},\text{C1},\text{C4},\text{N8}$ dihedral angle. Atoms' numbering is also shown. [Color figure can be viewed at wileyonlinelibrary.com]

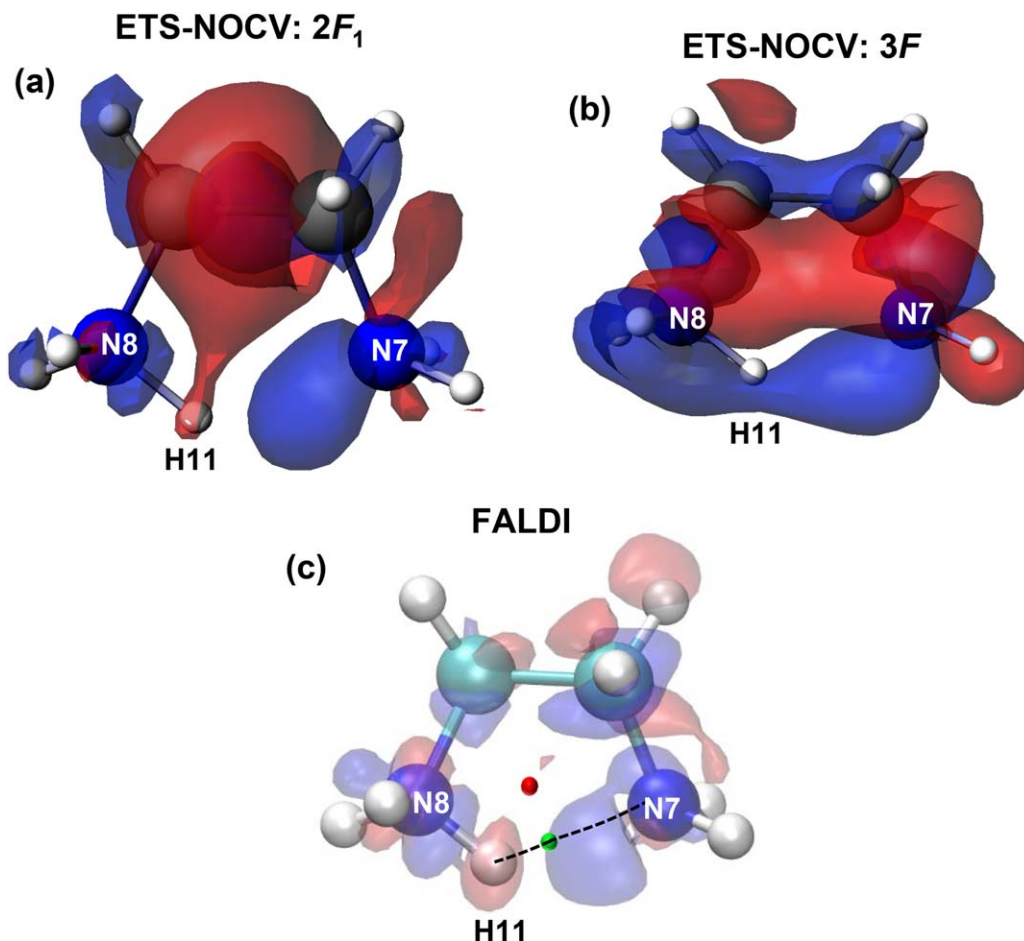


Figure 4. Total deformation densities: (a) and (b) computed in ADF using indicated partitioning scheme, (c) from FALDI, using the conformational approach. Red and blue regions indicate a decrease and increase in density, respectively, relative to the radical fragments in (a) and (b) and on the *ref* → *fin* structural change of Hen^+ in (c). All isosurfaces are at 0.0025 au. [Color figure can be viewed at wileyonlinelibrary.com]

cut off generating three, $-\text{NH}_2$, $-\text{CH}_2\text{CH}_2-$ and $-\text{NH}_3^+$ fragments (3F scheme; this is pictorially presented in Scheme S2 in the Supporting Information). Each scheme was chosen in such a way as to describe the formation of the $\text{N8}-\text{H11}\cdots\text{N7}$ intramolecular interaction.

As expected, these four partitioning schemes generated quite different pictures of the total deformation density (examples obtained from $2F_1$ and $3F$ partitioning schemes are shown in Fig. 4) because each fragmentation had to break different covalent bonds. This had a significant impact not only on density changes associated with the formation of the same $\text{N8}-\text{H11}\cdots\text{N7}$ intramolecular interaction, but also throughout a molecule—a full set of total deformation densities computed from four partitioning schemes is shown in Figure S1 in the Supporting Information. Clearly, selecting a specific fragmentation scheme is not always a trivial exercise as it might be very impactful with regards to a final interpretation of energetic components, such as binding energy or Pauli, orbital and electrostatic terms of an interaction, computed from EDA. Most likely, from a visual inspection and analysis of energy terms computed, one would select the total deformation density

generated from the $2F_1$ scheme. This is because it resulted in the picture visualizing deformation densities within a region of the intramolecular interaction best when related to chemist's general knowledge—Figure 4a. Such a heuristic approach is an easy choice for well-understood interactions, such as classical H-bonds, but is much more difficult to determine for unknown or controversial interactions, such as $\text{CH}\cdots\text{HC}$. Unavoidably, an additional and dominating contribution to the deformation density is observed which resulted from reconstruction of the covalent C—C bond when two promolecules, $-\text{CH}_2\text{NH}_2$ and $-\text{CH}_2\text{NH}_3^+$, were brought together from an infinite separation.

It is clear from Figure 4 that the use of promolecular reference states has a somewhat undesirable yet unavoidable effect on the intramolecular interaction of interest. The extent of this effect has been difficult to determine. Clearly, it is desirable to be able to obtain deformation densities for intramolecular interactions without needing to use radical reference states, which is the primary justification for this work. To achieve such deformation densities, FALDI makes use of real, chemically viable reference states, here from a linear to equilibrium conformer of Hen^+ —Figure 3.

FALDI-on-promolecules

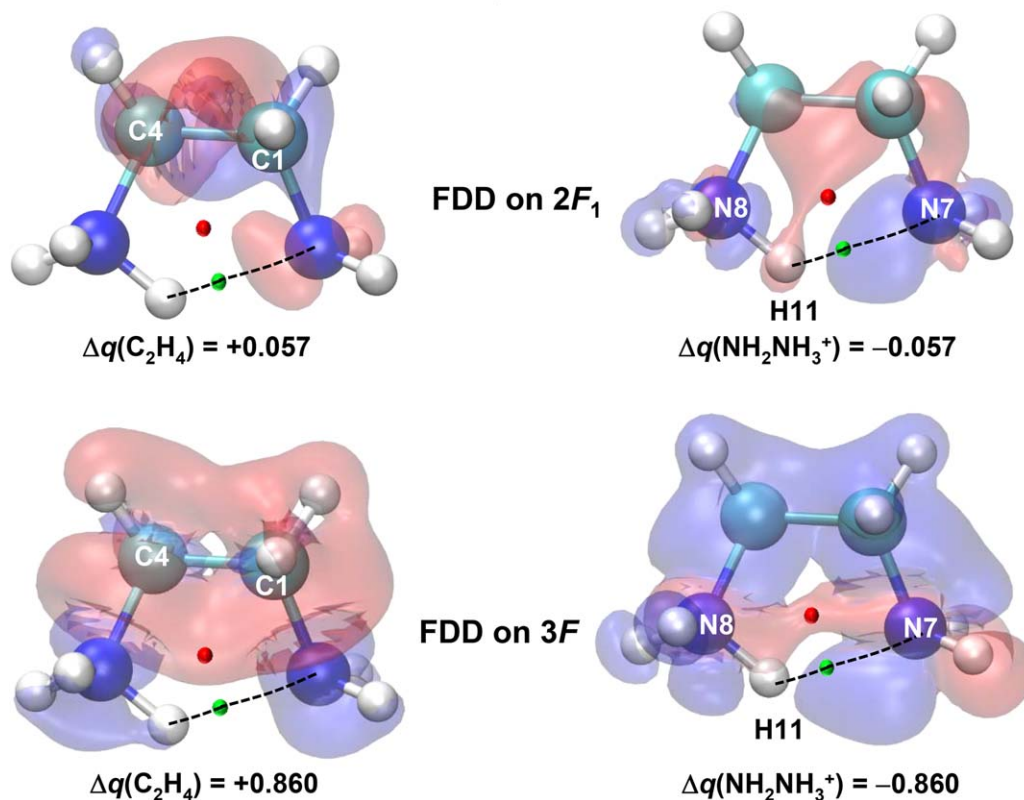


Figure 5. FALDI-on-promolecules generated Fragment-DD from the $2F_1$ and $3F$ partitioning schemes for $-\text{C}_4\text{H}_2-\text{C}_1\text{H}_2-$ and combined terminal groups using orthodox promolecules as a reference state. All isosurfaces are at 0.0025 au. [Color figure can be viewed at wileyonlinelibrary.com]

A 3D isosurface for the total deformation density (TDD) resulting from the conformational FALDI approach is shown in Figure 4c. Comparing the two pictures in Figure 4a (EDA) and 4c (FALDI) reveals that there are similar features in the $\text{H}_2\text{N}\cdots\text{HNH}_2^+$ region, namely (i) an accumulation of density is observed for N7 and N8 whereas H11 is losing density and (ii) polarization of terminal groups is observed which appears to be more significant for $-\text{N}_7\text{H}_2$ from ETS-NOCV whereas FALDI points at $-\text{N}_8\text{H}_3^+$. However, the FALDI-generated picture reveals additional regions that experienced a change in the density on a linear \rightarrow equilibrium structural change. Importantly, these regions correspond to the atomic population changes well as, for example, we obtained from QTAIM $\Delta N = +15, -8, -59,$ and -21 me for C1, C4, H2, and H3, respectively (both H-atoms of the C_1H_2 group). Such a picture is difficult to recover from an orthodox approach because it is largely distorted by the deformation density of a covalent bond formation.

To conclude our analysis of the intramolecular interaction region from the total deformation density perspective, it is clear that the FALDI-based approach displays similar features as those obtained from an orthodox approach, but without using radical reference states and without the potential pitfalls. Furthermore, FALDI density decomposition can also be applied on any number of fragments generated in an orthodox fashion, by cutting a molecule to radical-state promolecules (at

this stage, this is limited to wavefunctions generated by Gaussian). Although we are not going to extensively use the FALDI-on-promolecules approach in this work, it is important to stress that we were able to recover ADF-generated images of the total-DD using four partitioning schemes mentioned above; this is illustrated in Figures S2 in the Supporting Information. This gives us an assurance that our approach is working well and no major bugs are present in the in-house developed software package. Finally, a full set of fragment deformation densities (FDD), calculated by the FALDI-on-promolecules approach, was obtained for the $-\text{CH}_2\text{CH}_2-$ and $\text{H}_2\text{N}\cdots\text{HNH}_2^+$ fragments. It is presented in Figure S3 and S4 in the Supporting Information, showing how pictures recovered depend on a particular partition scheme used; for illustration purposes, FDDs obtained from $2F_1$ and $3F$ are shown in Figure 5. Summing up fragment-DDs from, for example, the $2F_1$ partitioning scheme, one obtains the total-DD shown in Figure 4a. This demonstrates that the FALDI decomposition can provide additional insight to orthodox deformation density studies by uncovering the origin of computed total-DD distribution.

Atomic FALDI deformation densities

It is important to realize that the total deformation density computed from the FALDI scheme, Figure 4c, does not depict details related to individual atoms or functional groups. This is because the total-DD distribution is the sum of either atomic-

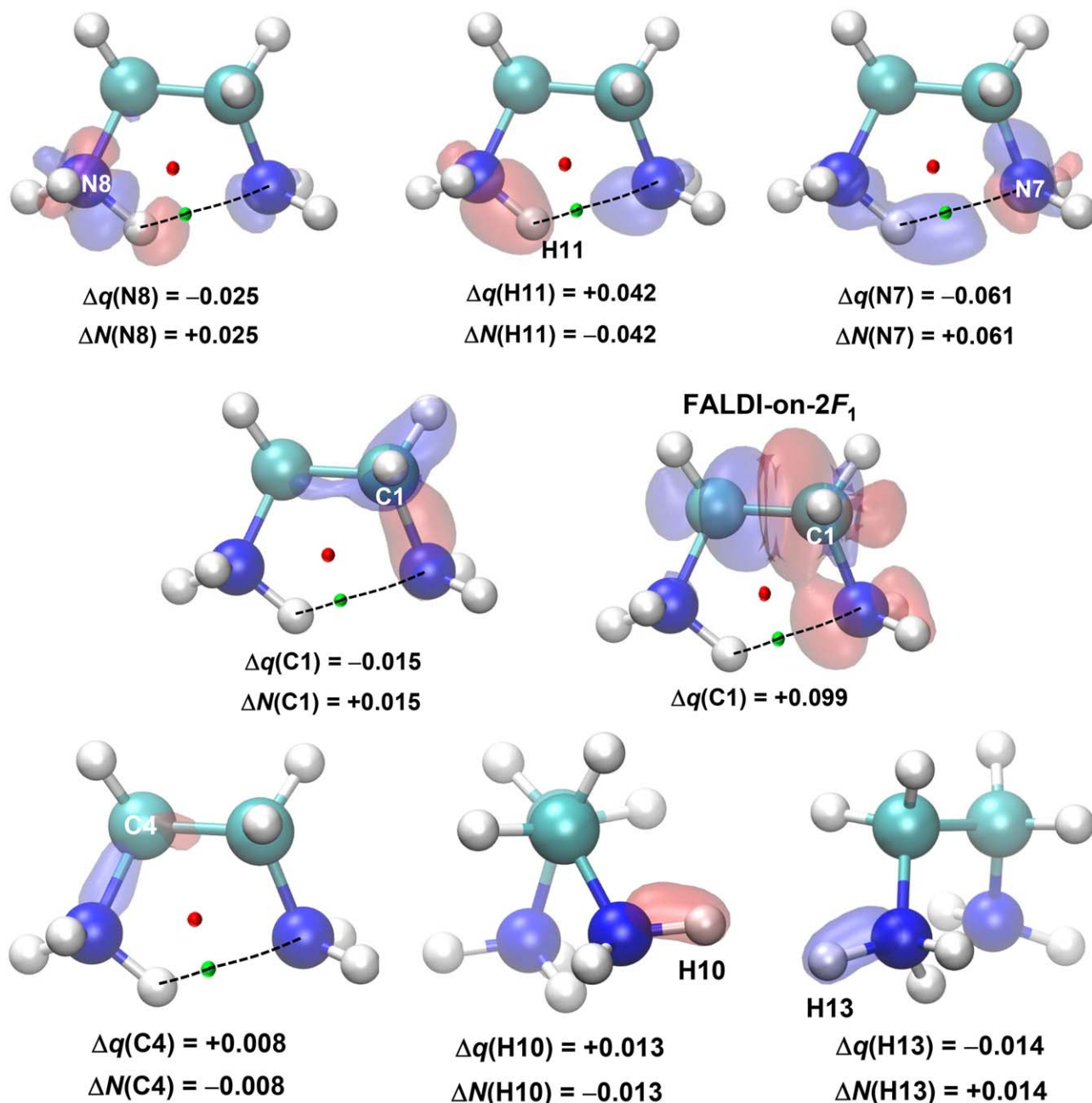


Figure 6. ADD distributions and changes in QTAIM atomic net charges and atomic populations (both in *e*) obtained for indicated atoms on the *ref* → *fin* structural change. Isosurfaces for C4, H10, and H13 are presented at 0.001 au; all other isosurfaces are at 0.0025 au. [Color figure can be viewed at wileyonlinelibrary.com]

and/or fragment-DD distribution. Hence, to uncover the origin of the conformational, from *ref* to *fin* state, deformation density in Hen^+ , in terms of individual atoms' contributions, we computed atomic deformation densities (ADDs) for each atom - a full set of FALDI-generated atomic-DDs is shown in Figure S5 in the Supporting Information, and for selected atoms in Figure 6. According to the IUPAC recommendation,^[13] a wide range of H-bonds should be represented as $\text{X-H}\cdots\text{Y-Z}$, where X-H represents the hydrogen bond donor and, in the case of an intramolecular H-bond, Y-Z represents a molecular fragment acting as the acceptor, where Y is bonded to Z .

Moreover, a classical intramolecular H-bond is commonly interpreted using the $\text{X-H}\cdots\text{Y}$ notation when H is bonded to electronegative atom, O, N or F.^[57] Following this recommendations, we have analyzed $\text{X} = \text{N8}$, $\text{H} = \text{H11}$, $\text{Y} = \text{N7}$, and $\text{Z} = \text{C1}$ as this selection affords us both notations and it was of great interest to find out if there are specific features of these atoms' atomic-DDs (Fig. 6) which could be linked with 4- and/or 3-atom representation. Comparing data shown in Figure S5 in the Supporting Information reveals that by far, in terms of 3D spaces occupied, the most significant changes in density were indeed obtained for atomic-DDs of C1, N7, H11, and N8.

As a matter of fact, these atoms are the only ones in Hen^+ for which the ADD is delocalized toward more than one neighboring atom. This is indicative of their most important contributions made to the conformational total-DD distribution change and can be used as a textbook example in support of the IUPAC recommendation that also illustrates, in 3D space, atomic contributions on the formation of a classical intramolecular bond.

The nature and mechanism of a classical intermolecular H-bonding, as $\text{X-H}\cdots\text{Y}$, was studied extensively for years. It has been established from, for example, EDA,^[30] DFT,^[58] and IQA studies^[59] that on formation of a $\text{X-H}\cdots\text{Y}$ bond some charge transfer (CT) from Y (here N7) to X-H (here N8-H11) always takes place. FALDI recovers this notion fully as atomic density of N7 is delocalized to the N8-H11 as well as N7-H11 bonding region. In the latter case, density is placed close to H11 along the AIL which must facilitate formation of the AIL. However, we also see in Figure 6 that N7 is also delocalizing some density in the N7-C1 region and this is counteracted by C1 which is removing its density from this bonding region and placing it mainly in the C1-H2 interatomic region. A significant interplay in density redistribution between N7 and C1 in combination with large space occupied by C1's atomic-DD further supports the 4-atom IUPAC notation.

An interesting picture is observed for N8 of the hydrogen bond donor. This atom is placing its density in the H11-N8 bonding region as well as on N7 (a proton acceptor) by removing it from H11 which is accompanied by charge redistribution, hence polarization of its own atomic basin. Furthermore, changes in density attributed to N8 near N7 and H11 are well separated and localized along the AIL.

It is known that H (H11) is losing charge and the FALDI-generated picture suggests that this atom's density is being delocalized by removing it not only from its own basin but also from the entire bonding region of the hydrogen bond donor H11-N8, as well as from the non-bonding region of N8. Noticeably, the removed density is placed entirely on the proton acceptor N7 and, importantly, it is located mainly along an AIL, facilitating N7-H11 bonding even further.

All these atomic density rearrangements provide the origin of polarization effects observed in Figure 4c in the entire N8-H11-N7-C1 region. However, it appears that pictures obtained for N7, H11, and N8 in Figure 6 also provide some support for the $\text{X-H}\cdots\text{Y}$ representation of a classical H-bonding. To this effect, we note that atomic-DDs of these atoms are mainly delocalized in the N8-H11-N7 region and, importantly, the two N atoms are the only ones which, not being neighbors, donated density through space to each other.

To complete the analysis of deformation densities computed for individual atoms, we would like to note that, excluding atoms of the N8-H11-N7-C1 bond, all other atoms show highly confined atomic-DDs which are placed almost entirely along a single covalent bond. To illustrate this, examples for C4 (to compare it with C1), H10, and H12 of the $-\text{NH}_2$ and $-\text{NH}_3^+$ terminal groups, respectively, are shown in Figure 6. Finally, an atomic-DD computed for C1 from the $2F_1$

partitioning scheme, marked as FALDI on $2F_1$, is also shown in Figure 6. It is immediately noticeable that FALDI-generated conformational atomic-DD for C1, when the *ref* \rightarrow *fin* structural change took place, is extremely different from that obtained using a FALDI-on-promolecules approach employing the $2F_1$ partitioning scheme. Whereas FALDI shows that the atomic-DD is delocalized in the immediate vicinity of C1 and neighboring atoms, totally unexpected, much larger and almost throughout a molecule atomic-DD was obtained from the FALDI-on-promolecules approach. Such an atomic-DD distribution nicely illustrates how reconstructing a C-C covalent bond has a detrimental impact on the picture recovered, especially in terms of its impact on the intramolecular NH-N interaction of interest. Furthermore, relative to the linear conformer of Hen^+ , deformation density of C1 from $2F_1$, when the FALDI-on-promolecules approach was used, has resulted in the change of the net atomic charge, $\Delta q(\text{C1}) = +0.099e$ which is totally different in value and trend when compared with $-0.015e$ computed from QTAIM.

Fragment FALDI deformation densities

Atomic resolution implemented in the FALDI scheme provides an invaluable insight on atoms' involvement in bonding. However, formation of an intramolecular interaction can also be explored from the perspective of functional groups. As showed in Figure 4c, formation of the intramolecular bond is a holistic, molecular wide event in terms of a charge redistribution and resultant polarisation effects. Hence, one would expect that the picture recovered using functional groups (FGs) should provide an additional and, to some extent, more general description. Atoms involved in H-bonding are members of three FGs and they all were used as fragments in FALDI's scheme; 3D representation of fragment-DDs attributed to the $-\text{C1H}_2-$, $-\text{N7H}_2$, and $-\text{N8H}_3^+$ FGs is shown in Figure 7.

A comparative analysis of fragment-DDs computed for the $-\text{N7H}_2$ and $-\text{N8H}_3^+$ functional groups (Fig. 7) with ADDs of N7, H11, and N8 atoms in Figure 6 leads to the conclusion that there are similar, in principle identical in nature, features for both atomic and fragment resolution. This means that our interpretation of atomic deformation densities can be entirely extended to fragment-DDs. This finding is of fundamental significance as it provides additional information on the origin of the total-DD shown in Figure 4c by providing evidence of a negligible contribution made by H-atoms not directly involved in the bond formation (H9 and H10 of $-\text{N7H}_2$, H12, and H13 of $-\text{N8H}_3^+$). The only difference is observed in the region of H-atoms of the $-\text{C1H}_2-$ fragment and the computed depletion of density correlates well with the largest decrease in the atomic population among all atoms of Hen^+ found for H2 whereas H11 experienced second largest outflow of density.

The combined deformation densities for two terminal groups, as NH_2NH_3^+ , produced a picture which is also consistent with a general description of a classical intermolecular $\text{X-H}\cdots\text{Y}$ bond. We observe a combined charge redistribution which resulted in larger(smaller) charge accumulation on a proton acceptor N7(donor N8) and density depletion on H11,

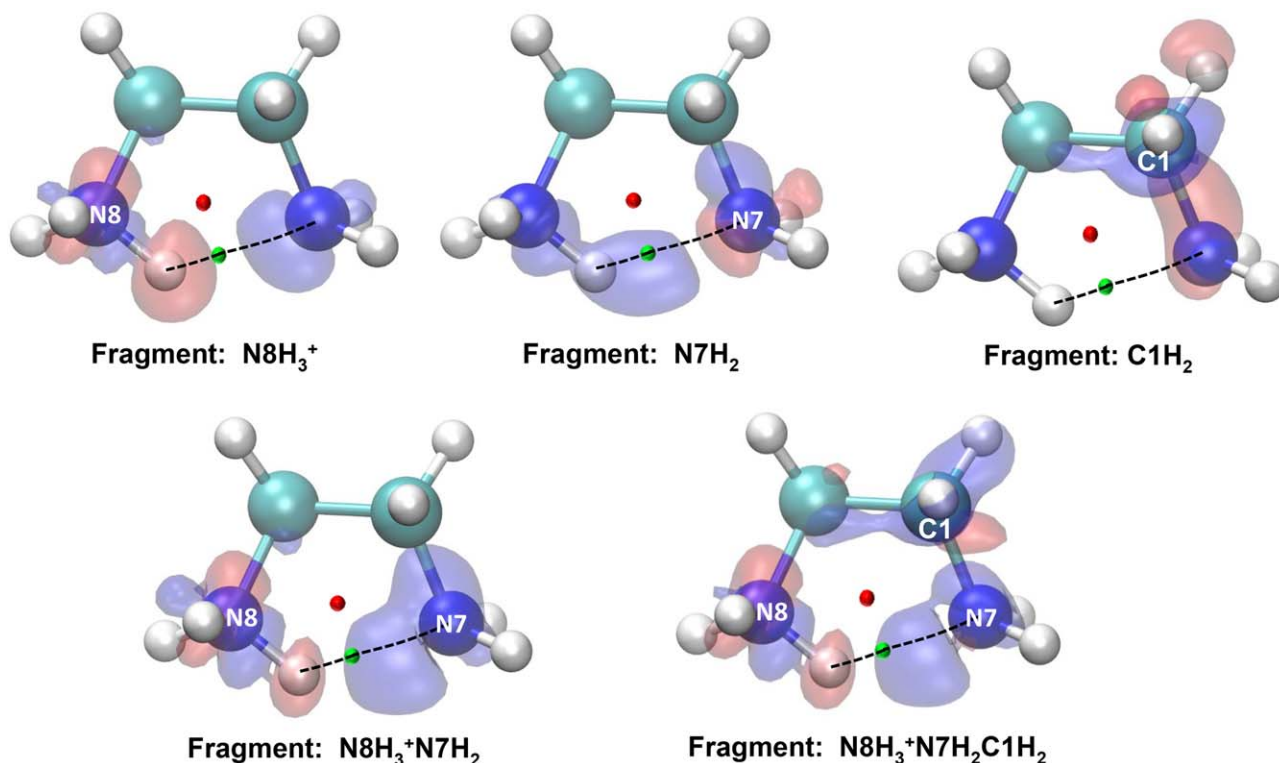


Figure 7. FDD distributions obtained for indicated fragments on the *ref* → *fin* structural change. All isosurfaces are at 0.0025 au. [Color figure can be viewed at wileyonlinelibrary.com]

a common feature also found from the IQA studies of a number of dimers using the full-valence CAS/6-311 + G(d,p) wavefunction.^[59] Moreover, a general trend in the atomic population change, when the structure of Hen^+ changed from the linear to equilibrium conformer, $\Delta N(X) > |\Delta N(\text{H})| > \Delta N(\text{Y})$ obtained here at B3LYP/6-311++G(d,p) is the same when compared with that computed as a difference in atomic populations between monomers and dimers.^[59] This shows that general features of the charge redistribution, here nicely illustrated by the fragment-DDs, and trends in computed atomic population changes are comparable and representative, regardless of level of theory used and the kind of classical H-bonding, either intermolecular or intramolecular.

In conclusion, the atomic- and fragment-based analyses of deformation densities provided an invaluable fundamental insight on the mechanism of an interaction formation. Furthermore, atomic- and fragment-DDs, by providing the origin, are extremely helpful in understanding and interpreting the overall picture obtained from the total deformation density. Regarding the two different representations ($\text{X}-\text{H}\cdots\text{Y}-\text{Z}$ and $\text{X}-\text{H}\cdots\text{Y}$) of the hydrogen bond, it appears that the four atom $\text{N8}-\text{H11}\cdots\text{N7}-\text{C1}$ description represents the intramolecular bonding better, because the atomic-DD distribution for C1 (Fig. 6) revealed that C1 also and significantly contributes to the density within the $\text{NH}\cdots\text{N}$ bonding region. Such a result cannot be obtained from a charge decomposition scheme, such as QTAIM, and is only revealed through FALDI's distributions in real space.

Diatomic and intrafragment interactions from the FALDI perspective

In the FALDI scheme, each atomic or fragment distribution can be decomposed into 1- and 2- center contributions, either through localized and delocalized distributions (LDD and DDD, respectively), or into intra-(self)atomic and interatomic contributions (SDD and IDD, respectively). The latter decomposition is particularly useful to investigate the changes on formation of a noncovalent and multi-center interaction. This is of special interest to us as it should provide a unique insight on a number of aspects of an interaction formation. Our main focus is on the $\text{N8}-\text{H11}\cdots\text{N7}-\text{C1}$ hydrogen bond (observed in the equilibrium structure of Hen^+) which is characterized by the presence of Bader's AIL. Figure 8 displays the overall contributions (including delocalized density) made by diatomic interactions (interatomic-DD isosurfaces), computed for four most relevant diatomic interactions. Figure S6 Supporting Information displays the relevant interatomic delocalized density contributions to the deformation density, showing the real-space distributions of QTAIM-defined delocalization indices.

It is important to stress that in the IQA world all diatomic fragments are treated on equal footing and we wondered whether our analysis, based on interaction deformation densities, can show us unique features one could link with the formation, or an absence, of a BP. From a general inspection of isosurfaces in Figure 8 it is immediately seen that red(blue) isosurfaces representing a decrease(increase) in density in the

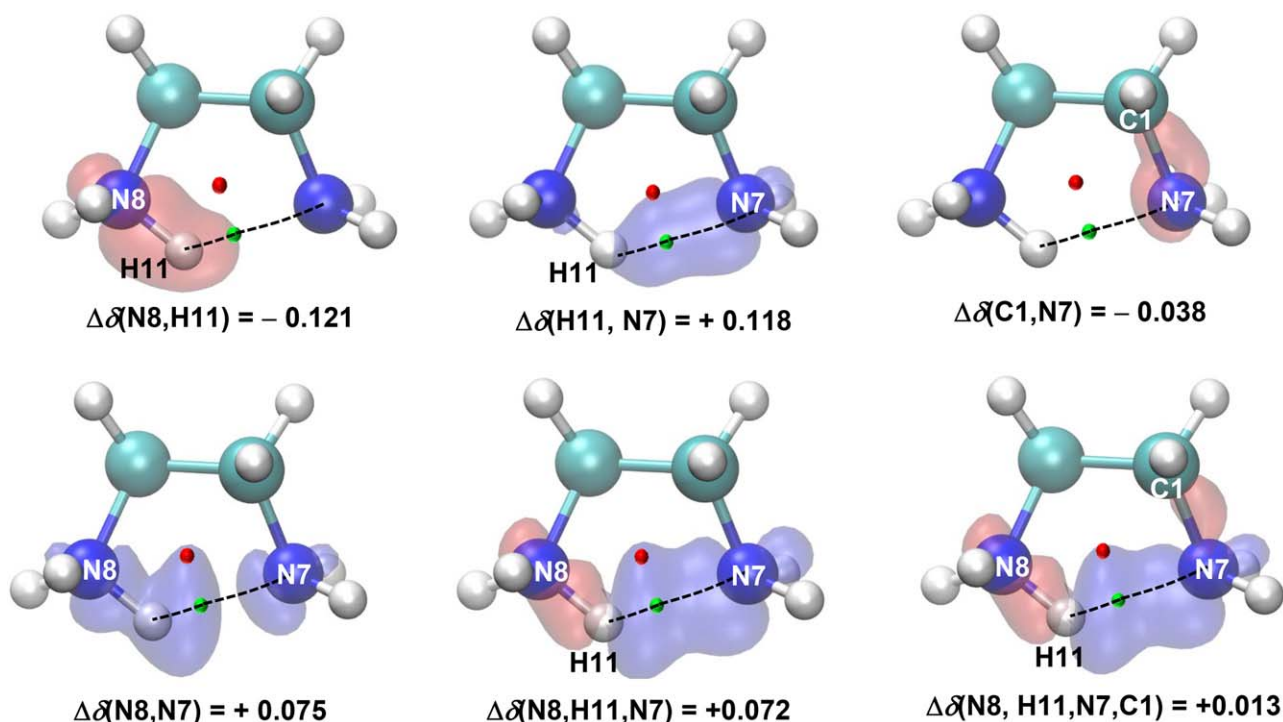


Figure 8. IDD distributions obtained for the indicated diatomic and intrafragment interactions. Red and blue regions indicate a decrease and increase in density, respectively, relative to the reference conformer. All isosurfaces are at 0.0025 au. Changes in QTAIM-defined delocalization indices are indicated. [Color figure can be viewed at wileyonlinelibrary.com]

interatomic region correlate perfectly well with the sign, negative(positive), of the delocalization indexes.

Because we analyze the outflow (red) and inflow (blue isosurface) of density from an interatomic region, it immediately appeals to the exchange-correlation (XC) term of the IQA-defined interatomic (or intrafragment) interaction energy. Looking at pictures recovered for the diatomic interaction in Figure 8 we note that the DI decreased for {C1,N7} and {N8,H11} fragments with the latter correlating perfectly well with our general knowledge, and (ii) increased for the {N7,H11} as well as {N7,N8} fragments, where the result obtained for the former corresponds to the formation of an intramolecular interaction in the form of Bader's BP. The above trends are fully supported by the computed $V_{XC}^{A,B}$ terms for relevant diatomic interactions, as we obtained $\Delta V_{XC}^{A,B} = +6.57$ and $+18.80$ kcal·mol⁻¹ for {C1,N7} and {N8,H11} interactions, and -16.59 and -8.02 kcal·mol⁻¹ for {N7,H11} and {N7,N8} fragments, respectively. The interaction-DD distributions, however, allow for investigation of the changes which each interaction contributes to the deformation density throughout all space. Comparing the IDD for the {N7,H11} and {N7,N8} fragments provides an important hint. The N7...N8 interaction-DD distribution extends through the N8—H11 bond and N7...H11 interaction. However, there is a fundamental difference between interaction-DD distributions of {N7,H11} and {N7,N8}: whereas the former has a BP the latter does not have a channel-like feature of the N7...H11 interaction-DD distribution even though the density shared between N7 and N8 shows a large

maximum exactly at the geometric middle point between the two atoms. In general, this correlates very well with density topology recovered from QTAIM and the concept of QTAIM-defined bond paths as privileged exchange channels proposed by Pendás et al.^[22] Importantly, it appears that defined here interaction- as well as delocalized-DD distributions might provide a powerful tool to investigate the underlying delocalization and interatomic density patterns corresponding to a presence/absence of a BP in real-space. One must recall that an attempt of using the value of the delocalization indices came short in some instances in supporting (or explaining) a presence/absence of BP.^[60] It is our intention to explore this area in future studies.

Conclusions

The simplicity and extreme usefulness of the general deformation density in revealing how charge is accumulated or depleted on the formation of an intermolecular interaction is unfortunately marred by a number of difficulties in interpreting intramolecular interactions using orthodox deformation densities. A necessity of breaking existing bonds to study the formation of an intramolecular interaction severely limits any EDA-based scheme to using radical reference states. This work introduces and implements fragment, atomic, localized, delocalized and intra- as well as interatomic contributions that are computed within the novel FALDI charge decomposition scheme as an alternative methodology which is not limited to

potentially unchemical reference states in studying intramolecular interactions. The FALDI scheme is a result of a paradigm shift from analyzing molecular deformation density obtained from reconstructing a molecule from radical fragments to computing decomposed density distributions in two structural states (*final* and *reference*) of a molecule which are then used to generate atomic, fragment as well as total deformation densities resulting from the structural *ref*→*fin* transformation. To achieve that we have made use of few concepts originating from the DAFH^[47,48] method and introduced a complete decomposition of the electron density into 1- and 2-center contributions, including direct distributions of QTAIM-defined localization and delocalization indices in real-space. To account for asymmetrical transformations of 2-center distributions, we arbitrarily implemented a first approximation to show that FALDI can be used for deformation density calculations, on which can be improved in the future.

As such, the derived expressions for the atomic, fragment and total deformation densities for any state of a molecule (giving static density distributions) can be used on EDA-generated fragments as well. Importantly, in the latter case, which we call FALDI-on-promolecules approach, EDA-generated deformation densities are fully recovered providing validation of the protocol developed in this work. In principle, applying our approach on the same intramolecular interaction revealed a picture with similar features as found from the orthodox EDA approach. However, because FALDI eliminates the interference of the reconstructing of a nearby covalent bond, the conformational deformation density isosurfaces displayed a number of details involving the H-bond which were either missing or masked when promolecular approaches were used.


As a case study, we used linear (as a *ref* state) and the lowest energy conformer (as a *fin* state) of protonated ethylenediamine, Hen^+ . The mechanism and origin of spontaneously formed intramolecular interaction in *fin*, $\text{N}-\text{H}\cdots\text{N}$, was uncovered using deformation densities on atomic and molecular fragment levels. We have shown, for the first time in real space, how four atoms contribute to the resultant molecular deformation density on the interaction formation. Interestingly, these atoms' contributions can be used as a textbook example in support of the IUPAC recommendation, namely $\text{X}-\text{H}\cdots\text{Y}-\text{Z}$ ($\text{N}-\text{H}\cdots\text{N}-\text{C}$ in the case studied here), in representing intramolecular H-bonding. We also uncovered the influence of the Z atom (here C1) on the density distribution in the bonding region of $\text{H}\cdots\text{N}$, a result which was previously difficult to obtain when the C—C or other bonds were cut in an orthodox deformation density experiment. Furthermore, we also found unique features which explain the commonly used $\text{N}-\text{H}\cdots\text{N}$ notation; the atomic deformation densities of these atoms are mainly delocalized in the entire $\text{N8}-\text{H11}\cdots\text{N7}$ region and, importantly, the two N atoms are the only ones which, not being neighbors, donated density through space to each other. A 3D picture of the deformation density computed for the $\text{N8}-\text{H11}\cdots\text{N7}$ fragment nicely explains why a BP is only observed between the H-atom and the proton acceptor N-atom even though both N-atoms delocalize their densities to

each other. Whereas there is a continued increase in density in the bonding region of $\text{H11}\cdots\text{N7}$, which is recovered by the presence of a BP between them, the interatomic region between N-atoms not only does not show such a channel of increased density but also a resultant (final) depletion in density is observed close to N8-atom along the trajectory between N8 and N7.

The added advantage of the FALDI scheme is in its ability of obtaining the total deformation from either atomic or/and fragment contributions. Such approach provides an invaluable insight on the origin and mechanism leading to or associated with the deformation density computed for an intramolecular interaction. This is of a fundamental significance as it should allow gaining an insight on the role played by a molecular environment (presence/absence of specific functionalities) in terms of density deformation leading to an intramolecular interaction. It is our conviction that FALDI might explain, on a fundamental level, the nature and origin of so many kinds of interactions. As a matter of fact, this is not limited to intramolecular ones as expressions derived can be equally used to understand all kinds of chemical bonds either in a final product or on the formation of these bonds, hence providing an insight on a mechanism leading to density sharing. Furthermore, delocalized as well as interatomic deformation densities (specifically defined within the FALDI scheme) should shed some light on the presence or absence of Bader's atomic interaction lines (or bond paths) that, in some instances, became a subject of heated debates when interpreted in terms of bonding or nonbonding character from a classical chemist's perspective. To this effect, the real-space nature of FALDI's delocalized density isosurfaces computed for the $\text{N}-\text{H}\cdots\text{N}$ region corroborated fully with the interpretation of AILs as privileged exchange channels^[22] and can provide significant support to this unorthodox interpretation; we are convinced that FALDI provides a promising method with which one should be able to elucidate the fundamentals behind the presence/absence of AILs and their interpretations in terms of chemical bonding. Plotting interatomic delocalized density in real space also opens up additional avenues for studying concepts such as aromaticity, resonance and long-range atomic communication. Finally, we must stress that the FALDI decomposition also provides a strong density-based investigative tool for both deformation as well as static electron densities, which we hope will find use with both experimentalists as well as theoreticians.

Keywords: deformation density · fragment · atom · localized · delocalized · and interatomic · domain averaged Fermi hole · intramolecular interactions · computational chemistry

How to cite this article: J. H. de Lange, I. Cukrowski. *J. Comput. Chem.* **2017**, *38*, 981–997. DOI: 10.1002/jcc.24772

 Additional Supporting Information may be found in the online version of this article.

- [1] J. J. Novoa, M.-H. Whangbo, J. M. Williams, *J. Chem. Phys.* **1991**, *94*, 4835.
- [2] K. N. Robertson, O. Knop, T. S. Cameron, *Can. J. Chem.* **2003**, *81*, 727.
- [3] R. H. Crabtree, *Science* **1998**, *282*, 2000.
- [4] R. Custelcean, J. E. Jackson, *Chem. Rev.* **2001**, *101*, 1963.
- [5] M. J. Calhorda, *Chem. Commun.* **2000**, 801.
- [6] T. B. Richardson, S. de Gala, R. H. Crabtree, P. E. M. Siegbahn, *J. Am. Chem. Soc.* **1995**, *117*, 12875.
- [7] R. H. Crabtree, P. E. M. Siegbahn, O. Eisenstein, A. L. Rheingold, *Acc. Chem. Res.* **1996**, *29*, 348.
- [8] S. J. Grabowski, W. A. Sokalski, J. Leszczyński, *Chem. Phys.* **2007**, *337*, 68.
- [9] U. Koch, P. L. A. Popelier, *J. Phys. Chem.* **1995**, *99*, 9747.
- [10] P. Hobza, Z. Havlas, *Chem. Rev.* **2000**, *100*, 4253.
- [11] I. Akorta, I. Rozas, J. Elguero, *Chem. Soc. Rev.* **1998**, *27*, 163.
- [12] M. J. Calhorda, *Chem. Commun.* **2000**, *10*, 801.
- [13] E. Arunan, G. R. Desiraju, R. A. Klein, J. Sadlej, S. Scheiner, I. Alkorta, D. C. Clary, R. H. Crabtree, J. J. Dannenberg, P. Hobza, H. G. Kjaergaard, A. C. Legon, B. Mennucci, D. J. Nesbitt, *Pure Appl. Chem.* **2011**, *83*, 1637.
- [14] P. Politzer, P. Lane, M. C. Concha, Y. Ma, J. S. Murray, *Mol. Model.* **2007**, *13*, 305.
- [15] S. Kawai, A. Sadeghi, F. Xu, L. Peng, A. Orita, J. Otera, S. Goedecker, E. Meyer, *ACS Nano* **2015**, *9*, 2574.
- [16] G. R. Desiraju, P. S. Ho, L. Kloo, A. C. Legon, R. Marquardt, P. Metrangolo, P. Politzer, G. Resnati, K. Rissanen, *Pure Appl. Chem.* **2013**, *85*, 1711.
- [17] F. Groenewald, C. Esterhuysen, J. Dillen, *Theor. Chem. Acc.* **2012**, *131*, 1.
- [18] W. Wang, B. Ji, Y. Zhang, *J. Phys. Chem. A* **2009**, *113*, 8132.
- [19] E. A. Zhurova, C. F. Matta, N. Wu, V. V. Zhurov, A. A. Pinkerton, *J. Am. Chem. Soc.* **2006**, *128*, 8849.
- [20] C. F. Matta, J. Hernández-Trujillo, T. H. Tang, R. F. W. Bader, *Chem. Eur. J.* **2003**, *9*, 1940.
- [21] R. F. W. Bader, *J. Phys. Chem. A* **2009**, *113*, 10391.
- [22] A. M. Pendás, E. Francisco, M. A. Blanco, C. Gatti, *Chem. Eur. J.* **2007**, *13*, 9362.
- [23] F. Cortés-Guzmán, J. Hernández-Trujillo, G. Cuevas, *J. Phys. Chem. A* **2003**, *107*, 9253.
- [24] J. Echeverría, G. Aullón, D. Danovich, S. Shaik, S. Alvarez, *Nat. Chem.* **2011**, *3*, 323.
- [25] J. Poater, M. Solà, F. M. Bickelhaupt, *Chem. Eur. J.* **2006**, *12*, 2889.
- [26] J. Poater, M. Solà, F. M. Bickelhaupt, *Chem. Eur. J.* **2006**, *12*, 2902.
- [27] P. Dem'yanov, P. Polestshuk, *Chem. Eur. J.* **2012**, *18*, 4982.
- [28] G. Frenking, S. Shaik, Eds. *The Chemical Bond: Fundamental Aspects of Chemical Bonding, Vol. 1*; Wiley: New York, **2014**.
- [29] I. Cukrowski, *Comput. Theory Chem.* **2015**, *1066*, 62.
- [30] K. Kitaura, K. Morokuma, *Int. J. Quantum Chem.* **1976**, *10*, 325.
- [31] T. Ziegler, A. Rauk, *Theor. Chim. Acta* **1977**, *46*, 1.
- [32] M. A. Blanco, A. M. Pendás, E. Francisco, *J. Chem. Theory Comput.* **2005**, *1*, 1096.
- [33] R. Moszynski, *Mol. Phys.* **1996**, *88*, 741.
- [34] R. F. W. Bader, In *Atoms in Molecules: A Quantum Theory*; Oxford University Press: Oxford, **1990**.
- [35] K. Fukui, T. Yonezawa, H. Shingu, *J. Chem. Phys.* **1952**, *20*, 722.
- [36] A. E. Reed, F. Weinhold, *J. Chem. Phys.* **1985**, *83*, 1736.
- [37] E. R. Johnson, S. Keinan, P. Mori-Sanchez, J. Contreras-García, A. J. Cohen, W. Yang, *J. Am. Chem. Soc.* **2010**, *132*, 6498.
- [38] A. Michalak, M. Mitoraj, T. Ziegler, *J. Phys. Chem. A* **2008**, *112*, 1933.
- [39] M. P. Mitoraj, A. Michalak, T. Ziegler, *J. Chem. Theory Comput.* **2009**, *5*, 962.
- [40] C. Foroutan-Nejad, S. Shahbazian, R. Marek, *Chem. Eur. J.* **2014**, *20*, 10140.
- [41] R. P. Feynman, *Phys. Rev.* **1939**, *56*, 340.
- [42] I. Cukrowski, J. H. de Lange, A. S. Adeyinka, P. Mangondo, *Comput. Theory Chem.* **2015**, *1053*, 60.
- [43] I. Cukrowski, P. Mangondo, *J. Comput. Chem.* **2016**, *37*, 1373.
- [44] I. Cukrowski, K. K. Govender, M. P. Mitoraj, M. Srebro, *J. Phys. Chem. A* **2011**, *115*, 12746.
- [45] I. Cukrowski, J. H. de Lange, M. P. Mitoraj, *J. Phys. Chem. A* **2014**, *118*, 623.
- [46] R. F. W. Bader, *Chem. Eur. J.* **2006**, *12*, 2896.
- [47] R. Ponec, *J. Math. Chem.* **1997**, *21*, 323.
- [48] R. Ponec, *J. Math. Chem.* **1998**, *23*, 85.
- [49] R. McWeeny, *Rev. Mod. Phys.* **1960**, *32*, 335.]
- [50] E. Francisco, A. M. Pendás, A. Costales, *Phys. Chem. Chem. Phys.* **2014**, *14*, 4586.
- [51] P. Bultinck, D. L. Cooper, R. Ponec, *J. Phys. Chem. A* **2010**, *114*, 8754.
- [52] A. M. K. Müller, *Phys. Lett. A* **1984**, *105*, 446.
- [53] M. J. Frisch, G. W. Trucks, H. B. Schlegel, G. E. Scuseria, M. A. Robb, J. R. Cheeseman, G. Scalmani, V. Barone, B. Mennucci, G. A. Petersson, H. Nakatsuji, M. Caricato, X. Li, H. P. Hratchian, A. F. Izmaylov, J. Bloino, G. Zheng, J. L. Sonnenberg, M. Hada, M. Ehara, K. Toyota, R. Fukuda, J. Hasegawa, M. Ishida, T. Nakajima, Y. Honda, O. Kitao, H. Nakai, T. Vreven, J. A. Montgomery, Jr., J. E. Peralta, F. Ogliaro, M. Bearpark, J. J. Heyd, E. Brothers, K. N. Kudin, V. N. Staroverov, R. Kobayashi, J. Normand, K. Raghavachari, A. Rendell, J. C. Burant, S. S. Iyengar, J. Tomasi, M. Cossi, N. Rega, J. M. Millam, M. Klene, J. E. Knox, J. B. Cross, V. Bakken, C. Adamo, J. Jaramillo, R. Gomperts, R. E. Stratmann, O. Yazyev, A. J. Austin, R. Cammi, C. Pomelli, J. W. Ochterski, R. L. Martin, K. Morokuma, V. G. Zakrzewski, G. A. Voth, P. Salvador, J. J. Dannenberg, S. Dapprich, A. D. Daniels, Ö. Farkas, J. B. Foresman, J. V. Ortiz, J. Cioslowski, D. J. Fox, *Gaussian 09, Revision D.01*; Gaussian, Inc.: Wallingford, CT, **2009**.
- [54] T. A. Keith, AIMAll (Version 16.05.18); TK Gristmill Software: Overland Park, KS, **2016**. Available at: aim.tkgristmill.com
- [55] W. Humphrey, A. Dalke, K. Schulten, *J. Mol. Graph.* **1996**, *14*, 33.
- [56] E. J. Baerends, T. Ziegler, A. J. Atkins, J. Autschbach, D. Bashford, A. Bérces, F. M. Bickelhaupt, C. Bo, P. M. Boerrigter, L. Cavallo, D. P. Chong, D. V. Chulhai, L. Deng, R. M. Dickson, J. M. Dieterich, D. E. Ellis, M. van Faassen, L. Fan, T. H. Fischer, C. Fonseca Guerra, M. Franchini, A. Ghysels, A. Giammona, S. J. A. van Gisbergen, A. W. Götz, J. A. Groeneveld, O. V. Gritsenko, M. Grüning, S. Gusarov, F. E. Harris, P. van den Hoek, C. R. Jacob, H. Jacobsen, L. Jensen, J. W. Kaminski, G. van Kessel, F. Kootstra, A. Kovalenko, M. V. Krykunov, E. van Lenthe, D. A. McCormack, A. Michalak, M. Mitoraj, S. M. Morton, J. Neugebauer, V. P. Nicu, L. Noodleman, V. P. Osinga, S. Patchkovskii, M. Pavanello, C. A. Peebles, P. H. T. Philipsen, D. Post, C. C. Pye, W. Ravenek, J. I. Rodríguez, P. Ros, R. Rüger, P. R. T. Schipper, H. van Schoot, G. Schreckenbach, J. S. Seldenthuis, M. Seth, J. G. Snijders, M. Solà, M. Swart, D. Swerhone, G. te Velde, P. Vernooijs, L. Versluis, L. Visscher, O. Visser, F. Wang, T. A. Wesolowski, E. M. van Wezenbeek, G. Wiesenekker, S. K. Wolff, T. K. Woo, A. L. Yakovlev, *ADF2014, SCM, Theoretical Chemistry*; Vrije Universiteit: Amsterdam, The Netherlands. Available at: <http://www.scm.com>
- [57] S. J. Grabowski, Ed. *Hydrogen Bonding: New Insights, Vol. 3*; Springer: The Netherlands, **2006**.
- [58] O. Gálvez, P. C. Gómez, L. F. Pacios, *J. Chem. Phys.* **2001**, *115*, 11166.
- [59] A. M. Pendás, M. A. Blanco, E. Francisco, *J. Chem. Phys.* **2006**, *125*, 184112.
- [60] V. Tognetti, L. Joubert, *J. Chem. Phys.* **2013**, *138*, 024102.

Received: 3 November 2016

Revised: 9 January 2017

Accepted: 2 February 2017

Published online on 2 March 2017

**Chapter 7. Exploring fundamental differences between red-
and blue-shifted intramolecular hydrogen bonds using
FAMSEC, FALDI, IQA and QTAIM.**


Published in:

Structural Chemistry, 2017, 28, 1429–1444.

Fundamentally distinct mechanisms of intramolecular red- and blue-shifted H-bonds in β -alanine are revealed using the FALDI electron density and FAMSEC energy decomposition techniques. Contributions made by atoms other than the standard IUPAC notation are shown to be important to the molecular electron density distributions as well as energy components.

Electronic supplementary information available at: <https://doi.org/10.1007/s11224-017-0956-5>.

Exploring fundamental differences between red- and blue-shifted intramolecular hydrogen bonds using FAMSEC, FALDI, IQA and QTAIM

Ignacy Cukrowski¹  · Daniël M. E. van Niekerk¹ · Jurgens H. de Lange¹

Received: 7 March 2017 / Accepted: 9 April 2017 / Published online: 25 May 2017
© Springer Science+Business Media New York 2017

Abstract We have discovered, using developed by us recently FALDI and FAMSEC computational techniques, fundamentally distinct mechanisms of intramolecular red- and blue-shifted H-bond formation that occurred in different conformers of the same molecule (amino-acid β -alanine) involving the same heteroatoms (O–H \cdots N and N–H \cdots O). Quantitative topological, geometric and energetic data of both H-bonds obtained with well-known QTAIM and IQA methodologies agree with what is known regarding H-bonding in general. However, the FALDI charge and decomposition scheme for calculating in real space 3D conformational deformation densities provided clear evidence that the process of electron density redistribution taking place on the formation of the stronger red-shifted H-bond is fundamentally distinct from the weaker blue-shifted H-bond. Contributions made by atoms of the X–H \cdots Y–Z fragment (IUPAC notation) as well as distinct atoms on the H-bond formation were fully explored. The FAMSEC energy decomposition approach showed that the atoms involved in formation of the red-shifted H-bond interact in a fundamentally different fashion, both locally and with the remainder of the molecule, as compared with those of the blue-shifted H-bond. Excellent correlations of trends obtained

with QTAIM, IQA, FAMSEC and FALDI techniques were obtained. Commentary regarding IUPAC recommended definition of an H-bond and validity of observed AILs (or bond paths) of the two H-bond kinds is also discussed.

Keywords Intramolecular hydrogen bond · FALDI · FAMSEC · Chemical bond · Deformation density · Interacting quantum fragments

Introduction

Amino acids are biologically important organic compounds that consist of three major components, including an amine ($-\text{NH}_2$) and carboxyl ($-\text{COOH}$) functional group and a side chain (or so-called R group) according to which they are classified. Due to their significance in natural biological systems, amino acids have been studied extensively, mostly from an analytical and synthetic perspective [1, 2]. β -amino acids, having the $-\text{NH}_2$ group chemically bonded to the second carbon atom in the side chain relative to the $-\text{COOH}$ group, are attractive building blocks in protein-protein and protein-RNA studies [1, 2]. β -alanine (or 3-aminopropanoic acid as per IUPAC definition) is most well-known for its use as a performance-enhancing supplement by athletes.

Although a recent computational study related to β -alanine has been reported by Waingeh *et al* [3], the focus was on obtaining conformational energies and determining solvent effects of β -peptides structures, *i.e.* the polymer products that may form in addition reactions of β -amino acid monomers. Furthermore, the studies utilised Hartree-Fock and unspecified Density Functional Theory methodology only to report the basic structural features of the compounds. However, their studies showed that, relative to the gas phase calculations, the inclusion of an implicitly simulated aqueous solvent (a variety

This paper is dedicated to Professor Lou Massa on the occasion of his Festschrift: A Path through Quantum Crystallography.

Electronic supplementary material The online version of this article (doi:10.1007/s11224-017-0956-5) contains supplementary material, which is available to authorized users.

✉ Ignacy Cukrowski
ignacy.cukrowski@up.ac.za

¹ Department of Chemistry, Faculty of Natural and Agricultural Sciences, University of Pretoria, Lynnwood Road, Hatfield, Pretoria 0002, South Africa

of known biological processes involving β -amino acids occur naturally in water) generally stabilised the conformers. Importantly, they concluded that ‘*intramolecular hydrogen bonding may play a significant role in the stability of the conformations.*’ Furthermore, a combined experimental (spectroscopic) and computational study by Eugenia Sanz *et al* [4] unambiguously confirmed the presence of intramolecular hydrogen bonds (H-bonds) in the gas phase molecular structures of abundant conformers of β -alanine. Besides the abovementioned reports [3, 4], other recent computational studies of β -alanine have focused on topics unrelated to the nature of, or influence that intramolecular H-bonding interactions may have in (de) stabilising different conformers [5, 6].

An important feature of the formation of an H-bond is the change that occurs for the X–H (where X is the H-bond donor) stretching frequency [7].¹ Most reported H-bonds are associated with a decrease of the X–H frequency and are therefore appropriately known as ‘red-shifted’ or ‘proper’ H-bonds. However, there are also numerous examples where the X–H frequency increases upon H-bond formation [8–36]. This unusual phenomenon was first reported in the 1950s [8, 9] but has only been investigated more rigorously since the nineties [10–36]. To distinguish them from classical H-bonds, names such as “anti-hydrogen bond” and “improper blue-shifting hydrogen bond” have been used. In the vast majority of reported blue-shifted H-bonds, the X atom is carbon, *i.e.* the donor group is C–H [10, 12, 13, 16, 19, 26–33]. Moreover, we note that (i) most reported blue-shifted H-bonds are intermolecular, although not exclusively [10, 34] and (ii) we are not aware of any study where red-shifted and improper blue-shifted H-bonds were identified in a single molecule.

Studies related to interpretation of blue-shifted H-bonds are currently in agreement that competing interactions ultimately determine the direction of the X–H frequency change. It is only on the nature of the competing interactions where there is some disagreement. For example, based on molecular orbital theory, Joseph and Jemmis proposed a ‘unified explanation’ of H-bonds [35]. They divided factors affecting X–H bonding in all X–H \cdots Y (where Y is the H-bond acceptor) interactions into two parts: (i) enhanced electrostatic attraction between atoms X and H in the presence of Y facilitates contraction of the X–H bond and (ii) the competing electrostatic attraction between H and Y that facilitates elongation of the X–H bond. More recently, from the study based on valence-bond theory, Chang *et al* concluded that H-bonding is dominated by electrostatic interaction, while polarisation plays the secondary role [36]. According to their results, it is the competition between the covalent and ionic components of an H-bond that

determines the direction of the X–H frequency change, with a comparatively stronger covalent structure favouring blue-shifted X–H frequencies.

Most importantly, however, the current consensus is that there is no fundamental difference (except X–H frequency change) between proper and improper H-bonds [31, 35–47]. According to literature reports, it is the relative dominance of one interaction above another which is responsible for either elongation (red shift) or contraction (blue shift) of the X–H bond, regardless of the interpretation of the exact nature of competing interactions.

Many techniques used for the study of intermolecular H-bonds are not suitable for the study of intramolecular H-bonds due to the lack of well-separated reference states. For instance, in order to calculate the binding energy for an intramolecular H-bond (as well as perform typical charge and energy decomposition analyses [48–50]), a different covalent bond is usually cut. This approach generates reference states containing radicals and inevitably influences the description of the intramolecular H-bond. Therefore, the study of intramolecular H-bonds in different conformers of, *e.g.*, β -alanine, requires the use of a suitable reference molecule, *ref*, in which there is clear evidence that intramolecular H-bonding is absent. There are numerous documented examples of how a reference molecule(s) can be utilised in order to estimate the energy of an intramolecular H-bond [51–57]. While the objective of this study is related to the relative strength of different intramolecular H-bonds, it is not the main objective. Our main focus is rather on understanding, on a fundamental level, the nature of intramolecular H-bonding and its influence on all the atoms in the molecule. To this effect, we will compare structures of β -alanine conformers in terms of deformation densities computed within the framework of the recently developed Fragment, Atomic, Localized, Delocalized and Interatomic (FALDI) electron density and deformation density decomposition technique [58]. This approach will allow us to understand the manner in which electron density is redistributed among atoms and molecular fragments upon conformational change leading to the H-bond formation. Additionally, by employing the Fragment Attributed Molecular System Energy Change (FAMSEC) energy decomposition [59], we will perform quantitative energy analysis to determine how the presence of an intramolecular interaction influences stability of (i) the entire molecule, (ii) ‘local’ fragments involved in the H-bond and (iii) the remainder of the atoms of the molecule, *i.e.* the atoms that are distant from the intramolecular interaction. To achieve our main goal, namely to explore and understand the fundamental nature of proper and improper H-bonding using interactions in β -alanine as a case study, we will also make use of the descriptors defined by the Interacting Quantum Atoms (IQA) [60] energy decomposition and Quantum Theory of Atoms in Molecules (QTAIM) [61].

¹ The IUPAC recommendation to depict classical (intra- and intermolecular) H-bonding is symbolically represented as a series of four chemically-bonded atoms X–H \cdots Y–Z

Theoretical Background

QTAIM [61] provides a thorough description of an open quantum system and is central to each of the methodologies used in this work. Similarly, IQA [60] partitions the energy of a molecule, E , into various intra- and interatomic components (one- and two-body components), including the intra-atomic (self) energy of an atom A , E_{self}^A , the interatomic energy of an interaction between atoms A and B , $E_{\text{int}}^{A,B}$, as well as electrostatic (classical) and exchange-correlation components of the latter, $V_{\text{cl}}^{A,B}$ and $V_{\text{XC}}^{A,B}$. However, we will not discuss QTAIM or IQA in any detail as these theories are well-established and thoroughly described in the literature.

We utilize two new approaches developed by us recently. The first gives expressions for a fragment attributed molecular system energy change (FAMSEC) [59] and is deeply rooted in the IQA framework and the theory of electronic separability of McWeeny [62]. FAMSEC describes the energy changes which a fragment \mathcal{G} (made up of two or more atoms) undergoes when a reference, *ref*, chemical state changes to its final, *fin*, state. FAMSEC defines the energy change *localized* to the fragment \mathcal{G} as,

$$E_{\text{attr-loc}}^{\mathcal{G}} = \Delta E_{\text{self}}^{\mathcal{G}} + \Delta E_{\text{int}}^{\mathcal{G}} \quad (1)$$

and the energetic effect the fragment \mathcal{G} makes with respect to the entire molecule by:

$$E_{\text{attr-mol}}^{\mathcal{G}} = E_{\text{attr-loc}}^{\mathcal{G}} + \Delta \sum_{X \in \mathcal{H}} E_{\text{int}}^{\mathcal{G},X} \quad (2)$$

where the sum in the final term runs over all atoms *not* contained in \mathcal{G} ; they constitute the molecular fragment \mathcal{H} . ‘Partitioning’ of a molecular system (without cutting any existing bonds) into two (or more) fragments is free of any restrictions; it is simply dictated by the choice of a \mathcal{G} fragment of interest.

The *loc*-FAMSEC term (Eq. 1, $E_{\text{attr-loc}}^{\mathcal{G}}$) accounts for both bonding and non-bonding regions within a fragment and gives an indication of how a fragment is directly affected (in terms of the self-energies of the atoms contained in the fragment and the intrafragment interactions between them) when a structural change occurs. On the other hand, the *mol*-FAMSEC term (Eq. 2, $E_{\text{attr-mol}}^{\mathcal{G}}$) gives the energy contribution which a fragment makes to a molecular system when *ref* changes to *fin*. It is important to stress that $E_{\text{attr-mol}}^{\mathcal{G}}$ must not be confused with the change in IQA additive atomic energies nor the strength of an intramolecular interaction between two or more atoms. Rather, $E_{\text{attr-mol}}^{\mathcal{G}}$ can be used to probe the contribution to the molecular energy from the perspective of any combination of atoms upon a chemical or physical change, both in terms of local fragment changes, $E_{\text{attr-loc}}^{\mathcal{G}}$, as well as the non-local effect which a fragment has on the remaining atoms of a molecule,

$\Delta \sum_{X \in \mathcal{H}} E_{\text{int}}^{\mathcal{G},X}$. Using these terms one can probe the contributions made by various fragments of various sizes in order to elucidate the energetic consequences of a change from *ref* to *fin*. More information on the calculation and interpretation of FAMSEC terms can be found in our previously published works [59, 63].

The second theory of ours partitions the electron density at any point \mathbf{r} in real 3D-space into fragment, atomic, localized, delocalized and interatomic (FALDI) [58] contributions. FALDI decomposition products can then be separately transformed using suitable transformation matrices to compute the change in electron density (*i.e.* the deformation density) from a *ref* to *fin* state. FALDI is therefore able to calculate deformation densities even for intramolecular interactions without the need to ‘cut’ the molecule into separated fragments, which are often chemically not viable due to the presence of free radicals.

FALDI utilizes a concept from Domain Averaged Fermi Hole (DAFH) analysis [64] related to the real-space distribution of the electron hole averaged over a QTAIM-defined atomic basin. However, whereas DAFH diagonalizes such a distribution to produce natural orbitals, FALDI uses the distribution directly in order to give the contribution of each atom to the total electron density at any given point \mathbf{r} :

$$\rho(\mathbf{r}) = \sum_i^M g_i(\mathbf{r}) \quad (3)$$

The $g_i(\mathbf{r})$ term stands for an atomic electron density distribution (atom-ED) associated with the i th atomic basin. By integrating $g_i(\mathbf{r})$ over entire molecular space the QTAIM-defined atomic population, $N(\Omega_i)$, is obtained that is equivalent to $N(\Omega_i)$ obtained by integrating the total electron density over a domain Ω_i . Atom-ED distributions are therefore the real-space distributions of the electrons found on average in an atomic domain. Importantly, FALDI decomposes each atom-ED further into electrons localized to the corresponding basin (localized-ED) and electrons delocalized between the corresponding basin and all other atomic basins (delocalized-ED):

$$g_i(\mathbf{r}) = \lambda_i(\mathbf{r}) + \sum_{X \neq i}^M \frac{1}{2} \delta_{i,X}(\mathbf{r}) \quad (4)$$

Localized-ED distributions ($\lambda_i(\mathbf{r})$) integrated over all space give the QTAIM-defined localization index ($\lambda(\Omega_i)$) whereas integrating diatomic delocalized-ED distributions ($\delta_{i,X}(\mathbf{r})$) over all space gives the QTAIM-defined diatomic delocalization index ($\delta(\Omega_i, \Omega_X)$). FALDI therefore not only provides real-space distributions of all the QTAIM-defined population statistics but can also reveal additional information on the density distribution of a chemical system that is not provided by their QTAIM counterparts.

The details on how these terms are calculated can be found in our recently published work [58].

FALDI also provides a novel scheme for calculating the deformation density resulting from a *ref* to *fin* conformational transformation using the terms in Eqs. 3 and 4; this kind of deformation density has been impossible to calculate directly previously. Since each atom as well as each interatomic interaction resides in different relative orientations and environments in two different chemical states, localized-ED and delocalized-ED distributions can be measured in a *fin* conformer and compared to uniquely transformed corresponding distributions in a *ref* conformer, giving localized deformation density (localized-DD) and interatomic delocalized deformation density (delocalized-DD) distributions:

$$\Delta_c \lambda(\mathbf{r}) = \sum_i^M [\text{fin} \lambda_i(\mathbf{r}) - \text{ref} \lambda_i(\mathbf{A}_i \mathbf{r})] \quad (5)$$

and

$$\Delta_c \delta(\mathbf{r}) = 2 \sum_i^{M-1} \sum_{j=i+1}^M [\text{fin} \delta_{i,j}(\mathbf{r}) - \text{ref} \delta_{i,j}(\mathbf{A}_{i,j} \mathbf{r})] \quad (6)$$

where \mathbf{A}_i and $\mathbf{A}_{i,j}$ are unique transformation matrices relating the relative position and orientation of each atom or interaction in *ref* to *fin*. The total, conformational deformation density is then simply the sum of all localized-DD and delocalized-DD terms. While the terms defined in Eqs. 5 and 6 are used for the calculation of total deformation density, they are also extremely useful for understanding the density changes between two different conformational states.

Finally, we present here for the first time a visualization of Pendás *et al*'s concept of privileged exchange channels [65] using FALDI. A FALDI-based privilege indicator is calculated by taking the delocalized-ED value of an interaction of interest (the primary interaction) at any coordinate \mathbf{r} and subtracting the value of (i) the largest competing secondary delocalized-ED interaction at \mathbf{r} , or (ii) the largest delocalized-ED interaction other than the primary interaction at \mathbf{r} . The result is a distribution in real-space of where the delocalized density associated with the primary interaction is dominant with regards to either secondary interactions or all other interactions.

Computational details

All geometry optimizations (using very tight convergence criteria) and electronic structure calculations were performed in Gaussian 09, revision D [66] at the RMP2/aug-cc-pvdz and RB3LYP/aug-cc-pvdz level of theory using an implicit solvent model (PCM) in water. Empirical dispersion corrections of Grimme (GD3) [67] were included in all B3LYP geometry

optimisations and frequencies calculations. All six geometry optimized structures correspond to energy minima as no negative frequencies were obtained. Cartesian coordinates for all optimized molecules as well as promolecules are included in Tables S1–S6 in PART 1 of the Supplementary Information (SI). AIMAll version 16.10.31 [68] was used to calculate topological properties, QTAIM molecular graphs and atomic populations as well as IQA descriptors in case of B3LYP wavefunctions. In case of the MP2-optimised structures, IQA analyses were conducted using TWOe-14 program [69, 70] developed by Polestshuk; the BBC1 approximation [71] of the two-electron density matrix (2EDM) was used to compute IQA-defined V_{ee} energy contributions (intra- and interatomic, V_{ee}^A and $V_{ee}^{A,B}$, respectively). FAMSEC parameters were generated from IQA data using in-house software. AIMAll was also used to calculate atomic overlap matrices for all systems at the B3LYP level. Atomic overlap matrices were used to perform the FALDI decomposition and conformational deformation densities calculations using in-house software. All FALDI isosurfaces were visualized using VMD [72].

All results, unless stated otherwise, are presented at MP2 level, with corresponding B3LYP data in the PART 2 of the SI. FALDI calculations are very time consuming for MP2 wavefunctions. For this reason all FALDI data has been calculated on B3LYP atomic overlap matrices; however, we have found excellent agreement between B3LYP and MP2 trends in IQA, QTAIM and FAMSEC results.

Finally, we utilize an approach described previously [73] to analyse the density cross-section of a bond. This approach simply involves calculating the Hessian matrix at the bond critical point (BCP), following along the 2nd eigenvector by set increments (usually 0.1 Bohr) and then recalculating the Hessian and repeating the process. We use in-house software for this approach.

Results and discussions

We decided to explore and compare the mechanism leading to, and properties of, two intramolecular X–H···Y–Z bonding interactions that are present in different conformers of β -alanine; the four atoms are O–H···N–C and N–H···O–C in the lower- and higher energy conformer (**LEC**², and **HEC**), respectively. These two *fin* states of β -alanine in water (PCM) are similar to the gas phase structures reported by Eugenia Sanz *et al* [4] and are presented as molecular graphs in Table 1, where $\Delta E = E^{\text{fin}} - E^{\text{ref}}$, X–H stretching frequencies, interatomic distances and angles in the vicinity of the H-bonding and electron densities at selected BCPs are also shown.

² **LEC** is also the lowest energy conformer (global energy minimum structure) of β -alanine (MP2 level).

Table 1 Molecular graphs and selected geometric features and properties of *fin* structures of β -alanine investigated in this work. ^a

Descriptor	<i>fin</i> structure
$\Delta E = -5.9 \text{ kcal}\cdot\text{mol}^{-1}$ $\nu(\text{X-H}) = 2687 \text{ cm}^{-1}$ (-1030 cm^{-1})	
$d(\text{W-X}) = 1.3455 \text{ \AA}$ (-0.0166 \AA) $d(\text{X-H}) = 1.0240 \text{ \AA}$ ($+0.0487 \text{ \AA}$) $d(\text{H}\cdots\text{Y}) = 1.6326 \text{ \AA}$ $d(\text{Y-Z}) = 1.4835 \text{ \AA}$ ($+0.0112 \text{ \AA}$)	
$\angle(\text{X-H}\cdots\text{Y}) = 156.23^\circ$	
$\rho_{\text{BCP}}(\text{X-H}) = 0.2884 \text{ a.u.}$ (-0.0537 a.u.) $\rho_{\text{BCP}}(\text{H}\cdots\text{Y}) = 0.0649 \text{ a.u.}$	
$\Delta E = -1.0 \text{ kcal}\cdot\text{mol}^{-1}$ $\nu(\text{X-H}) = 3497 \text{ cm}^{-1}$ ($+9 \text{ cm}^{-1}$)	
$d(\text{W-X}) = 1.4757 \text{ \AA}$ ($+0.0034 \text{ \AA}$) $d(\text{X-H}) = 1.0220 \text{ \AA}$ (-0.0002 \AA) $d(\text{H}\cdots\text{Y}) = 2.4387 \text{ \AA}$ $d(\text{Y-Z}) = 1.2260 \text{ \AA}$ ($+0.0010 \text{ \AA}$)	
$\angle(\text{X-H}\cdots\text{Y}) = 117.21^\circ$	
$\rho_{\text{BCP}}(\text{X-H}) = 0.3278 \text{ a.u.}$ ($+0.0008 \text{ a.u.}$) $\rho_{\text{BCP}}(\text{H}\cdots\text{Y}) = 0.0116 \text{ a.u.}$	

^a All values were obtained at the MP2 level. ΔE is the difference in molecular electronic energies, ${}^{\text{fin}}E - {}^{\text{ref}}E$, where the *ref* structure is shown in Fig. S4 in PART 3 of the SI. The values given in brackets refer to the change that occurs when going from *ref* to *fin*

The interatomic $\text{H}\cdots\text{Y}$ distance in **LEC** (1.6326 \AA) is significantly smaller, by 1.1174 \AA , than the sum of the van der Waals (vdW) radii of H and N.³ The $\text{H}\cdots\text{Y}$ distance in **HEC** (2.4387 \AA) is only 0.2813 \AA smaller in magnitude than the sum of the vdW radii of atoms involved. This result, together with the observed atomic interaction line (AIL) between H and Y for both conformers and all descriptors shown in Table 1, provides very clear evidence that (i) intramolecular H-bonds are present in both cases and (ii) strongly suggests that the red-shifted H-bond in **LEC** is significantly stronger than the blue-shifted H-bond in **HEC** – descriptors in Table 1 are discussed in detail in PART 3 in the Supplementary Information (SI) where the molecular graph of the *ref* structure (a ‘linear’ conformer of β -alanine, **Lin**) is also shown, Figure S4.

³ vdW radii taken as H = 1.20 \AA , N = 1.55 \AA and O = 1.52 \AA [74].

Exploring the changes of the atomic electron population and bond charge polarization

To gain insight on how the formation of **LEC** and **HEC** compares in terms of charge transfer, we analysed the changes in atomic electron population, $\Delta N(\text{A}) = N(\text{A})_{\text{fin}} - N(\text{A})_{\text{ref}}$; the MP2 data is shown in Fig 1.

It is clear that atoms of **LEC** experienced much larger change in the electron charge transfer/distribution; note that only N11 (Y) and atoms of the methylene bridge (C2, H3 and H4, which are relatively distant from the vicinity of the H-bonding) show minimal changes in their electron population. By contrast, the major changes observed in **HEC** occur distant from the intramolecular H-bonding (atoms H9 and C2) and are rather small in magnitude relative to the changes observed in **LEC**. Comparing $\Delta N(\text{A})$ for the $\text{W-X-H}\cdots\text{Y-Z}$ atoms of **LEC** and **HEC**, *i.e.* in the vicinity of the intramolecular

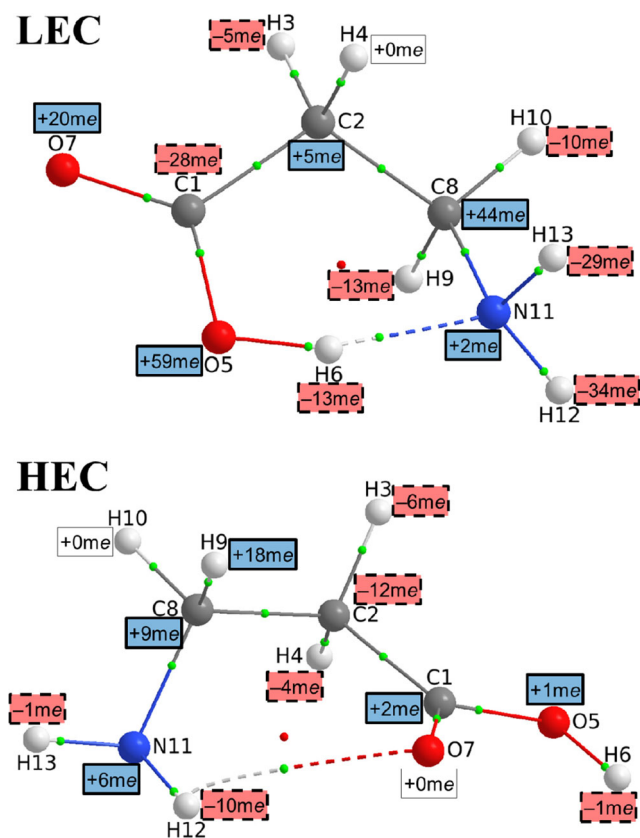


Fig. 1 Molecular graphs of *fin* structures of **LEC** and **HEC** showing the changes (at MP2) in atomic electron population, $\Delta N(A)$, on the *ref* (**Lin**) to *fin* structural change. Colour coding: blue and solid frame = increase, red and dashed frame = decrease, no colour and solid frame = no change

interaction, we see that significant differences between **LEC** and **HEC**, in terms of atomic electron population changes, i.e. $|\Delta\Delta N(A)| = \Delta N(A)_{fin} - \Delta N(A)_{ref}$, have occurred:

- atom W; an outflow/inflow of electrons in **LEC/HEC** took place and the difference in magnitude is large, i.e. $|\Delta\Delta N(A)| = 37 me$,
- atom X; an inflow of electrons in both conformers is observed, but the relative increase in **LEC** is much larger with $|\Delta\Delta N(A)| = 53 me$,
- atom H; an outflow of electrons by approximately the same magnitude of $\pm 12 me$ ($|\Delta\Delta N(A)| = 3 me$) in both conformers is observed,
- atom Y; the change is very small and comparable ($|\Delta\Delta N(A)| = 2 me$) in both conformers,
- atom Z; electron population increased in **LEC** much more as we obtained $|\Delta\Delta N(A)| = 42 me$.

Importantly, the dissimilarities in the changes observed for W, X and Z atoms strongly suggest that they might play an important role with regards to the type of intramolecular H-bond formation in these two conformers of β-alanine. Considering the entire terminal functional groups of **LEC**,

the electron population of the donor –COOH increased by +38 *me* whereas the acceptor –NH₂ group decreased by –61 *me*. By contrast, these two moieties' electron population in **HEC** changed slightly; a decrease by –5 *me* is observed in the case of the donor –NH₂ group and negligible increase, by +2 *me*, was found for the acceptor –COOH group.

We have also analysed the extent to which the 'chemical bonds' became charge-polarised, on structural transformation and the MP2 data of interatomic charge polarisation, as $\Delta|Q(A) - Q(B)|$, for each 'chemical bond' in **LEC** and **HEC** (relative to *ref* structure **Lin**) is shown in Fig 2. By far larger changes took place in the case of **LEC** where the sum total of charge polarisation of all the 'chemical bonds' (excluding the H...Y interaction), $\sum(\Delta|Q(A) - Q(B)|) = +104 me$, indicates that the molecule as a whole has become much more polarised. On formation of **HEC**, the sum total is a small negative value (–3 *me*), indicating that the molecule has become slightly less charge-polarised.

The bond charge polarisation with regards to the W–X–H...Y fragment increased by +177 *me* in **LEC** and in case of the Y–Z bond it decreased by –41 *me*. Very different values are observed in **HEC**, where the W–X–H...Y fragment experienced a small increase of +23 *me* due to small (–3*me*) charge

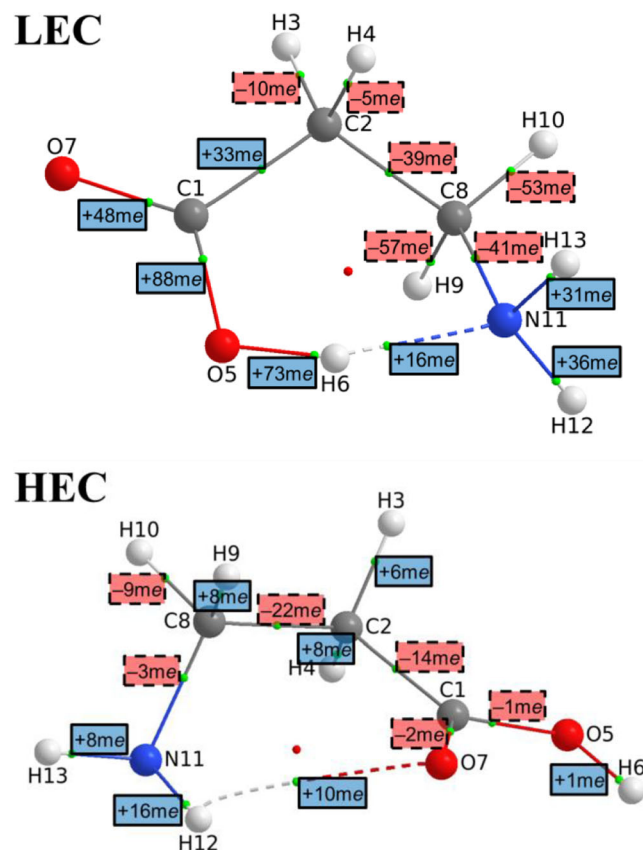


Fig. 2 Molecular graphs of *fin* structures of **LEC** and **HEC** showing the changes (at MP2) in charge polarisation between chemically bonded atoms, $\Delta|Q(A) - Q(B)|$, on the *ref* (**Lin**) to *fin* structural change. Colour coding: blue and solid frame = increase, red and dashed frame = decrease

polarization decrease found for the W–X bond (+88 *me* was found in **LEC**). It is notable here that, relative to **Lin**, the X–H bond becomes more charge-polarised on formation of both H-bonds, ‘red-shifted’ in **LEC** (increased bond length, decreased ρ_{BCP}) and ‘blue-shifted’ in **HEC** (decreased bond length, increased ρ_{BCP}) despite them having strikingly opposite features to each other, Table 1.

FALDI-based atomic deformation densities of the W–X–H...Y–Z fragment

The FALDI approach, as discussed in the Theoretical Background (Section 2), allows a real-space visualization of the contributions of each fragment and atom as well as localized and delocalized density to the total deformation density. We have decided to focus on the atomic and interatomic delocalized contributions of the X–H...Y interaction, as well as the atomic contributions made by the adjacent carbon atoms (W and Z) of the *fin* conformers **LEC** and **HEC**, relative to the *ref* structure, **Lin**.

Figure 3 shows 3D isosurfaces of the FALDI-defined atomic contributions to the deformation density (atom–DD) for atoms X, H and Y at B3LYP level. These isosurfaces are a direct visualization in real-space of the total change in QTAIM-defined atomic population and presents considerably more information than the scalar net change in population $\Delta N(A)$, Fig. 1. Atom X = O5 in **LEC** gains an overall net

+57 *me* when the intramolecular X–H...Y (H-bond) is formed. Importantly, however, Fig. 3 reveals that atom X is extremely polarized, with large increase in density along the W–X bond as well as outside of the X–H...Y interatomic region. Atom X also increases the density at the H-bond acceptor, atom Y = N11. On the other hand, X decreases the total density along the X–H bond as well as along the H...Y interaction. Atom X = N11 in **HEC** shows several similar patterns as in **LEC**, namely it (i) decreases density along the H...Y interaction, (ii) increases density along the W–X bond, (iii) increases density outside of the H...Y interatomic region and (iv) increases density in the lone-pair region of atom Y. However, there are a few distinct and fundamentally important differences. Unlike in **LEC**, atom X in **HEC** increases density along the X–H (N11–H12) bond and decreases density along its other bonded hydrogen atom. In addition, atom X in **HEC** shows considerably more delocalized changes throughout the carbon backbone of the molecule. As a result of these differences, atom X (N11) in **HEC** gains considerably fewer electrons (+5 *me*) and is far less polarized than atom X (O5) in **LEC**.

Atom H shows very similar patterns in **LEC** and **HEC** in that a comparable number of electrons are lost in both conformers, a common feature of H-bonding. Figure 3 shows that the loss of electrons occurred along the X–H bond and despite increase of density from H in the lone-pair region of atom Y.

The change that occurred at atom Y shows some similarities in the two *fin* conformers in that it decreases density around its own nucleus, specifically at its own lone-pair region. In **LEC**, Y = N11 increases density along the H...Y interatomic region in a channel fashion as well as along the X–H bond. In **HEC**, however, Y = O7 only increases density along the X–H bond and has a considerably lesser effect at the H...Y interatomic region, in that no discernible channel is observed (even at much lower isosurfaces). We therefore see that atom Y interacts with X and H in a very different fashion in **HEC** as compared to **LEC**. Note also that atom Y in **HEC** loses some density due to an interaction which was present in the **Lin** structure but is absent in the **HEC** structure – a feature which is easy to miss with traditional QTAIM analyses. This loss of density is, in principle, unrelated to the H-bond formation but still decreases the total population change of atom Y. Interestingly, while the net population change of the Y atoms in both conformers is relatively small in comparison to atom X, FALDI reveals that the net population change of atom Y is the result of large but opposing changes in atomic charges.

3D isosurfaces of the FALDI-defined atom–DD for the W and Z carbons bonded to X and Y are shown in Figure S5 in PART 4 of the SI. Atom W in **LEC** loses a significant –27 *me* relative to **Lin**. FALDI reveals that, despite an increase of density along the W–X bond, this net loss is mostly due to a decrease in density along the carbon backbone. On the other hand, atom W in **HEC**, with an increase in population by +9 *me*, does not significantly affect the density of the W–X bond

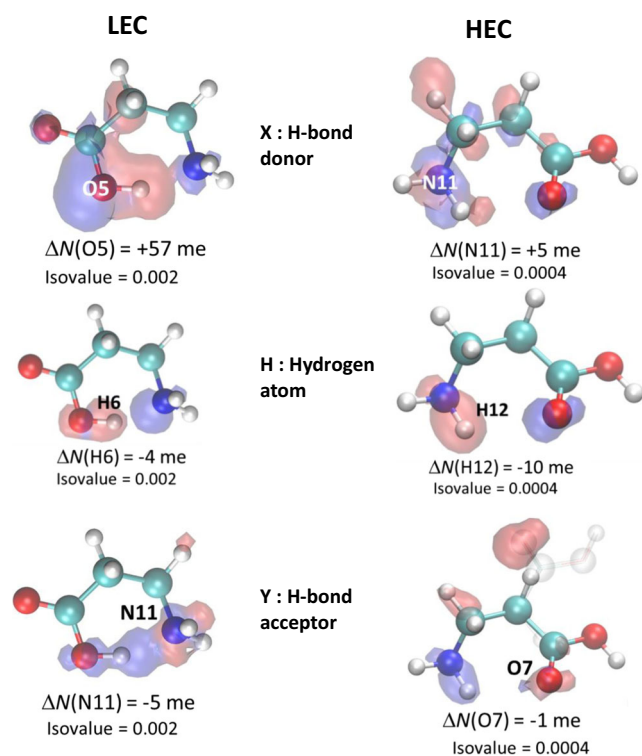


Fig. 3 Relative to **Lin**, FALDI atomic deformation density isosurfaces for selected atoms in **LEC** and **HEC** and changes in atomic populations calculated at the B3LYP level.

or the carbon backbone. Atom Z in **LEC** gained +44 *me* mostly due to an increase with its bonded carbon neighbour (within the carbon backbone), and decreased density along the Z–Y bond. The influence of atoms Z and W in **LEC** therefore seem to be exact opposite of each other – whereas atom W removes density from the backbone but places it along the W–X bond, atom Z removes density from the Z–Y bond but places it in the backbone. By contrast, neither atom W nor atom Z in **HEC** seems to alter the density of the W–X and Z–Y bonds significantly.

In summary of the atom–DD distributions, we note a few interesting features of the H-bonding interactions which are uncovered by FALDI. Firstly, the opposing donations, (back-donations) and polarizations of atoms X, H and Y of the X–H...Y interatomic region leads to increased electrostatic polarization throughout the molecule. For instance, in **LEC** atom X decreases density near atom H but increases density near its own nucleus and near atom Y. Atom H removes density near its own nucleus but increases density near atom Y. Atom Y removes density from its own nucleus but increases density at atom X and along the X–H bond. Secondly, we note that atom Y seems to be mostly responsible for the formation of a density channel along the H...Y interaction, a channel which forms in **LEC** but not in **HEC**. Thirdly, the influence of atoms W and Z is clearly revealed with FALDI. In **LEC**, W reinforces the W–X bond whereas Z removes density from the Z–Y bond, features which do not occur in **HEC**. We will investigate these features more in the following sections, starting with 3D isosurfaces of the interatomic delocalized deformation density.

FALDI-based interatomic delocalized deformation densities of X–H...Y fragment

Figure 4 shows 3D isosurfaces of the FALDI-defined delocalized deformation densities (delocalized–DD) for all diatomic interactions of the X–H...Y interaction for both **LEC** and **HEC**; they were computed at the B3LYP level relative to the **Lin** structure.

The delocalized–DD distributions are real-space distributions of QTAIM-defined delocalization indices and can be interpreted as the density analogue of IQA-defined exchange-correlation (XC) interaction energies, $V_{XC}^{A,B}$; for convenience and to facilitate the discussion these terms are included in Fig. 4.

The first set of isosurfaces in Fig. 4 displays the change in delocalized density between atoms H and Y, i.e. the region where H-bonding takes place. In **LEC**, a clear XC channel (a blue isosurface linking H and N atoms) is formed, resulting in an increase of 167 *me* shared between these atomic basins and an associated XC stabilization, $V_{XC}^{H6,N11} = -26.4 \text{ kcal}\cdot\text{mol}^{-1}$. The formation of such a channel is very reminiscent of Pendás

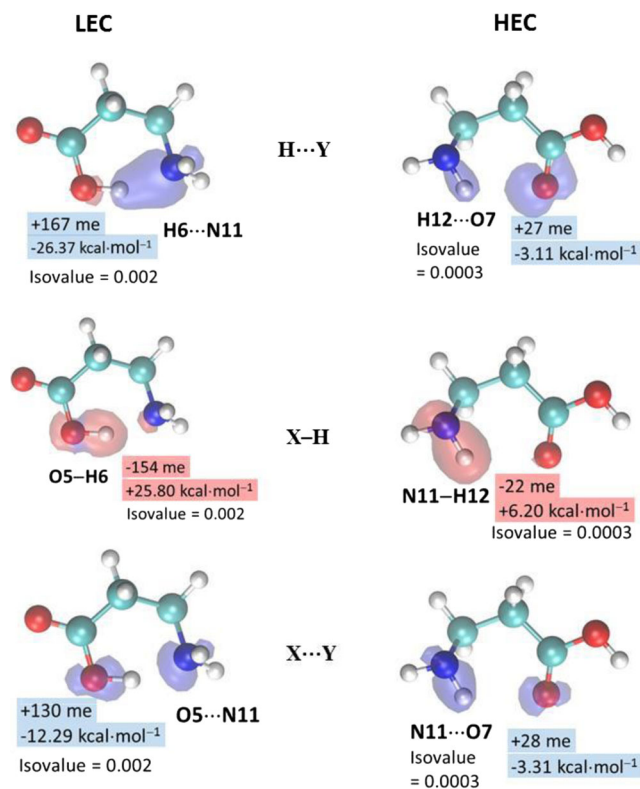


Fig. 4 FALDI interatomic delocalized deformation density isosurfaces for selected interactions in **LEC** and **HEC** relative to **Lin**. Changes in delocalization indices as well as IQA interatomic exchange-correlation energies are shown; all calculated at the B3LYP level

et al's concept of the AIL as “a privileged exchange channel” [65]. To our knowledge, FALDI is the first technique which can detect and visualize these channels as delocalized density distributions in real space. Note that the channel extends just between H6 and N11 and a small amount of delocalized density is removed close to atom X. In stark contrast to **LEC**, the change in density delocalized between atoms H and Y in **HEC** (i) does not form a channel between H12 and O7 (even at very low isovalues) but rather (ii) increases density along the X–H and Z–Y bonds. In comparison with **LEC**, the amount of density shared is an order of magnitude smaller (27 *me*) and the XC stabilization is only $-3.1 \text{ kcal}\cdot\text{mol}^{-1}$. We see therefore that the manner in which density is shared between atoms of the X–H...Y fragment is fundamentally different in the two conformers.

The remainder of the delocalized–DD isosurfaces are qualitatively quite similar for the two conformers, although at much different magnitudes. For example, density delocalized between atoms X and H generally decreases along the X–H bond (by -154 and -22 me) and, as a result, XC destabilization is observed with $V_{XC}^{O5,H6} = +25.80$ and $V_{XC}^{N11,H12} = +6.2 \text{ kcal}\cdot\text{mol}^{-1}$ in **LEC** and **HEC**, respectively. Furthermore, an increase in long-range delocalization between atoms X and Y is also observed (by -130 and -28 me ,

resulting in $V_{XC}^{O5,N11} = -12.3$ and $V_{XC}^{N11,O7} = -3.3$ kcal·mol⁻¹ for **LEC** and **HEC**, respectively) mostly with increased density along the X–H bond and close to the Y nucleus but without the presence of any form of an interatomic XC channel.

Delocalized–DD isosurfaces for the W–X and Z–Y interactions are shown in Figure S6 in PART 4 of the SI. Notably, atoms W and X experience *increased* delocalized density in **LEC** along the W–X bond (by 46 *me* and XC stabilization by -8.4 kcal·mol⁻¹) whereas they experience *decreased*, as well as highly polarized, delocalized density in **HEC** (by -2 *me* and XC destabilization by +0.9 kcal·mol⁻¹). Atoms Z and Y experience decreased delocalized density between them in both conformers, i.e. along the Z–Y bond (by -27 and -6 *me* for **LEC** and **HEC** with XC destabilization by +6.2 and +0.7 kcal·mol⁻¹, respectively).

From the atom–DD and delocalized–DD distributions (Figs. 2, 3, 4 and Figs. S5–S6 in PART 4 of the SI) it is clear that the manner in which density is either accumulated, depleted or delocalized along the W–X–H...Y–Z fragment is significantly different in the red- and blue-shifted H-bonds of **LEC** and **HEC**, respectively. In order to elucidate the nature of these differences, we now turn to a more quantitative approach, by analyzing 1D cross-sections of the FALDI-based deformation density decomposition terms of selected interactions.

1D FALDI cross-sections of X–H...Y interactions

Relative to **Lin**, the change in QTAIM properties (at B3LYP level) at the BCP of the X–H bond for each conformer, are detailed in Table 2. The electron density at the BCP decreased by -0.0539 *e* for the red-shifted X–H bond in **LEC**, and increased by 0.0010 *e* for the blue-shifted X–H bond in **HEC**. These changes, $\Delta\rho_{BCP}$ are exactly as expected for the red- and blue-shifted H-bonds [7]. For **LEC**, the positive change in the Laplacian and negative change in the $|V|/G$ ratio indicates a less open-shell, less covalent, hence more electrostatic interaction [75–77]. This is corroborated with changes in the IQA-defined energy terms, (i) destabilizing $\Delta V_{XC}^{A,B} = +25.8$ kcal·mol⁻¹, (ii) stabilizing $\Delta V_{cl}^{A,B} = -15.8$ kcal·mol⁻¹ and (iii) decreasing delocalization index, $\Delta DI(A,B) = -0.1543e$. The resultant weakening of the X–H bond, consistent with red-shifted H-bonds, is reflected well

with the destabilizing in nature change in the diatomic interaction energy, $\Delta E_{int}^{A,B} = +10.1$ kcal·mol⁻¹. However, a set of

interesting results is seen for the blue-shifted X–H bond in **HEC**, namely a small increase in the ρ_{BCP} value is observed (+0.0010 *e*), a decrease in the Laplacian and an increase in the $|V|/G$ ratio; this suggests a more covalent, more open-shell, hence less electrostatic interaction. Contrary to this finding, the DI has decreased (-0.0224 *e*), the $\Delta V_{XC}^{A,B}$ term is destabilizing (+2.6 kcal·mol⁻¹) and the $\Delta V_{cl}^{A,B}$ term is stabilizing (-4.7 kcal·mol⁻¹). It would appear as if the X–H (N11–H12) bond in **HEC** became stronger (as expected for a blue-shifted H-bond) with more covalent and less electrostatic character, even though the overall XC energy and the number of shared electrons between atoms X and H decreased and the electrostatic attraction increased. These changes appear to be quite contradicting and in search for the origin of these trends we made use of 1D FALDI cross-sections discussed below.

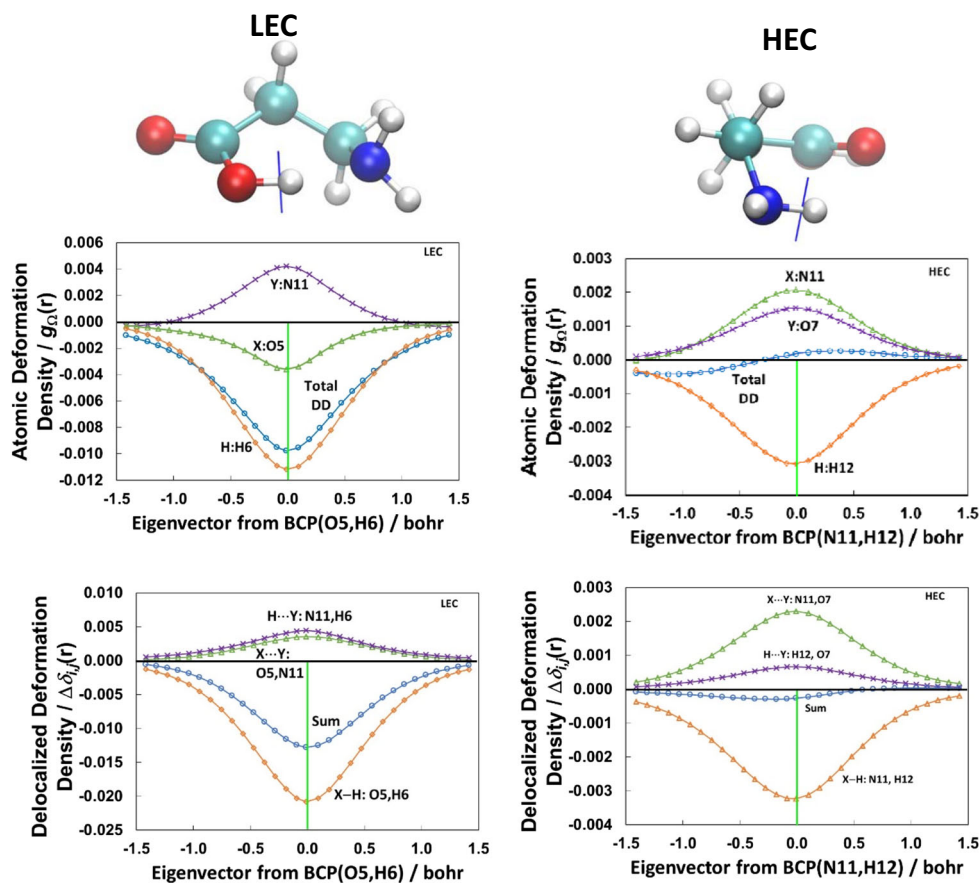
Figure 5 shows the total deformation density and its FALDI-based decomposition. The cross-sections start at the BCP between atoms X and H of **HEC** and **LEC**. Atomic and delocalized deformation densities are measured against the exactly transformed vectors in the *ref* state, **Lin**. The cross-section follows the λ_2 -eigenvector, as described in the Computational Methods (Section 3). The position of the BCP is at 0.0 on the X-axis as indicated by a green line and positive values were obtained by following the vector in the outward of molecule direction. The top two graphs give the total deformation density, as well as the contributions to the deformation density made by atoms X, H and Y. The bottom two graphs illustrate the delocalized interatomic contributions which the X–H, X...Y and H...Y interactions as well as their sum made to the deformation density.

First and foremost, we notice that the total deformation density (total-DD) at the BCP is negative for the X–H bond in **LEC** but very slightly positive in **HEC**. This is in line with the changes in electron density at the BCP presented in Table 2. Importantly, FALDI can decompose the total-DD and discover its origin. We notice that in both conformers atom H decreases while atom Y increases density at the BCP. However, we discovered a fundamentally different mechanism at the atom X; it *decreases* in **LEC** but *increases* density at the BCP in **HEC**, leading to resultant decreased and increased deformation density computed for **LEC** and **HEC**,

Table 2 Changes in QTAIM properties at the BCP of the X–H bond at B3LYP level

Form	$\Delta\rho_{BCP}$ (X–H) <i>au</i>	$\Delta\bar{v}^2\rho_{BCP}$ (X–H)	$\Delta V /$ G	ΔDI (X,H)	$\Delta E_{int}^{X,H}$ <i>kcal·mol⁻¹</i>	$\Delta V_{XC}^{X,H}$	$\Delta V_{cl}^{X,H}$
LEC (O5,H6)	-0.0539	0.5717	-3.110	-0.1543	+10.2	+25.8	-15.8
HEC (N11,H12)	0.0010	-0.0134	0.152	-0.0224	-2.1	+2.6	-4.7

Fig. 5 Cross-sections along the path defined by the λ_2 eigenvector at the BCP of the X–H bond of **LEC** and **HEC** conformers, as shown by the blue line in the ball-and-stick representation at the top. The total deformation density as well as the change in selected FALDI atomic density, relative to **Lin**, is shown in the middle; and the change in selected FALDI interatomic delocalized densities is shown at the bottom; all calculated at the B3LYP level



respectively. Hence, the increased electron density observed at the BCP of the X–H bond previously shown for blue-shifted H-bonds [34] therefore seems to originate from both atoms, X and Y, which is a novel finding.

Secondly, we see large differences in the manner in which electron density is delocalized at the BCP of the X–H bond. In both conformers, the density delocalized directly along the X–H bond is removed from the BCP, whereas density shared between atoms X and Y as well as between atoms H and Y is increased. In other words, both the X...Y long-distance and H...Y direct interactions increased density along the X–H bond. The ratio of increased and decreased delocalized density differs for the two conformers, however, with the X...Y interaction contributing, relative to the other interactions (shown in Fig. 5), much more in **HEC** conformer than in **LEC** conformer. The X...Y interaction is therefore largely responsible for net increase in total density at the X–H BCP in **HEC**. This finding provides new evidence with regards to the mechanism of blue-shifted H-bonds.

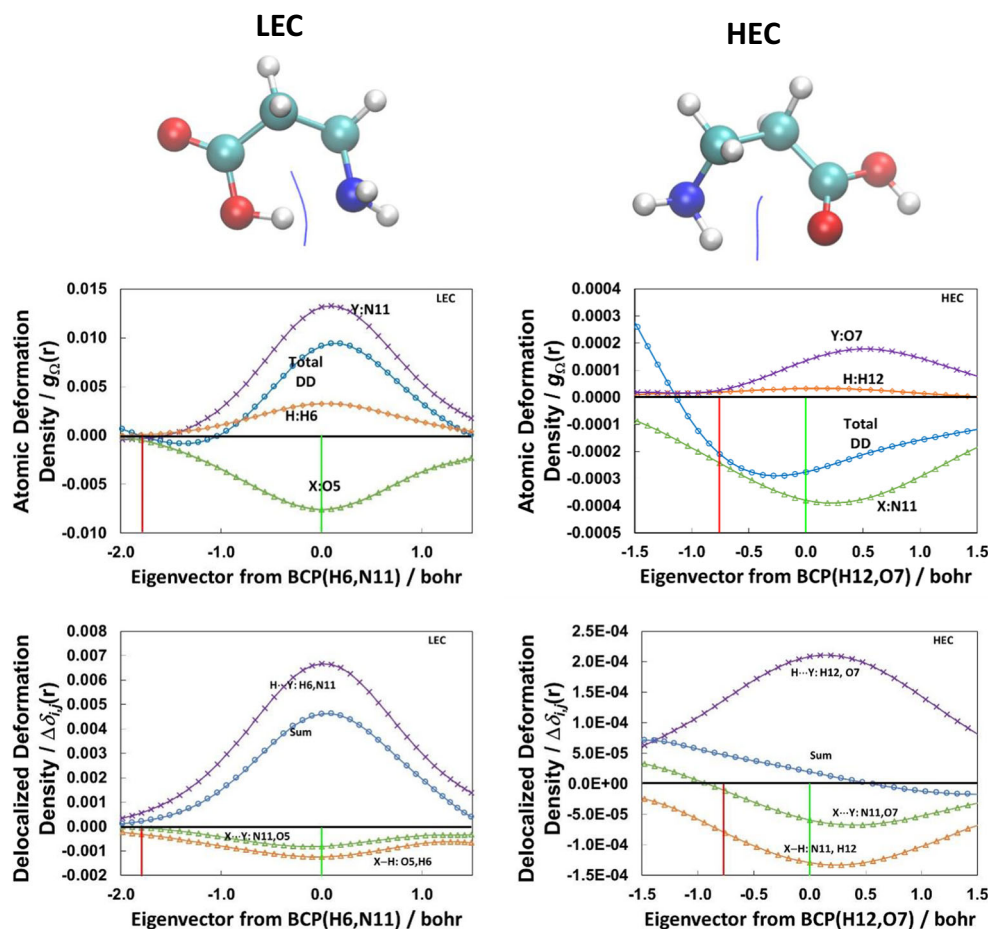
Figure 6 shows the cross-section along the λ_2 -eigenvector originating from the BCP between atoms H and Y directly involved in the intramolecular H-bond formation. We note first a very important fundamental difference: the total-DD *increases* in **LEC** but *decreases* in **HEC**, despite the presence of an AIL in both conformers. We have previously shown [73]

that the deformation density is a much better measure of the concentration of density in terms of Feynman's theorem [78] during the formation of an inter- or intramolecular interaction. Therefore, despite the formation of an AIL between atoms H and Y in both conformers, only the AIL in **LEC** can be seen as a true, or purposeful, accumulation of electron density on a spontaneous intramolecular bond formation whereas the AIL in **HEC** can be seen as a resultant, or residual, density that has not been removed on a spontaneous intramolecular bond formation (note that **HEC** is a stationary point on the potential energy surface without negative imaginary frequencies). This statement is supported by the isosurfaces in Figs. 3, 4, which clearly show the formation of the XC channel between atoms H and Y for **LEC** but not for **HEC**.

The origin of the total-DD at the H...Y BCP can be investigated by analysing the atom-DDs shown in Fig. 6. The mechanism leading to the total-DD appears to be very much the same in both conformers; atom X decreases density whereas atoms H and Y increase density at the BCP. Clearly, it is the ratio of these contributions which determines the sign of the total-DD at the BCP. A comparatively small increase from atoms Y and H relative to a large decrease from atom X in **HEC** leads to the observed negative deformation density.

Finally, we look at the changes in delocalized-DD at the H...Y BCP. The only factor increasing density in this region is

Fig. 6 Cross-sections along the path defined by the λ_2 eigenvector at the BCP of the H...Y interaction of **LEC** and **HEC** conformers. The total deformation density as well as the change in selected FALDI atomic density, relative to **Lin**, is shown at the top, and the change in selected FALDI interatomic delocalized densities is shown at the bottom. Positions of the BCP and ring critical point are indicated by a green and red line, respectively; all calculated at the B3LYP level



the density shared directly between atoms H and Y, whereas the density shared by atoms X,H and X,Y decreases the density. Relative to **HEC**, more significant contribution comes from the H...Y interaction in **LEC** and this leads to an overall much larger delocalized density at the BCP in this conformer. Again, these findings corroborate very well the observed XC channel between interacting atoms of H and Y only in the **LEC**.

Validity of the AIL between atoms H and Y

The results described above place some doubt regarding the presence of the H...Y AIL in *both* **LEC** and **HEC**. The orthodox interpretation of an AIL – that it represents a bonding interaction – has been slowly replaced during recent years by an interpretation given by Pendás *et al* that an AIL represents a privileged exchange channel [65]. Tognetti and Joubert have found [79] a correlation between the presence of an AIL and the ratio of the IQA-defined XC interaction energy of the primary interaction (here H...Y) and the largest (in absolute value) XC interaction energy of any competing secondary interaction, called by them a β parameter. In their systems, they found that a β parameter larger than 1.35 was

consistently found with the presence of an AIL. Following their approach, we have calculated the β parameter for the H...Y interaction in **LEC** to be 2.14 and in **HEC** to be 1.07. The H...Y interactions in β -alanine conformers are quite different from the interactions studied by Tognetti and Joubert; hence, we probably cannot use the same cut-off of $\beta > 1.35$ for the presence of an AIL. It is clear, however, that the H...Y interaction in **HEC** is much more contested and less privileged than the corresponding interaction in **LEC**. As an alternative to the approach by Tognetti and Joubert, we can compute and visualise privilege using FALDI-defined the delocalized electron density distribution of the H...Y interaction relative to either a selected single competing interaction, a set of selected secondary interactions (here X...Y, X...Z, W...Y, X...H, and W...H) or all remaining interactions. This approach is detailed in the Theoretical Background (Section 2). Such visualizations of privilege are shown in Fig. 7 (relative to all secondary interactions) and Fig. S7 in PART 4 of the SI, and as mentioned previously, to our knowledge, FALDI is the first approach which can directly visualize Pendás *et al*'s concept of privilege. In both molecules we see that the H...Y delocalized density is dominant (privileged) at or near the H...Y BCP, relative to competing secondary

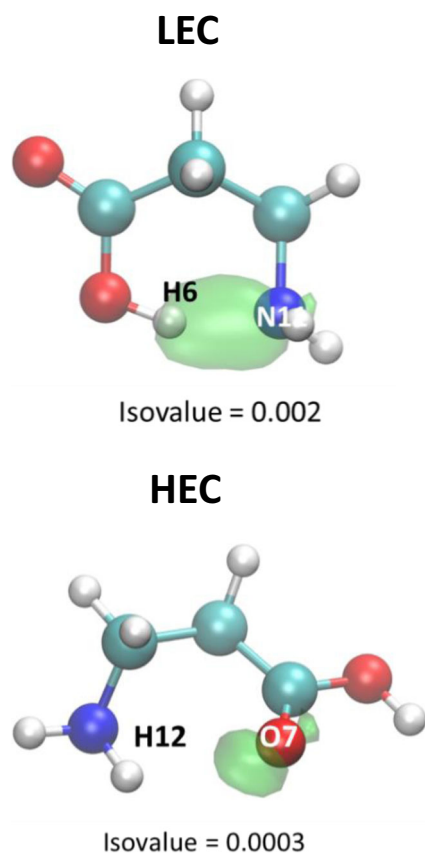


Fig. 7 FALDI-defined privilege of the H...Y interaction, relative to local secondary interactions (X...Y, X...Z, W...Y, H...W and H...Z) for **LEC** and **HEC** calculated at the B3LYP level

interactions. Since an AIL is present between H and Y atoms in both conformers, finding privileged delocalized density from FALDI's perspective supports Pendás *et al*'s AIL interpretation. We note, however, that the H...Y interaction in **LEC** forms a privileged *channel*, whereas in **HEC** only the region corresponding to the lone pair of atom Y is privileged (and to a much lesser extent, noting the difference in the isovalues). In comparison to all other delocalized-ED distributions in the molecule (Fig. S7 in PART 4 of the SI), the H...Y interaction in **LEC** is only dominant close to the lone-pair region of atom Y whereas it is not dominant at all in **HEC**.

We conclude this section by stating that the AIL between atoms H and Y in **LEC** is a result of (i) an inflow of density in the bonding region and (ii) a *privileged* channel of delocalized electron density across both basins that truly signifies a strong covalent aspect of intramolecular H-bonding. On the other hand, the observed AIL in **HEC** is most likely merely a topological phenomenon, despite an outflow of density and general lack of a channel of privileged density. Therefore, the H-bond in **HEC** shows comparatively little to no covalent character, mostly due to the fact that atom X donates more density into the X–H bond than into the H...Y bonding region. This is a fundamental difference between the red-shifted

intramolecular H-bond in **LEC** and the blue-shifted intramolecular H-bond in **HEC**, a novel finding given that both interactions are found in the same molecular system.

FAMSEC-based interpretation of the W–X–H...Y–Z region

The FALDI-based analysis has revealed in real space the atoms and molecular fragments that experienced most significant changes in density and this, in turn, has an influence on computed FAMSEC energy terms. This is because $\Delta N(A)$ and $\Delta_c \delta(\mathbf{r})$ descriptors will contribute (indirectly) to the computed changes in self-atomic, hence self-fragment ($\Delta E_{\text{self}}^{\mathcal{G}}$) and diatomic, hence intrafragment interaction energies ($\Delta E_{\text{int}}^{\mathcal{G}}$) when a conformational change from *ref* to *fin* takes place. Accordingly, we selected most relevant fragments containing atoms that indeed experienced most significant changes in both conformers, **LEC** and **HEC**, and computed FAMSEC-defined energy terms are indicated in Table 3.

At first glance it is immediately clear that data in Table 3 reflects the differences between the red- and blue-shifted H-bonding discussed in details in previous sections. Furthermore, there are many excellent correlations between trends in the computed FAMSEC energy terms and FALDI-as well topological-based analyses. To this effect, note that values obtained for the **LEC** (with 'proper' H-bond) are larger, in some cases almost an order of magnitude, when compared with those computed for the **HEC** (with 'improper' H-bond). Furthermore, the larger change in atomic populations found in **LEC** are reflected in larger $\Delta E_{\text{self}}^{\mathcal{G}}$ values for all molecular fragments in Table 3. Similarly, most significant interatomic deformation densities in **LEC** are reflected by much larger intrafragment interaction energy changes, the $\Delta E_{\text{int}}^{\mathcal{G}}$ term, in this conformer.

We will focus now on most important differences between red- and blue-shifted H-bonds from the FAMSEC perspective. To this effect let us consider the $\mathcal{G} = \{X, H\}$ fragment and we note that:

- $(\Delta E_{\text{self}}^{\mathcal{G}})_{\text{LEC}} \gg (\Delta E_{\text{self}}^{\mathcal{G}})_{\text{HEC}}$ and this correlates well with trends found for changes in (i) atomic electron population $\Delta N(A)$, Fig. 1 and (ii) atomic deformation densities of O- and N-atoms in **LEC** and **HEC**, respectively, shown in Fig. 3.
- The intrafragment interaction energy changed unfavourably for **LEC** but became more attractive in **HEC** reflecting the fact (discussed in details in the previous sections) that the X–H bond became weaker in **LEC** but stronger in **HEC**.
- This fragment's contribution to the energy of β -alanine was significant and of stabilizing nature only in the case of the **LEC**. This can be linked with large polarization

Table 3 Energy components used for the interpretation of selected important molecular fragments in **LEC** and **HEC**^a

Molecular fragment G		ΔE_{self}^G	ΔE_{int}^G	$\Delta E_{\text{attr-loc}}^G$	$\Delta \sum_{X \in \mathcal{H}} E_{\text{int}}^{G,X}$	$\Delta E_{\text{attr-mol}}^G$
LEC						
{O5,H6}	X–H	39.0	4.2	43.3	–69.8	–26.5
{H6,N11}	H··Y	37.2	–133.1	–95.9	125.0	29.1
{O5,H6,N11}	X–H··Y	64.4	–42.2	22.1	–85.5	–63.3
{O5,H6,N11,C8}	X–H··Y–Z	57.9	–35.2	22.8	–78.1	–55.4
{C1,O5,H6,N11}	W–X–H··Y	80.5	–150.5	–70.1	57.5	–12.5
HEC						
{N11,H12}	X–H	8.0	–1.8	6.2	–4.5	1.8
{H12,O7}	H··Y	5.8	–33.1	–27.3	50.0	22.7
{N11,H12,O7}	X–H··Y	10.4	7.7	18.2	–31.0	–12.9
{N11,H12,O7,C1}	X–H··Y–Z	10.6	–11.0	–0.4	2.2	1.8
{C8,N11,H12,O7}	W–X–H··Y	8.3	3.1	11.4	–21.5	–10.1

^a All values in kcal·mol^{–1} at MP2

effects that must facilitate the strengthening of interactions with remaining atoms of the **LEC**, as reflected by the large and negative (attractive) $\Delta E_{\text{int}}^{G,H}$ value.

- d) As one would expect, due to $(\Delta E_{\text{self}}^G)_{\text{LEC}} \gg (\Delta E_{\text{self}}^G)_{\text{HEC}}$, the {X,H} fragment became significantly more destabilized in the **LEC** as measured by the *loc*-FAMSEC term.

Besides clear differences, there must be several similarities because these two interactions represent an intramolecular H-bonding taking place in the same molecule and involve the same electronegative atoms, O and N. Indeed, FAMSEC recovers this notion fully as we observe similar trends in some energy terms in both conformers. Focusing on most important findings we note that:

- a) In case of the $G = \{H,Y\}$ fragment, (i) $\Delta E_{\text{int}}^G < 0$ and is several times larger (in absolute term) in **LEC**; this correlates very well with the interatomic delocalised deformation density (Fig. 4), which is also several times larger in **LEC**; (ii) this fragment was stabilized much more in **LEC** as we found *loc*-FAMSEC of about –95.9 and –27.3 kcal·mol^{–1} for **LEC** and **HEC**, respectively. This fragment became stabilized in both conformers because in each case the favourable diatomic interaction energy change ($\Delta E_{\text{int}}^G < 0$) compensated over an increase in self-atomic energies ($\Delta E_{\text{self}}^G > 0$). This is consistent with the presence of an AIL in both conformers and correlates well with the relative strength of the two H-bonds.
- b) The $G = \{X,H,Y\}$ fragment representing the often used three atom notation, X–H··Y, as expected, stabilized the molecule and contribution made in **LEC** is several times larger with *mol*-FAMSEC of about –63.3 and

–12.9 kcal·mol^{–1} for **LEC** and **HEC**, respectively. This fragment itself became destabilized on H-bonding and the *loc*-FAMSEC term is positive and of comparable value in both conformers.

According to IUPAC, the X, H, Y and Z atoms should be considered when describing an H-bond. It was then interesting to find out how this representation recovers the nature of the red- and blue-shifted H-bonds from the FAMSEC perspective. The 4-atom IUPAC fragment for **LEC** yields a local destabilization of +22.8 kcal·mol^{–1} but an overall molecular stabilization of –55.4 kcal·mol^{–1}. It is clear that including atom Z with the X–H··Y fragment does not significantly change the local energetics of the H-bond, and slightly decreases the molecular stabilization from the perspective of the fragment. Hence, a general description of H-bonding and conclusions arrived at are very much the same regardless whether X–H··Y or X–H··Y–Z representation is used; note that all five descriptors in Table 3 are similar for the two molecular fragments. A very different picture emerged in the case of **HEC** where 4-atom representation changed not only the values but also signs of most of the FAMSEC terms. Possibly most unexpected is the change from stabilizing to destabilizing molecule contribution made by the blue-shifted H-bond when 3- and 4-atom (IUPAC) representation was used, respectively. It appears that the IUPAC recommendation is not suitable for blue-shifted intramolecular H-bond in this case.

As discussed in preceding sections, we found the W-atom to be largely affected by the formation of the intramolecular H-bond in the **LEC**. Hence, we decided to consider FAMSEC computed energy components of the four-atom fragment W–X–H··Y. In contrast to the X–H··Y–Z fragment, the W–X–H··Y fragment is highly stabilized in **LEC** (*loc*-

FAMSEC = $-70.1 \text{ kcal}\cdot\text{mol}^{-1}$). This is mostly a result of very favourable local or intrafragment interaction stabilization which can be linked with large charge-polarization taking place on the H-bonding. This fragment also contributes to molecular stabilization ($\text{mol-FAMSEC} = -12.5 \text{ kcal}\cdot\text{mol}^{-1}$) and is the only fragment involving atoms H and Y to show both local and molecular stabilization in **LEC** showing again the importance of the W-atom. By contrast, this atom has not been influenced by the blue-shifted H-bond formation. This is also seen from FAMSEC analysis; the addition of W to the X–H \cdots Y fragment had no significant influence on the magnitude of all indices and their sign remained unchanged.

A few notable conclusions regarding the energetic changes (both local and non-local) of H-bond formation in β -alanine are evident from the discussion above:

1. The $\mathcal{G} = \{X,H\}$ fragment is locally destabilised in both conformers, but considerably less so in **HEC**. However, this fragment contributes to molecular stabilization only in **LEC**.
2. The three atoms directly involved in H-bonding, X,H and Y, are locally strained in both conformers by similar amount. Due to favourable interactions of the $\{X,H,Y\}$ fragment with the remaining atoms of the molecule, however, formation of the H-bond exerts an overall stabilizing influence on the entire molecular system that is much larger in the case of the red-shifted H-bond.
3. Including atom Z as a part of the H-bonding fragment does not significantly change the molecular energetics in **LEC**, but leads to molecular destabilization in **HEC**.
4. Including atom W as a part of the H-bonding fragment results in a very large local stabilization as well as an overall molecular stabilization in **LEC**, whereas in **HEC** it does not significantly change the energetics.

Clearly, upon formation of the H-bond the atoms involved in the red-shifted H-bond interact in a fundamentally different manner, both locally as well as with the rest of the molecule, in comparison with the blue-shifted H-bond.

Conclusions

We have presented a rare example of a molecule, the amino acid β -alanine, which can form a red- or blue-shifted intramolecular H-bond, depending on the *fin* conformer that is formed; in both cases the same heteroatoms are involved, O and N, acting as either an H-bond donor (O–H or N–H) or as H-bond acceptor and vice versa. We have shown that both the lower energy conformer (**LEC**) and the higher energy conformer (**HEC**) are stabilized relative to the fully linear molecule (**Lin**) and that intramolecular H-bonds are formed; a red-shifted H-bond is observed for **LEC** and a blue-shifted H-

bond is observed for **HEC**. Interestingly, the energy difference between **LEC** and **HEC** is quite large ($-4.9 \text{ kcal}\cdot\text{mol}^{-1}$, as calculated by MP2), despite many reports in literature which state that there is no fundamental difference between red-shifted and blue-shifted H-bonds. We have therefore investigated, using newly developed methods, the charge-distribution and energetic consequences of the H-bond formation in β -alanine in order to determine whether the nature of the observed H-bonds is fundamentally equivalent.

We have found several similarities between the red-shifted H-bond in **LEC** and the blue-shifted H-bond in **HEC**, all of which generally agrees with literature and the IUPAC recommended criteria to define an H-bond. Both H-bonds (i) show the presence of an AIL, (ii) are dominated by electrostatic interactions (as measured by the components of the IQA-defined diatomic interaction energy) and (iii) show distinctive changes in QTAIM-defined atomic populations at the H-bond donor (X), hydrogen atom (H) and H-bond acceptor (Y). Specifically, a large inflow of density is seen at atom X, a large outflow of density is seen at atom H, and atom Y remains generally unchanged, for both **LEC** and **HEC** relative to the **Lin** conformer. We have also evaluated the observed H-bonds in terms of a number of descriptors and criteria for H-bonding listed by IUPAC; according to the computed properties obtained, both were found to be in full agreement with the recommended IUPAC definition.

We have, however, found quite a large number of interesting and fundamental differences between these two H-bonds, including different charge rearrangement and delocalization patterns along the (i) H \cdots Y interaction as well as (ii) the X–H bond, and (iii) a different manner of interaction of the X–H \cdots Y fragment with the remaining atoms in the molecule, specifically the carbon atoms bonded to X and Y (W and Z, respectively).

The newly developed FALDI charge decomposition scheme for calculating conformational deformation densities was utilized to investigate the changes in electron density and delocalization patterns of the two *fin* conformers. FALDI revealed a very distinctive difference between the red- and blue-shifted H-bonds in terms of the manner in which electrons are redistributed when the H-bond is formed: whereas atom Y donates density into the interatomic regions of the H \cdots Y interaction as well as the X–H bond in **LEC**, atom Y of **HEC** donates density predominantly into the X–H bond, with a negligible contribution into the H \cdots Y bonding region (Figs. 3 and 6). Similarly, the manner in which density is delocalized between atoms H and Y upon H-bond formation was found to be very different: a channel of delocalized density is clearly formed along the H \cdots Y interaction in **LEC**, whereas density between atoms H and Y in **HEC** is mostly delocalized along the X–H bond and the Y lone-pair region (Figs. 4 and 6). Due to these differences, a net influx of density is seen along the H \cdots Y interaction of the red-shifted H-bond,

which is consistent with an interaction of increasing covalent character, whereas an outflow of density is seen between atoms H and Y for the blue-shifted H-bond. We have also investigated the privilege of the exchange-correlation interaction between atoms H and Y (Figs. 7 and S7 in PART 4 of the SI), in line with the concept of Pendás et al. of the AIL as a *privileged exchange channel*. We found that the red-shifted H-bond in **LEC** is privileged relative to all other interactions in the molecule, while this feature is clearly lacking for the blue-shifted H-bond in **HEC**. For these abovementioned reasons, we regard the blue-shifted intramolecular H-bond in **HEC** to have a very small covalent component and show a fundamentally different change in charge distribution as compared to the red-shifted H-bond in **LEC**, leading to a weaker intramolecular H-bond in **HEC**.

We have also found that, according to changes in various QTAIM descriptors at the BCP of the X–H bond (Table 2), the red-shifted X–H bond becomes weaker and more electrostatic and the blue-shifted X–H bond becomes stronger and more covalent. However, in both conformers the number of electrons shared by X and H decreases, together with a decrease in IQA exchange-correlation stabilization. Therefore, the increase in covalency, bond strength and the origin of the blue-shift of the X–H bond in **HEC** is a result of increased density from atom Y, rather than from atom X, which is a novel discovery realizable by FALDI.

Finally, using the FAMSEC energy decomposition approach, we have shown that the relative strength of the red-shifted H-bond in **LEC** is not only a result of local changes among atoms X, H and Y, but also non-local changes in the interactions of the 3-atom fragment with the remaining atoms of the molecule. In both H-bonds investigated, a local destabilization of the X–H...Y fragment is observed of roughly the same magnitude. However, this fragment shows very favourable interactions with the remainder of the molecule, resulting in an overall molecular stabilization, but considerably more so for **LEC** than for **HEC**. Importantly, FAMSEC therefore reveals that the molecular stabilization afforded by the formation of an intramolecular interaction is not a local event but rather inclusive of the entire molecule. Specifically, FAMSEC data shows that for the H-bond in **LEC**, the W carbon bonded to atom X plays a very important role in stabilizing the molecule. This is a counter-intuitive result which we will investigate more thoroughly in the future, since IUPAC recommends that atom Z, rather than atom W, might be important in certain H-bonds. FALDI also shows considerably different charge rearrangements of the carbon backbone for **LEC** and **HEC**, as well as different delocalization patterns across the W–X and Z–Y bonds. Finally, changes in diatomic polarization reveals that formation of the H-bond in **LEC** results in an overall polarization of both the X–H...Y fragment as well as the carbon backbone, whereas **HEC** becomes slightly less polarized overall. Stronger electrostatic

interactions throughout the entire molecule is observed in **LEC**, providing a possible explanation for the considerably stronger interactions of the X–H...Y fragment with the remainder of the molecule as observed by FAMSEC. Therefore, we note that the red-shifted H-bond in **LEC** interacts in a fundamentally different fashion with the remainder of the molecule in comparison with the blue-shifted H-bond in **HEC**, leading to a considerably stronger intramolecular H-bond and more stable molecule overall.

In conclusion, we observe very different mechanisms of formation for different H-bonds that occur in two different conformers of β -alanine. While we cannot yet show whether these are general differences between red- and blue-shifted intramolecular H-bonds or whether it is specific for β -alanine, we have shown the usefulness of FALDI and FAMSEC in providing a novel view of H-bonding and providing critical information regarding the origin of density and energetic changes in the formation of intramolecular interactions.

Acknowledgments This work is based on the research supported in part by the National Research Foundation of South Africa (Grant Number 105855).

Compliance with ethical standards

Conflict of Interest The authors declare that they have no conflict of interest.

References

1. Coppola GM, Schuster HF (1987) In asymmetric synthesis: construction of chiral molecules using amino acids. Wiley, New York
2. Blaskovich MA (2010) In handbook on syntheses of amino acids: general routes for the syntheses of amino acids, 1st edn. New York, Oxford University Press
3. Waingeh VF, Ngassa FN, Song J (2015) Open J Phys Chem 5:122–131
4. Eugenia Sanz M, Lesarri A, Isabel Peña M, Vaquero V, Cortijo V, López JC, Alonso JL (2006) J Am Chem Soc 128:3812–3817
5. Abirami S, Xing YM, Tsang CW, Ma NL (2005) J Phys Chem A 109:500–506
6. Piekarski DG, Díaz-Tendero S (2017) Phys Chem Chem Phys 19: 5465–5476
7. Arunan E, Desiraju GR, Klein RA, Sadlej J, Scheiner S, Alkorta I, Clary DC, Crabtree RH, Dannenberg JJ, Hobza P, Kjaergaard HG, Legon AC, Mennucci B, Nesbitt DJ (2011) Pure Appl Chem 83: 1637–1641
8. Pinchas S (1955) Anal Chem 27:2–6
9. Schneider WG, Bernstein HJ (1956) Trans Faraday Soc 52:13–18
10. Hobza P, Spirko V, Selzle HL, Schlag EWJ (1998) Phys Chem A 102:2501–2504
11. Hobza P, Havlas Z (2000) Chem Rev 100:4253–4264
12. Caminati W, Melandri S, Moreschini P, Favero PG (1999) Angew Chem Int Ed 38:2924–2925
13. Hobza P, Havlas Z (1999) Chem Phys Lett 303:447–452
14. Jemmis ED, Giju KT, Sundararajan K, Sankaran K, Vidya V, Viswanathan KS, Leszczynski JJ (1999) Mol Struct 510:59–68

15. Jemmis ED, Subramanian G, Nowek A, Gora RW, Sullivan RH, Leszczynski JJ (2000) *Mol Struct* 556:315–320
16. van der Veken BJ, Herrebout WA, Szostak R, Shchepkin DN, Havlas Z, Hobza PJ (2001) *Am Chem Soc* 123:12290–12293
17. Delanoye SN, Herrebout WA, van der Veken BJ (2002) *J Am Chem Soc* 124:7490–7498
18. Hobza P, Havlas Z (2002) *Theor Chem Accounts* 108:325–334
19. Delanoye SN, Herrebout WA, van der Veken BJ (2002) *J Am Chem Soc* 124:11854–11855
20. Matsuura H, Yoshida H, Hieda M, Yamanaka S, Harada T, Shinya K, Ohno K (2003) *J Am Chem Soc* 125:13910–13911
21. Alonso JL, Antolinez S, Blanco S, Lesarri A, Lopez JC, Caminati W (2004) *J Am Chem Soc* 126:3244–3249
22. Diana E, Stanghellini PL (2004) *J Am Chem Soc* 126:7418–7419
23. Barnes AJ (2004) *J Mol Struct* 704:3–9
24. Castellano RK (2004) *Curr Org Chem* 8:845–865
25. Kryachko ES (2006) In: Grabowski SJ (ed) *Hydrogen bonding - new insights*. Springer, Dordrecht **Chapter 8**
26. Nishio M, Hirota M, Umezawa Y (1998) In the CH/interaction. Evidence, nature, and consequences. Wiley-VCH, New York
27. Buděšínský M, Fiedler P, Arnold Z (1989) *Synthesis* 11:858–860
28. Boldeskul IE, Tsybmal IF, Ryltsev EV, Latajka Z, Barnes AJ (1997) *J Mol Struct* 436–437:167–171
29. Hobza P, Špirko V, Havlas Z, Buchhold K, Reimann B, Barth HD, Brutschy B (1999) *Chem Phys Lett* 299:180–186
30. Reimann B, Buchhold K, Vaupel S, Brutschy B, Havlas Z, Spirko V, Hobza P (2001) *J Phys Chem A* 105:5560–5566
31. Gu Y, Kar T, Scheiner S (1999) *J Am Chem Soc* 121:9411–9422
32. Karger N, Amorim da Costa AM, Ribeiro-Claro PJA (1999) *J Phys Chem A* 103:8672–8677
33. Zierkiewicz W, Michalska D, Havlas Z, Hobza P (2002) *ChemPhysChem* 3:511–518
34. Wojtulewski S, Grabowski SJ (2005) *Chem Phys* 309:183–188
35. Joseph J, Jemmis ED (2007) *J Am Chem Soc* 129:4620–4632
36. Chang X, Zhang Y, Weng X, Su P, Wu W, Mo Y (2016) *J Phys Chem A* 120:2749–2756
37. Scheiner S, Kar T (2002) *J Phys Chem A* 106:1784–1789
38. Dykstra CE (1988) *Acc Chem Res* 21:355–361
39. Masunov A, Dannenberg JJ, Contreras RH (2001) *J Phys Chem A* 105:4737–4740
40. Hermansson K (2002) *J Phys Chem A* 106:4695–4702
41. Qian WL, Krimm S (2002) *J Phys Chem A* 106:6628–6636
42. Qian WL, Krimm S (2005) *J Phys Chem A* 109:5608–5618
43. Cubero E, Orozco M, Hobza P, Luque FJ (1999) *J Phys Chem A* 103:6394–6401
44. Li XS, Liu L, Schlegel HB (2002) *J Am Chem Soc* 124:9639–9647
45. Alabugin IV, Manoharan M, Peabody S, Weinhold F (2003) *J Am Chem Soc* 125:5973–5987
46. Bent H (1961) *Chem Rev* 61:275–311
47. Mo Y, Wang C, Guan L, Braïda B, Hiberty PC, Wu W (2014) *Chem Eur J* 20:8444–8452
48. Kitaura K, Morokuma K (1976) *Int J Quantum Chem* 10:325–340
49. Mitoraj M, Michalak AA (2007) *J Mol Model* 13:347–355
50. Mitoraj M, Michalak A, Ziegler T (2009) *J Chem Theory Comput* 5:962–975
51. Buemi G, Zuccarello F (2002) *J Mol Struct (THEOCHEM)* 581: 71–85
52. Lipkowski P, Koll A, Karpfen A, Wolschann P (2002) *Chem Phys Lett* 360:256–263
53. Jabłoński M, Monaco G (2013) *J Chem Inf Model* 53:1661–1675
54. Jabłoński M, Kaczmarek A, Sadlej AJ (2006) *J Phys Chem A* 110: 10890–10898
55. Jabłoński M (2000) MSc Dissertation, Nicolaus Copernicus University, Toruń, Poland
56. Nowroozi A, Raissi H, Farzad F (2005) *J Mol Struct (THEOCHEM)* 730:161–169
57. Espinosa E, Molins E, Lecomte C (1998) *Chem Phys Lett* 285:170–173
58. De Lange JH, Cukrowski I (2017) Towards deformation densities for intramolecular interactions without radical reference states using the fragment, atom, localized, delocalized and interatomic charge density decomposition scheme. *J Comp Chem*. doi:10.1002/jcc.24772
59. Cukrowski I (2015) *Comp Theory Chem* 1066:62–75
60. Blanco MA, Pendás AM, Francisco E (2005) *J Chem Theory* 1: 1096–1109
61. Bader RFW (1990) *Atoms in molecules: a quantum theory*. Oxford University Press, Oxford
62. McWeeny R (1992) *Methods of molecular quantum mechanics*, 2nd edn. Academic Press, London
63. Cukrowski I, Sagan F, Mitoraj MP (2016) *J Comp Chem* 37(32): 2783–2798
64. Ponec R (1997) *J Math Chem* 21:323–333
65. Pendás AM, Francisco E, Blanco MA, Gatti C (2007) *Chem Eur J* 13:9362–9371
66. Frisch MJ, Trucks GW, Schlegel HB, Scuseria GE, Robb MA, Cheeseman JR, Scalmani G, Barone V, Mennucci B, Petersson GA, Nakatsuji H, Caricato M, Li X, Hratchian HP, Izmaylov AF, Bloino J, Zheng G, Sonnenberg JL, Hada M, Ehara M, Toyota K, Fukuda R, Hasegawa J, Ishida M, Nakajima T, Honda Y, Kitao O, Nakai H, Vreven T, Montgomery Jr JA, Peralta JE, Ogliaro F, Bearpark M, Heyd JJ, Brothers E, Kudin KN, Staroverov VN, Kobayashi R, Normand J, Raghavachari K, Rendell A, Burant JC, Iyengar SS, Tomasi J, Cossi M, Rega N, Millam JM, Klene M, Knox JE, Cross JB, Bakken V, Adamo C, Jaramillo J, Gomperts R, Stratmann RE, Yazyev O, Austin AJ, Cammi R, Pomelli C, Ochterski JW, Martin RL, Morokuma K, Zakrzewski VG, Voth GA, Salvador P, Dannenberg JJ, Dapprich S, Daniels AD, Farkas Ö, Foresman JB, Ortiz JV, Cioslowski J, Fox DJ (2009) *Gaussian 09*, Revision D.01. Gaussian, Inc., Wallingford
67. Grimme S (2011) *Wiley Interdisciplinary Reviews: Computational Molecular Science* 1(2):211–228
68. Keith TA (2017) *AIMAll (Version 16.10.31)*. TK Gristmill Software, Overland Park (aim.tkgristmill.com)
69. Polestshuk PM (2013) *J Comp Chem* 34:206–219
70. Polestshuk PM (2013) *J Chem Phys* 139:054108
71. Buijse MA, Baerends EJ (2002) *Mol Phys* 100:401–421
72. Humphrey W, Dalke A, Schulten K (1996) *J Molec Graphics* 14: 33–38
73. Cukrowski I, de Lange JH, Adeyinka AS, Mangondo P (2015) *Comp Theo Chem* 1053:60–76
74. Bondi A (1964) *J Phys Chem* 68:441–451
75. Bader RFW, Essén H (1984) *J Chem Phys* 80:1943–1960
76. Espinosa E, Alkorta I, Elguero J, Molins E (2002) *J Chem Phys* 117:5529–5542
77. Jenkins S, Morrison I (2000) *Chem Phys Lett* 317:97–102
78. Feynman RP (1939) *Phys Rev* 56:340–344
79. Tognetti V, Joubert L (2013) *J Chem Phys* 138(2):024102–024109

Chapter 8: Conclusions

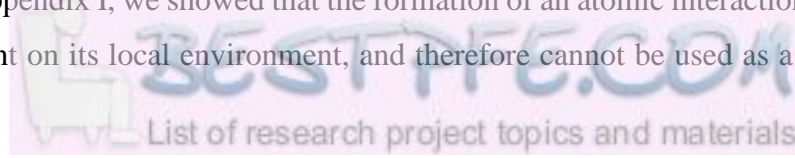
Summary

The primary novel development of this work is the derivation and implementation of the Fragment, Atomic, Localized, Delocalized and Interatomic (FALDI) electron density decomposition. FALDI is a quantum chemical analytical scheme that is atom-centric and density-based. The FALDI scheme decomposes the electron density at any given coordinate into various 1- and 2-centre contributions related to the correlated probability of finding two electrons simultaneously at two coordinates – the electron pair density. At its base level, FALDI provides real-space, molecular-wide distributions of electrons localized to a single atom or electrons delocalized amongst two different atoms, thereby providing a holistic approach to a quantum mechanical definition of an atom in a molecule.

This thesis discussed and derived the basic concept underlying FALDI as well as various implementations and applications of the theory. Generally, the work can be divided into two aspects: FALDI analysis of static (single state) electron density distributions, and FALDI analysis of deformation (two state) density distributions.

Three different topics regarding static electron density analysis using FALDI were covered. The first concerned the description of localized and delocalized electrons of an atom in a molecule. In Chapter 3, we showed that the popular localization indices (LIs)^{1,2} of the Quantum Theory of Atoms in Molecules (QTAIM)³ is inherently flawed and misinterpreted. Using visualizations of FALDI's localized electron density (*loc*-ED) distributions, we proved that QTAIM LIs describe a certain degree of *delocalized* electrons as well. We then developed an approach to calculate *exclusively* localized and delocalized electrons. We showed that our approach not only recovers classically expected core, non-bonded and valence electron counts for simple molecules, but also shed some classically unexpected light on the nature of aromatic electrons in benzene and the involvement of core electrons in formamide. In addition, our diagonalized FALDI distributions provide a very clear, atom-centric and density-based analytical tool to quantify and visualize electrons distributed in various modes, such as σ - and π -bonding distributions.

We also addressed a major issue regarding the measurement of electron density concentration. In Appendix I, we showed that the formation of an atomic interaction line (AIL) is strongly dependent on its local environment, and therefore cannot be used as a measure of



molecular stabilization in line with Feynman's theorem⁴, as Bader often argued it could.^{3,5,6} In Chapters 4 and 5, we showed that a much more exact measure of concentration can be made via the partial second derivatives of FALDI localized and delocalized density components. Such a measure of concentration is inherently non-relative and holistic, and does not suffer from a dependence on the local environment as an AIL. In this regard, we managed to develop a methodology for classifying each FALDI component as whether it concentrates, depletes or lowers the electron density, relative to a specific coordinate. We showed that the origin of any concentration or depletion is associated with the interference patterns of molecular orbitals simultaneously overlapping two or more atomic basins. We thus concluded that our classification scheme can be linked to molecular orbital bond theory, and we therefore established a strong link between quantum chemical topology (QCT)⁷ and conceptual molecular orbital theory. We were therefore justified in labelling each of our FALDI components as bonding, non-bonding and anti-bonding, relative to a specific coordinate in space.

Using this classification, we investigated the multi-nature character of a number of AILs describing conventional interactions in Chapter 4. We recovered the classical 3-atom nature of an H-bond, and also showed the role which other atoms and atom-pairs play in the electron density description of an intramolecular H-bond. We also fully recovered the three-centre nature of B–H–B bonds in diborane, but also showed how electrons delocalized between the H···H contact as well as between the B···B contact contribute to the AILs between B and H atoms. Finally, we also illustrated the comparatively larger multi-centre character of a C=M bond in a Fischer carbene than a Schrock carbene.

We extended our bonding, non-bonding and anti-bonding classification scheme further in Chapter 5, where we developed a tool with which one can investigate *why* an AIL is present in some interactions but absent in others. The proposed $CP(\mathbf{r})$ function is an AIL indicator that takes into account which FALDI components *facilitate* or *hinder* formation of an AIL. Using the $CP(\mathbf{r})$ in three case studies, we showed that the presence of an AIL is a result of an increased rate of change of facilitating (FALDI's bonding density distributions) relative to the rate of change of depleting and 'disruptive' (FALDI's nonbonding and antibonding distributions, respectively). Our criterion provides an additional understanding of an AIL, as well as the general electron density distributions in internuclear spaces. Since we can also link FALDI's bonding, nonbonding and antibonding distributions to trends in molecular orbital interference

patterns as well as the forces acting on nuclei, we hope that the $CP(\mathbf{r})$ function will provide a strong and interpretive tool in the future to investigate chemical bonding.

In Appendix 1, we suggested that the deformation density – the change in electron density between a bound and unbound state – is also a better measure of the accumulation of density in an internuclear region for the fulfilment of Feynman's theorem.⁴ However, orthodox deformation densities is only truly sensible for the study of intermolecular bonds, where a well-defined reference state is chemically viable. Using the FALDI decomposition, we developed a scheme for the calculation of deformation densities resulting from conformational change rather than fragmentation. We derive our conformational deformation density approach in Chapter 6, and demonstrate that it is necessary to have molecular-wide 1-centre and 2-centre contributions, which can be separately transformed from a reference state to a final state, in order to calculate a sensible change in density. We compare orthodox, fragment-based deformation densities with our FALDI-based approach for the formation of an intramolecular H-bond in ethylene diamine, and showed that while both approaches capture the essential charge changes related to H-bond formation, the orthodox approach displays a large degree of interference due to the use of radical reference states. We also note that our approach can be used in conjunction to the popular Extended Transition State coupled with Chemical Valence (ETS-NOCV) approach,⁸ for validating as well as extending ETS-NOCV results. The ETS-NOCV approach is used in Appendices 2 and 3 for the study of gold-hydride bonds as well as elucidating the nature of carbene bonds.

Finally, Chapter 7 applies our FALDI-based conformational deformation density on the formation of a red-shifted and a blue-shifted intramolecular H-bond in the amino acid β -alanine. In conjunction with the Fragment Attributed Molecular System Energy Change (FAMSEC) energy decomposition,⁹ we elucidated the effect of W and Z atoms in describing a multi-centre, $WX-H\cdots YZ$ H-bond. In addition, we showed that the fundamental nature of the red-shifted H-bond is significantly different than the nature of the blue-shifted H-bond, a hypothesis contrary to some literature suggestions.

The FALDI decomposition, as a whole, represents an extension of Baders' concept of a quantum atom in a molecule. Through the FALDI decomposition, an atom in a molecule defined by the topological condition of a zero-flux surface³ consists of (i) a nucleus signified by a local maxima in the electron density, (ii) a set of core electrons localized *exclusively* to the atomic basin, (iii) a set of non-bonded electrons, predominantly localized to the basin through constructive interference of molecular-wide functions and (iv) a set of delocalized

electrons that can be found in other atomic basins as well. Each of the electronic components can be quantified, either as an integrated total or along a 1D vector as well as visualized in 3D real-space using FALDI. In addition, each electronic component can be decomposed in a number of partially occupied functions, giving exact orbital density occupations such as core $2p$ or π -bonding electron counts. The density of each atom, as well as the density shared by each atom-pair, can contribute to the concentration, depletion or removal of electron density throughout the entire molecule as a result of (de)constructive interference of molecular orbitals overlapping two atomic basins simultaneously. Therefore, the exact manner in which an atom or an atom-pair contributes to the bonding, non-bonding or antibonding modes of any chemical interaction can be elucidated, and the manner in which multiple atoms or atom-pairs contribute simultaneously, *i.e.* the multi-centre nature of an interaction, can be determined. Finally, the density that is shared by two atomic basins can be visualized in real-space, and often resembles channels of delocalized density. Such channels are reminiscent of a relatively recent interpretation of an AIL, Pendás *et al*'s concept of privileged exchange channels.¹⁰

We suspect that we have only barely touched the surface of the topics that can be investigated using the FALDI decomposition. We hope that it will provide additional analytical tools for theoretical and computational researchers, as well as establish a stronger bridge between conceptual and theoretical chemistry.

Implications

As mentioned in Chapter 1, the divide between quantum chemistry (an intrinsically holistic science) and general, experimental chemistry (an intrinsically atomistic science) is quite large and deceptively difficult to bridge. Specifically, the cornerstones of chemistry – atoms and bonds – are ill-defined in molecular quantum chemistry. A strong and universal quantum theory of an atom in a molecule provides a very good link between quantum and conceptual chemistry.

FALDI provides an extension of QTAIM's atoms, in that the holistic nature of electrons within a molecule is fully taken into account. FALDI provides a detailed view of how electrons found on average within an atomic basin are distributed throughout a molecule, whether they are localized or delocalized, and how they are distributed relative to chemical interactions. FALDI therefore strengthens the link created by the inception of QTAIM between conceptual chemistry and molecular quantum chemistry. FALDI also provides a very detailed description of electron density distributions with relation to chemical interactions, *viz.* chemical bonding, from a fully atomic *and* quantum mechanical perspective.

We note, however, that a severe paradigm shift is associated with the electron density distributions in internuclear regions and chemical bonding, as discussed in Chapters 4 and 5. FALDI analyses in this thesis have revealed the very prominent role of multicenter descriptions of chemical interactions, even for seemingly ‘pure’ diatomic bonds. If we are to arrive at a universal theory of chemical bonding, then it is very likely that predominantly diatomic bond models will become archaic.

Future Work

While this thesis explores a large number of topics related to both the FALDI decomposition scheme as well as QTAIM, most of the topics can be further explored as well as applied to a larger set of systems. That said, there are a few technical details related to the implementation of FALDI which is of quite a high priority to us.

Most importantly is the implementation of FALDI using multi-determinant wavefunctions. Currently, the *orthodox* FALDI decomposition scheme can be applied to any wavefunction using canonical orbitals *or* partially occupied, natural orbitals.¹¹ However, Localized-Delocalized-Overlap (LDO, Chapter 3) free *loc*-ED and *deloc*-ED distributions are currently limited to Hartree-Fock or Density Functional Theory wavefunctions. While the full implementation of FALDI for multi-determinant wavefunctions should be relatively straightforward (following along the lines of the correlated implementations of Domain Averaged Fermi Holes¹²⁻¹⁵), it will require significant re-design of the current computational algorithm that we have implemented.

Our FALDI code itself was developed in various stages throughout the development of the FALDI scheme. While the code has been parallelized, as well as compiled on both UNIX and Windows, the memory-handling of the code is not optimized for scaling to larger molecular systems. We therefore hope to redesign our software in order to fully incorporate all of the features of FALDI in a computationally efficient manner.

In terms of the development of the theory itself, we wish to further investigate the topology of specific FALDI components. Topological analysis is a useful tool to condense information and reveal trends across multiple systems, and topological analysis of specific FALDI components might reveal fundamental properties of these distributions. We also want to extend the FALDI scheme to the decomposition of other scalar fields related to the electron density, such as the kinetic energy density or Bader’s virial field.³ We hope that such developments can lead to improved tools with which concepts, such as chemical bonding, can be explored.

The conformational deformation density introduced in this thesis show quite some promise for the study of intramolecular bonds, or for calculating changes in density related to conformational changes (such as along normal modes, or for perturbed geometries in excited states). While orthodox, fragment-based deformation densities have been used before to study such systems, we wish to revisit many previous studies using our conformational approach. In addition, we wish to explore the full range of our approach in an applied fashion in conjunction with experimental studies.

The FALDI scheme inherently allows for a careful investigation of long-range atom communication, specifically in terms of through-space or through-bond mechanisms. Long-range communications are particularly prevalent in projects involving semi-conductors and photochemical applications. Therefore, we expect the FALDI approach to provide very useful information where long-range communication is important.

Finally, we aim to use FALDI in exploring some fundamental and conceptual aspects of atoms in molecules and interactions between atoms. Concepts such as aromaticity, resonance and valency are relatively well-understood at a conceptual level, but difficult to express using molecular quantum mechanics. We expect FALDI to be able to provide some insight regarding many general chemistry concepts fundamentally related to an atom or the bonds between atoms.

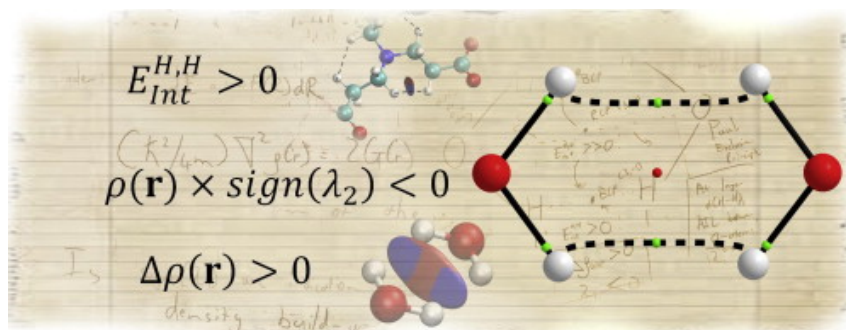
References

1. R. F. Bader; M. E. Stephens. *J. Am. Chem. Soc.* **1975**, *97*, 7391-7399.
2. R. Daudel; R. Bader; M. Stephens; D. Borrett. *Can. J. Chem.* **1974**, *52*, 1310-1320.
3. R. F. Bader. In *Atoms in molecules*; Wiley Online Library, **1990**.
4. R. P. Feynman. *Physical Review* **1939**, *56*, 340.
5. R. F. Bader. *J. Phys. Chem. A* **2009**, *113*, 10391-10396.
6. R. F. Bader. *J. Phys. Chem. A* **1998**, *102*, 7314-7323.
7. P. L. Popelier. In *The Chemical Bond II*; Springer, **2016**, p 71-117.
8. M. P. Mitoraj; A. Michalak; T. Ziegler. *J. Chem. Theory Comput.* **2009**, *5*, 962-975.
9. I. Cukrowski. *Comput. Theor. Chem.* **2015**, *1066*, 62-75.
10. A. M. Pendás; E. Francisco; M. A. Blanco; C. Gatti. *Chem. Eur. J.* **2007**, *13*, 9362-9371.
11. A. Müller. *Phys. Lett. A* **1984**, *105*, 446-452.
12. P. Bultinck; D. L. Cooper; R. Ponec. *J. Phys. Chem. A* **2010**, *114*, 8754-8763.
13. E. Francisco; A. M. Pendás; A. Costales. *PCCP* **2014**, *16*, 4586-4597.
14. R. Ponec; D. L. Cooper. *Faraday Discuss.* **2007**, *135*, 31-42.
15. R. Ponec; D. L. Cooper. *J. Phys. Chem. A* **2007**, *111*, 11294-11301.

Appendix I. Evaluating common QTAIM and NCI interpretations of the electron density concentration through IQA interaction energies and 1D cross-sections of the electron and deformation density distributions

Published in:

Computational and Theoretical Chemistry, **2015**, 1053, 60–76.



The internuclear electron density distributions of various inter- and intramolecular interactions were investigated using QTAIM, IQA and NCI techniques. A novel method for examining cross-sections of the electron density along the vector defined by the second eigenvalue of the Hessian matrix is introduced. The existence of atomic interaction lines is shown to be extremely dependent on the local environment and is mostly independent of the nature of the interaction. The deformation density is suggested as a more trustworthy measure of electron accumulation in terms of chemical bonding than the concentration of electron density as used to define QTAIM “bond paths” or NCI “regions of attraction”.

Electronic supplementary information available at: <https://doi.org/10.1016/j.comptc.2014.10.005>.



Contents lists available at ScienceDirect

Computational and Theoretical Chemistry

journal homepage: www.elsevier.com/locate/comptc

Evaluating common QTAIM and NCI interpretations of the electron density concentration through IQA interaction energies and 1D cross-sections of the electron and deformation density distributions



Ignacy Cukrowski*, Jurgens H. de Lange, Adedapo S. Adeyinka, Paidamwoyo Mangondo

Department of Chemistry, Faculty of Natural and Agricultural Sciences, University of Pretoria, Lynnwood Road, Hatfield, Pretoria 0002, South Africa

ARTICLE INFO

Article history:

Received 15 July 2014

Received in revised form 2 October 2014

Accepted 2 October 2014

Available online 12 October 2014

Keywords:

QTAIM

IQA

NCI

Deformation density

Chemical bonding

Bond path

ABSTRACT

Nine kinds of inter- and intramolecular interactions were investigated by exploring the topology of electron density in the interatomic regions using standard protocols of QTAIM, IQA and NCI techniques as well as in-house developed cross-sections of the electron and deformation density distributions. The first four methods provide the properties of the resultant density distribution in a molecular system whereas the later illustrates the process, inflow or outflow of density from fragments to the interatomic region of an interaction on its formation in a molecular system. We used (i) the QTAIM-defined atomic interaction line, AIL (presence or absence), (ii) IQA-defined interaction energy, $E_{int}^{A,B}$, and its components, classical $V_{cl}^{A,B}$ and exchange–correlation $V_{xc}^{A,B}$ term, (iii) NCI-defined isosurfaces to identify local regions of accumulated ($\lambda_2 < 0$) or depleted ($\lambda_2 > 0$) density relative to immediate environment, and (iv) deformation density for which $\Delta\rho(\mathbf{r}) > 0$ indicates an inflow or otherwise an outflow of density on the interaction formation to explore the nature of the interactions. We found (i) AILs for highly attractive and repulsive interactions, regardless whether an inflow ($\Delta\rho(\mathbf{r}) > 0$) or outflow of density into the interatomic region, (ii) no correlation between the signs of λ_2 and $E_{int}^{A,B}$; both, highly repulsive and attractive, interactions might have locally depleted density and *vice versa*, (iii) locally accumulated density ($\lambda_2 < 0$) does not imply that this is the result of an inflow ($\Delta\rho(\mathbf{r}) > 0$) of density and this equally applies to attractive and repulsive interactions either with or without an AIL. Results obtained demonstrate that the molecular environment can change the character of an interaction radically, from (i) attractive to repulsive, (ii) $\lambda_2 < 0$ to $\lambda_2 > 0$, or (iii) $\Delta\rho(\mathbf{r}) > 0$ to $\Delta\rho(\mathbf{r}) < 0$; hence, none of the topological indices used here, either separately or combined, can be used to definitely predict the (de)stabilizing nature of an interaction except highly repulsive ones for which the absence of AIL, interatomic density depletion and outflow of density on interaction formation are observed.

© 2014 Elsevier B.V. All rights reserved.

1. Introduction

The analysis of the topology of the electron density, for instance as it is used in the Quantum Theory of Atoms in Molecules (QTAIM) [1] and the more recent Non-Covalent Interactions (NCI) [2–4] method, is commonly used to identify and classify inter- and intramolecular interactions in molecular systems. Due to the relatively low computational costs, these methods (under the umbrella of Quantum Chemical Topology (QCT) [5]) have found widespread use in all fields of chemistry, ranging from drug-design [6] to catalysis [7] to large biological systems [8]. In QTAIM, the presence of a bridge of maximal electron density between two atoms, commonly referred to as a bond path or an atomic interaction line (AIL), is

observed for most cases where a classical chemist would expect a chemical bond. Consequently, many chemists commonly use the presence of an AIL as an indication of a chemical bond [9–12] or, at the very least, a bonding interaction [13,14]. Numerous cases exist, however, where either (i) classical chemists expect a bonding interaction (or it is shown through other methods, such as energy decomposition schemes) but no AIL is present [15], or (ii) steric repulsion is believed to exist, but an AIL is seen regardless [16–26]. These problem cases have resulted in a very long debate, questioning on one hand the validity and interpretation of QTAIM results [27–31] and on the other hand the nature of classical chemical concepts, such as steric repulsion [32–36]. The chemical bond itself also came into question since, as Bader put it, ‘Why should a bond path, which recovers all Lewis structures, not be associated with bonding in other cases?’ [28]. Although many regard the debate to

* Corresponding author.

be stale [37,38], new papers are still being published regarding the interpretation and physical nature of AILs [39–46].

NCI managed to solve one branch of QTAIM-associated problems, by showing that the absence of an AIL does not imply that electron density cannot be concentrated in the bonding region of an interaction. NCI identifies inter- and intramolecular interactions by finding regions of low electron density between atoms where the reduced density gradient (RDG) tends to zero [2]. These regions are then classified as either “stabilizing”, when electron density is concentrated, or “destabilizing”, when electron density is depleted [2–4,47,48]. NCI therefore supplements typical QTAIM analysis in three ways: (i) it identifies an interaction in 3D space, whereas QTAIM only shows bridges, (ii) it can detect electron density concentration, despite the absence of an AIL, and (iii) it can also identify interactions due to regions of electron depletion. NCI can also be used to approximately analyse interactions based only on the geometries (without the need for an electronic structure calculation) thereby allowing it to be used for very large systems. However, NCI will always show a region of concentration wherever an AIL is present [49], and is thus marred by the same problem of interpretation with regards to controversial interactions (such as the CH \cdots HC interactions in the bay of biphenyl). Both NCI and QTAIM are very attractive tools for a computational chemist to use, for their relative simplicity, insight and low computational cost but interpreting the results of these methods, especially in the realm of potentially new and not-yet-understood interactions, is still very unclear.

The so-called orthodox interpretation of an AIL, as given by Bader [50], is that it signals a *bonding interaction*, and only at equilibrium geometries (when no net forces are acting on the atoms) it can be related to a chemical bond. Bader arrived [50] to this statement by first pointing out that the sign of the eigenvalues λ_1 , λ_2 and λ_3 , of the Hessian matrix (the ordered matrix of second derivatives in 3D space), as well as the sum of eigenvalues, the Laplacian ($\nabla^2\rho(\mathbf{r})$), can be related to the concentration or depletion of electron density in a specific axis or at a point, respectively. Specifically, when $\nabla^2\rho(\mathbf{r}) > 0$, the second-order change in the electron density is positive at \mathbf{r} , the density at \mathbf{r} is less than the average of its surrounding density, and the electron density is said to be *depleted*; similarly, electron density is *concentrated* at \mathbf{r} when $\nabla^2\rho(\mathbf{r}) < 0$. The same applies to the individual component eigenvalues of the Hessian matrix, but along a specific axis. The topological condition for an AIL to be present is that density is depleted *along* the AIL ($\lambda_1 > 0$), but concentrated *across* it (λ_2 and $\lambda_3 < 0$). By convention, $\lambda_1 \geq \lambda_2 \geq \lambda_3$, and $\lambda_1 > 0$ between any two atoms, hence λ_2 is of particular importance because its sign will determine whether electron density is concentrated or depleted across an interaction; this is also the base of classification used by NCI. Bader then linked [1,50] the concentration of density (as measured by the second-derivative of the electron density) through the local statement of the virial theorem, to a concept of bonding: that a “build-up” of charge is observed in the bonding region upon formation of a chemical bond [51–55]. Through this reasoning Bader then suggested that a concentration and depletion of electron density is stabilizing and destabilizing, respectively, and therefore that the presence of an AIL (a maximal concentration of density) can be regarded as a bonding interaction. The same interpretation was then applied in NCI, with regions of concentration deemed as stabilizing and attractive, and regions of depletion often referred to as steric strain [2,47–49].

While there have been debates with regards to the nature of the energetic stabilization which occurs upon bond formation (whether it is potential [1,51,52] or kinetic in origin [56,57]), there can be little doubt that one of the key features of any form of chemical bonding is increased charge density in the bonding region. This is true even for atoms bound only by dispersion,

where, as Feynman [53] puts it, “each atom is attracted to the distortion, centred in the bonding region, of its own charge density”, as well as very electrostatic or ionic interactions, where the increased density is mainly localized to one atom (but still more so within the bonding region). However, it is not clear how this “build-up” of charge can be measured. Is the concentration or depletion of density, as used by the orthodox interpretation of an AIL or NCI regions of interactions, truly indicative of increased or decreased electron density in the bonding region, respectively, and thus synonymous with energetic stabilization or destabilization? Is it a measure of the electron density of a small region relative only to its environment, or can it be linked with the electron density relative to an unbound state? Finally, Pendás et al. [38] have provided an alternative interpretation of an AIL, which suggests that an AIL signals a privileged exchange–correlation channel. Their interpretation provides an elegant alternative to the orthodox QTAIM interpretation of AILs as bonding interactions. Their interpretation has been put to the test by Tognetti and Joubert [58] who measured the QTAIM-defined delocalization indices as well as the exchange–correlation contribution to the IQA-defined diatomic interaction energy between competing (close) pairs of atoms, and found that Pendás’ interpretation holds with a small margin of ambiguity.

In this work we will investigate Bader’s claim, as it is commonly used in QTAIM and NCI literature, by careful investigation of the electron density and its changes in a wide range of interactions in various molecular systems, ranging from equilibrium to non-equilibrium geometries, as well as several controversial CH \cdots HC interactions in different environments. QTAIM and NCI analyses, as well as the changes observed with changing geometries and environments, will be compared with results from the Interacting Quantum Atoms [59,60] (IQA) energy decomposition technique, as well as investigated carefully with one dimensional cross-sections of the electron density. We also investigate the use of the deformation density as an alternative measure of the “build-up” of charge in the bonding region.

2. Methods and computational details

All geometry optimizations and electronic structure calculations were performed in Gaussian 09, revision D [61] at the RMP2/6-311++G(d,p) level of theory in solvent (PCM/UFF) except water dimer where RMP2/6-31+G(d,p) in the gas phase was used. QTAIM and IQA analyses were carried out in AIMAll [62] using the Proaim integration algorithm with very high angular quadrature outside the beta sphere for IQA calculations. NCI calculations were carried out using NCIPLOT 2.0 [4] and corresponding isosurfaces were visualized in VMD 1.9.1 [63]. Finally, one-dimensional cross-sections of the electron and deformation densities along λ_2 eigenvectors were performed using in-house software.

In order to calculate the cross-sections of the electron and deformation densities, the geometric interaction point (GIP) was determined which corresponds to the point of lowest density directly between two nuclei. The eigenvector corresponding to the λ_2 eigenvalue of the Hessian matrix was then calculated, and two new coordinates were generated at a specific distance (usually 0.05 au) in both directions along this vector. The electron densities were then recorded at these points and new coordinates generated based on the eigenvectors corresponding to the λ_2 eigenvalues at these points. This process was repeated until a pre-determined length (usually 2 Å in both directions) was reached. For brevity, the entire path followed through this process is referred to the λ_2 -eigenvector. The λ_2 -eigenvector therefore will always originate from the GIP (which occasionally may coincide with a QTAIM-defined bond critical point, BCP) and will pass through any corresponding NCI-defined interaction critical point (ICP) or BCP, ring

critical point (RCP) and cage critical point (CCP). However, in congested molecules the λ_2 -eigenvector corresponds to the cross-sections of multiple interactions and in such cases the path followed for the cross-section was calculated as a straight line along the initial λ_2 -eigenvector at the GIP. In order to calculate the cross-sections of the deformation density, the electron density for each fragment was calculated along the same λ_2 -eigenvector as for the cross-section of the molecular electron density. The cross-section of the molecular density was then subtracted from the sum of fragment densities to give the cross-section of the deformation density.

To generate a wide range of structures for water dimers in four different conformations, selected interatomic distances in each conformer were fixed at preselected values and the structures were optimized with geometrical constraints shown in Table S1 of the SI. The deformation density was generated from single point calculations (SPCs) carried out on each monomer.

Two conformers of (un)protonated 2,2'-bipyridine were generated by keeping the N,C,C,N dihedral angle (DA) fixed at $DA(N,C,C,N) = 0^\circ$ and 180° , corresponding to *s-cis* and *s-trans* forms, respectively. Deformation densities were calculated by fragmenting each structure into two radical pyridine fragments and carrying out SPCs at UMP2 level with duplet multiplicities, as shown in Fig. S1 of the SI.

A conformational analysis of nitrilotri-3-propionic acid (NTPA) was carried out using Spartan '10 [64] and the MMFFaq force field. Deformation densities were obtained from SPCs carried out on four radical fragments, three duplet $(\text{CH}_2)_2\text{COO}^-$ and one quartet N-tom fragment as shown in Fig. S2 of the SI.

Deformation densities of monoprotonated aliphatic polyamine, triethylenetetramine (2,2,2-tet) were calculated by fragmenting each conformer into three radical fragments (corresponding to two duplet fragments, $(\text{CH}_2)_2(\text{NH}_3)$ and $(\text{CH}_2)_2(\text{NH}_2)$, and a triplet $(\text{NH})(\text{CH}_2)_2(\text{NH})$ fragment, as shown in Fig. S3 of the SI.

Cross-sections of the electron and deformation densities of selected interactions were calculated along the λ_2 -eigenvector at the GIP except water dimers for which BCP was used to generate the initial value of the eigenvector.

3. Results and discussion

3.1. Water dimers

Fig. 1 shows four water dimers, **d1** to **d4**, where water molecules were arranged in various relative configurations to test different competing intermolecular interactions. Dimer **d1** represents the lowest energy equilibrium structure, with the molecules bonded with a classical intermolecular O–H hydrogen bond. The remaining dimers were selected with the aim to simulate intermolecular interactions in a crowded (strained) environment: (i) dimer **d2** was prepared to test an $\text{O}\cdots\text{O}$ interaction, with hydrogens (and oxygen lone-pairs) arranged in a perpendicular manner, (ii) dimer **d3** was constructed to study the competition between $\text{O}\cdots\text{H}$ and $\text{O}\cdots\text{O}$ interactions in the same space, with water molecules approaching in the plane, and (iv) in dimer **d4**, the head-on approach of hydrogens in a planar arrangement allowed for studying $\text{H}\cdots\text{H}$ interactions. In each dimer, the distance of the primary

interaction was varied: $d(\text{H5}\cdots\text{O1})$ in **d1**, $d(\text{O1}\cdots\text{O4})$ in **d2** and **d3**, and $d(\text{H2}\cdots\text{H4}) = d(\text{H5}\cdots\text{H6})$ in **d4**.

3.1.1. Energy profiles and molecular graphs

The electronic energy of dimer **d1** exhibits a global minimum at $d(\text{O}\cdots\text{H}) = 1.946 \text{ \AA}$ but the electronic energy of dimers **d2**, **d3** and **d4** (as shown in Fig. 2) continuously increases as $d(\text{A}\cdots\text{B})$ decreases, demonstrating that these dimers are truly in unfavourable conformations (with constraints removed in the optimization operations, dimers **d2–d4** revert to the **d1** configuration). The variation in QTAIM-defined molecular structures is also shown in Fig. 2. AILs are found for the $\text{O}\cdots\text{H}$ and $\text{O}\cdots\text{O}$ interactions in **d1** and **d2**, respectively. Whilst the AIL between O1 and H5 in **d1** is entirely expected and easily interpreted as a classical (stabilizing) H-bond, the interaction between O1 and O4 in **d2** is clearly destabilizing the dimer, hence the significance of the AIL between these atoms is difficult to interpret. It is important to note that the general feature of topology of the electron density between A and B in **d1** as well as in **d2** remains essentially the same at all $d(\text{A}\cdots\text{B})$ distances – a single AIL is always observed. A different picture is observed for **d3** where initially a single and straight AIL is seen at $d(\text{O}\cdots\text{O}) < \sim 2.4 \text{ \AA}$, which splits into two AILs at $d(\text{O}\cdots\text{O}) \sim 2.4 \text{ \AA}$ and as a result two BCPs and a RCP are present.

However, regardless of the interatomic distance, AILs are always linking oxygen atoms. Finally, in **d4**, AILs are initially observed for the $\text{H}\cdots\text{H}$ interactions at $d(\text{H}\cdots\text{H}) \leq \sim 2.0 \text{ \AA}$, with a RCP between oxygen atoms in the middle of the intermolecular six-membered ring. At distances larger than about 2.0 \AA , AILs are rather seen between oxygen atoms; initially, at $d(\text{H}\cdots\text{H}) \sim 2.4 \text{ \AA}$ a bifurcated AIL (including RCP) is observed which changes to a single AIL at $d(\text{H}\cdots\text{H}) \geq 2.8 \text{ \AA}$.

It is fairly clear from Fig. 2 that the presence of AILs and their interpretation is not quite obvious. This is because (i) AILs seem to appear between atoms involved in both, classically attractive and repulsive, interactions and (ii) in the case of **d3** and **d4**, the change in the molecular graphs does not seem to correlate with any significant change in the electronic energy which decreases monotonically throughout. Also, the appearance of bifurcated AILs in **d3** and **d4** cannot be easily explained, although (following Bader [1]) they might be examples of “catastrophe points” signalling unstable metafolds. The traditional interpretation of Bader, which states that AILs signify “bonding” interactions [50], is difficult to apply to most of these interactions; it is only for the equilibrium structure of **d1** where the AIL can be truly interpreted as resembling a chemical bond. We therefore turn to NCI for additional insight.

3.1.2. NCI analysis

The NCI regions of interaction (colour-coded blue for $\lambda_2 < 0$ and red for $\lambda_2 > 0$) for each water dimer at selected $d(\text{A}\cdots\text{B})$ values are shown in Fig. 3; for a full set of NCI plots see Figs. S4–S7 in the SI. Superficially, NCI correlates well with the molecular graphs: an AIL is seen when $\lambda_2 < 0$ and the density is said to be concentrated (in the QTAIM and NCI terminology). This is not surprising and has been pointed out before [50]. The spatial property of NCI-regions expands the analysis and is of great help in monitoring variation

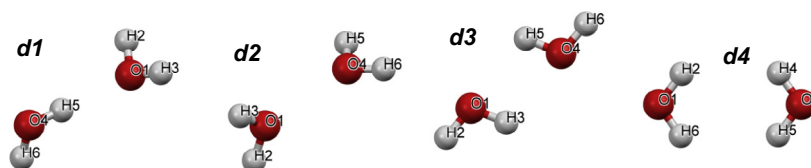


Fig. 1. Ball-and-stick representation of water dimers considered in this work.

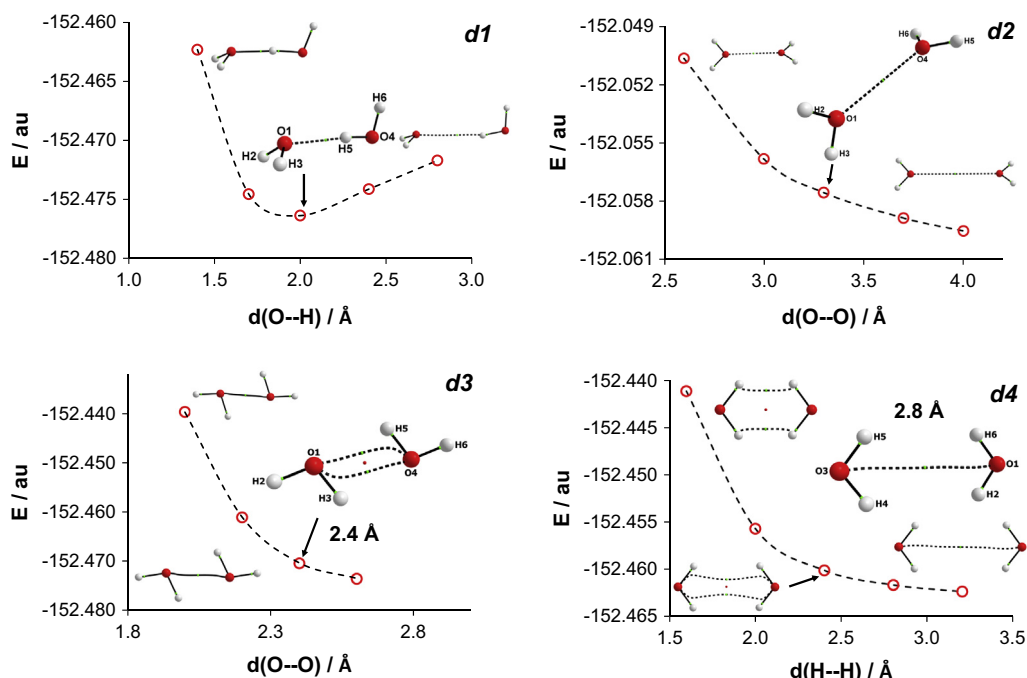


Fig. 2. Variation in E with interatomic distance for the indicated water dimers also showing representative molecular graphs.

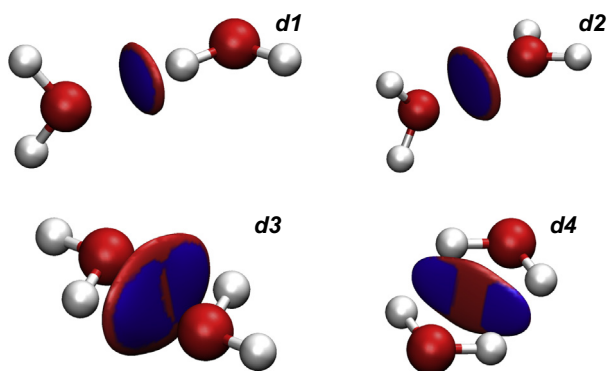


Fig. 3. NCI isosurfaces (with RDG isovalue = 0.9 au) for water dimers: **d1**) $d(\text{O}\cdots\text{H}) = 2.0 \text{ \AA}$; **d2**) $d(\text{O}\cdots\text{O}) = 1.6 \text{ \AA}$; **d3**) $d(\text{O}\cdots\text{O}) = 2.4 \text{ \AA}$; **d4**) $d(\text{H}\cdots\text{H}) = 2.0 \text{ \AA}$. Isosurfaces are coloured from blue to red by $-0.03 \leq \rho(\mathbf{r}) \times \text{sign}(\lambda_2) \leq +0.03 \text{ au}$. (For interpretation of the references to colour in this figure legend, the reader is referred to the web version of this article.)

in the electron density distributions throughout a molecular system. For instance, in **d3** at $d(\text{O}\cdots\text{O}) = 2.4 \text{ \AA}$, a very small region is seen directly between O-atoms where $\lambda_2 > 0$, whereas large regions, with $\lambda_2 < 0$, are seen between the $\text{H}\cdots\text{O}$ interactions. This observation clearly shows that, even though the AIL always links O-atoms for all $d(\text{O}\cdots\text{O})$ in **d3**, AIL might be influenced by the $\lambda_2 < 0$ regions involving the $\text{H}\cdots\text{O}$ interactions which, in turn, can give rise to features such as bent AILs as well as splitting at $d(\text{O}\cdots\text{O}) = 2.4 \text{ \AA}$ (see Fig. 2c). Furthermore, regions where $\lambda_2 < 0$ are seen for the $\text{H}\cdots\text{H}$ interactions, with a clear region of $\lambda_2 > 0$ for the $\text{O}\cdots\text{O}$ interaction in **d4** and in this case it correlates with the presence of AILs linking H-atoms at short distances. However, as $d(\text{H}\cdots\text{H})$ increases, the region where $\lambda_2 > 0$ vanishes and is replaced by a homogeneous $\lambda_2 < 0$ region, which is spread out between the $\text{H}\cdots\text{H}$ and $\text{O}\cdots\text{O}$ interactions as shown in Fig. S7 of the SI.

A clear interpretation of NCI-defined isosurfaces in terms of bonding interactions might be confusing because regions where

(i) $\lambda_2 < 0$ have been described as “concentrating”, “stabilizing” or “attractive”, whereas (ii) $\lambda_2 > 0$ are referred to as “depletion”, “strain” or “destabilization” [2–4,47–49]. It appears that, in the NCI interpretations, the locally increased density became synonymous with attractive and stabilizing interaction (opposite interpretation applies to $\lambda_2 > 0$). Using these interpretations, however, one would have to attribute both the $\text{O}\cdots\text{H}$ (in **d1**) and $\text{O}\cdots\text{O}$ (e.g., in **d2**), as “attractive” interactions. Hence, it is reasonable to question whether it is correct to state that a concentration of density (implying $\lambda_2 < 0$) is indeed attractive or stabilizing and to gain further insight we now turn to the IQA method.

3.1.3. IQA analysis

Table 1 shows the interaction energies, $E_{\text{int}}^{\text{A,B}}$, as well as its components, the electrostatic term $V_{\text{cl}}^{\text{A,B}}$ and exchange–correlation term, $V_{\text{xc}}^{\text{A,B}}$. A few interesting patterns are observed within the IQA analysis of the water dimers: (i) all $\text{O}\cdots\text{H}$ interactions, especially the AIL-linked $\text{O1}\cdots\text{H5}$ interaction in **d1**, are highly attractive ($E_{\text{int}}^{\text{A,B}} < 0$) and electrostatic in nature ($|V_{\text{cl}}^{\text{A,B}}| \gg |V_{\text{xc}}^{\text{A,B}}|$), (ii) all $\text{O}\cdots\text{O}$ and $\text{H}\cdots\text{H}$ interactions are repulsive and (iii) except for the $\text{O}\cdots\text{H}$ interactions in **d1** and **d3**, IQA and NCI results do not correlate. The last observation shows that when $\lambda_2 < 0$ in the bonding region of an interaction, it does not necessarily result in the two atoms being physically attracted towards each other. To support this, let us consider interactions in **d4** as an example. At $d(\text{H}\cdots\text{H}) = 1.6 \text{ \AA}$, IQA shows a repulsion of +62.0 kcal/mol between each hydrogen pair, despite $\lambda_2 = -0.0210 \text{ au}$. On the other hand, one observes $\lambda_2 = 0.0176 \text{ au}$ in the bonding region for the $\text{O}\cdots\text{O}$ interaction and this correlates well with a large repulsion of +166.9 kcal/mol at $d(\text{H}\cdots\text{H}) = 1.6 \text{ \AA}$ as well as with a common perception of steric hindrance even though O-atoms are not involved in a direct contact. However, at $d(\text{H}\cdots\text{H}) = 2.8 \text{ \AA}$, the large repulsion between oxygens is still present (+126.7 kcal/mol) but now we observe $\lambda_2 < 0$ in the bonding region as well as an AIL.

The interpretation that AILs and NCI regions of density concentration are stabilizing in nature [1,2,50] rests upon the concept that an increase in charge density in the bonding region of an interaction is associated with typical bonding mechanisms. Hence, the

Table 1
Analysis of interactions in water dimers, **d1–d4**, in terms of interaction energies and electron density in the interatomic bonding region.

Dimer	Distance Å	Interaction A...B	$E_{\text{int}}^{\text{A,B}}$ ^a	$V_{\text{cl}}^{\text{A,Ba}}$	$V_{\text{XC}}^{\text{A,Ba}}$	AIL	$\rho(\mathbf{r}) \times \text{sign}(\lambda_2)^{\text{b}}$	$\Delta\rho(\mathbf{r})_{\text{GIP}}^{\text{c}}$
d1	1.946	O1...H5	−126.1	−116.3	−9.8	Yes	−0.0240	+0.0010
		O1...O4	158.4	163.3	−4.9	No	−	−
d2	2.6	O1...O4	157.2	168.6	−11.4	Yes	−0.0178	−0.0036
		O1...H5	−76.2	−76.1	−0.1	No	−	−
d3	2.0	O1...O4	154.1	191.0	−36.9	Yes	−0.0524	−0.0094
		O1...H5	−121.3	−117.3	−4.0	No	−0.0406	−0.0069
d4	1.6	H5...H6	62.0	64.7	−2.6	Yes	−0.0210	+0.0007
		O1...O3	166.9	175.5	−8.6	No	+0.0176	−0.0015
	2.4	O1...H5	−103.0	−100.3	−2.7	No	−0.0233	−0.0001
		H5...H6	45.2	45.5	−0.5	No	−0.0032	+0.0002
	2.8	O1...O3	140.0	141.8	−1.8	Yes ^d	+0.0037	+0.0001
		O1...H5	−78.7	−78.2	−0.4	No	−0.0036	+0.0002
		H5...H6	39.6	39.7	−0.2	No	−0.0013	+0.0001
		O1...O3	126.7	127.6	−0.8	Yes	−0.0016	+0.0001
		O1...H5	−70.0	−69.7	−0.1	No	−0.0015	+0.0001

^a Diatomic interaction energies and decomposed components, all in kcal/mol.^b Values in au at GIP.^c The deformation density in au at GIP.^d The AIL is bifurcated into two O...O AILs, with 2 BCPs and a RCP.

sign of λ_2 gives an indication of bonding interactions for the most commonly accepted chemical bonds, such as the O...H interaction in **d1**. However, since the sign of λ_2 gives strictly the local density increase (or decrease) relative to adjacent density regions, one might wonder whether its interpretation in terms of attractive (or stabilizing) contribution is equally applicable for all interactions. Specifically, in highly congested systems (such as the **d3** and **d4** water dimers) or isolated interactions in non-equilibrium geometries (such as the O...O interaction in the **d2** water dimer) the use of the sign of λ_2 only shows a local maximum, minimum (or inflection point) of electron density, but does not give any indication of an increase due to an inflow (or decrease caused by an outflow) in the density upon the formation of an interaction.

Hence, we decided to investigate two aspects of the density distribution with closer focus on: (i) the resultant distribution of density at a specific state or geometry of a molecular system and (ii) the processes which transform the density from the initial (non-interacting fragments) to final topology of molecular state under consideration. Within this framework, a resultant electron concentration shows where the electron density is at a local maximum, whereas the processes at work show how the density contribution came to be. In order to study these phenomena, we report here the 1D density cross-sections of specific interactions in the water dimers, as well as the 1D cross-sections of the deformation density of each dimer, using water monomers as initial constructor states, according to the methodology set out in Section 2.

3.1.4. Density cross section and deformation density analysis

Fig. 4(a) shows the density cross-sections of the O...H and O...O interactions in **d1** and **d2**. Remarkably, there is no qualitative difference between the density cross-sections perpendicular to the A...B axis of the **d1** and **d2** dimers: a local maximum is seen directly between atoms involved. Because of that, the observed topology generates a point in space where the first order change crosses zero, resulting in a bond critical point, and a region where the second-order change is negative, as shown in Fig. S8 of the SI. Furthermore, an almost identical variation obtained for the first and second order changes in **d1** and **d2** indicates that the resultant electron density distribution is qualitatively identical for these two radically different interactions. However, the deformation density ($\Delta\rho(\mathbf{r})$) cross-sections, shown in Fig. 4b, uncover the different nature of these two interactions. In **d1**, forming the O...H interaction resulted in $\Delta\rho(\mathbf{r}) > 0$ with an inflow of electron density into the

bonding region which is consistent with the concept of chemical bonding. On the other hand, forming the O...O interaction in **d2** resulted in a negative deformation density. This appears to correlate well with the repulsive nature of this interaction for which it is favourable for electron density to be removed (dissipated) from the bonding region of the O...O interaction. The deformation density thus shows two very different processes which give rise to similar final density distributions.

The understanding and interpretation of NCI plots, as well as molecular graphs, for dimers **d3** and **d4** is facilitated greatly by cross-sections of the electron density shown for **d4** in Fig. 5 and for **d3** in Fig. S9 in the SI. At short d(H...H), e.g., 1.6 Å, the cross-section of the electron density in **d4** shows two clear peaks, corresponding to the BCPs between hydrogen atoms, and a local minimum, corresponding to the RCP between oxygen atoms. As d(H...H) gradually increases, the density at BCPs corresponding to the H...H interactions shows a faster decline than density attributed to the RCP of the O...O interaction. Finally, at d(H...H) \geq 2.8 Å, a single local maximum is observed which corresponds to the BCP of the O...O interaction. The patterns observed in the first- and second-order changes in the electron distribution of **d4** show very much what one would expect from the above analysis: the first order change crosses the X-axis three times at short d(H...H), corresponding to two BCPs and a RCP, and the second order change shows clear regions of concentration between H-atoms and a region of depletion between O-atoms. As d(H...H) increases, the first order change reduces to one critical point, and only a region of concentration (spanning over all three interactions) is seen in the 2nd order change. Strikingly, the general pattern of topology remains relatively constant across all values of d(H...H); only the relative values differ in the second order change at d(H...H) = 2.8 Å (where only concentration is observed) and at d(H...H) = 1.6 Å showing that the same mechanisms governing the electron distribution are present for the range of d(H...H) examined in this study; the second order change is always lowest between H-atoms. This point is emphasized by examining the cross-sections of the deformation density for **d4**, as shown in Fig. 6 (and for **d3** in Fig. S10 in the SI). At short d(H...H), a clear inflow and outflow of density is observed for the H...H and O...O interaction, respectively. As d(H...H) increases, the interplay between an outflow of density from the interatomic region of the H...H interactions and inflow of density into the bonding region of the O...O interaction, gradually brings the accumulation peaks closer together which finally results in a

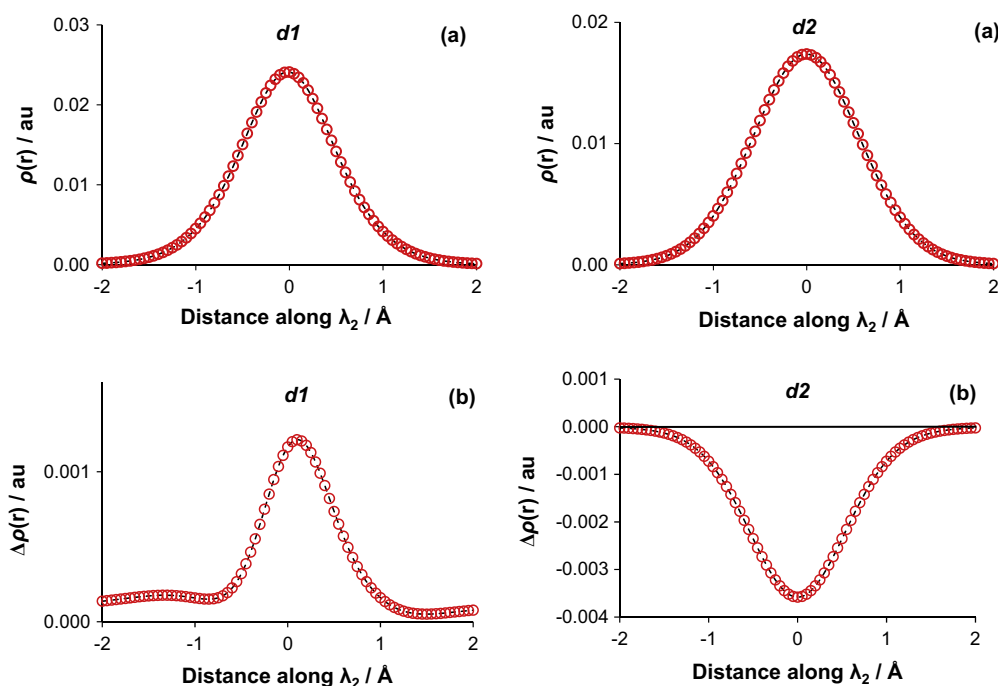


Fig. 4. Cross section of (a) the electron density and (b) the deformation density along λ_2 eigenvector for **d1** at $d(\text{O}---\text{H}) = 1.946 \text{ \AA}$ and **d2** at $d(\text{O}---\text{O}) = 2.6 \text{ \AA}$. The origin of the cross-sections for **d1** and **d2** are the BCP(O1,H5) and BCP(O1,O4), respectively.

net overall accumulation at $d(\text{H}---\text{H}) = 2.8 \text{ \AA}$. It seems that the deformation density patterns (as well as the resulting patterns observed in the second order change of the molecular electron density) are primarily a result of the kind of atoms involved, with the distance between them only determining the density at critical points and the net observed effect.

From the above considerations and data shown in Table 1 it is clear that the presence of an AIL does not necessarily mean that:

- Atoms are involved in an attractive (or stabilizing) interaction with $E_{\text{int}}^{\text{A,B}} < 0$; only in the case of O1 and H5 of **d1** we observe an AIL and $E_{\text{int}}^{\text{A,B}} < 0$.
- The interaction is strongest among all, as measured by $E_{\text{int}}^{\text{A,B}}$, e.g., in **d4** with $d(\text{H5}---\text{H6}) = 1.6 \text{ \AA}$, an AIL is observed between H-atoms involved in the weakest and repulsive interaction even though there is highly attractive and stronger interaction present in this molecular system (O1...H5 with $E_{\text{int}}^{\text{A,B}} = -103 \text{ kcal/mol}$).
- A positive density deformation (which shows an inflow of density into an interatomic region on the formation of an interaction) should be expected, e.g., (i) in the case of **d2**, an outflow of density, $\Delta\rho(\mathbf{r}) < 0$, is observed between O-atoms linked by an AIL at any $d(\text{O1,O4})$, or (ii) in the case of **d3** at $d(\text{O1,O4}) = 2.0 \text{ \AA}$, one observes AIL between O1 and O4 while $\Delta\rho(\mathbf{r}) < 0$. Note that these two interactions exhibit highly repulsive character.

The analysis of deformation density, $\Delta\rho(\mathbf{r})$, provides not only an important insight on the mechanism of density distribution in the final structure of a molecular system but also might be more intuitive for a classical chemist in interpreting interactions in terms of bond formation. However:

- The sign of $\Delta\rho(\mathbf{r})$ cannot be used to predict the character of an interaction in the final structure as there is no correlation between the signs of $\Delta\rho(\mathbf{r})$, $E_{\text{int}}^{\text{A,B}}$ and λ_2 . For instance, an inflow of density, $\Delta\rho(\mathbf{r}) > 0$, and accumulated density in the interatomic region, $\lambda_2 < 0$ (both indices are synonymous

with a formation of a chemical bond or bonding interaction) is observed in (i) **d4** for highly repulsive interactions H5...H6 at any distance and O1...O3 at $d \geq 2.8 \text{ \AA}$, as well as (ii) **d1** for highly attractive O1...H5 interaction, a classical intermolecular H-bond.

- An outflow of density, as predicted by $\Delta\rho(\mathbf{r}) < 0$, is not synonymous with either the repulsive interaction or a local resultant depletion in the density as indicated by $\lambda_2 > 0$. For instance, for $\Delta\rho(\mathbf{r}) < 0$ we still observe $\lambda_2 < 0$ for two interactions in **d3**, namely for highly repulsive O1---O4 with an AIL and highly attractive ($E_{\text{int}}^{\text{A,B}} = -121 \text{ kcal/mol}$) O1...H5 without an AIL.

3.2. Bipyridine

We change our focus from inter- to intramolecular interactions in *s-cis* and *s-trans* forms of bpy (L) and its protonated forms, HL and H₂L (signs are omitted for simplicity), because they provide many contacts of different nature which will allow us to examine the electron density distributions in different molecular as well as immediate environments. From the data shown in Table S2 and Fig. S11 of the SI it follows that there are two genuine equilibrium structures among those examined here, namely *s-trans* L and *s-cis* HL. This means that we will be able to compare properties of intramolecular interactions formed by spontaneous change in the configuration of a molecule against forced-to-be contacts in non-equilibrium conformers obtained by rotating the rings along the N,C,N dihedral angle.

As shown in Fig. 7, the molecular graphs do not exhibit AILs for all close contacts even though a distance criterion, $d(\text{A}---\text{B}) < \text{sum of the van der Waals radii}$, is met in all cases. From the NCI perspective (as shown in Fig. 8 and Fig. S12 of the SI), all contacts show regions where the reduced density gradient approaches zero, indicative of atoms being involved in an interaction.

It was then of importance to examine the cross-sections of the electron density and results obtained for selected interactions without an AIL are shown in Fig. 9a, and those with AIL are shown

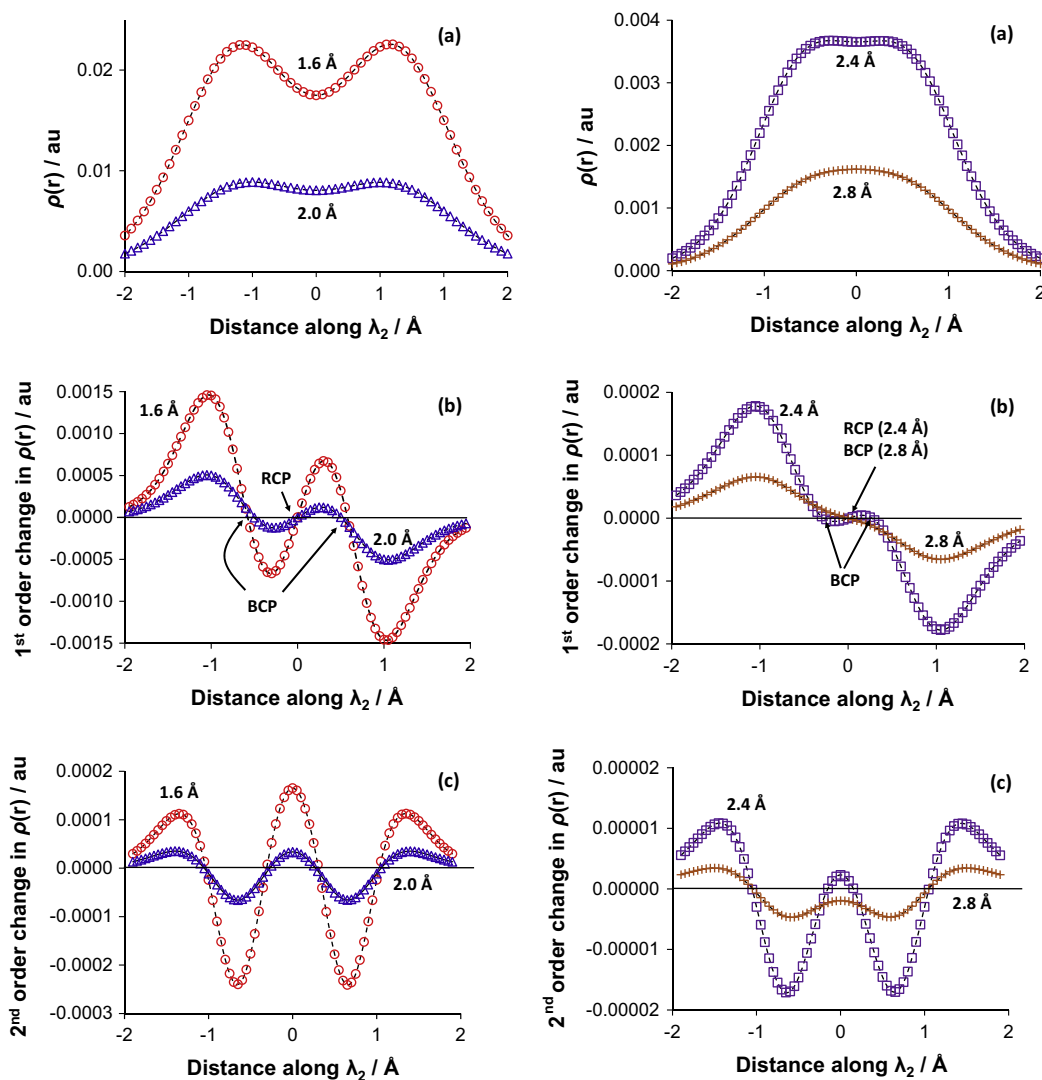


Fig. 5. Cross-section of the (a) electron density, (b) its first and (c) second order changes, along the λ_2 eigenvector for d_4 for indicated distances of $d(\text{H}\cdots\text{H})$. The origin of the cross-section is either RCP or BCP between O1 and O3 atoms.

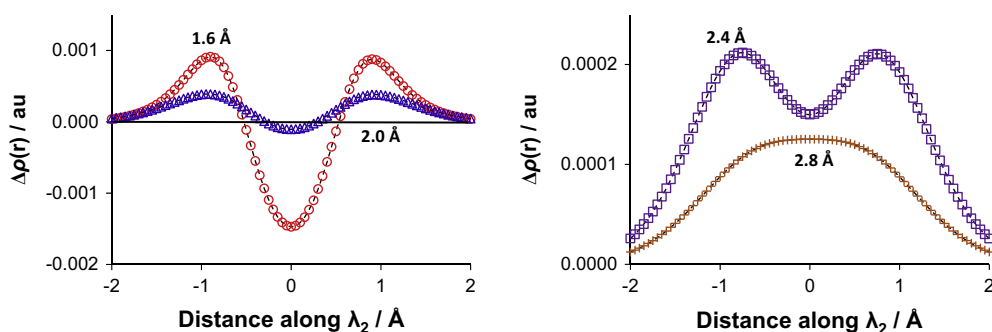


Fig. 6. Cross-section of the deformation density along the λ_2 eigenvector for indicated distances of d_4 . The origin of the vector is either RCP or BCP between O1 and O3 atoms.

in Fig. 9b (corresponding first- and second-order changes are shown in Figs. S13 and S14 of the SI). Focusing on contacts without AILs, the $\text{CH}\cdots\text{N}$ interaction in *s-trans* L shows a clear concentration in the bonding region, but it is not sufficient to increase the density relative to a preceding point, hence no AIL is observed; this is a common feature for all interactions where density is locally increased but an AIL is not present. A very useful picture is obtained for the $\text{N}\cdots\text{N}$ interaction in *s-cis* L; it can be seen that

exactly in the bonding region the density is only depletive and it increases somewhat outside the ring and this correlates well with the relevant NCI isosurface shown in Fig. 8.

Regarding interactions with AILs, we always observe an increased density in the bonding region; this is clearly visible for the $\text{NH}\cdots\text{N}$ (most pronounced change) and $\text{CH}\cdots\text{HC}$ interactions in *s-cis* L, but only a very slight increase is seen for the $\text{NH}\cdots\text{HN}$ interaction in *s-cis* H_2L . One can also observe that the maximum

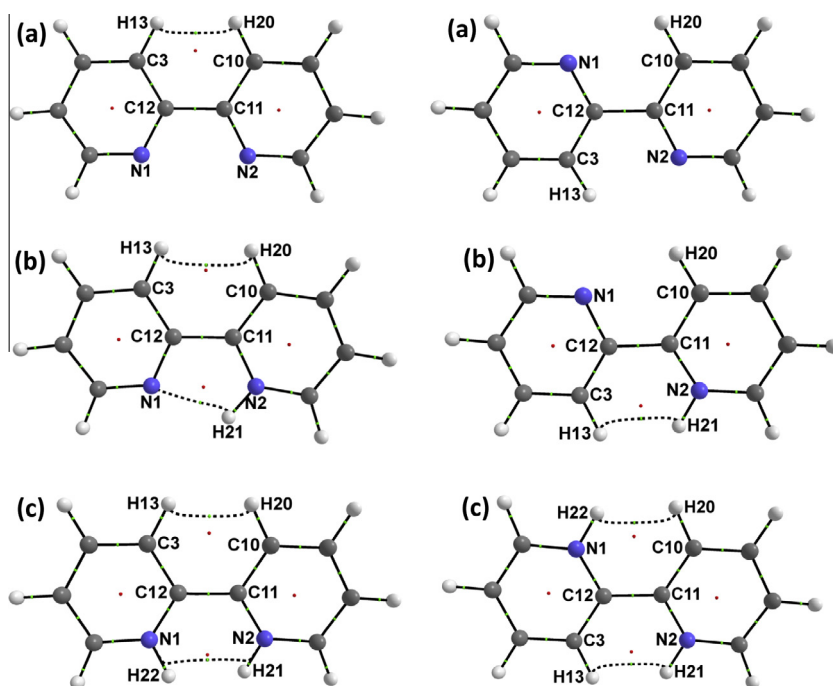


Fig. 7. Molecular graphs of the *s-cis* and *s-trans* forms of (a) bipyridine, L, (b) HL and (c) H_2L .

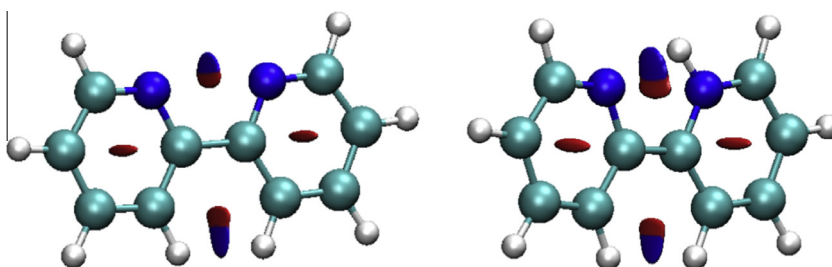


Fig. 8. NCI isosurfaces of the *s-cis* forms of bpy (L) and HL, with a RDG isovalue = 0.5 au and isosurfaces coloured from blue to red using $-0.03 \leq \rho(r) \times \text{sign}(\lambda_2) \leq +0.03$ au. (For interpretation of the references to colour in this figure legend, the reader is referred to the web version of this article.)

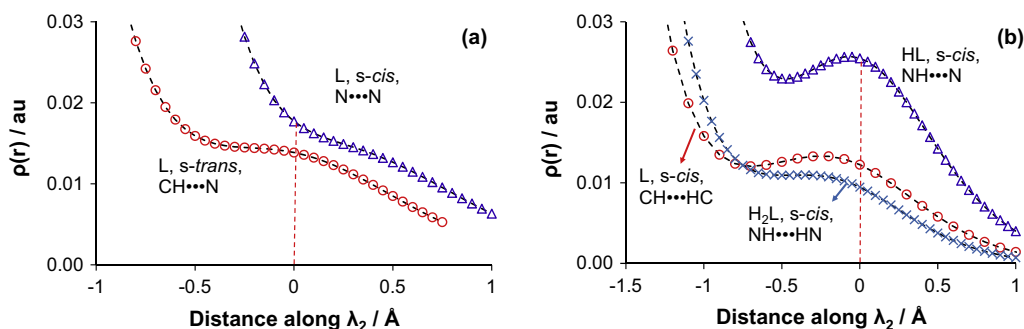


Fig. 9. Cross-sections of the electron density along the λ_2 eigenvector for indicated interactions (a) without a bond path, and (b) with a bond path present, in indicated forms of bpy. Dashed red line indicates Geometric Interaction Point (GIP) – point of lowest density directly between two atoms. (For interpretation of the references to colour in this figure legend, the reader is referred to the web version of this article.)

density (which correlates with a BCP) is shifted inside the respective ring from the GIP - point of lowest density directly between two nuclei.

The most informative picture is again observed for the cross-sections of the deformation density, although some care must be taken in the case of intramolecular interactions, since the fragments used to generate the deformation density (in this

case, radical pyridine fragments) are unphysical reference states. However, even using fragments which are unlikely to exist in reality, the protocol used here is similar to that employed in frequently utilized energy decomposition techniques, such as ETS [65] and EDA [66]; hence, it should provide sufficient information to make qualitative conclusions related to the nature of these interactions.

Fig. 10(a) shows the deformation densities for the CH···N and N···N interactions in *s-trans* and *s-cis* bpy, respectively, which are not linked by an AIL; an outflow of density from the bays as well as from the bonding interatomic regions is observed. The very repulsive N···N interaction shows a maximum decrease in density within the N···N bonding region, clearly showing that it is preferable to remove density from the electron-rich N···N interaction upon its formation. This observation correlates well with the nature of this interaction as well as chemists' intuition, hence gives some credibility of this analysis, even though unphysical reference states were used. On the other hand, for the CH···N interaction, the density depletion is greatest between the N1 and C10 atoms of the bay, and is approaching zero outside the bonding region.

Considering the deformation density cross-sections in Fig. 10b for the CH···HC, NH···HN and NH···N interactions, all with an AIL present, a slight inflow of density is observed in the bonding region. This shows that, upon their formation, it is favourable to increase the density within these regions and in general, correlates well with the picture obtained from the analysis of the electron density cross-sections and the presence of AILs. However, using pyridine radical reference states, it is impossible to state with certainty whether density truly increases between these atoms in their interaction regions, but it is reasonable to infer that no significant density changes occur upon the formation of these interactions. On the other hand, it is important to note that a much larger and significant outflow of density takes place in the interatomic regions of neighbouring C- and N-atoms of the bay, as shown in Fig. 10(b); this observation suggests that these atoms play larger roles than what is typically expected in the overall density distribution of the bay. In addition, the outflow of density in these neighbouring regions will significantly change the curvature of the electron density for the intramolecular interactions of interest, thereby possibly facilitating the appearance of AILs and regions of concentration. This concept is illustrated for the CH···HC interaction in *s-cis* bpy in Fig. S15 of the SI.

Finally, it is informative to discuss collated results shown in Table 2. There is only one case, the N···N interaction in *s-cis* bpy, for which a fully consistent description emerges; it is characterized by a large repulsive interaction energy of +255.9 kcal/mol, absence of an AIL, a region of depleted density directly in the bonding region between the N-atoms ($\lambda_2 > 0$) and an outflow of density takes place on its formation, $\Delta\rho(\mathbf{r}) < 0$. When these indices are combined, this interaction might be seen as a classic case of intramolecular repulsive steric contact. However, if this set of indices is used as a reference then the very electron-poor NH···HN contact in *s-cis* H₂L (also with $E_{\text{int}}^{\text{A,B}} \gg 0$) does not conform to this criterion because density in the interatomic region is accumulated ($\lambda_2 < 0$), an inflow of density takes place on the formation of this contact

($\Delta\rho(\mathbf{r}) > 0$) and an AIL is linking H-atoms. It is obvious that using general chemical wisdom and intuition, these two contacts must be seen as destabilizing a molecule.

Let us analyse the CH···HC contacts which are often also seen as steric hindrance and became a subject of heated scientific debate when their nature in, e.g., biphenyl goes [16,17,27–29,33,34]. We note with interest that in all three *s-cis* (de)protonated forms of bpy these contacts are characterized by the presence of AILs, favourable and XC-dominated interaction energy ($E_{\text{int}}^{\text{A,B}} < 0$), an increased density in the interatomic region ($\lambda_2 < 0$) and an inflow of density on these contacts formation; remarkably, this is exactly the same set of indices as observed for a spontaneous formation of a classical intermolecular H-bond in the water dimer **d1**.

Considering the CH···N interactions, we found that they are characterized by a different set of descriptors when compared with those discussed for the CH···HC or NH···HN contacts. Also, the set of descriptors has not changed for the CH···N interaction when going from the equilibrium *s-cis* L to non-equilibrium *s-trans* HL. Even though the CH···N interactions contribute significantly more, when measured by the $E_{\text{int}}^{\text{A,B}}$ term, to the overall stability of a molecule than the CH···HC ones:

- (a) Atoms involved in the interaction are not linked by an AIL even though density is accumulated, $\lambda_2 < 0$.
- (b) An outflow of density takes place on the contact formation, $\Delta\rho(\mathbf{r}) < 0$.

An analysis of data shown in Table 2 also shows an influence of a molecular environment on the nature and strength of an interaction. For instance, we observe weakening of the CH···HC interactions when going from unprotonated ($E_{\text{int}}^{\text{A,B}} = -2.9$ kcal/mol) to diprotonated bpy ($E_{\text{int}}^{\text{A,B}} = -1.5$ kcal/mol) and this is almost entirely due to an increase in a classical term from virtually zero in L to +1.2 kcal/mol in H₂L. More apparent change, also mainly caused by an increase in the value of $V_{\text{cl}}^{\text{A,B}}$, involves the CH···HN interaction which changed its nature from attractive in HL ($E_{\text{int}}^{\text{A,B}} = -0.7$ kcal/mol) to repulsive in H₂L ($E_{\text{int}}^{\text{A,B}} = +3.7$ kcal/mol) even though in both cases $\Delta\rho(\mathbf{r}) > 0$ and $\lambda_2 < 0$ are observed between H-atoms involved with the $V_{\text{xc}}^{\text{A,B}}$ term virtually unchanged.

In general, as observed for the water dimers, (i) there is no direct correlation between all indices discussed here, e.g., $E_{\text{int}}^{\text{A,B}} < 0$ or $E_{\text{int}}^{\text{A,B}} > 0$ is not synonymous with the presence or absence of AIL, respectively, (ii) locally increased density, as identified by NCI, does not imply that this is the result of the density inflow into the interatomic region and also (iii) different mechanisms, through which electron density is distributed between atoms, also take place in case of intramolecular interaction.

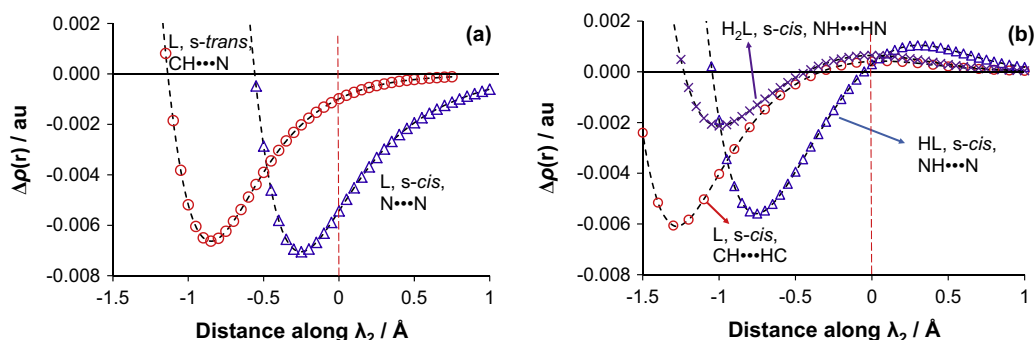


Fig. 10. Cross-sections of the deformation density along the λ_2 eigenvector for selected interactions (a) without bond path in deprotonated bpy and (b) with a bond path in indicated forms of bpy. Dashed red lines indicate the geometric interaction point, GIP. (For interpretation of the references to colour in this figure legend, the reader is referred to the web version of this article.)

Table 2

Analysis of interactions in bpy and its protonated forms in terms of interaction energies and electron density in the interatomic region.

Molecule	Form	Interaction	Distance Å	$E_{\text{int}}^{\text{A,B}}$	$V_{\text{cl}}^{\text{A,B}}$	$V_{\text{xc}}^{\text{A,B}}$	AIL	$\rho(\mathbf{r}) \times \text{sign}(\lambda_2)^{\text{b}}$	$\Delta\rho(\mathbf{r})_{\text{GIP}}^{\text{c}}$
bpy	<i>s-cis</i>	CH···HC	1.98	-2.9	0.0	-3.0	Yes	-0.0123	+0.0004
		N···N	2.72	255.9	264.4	-8.5	No	+0.0177	-0.0054
Hbpy	<i>s-trans</i>	CH···N	2.47	-14.7	-10.4	-4.3	No	-0.0139	-0.0010
	<i>s-cis</i>	CH···HC	2.19	-1.5	0.4	-1.9	Yes	-0.0083	+0.0004
		N···HN	2.08	-128.3	-123.0	-5.4	Yes	-0.0255	+0.0005
	<i>s-trans</i>	CH···HN	1.96	-0.7	1.1	-1.7	Yes	-0.0111	+0.0009
CH···N		2.43	-25.4	-20.9	-4.4	No	-0.0149	-0.0008	
H ₂ bpy	<i>s-cis</i>	CH···HC	1.98	-1.5	1.2	-2.6	Yes	-0.0116	+0.0007
		NH···HN	1.95	41.4	42.2	-0.9	Yes	-0.0095	+0.0006
	<i>s-trans</i>	CH···HN	1.94	3.7	5.4	-1.7	Yes	-0.0118	+0.0009

^a Diatomic interaction energies and decomposed components, all in kcal/mol.^b Values in au at GIP.^c The deformation density in au at GIP.

3.3. NTPA

This common tetradentate ligand, has some conformational space in its free form but must undergo preorganization to form complexes with transition metals. It is known that on the complex formation the CH···HC steric contacts are present and this is commonly used to reason why NTPA forms weaker complexes with most metal ions than the slightly smaller (and less congested) NTA (nitrilotriacetic acid) [67–69]. We decided to examine here two, the lowest and highest energy conformers of the free and deprotonated NTPA (LEC and HEC, respectively) and found several CH···HC contacts in both conformers but only one with an AIL – see Fig. 11.

The number of the CH···HC interactions presenting concentrated density within its bonding region was expanded upon NCI analysis (Fig. 12) which also revealed two CH···HC interactions in HEC which show only depletion. We therefore selected three examples of the CH···HC interactions: (i) CH₂···H18C in LEC, which contains concentrated density but no AIL (note that there are three almost identical interactions of this type in LEC), (ii) CH₁₆···H19C in HEC, which contains concentrated density as well as an AIL, and (iii) CH₂···H9C in the HEC, which shows no AIL and only presents an NCI region of density depletion.

Interestingly, the IQA data (Table 3) reveals that all three interactions are attractive, with $E_{\text{int}}^{\text{A,B}} = -3.3, -3.2$ and -1.6 kcal/mol, respectively, and similarly to the CH···HC interactions in all forms of bpy, they are dominated by the $V_{\text{xc}}^{\text{A,B}}$ component.

Cross-sections of the electron density, as shown in Fig. 13, revealed a few very interesting features. The electron density at GIP for each CH···HC interaction is almost identical, with $\rho(\mathbf{r}) \sim 0.01$ au. However, the topology of the interactions differ,

predominantly in the region preceding the GIP. In CH₁₆···H19C, where an AIL is present, the neighbouring region shows the largest depletion, followed by CH₂···H18C, the interaction without an AIL but showing concentration in the bonding region. Finally, CH₂···H9C in HEC shows a mostly uniformly declining electron density, with no shoulder in the bonding region (and hence no concentration), but also no valley in the neighbouring regions (hence no AIL). It is thus clear that the appearance of concentration regions for these interactions is mostly dependant on the density distribution of the local environment.

Fig. 14 shows the deformation density for the three CH···HC interactions of NTPA. Surprisingly, all three interactions show somewhat negative deformation densities with the largest outflow from the bonding region of CH₂···H9C in HEC where identified by NCI depletion in density is observed but, like the CH···HC interactions in bpy, the largest changes occur in neighbouring regions. Regardless of the different mechanisms, however, in all cases these interactions exhibit $E_{\text{int}}^{\text{A,B}} < 0$ and are almost entirely dominated by the $V_{\text{xc}}^{\text{A,B}}$ term.

In general, there is no obvious correlation between the presence (or absence) of AIL and the signs of $\Delta\rho(\mathbf{r})$, λ_2 and $E_{\text{int}}^{\text{A,B}}$ (as also observed for all other molecular systems discussed above), hence, the properties of topologies discussed here cannot be used to conclusively describe the chemical character of the CH···HC contacts or their impact on the stability of a molecule. Interestingly, however, these contacts exist already in the LEC of NTPA where, in principle, they could be avoided by just a slight rotation of the –CH₂– fragments but clearly that would result in some energy penalty: (i) either even larger strain than that caused by these contacts or (ii) the loss of three stabilizing CH···HC interactions in LEC, amounting to -10 kcal/mol.

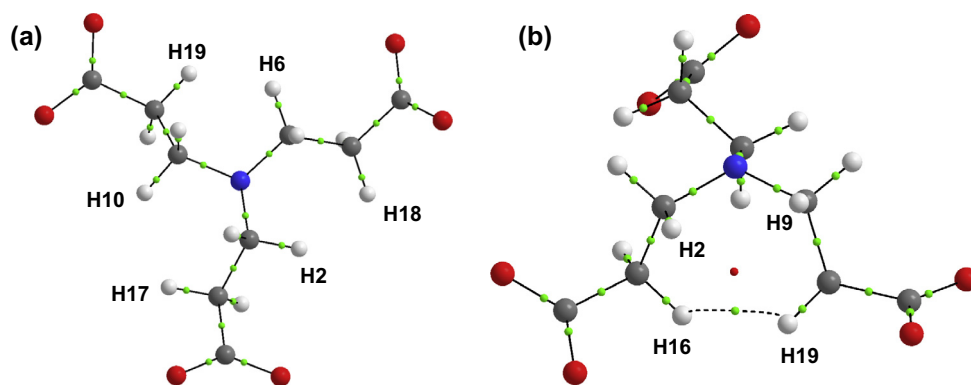


Fig. 11. Molecular graphs of (a) the lowest and (b) highest energy conformer of NTPA.

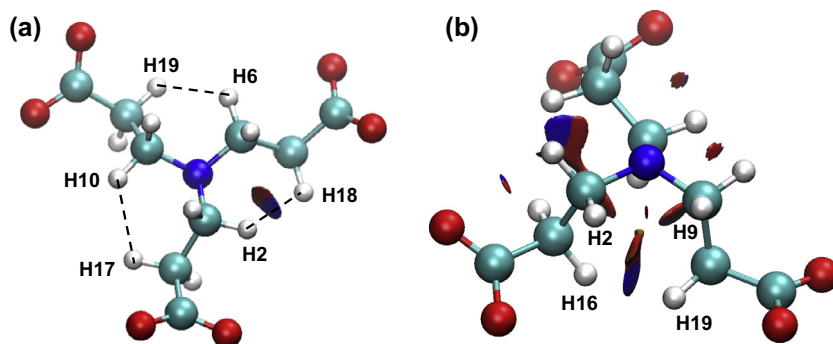


Fig. 12. NCI isosurfaces of (a) the lowest and (b) highest energy conformer of NTPA with a RDG isovalue = 0.5 au and isosurfaces coloured from blue to red using $-0.03 \leq \rho(\mathbf{r}) \times \text{sign}(\lambda_2) \leq +0.03$ au. (For interpretation of the references to colour in this figure legend, the reader is referred to the web version of this article.)

Table 3
Analysis of interactions in the LEC and HEC of NTPA in terms of interaction energies and electron density in the interatomic region.

Form	Interaction	Distance (Å)	$E_{\text{int}}^{\text{A,Bb}}$	$V_{\text{cl}}^{\text{A,Bb}}$	$V_{\text{XC}}^{\text{A,Ba}}$	AIL	$\rho(\mathbf{r}) \times \text{sign}(\lambda_2)^{\text{b}}$	$\Delta\rho(\mathbf{r})_{\text{GIP}}^{\text{c}}$
LEC	CH2...H18C	2.11	-3.3	0.1	-3.4	No	-0.0105	-0.0007
HEC	CH16...H19C	2.13	-3.2	0.1	-3.2	Yes	-0.0103	-0.0012
	CH2...H9C	2.27	-1.6	0.2	-1.8	No	+0.0105	-0.0035

^a Diatomic interaction energies and decomposed components, all in kcal/mol.

^b Values in au at GIP.

^c The deformation density in au at GIP.

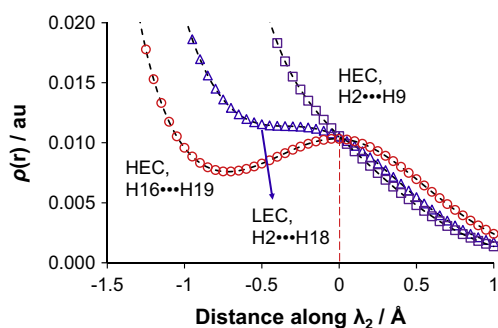


Fig. 13. Cross-sections of the electron density along the λ_2 eigenvector for indicated interactions in the lowest and highest energy conformers of NTPA. The dashed red line indicates the GIP.

3.4. 2,2,2-Tet

Triethylenetetramine (*trien*,) is a member of the homologous series of linear aliphatic polyamines (LAP), most of which are found in living organisms and play important roles in regulating cell proliferation and differentiation [70,71]. It is also a well-known copper chelator and has been used extensively in the treatment of Wilson's disease [72,73]. Due to the large conformational space available to this molecule, as well as the possibility of various intramolecular interactions (e.g., NH...N, CH...HC, etc.) forming upon its protonation, we have found it suitable to study the electron density distributions of intramolecular interactions.

Fig. 15 shows the molecular graphs of the lower (L1) and higher (L2) energy conformers. Both of them show a very strong (or leading) classical intramolecular NH...N hydrogen bonds, with an AIL present, but these conformers differ in the overall congestion of the molecule. As a result, L1 forms an additional NH...N interaction (with an AIL) and both conformers have additional CH...HC and CH...N interactions.

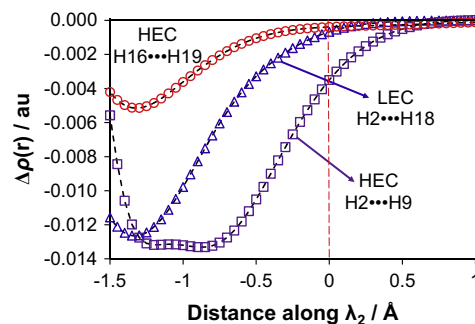


Fig. 14. Cross-sections of the deformation density along the λ_2 eigenvector for the indicated interactions in the lowest and highest energy conformers of NTPA. Red dashed line indicates the GIP. (For interpretation of the references to colour in this figure legend, the reader is referred to the web version of this article.)

The NCI-plots for each conformer, shown in Fig. 16, disclose an abundance of intramolecular interactions involving N-and H-atoms. Focusing on the CH...HC interactions, it can be seen that besides those with the presence of AILs, there also exist interactions just showing regions of concentration as well as regions of depletion.

Cross-sections of the electron density for the NH...N, CH...N and CH...HC interactions are shown in Fig. 17(a–c). A clear concentration and local maximum in the density is seen in L1 for the leading NH29...N28 interaction, whilst only a slight increase in the density is observed for the weaker NH2...N27 interaction; both maxima correspond to the observed BCP.

The difference between these two interactions, in terms of density cross-sections, might be rationalized in terms of the local environment; NH29...N28 is on the 'outskirts' of a molecule, whereas NH2...N27 occurs within the congested ring in the presence of numerous other interactions. For both interactions $\Delta\rho(\mathbf{r}) > 0$, but influence of the environment on the shape of the deformation

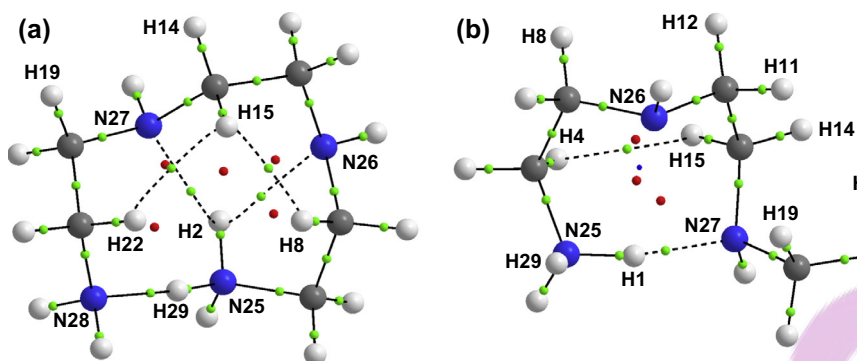


Fig. 15. Molecular graphs of (a) the lower energy L1 and (b) higher energy L2 conformer of 2,2,2-tet.

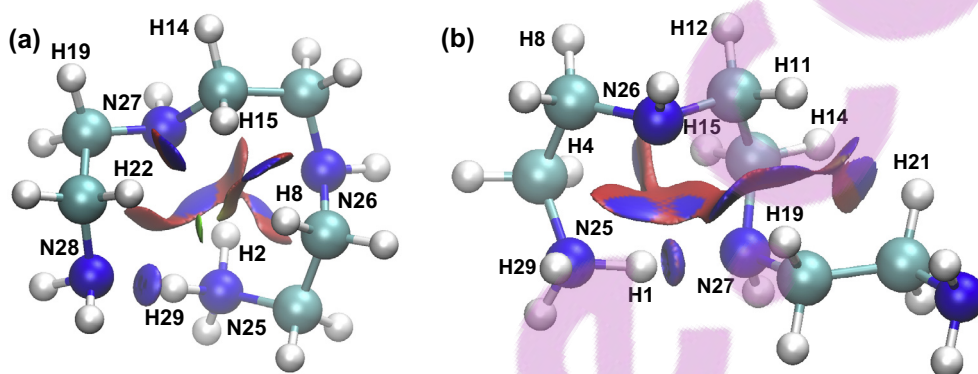


Fig. 16. NCI isosurfaces of (a) the lower L1 and (b) higher energy L2 conformer of 2,2,2-tet with a RDG isovalue = 0.5 au and isosurfaces coloured from blue to red using $-0.03 \leq \rho(r) \times \text{sign}(\lambda_2) \leq +0.03$ au. (For interpretation of the references to colour in this figure legend, the reader is referred to the web version of this article.)

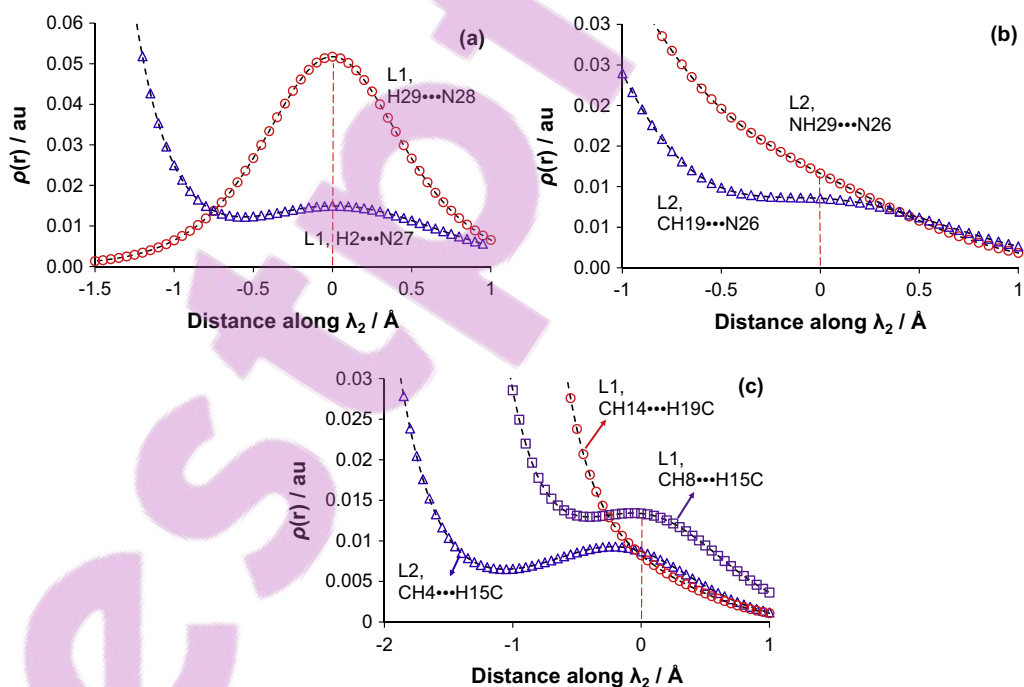


Fig. 17. Cross-sections of the electron density along the λ_2 -eigenvector for indicated (a) H...N interactions with an AIL, (b) XH...N interactions without an AIL and (c) CH...HC interactions in the lower energy conformer, LEC, of 2,2,2-tet.

densities can be easily deduced from Fig. 18(a). Two other H...N interactions, CH19...N26 and NH29...N26 in L2, but without AILs present, are presented in Fig. 17b. Regions of concentration and

depletion are observed, respectively, but the deformation density cross-sections in Fig. 18b show a very slight inflow of density for CH19...N26 but only an outflow of density for NH29...N26. A large

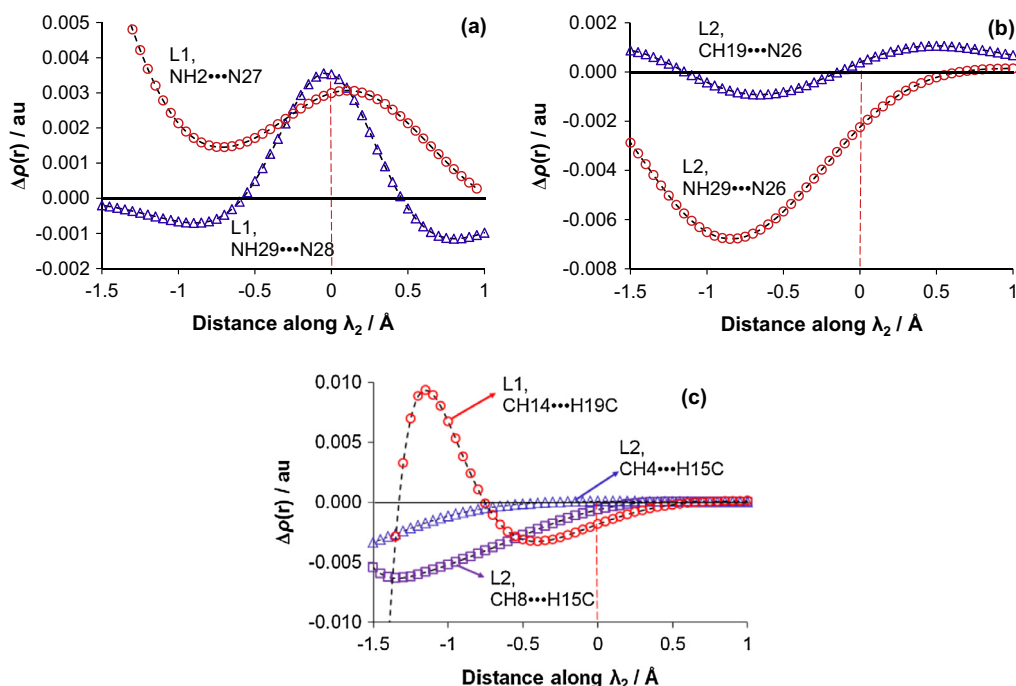


Fig. 18. Cross-sections of the deformation density along the λ_2 -eigenvector for indicated (a) XH...N with AIL present, (b) XH...N without AIL present and (c) CH...HC interactions in the lowest energy conformer of 2,2,2-tet. Red dashed lines indicate the GIP. (For interpretation of the references to colour in this figure legend, the reader is referred to the web version of this article.)

spectrum of various H...N interactions with different indices are therefore observed in these molecules.

The density cross-sections of selected CH...HC interactions (Fig. 17c) show a variation similar to what was seen in NTPA, with clear increases in the electron density showing an AIL and the absence of any shoulders showing regions of depletion. The deformation densities (Fig. 18c) show a slight outflow of density in the interaction regions but, like the CH...HC interactions in NTPA and bpy, much larger changes in the neighbouring regions between C atoms except for CH14...H19C, where the cross-section passes close to the lone pair of a nitrogen atom).

The full list of interacting atoms (as identified by NCI) is shown in Table 4, together with their IQA interaction energies. It is important to stress that, while the interaction energies of all intramolecular interactions vary greatly, there is not a single CH...HC

interaction which is repulsive and all are showing dominating contribution of the $V_{XC}^{A,B}$ term as found in bpy and NTPA; note that $E_{int}^{A,B} < 0$ is observed in all molecular systems studied here, regardless whether density concentration or depletion is observed in the bonding region, contradicting the MM-based notion of highly repulsive nature of this kind of interaction.

All NH...N interactions are characterized by large and negative interaction energies but H29...N26 ($E_{int}^{A,B} = -61.4$ kcal/mol in L2) does not have an AIL (most likely due to interatomic distance of 2.74 Å) and has a unique and somewhat unexpected set of NCI and deformation density indices, namely a local depletion in electron density ($\rho(\mathbf{r}) \times \text{sign}(\lambda_2) = +0.0116$ au) and an outflow of density on this interaction formation is observed, $\Delta\rho(\mathbf{r}) < 0$. Furthermore, there is no significant inflow of density on the formation of the H2...N26 interaction in L1 even though it is the second

Table 4
Analysis of interactions in the protonated lower (L1) and higher (L2) energy conformers of 2,2,2-tet and its protonated forms in terms of interaction energies and electron density in the interatomic region.

Form	Interaction	Atoms A, B	Distance (Å)	$E_{int}^{A,Ba}$	$V_{cl}^{A,Ba}$	$V_{XC}^{A,Ba}$	AIL	$\rho(\mathbf{r}) \times \text{sign}(\lambda_2)^b$	$\Delta\rho(\mathbf{r})_{GIP}^c$
L1	NH...N	H29, N28	1.741	-131.8	-107.5	-24.3	Yes	-0.0517	+0.0035
	NH...N	H2, N27	2.379	-78.2	-73.5	-4.7	Yes	-0.0150	+0.0026
	NH...N	H2, N26	2.136	-89.8	-81.6	-8.2	Yes	-0.0239	+0.0000
	CH...HC	H8, H15	2.034	-3.6	+0.0	-3.6	Yes	-0.0134	-0.0006
	CH...HC	H15, H22	2.133	-3.0	+0.1	-3.1	Yes	-0.0098	+0.0000
	CH...HC	H14, H19	2.490	-0.9	+0.2	-1.1	No	+0.0082	-0.0018
L2	NH...N	H1, N27	1.654	-145.8	-116.5	-29.3	Yes	-0.0656	+0.0144
	NH...N	H29, N26	2.736	-61.4	-60.5	-0.9	No	+0.0116	-0.0022
	CH...N	H19, N26	2.711	-5.0	-1.9	-3.1	No	-0.0086	+0.0004
	CH...HC	H4, H15	2.156	-2.7	+0.1	-2.8	Yes	-0.0087	+0.0001
	CH...HC	H8, H12	2.426	-1.1	+0.2	-1.3	No	+0.0082	-0.0017
	CH...HC	H14, H21	2.273	-2.0	+0.1	-2.1	No	-0.0083	-0.0001
	CH...HC	H11, H19	2.344	-1.4	+0.1	-1.5	No	-0.0083	-0.0004
	CH...HC	H11, H21	2.553	-0.9	+0.0	-1.0	No	-0.0045	-0.0000

^a Diatomic interaction energies and decomposed components, all in kcal/mol.

^b Values in au at GIP.

^c The deformation density in au at GIP.

strongest (in stabilizing manner), has large locally increased density ($\rho(\mathbf{r}) \times \text{sign}(\lambda_2) = -0.0239$ au) and atoms involved are linked by the AIL. The data obtained for the NH...N interactions show that (i) positive values of ($\rho(\mathbf{r}) \times \text{sign}(\lambda_2)$) and (ii) outflow or no change in the deformation density, $\Delta\rho(\mathbf{r}) \leq 0$ are not synonymous with destabilizing interaction; hence, former describes the resultant local density distribution and the latter explains the process of the resultant density formation, in- or outflow of density on an interaction formation and both these indices illustrate how a molecular system has minimized its energy in terms of density distribution.

Similar observations, related to significance of $\rho(\mathbf{r}) \times \text{sign}(\lambda_2)$ and $\Delta\rho(\mathbf{r})$, apply to CH...HC interactions, all characterized by $E_{\text{int}}^{A,B} < 0$ with dominant $V_{\text{XC}}^{A,B}$ term and various combinations of resultant local density and its formation. For instance, let us focus on two, H8...H15 and H14...H19 in L1, where an inflow of density is observed but only former has $\rho(\mathbf{r}) \times \text{sign}(\lambda_2) < 0$ and AIL. In some other cases, $\Delta\rho(\mathbf{r}) \sim 0$ but density is locally increased with either AIL present or not. From the analysis of weaker intramolecular interactions, as identified by NCI, it would also appear that density is preferentially removed from peripheral or long-distance contacts (H14...H19, H29...N26, H8...H12) in favour of contacts with shorter distances which are localized within a ring formed by the leading NH...N interaction.

From a chemist perspective it would be of importance to understand parameters controlling relative stability of conformers. A first attempt might be made by comparing the strength of the leading and 'truly' chemical in nature intramolecular H-bond. Unfortunately, inspection of data in Table 4 reveals that this is not the case as all indices are in favour of the NH...N interaction in the higher energy conformer for which we observe stronger by -14 kcal/mol interaction, much more significant covalent contribution, by about -5 kcal/mol, significantly larger density accumulation in the interatomic region (about -0.015 au) which resulted from a large inflow of density. The only reasonable explanation we were able to come up with is the presence of three highly stabilizing NH...N interactions in L1 whereas only two are observed in L2. However, if these were the only significant changes then L1 should be more stable, by ~ 100 kcal/mol, than L2 but this is not the case. Hence, L1 must have paid some energy penalties (not reflected in Table 4) which largely reduced the decrease in the final energy of the L1 conformer. Clearly, any rigorous attempt to explain and quantify conformational preference is not an easy, if at all possible, task when polyatomic molecular structures are considered. In this regard, the NCI is very useful in identifying regions with increased density in the interatomic region from which additional and possibly significant interactions can be identified. However, the appearance of blue regions in the NCI plots must be always accompanied by red ones (with depleted density) and interpretation of significance of the latter might be more difficult for chemists' purposes, in terms of stabilizing or unfavourable character of an interaction, as exemplified by, e.g., the highly stabilizing H29...N26 interaction in L2.

4. Conclusions

Numerous inter- (in water dimers) and intramolecular (in(de)protonated forms of bpy, NTPA and singly protonated 2,2,2-tet) interactions of different kind (O...H, NH...N, CH...HC, CH...HN, NH...HN, CH...N, H...H, O...O and N...N) were investigated by exploring topology of electron density in the interatomic regions using standard protocols as implemented in QTAIM, IQA and NCI as well as density cross section along the eigenvector corresponding to the λ_2 eigenvalue of the Hessian matrix, starting from the geometric interaction point (the lowest density directly

between two nuclei). All these techniques are concerned with the properties of the resultant density distribution in a molecular system. To gain further insight, we have also implemented here an analysis of deformation density from which the process, inflow or outflow of density from fragments to the interatomic region of an interaction of interest in a molecule or molecular system could be uncovered. Our main interest was to find out whether there are well-defined relationships between (i) QTAIM-defined an atomic interaction line, AIL (presence or absence), (ii) IQA-defined interaction energy, $E_{\text{int}}^{A,B}$, and its components, classical $V_{\text{cl}}^{A,B}$ and exchange-correlation term $V_{\text{XC}}^{A,B}$, (iii) NCI-defined isosurfaces used to identify local regions of accumulated ($\lambda_2 < 0$) or depleted ($\lambda_2 > 0$) density relative to immediate environment, and (iv) deformation density which for $\Delta\rho(\mathbf{r}) > 0$ indicates an inflow and $\Delta\rho(\mathbf{r}) < 0$ indicates an outflow of density on the interaction formation.

The analysis of data presented in Table 5, where a full set of combined indices obtained for all interactions is shown, leads us to the following final conclusions:

- the presence of an AIL is observed for many interactions, regardless whether (i) they are highly attractive or repulsive as measured by the value and sign of $E_{\text{int}}^{A,B}$, (ii) an inflow or outflow of density takes place into the interatomic region,

Table 5
Comparative analysis of all interactions investigated in this work.^a

Structure	Interaction	Dominant term	λ_2	$\Delta\rho(\mathbf{r})_{\text{GIP}}$
<i>Attractive ($E_{\text{int}}^{A,B} < 0$) with AIL</i>				
d1	O...H	V_{cl}	neg	pos
L1 2,2,2-tet	NH...N	V_{cl}	neg	pos
s-cis Hbpy	NH...N	V_{cl}	neg	pos
s-cis bpy				
s-cis Hbpy				
s-cis H ₂ bpy				
L1 2,2,2-tet	CH...HC	V_{XC}	neg	pos
L2 2,2,2-tet	CH...HN	V_{XC}	neg	pos
s-trans Hbpy				
HEC NTPA				
L1 2,2,2-tet				
L2 2,2,2-tet	CH...HC	V_{XC}	neg	neg
<i>Repulsive ($E_{\text{int}}^{A,B} > 0$) with AIL</i>				
d4	H...H	V_{cl}	neg	pos
d4	O...O	V_{cl}	neg	pos
s-trans H ₂ bpy	NH...HN	V_{cl}	neg	pos
s-trans H ₂ bpy	CH...HN	V_{cl}	neg	pos
d2, d3	O...O	V_{cl}	neg	neg
d4	O...O	V_{cl}	pos ^b	pos
<i>Attractive ($E_{\text{int}}^{A,B} < 0$) without AIL</i>				
d4	O...H	V_{cl}	neg	pos
L2 2,2,2-tet	CH...N	V_{XC}	neg	pos
s-trans bpy	CH...N	V_{cl}	neg	neg
s-trans Hbpy				
d3 d4	O...H	V_{cl}	neg	neg
LEC NTPA	CH...HC	V_{XC}	neg	neg
L2 2,2,2-tet				
L1 2,2,2-tet	CH...HC	V_{XC}	neg	~ 0
L2 2,2,2-tet				
L2 2,2,2-tet	CH...HC	V_{XC}	pos	neg
HEC NTPA	CH...HC	V_{XC}	pos	neg
L1 2,2,2-tet				
L2 2,2,2-tet				
L2 2,2,2-tet	NH...N	V_{cl}	pos	neg
<i>Repulsive ($E_{\text{int}}^{A,B} > 0$) without AIL</i>				
d4	H...H	V_{cl}	neg	pos
d4	O...O	V_{cl}	pos	neg
s-cis bpy	N...N	V_{cl}	pos	neg

^a neg and pos stand for the negative and positive, respectively, signs of the λ_2 and $\Delta\rho(\mathbf{r})_{\text{GIP}}$ values.

^b This is at the GIP = RCP in this dimer where bifurcated AIL is observed.

- there is no correlation between the signs of λ_2 and $E_{\text{int}}^{\text{A,B}}$; both, highly repulsive and attractive, interactions might have locally depleted density and *vice versa*,
- locally accumulated density, with $\lambda_2 < 0$, does not imply that this is the result of an inflow ($\Delta\rho(\mathbf{r}) > 0$) or outflow of density, and this equally applies to attractive and repulsive interactions either with or without an AIL.

From a chemist's perspective:

- the first three interactions in Table 5 can be interpreted as H-bonds (either inter- or intramolecular) and they all are characterized by the presence of AIL, $E_{\text{int}}^{\text{A,B}} \ll 0$ dominated by the $V_{\text{cl}}^{\text{A,B}}$ term, $\lambda_2 < 0$ and $\Delta\rho(\mathbf{r}) > 0$. There are also other two interactions, CH \cdots HC and CH \cdots HN which have exactly the set of indices (but their interaction energy is dominated by the $V_{\text{xc}}^{\text{A,B}}$) and classically the former is interpreted as steric hindrance and the latter as another kind of a H-bond.
- the last two interactions in Table 5 represent classical non-bonded and repulsive contacts which are characterized by the absence of AIL, $E_{\text{int}}^{\text{A,B}} \gg 0$ dominated by the $V_{\text{cl}}^{\text{A,B}}$ term, locally depleted density ($\lambda_2 < 0$) and an outflow of density from the interatomic region ($\Delta\rho(\mathbf{r}) < 0$). One must note that there are also attractive interactions ($E_{\text{int}}^{\text{A,B}} < 0$) without AILs, for which also locally depleted density and outflow of density from the interatomic region is observed, and one of them, NH \cdots N in 2,2,2-tet, would easily be interpreted as an intramolecular H-bond,
- the O \cdots O interaction in **d4** is highly repulsive and would be classified by any chemist as highly destabilizing a molecular system but, at the same time, is characterized by three identical topological features as found for classical H-bonds, namely (i) the presence of an AIL, locally increased density in and an inflow into the interatomic region,
- the molecular environment can change the description, hence a character, of an interaction radically as exemplified by CH \cdots HC for which the set of descriptors varies from that observed in the case of classical H-bonds and changes to the set characterizing a destabilizing a molecule interaction, except the interaction energy between H-atoms involved which is always negative,
- none of the indices (IQA, QTAIM, etc.), either separately or combined, can be used to predict the (de)stabilizing nature of an interaction except two limiting cases, the first and last interaction shown in Table 5.

The interpretation that the signs of λ_2 or $\Delta\rho(\mathbf{r})$ can be used as indications of “stabilizing”, “attractive” or even “bonding” rests on the concept that an increase in density in the bonding region of an interaction is an indication of a bonding mechanism. In this work, we have presented two different techniques to measure an increase in density in the bonding region: the sign of λ_2 (as it is used in NCI and the interpretation of an AIL) and the sign of $\Delta\rho(\mathbf{r})$. The former indicates increased density relative to the local environment of an interaction, whereas the latter indicates increased density relative to non-interacting fragment states. We note that the combination of the two methods gives a much greater insight into the electron distribution of inter- and intramolecular interactions; this is particularly true for all of the CH \cdots HC interactions investigated in this work. Even though the electron density distributions of these interactions show a wide range of different indices, we note that, in cases where a concentration of density or even an AIL is seen, a large outflow of density is observed between the neighbouring C-atoms. It appears that formation of an AIL does not have to be an output of the inflow of density into the interatomic region, as traced by the deformation density, but might be also an ‘artefact’ of density depletion between neighbouring atoms.

Clearly, care must be taken when using any *local* theoretical index (i.e. the value of the electron density or deformation density at a single coordinate), because the description of any interaction is highly influenced by its local environment. This is particularly true for congested systems, with many intramolecular interactions present in the same space. It is obvious that to fully uncover the chemical character of an interaction it would be necessary and informative to include additional physical properties and expand on methodologies used.

On a final note, we can also ask whether the presence of an AIL corresponds in any way with the delocalization or exchange interaction energy between competing pairs of atoms. Such a correspondence was suggested by Pendás et al. [38] and investigated in more detail by Tognetti and Joubert. [58] From the data obtained in this work, it would appear that Pendás' interpretation of an AIL holds true – the interactions for which $V_{\text{xc}}^{\text{A,B}}$ is the largest in magnitude does indeed show the presence of an AIL. For example, in **d1**, $V_{\text{xc}}^{\text{O1,H5}} = -9.8$ kcal/mol, whereas $V_{\text{xc}}^{\text{O1,O4}} = -4.9$ kcal/mol. However, we have found one case in **d4** with $d(\text{H}\cdots\text{H}) = 1.6$ Å, where the H \cdots H interaction presenting an AIL has a less negative $V_{\text{xc}}^{\text{A,B}}$ value than its competing O \cdots O interaction; $V_{\text{xc}}^{\text{H5,H6}} = -2.6$ kcal/mol, whereas $V_{\text{xc}}^{\text{O1,O3}} = -8.6$ kcal/mol. Whether this observation is a result of a structure which is far from equilibrium or whether it is a special case where Pendás' interpretation (as determined by the methodology of Tognetti and Joubert) does not hold is a question we will investigate more thoroughly in the future.

Acknowledgments

This work is based on the research supported in part by the National Research Foundation of South Africa (Grant Number 87777) and the University of Pretoria.

Appendix A. Supplementary material

Supplementary data associated with this article can be found, in the online version, at <http://dx.doi.org/10.1016/j.comptc.2014.10.005>.

References

- [1] R.W.F. Bader, *Atoms in Molecules: A Quantum Theory*, Oxford University Press, Oxford, UK, 1990.
- [2] E.R. Johnson, S. Keinan, P. Mori-Sánchez, J. Contreras-García, A.J. Cohen, W.J. Yang, Revealing noncovalent interactions, *Am. Chem. Soc.* 132 (2010) 6498–6506.
- [3] N. Gillet, R. Chaudret, J. Contreras-García, W. Yang, B. Silvi, J.P.J. Piquemal, Coupling quantum interpretative techniques: another look at chemical mechanisms in organic reactions, *Chem. Theory Comput.* 8 (2012) 3993–3997.
- [4] J. Contreras-García, E.R. Johnson, S. Keinan, R. Chaudret, J.P. Piquemal, D. Beratan, W.J. Yang, NCIPlot: a program for plotting noncovalent interaction regions, *Chem. Theory Comput.* 7 (2011) 625–632.
- [5] P.L.A. Popelier, Quantum chemical topology: on bonds and potentials, in: D. Wales (Ed.), *Intermolecular Forces and Clusters I*, Springer-Verlag, Berlin, 2005, pp. 1–56.
- [6] N. Sukumar, C.M. Breneman, QTAIM in drug discovery and protein modelling, in: C.F. Matta, R.J. Boyd (Eds.), *The Quantum Theory of Atoms in Molecules: From Solid State to DNA and Drug Design*, Wiley-VCH Verlag GmbH & Co. KGaA, Weinheim, 2007, pp. 471–498.
- [7] M. Vafaezadeh, Z.B. Dizicheh, M.M. Hashemi, Mesoporous silica-functionalized dual Brønsted acidic ionic liquid as an efficient catalyst for thioacetalization of carbonyl compounds in water, *Catal. Commun.* 41 (2013) 96–100.
- [8] C.D.M. Churchill, D.M. Cassandra, L.R. Rutledge, S.D. Wetmore, Effects of the biological backbone on stacking interactions at DNA-protein interfaces: the interplay between the backbone π and $\pi\pi$ components, *Phys. Chem. Chem. Phys.* 12 (2010) 14515–14526.
- [9] S.M. LaPointe, S. Farrag, H.J. Bohórquez, R.J. Boyd, QTAIM study of an α -helix hydrogen bond network, *J. Phys. Chem. B* 113 (2009) 10957–10964.
- [10] M. Mandado, A.M. Graña, R.A. Mosquera, Do 1, 2-ethanediol and 1, 2-dihydroxybenzene present intramolecular hydrogen bond?, *Phys. Chem. Chem. Phys.* 6 (2004) 4391–4396.

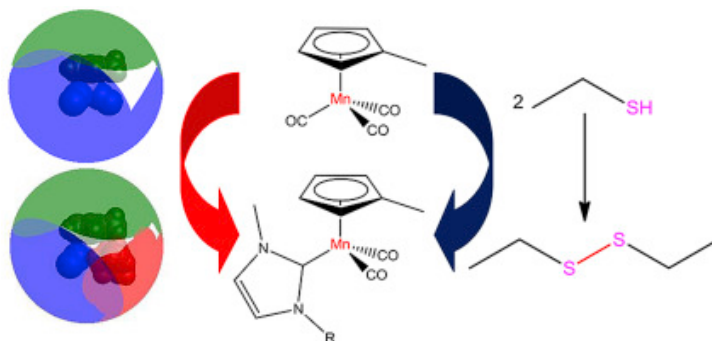
Appendix 1

- importance of short H-H nonbonded van der Waals contacts in controlling metal-ion selectivity. A thermodynamic, molecular mechanics and crystallographic study, *Inorg. Chem.* 46 (2007) 4749–4757.
- [68] J.C.A. Boeyens, C.C. Fox, R.D. Hancock, Refinement of the structure of the nickel perchlorate complex of 1,4-diazacyclooctane, $[\text{Ni}(\text{Daco})_2](\text{ClO}_4)_2 \cdot 2\text{H}_2\text{O}$ by empirical force-field methods, *Inorg. Chim. Acta* 87 (1984) 1–4.
- [69] A.E. Martell, R.D. Hancock, *Metal Complexes in Aqueous Solutions*, Plenum Press, New York, 1996.
- [70] E. Agostinelli, M.P.M. Marques, R. Calheiros, F.P.S.C. Gil, G. Tempera, N. Viceconte, V. Battaglia, S. Grancara, A. Toninello, Polyamines: fundamental characters in chemistry and biology, *Amino Acids* 38 (2010) 393–403.
- [71] U. Bachrach, The early history of polyamine research, *Plant Phys. Biochem.* 48 (2010) 490–495.
- [72] L.A.E. Batisa de Carvalho, M.P.M. Marques, J. Tomkinson, Transverse Acoustic modes of biogenic and α,ω -polyamines: a study by inelastic neutron scattering and Raman spectroscopies coupled to DFT calculations, *J. Phys. Chem. A* 110 (2006) 12947–12954.
- [73] G.J.S. Cooper, Therapeutic potential of copper chelation with triethylenetetramine in managing diabetes mellitus and Alzheimer's disease, *Drugs* 71 (2011) 1281–1320.

**Appendix II. Synthesis, structure and DFT study of
asymmetrical NHC complexes of cymantrene derivatives
and their application in the dehydrogenative dimerization
reaction of thiols**

Published in:

Journal of Organometallic Chemistry, **2017**, 840, 11–22.



Synthesis, X-ray study, structural analysis and catalytic study of cymantrene derived N-heterocyclic carbene complexes.

Electronic supplementary information available at:

<https://doi.org/10.1016/j.jorganchem.2017.03.047>.



Synthesis, structure and DFT study of asymmetrical NHC complexes of cymantrene derivatives and their application in the dehydrogenative dimerization reaction of thiols



Roan Fraser, Petrus H. van Rooyen, Jurgens de Lange, Ignacy Cukrowski, Marilé Landman*

Department of Chemistry, University of Pretoria, Private Bag X20, Hatfield, 0028, South Africa

ARTICLE INFO

Article history:

Received 11 January 2017

Received in revised form

15 March 2017

Accepted 25 March 2017

Available online 28 March 2017

Keywords:

N-heterocyclic carbene

Cymantrene derivatives

DFT

Steric parameters

Bond order

ABSTRACT

Asymmetrical NHC complexes of cymantrene and methylcymantrene have been synthesised through the photochemical substitution of carbonyl ligands in the presence of the imidazol-2-ylidene salts. The carbene substituents have been varied between compact (**L1**) and bulky (**L2** and **L3**) substituents to produce an array of differently sized carbene ligands. The solid state crystal structures of three of the complexes confirmed the bonding pattern of the ligand towards available metal centres and an in-depth DFT study provided insight into electronic and steric aspects. Application of the Extended Transition State coupled with Natural Orbitals for Chemical Valence (ETS-NOCV) energy decomposition technique indicated various NOCV channels for each Mn–L bond (L = 3-ethyl-1-methylimidazolylidene carbene, triphenylphosphine or acetonitrile), describing the density and energy changes of specific (σ and π) attributes of each bond. N-heterocyclic carbenes of cymantrene derivatives and their triphenylphosphine-substituted analogue are equivalent σ -donors, with 53% and 56%, respectively, of the total binding energy originating from σ -donation. However, NHC complexes show considerably less π character in the metal-carbene bond. Hydrogen interactions in the NHC complexes were also identified in the ETS-NOCV calculations and provided quantification of the hydrogen interactions witnessed in the solid state structures. Calculated Wiberg bond indices, bond dissociation enthalpies, percentage buried volumes and percentage sigma and pi-bonding characteristics quantified the bonding and electronic aspects of the ligand-metal interactions within the complex.

© 2017 Elsevier B.V. All rights reserved.

1. Introduction

Since the isolation of the first stable, free N-heterocyclic carbene (NHC) by Arduengo in 1991, NHC's have transformed the field of organometallic chemistry [1]. The adjustability of the steric and electronic properties of these ligands has resulted in their persistent use for the synthesis and stabilization of metal complexes capable of cleaving very inert bonds [2]. The majority of synthetic pathways in the synthesis of transition metal (TM) NHC complexes have been thermally initiated [3] whereas photochemical induced pathways have, however, been mostly ignored. This aspect is surprising, especially if taken into consideration the similarities between tertiary phosphines and NHC ligands and the applicability of photochemical reactions in producing highly reactive, coordinatively unsaturated TM-PR₃ species [3]. The photolysis and the

subsequent isomerisation of ruthenium NHC complexes have been reported and indicate the ability of photochemical processes to produce isomeric variations of target complexes (Fig. 1) [3].

Methylcyclopentadienyl manganese tricarbonyl (MMT), and to a far lesser extent, cymantrene have been successfully applied in the fuel industry as supplements in unleaded gasoline. MMT not only increases octane ratings but are particularly useful as anti-knocking agents, improving combustion of fuels [4]. Studies on carbene complexes of MMT and cymantrene complexes are limited in literature and mainly focus on the synthesis of novel, symmetrical N-heterocyclic carbene (NHC's) complexes of MMT and cymantrene (Fig. 2) [4–7]. The synthesis of symmetrical NHC complexes of MMT has been reported as early as 1977 when Lappert [8] prepared complexes of manganese from the Wanzlick dimeric NHC ligand under high thermal conditions. The complexes were stable above 180 °C and displayed exceptional inertness against thermal decomposition. A small variety of symmetrical NHC cymantrene derived carbene complexes have been synthesised by means of photochemical processes and have even found application in the

* Corresponding author.

E-mail address: marile.landman@up.ac.za (M. Landman).

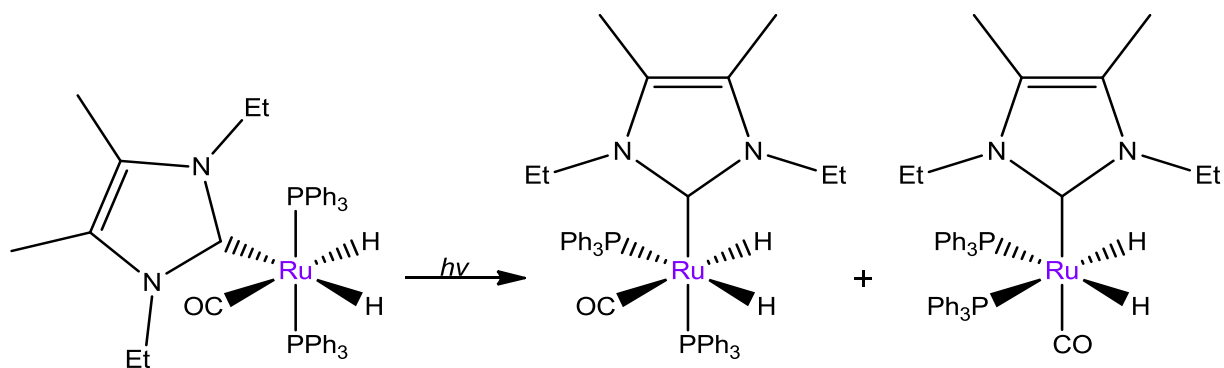


Fig. 1. Isomerisation of Ru-NHC complexes afforded through photochemical processes [3].

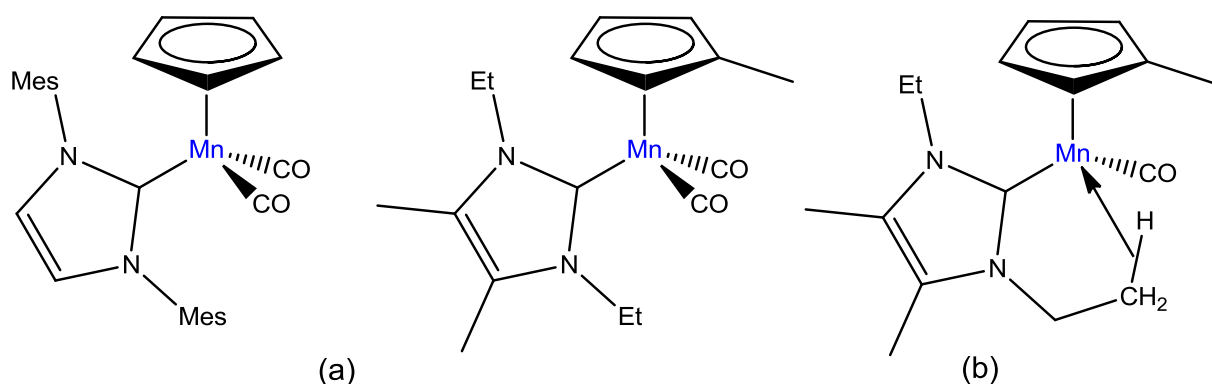


Fig. 2. NHC complexes of cymantrene and MMT (a) and agostic interaction of the cymantrene NHC complex (b).

hydrosilylation of aldehydes and ketones [4]. The study found that the incorporation of at least one mesityl group leads to the most selective and active systems. DFT calculations also indicated the presence of an agostic stabilization when a second carbonyl ligand is removed by photolytic irradiation [5].

Since agostic interactions are also witnessed in the triphenylphosphine analogue [5] and both $\text{Cp}^*\text{Mn}(\text{CO})\text{PPh}_3$ and $\text{Cp}^*\text{Mn}(\text{CO})$ NHC stabilize carbonyl expulsion through agostic interactions rather than with solvent ligation [6], both analogues can be seen as quite similar in chemical nature. Although the synthetic methodology and catalytic potential of symmetric NHC complexes of cymantrene and MMT have been determined for a variety of

different reactions and conditions, very limited understanding exists for the structural and electronic effects of different unsymmetrical NHC ligands towards the metal centre. For this purpose, asymmetrical NHC complexes with increasing steric bulk have been synthesised (Fig. 4) and studied with theoretical calculations. This study reports the synthesis of the six novel asymmetrical NHC complexes of cymantrene and MMT, the synthesis of the acetonitrile and triphenylphosphine analogues of the NHC complexes, X-ray crystal structures of three of the complexes and a DFT study (Fig. 3). The triphenylphosphine and acetonitrile analogues were synthesised to form a baseline to which the percentage sigma and pi-bonding characteristics of the NHC complexes could be compared.

2. Experimental

2.1. General

All reactions, unless noted otherwise, were performed under inert nitrogen or argon atmospheres using typical Schlenk techniques [9]. All solvents used, were freshly distilled, dried and collected under inert conditions. Column chromatography was carried out under inert nitrogen and argon atmospheres using silica gel (particle size 0.063–0.200 mm) as the stationary phase. Percentage yields were calculated relative to the limiting reactant. Crystallization was done using hexane:DCM or hexane:diethyl ether diffusion methods. The reagents $\text{CpMn}(\text{CO})_3$, $\text{MeCpMn}(\text{CO})_3$, *n*-butyl lithium (1.6 M solution in hexane) and other commercial reagents were used as purchased. Complexes **B1** [10] and **C1** [11] were synthesised according to literature procedures. NMR spectra were recorded on a Bruker ARX-300. NMR spectra were recorded in

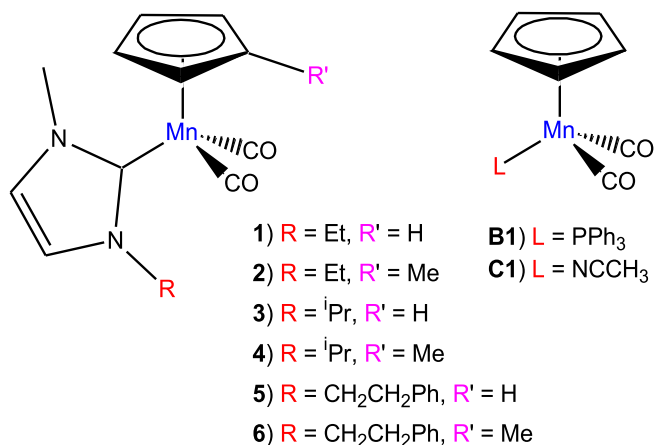


Fig. 3. Cymantrene derived NHC complexes of this study.

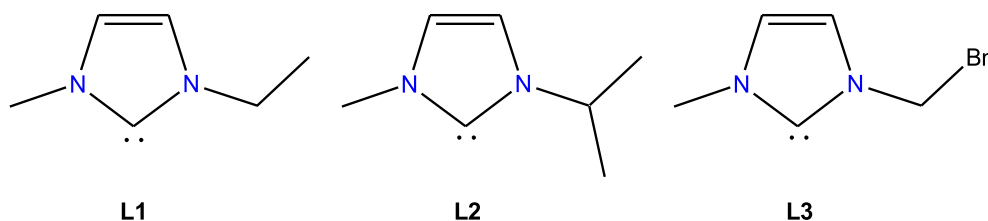


Fig. 4. NHC ligands used in this study.

CD₃CN using the deuterated solvent peak as internal reference. The ¹H and ¹³C NMR spectra were measured at 300.1 and 75.5 MHz, respectively. IR spectra were recorded on a Perkin Elmer Spectrum RXI FT-IR spectrophotometer as KBr pellets or in hexane and only the vibration bands in the carbonyl-stretching region (ca. 1500–2200 cm⁻¹) are reported.

2.2. Synthesis of complexes 1–6

2.2.1. Synthesis of **1**, CpMn(CO)₂L1

All complexes were synthesised according to a similar methodology as reported by Lukan [4]. CpMn(CO)₃ (0.612 g, 3.0 mmol) was dissolved in 40 ml of dry THF and irradiated for 60 min at room temperature. Imidazol-2-ylidene **L1** (0.714 g, 3.0 mmol) was added to the reaction mixture via cannula and the reaction allowed to stir for 90 min. The reaction colour turned to deep brown and the mixture was subsequently filtered through a small aluminium oxide column. The solvent was evaporated, the product redissolved and purified with column chromatography with hexane:ether eluent to recover **1** as an orange oil. Yield (0.267 g (31%)) ¹H NMR(CD₃CN): δ 7.33 (s, 1H, NCH=CHN), 7.30 (s, 1H, NHC=CHN), 4.44 (s, 5H, Cp), 4.27 (q, 2H, J_{HH} = 7.3, NCH₂CH₃), 3.75 (s, 3H, NCH₃), 1.30 (t, 3H, J_{HH} = 7.3, NCH₂CH₃). ¹³C{¹H} NMR: δ 235.22 Mn(CO)₂, 195.7 NCN, 124.6 NC=CN, 121.5 NC=CN, 82.6 Cp, 65.4 NCH₃, 45.5 NCH₂CH₃, 16.7 NCH₂CH₃. IR (cm⁻¹): 1922 ν(CO), 1856 ν(CO). HRESI⁺-MS, m/z: 287.0513 (calcd. 287.0592).

2.2.2. Synthesis of **2**, MeCpMn(CO)₂L1

A similar methodology as for **1** was followed. Imidazol-2-ylidene **L1** (0.714 g, 3.0 mmol) was added to photo-irradiated MeCpMn(CO)₃ (0.654 g, 3.0 mmol). A single brown-orange oily product of complex **2** was isolated. Yield: 0.271 g (30%) ¹H NMR, ppm (CD₃CN): δ 7.20 (s, 1H, NHC=CHN), 7.15 (s, 1H, NHC=CHN), 4.34 (s br, 2H, NCH₂CH₃), 4.09 (s, 2H, Cp), 4.02 (s, 2H, Cp), 3.36 (s, 3H, NCH₃), 2.86 (s, 3H, Cp-CH₃), 1.48 (s br 3H, NCH₂CH₃). ¹³C{¹H} NMR, ppm: δ 234.7 Mn(CO)₂, 200.7 NCN, 129.0NC = CN, 128.6 NC=CN, Cp 101.4, Cp 81.5, Cp 79.8, 65.0 NCH₃; NCH₂CH₃ 52.27, Cp-CH₃ 37.5, NCH₂CH₃ 13.7. IR (cm⁻¹): 1918 ν(CO), 1852 ν(CO). HRESI⁺-MS, m/z: 303.0939 (calcd. 303.0905).

2.2.3. Synthesis of **3**, CpMn(CO)₂L2

A similar methodology as for **1** was followed. Imidazol-2-ylidene **L2** (0.0481 g, 3.0 mmol) was added to photo-irradiated MeCpMn(CO)₃ (0.612 g, 3.0 mmol). A single yellow solid product of complex **3** was isolated (yield: 0.271 g; 30%). ¹H NMR, ppm (CD₃CN): δ 7.42 (s, 1H, NHC=CHN), 7.32 (s, 1H, NCH=CHN), 4.45 (s, 5H, Cp), 3.76 (s, 3H, NCH₃), 3.60 (m, 2H, NCH(CH₃)₂), 1.32 (s, 6H, NCH(CH₃)₂). ¹³C{¹H} NMR, ppm: δ 235.1 Mn(CO)₂, 193.5 NCN, 124.90 NC=CN, 118.7 NC=CN, Cp 82.5, 67.5 NCH₃, 51.9 NCH(CH₃)₂, 25.6 NCH(CH₃)₂. IR (cm⁻¹): 1922 ν(CO), 1856 ν(CO). HRESI⁺-MS, m/z: 301.0789 (calcd. 301.0748).

2.2.4. Synthesis of **4**, MeCpMn(CO)₂L2

A similar methodology as for **1** was followed. Imidazol-2-

ylidene **L2** (0.481 g, 3.0 mmol) was added to photo-irradiated MeCpMn(CO)₃ (0.654 g, 3.0 mmol). A single yellow solid product of complex **4** was isolated (yield: 0.255 g; 27%). ¹H NMR, ppm (CD₃CN): δ 6.85 (s, 1H, NCH=CHN), 6.83 (s, 1H, NCH=CHN), 3.96 (s, 2H, Cp), 3.86 (s, 3H, NCH₃), 3.85 (s, 2H, Cp), 3.76 (s br, 2H, NCH(CH₃)₂), 2.89 (s, 3H, Cp-CH₃), 1.33 (d, 6H, J_{HH} = 6.3, NCH(CH₃)₂). ¹³C{¹H} NMR, ppm: δ 235.1 Mn(CO)₂, 195.0 NCN, 124.9 NC=CN, 124.1 NC=CN, 34.7 Cp-CH₃, 102.8 Cp, 81.9 Cp, 80.4 Cp, 60.5 NCH₃, 52.4 NCH(CH₃)₂, 13.7 NCH(CH₃)₂. IR (cm⁻¹): 1943 ν(CO), 1852 ν(CO). HRESI⁺-MS, m/z: 317.1081 (calcd. 317.1062).

2.2.5. Synthesis of **5**, CpMn(CO)₂L3

A similar methodology as for **1** was followed. Imidazol-2-ylidene **L1** (0.801 g, 3.0 mmol) was added to photo-irradiated MeCpMn(CO)₃ (0.612 g, 3.0 mmol). A single yellow solid product of complex **3** was isolated (yield: 0.381 g; 35%). ¹H NMR, ppm (CD₃CN): δ 7.45 (s, 1H, NHC=CHN), 7.34 (s br, 5H, Ph), 7.26 (s, 1H, NHC=CHN), 4.44 (m, 2H, NCH₂Bn), 4.38 (s, 5H, Cp), 3.75 (s, 3H, NCH₃), 3.03 (m, 2H, NCH₂CH₂Ph). ¹³C{¹H} NMR, ppm: δ 235.2 Mn(CO)₂, 195.1 NCN, 138.9 Ph(ips), 129.3 Ph(meta), 129.0 Ph(ortho), 127.0 Ph(para), 124.5 NC=CN, 122.1 NC=CN, 82.7Cp, 64.4 NCH₃, 52.0 NCH₂Bn, 40.8 NCH₂CH₂Ph. IR (cm⁻¹): 1921 ν(CO), 1855 ν(CO). HRESI⁺-MS, m/z: 365.1033 (calcd. 365.1062).

2.2.6. Synthesis of **6**, MeCpMn(CO)₂L3

A similar methodology as for **1** was followed. Imidazol-2-ylidene **L1** (0.801 g, 3.0 mmol) was added to photo-irradiated MeCpMn(CO)₃ (0.654 g, 3.0 mmol). A single yellow solid product of complex **6** was isolated (yield: 0.374 g; 33%). ¹H NMR, ppm (CD₃CN): δ 7.37 (s br, 4H, Ph), 7.46 (s, 1H NHC=CHN), 7.25 (s, 1H NCH=CHN), 4.46 (m, 2H, NCH₂Bn), 4.26 (s br, 5H, Cp), 3.75 (s, 3H, NCH₃), 3.05 (m, 2H, NCH₂CH₂Ph), 2.51 (s, 3H, Cp-CH₃). ¹³C{¹H} NMR, ppm: δ Mn(CO) 235.3, 196.5 NCN, 124.6 NC=CN, 122.2 NC=CN, 138.9 Ph(ips), 129.3 Ph(meta), 129.0 Ph(ortho), 127.0 Ph(para), 103.2 Cp, 82.1 Cp, 80.4 Cp, 64.4 NCH₃, 52.1 NCH₂Bn, 40.8 NCH₂CH₂Ph, 35.6 Cp-CH₃. IR (cm⁻¹): 1917 ν(CO), 1852 ν(CO). HRESI⁺-MS, m/z: 379.1248 (calcd. 379.1218).

2.3. X-ray crystallography

Data for complexes **3** and **6** and **C1** were collected at 150 K on a Bruker D8 Venture kappa geometry diffractometer, with duo μ s sources, a Photon 100 CMOS detector and APEX II control software using Quazar multi-layer optics, monochromated Mo-K α radiation and by means of a combination of ϕ and ω scans. Data reduction was performed using SAINT+ and the intensities were corrected for absorption using SADABS [12]. The structures were solved by intrinsic phasing using SHELXTS and refined by full-matrix least squares using SHELXTL and SHELXL-2013 [13]. In the structure refinement, all hydrogen atoms were added in calculated positions and treated as riding on the atom to which they are attached. All nonhydrogen atoms were refined with anisotropic displacement parameters, all isotropic displacement parameters for hydrogen atoms were calculated as X \times U_{eq} of the atom to which they are

attached, $X = 1.5$ for the methyl hydrogens and 1.2 for all other hydrogens. Crystallographic data and refinement parameters are given in Table 1. Ortep drawings [14] of the three structures are included in Fig. 5, Fig. 6 and Fig. 9. The crystal structures (cif) have been deposited at the Cambridge Crystallographic Data Centre and allocated the deposition numbers: CCDC 1517726–1517728. Data collection, structure solution and refinement details are available in each cif.

2.4. Molecular modelling

The calculations reported in this paper were obtained using the Gaussian 09 [15] suite of programs. Calculations were carried out in the singlet spin state using the hybrid functional B3LYP [16,17]. Geometries of the neutral complexes were optimized in gas phase with the triple- ζ basis set 6-311G* on all atoms except for the metal atoms. Stuttgart/Dresden (SDD) pseudopotential was used to describe the metal electronic core, while the valence electrons were described using def2-TZVPP [18]. No symmetry constraints were applied and only the default convergence criteria were used during the geometric optimizations. Vibrational frequencies [19] were calculated for the optimized geometries and no imaginary frequencies were observed, confirming true minima. Donor-acceptor interactions have been computed using the natural bond order (NBO) method [20]. For the ETS-NOVC analysis, complexes **1**, **B1** and **C1** were optimized in ADF 2014.01 [21], using BP86 with a triple- ζ basis set and with up to 2p frozen cores on metal atoms, in the gas phase. Optimized structures were then investigated using the Extended Transition State coupled with Natural Orbitals for Chemical Valence (ETS-NOCV) [22] energy decomposition technique. Mn–L bonds were broken and the corresponding fragments were used as promolecules, without any adjustment of fragment occupations.

2.5. General procedure for the dimerization of thiols

On the basis of literature [23] and for purposes of the comparison of computed percentage buried volume and solid angle predictions to experimental obtainable results, 3 mol% of catalyst, in the presence of the ethylthiol and cyclohexane were irradiated in an inert argon atmosphere for the duration of 2.5 h. The resulting solution was analysed directly by GC/MS using hexadecane as internal standard upon which the dimerization yields were based. All reported yields are based on the average of three runs.

Table 1
Selected bond lengths and angles.

	3	6^a
Bond length (Å)		
Mn–CO _x (x = 1–2)	1.7565 (19)	1.761 (4)
Mn–C6	1.9904 (17)	1.990 (3)
N1–C6	1.363 (2)	1.373 (4)
N2–C6	1.367 (2)	1.377 (5)
Bond angle (°)		
C1–Mn–C2	87.96 (9)	89.44 (15)
N1–C6–N2	103.08 (14)	102.6 (3)
N1–C6–Mn	128.79 (12)	128.6 (2)
N2–C6–Mn	128.12 (12)	128.6 (2)
Torsion angle (°)		
Mn–C6–N1–C7	–179.94 (12)	–0.5 (4)
Mn–C6–N2–C8	–179.97 (12)	0.6 (4)
Plane angle (°)		
Carbene/Cp	31.77	30.40

^a Bond lengths and angles are average values calculated due to the presence of two units per cell.

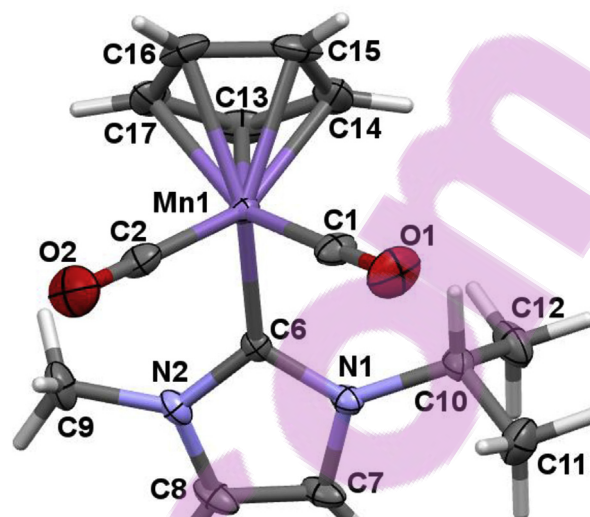


Fig. 5. Perspective view of **3** with thermal ellipsoids drawn at the 50% probability level.

3. Results and discussion

3.1. Synthesis and characterization

Complexes **1–6** were prepared in reasonable yields by photochemical substitution of a carbonyl ligand with the free NHC ligand, generated in situ from the reaction between an imidazolium salt and ^tBuOK (Scheme 1). The imidazolium salts (**L1–L3**) were prepared according to literature procedures [24].

The infrared (IR) spectrum of the complexes have been recorded using hexane as the solvent, and indicated the presence of two stretching frequencies. Both stretching frequencies are attributed to the carbonyl ligands of the Mn(CO)₂-moiety. The observations of these stretching frequencies are supported by literature [4,5]. The structural predictions were also confirmed with X-ray diffraction studies of three complexes and will be presented in the next sections.

3.2. Spectroscopic characterization

Using NMR spectroscopy, with CD₃CN as solvent, the structural aspects of the NHC complexes could be investigated. The ¹H NMR spectroscopic peaks for both the imidazolium salts and the complexed ligands had similarity in their spectral pattern and chemical shifts. The imidazolium ligand salts had a characteristic carbene carbon proton peak around $\delta = 9$ ppm, which disappeared instantly upon deprotonation and coordination to the metal centres, indicating the formation of the desired carbene complexes. The proton peaks on the C4 and C5 ring positions of the imidazolylidene ligand of **1–6** were also clearly visible at chemical shifts between $\delta = 6.83$ and $\delta = 7.46$ ppm. The ¹³C NMR of complexes **1–6** indicated the presence of a single distinct CO peak at ca. 235 ppm, a down-field shift of 10 ppm from the MMT and cymantrene starting synthons. The distinct carbene carbon peak can be witnessed at ca. 195 ppm. The NMR spectroscopy data is in accordance with literature [4,5]. The IR spectra of **1–6** were measured in hexane and indicated two stretching frequencies attributed to the CpMn(CO)₂ moiety carbonyl stretching frequencies. The stretching frequencies for the two carbonyls ligands were observed at ca. 1850 (symmetric A') and 2020 (antisymmetric A'') cm⁻¹.

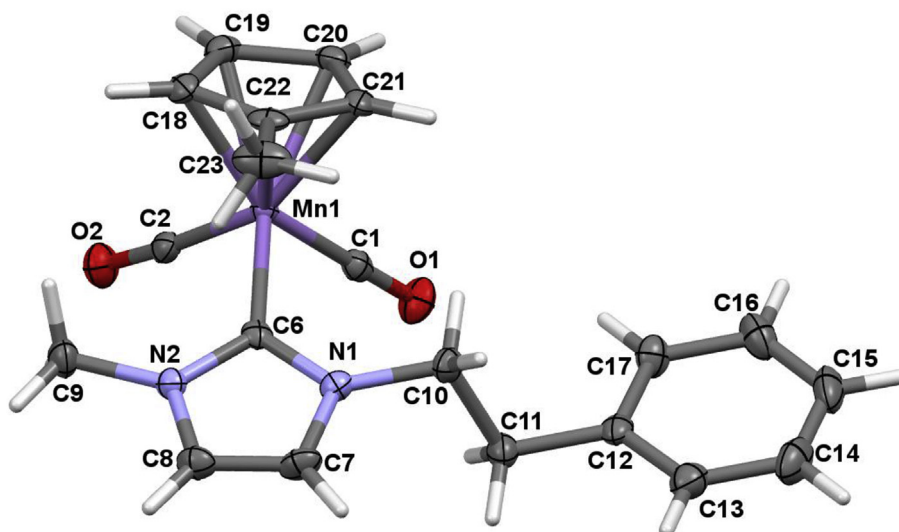


Fig. 6. Perspective view of **6** (molecule A) with thermal ellipsoids drawn at the 50% probability level.

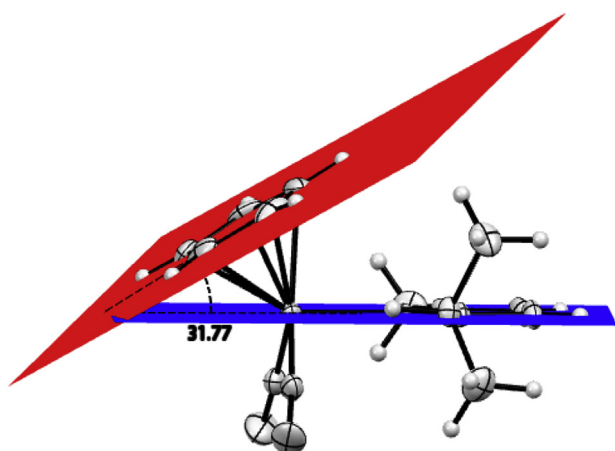


Fig. 7. The angle ($^{\circ}$) between the Cp and carbene planes of **3**.

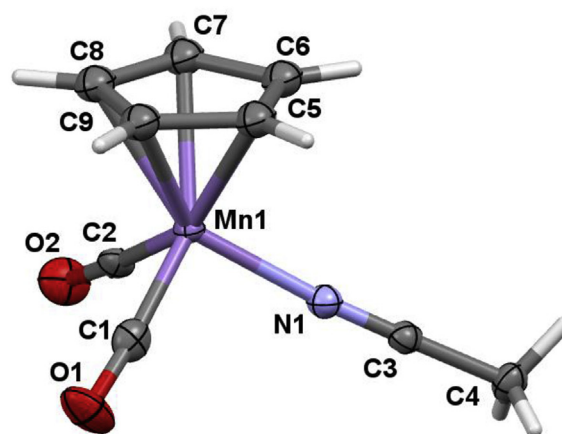


Fig. 9. Perspective view of **1** with thermal ellipsoids drawn at the 50% probability level.

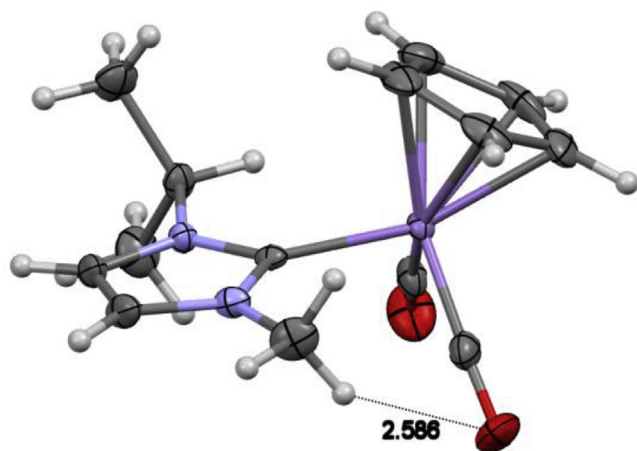
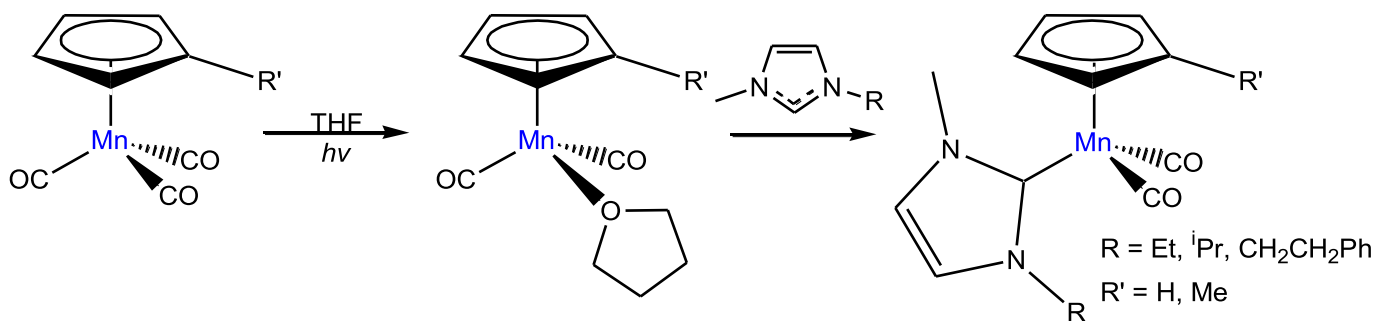


Fig. 8. Hydrogen interactions (in Å) witnessed in **3**.

3.3. Single crystal X-ray diffraction studies

Selected structural parameters are summarized in Table 1. The conformation of the carbene moiety, as represented by the C7-N1-C6-Mn dihedral angles, deviate from planarity by less than 1° (**3**, see Fig. 5) and 7° (**6**, see Fig. 6). The carbene-metal bond lengths were determined to be 1.9904 (17) Å and 1.990 (3) Å respectively and seem to be insensitive to the size of the carbene substituents. The carbene-metal bond lengths are slightly shorter compared to published literature on symmetrical NHC cymantrene derived complexes [5]. The angles between the carbene plane (Mn, C6, N1 and N2) and the Cp ring were measured as 31.77° for **3** and 30.40° for **6** (Fig. 7). Complex **6** crystallized with two molecular units (molecule A and molecule B) in the asymmetric unit and displays intramolecular hydrogen interactions between the carbene substituents and the carbonyl groups.

The incidence of hydrogen interactions can also be witnessed in both **3** and in **6** between the methyl group on the N substituent and the carbonyl ligands of the manganese metal atom. The presence of these hydrogen interactions will be quantified using the (ETS-NOCV) [22] energy decomposition technique in the DFT study section (Fig. 8).



Scheme 1. Synthesis of group VII NHC complexes.

During the synthesis of complex **C1** a single crystal, suitable for X-ray diffraction, was also obtained. **C1** crystallized in a P2₁/c space group and displays a linearly coordinated nitrile functionality (Fig. 9). The Mn–N–C3 displays a bond angle of nearly 180° (175.6°) and a C1–M–C2 bond angle of 91.37° which is bigger compared to the NHC ligated complexes **3** and **6**.

3.4. Theoretical study

Theoretical aspects of manganese carbene complexes are well described in literature [4,25,26]. Computational studies typically focus on the interactions of the frontier orbitals and the predictions that can be made from these interactions on the oxidation and reduction potential trends witnessed for metal centres [26]. Theoretical studies by Whittlesey [5] focused on aspects of agostic interactions witnessed in MMT NHC complexes. These studies have, however, been confined to electronic parameters and limited data have been provided on the steric aspects of NHC-substituted complexes of cymantrene and MMT. A DFT study has thus been considered to describe not only the electronic influences that the carbene moiety imparts on the coordination sphere of metal centres but also structural and steric influences by these ligands on the metal moiety. Complexes **1–6**, with varying steric bulk on one of the nitrogen substituents of the carbene ligand, have been studied. The calculated properties of the novel complexes **1–6** and **C1** were compared with those of literature complexes **A2** [4] and **B1** [10] as well as theoretical complex **A1** (Fig. 10).

3.4.1. Ligand steric parameters

In this study the steric characteristics of NHC ligands have been determined using two different methods, namely the percentage buried volume (%V_{bur}) and the solid angle measurement of the ligands [27a,28,29]. Increasing the bulkiness of the substituents on the N atoms of the ligand should result in a greater %V_{bur} in relation to the metal–ligand bond distance. The %V_{bur} values were found to be similar irrespective of the identity or bulkiness of R-group

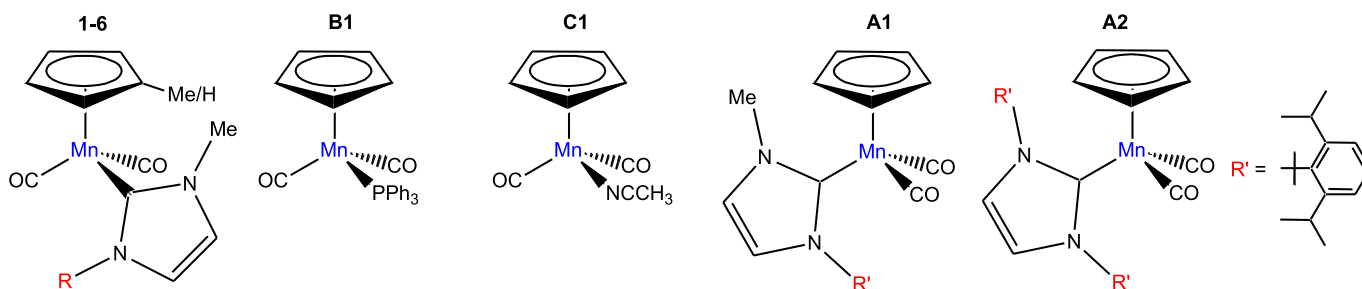
substituents on the N atoms of the NHC ligands (26% for **L1**, 25% for **L2** and ca. 26% for **L3**). The %V_{bur} was slightly higher (28.5%) for **A1** and significantly higher (33%) for **A2** [4]. Therefore the %V_{bur} values are elevated only when both N-substituents are bulky. Due to size and rotation possibilities, steric repulsion is minimized by rotating the bulky substituents away from the coordination sphere of the manganese metal centre. The steric contour map of complex **3** (Fig. 11(b)), generated with SambVca2 [27b], indicates that the NHC ligand is not seen to be sterically crowding the metal centre. Complexes **1** and **5** show similar steric contour maps (see SI).

Although groups are increasingly bulkier, only hydrogen atoms are allowed to penetrate the coordination centre, while the alkyl and aryl groups are accommodated away from the coordination sphere, minimizing the steric requirements of the substituents. Since the %V_{bur} of all the complexes are similar in value, and the NHC ligands occupy only a quarter of the total available space around the manganese atom, the deduction can be made that the steric demands of the NHC ligands have little consequence on available catalytic space.

Solid angle measurements of ligand steric parameters [30] have been attempted to establish a correlation between the steric bulk of a ligand and chemical and physical characteristics of inorganic and organometallic systems [29,31,32]. Shielded regions would severely limit metal–substrate interactions and affect the catalytic potential of the pre-catalyst. The solid angle parameters are provided in Table 2.

The G_M of **1**, **3**, **5** and the cymantrene starting synthon have been visualized and presented in Fig. 12.

The solid angles of **1–6** indicate the size of the ligand increases in the order of **L1** ≈ **L2** < **L3**. The G_M and G_(γ) of the cymantrene synthon has also been calculated and indicates a small decrease in both parameters after the coordination of the NHC moiety. As expected, the G_M and G_(γ) increase when two ethyl groups occupy the carbene nitrogen substituents positions compared to the ethyl methyl substituted ligand Fig. 13. The G_(M) predictions for **1–6** have similar values as also seen in the %V_{bur}. Although the solid angles

Fig. 10. NHC complexes **1–6**, **A1**, **A2**, phosphine complex **B1** and acetonitrile complex **C1** of the theoretical study.

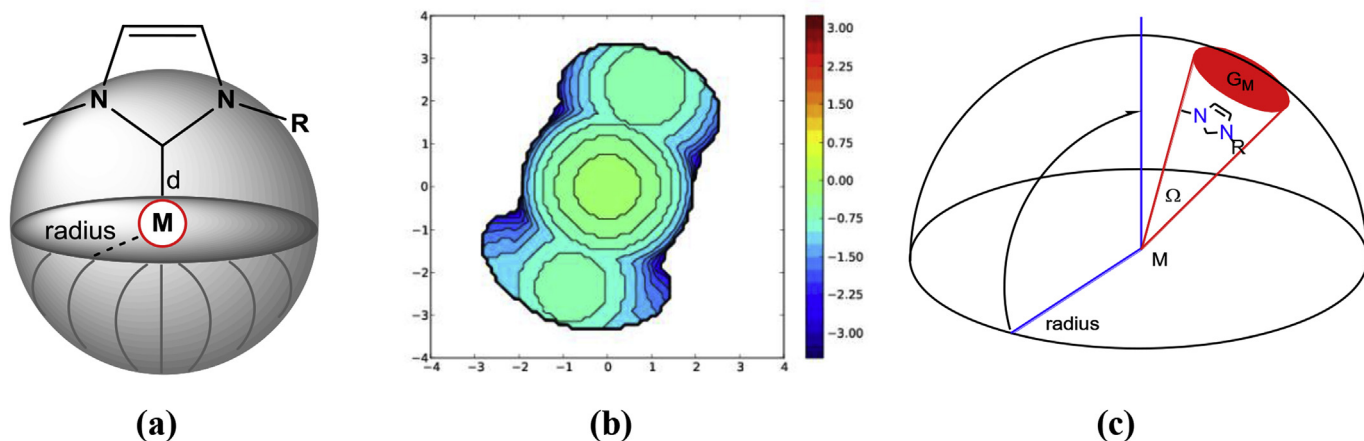


Fig. 11. (a) Graphical representation of the sphere defining the $\%V_{\text{bur}}$ of metal complexes **1–6**; (b) steric contour map of **3**; and (c) representation of the solid angle and G_M of a complex.

Table 2
Solid angle parameters for **1–6**.

Ligand	Complex	Solid Angle Steradians ^a	$G_M(\text{Complex})\%$	$G_{(\gamma)}\%$
1	1	3.11	96.88	12.89
1	2	3.20	96.91	13.19
2	3	3.06	96.70	13.87
2	4	3.18	96.93	14.14
3	5	3.34	96.35	15.50
3	6	3.34	96.55	16.03
	A1	4.05	98.04	18.79
	A2	4.92	98.60	25.69
	CpMn(CO) ₃	–	97.07	16.66
	MeCpMn(CO) ₃	–	95.41	12.08

^a Solid angle of the NHC ligand.

indicate a similar size of **L1** and **L2**, the increasing $G_{(\gamma)}$ values is indicative of increasing steric bulk of the ligands in the order of **L1** < **L2** < **L3** < **L_{A1}** < **L_{A2}**.

3.4.2. Wiberg bond indices and bond dissociation energies (BDEs)

Literature exists for the determination and applicability of Wiberg bond orders in the endeavour to study NHC ligands [33,34] and the coordination to metal centres [35,36]. The Wiberg bond indices quantified single or double bond character and can be utilized to determine bond strength orders (BSOs). From our calculated results, the Wiberg bond indices (see Table S1 in SI) indicate a relatively strong sigma-donation from the NHC ligand towards the metal centre ($BO = 0.73–0.78$). The indices are similar in all the NHC complexes and show no variation despite steric difference between the carbene nitrogen substituents. These values correlate

well with dimeric Mn NHC complexes reported recently [29]. The bonding interaction of the NHC ligands was determined to be similar to that of phosphine ligands (M–L bond order of 0.77) and stronger in comparison to the nitrile ligand analogues such as **C1** ($BO = 0.66$). These values are, however, in line with reported literature values [35].

The bond dissociation energies [29,37] for **1–6** are listed in Table S1 in SI. From the data presented, NHC ligands bound more tightly towards the manganese centre bearing cyclopentadienyl ligands compared to the methylcyclopentadienyl analogues. NHC ligands with ethyl phenyl substituents had greater BDEs followed by isopropyl and finally ethyl groups respectively. The dissociation energies thus decreases in the following trend: CpMn-**L3** > MeCpMn-**L3** > CpMn-**L2** > CpMn-**L1** > MeCpMn-**L2** > MeCpMn-**L1**.

The average bond dissociation energy for the NHC ligands were significantly greater compared to both phosphine and nitrile ligands despite the similarity in Wiberg bond orders. The heightened BDEs are ascribed to the superior coordination interactions offered by NHC ligands. Complexes with larger substituents on the nitrogen backbone of the ligands tend to display greater BDE compared to smaller substituents. This finding is supported by literature [38] and the steric effects of the heteroatomic substituents are well described. Increasing the bulkiness of the nitrogen substituents leads to increases in the stability of the NHC ligands and greater donation to the ligated metal centre.

3.4.3. Extended Transition State coupled with Natural Orbitals for Chemical Valence (ETS-NOCV)

ETS-NOCV is a powerful computational tool with which the

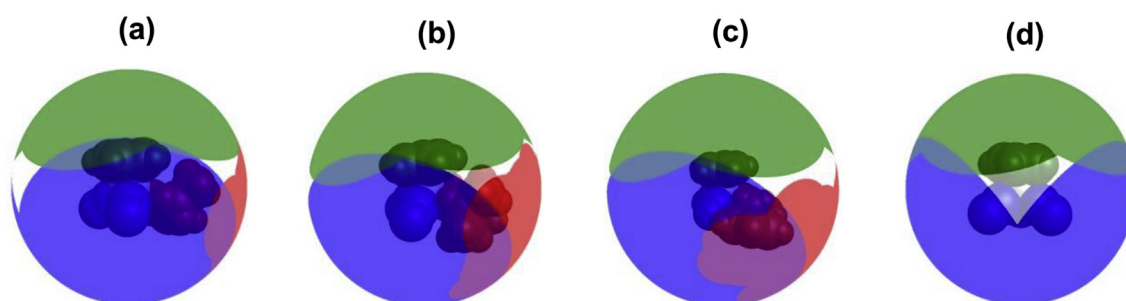


Fig. 12. The $G_M(\text{Complex})$ of **1** (a), **3** (b) and **5** (c) and CpMn(CO)₃ (d).

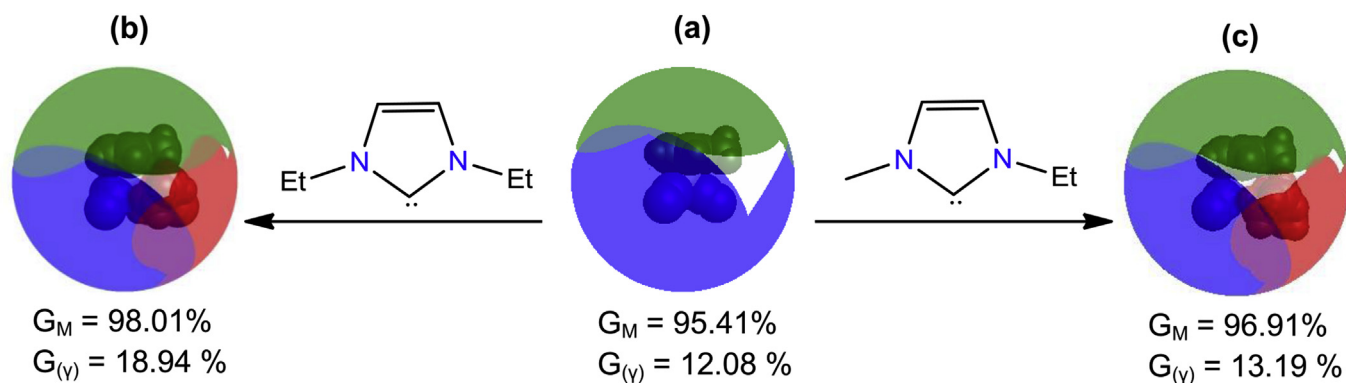


Fig. 13. Solid angle parameters of the (a) MeCpMn(CO)₃, (b) diethyl substituted NHC and (c) complex **2**.

formation of an M–C bond can be investigated and analysed in terms of the absorbed or released interaction energy, ΔE_{Int} , as well as the change in electron density, commonly known as the deformation density, $\Delta\rho$, associated with bond formation [21,22]. Both ΔE_{Int} and $\Delta\rho$ can be decomposed into different components to aid interpretation of a bond formation process. The interaction energy can be decomposed into three terms,

$$\Delta E_{Int} = \Delta E_{Estat} + \Delta E_{Pauli} + \Delta E_{Orb} + \Delta E_{Disp} \quad (1)$$

where ΔE_{Estat} gives the change in electrostatic energy upon bringing unperturbed promolecules from an infinite separation to the final bonding distance, ΔE_{Pauli} gives the change in energy required to orthogonalize (ensuring antisymmetry) the promolecular (ensuring antisymmetry) wavefunctions and is commonly known as Pauli repulsion, ΔE_{Orb} gives the change in energy related to the minimization of the energy of the final structure and is commonly known as the orbital interaction term and ΔE_{Disp} is the dispersion energy, usually calculated through empirically-derived functionals. The electrostatic and Pauli energy changes are often combined into a single value, ΔE_{Steric} , to give an indication of the steric (electrostatic + electronic) interaction between promolecules. Similarly, the deformation density can be decomposed into two terms,

$$\Delta\rho = \Delta\rho_{Pauli} + \Delta\rho_{Orb} \quad (2)$$

where each term gives the change in density associated with the energetic term of Eq. (1) (no density change is observed with the change in electrostatic energy) [21,22]. The various decomposition terms of Eq. (1) can be used to compare the properties associated with the formation of different M–C bonds, and the associated density changes can be used for visual inspection [21,22]. Of more interest to us, however, is the further decomposition of the ΔE_{Orb} and $\Delta\rho_{Orb}$ terms into contributions from natural orbitals, as given by the NOCV addition to ETS. Specifically, the total $\Delta\rho_{Orb}$ term can be decomposed into i natural orbitals,

$$\Delta\rho_{Orb} = \sum_i \Delta\rho_i \quad (3)$$

and each NOCV channel is associated with a specific change in energy, ΔE_{Orb}^i . The highest occupied NOCV channels can usually be associated with specific components of molecular orbital interactions between promolecules, such as σ and π bonding, giving associated deformation density channels and energy changes for these components, i.e. $\Delta\rho_\sigma$ and ΔE_{Orb}^σ describing a σ -bonding component of an M–C bond [21,22]. These features of the ETS-

NOCV approach allow qualitative as well as quantitative comparison of specific attributes of different M–C bonds in various systems [21,22].

In this section the bond characteristics of three different ligand systems coordinated to a CpMn(CO)₂ moiety were probed. The formation of various Mn–L bonds in **1**, **B1** and **C1** was investigated theoretically using ETS-NOCV. Of primary interest is the various NOCV channels of each Mn–L bond, describing the density and energy changes of specific (σ and π) attributes of each bond. The primary NOCV channels for the NHC (structure **1**) are shown in Fig. 14. $\Delta\rho_\sigma$ describes the clear σ -donation from the ligand to the metal with an associated energy change of $-146.86 \text{ kJ}\cdot\text{mol}^{-1}$, whereas $\Delta\rho_{\pi 1}$ and $\Delta\rho_{\pi 2}$ describe the π -back donation from metal to ligand for two different axes, with a combined energy contribution of $-59.50 \text{ kJ}\cdot\text{mol}^{-1}$. Finally, $\Delta\rho_4$ shows the formation of two hydrogen CH \cdots C interactions, contributing $-5.69 \text{ kJ}\cdot\text{mol}^{-1}$ to the total interaction energy. The NOCV channels for the remaining structures **B1** and **C1** are qualitatively very similar, except for the lack of CH \cdots C interactions in **C1**. The presence of hydrogen interactions was also witnessed in the solid-state crystal structures of **3** and **6**.

In Table 3, decomposition of the total interaction energy into relevant components for each structure is shown; for a complete ETS-NOCV decomposition. Comparing first the total interaction energies, ΔE_{Int} , **1** forms the strongest M–L bond, with the phosphine **B1** and the acetonitrile **C1** weaker by $+29.12$ and $+125.10 \text{ kJ}\cdot\text{mol}^{-1}$, respectively. The biggest contribution to the strength of **1** is a very large electrostatic contribution ($-485.26 \text{ kJ}\cdot\text{mol}^{-1}$ as opposed to -348.61 and $-227.61 \text{ kJ}\cdot\text{mol}^{-1}$ in **B1** and **C1**, respectively, as seen in Table 3). Electronically, however, **1** and **B1** is equivalent, with a total orbital interaction of -233.47 and $-237.61 \text{ kJ}\cdot\text{mol}^{-1}$, respectively. Interestingly, the σ -donation of both **1** and **B1** is very similar (differing by $-7.41 \text{ kJ}\cdot\text{mol}^{-1}$ in favour of **1**) but **1** experiences considerably weaker π -back bonding (differing by $-16.78 \text{ kJ}\cdot\text{mol}^{-1}$ in favour of **B1**). On the other hand, **B1** and **C1** show equivalent π contributions, but **C1** forms a considerably weaker σ bond than the other structures. Therefore, the combination of large electrostatic attractions coupled with comparatively small electronic steric repulsions result in **1** forming a stronger M–L bond than **B1**, despite comparative orbital and dispersion interactions.

The ratio of the σ contributions over π contributions for each structure is shown in Table 3. This metric gives us a direct indication of the relative σ -donation over π -back bonding capability of each system. Clearly, **1** shows by far the most σ character (2.47 times more σ -bonding than π -bonding), whereas the phosphine **B1** is slightly more prevalent for σ -bonding (1.83) and the **C1** is more or less equivalent for both σ and π (1.11). However, since the total

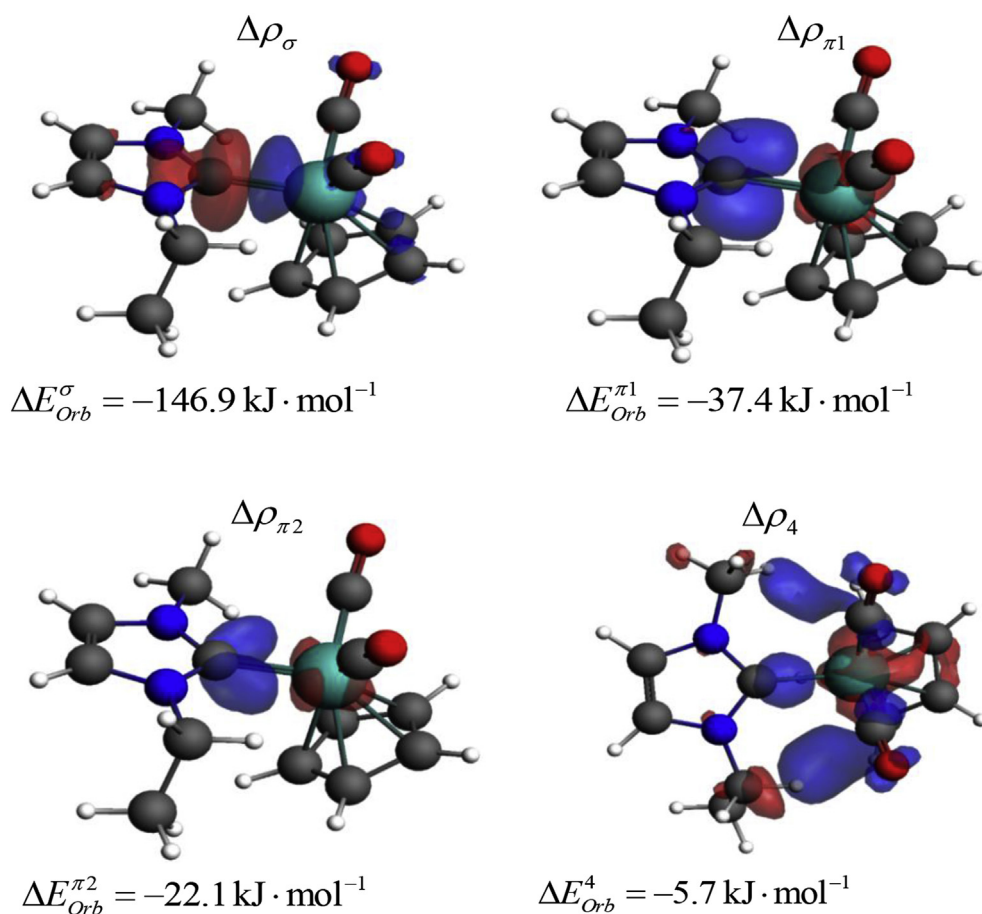


Fig. 14. Primary NOCV channels and associated orbital energy changes for **1**. Blue and red regions indicate an accumulation and depletion of electron density, respectively. Iso-surfaces for $\Delta\rho_\sigma$, $\Delta\rho_{\pi 1}$, $\Delta\rho_{\pi 2}$ and $\Delta\rho_4$ are 0.002 au, 0.001 au, 0.001 au and 0.00015 au, respectively. (For interpretation of the references to colour in this figure legend, the reader is referred to the web version of this article.)

Table 3
Selected ETS-NOCV energy contributions.

	ΔE_{Int}^a	ΔE_{Elstat}^a	ΔE_{Pauli}^a	ΔE_{Steric}^a	ΔE_{Orb}^a	ΔE_{Disp}^a
1	-276.14	-485.26	+493.96	+8.70	-233.47	-51.35
B1	-247.02	-348.61	+405.68	+57.07	-237.61	-66.46
C1	-151.04	-227.61	+265.27	+37.66	-173.64	-15.21
	$\Delta E_{Orb}^{\sigma a}$	$\Delta E_{Orb}^{\pi a}$	σ/π^b	$\% \sigma^c$	$\% \pi^d$	
1	-35.10	-14.22	2.47	53%	22%	
B1	-33.33	-18.23	1.83	56%	31%	
C1	-20.40	-18.40	1.11	13%	12%	

^a All values in $\text{kJ}\cdot\text{mol}^{-1}$.

^b Ratio of ΔE_{Orb}^{σ} over ΔE_{Orb}^{π} .

^c Percentage of σ contribution to ΔE_{Int} .

^d Percentage of π contribution to ΔE_{Int} .

interaction energies of each system differ, the final columns of [Table 3](#) present each attribute of bonding as a percentage of the total interaction energy, allowing direct comparison between different ligands.

Complexes **1** and **B1** are equivalent σ -donors, with 53% and 56% of the total binding energy originating from σ -donation, respectively. However, **1** shows considerably less π character than **B1**, with 22% π -back donation for **1** and 31% for **B1**. The acetonitrile **C1** shows equivalent σ and π character (13% and 12%, respectively), and overall lower contributions from electronic interactions. The remaining contributions to the total interaction energy includes

energetically weaker electronic interactions (such as weak non-covalent interactions and various polarizations), as well as steric effects (including electrostatic interactions and Pauli repulsion). The stronger M-L bond in **1** illustrates the superior ability of the NHC ligand to stabilize the metal centres compared to phosphine and acetonitrile ligands. The ETS-NOCV results also mirror findings of the bond dissociation energies were NHC-M complexes display strong M-L bonds.

3.5. Catalytic study

Catalytic applications of cymantrene [39] include dehydrocoupling reactions of amine-borane adducts [40], dehydrogenative silane alcoholysis [41] and the photoconversion of thiols into disulfides [23]. Of the three reactions mentioned, the final process was chosen to evaluate the catalytic activity of our complexes.

Organosulfur chemistry has always been of particular interest both in the field of chemistry and biology [42]. The transformation of sulfur-containing compounds has attracted much research interest and specifically the oxidation of thiols to disulfides has remained an area of importance [43]. Reactions focussing explicitly on the dimerization of sulfides into disulfides normally require a basic catalyst [44], stoichiometric amounts of oxidants [45] or toxic reagent and long reaction times. Apart from the high demand of these reaction conditions, many synthetic methodologies generate elevated levels of unwanted side-products. The side-products are commonly produced as a result from over oxidation, producing

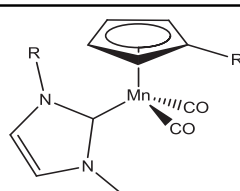
sulfoxides, sulfones, thiosulfates and thiosulfonates [46–48]. Literature examples have been reported for the employment of rhodium(I) transition-metal complexes that illustrated the ability to selectively oxidize thiols into disulfides as an attractive alternative to the use of hazardous oxidants [23], but such processes have been fairly unexploited. The UV photolysis of cymantrene with thiols at room temperature offered a viable, greener alternative to classic published method of dimerization of thiols and produced H₂ as the only side product [23]. Pre-catalysts **1–6** have been investigated for application in the dimerization of thiols into disulfides [23]. Based on literature [23] and for purposes of the simple comparison of %V_{bur} and solid angle predictions to experimental obtainable results, 3 mol% of catalyst, in the presence of the substrate and cyclohexane were photo-irradiated in an inert argon atmosphere for the duration of 2.5 h to test for catalytic activity.

All six complexes displayed catalytic activity in the dimerization of thiols into disulfides (Table 4). Although lower yields were obtained for complexes **3** and **4**, complexes **5** and **6** displayed superior activity with yields of ca. 47% and turn over frequencies (TOF) of 49 h⁻¹. The obtained yields were lower in comparison to literature [23] (ca. 99% for alkyl thiols) for the CpMn(CO)₃-photoconversion of thiols. Complexes displayed diminished activity over the 150 min reaction period, which might indicate the decomposition of the catalysis under the harsh photo-irradiation conditions. The higher catalytic activity of **5** and **6** could thus be explained by the greater stability of these complexes where decomposition is concerned, displaying higher BDE of the metal-carbene bond and slightly larger HOMO-LUMO band gaps (see SI) compared to complexes **1–4**. The dimerization occurs through the substitution of a carbonyl ligand for an ethylthiol group. The ligand exchange can occur at two different carbonyl ligand positions in reference to the substituents on the NHC ligand. Bond dissociation energies of the metal-carbonyl bonds indicate similar dissociation energies for carbonyl ligands CO_a and CO_b (Fig. 15). It can thus be hypothesized that ligand exchange could occur at either carbonyl ligand to initiate the catalytic cycle.

The ligand steric parameter results indicate that the steric trend increases in the order **L1** < **L2** < **L3** and literature associates the steric influences of NHC substituents with the greater stability these ligands afford to the metal moiety. The solid angle and %V_{bur} parameters thus correlate with the stability associated with the pre-catalysts and therefore might suggest a probable explanation for the catalytic activity witnessed. Although the ligands increase in bulkiness, the steric groups do not directly influence the coordination space of the metal moiety (as indicated by the solid angle).

Table 4
Dimerization of ethylthiol by manganese(I) NHC complexes **1–6**.

$$\text{Et-SH} \xrightarrow[\text{Cyclohexane cat}]{h\nu} \text{Et-S-S-Et}$$

Catalyst ^{a,c}	Complex	R	R'	Cat. (mol%)	Conversion ^b (%)
	1	Et	H	3	28
	2	Et	Me	3	22
	3	ⁱ Pr	H	3	16
	4	ⁱ Pr	Me	3	6
	5	CH ₂ CH ₂ Ph	H	3	47
	6	CH ₂ CH ₂ Ph	Me	3	48

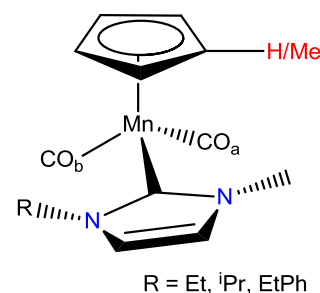


Fig. 15. Possible carbonyl substitution positions CO_a and CO_b available on **1–6**.

The ligands thus afford greater stability while not crowding the metal atom. Complexes **5** and **6** contain the most steric ligand **L3**, according to the steric parameters calculated, which then implies that the most stable complexes were found to have the best catalytic activity. A feasible catalytic cycle is proposed in Fig. 16, describing the catalytic conversion of the thiol substrates into disulfides. The cycle is based on experimental data obtained from the similar study on the dimerization of thiols using cymantrene only as catalyst [23,49]. In the article by Zhang et al. [49], an in-depth DFT study on the key intermediates and two possible pathways for this conversion, is described. Their results correlate with the experimental observations of Tan et al. [23]. The cycle is initiated with the photo-induced substitution of a carbonyl ligand for a thiol substrate and terminates with the liberation of disulfides and the regeneration of the active catalyst species. The process is dependent on the availability and lability of carbonyl ligands of the pre-catalyst species and thus might explain the lower activity of our pre-catalysts in comparison with the cymantrene analogue.

4. Conclusion

NHC complexes **1–6** were synthesised in satisfactory yields from MMT and cymantrene synthons. The molecular structures of the novel complexes were confirmed with NMR and IR spectroscopy, and single crystal X-ray diffraction studies of **3** and **6**. Through DFT calculations, it was possible to describe the steric influences the NHC ligands impose on the metal synthon. Wiberg bond indices indicated orders of ca. 0.7 for the NHC complexes, which is similar to bonding aspects of triphenylphosphine. Both ligands thus display negligible π -back donation from the metal centre. The frontier orbital analysis indicated increases in the band gaps upon

^a General reaction conditions: Ethylthiol (2.0 mmol), Catalyst (0.06 mmol), Cyclohexane (10 ml), Room temperature, 150 min.

^b Conversion based on internal standard.

^c TOF, as cited in text, was calculated after the first 10 min of the catalytic reaction.

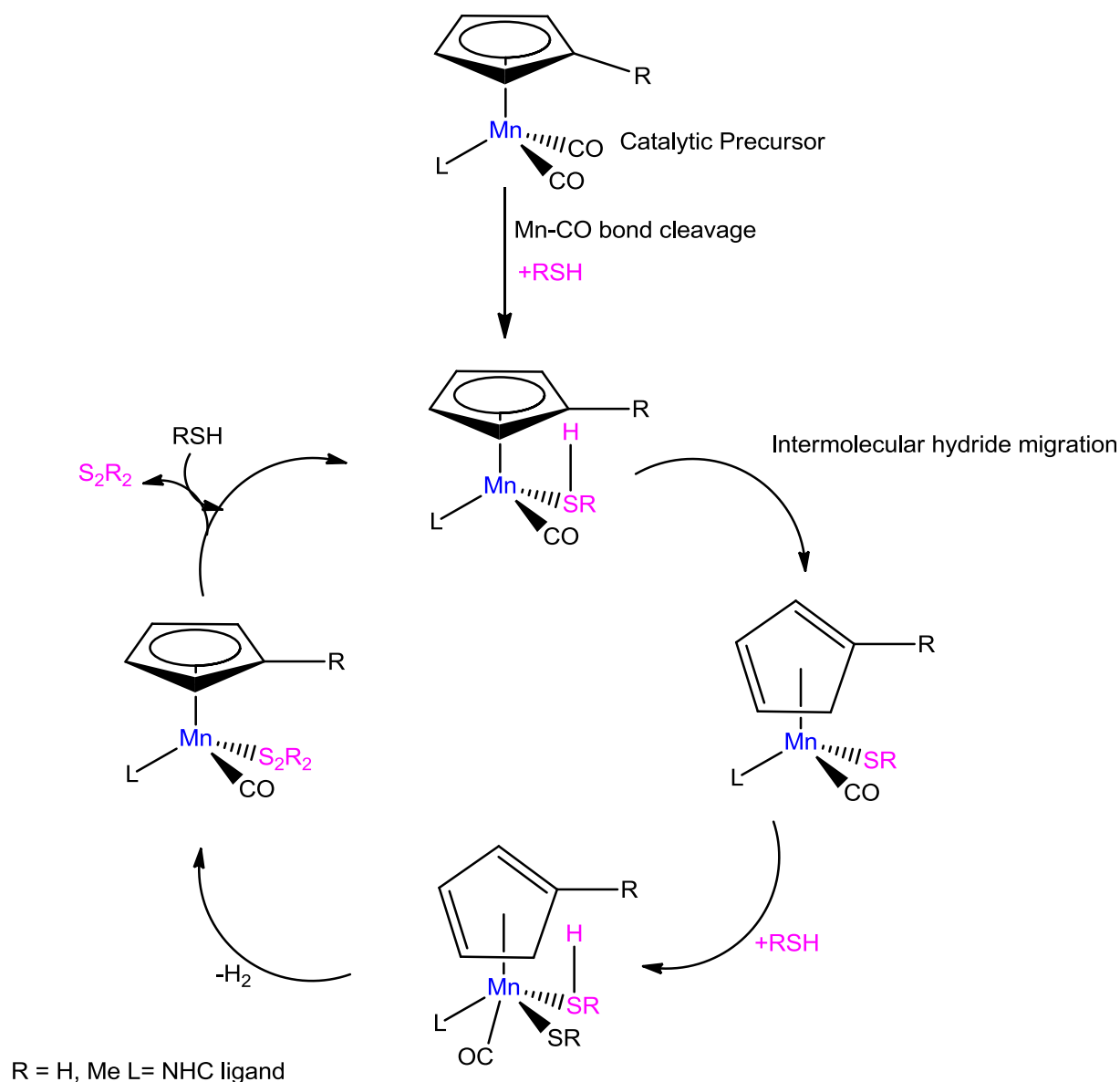


Fig. 16. Catalytic cycle associated with the dimerization of thiol substrates.

the substitution of NHC ligands with larger molecular masses (see SI). Lower mass ligands had smaller band gaps. The increases in the band gaps may indicate higher stability of complexes **5** and **6** or greater inertness towards decomposition pathways. Finally, BDE energies indicated a linear relationship between the associated energies and the molar mass of the NHC moiety. The BDE of the NHC-metal bonds were higher in cymantrene complexes compared to MMT analogues.

Acknowledgements

This work has received financial support from the South African National Research Foundation (Grant nr. 93638) and the University of Pretoria.

Appendix A. Supplementary data

Supplementary data related to this article can be found at <http://dx.doi.org/10.1016/j.jorganchem.2017.03.047>.

References

- [1] (a) A.J. Arduengo, R.L. Harlow, M. Kline, *J. Am. Chem. Soc.* 113 (1991) 361; (b) A. Igau, H. Grutzmacher, A. Baceiredo, G. Bertrand, *J. Am. Chem. Soc.* 110 (1988) 6463; (c) G. Bertrand, R. Reed, *Coord. Chem. Rev.* 137 (1994) 323.
- [2] L. Cavallo, A. Correa, C. Costabile, H. Jacobsen, *J. Organomet. Chem.* 690 (2005) 5407.
- [3] K.A.M. Ampt, S. Burling, S.M.A. Donald, S. Douglas, S.B. Duckett, S.A. Macgregor, R.N. Perutz, M.K. Whittlesey, *J. Am. Chem. Soc.* 128 (2006) 7452.
- [4] J. Zheng, S. Elangovan, D.A. Valyaev, R. Brousses, V. César, J. Sortais, C. Darcel, N. Lugan, G. Lavigne, *Adv. Synth. Catal.* 356 (2014) 1093.
- [5] M. Batool, T.A. Martin, A.G. Algarra, M.W. George, S.A. Macgregor, M.F. Mahon, M.K. Whittlesey, *Organometallics* 31 (2012) 4971.
- [6] M. Batool, T.A. Martin, N.A. Naser, M.W. George, S.A. Macgregor, M.F. Mahon, M.K. Whittlesey, *Chem. Commun.* 47 (2011) 11225.
- [7] D.A. Valyaev, D. Wei, S. Elangovan, M. Cavaillès, V. Dorcet, J.-B. Sortais, C. Darcel, N. Lugan, *Organometallics* 35 (2016) 4090.
- [8] M.F. Lappert, P.L. Pye, *J. Chem. Soc. Dalton Trans.* (1977) 2172.
- [9] D.F. Schriver, M.A. Drezdson, *The Manipulation of Air-sensitive Compounds*, second ed., Wiley, New York, USA, 1986.
- [10] M.D. Raush, B.H. Edwards, R.D. Rogers, J.L. Atwood, *J. Am. Chem. Soc.* 105 (1983) 3882.

Appendix II.

- [11] J.W. Hershberger, C. Amatore, J.K. Kochi, *J. Organomet. Chem.* 250 (1983) 345.
- [12] APEX2 (Including SAINT and SADABS), Bruker AXS Inc., Madison, WI, 2012.
- [13] G.M. Sheldrick, *Acta Crystallogr. A64* (2008) 112.
- [14] L.J.J. Farrugia, *Appl. Crystallogr.* 30 (1997) 565.
- [15] M.J. Frisch, G.W. Trucks, H.B. Schlegel, G.E. Scuseria, M.A. Robb, J.R. Cheeseman, G. Scalmani, V. Barone, B. Mennucci, G.A. Petersson, H. Nakatsuji, M. Caricato, X. Li, H.P. Hratchian, A.F. Izmaylov, J. Bloino, G. Zheng, J.L. Sonnenberg, M. Hada, M. Ehara, K. Toyota, R. Fukuda, J. Hasegawa, M. Ishida, T. Nakajima, Y. Honda, O. Kitao, H. Nakai, T. Vreven, J.A. Montgomery (Jr.), J.E. Peralta, F. Ogliaro, M. Bearpark, J.J. Heyd, E. Brothers, K.N. Kudin, V.N. Staroverov, T. Keith, R. Kobayashi, J. Normand, K. Raghavachari, A. Rendell, J.C. Burant, S.S. Iyengar, J. Tomasi, M. Cossi, N. Rega, J.M. Millam, M. Klene, J.E. Knox, J.B. Cross, V. Bakken, C. Adamo, J. Jaramillo, R. Gomperts, R.E. Stratmann, O. Yazyev, A.J. Austin, R. Cammi, C. Pomelli, J.W. Ochterski, R.L. Martin, K. Morokuma, V.G. Zakrzewski, G.A. Voth, P. Salvador, J.J. Dannenberg, S. Dapprich, A.D. Daniels, O. Farkas, J.B. Foresman, J.V. Ortiz, J. Cioslowski, D.J. Fox, Gaussian 09, Revision D.01, Gaussian Inc., Wallingford CT, 2010.
- [16] A.D. Becke, *J. Chem. Phys.* 98 (1993) 5648.
- [17] C. Lee, W. Yang, R.G. Parr, *Phys. Rev. B* 37 (1988) 785.
- [18] F. Weigend, R. Ahlrichs, *Phys. Chem. Chem. Phys.* 7 (2005) 3297.
- [19] J.W. Mclver, A.K. Komornicki, *J. Am. Chem. Soc.* 94 (1972) 2625.
- [20] (a) J.P. Foster, F. Weinhold, *J. Am. Chem. Soc.* 102 (1980) 7211;
(b) A.E. Reed, F. Weinhold, *J. Chem. Phys.* 83 (1985) 1736;
(c) A.E. Reed, R.B. Weinstock, F. Weinhold, *J. Chem. Phys.* 83 (1985) 735;
(d) A.E. Reed, L.A. Curtiss, F. Weinhold, *Chem. Rev.* 88 (1988) 899.
- [21] E.J. Baerends, T. Ziegler, J. Autschbach, D. Bashford, A. Bérces, F.M. Bickelhaupt, C. Bo, P.M. Boerrigter, L. Cavallo, D.P. Chong, L. Deng, R.M. Dickson, D.E. Ellis, M. van Faassen, L. Fan, T.H. Fischer, C. Fonseca Guerra, A. Ghysels, A. Giannina, S.J.A. van Gisbergen, A.W. Götz, J.A. Groeneveld, O.V. Gritsenko, M. Grüning, S. Gusarov, F.E. Harris, P. van den Hoek, C.R. Jacob, H. Jacobsen, L. Jensen, J.W. Kaminski, G. van Kessel, F. Kootstra, A. Kovalenko, M.V. Krykunov, E. van Lenthe, D.A. McCormack, A. Michalak, M. Mitoraj, J. Neugebauer, V.P. Nicu, L. Noodleman, V.P. Osinga, S. Patchkovskii, P.H.T. Philipsen, D. Post, C.C. Pye, W. Ravenek, J.I. Rodríguez, P. Ros, P.R.T. Schipper, G. Schreckenbach, J.S. Seldenthuis, M. Seth, J.G. Snijders, M. Solà, M. Swart, D. Swerhone, G. te Velde, P. Vernooijs, L. Versluis, L. Visscher, O. Visser, F. Wang, T.A. Wesolowski, E.M. van Wezenbeek, G. Wiesenekker, S.K. Wolff, T.K. Woo, A.L. Yakovlev, ADF2012, SCM, Theoretical Chemistry, Vrije Universiteit, Amsterdam, The Netherlands, <http://www.scm.com>.
- [22] M. Mitoraj, A. Michalak, T. Ziegler, *J. Chem. Theory Comput.* 5 (2009) 962.
- [23] K.Y.D. Tan, J.W. Kee, W.Y. Fan, *Organometallics* 29 (2010) 4459.
- [24] F.P. Malan, E. Singleton, P.H. van Rooyen, M. Landman, *J. Organomet. Chem.* 813 (2016) 7.
- [25] N. Lugan, I. Fernández, R. Brousses, D.A. Valyaev, G. Lavigne, N.A. Ustynyuk, *Dalton Trans.* 42 (2013) 898.
- [26] (a) B. Tumanskii, D. Sheberla, G. Molev, Y. Apeloig, *Angew. Chem. Int. Ed.* 46 (2007) 7408;
(b) R. Fraser, P.H. van Rooyen, M. Landman, *Polyhedron* 118 (2016) 133;
(c) R. Fraser, P.H. van Rooyen, M. Landman, *J. Coord. Chem.* 69 (2016) 2972.
- [27] (a) H. Clavier, A. Correa, L. Cavallo, E.C. Escudero-Adán, J. Benet-Buchholz, A.M.Z. Slawin, S.P. Nolan, *Eur. J. Inorg. Chem.* (2009) 1767;
(b) L. Falivene, R. Credendino, A. Poater, A. Petta, L. Serra, R. Oliva, V. Scarano, L. Cavallo, *Organometallics* 35 (2016) 2286.
- [28] A. Poater, B. Cosenza, A. Correa, S. Giudice, F. Ragone, V. Scarano, L. Cavallo, *Eur. J. Inorg. Chem.* (2009) 1759.
- [29] R. Fraser, C.G.C.E. van Sittert, P.H. van Rooyen, M. Landman, *J. Organomet. Chem.* 835 (2017) 60.
- [30] G.K. Fukin, I.A. Guzei, E.V. Baranov, *J. Coord. Chem.* 9 (2007) 937.
- [31] I. Guzei, M.E. Sánchez-Castro, A. Ramírez-Monroy, M. Cervantes-Vásquez, I.R.A. Figueroa, M.A. Paz-Sand, *Inorg. Chim. Acta* 359 (2006) 701.
- [32] I.A. Guzei, M. Wendt, *Dalton Trans.* (2006) 3991.
- [33] D.M. Andrada, N. Holzmann, T. Hamadi, G. Frenking, *Beilstein J. Org. Chem.* 11 (2015) 2727.
- [34] D. Setiawan, R. Kalescky, E. Kraka, D. Cremer, *Inorg. Chem.* 55 (2016) 2332.
- [35] A. Baishya, V.R. Mundlapati, S. Nembenna, H.S. Biswal, *J. Chem. Sci.* 126 (2014) 1781.
- [36] G. Occhipinti, H. Bjørsvik, K.W. Törnroos, A. Fürstner, V.R. Jensen, *Organometallics* 26 (2007) 4383.
- [37] X. Qi, Y. Feng, L. Liu, Q. Guo, *Chin. J. Chem.* 23 (2005) 194.
- [38] R.W. Alder, M.E. Blake, L. Chaker, J.N. Harvey, F. Paolini, J. Schutz, *Angew. Chem. Int. Ed.* 43 (2004) 5896.
- [39] For recent reviews on the use of manganese catalysts in organic chemistry, see (a) R.I. Khusnutdinov, A.R. Bayguzina, U.M. Dzhemilev, *Russ. J. Org. Chem.* 48 (2012) 309;
(b) D.A. Valyaev, G. Lavigne, N. Lugan, *Coord. Chem. Rev.* 308 (2016) 191.
- [40] T. Kakizawa, Y. Kawano, K. Naganeyama, M. Shimoi, *Chem. Lett.* 40 (2011) 171.
- [41] B.T. Gregg, A.R. Cutler, *Organometallics* 13 (1994) 1039.
- [42] R.J. Cremlyn, *An Introduction to Organosulfur Chemistry*, Wiley, New York, 1996.
- [43] G.H. Whitham, *Organosulfur Chemistry*, Oxford University Press, Oxford, 1995.
- [44] A.V. Joshi, S. Bhusare, M. Baidossi, N. Qafisheh, Y. Sasson, *Tetrahedron Lett.* 46 (2005) 3583.
- [45] A.R. Ramesha, S. Chandrasekaran, *J. Org. Chem.* 59 (1994) 1354.
- [46] N. Iranpoor, D. Mohajer, A.R. Rezaeifard, *Tetrahedron Lett.* 45 (2004) 3811.
- [47] F. Freeman, C.N. Angeletakis, *J. Am. Chem. Soc.* 105 (1983) 4039.
- [48] F. Lazzaro, M. Crucianelli, F.D. Angelis, V. Neri, R. Saladino, *Tetrahedron Lett.* 45 (2004) 9237.
- [49] Z. Zhang, W. Li, J. Liu, X. Chen, Y. Bu, *J. Organomet. Chem.* 706–707 (2012) 89.

Appendix III. Gold (I) Hydrides as Proton Acceptors in Dihydrogen Bond Formation

Published in:

ChemPhysChem, **2017**, *18*, 2288–2294.

Au–H···H interactions are investigated using a variety of methods, including QTAIM, IQA and ETS-NOCV.

Electronic supplementary information available at: <https://doi.org/10.1002/cphc.201700383>.

Gold(I) Hydrides as Proton Acceptors in Dihydrogen Bond Formation

Ignacy Cukrowski,^{*[a]} Jurgens H. de Lange,^[a] Ferdinand Groenewald,^[b] and Helgard G. Raubenheimer^{*[b]}

Wavefunction and DFT calculations indicate that *anionic* dihydride complexes of Au^I form strong to moderate directed Au–H...H bonds with one or two HF, H₂O and NH₃ prototype proton donor molecules. The largely electrostatic interaction is influenced by relativistic effects which, however, do not increase the binding energy. Very weak Au...H associations—exhibiting a corresponding bond path—occur between *neutral* AuH and HF units, although ultimately F becomes the preferred donor atom in the most stable structure. Increasing the hydricity of AuH by attachment of an electron donating NHC

ligand effects Au–H...H bonding of moderate strength only with HF, whereas competing Au...H interactions dominate for H₂O and NH₃. Rare η^2 coordinated and HX (X = F or OH) associated H₂ complexes are produced during interaction with a single ion of stronger acidity, H₂F⁺ or H₃O⁺. Theoretically, reaction of excess [AuH₂][−] as proton acceptor with H₃O⁺ or NH₄⁺ in 3:1 or 4:1 ionic ratios, respectively, affords H...H bonded analogues of Eigen-type adducts. Outstanding analytical relationships between selected bonding parameters support the integrity of the results.

1. Introduction

The chemistry of Au^I complexes is enriched by the important role played by Au...Au interactions, a phenomenon that has been investigated in great detail.^[1,2] Recently the possibility of equally strong Au...H hydrogen bond formation has been recognized as a viable interaction in its own right. Examples have been investigated experimentally in the condensed phase,^[3] and theoretically for simple^[4] as well as complicated^[3] systems. [M]–H...HX ([M] = transition metal fragment; X = rest of proton donor molecule) dihydrogen bonding, discovered in the 1990s^[5] and later reported for various metals after theoretical and experimental investigations, is presently a topic attracting increased research attention among a large and growing number of participants.^[6] Bonding^[7] and mechanistic^[8] aspects, proton transfer,^[9] packing in crystals,^[10] and biochemical investigations^[11] have all been receiving attention. With two exceptions, dihydrogen bonding is currently not known for group 11 and 12 transition metal hydride complexes.^[8b,12] The nearest resemblance of such an interaction in dynamic gold chemistry, has been postulated for a regenerated gold hydride intermedi-

ate that is stabilized by a protonated ethanol solvent molecule within a calculated catalytic cycle of olefin hydrogenation.^[13] Subsequently, Grabowski and Ruipérez^[14] theoretically found the intermediate complexes FH...HCu and FH...HAg upon H₂ cleavage by the two fluorides, MF (M = Cu, Ag). In the context of supramolecular interactions where gold complexes feature prominently,^[15] this lack of fundamental knowledge regarding dihydrogen interactions, constitutes a severe shortcoming. If appropriately addressed and accurately resolved, important further developments could follow. Hence, we embarked on such a study involving Au^I hydrides.

Only a few hydrides of Au^I are known.^[3] From them, we selected as potential *anionic* proton acceptors the dihydride [AuH₂][−] (**1**),^[16] the stable, isolobal, cluster-like [AuAuH][−] (**2**),^[17] and a complex [C₆F₅AuH][−] (**3**), which has not yet been synthesized. Furthermore, we included *neutral* AuH (**4**)^[18] and the simplified compound [(MeNCH=CHNMeC)AuH] (**5**) as model for the known carbene complex [(ArNCH=CHNArC)AuH] (Ar = 2,6-(iPr)₂C₆H₃).^[19] The conventional proton donors in hydrogen bonding, HF, H₂O, H₃N as well as their corresponding protonated analogues were employed. This article focusses primarily on the involvement of HF and H₂F⁺ in dihydrogen bonding with the selected Au^I hydrides, although results obtained with the other proton donors are referred to by way of comparison.

Our results highlight the following: 1) a number of previously unreported 1:1, 1:2 and *n*:1 (*n* ≥ 3) proton acceptor:proton donor interactions realized in isolated systems (full set of structural data for monomers and adducts is provided in Section S1 in the Supporting Information); 2) various competitive and/or 3) stabilizing secondary interactions, and 4) unexpected proton transfers. A major aim of our work was to determine stability trends and bonding preferences between the chosen proton

[a] Prof. I. Cukrowski, J. H. de Lange
Department of Chemistry
Faculty of Natural and Agricultural Sciences
University of Pretoria, Lynnwood Road
Pretoria 0002 (South Africa)
E-mail: ignacy.cukrowski@up.ac.za

[b] F. Groenewald, Prof. H. G. Raubenheimer
Department of Chemistry and Polymer Science
University of Stellenbosch
Private Bag X1, Matieland 7602 (South Africa)
E-mail: hgr@sun.ac.za

Supporting Information and the ORCID identification number(s) for the author(s) of this article can be found under <https://doi.org/10.1002/cphc.201700383>.

donors and acceptors that could ultimately be useful in future experimental investigations and applications.

2. Computational Details

Herein we report results of DFT calculations performed on all the products shown as ball-and-stick representations in Section S2 of the Supporting Information (SI) mainly by using the Gaussian09 rev. D01 program with a “nosymm” keyword, the UB3LYP density functional with Grimme’s D3 empirical dispersion correction, aug-cc-pVDZ basis set and SDD pseudopotential for gold.^[20] Coordinates of optimised structures are provided in Section S3 of the Supporting Information. Unless specified otherwise, all reported structures represent a stationary point on the potential energy surface—no imaginary negative frequencies are present. Bader’s QTAIM^[21] analysis, as implemented in the AIMAll program,^[22] was performed. The ETS-NOCV energy partitioning^[23] was executed in the ADF program,^[24] by performing a single-point calculation on Gaussian-optimized structures using the B3LYP functional, triple- ζ with polarization function basis set without the frozen core approximation (all electrons) and the scalar relativistic zero-order-regular approximation for relativistic effects (for further computational details see Section S4 in the Supporting Information). Taking into account the limitations of both DFT and wavefunction methods with regard to absolute energies and even structural information,^[7b,25] we used these methods here in a comparative sense. The integrity of the results for the smallest adducts was satisfactorily verified at the UCCSD/aug-cc-pVDZ/SDD level and data for $d(\text{H}\cdots\text{H})$ and binding energies, E_{bind} , are given in Table S15 in the Supporting Information. Our approach in dealing with the role of relativistic effects is described in the main text.

3. Results and Discussion

3.1. Adducts with Anionic and Neutral Gold Hydrides

Optimized 1:1 structures for the adducts formed between the chosen Au^{I} hydrides and the HF molecule are shown in Figure 1 together with their bond distances, relevant angles and binding energies.^[14] Strong (ca. 20 kcal mol⁻¹)^[26] dihydrogen bonding occurs between the anionic gold dihydride and HF in (1).HF. The strength of the interaction is reduced by 35% when HF is replaced by H₂O^[27] and again by 45% when NH₃ is substituted for H₂O (Figure S2, Section S5 in the Supporting Information). These changes are percentage-wise much larger than the parallel increases in gas-phase deprotonation energies along the series HF (371 kcal mol⁻¹) to NH₃ (403 kcal mol⁻¹).^[28]

The anionic digold hydride $[\text{AuAuH}]^-$ (2), is isolobal to $[\text{AuH}_2]^-$.^[3] The higher negative net atomic charge ($-0.610e$) calculated for the terminal Au atom, compared to the $-0.222e$ charge on the hydride hydrogen leads to a competitive situation during interaction with HF. The latter hydrogen atom, counter intuitively, was found to be the preferred point of attack and bond formation. Notably, the gold atom does not

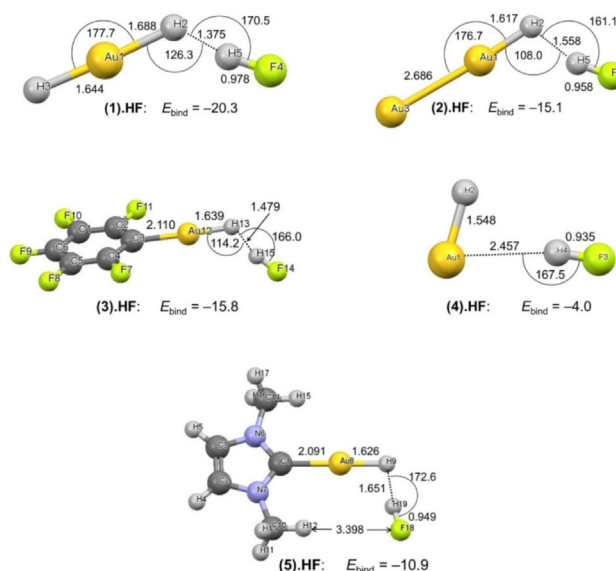


Figure 1. Optimized structures, bond distances (Å), angles (°) and binding energies (kcal mol⁻¹) for HF adducts of gold hydrides (1)–(5).

carry a higher negative charge in free $[\text{AuH}_2]^-$ ($-0.232e$) where the hydride hydrogen ($-0.384e$) is preferred as proton acceptor as expected. The binding energy for (2).HF (-15.1 kcal mol⁻¹; Figure 1) is comparable to the binding energy between the same proton donor and (3) (-15.8 kcal mol⁻¹), despite gold bearing an electron withdrawing C₆F₅ group in (3).HF. Using H₂O as proton donor, the interaction with (3) weakens (-11.1 kcal mol⁻¹), although the association is strengthened by the presence of an additional 2.259 Å interaction between the second proton of H₂O and a fluorine atom of C₆F₅ (for (3).H₂O, see Figure S3, Section S5 in the Supporting Information).

When the hydricity^[29] of the chosen gold complex is decidedly reduced, as in *neutral* AuH, the interaction with HF and other proton donors changes significantly and no stable H \cdots H bonds are formed. Adduct (4).HF in Figure 1 represents the weakly bonded structure at a local energy minimum; in the ensuing more stable product, an F-coordinated HF complex of AuH, HAu(FH), the Au \cdots H bond is abolished.^[14,30] H₂O and NH₃ also form classical Lewis adducts (4).H₂O and (4).NH₃ of increasing stability, in which charge is transferred to AuH during dative bonding (Figure 2; additional data for (4).H₂O and (4).NH₃ are available in the Supporting Information, Section S5, Figures S4–S5).

Installing a well-known electron donating NHC at gold in (4), to afford the model complex (5), is sufficient to effect dihydrogen interaction of modest strength only with HF in (5).HF (Figure 1). In fact, the other classical hydrogen bonding donors H₂O (Figure 2) and NH₃ (for (5).NH₃, see the Supporting Information, Section S5, Figure S6) prefer to weakly interact simultaneously with the central gold atom (Au \cdots H) and a hydrogen atom of the methyl group of the ligand (CH \cdots X, X=N or O).

The H \cdots H bond distances vary between 1.375 Å and 1.651 Å, inversely to the absolute values of the binding energies of the adducts (1)–(3) and (5). (Au)H \cdots H–F angles in all HF adducts are approximately linear (161–173°) which is not always the

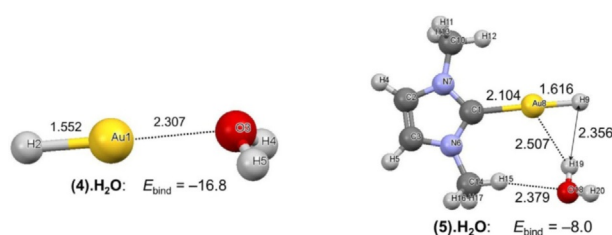


Figure 2. Selected distances (Å) and binding energies (kcal mol^{-1}) for indicated adducts.

case for this class of interactions involving transition metals.^[31] However, angles between 168° and 178° have been indicated as typical for transition metal hydrides involved in dihydrogen bonding when competitive $\text{Au}\cdots\text{H}$ bonding is weak.^[7a] The approximate linear arrangement as well as minimal differences in the $(\text{Au})\text{H}\cdots\text{H}-\text{F}$ angles in the HF adducts optimized with and without D3 empirical dispersion of Grimme, provide evidence that dispersion forces do play a role but are not dominating the $\text{H}\cdots\text{H}$ bonding. For instance, we obtained $\Delta(\text{angles})$ [i.e., (angle with Grimme's D3 dispersion) – (angle without Grimme's D3 dispersion)] of 0.7, 0.2, 0.7, and 1.2° for (1).HF, (2).HF, (3).HF, and (5).HF, respectively. Furthermore, the contribution made by dispersion was estimated as $-1.03 \pm 0.04 \text{ kcal mol}^{-1}$ in adducts (1).HF, (2).HF and (3).HF and $1.28 \text{ kcal mol}^{-1}$ in (5).HF—for details see commented Table S16, Section S5 of the Supporting Information.

3.2. The Role of Relativistic Effects

Relativistic effects are important in gold chemistry.^[32] We have previously shown that such effects strongly influence $\text{Au}\cdots\text{H}$ interactions and, on occasion, even determine the interaction mode.^[4] Following the same strategy as before for AuH_2^- and the adduct (1).HF, calculations were carried out using a scalar-relativistic effective core potential (ECP60MDF) and comparable non-relativistic pseudopotential (ECP60MHF) for gold at UB3LYP and UCCSD levels of theory, respectively (see Supporting Information, Section 6 for details). Although there were differences in the numerical values generated at the two levels of theory, the trends were unambiguously identical. Furthermore, UB3LYP-GD3/SDD and UB3LYP/ECP60MDF gave similar results for energies and bond distances. Non-metal atoms were modelled by the aug-cc-pVDZ basis set. Relativistic effects are responsible for a shortening of all bonds to the gold atom.

During adduct formation between AuH_2^- and HF, the Au-H1 bond is lengthened and Au-H(2) shortened (Figure 2) by the same amount (with and without consideration of relativistic effects). Both these bonds are strengthened by relativistic effects, causing a longer H1 \cdots H3 separation for the dihydrogen bond with ECP60MDF than with the ECP60MHF basis set. Overall, a positive, destabilizing contribution of not more than $1.7 \text{ kcal mol}^{-1}$ to the binding energy of (1).HF can be attributed to relativistic effects. It is therefore not surprising that preliminary calculations also indicated that adduct formation between HF and “non-relativistic” AgH_2^- ^[33] is stronger than with AuH_2^- as proton acceptor. These results also indicate that selected Ag^I hydride complexes could be beneficially included in the experimental search for examples of dihydrogen interactions involving the group 11 metals.

3.3. Energy Partitioning

The ETS-NOCV energy partitioning Scheme revealed (see Section S7 in the Supporting Information) that the bonding energy between monomers, ΔE_{total} , hinges predominantly on electrostatic interactions, ΔE_{elstat} ($-23.4 \text{ kcal mol}^{-1}$), with significant orbital exchange ΔE_{orb} ($-16.4 \text{ kcal mol}^{-1}$). These two contributions overcompensate the repulsion influence, ΔE_{Pauli} ($18.7 \text{ kcal mol}^{-1}$). The ΔE_{total} values of -21.1 and $-11.9 \text{ kcal mol}^{-1}$ for (1).HF and (1).H₂O, respectively, compare well with Gaussian-computed binding energies, E_{bindr} -20.3 and $-13.2 \text{ kcal mol}^{-1}$. It should be mentioned that E_{bind} for (1).HF and (2).HF calculated at the UCCSD level is, respectively smaller and larger than the DFT values (computed with Grimme's D3 empirical dispersion correction in Gaussian) by 1.1 and $0.4 \text{ kcal mol}^{-1}$, Table S15 in The Supporting Information, suggesting again that dispersion indeed contributes minimally to the $\text{H}\cdots\text{H}$ bonding.

3.4. The Role of Charge Transfer

Relative to the isolated monomers, the difference in net atomic charges between covalently bonded atoms A and B increases in most adducts, $\Delta\Delta q(A,B) > 0$; hence, the interatomic regions become polarised increasing the relative role of electrostatic interaction between A and B. It is seen in Table 1 for (1).HF (and for other adducts with (1) in the Supporting Information, Section S8) that the atomic electron population N for the gold atoms decreases the most whereas the fluorine

Table 1. Analysis of QTAIM-defined net atomic charges (q in e) and electron population (N in m_e) in $[\text{AuH}_2^-]$, HF and (1).HF. $\Delta N(A)$ and $\Delta\Delta q(A,B)$, respectively, indicates a change in atomic electron population and, computed relative to isolated monomers, the difference in atomic net charges between indicated atoms.

Atom A	(1) and HF $q(A)$	$ \Delta q(A,B) $	$q(A)$	(1).HF $\Delta N(A)$	$ \Delta q(A,B) $	$\Delta\Delta q(A,B)$
Au1	-0.232	-	-0.159	-73	-	-
H2	-0.384	Au1,H2	-0.380	-4	Au1,H2	0.221
H3	-0.384	Au1,H3	-0.331	-53	Au1,H3	0.172
F4	-0.705	H2,H5	-0.793	88	H2,H5	1.044
H5	0.705	F4,H5	0.663	42	F4,H5	1.457

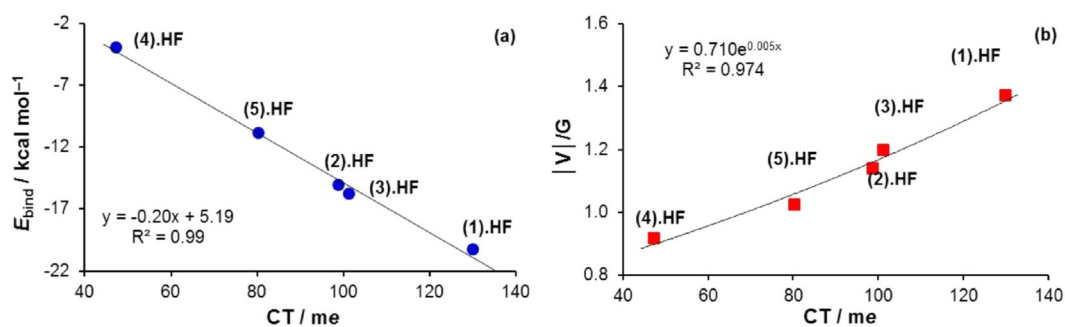


Figure 3. Correlations between: a) binding energy, b) quotient of the local electron potential and kinetic energy densities at the BCP of directly interacting atoms in the 1:1 adducts and the charge transfer (CT) from Au-containing complex to HF.

atoms gain most negative charge in adducts with the H...H bonding. In most adducts the $N(\text{H})$ of HF increases by 26 ± 2 me; however, in (1).HF an increase of over 60% is found. Moreover, for adducts (1)–(3) and (5), the net atomic charge difference $\Delta q(\text{A},\text{B})$ is always largest for atoms of HF and second largest for H atoms involved in dihydrogen bonding. Importantly, significant electronic charge transfers (CTs), essentially from Au atoms, occurred to the HF molecule (e.g., in case of (1).HF, $\text{CT} = \Delta N(\text{F}) + \Delta N(\text{H}) = 0.130e$, Table 1).

Excellent correlations between the CT and 1) binding energy (Figure 3 a) and 2) the ratio of the local electron potential, $V(r)$, over kinetic, $G(r)$, energy density at the bond critical point (BCP) between directly interacting atoms of the complexes (Figure 3 b), are observed for the H...H bonded adducts as well as (4).HF. Based on topological properties at BCPs, the H...H bonding can be interpreted as a closed shell interaction^[34] (ρ_{BCP} of 0.035 ± 0.008 au and small positive values of the Laplacian, $\nabla^2 \rho_{\text{BCP}}$ of 0.054 ± 0.003 au). Some covalent character in the H...H bonding is indicated by $|V(r)|/G(r) > 1$,^[35] the quotient being largest (1.37) for (1).HF and smallest (1.02) for (5).HF which contrasts with a value of only 0.92 obtained for Au...H bonding in (4).HF (Figure 3 b).

3.5. Competing Reactions

Employing the stronger proton donor H_2F^+ in a computationally modelled reaction with $[\text{AuH}_2]^-$, spontaneously gave an H_2 molecule uniquely coordinated to Au^I in (6) (Figure 4), while the remaining gold hydride formed a dihydrogen bond with the released HF unit, but at a significantly longer bond distance (1.821 Å) than in (1).HF (1.375 Å). Besides, with H_3O^+ re-

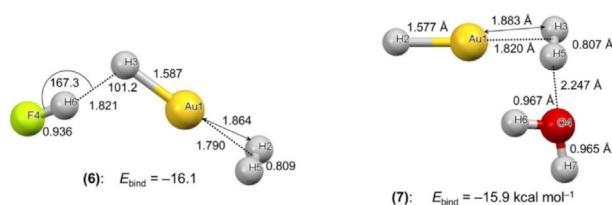


Figure 4. Bond distances (Å), angles (°) and binding energy (kcal mol⁻¹) for products (6) and (7) where E_{bind} for, for example, (6) is $E(\text{6}) - [E(\text{AuH}) + E(\text{HF}) + E(\text{H}_2)]$.

acting as proton donor towards $[\text{AuH}_2]^-$ in a 1:1 ratio, a gold-coordinated H_2 molecule was also formed, (1) + $\text{H}_3\text{O}^+ \rightarrow \text{HAu}(\eta^2\text{-H}_2) + \text{H}_2\text{O}$, but one hydrogen atom of the H_2 molecule remained associated with the oxygen atom of the liberated H_2O molecule at 2.247 Å whereas an H-atom of the H_2O molecule is in plane with the $\text{HAu}(\eta^2\text{-H}_2)$ complex due to H...Au long-distance interaction—see product (7) in Figure 4. Similar features are present in the product formed between $\text{HAu}(\mu^2\text{-H}_2) + \text{NH}_3$ (see product (8) in Figure S7, Section 5 of the SI) that is also spontaneously formed in reaction of (1) with NH_4^+ . The binding energy, E_{bind} , for products (6), (7) and (8) was calculated as $E(\text{HAu}(\eta^2\text{-H}_2)) - [E(\text{AuH}) + E(\text{Z}) + E(\text{H}_2)]$, where $\text{Z} = \text{HF}, \text{H}_2\text{O}, \text{NH}_3$.

Although reactions between (1) and H_2F^+ or H_3O^+ have not yet been studied, the Y-shaped $\text{HAu}(\eta^2\text{-H}_2)$ motif shown in Figure 4 has been reported to be the more stable equilibrium structure.^[36] As mentioned earlier, H_2 activation at coinage metal fluorides, MF ($\text{M} = \text{Cu}, \text{Ag}, \text{Au}$), has been studied by quantum chemistry.^[14] A similar Y-shaped structure to the fragment in Figure 4, with a H–H bond length of 0.955 Å (compared to our 0.809 Å distance) was identified. In the case of the $\text{FAu}(\eta^2\text{-H}_2)$ complex, a significant energy barrier offers resistance against splitting of the dihydrogen bond and formation of a F-donor $\text{HAu}(\text{FH})$ adduct. The results indicate that a weaker side-on bond is formed with the gold hydride than with AuF. Consequently, attachment of a weakly donating or electron withdrawing ligand could be a prerequisite for isolating such a compound in the condensed phase. Convincing evidence for the mechanistic relationship between the protonation of transition metal hydrides and dihydrogen coordination has been reported.^[6c,37]

In view of the formation of adduct (6) by protonation of the gold dihydride anion with H_2F^+ (and a reviewer's suggestion), we also considered various protonations and one oxidative addition by HF as alternative reaction modes for (1), (2) and (4). The selected reactions and relevant reaction energies, ΔE_r , are included in Table 2.

Except for the first reaction, all other conversions are energetically prevented from being considered as viable alternatives with $\Delta E_r > 0$. For the first reaction, the favourable reaction energy is only half the value for (1).HF formation. Furthermore, an energy barrier E^\ddagger of about +34 kcal mol⁻¹ prevents rapid breaking of the strong, existing bonds during the conver-

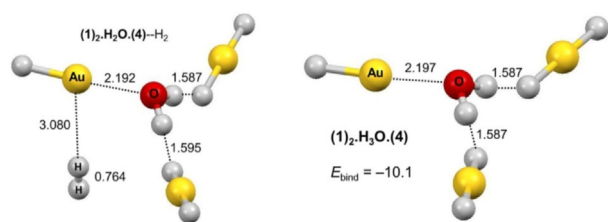


Figure 6. Selected distances (Å) for the $(1)_2\text{H}_2\text{O}(\cdot 4)\text{-H}_2$ and $(1)_2\text{H}_2\text{O}(\cdot 4)$ structures. The binding energy (kcal mol^{-1}) for $(1)_2\text{H}_2\text{O}(\cdot 4)$ is also provided.

mol^{-1} obtained for hydronium ion containing $(1)_3\text{H}_3\text{O}^+$; note also that $d(\text{H,H}) = 1.587 \text{ \AA}$ in $(1)_2\text{H}_2\text{O}(\cdot 4)$ is over 0.22 \AA longer when compared with the same bonds in $(1)_3\text{H}_3\text{O}^+$. Interestingly, the reaction $3\text{AuH}_2^- + \text{H}_3\text{O}^+ \rightarrow (\text{AuH}_2^-)_2\text{H}_2\text{O}\cdot\text{AuH} + \text{H}_2$ is slightly more favourable ($\Delta E_r = -161.6 \text{ kcal mol}^{-1}$) when compared with $E_{\text{bind}} = \Delta E_r = -157.1 \text{ kcal mol}^{-1}$ computed for the formation of $(1)_3\text{H}_3\text{O}^+$. Due to an energy barrier of about $+20 \text{ kcal mol}^{-1}$, however, the direct conversion of $(1)_3\text{H}_3\text{O}^+$ to $(1)_2\text{H}_2\text{O}(\cdot 4) + \text{H}_2$ must be seen as highly unlikely.

4. Conclusions

The use of gold(I) hydrides in dihydrogen bond formation was investigated using quantum chemistry, in various carefully selected systems that involved conventional hydrogen bond donors. These early results obtained for various types of adducts formed, their structures and relative stabilities (all of which are particularly important for reactions in the gas phase) are considered significant and useful. Despite that fact that most reactions carried out in solution are generally considerably complicated as a result of classical hydrogen bonding and van der Waals interaction, some of the unique products reported in this study could correspond to key intermediates or transition states during proton transfers, or serve as building blocks (synthons) for crystallization. Most importantly, dihydrogen interaction between *anionic* Au^{I} hydrides and well-chosen proton donors present in different ratios in isolated systems was found strong enough to warrant further experimental exploration in the gas and solid phases. Whether such is the case with hydrides of neighbouring Ag^{I} and Hg^{I} , should be investigated further using quantum mechanics. Finally, under ideal experimental conditions, and fostered by a weakly donating or, preferably, electron attracting ligand, the deliberate preparation of side-on dihydrogen complexes of Au^{I} could be realized in the condensed phase.

Acknowledgements

The work reported here was financially supported (IC and JHL) in part by the National Research Foundation of South Africa (Grant Number 105855).

Conflict of interest

The authors declare no conflict of interest.

Keywords: dihydrogen bonds · Eigen complex analogues · gold hydrides · quantum chemical calculations · σ -dihydrogen gold complexes

- [1] H. Schmidbaur, A. Schier, *Chem. Soc. Rev.* **2012**, *41*, 370–412.
- [2] P. Pyykkö, *Chem. Soc. Rev.* **2008**, *37*, 1967–1997.
- [3] H. Schmidbaur, H. G. Raubenheimer, L. Dobrzańska, *Chem. Soc. Rev.* **2014**, *43*, 345–380.
- [4] F. Groenewald, J. Dillen, H. G. Raubenheimer, C. Esterhuysen, *Angew. Chem. Int. Ed.* **2016**, *55*, 1694–1698; *Angew. Chem.* **2016**, *128*, 1726–1730.
- [5] D. Milstein, J. C. Calabrese, I. D. Williams, *J. Am. Chem. Soc.* **1986**, *108*, 6387–6389.
- [6] See for example: a) R. H. Crabtree, P. E. M. Sigbaum, O. Eisenstein, A. L. Rheingold, T. F. Koetzle, *Acc. Chem. Res.* **2001**, *101*, 1963–1980; b) R. Custelcean, J. E. Jackson, *Chem. Rev.* **2001**, *101*, 1963–1980; c) N. V. Belkova, E. S. Shubina, L. M. Epstein, *Acc. Chem. Res.* **2005**, *38*, 624–631; d) M. J. Calhorda in *Hydrogen Bonding—New insights* (Ed. S. Grabowski), Springer, Berlin, **2006**, pp. 245–262.
- [7] a) O. A. Filippov, N. V. Belkova, L. Epstein, A. Lledes, E. S. Shubina, *ChemPhysChem* **2012**, *13*, 2677–2687; b) E. Fabiano, L. A. Constantin, F. D. Sala, *J. Chem. Theory Comput.* **2014**, *10*, 3151–3162.
- [8] a) A. G. Algarra, M. G. Basallote, M. Feliz, M. J. Fernández-Triayillo, R. Llusar, V. Safront, *Chem. Eur. J.* **2010**, *16*, 1613–1623; b) T. E. Golub, O. A. Filippov, E. I. Gutsul, N. V. Belkova, L. M. Epstein, A. Rossin, M. Peruzzini, E. S. Shubina, *Inorg. Chem.* **2012**, *51*, 6486–6497; c) K. S. Sandhya, C. H. Suresh, *Dalton Trans.* **2012**, *41*, 11018–11025.
- [9] G. A. Silantyev, O. A. Filippov, P. M. Tolstoy, N. V. Belkova, L. M. Epstein, K. Weisz, E. M. Shubina, *Inorg. Chem.* **2013**, *52*, 1787–1797.
- [10] M. Owczarek, I. Majez, R. Jakubas, *CrystEngComm* **2014**, *16*, 7638–7648.
- [11] a) T. Liu, X. Wang, C. Hoffmann, D. L. Du Bois, R. M. Bullock, *Angew. Chem. Int. Ed.* **2014**, *53*, 5300–5304; *Angew. Chem.* **2014**, *126*, 5404–5408; b) T. B. Rauchfuss, *Acc. Chem. Res.* **2015**, *48*, 2107–2116.
- [12] V. I. Bakhmutov, *Dihydrogen Bonds—Principles, Experiments and Applications*, Wiley-Interscience, Hoboken, **2008**.
- [13] A. Comas-Vives, G. Ujaque, *J. Am. Chem. Soc.* **2013**, *135*, 1295–1305.
- [14] S. J. Grabowski, F. Ruipérez, *Phys. Chem. Chem. Phys.* **2016**, *18*, 12810–12818.
- [15] M. J. Katz, K. Sakai, D. B. Leznoff, *Chem. Soc. Rev.* **2008**, *37*, 1884–1895.
- [16] H.-T. Liu, Y.-L. Wang, X.-G. Xiong, P. D. Dau, Z. A. Piazza, D.-L. Huang, C.-Q. Xu, J. Li, L.-S. Wang, *Chem. Sci.* **2012**, *3*, 3286–3295.
- [17] X. Wang, L. Andrews, *J. Phys. Chem. A* **2003**, *107*, 8492–8505.
- [18] P. Schwerdtfeger, M. Dolg, W. H. E. Schwarz, *J. Chem. Phys.* **1989**, *91*, 1762–1774.
- [19] E. Y. Tsui, P. Müller, J. P. Sadighi, *Angew. Chem. Int. Ed.* **2008**, *47*, 8937–8940; *Angew. Chem.* **2008**, *120*, 9069–9072.
- [20] M. J. Frisch, G. W. Trucks, H. B. Schlegel, G. E. Scuseria, M. A. Robb, J. R. Cheeseman, G. Scalmani, V. Barone, B. Mennucci, G. A. Petersson, H. Nakatsuji, M. Caricato, X. Li, H. P. Hratchian, A. F. Izmaylov, J. Bloino, G. Zheng, J. L. Sonnenberg, M. Hada, M. Ehara, K. Toyota, R. Fukuda, J. Hasegawa, M. Ishida, T. Nakajima, Y. Honda, O. Kitao, H. Nakai, T. Vreven, J. A. Montgomery, Jr., J. E. Peralta, F. Ogliaro, M. Bearpark, J. J. Heyd, E. Brothers, K. N. Kudin, V. N. Staroverov, T. Keith, R. Kobayashi, J. Normand, K. Raghavachari, A. Rendell, J. C. Burant, S. S. Iyengar, J. Tomasi, M. Cossi, N. Rega, J. M. Millam, M. Klene, J. E. Knox, J. B. Cross, V. Bakken, C. Adamo, J. Jaramillo, R. Gomperts, R. E. Stratmann, O. Yazyev, A. J. Austin, R. Cammi, C. Pomelli, J. W. Ochterski, R. L. Martin, K. Morokuma, V. G. Zakrzewski, G. A. Voth, P. Salvador, J. J. Dannenberg, S. Dapprich, A. D. Daniels, O. Farkas, J. B. Foresman, J. V. Ortiz, J. Cioslowski, and D. J. Fox, Gaussian 09, revision D.01, Gaussian, Inc., Wallingford CT, 2013.
- [21] R. F. W. Bader, *Atoms in Molecules: A Quantum Theory*, Oxford University Press, Oxford, **1990**.
- [22] A. Keith, AIMAll (Version 14.06.21), TK Gristmill Software, Overland Parks KS, USA, 2014 (<http://www.aim.tkgristmill.com>).
- [23] a) M. Mitoraj, A. Michalak, *J. Mol. Model.* **2007**, *13*, 347–355; b) M. Mitoraj, A. Michalak, T. Ziegler, *J. Chem. Theory Comput.* **2009**, *5*, 962–975.
- [24] E. J. Baerends, T. Ziegler, J. Autschbach, D. Bashford, A. Bérces, F. M. Bickelhaupt, C. Bo, P. M. Boerrigter, L. Cavallo, D. P. Chong, L. Deng,

- R. M. Dickson, D. E. Ellis, M. van Faassen, L. Fan, T. H. Fischer, C. Fonseca Guerra, M. Franchini, A. Ghysels, A. Giammona, S. J. A. van Gisbergen, A. W. Götz, J. A. Groeneveld, O. V. Gritsenko, M. Grüning, S. Gusarov, F. E. Harris, P. van den Hoek, C. R. Jacob, H. Jacobsen, L. Jensen, J. W. Kaminiski, G. van Kessel, F. Kootstra, A. Kovalenko, M. V. Krykunov, E. van Lenthe, D. A. McCormack, A. Michalak, M. Mitoraj, S. M. Morton, J. Neugebauer, V. P. Nicu, L. Noodleman, V. P. Osinga, S. Patchkovskii, M. Pavanello, P. H. T. Philipsen, D. Post, C. C. Pye, W. Ravenek, J. I. Rodríguez, P. Ros, P. R. T. Schipper, H. van Schoot, G. Schreckenbach, J. S. Seldenthuis, M. Seth, J. G. Snijders, M. Solà, M. Swart, D. Swerhone, G. te Velde, P. Vernooijs, L. Versluis, L. Visscher, O. Visser, F. Wang, T. A. Wesolowski, E. M. van Wezenbeek, G. Wiesenekker, S. K. Wolff, T. K. Woo, A. L. Yakovlev, ADF2014.01 SCM, Theoretical Chemistry, Vrije Universiteit, Amsterdam, The Netherlands, 2014, <http://www.scm.com>.
- [25] a) R. F. W. Bader, *Found. Chem.* **2011**, *13*, 11–37; b) G. Frenking, G. F. Caramori, *Angew. Chem. Int. Ed.* **2015**, *54*, 2596–2599; *Angew. Chem.* **2015**, *127*, 2632–2635; c) F. Weinhold, R. A. Klein, *Angew. Chem. Int. Ed.* **2015**, *54*, 2600–2602; *Angew. Chem.* **2015**, *127*, 2636–2638.
- [26] T. Steiner, *Angew. Chem. Int. Ed.* **2002**, *41*, 48–76; *Angew. Chem.* **2002**, *114*, 50–80.
- [27] Compare Ref. [4] for a similar result obtained by using another basis set.
- [28] J. E. Huheey, E. A. Keiter, R. L. Keiter, *Inorganic Chemistry: Principles Structure and Reactivity*, Harper Collins College Publishers, New York, **1993**, p. 332.
- [29] H. Jacobsen, H. Berke in *Recent Advances in Hydride Chemistry* (Eds.: M. Peruzzini, R. Poli) Elsevier, Amsterdam, **2001**, pp. 89–116.
- [30] P. M. Minaev, T. N. Gribanova, *J. Inorg. Chem. (in Russian)* **2001**, *46*, 1521–1530.
- [31] T. B. Richardson, S. de Gala, R. H. Crabtree, P. E. M. Siegbahn, *J. Am. Chem. Soc.* **1995**, *117*, 12875–12876.
- [32] a) P. Pyykkö, *Angew. Chem. Int. Ed.* **2004**, *43*, 4412–4456; *Angew. Chem.* **2004**, *116*, 4512–4557;; b) P. Schwerdtfeger, M. Lein in *Gold Chemistry: Applications and Future Directions in the Life Sciences* (Ed.: F. Mohr), Wiley-VCH, Weinheim, **2009**, pp. 183–247; c) P. Schwerdtfeger, P. D. W. Boyd, A. K. Burrell, W. T. Robinson, M. J. Taylor, *Inorg. Chem.* **1990**, *29*, 3593–3607.
- [33] P. Pyykkö, J.-P. Desclaux, *Acc. Chem. Res.* **1979**, *12*, 276–281.
- [34] E. Espinosa, I. Alkorta, J. Elguero, E. Molins, *J. Chem. Phys.* **2002**, *117*, 5529–5542.
- [35] S. Jenkins, I. Morrison, *Chem. Phys. Lett.* **2000**, *317*, 97–102.
- [36] a) C. A. Bayse, *J. Phys. Chem. A* **2001**, *105*, 5902–5905; b) L. Andrews, *Chem. Soc. Rev.* **2004**, *33*, 123–132.
- [37] M. Besora, A. Lledos, F. Maseras, *Chem. Soc. Rev.* **2009**, *38*, 957–966.
- [38] a) M. Eigen, *Angew. Chem. Int. Ed. Engl.* **1964**, *3*, 1–19; *Angew. Chem.* **1963**, *75*, 489–508; b) R. Parthasarathi, V. Subramanian, N. Sathyamurthy, *J. Phys. Chem. A* **2007**, *111*, 13287–13290.
- [39] a) G. Zundel, *Z. Phys. Chem. (Muenchen Ger.)* **1968**, *58*, 225–245; b) G. Zundel, *Adv. Chem. Phys.* **2000**, *111*, 1–217.

Manuscript received: April 11, 2017

Revised manuscript received: May 19, 2017

Accepted manuscript online: May 25, 2017

Version of record online: July 6, 2017